# HAIR BUNDLES - DEVELOPMENT, MAINTENANCE, AND FUNCTION

EDITED BY: Zhigang Xu, Anthony Wei Peng and Wei Xiong
PUBLISHED IN: Frontiers in Cell and Developmental Biology

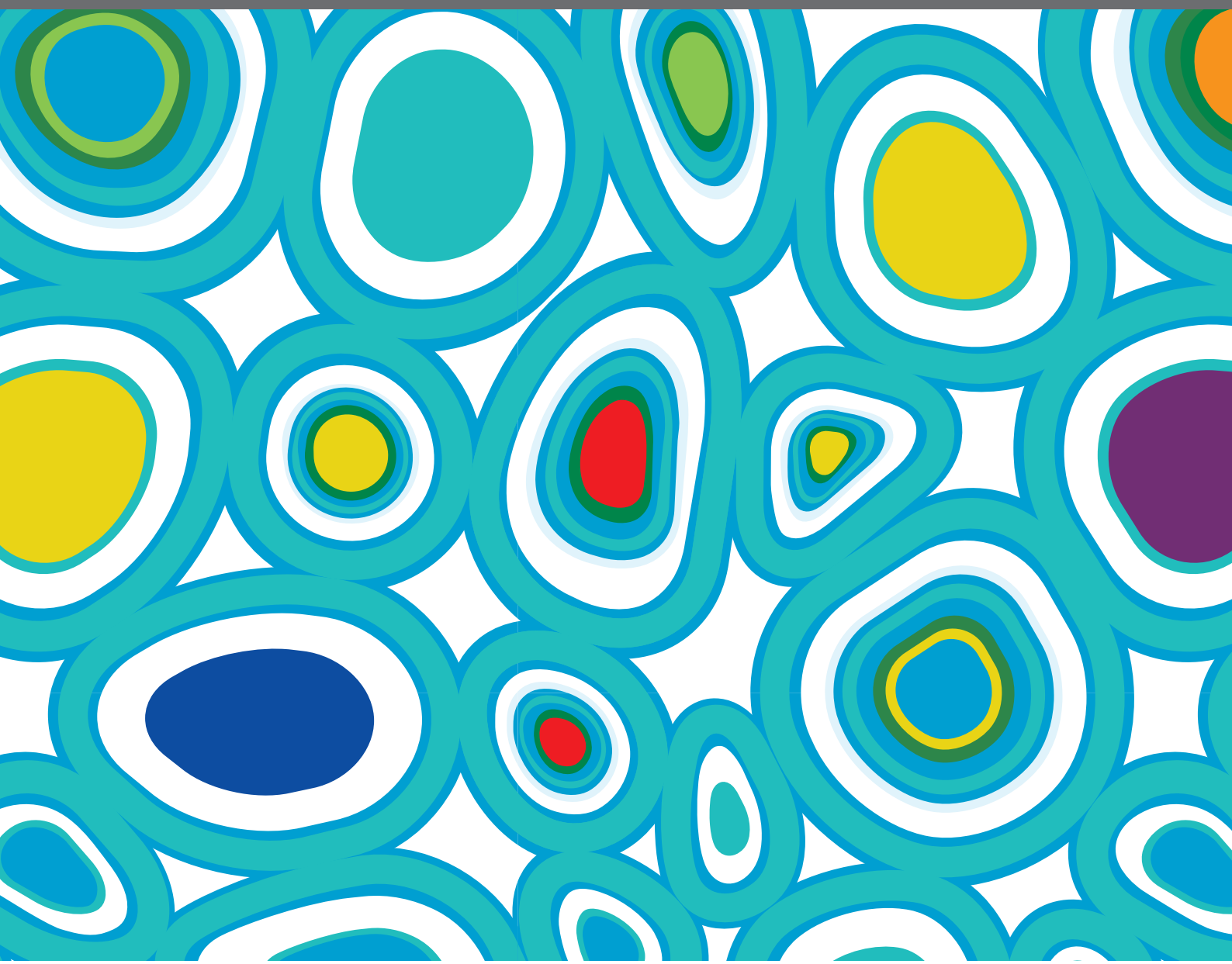

frontiers Research Topics

**Frontiers eBook Copyright Statement**

The copyright in the text of individual articles in this eBook is the property of their respective authors or their respective institutions or funders. The copyright in graphics and images within each article may be subject to copyright of other parties. In both cases this is subject to a license granted to Frontiers.

The compilation of articles constituting this eBook is the property of Frontiers.

Each article within this eBook, and the eBook itself, are published under the most recent version of the Creative Commons CC-BY licence. The version current at the date of publication of this eBook is CC-BY 4.0. If the CC-BY licence is updated, the licence granted by Frontiers is automatically updated to the new version.

When exercising any right under the CC-BY licence, Frontiers must be attributed as the original publisher of the article or eBook, as applicable.

Authors have the responsibility of ensuring that any graphics or other materials which are the property of others may be included in the CC-BY licence, but this should be checked before relying on the CC-BY licence to reproduce those materials. Any copyright notices relating to those materials must be complied with.

Copyright and source acknowledgement notices may not be removed and must be displayed in any copy, derivative work or partial copy which includes the elements in question.

All copyright, and all rights therein, are protected by national and international copyright laws. The above represents a summary only. For further information please read Frontiers' Conditions for Website Use and Copyright Statement, and the applicable CC-BY licence.

ISSN 1664-8714
ISBN 978-2-88971-968-6
DOI 10.3389/978-2-88971-968-6

## About Frontiers

Frontiers is more than just an open-access publisher of scholarly articles: it is a pioneering approach to the world of academia, radically improving the way scholarly research is managed. The grand vision of Frontiers is a world where all people have an equal opportunity to seek, share and generate knowledge. Frontiers provides immediate and permanent online open access to all its publications, but this alone is not enough to realize our grand goals.

## Frontiers Journal Series

The Frontiers Journal Series is a multi-tier and interdisciplinary set of open-access, online journals, promising a paradigm shift from the current review, selection and dissemination processes in academic publishing. All Frontiers journals are driven by researchers for researchers; therefore, they constitute a service to the scholarly community. At the same time, the Frontiers Journal Series operates on a revolutionary invention, the tiered publishing system, initially addressing specific communities of scholars, and gradually climbing up to broader public understanding, thus serving the interests of the lay society, too.

## Dedication to Quality

Each Frontiers article is a landmark of the highest quality, thanks to genuinely collaborative interactions between authors and review editors, who include some of the world's best academicians. Research must be certified by peers before entering a stream of knowledge that may eventually reach the public - and shape society; therefore, Frontiers only applies the most rigorous and unbiased reviews.
Frontiers revolutionizes research publishing by freely delivering the most outstanding research, evaluated with no bias from both the academic and social point of view. By applying the most advanced information technologies, Frontiers is catapulting scholarly publishing into a new generation.

## What are Frontiers Research Topics?

Frontiers Research Topics are very popular trademarks of the Frontiers Journals Series: they are collections of at least ten articles, all centered on a particular subject. With their unique mix of varied contributions from Original Research to Review Articles, Frontiers Research Topics unify the most influential researchers, the latest key findings and historical advances in a hot research area! Find out more on how to host your own Frontiers Research Topic or contribute to one as an author by contacting the Frontiers Editorial Office: frontiersin.org/about/contact

# HAIR BUNDLES - DEVELOPMENT, MAINTENANCE, AND FUNCTION

Topic Editors:
**Zhigang Xu,** Shandong University, China
**Anthony Wei Peng,** University of Colorado Anschutz Medical Campus, United States
**Wei Xiong,** Tsinghua University, China

**Citation:** Xu, Z., Peng, A. W., Xiong, W., eds. (2021).
Hair Bundles - Development, Maintenance, And Function.
Lausanne: Frontiers Media SA. doi: 10.3389/978-2-88971-968-6

# Table of Contents

frontiers in Cell and Developmental Biology

EDITORIAL
published: 15 November 2021
doi: 10.3389/fcell.2021.800410

# Editorial: Hair Bundles—Development, Maintenance, and Function

*Zhigang Xu*[1]*, *Anthony W. Peng*[2] *and Wei Xiong*[3]

[1]Shandong Provincial Key Laboratory of Animal Cell and Developmental Biology, School of Life Sciences, Shandong University, Qingdao, China, [2]Department of Physiology and Biophysics, University of Colorado Anschutz Medical Campus, Aurora, CO, United States, [3]School of Life Sciences, IDG/McGovern Institute for Brain Research at Tsinghua, Tsinghua University, Beijing, China

**Keywords: hair cells, hair bundles, stereocilia, kinocilium, mechano-electrical transduction**

## Editorial on the Research Topic

## Hair Bundles—Development, Maintenance, and Function

Hair bundles are hairy-looking cell protrusions at the apical surface of mechanosensitive hair cells, consisting of hundreds of actin-based stereocilia and one microtubule-based kinocilium in each cell (Flock and Cheung, 1977). The kinocilium is important for hair bundle development as well as planar cell polarity (PCP) establishment, while the stereocilia are indispensable for mechano-electrical transduction (MET) (Hudspeth and Jacobs, 1979; Jones et al., 2008). The tightly-regulated process of hair bundle development started to be appreciated after Lew Tilney's seminal work (Tilney et al., 1992). With the rapid progress of genetic, proteomic, and microscopic techniques, many proteins have been identified to play important roles in the development, maintenance, and/or function of hair bundles (Barr-Gillespie, 2015; McGrath et al., 2017; Velez-Ortega and Frolenkov, 2019). Nevertheless, a lot more remain unknown about this fantastic subcellular structure responsible for sound and balance detection.

In the present Research Topic, Landin Malt et al. show that non-canonical Wnt signaling regulates cochlear outgrowth and PCP through Gsk3β inhibition. Zhang et al. investigate the role of RNA-binding protein RBM24 in hair cell development, and show that Rbm24a deficiency in zebrafish affects development of hair cells as well as stereocilia through regulating the stability of its downstream target mRNAs. Li et al. show that GRXCR2 interacts with CLIC5 at the base of stereocilia and plays an essential role in stereocilia development. Kannan-Sundhari et al. reveal that bromodomain protein BRD4 is essential for stereocilia development as well as hair cell function, and Liu et al. show that lysyl oxidase LOXL3 inactivation leads to hair cell deficits including stereocilia disorganization. Wang and Zhou review the role of kinocilia in the development of hair cells and related diseases, while Cirilo et al. review the functional role of class III myosins in the stereocilia. Together, these works help us to learn more about the underlying mechanism of hair bundle development and maintenance.

The mechanic stimuli such as sound deflect hair bundles, then open the MET channels localized at the tips of shorter row stereocilia, resulting in influx of cations into the hair cells (Hudspeth and Jacobs, 1979; Beurg et al., 2009). Peng et al. show that hair bundles stimulated with a fluid jet exhibit spatial non-uniformities and two viscoelastic-like mechanisms, which are important for us to understand the mechanics of the mammalian hair bundles. TMC1/TMC2 have been suggested to be the pore-forming components of MET channels (Pan et al., 2018; Jia et al., 2020). In the zebrafish, there are one Tmc1 and two Tmc2 orthologs, and Zhu et al. show that Tmc reliance is biased by the hair cell subtype and position in the zebrafish inner ear. These works shed light on the mechanism of how stereocilia respond to mechanical stimuli and result in MET.

Our understanding of the hair bundles cannot improve without technical advances. Electron microscopy (EM) has been extensively used to understand the development, maintenance, and

OPEN ACCESS

***Edited and reviewed by:***
*Philipp Kaldis,*
*Lund University, Sweden*

***Correspondence:**
*Zhigang Xu*
*xuzg@sdu.edu.cn*

***Specialty section:***
*This article was submitted to Cell Growth and Division, a section of the journal Frontiers in Cell and Developmental Biology*

***Received:*** *23 October 2021*
***Accepted:*** *28 October 2021*
***Published:*** *15 November 2021*

***Citation:***
*Xu Z, Peng AW and Xiong W (2021) Editorial: Hair Bundles—Development, Maintenance, and Function. Front. Cell Dev. Biol. 9:800410. doi: 10.3389/fcell.2021.800410*

function of hair bundles. Ivanchenko et al. systematically summarize different EM techniques commonly used in studying hair bundles such as scanning electron microscopy (SEM), transmission electron microscopy (TEM), and focused-ion-beam scanning electron microscopy (FIB-SEM), and provide detailed protocols for sample preparation, treatment, and imaging. Miller et al. compare stereocilia measurements from living tissue, tissue mildly-fixed for fluorescent imaging, or tissue strongly-fixed for SEM, and illustrate the requirement of high accuracy to understand hair bundle mechanotransduction. Lin et al. turn to structural biology and reveal that the harmonin homology domain (HHD) of PDZD7 binds lipid and mediates the localization of PDZD7 to the plasma membrane, therefore provide mechanistic explanations for human deafness-associated mutations in PDZD7.

In the present Research Topic, researchers also show some other interesting findings. Li et al. show that albeit specially expressed in the inner ear hair cells and localized at the tips of stereocilia, annexin A4 (ANXA4) is dispensable for development and function of stereocilia and hair cells. Moreover, Gilbert et al. show that actin crosslinking family protein 7 (ACF7) is localized to the cuticular plate and the circumferential band in hair cells, but its inactivation does not have a significant effect on the hair bundle or hair cells. These studies suggest that not all hair cell-specific or hair bundle-enriched proteins are essential for hair cells to develop or function. Nevertheless, possibilities remain that these proteins are required for hair cell processes that were not examined in these studies.

In summary, this Research Topic presents some recent advances in the development, maintenance, and function of hair bundles. However, despite the rapid progress in this field, there is much more to learn. For example, how are the heights of stereocilia in different rows precisely controlled? How are the stereocilia row numbers determined? How is the MET machinery organized and regulated? We hope that we can have answers for these questions in the near future.

## AUTHOR CONTRIBUTIONS

All authors listed have made a substantial, direct and intellectual contribution to the work, and approved it for publication.

## ACKNOWLEDGMENTS

We thank all the contributing authors and reviewers for their support in this Research Topic.

## REFERENCES

Barr-Gillespie, P.-G. (2015). Assembly of Hair Bundles, an Amazing Problem for Cell Biology. *MBoC* 26 (15), 2727–2732. doi:10.1091/mbc.E14-04-0940

Beurg, M., Fettiplace, R., Nam, J.-H., and Ricci, A. J. (2009). Localization of Inner Hair Cell Mechanotransducer Channels Using High-Speed Calcium Imaging. *Nat. Neurosci.* 12 (5), 553–558. doi:10.1038/nn.2295

Flock, A., and Cheung, H. C. (1977). Actin Filaments in Sensory Hairs of Inner Ear Receptor Cells. *J. Cel Biol* 75 (2 Pt 1), 339–343. doi:10.1083/jcb.75.2.339

Hudspeth, A. J., and Jacobs, R. (1979). Stereocilia Mediate Transduction in Vertebrate Hair Cells (Auditory System/cilium/vestibular System). *Proc. Natl. Acad. Sci.* 76 (3), 1506–1509. doi:10.1073/pnas.76.3.1506

Jia, Y., Zhao, Y., Kusakizako, T., Wang, Y., Pan, C., Zhang, Y., et al. (2020). TMC1 and TMC2 Proteins Are Pore-Forming Subunits of Mechanosensitive Ion Channels. *Neuron* 105 (2), 310–321. doi:10.1016/j.neuron.2019.10.017

Jones, C., Roper, V. C., Foucher, I., Qian, D., Banizs, B., Petit, C., et al. (2008). Ciliary Proteins Link Basal Body Polarization to Planar Cell Polarity Regulation. *Nat. Genet.* 40 (1), 69–77. doi:10.1038/ng.2007.54

McGrath, J., Roy, P., and Perrin, B. J. (2017). Stereocilia Morphogenesis and Maintenance through Regulation of Actin Stability. *Semin. Cel Dev. Biol.* 65, 88–95. doi:10.1016/j.semcdb.2016.08.017

Pan, B., Akyuz, N., Liu, X.-P., Asai, Y., Nist-Lund, C., Kurima, K., et al. (2018). TMC1 Forms the Pore of Mechanosensory Transduction Channels in Vertebrate Inner Ear Hair Cells. *Neuron* 99 (4), 736–753. doi:10.1016/j.neuron.2018.07.033

Tilney, L. G., Tilney, M. S., and DeRosier, D. J. (1992). Actin Filaments, Stereocilia, and Hair Cells: How Cells Count and Measure. *Annu. Rev. Cel. Biol.* 8, 257–274. doi:10.1146/annurev.cb.08.110192.001353

Vélez-Ortega, A. C., and Frolenkov, G. I. (2019). Building and Repairing the Stereocilia Cytoskeleton in Mammalian Auditory Hair Cells. *Hearing Res.* 376, 47–57. doi:10.1016/j.heares.2018.12.012

**Conflict of Interest:** The authors declare that the research was conducted in the absence of any commercial or financial relationships that could be construed as a potential conflict of interest.

**Publisher's Note:** All claims expressed in this article are solely those of the authors and do not necessarily represent those of their affiliated organizations, or those of the publisher, the editors and the reviewers. Any product that may be evaluated in this article, or claim that may be made by its manufacturer, is not guaranteed or endorsed by the publisher.

*Copyright © 2021 Xu, Peng and Xiong. This is an open-access article distributed under the terms of the Creative Commons Attribution License (CC BY). The use, distribution or reproduction in other forums is permitted, provided the original author(s) and the copyright owner(s) are credited and that the original publication in this journal is cited, in accordance with accepted academic practice. No use, distribution or reproduction is permitted which does not comply with these terms.*

frontiers in Cell and Developmental Biology

ORIGINAL RESEARCH
published: 08 September 2020
doi: 10.3389/fcell.2020.576654

# Bromodomain Protein BRD4 Is Essential for Hair Cell Function and Survival

*Abhiraami Kannan-Sundhari[1,2], Clemer Abad[3], Marie E. Maloof[4], Nagi G. Ayad[4], Juan I. Young[2,3], Xue Zhong Liu[1,2,3]* and Katherina Walz[2,3]**

[1] Department of Otolaryngology, Miller School of Medicine, University of Miami, Miami, FL, United States, [2] The Dr. John T. Macdonald Foundation Department of Human Genetics, University of Miami, Miami, FL, United States, [3] John P. Hussman Institute for Human Genomics, University of Miami, Miami, FL, United States, [4] The Miami Project to Cure Paralysis, Department of Neurological Surgery, Miller School of Medicine, University of Miami, Miami, FL, United States

Hair cells (HCs) play crucial roles in perceiving sound, acceleration, and fluid motion. The tonotopic architecture of the sensory epithelium recognizes mechanical stimuli and convert them into electrical signals. The expression and regulation of the genes in the inner ear is very important to keep the sensory organ functional. Our study is the first to investigate the role of the epigenetic reader *Brd4* in the mouse inner ear. We demonstrate that HC specific deletion of *Brd4 in vivo* in the mouse inner ear is sufficient to cause profound hearing loss (HL), degeneration of stereocilia, nerve fibers and HC loss postnatally in mouse; suggesting an important role in hearing function and maintenance.

**Keywords: Brd4, hearing loss, hair cell loss, hair cells, function, survival**

OPEN ACCESS

***Edited by:***
*Wei Xiong,*
*Tsinghua University, China*

***Reviewed by:***
*Bo Zhao,*
*Indiana University, United States*
*Jiangang Gao,*
*Shandong University, China*

****Correspondence:***
*Xue Zhong Liu*
*x.liu1@med.miami.edu*
*Katherina Walz*
*KWalz@med.miami.edu*

***Specialty section:***
*This article was submitted to Cell Growth and Division, a section of the journal Frontiers in Cell and Developmental Biology*

***Received:*** *26 June 2020*
***Accepted:*** *18 August 2020*
***Published:*** *08 September 2020*

***Citation:***
*Kannan-Sundhari A, Abad C, Maloof ME, Ayad NG, Young JI, Liu XZ and Walz K (2020) Bromodomain Protein BRD4 Is Essential for Hair Cell Function and Survival. Front. Cell Dev. Biol. 8:576654. doi: 10.3389/fcell.2020.576654*

## INTRODUCTION

The inner ear is a complex sensory organ that is involved in hearing and vestibular balance. The complex mechanical-electrical transduction process that takes place in the inner ear is not completely understood (Tekin et al., 2001). The cochlea comprises the organ of Corti, that contains specialized mechanosensory HCs that recognize mechanical stimuli and convert them into electrical signals. The expression and tight regulation of the genes in the inner ear is very important to keep the sensory organ functional, playing a major role in the development, differentiation and morphogenesis (Wu and Kelley, 2012). Epigenetic mechanisms have been implicated various developmental disorders (Ong and Corces, 2014). Although research on epigenetic pathways in the inner ear is very limited, a few studies have shown that it plays a crucial role in hair cell (HC) development, maintenance, function, survival and regeneration (Doetzlhofer and Avraham, 2017). Hearing loss (HL) is a common sensorineural disorder in humans. Approximately 70% of HL is congenital with an incidence of ∼1 in 500 in newborns in industrialized nations. Despite the number of genes that have been associated with HL, many cases remain unexplained. HL has been associated with genes that are involved in DNA methylation, histone modification and chromatin remodeling (Layman et al., 2015). BRD4 is a chromatin-binding protein that belongs to the family of bromodomain and extra terminal proteins (BET) that recognize and bind acetylated histones to facilitate gene transcription. It is amongst the most studied of the BET reader proteins. The domains of mammalian BET proteins are highly conserved, including mice (Wu and Chiang, 2007). Most of the current research on *BRD4* focuses its role in several cancers (Sanchez and Zhou, 2009; Wang and Filippakopoulos, 2015; Taniguchi, 2016). The importance of BET protein BRD4 has been

investigated and characterized in the developmental processes of different cell types (Lee et al., 2017; Penas et al., 2019). *BRD4* has been associated with HL in previous studies (de Souza et al., 2018; Olley et al., 2018), despite which, its role in HC development has not yet been studied. In this study, we provide evidence that *Brd4* is necessary for the function and maintenance of the inner ear by studying a HC specific knock-out mouse model.

## MATERIALS AND METHODS

### RNA Isolation

*Brd4*$^{+/+}$ and *Atoh1-Brd4*$^{-/-}$ cochlear sensory epithelium were isolated and immediately transferred to 250 μL TriZol (Invitrogen). These samples were subject to ultrasonic homogenization for complete dissociation and lysis. 200 μL chloroform was added to the lysate-TriZol mixture and mixed gently incubated at room temperature (RT) for 5 min and centrifuged at maximum speed for 20 min at 4°C. Clear supernatant (the aqueous layer) was transferred to fresh tubes and equal volume of 70% ethanol was added and mixed well. This mixture was transferred to spin columns from the RNeasy mini kit (Qiagen) and processed according to the manufacturer's instructions (catalog #74104). RNA yield was quantified with a nanodrop spectrophotometer (ND-1000, Thermo Fisher).

### cDNA Synthesis and Real Time PCR (RT-PCR)

RNA was reverse transcribed into cDNA using qScript$^{TM}$ XLT cDNA SuperMix, cDNA Reverse Transcription Kit (QuantaBio #95161-500). Adjusted volumes of RNA with a final concentration of 500 ng/μL was added into each reaction. RT-PCR was performed relative to *mGapdh* as control. Primers for the reaction was designed using Primer3[1]. *In silico* PCR was performed using the UCSC genome browser[2] to confirm their specificity, amplicon size and detection of any primer dimers. RT-PCR Primers: Ex 5-6F: ATGGCAGAAGCTCTGGAGAA, Ex 5-6R: TTGGTACCGTGGATACACCA, mGapdh-F: ACCCA GAAGACTGTGGATGG, mGapdh-R: CACATTGGGGGTAGG AACAC.

### Cochlear Extraction and Sectioning

P0 mouse cochleae were dissected in 4°C 1× PBS and fixed overnight at 4°C in PBS containing 4% paraformaldehyde. 45 μm sections were obtained using a vibrotome (Leica VT 1200S).

### Generation and Genotyping of *Brd4* Conditional Knock Out Mice

Brd4$^{tm1a}$(EUCOMM)Wtsi (MGI ID: 4441798) heterozygous mice were obtained through the Knockout Mouse Project Repository (KOMP) at Baylor University from Dr. John Seavitt. These mice were bred to B6.Cg-Tg(ACTFLPe)9205Dym/J (The Jackson Laboratory Stock #005703) mice to remove the neomycin cassette and LacZ reporter gene to generate *Brd4*$^{tm1c}$ heterozygous mice. The *Brd4*$^{tm1c}$ mice (hereafter referred to as *Brd4*$^{fl/fl}$) were crossed with B6.Cg-Tg(Atoh1-cre)1Bfri/J (The Jackson Laboratory Stock #011104) mice, hereafter referred to as Atoh1-cre, to obtain conditional cre expression in the HCs (**Figure 1C**). The mice were bred accordingly to generate *Brd4*$^{fl/fl;Atoh1-cre+/-}$ (referred to as *Atoh1-Brd4*$^{-/-}$) and control littermates. Tails were collected and labeled for gDNA extraction. They were incubated overnight at 56°C in 500 μL of TEL buffer and Proteinase K (20 mg/ml). The samples were centrifuged at maximum speed for 10 min. The supernatant was transferred to fresh tubes and DNA was precipitated using 100% Ethanol. The samples were centrifuged again at maximum speed for 5 min to pellet the DNA, then washed again with 70% ethanol for 2 min. The pellet was air dried for 20–30 min and dissolved in 150 μL of TE buffer (10 mM Tris–HCl pH 8.0, 0.1 mM EDTA pH 8.0). Standard PCR reactions were used to genotype the mice. Genotyping primers: Brd4-F-TCAGAGTGCTAGGGATTACAGG, Brd4- R-CTAGTTACAACGGCTTCTGTC, Cre-F-AGAACCTGAAGAT GTTCGCG, Cre-R-GGCTATACGTAACAGGGTGT.

PCR conditions: Initial Denaturation: 94°C for 4 min; Annealing: 94°C for 30 s, 60°C for 30 s, 72°C for 1 min repeated for 35 cycles; final extension: 72°C for 7 min; hold at 4°C ∞.

### Quantitative Real Time PCR (qRT-PCR)

Quantitative real time PCR (qRT-PCR) was performed using 2x Taqman Gene Expression Master Mix (Applied Biosystems/Invitrogen #4369016) with Taqman probes designed with the Taqman gene expression assay tool. Data were collected using the QuantStudio$^{TM}$ 6 Flex Real-Time PCR System (Applied Biosystems/Invitrogen 4485694). Data analysis was done to asses fold change in gene expression with the comparative cycle threshold (ΔΔCt) method relative to housekeeping gene *Gapdh* cycle threshold values. Results were compared to gene expression in *Brd4*$^{+/+}$ samples. qRT-PCR primers: Assay ID: Mm00480392_m1; Brd4 Ex5-6, FAM- MGB, Assay ID: Mm99999915_g1; Gapdh Ex 2-3; VIC-MGB.

### Section and Whole Mount Immunostaining

Sections from P0 and whole cochlear tissues collected from P8, P14, P16 and P21 *Brd4*$^{+/+}$ and *Atoh1-Brd4*$^{+/-}$ mice were fixed and immunolabeled. The tissues were permeabilized with 0.5% for 20 min, blocked for 1.5 h with a combination of 5% BSA and 0.1% Triton X-100 and incubated overnight at 4°C with primary antibodies. Immunolabeling of the primaries were done using secondary antibodies for 1.5 h at RT. The samples were then washed and incubated with DAPI (Calbiochem) for 5 min at RT. Specimens were washed with PBS and mounted in fluorescence mounting medium (Dako, # S3023). Preparations were imaged using a 63× objective with a Leica SP5 Inverted Confocal. Primary antibodies used are as follows: (1) Brd4 visualization: Rabbit anti-phospho-Brd4-S492/494 (1/50, Millipore, #ABE1453), (2) HC specific marker: Mouse monoclonal anti-Myo7a (1/400, Developmental Studies

[1]http://bioinfo.ut.ee/primer3-0.4.0/

[2]https://genome.ucsc.edu/cgi-bin/hgPcr

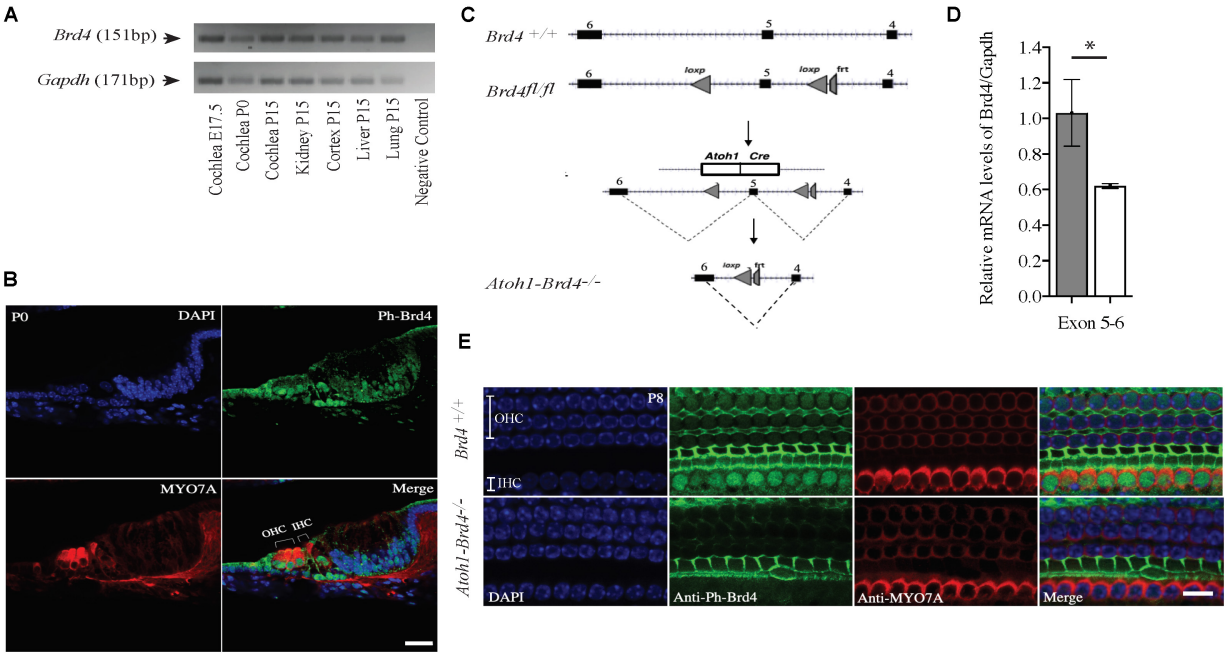


**FIGURE 1 |** Mouse *Brd4* expression, generation, and confirmation of HC specific knockout. **(A)** Expression of *mBrd4* (Exon 5-6) in the cochlea during the different developmental stages (E17.5 to P15) is observed relative to *mGapdh*. **(B)** Immunostaining of $Brd4^{+/+}$ section ($n$ = 3) show *Brd4* expression (green) in nucleus of every cell-type in the inner ear as indicated by its colocalization with DAPI (blue, nuclei), including hair cells, labeled with HC specific Myo7a (red) (Scale = 10 μM). **(C)** $Brd4^{tm1c}$ mice (referred to as $Brd4^{fl/fl}$) were crossed with B6.Cg-Tg (Atoh1-cre) 1Bfri/J (The Jackson Laboratory Stock #011104) mice (referred to as Atoh1-cre), to obtain *Atoh1-*$Brd4^{-/-}$ HC specific knockout and control littermates. **(D)** qRT-PCR results showed that *mBrd4* (Exon 5-6) levels were decreased significantly in (white) *Atoh1-*$Brd4^{-/-}$ compared to (gray) $Brd4^{+/+}$ samples (triplicates of each $n$ = 3, $Brd4^{+/+}$ and $n$ = 4, *Atoh1-*$Brd4^{-/-}$ samples). **(E)** Z-stack of P8 ($n$ = 3) cochlea immunostained with Brd4 (green), the HC marker Myosin7a (red) and DAPI (blue, nuclei). Results showed Brd4 was absent in the IHCs and OHCs of the *Atoh1-*$Brd4^{-/-}$ mice (Scale = 10 μM). (Standard $T$-test was performed to determine the significance of the experiment, $^{*}p < 0.05$, $^{**}p < 0.01$, $^{***}p < 0.001$, ns-not significant).

Hybridoma Bank at the University of Iowa, #138-1), (3) Neuronal fibers visualization: chicken polyclonal anti-Neurofilament (NF) (1/300, Millipore, #AB5539), (4) Synaptic ribbon visualization: mouse monoclonal Anti-Ctbp2 (1/300, BD Biosciences, #612044) and rabbit polyclonal anti-Glur2 (1/300, Millipore, # 07-598). Secondary antibodies used are as follows: (1) anti-rabbit Alexa Fluor® 488 (1/400, Invitrogen, # A32731), (2) anti-chicken Alexa Fluor® 488 (1/300, Invitrogen, # A32931), (3) anti-mouse Alexa Fluor® 488 (1/400, Invitrogen, # A32723), (4) anti-rabbit Alexa Fluor® 568 (1/400, Invitrogen, # A-11008), (5) anti-mouse Alexa Fluor® 568 (1/400, Invitrogen, # A-21124), (6) Alexa Fluor® Phalloidin 568 (1/100; Invitrogen, #A12380).

## Scanning Electron Microscopy (SEM)

P8 mouse cochleae from $Brd4^{+/+}$ and *Atoh1-*$Brd4^{-/-}$ were fixed in 3% glutaraldehyde in PBS overnight at 4°C. Samples were rinsed with PBS twice to remove the fixative well. Samples were fixed in 1% Osmium Tetroxide (OsO4) between 30 and 60 min, rinsed with distilled, de-ionized water for 10 min (2×), followed by treatment in 0.5% thiocarbohydrazide for 15–20 min. The process was repeated until the last OsO4 treatment was complete. The samples were rinsed well with water to remove any chemical residues and dehydrated in absolute EtOH serially from 50%, 70% up to 100% for 10 min each. The samples were then treated with HMDS for 5 min. Air contact was avoided to ensure there was no sample re-hydration. Once they were dried, the samples were mounted on scanning electron microscopy (SEM) stubs, the cochlea facing up and kept in a vacuum chamber till the time they were sputter coated with Palladium (Pd) (60:40) using Edwards S150B unit at 750 V and 40 mA for 30 min. Samples were imaged using an XL-30 field emission scanning electron microscope.

## Audio Brainstem Response (ABR) and Distorted Product Otoacoustic Emission (DPOAE) Evaluation

Mouse ($Brd4^{+/+}$ and *Atoh1-*$Brd4^{+/-}$) audio brainstem responses (ABRs) and distorted product otoacoustic emissions (DPOAEs) were conducted using a Smart EP Universal Smart Box (Intelligent Hearing Systems, Miami, FL, United States). ABR stimuli were 0.1 ms duration clicks or 0.1 ms duration pure tone pips presented at frequencies 8, 16, and 24 kHz. Click stimuli were enveloped with a rectangular window, while pips were enveloped with a Blackman window. Stimuli began at 20 dB SPL amplitude and increased at 10 dB steps up to 100 dB SPL. A total of 600 sweeps were averaged for each frequency and amplitude. ABR thresholds were determined for each stimulus frequency by identifying the lowest intensity producing a recognizable ABR pattern (at least two consistent

peaks above the baseline). For DPOAEs, specific acoustic stimuli were delivered monaurally through plastic tubes channeled from high-frequency transducers. Five hundred and twelve sweeps of DPOAE at frequencies 2f1–f2 were recorded in response to two level primary tones (55 and 65 dB, respectively), f1 and f2, with f2/f1 = 1.20 and frequencies, $\sqrt{(ff1 \times ff2)}$ ranging from 8 kHz to 24 kHz. *T*-test was performed for significance of experiment.

# RESULTS

## *Brd4* Is Expressed in the Mouse Cochlea

In order to understand the spaciotemporal expression of the *Brd4* in the inner ear (IE), we analyzed its expression in wild type (WT) mice by RT-PCR and immunofluorescence. Expression of *Brd4* was studied by RT-PCR (**Figure 1A**) using mRNA obtained from mice cochlear tissues collected at embryonic stage E17.5, and postnatal stages P0 and P15. *Brd4* was detected in the $Brd4^{+/+}$ mouse cochlea at E17.5, P0 and P15. Immunostaining (**Figure 1B**) of cochlear sections of P0 mice showed ubiquitous localization of phosphorylated-Brd4 (green) in the nuclei of cells, including HCs, identified by the specific marker Myo7a (red).

## Generation of HC-Specific *Brd4* Knock-Out Mice

To bypass embryonic lethality (Houzelstein et al., 2002) and investigate the function of *Brd4* in HCs, *Brd4* conditional knock-out mice were successfully generated as previously described (Penas et al., 2019; **Figure 1C**). $Brd4^{fl/fl}$ were crossed with Atoh1-cre mice, that expressed Cre in developing HCs at approximately E13.5 (Woods et al., 2004) to obtain cell specific expression of cre in the HCs. The mice were bred accordingly to generate HC specific knockout *Atoh1-Brd4*$^{-/-}$ and control littermates. In order to confirm the decrease in *Brd4* expression in *Atoh1-Brd4*$^{-/-}$ mice we performed qRT-PCR using inner ear cDNA from P3 mice as template. A significant decrease in the levels of *Brd4* mRNA in *Atoh1-Brd4*$^{-/-}$ mice compared to $Brd4^{+/+}$ was observed (**Figure 1D**) and between $Brd4^{fl/fl}$ and *Atoh1-Brd4*$^{-/-}$ while there was no significant decrease observed between $Brd4^{+/+}$ and $Brd4^{fl/fl}$ (**Supplementary Figures 1A,B**). To visualize the HC specific deletion of *Brd4* in *Atoh1-Brd4*$^{-/-}$ mice, we performed whole mount immunostaining on P8 cochlea. As expected, a clear deletion of *Brd4* in the outer hair cells (OHCs) and inner hair cells (IHCs) of the *Atoh1-Brd4*$^{-/-}$ mice compared to $Brd4^{+/+}$ was observed (**Figure 1E**).

## Auditory Neuropathy in HC-Specific *Brd4* Knock-Out Mice

To assess whether the cell-specific deletion of *Brd4* affected the hearing capacity we measured ABRs and DPOAEs. At P21, the ABR thresholds for click response in $Brd4^{+/+}$ mice was ∼65 dB SPL (decibel sound pressure level) whereas in *Atoh1-Brd4*$^{-/-}$ it was ∼100 dB SPL. Similarly, for the pure-tone frequencies, *Atoh1-Brd4*$^{-/-}$ mice had significantly elevated ABR thresholds (∼100 dB SPL) compared with control mice (**Figure 2A**). Thus, the *Atoh1-Brd4*$^{-/-}$ mice were profoundly deaf, indicating the important role of *Brd4* in HCs. The DPOAE recordings (**Figure 2B**) produced by OHCs in the *Atoh1-Brd4*$^{-/-}$ mice had reduced amplitudes compared to the control group at P21; clearly suggesting a functional defect of OHC in the mutant mice. To exclude the effect of the floxed allele the hearing phenotype for $Brd4^{fl/fl}$ mice was tested., A significant difference in the ABR and DPOAE was observed between $Brd4^{fl/fl}$ and *Atoh1-Brd4*$^{-/-}$ while there was no significant decrease observed between $Brd4^{+/+}$ and $Brd4^{fl/fl}$ (**Supplementary Figures 1C–F**); indicating that the floxed allele alone is not responsible for the HL observed in the HC-specific *Brd4* knock-out mice.

## Stereociliary Structure, Innervation Pattern, and Ribbon Synapses of Hair Cells Are Disrupted in HC-Specific *Brd4* Knock-Out Mice

To determine whether *Brd4* deletion cause morphological defects, we examined the HC in *Atoh1-Brd4*$^{-/-}$ mice. Confocal microscopy and SEM images revealed that the stereocilia bundles in *Atoh1-Brd4*$^{-/-}$ mice were abnormal compared to those in control mice. Confocal images of the middle region of cochlea showed morphological changes (**Figure 2C**) over time in between $Brd4^{+/+}$ and *Atoh1-Brd4*$^{-/-}$ starting with a mild disorganization in the stereociliary bundles at P8 in both IHCs and OHCs, to complete degeneration by P21. The SEM imaging confirmed the structural disorganization at P8 (**Figure 2D**). Morphological changes were also observed in the basal and apical regions (**Supplementary Figure 2**). In order to further examine the HL phenotype in the *Atoh1-Brd4*$^{-/-}$ mice, we examined how the *Brd4* inactivation affects innervation of the inner ear. Confocal images of cochleae collected and immunolabeled with anti-neurofilament (NF) antibody, from $Brd4^{+/+}$ and *Atoh1-Brd4*$^{-/-}$ mice at P16 and P21 revealed severe disorganization of the neurofilament bundles and degeneration by P21 (**Figure 3A**). To determine if the synapses between HCs and the nerve terminals were affected, we collected the sensory epithelium from P14, P16, and P21 of $Brd4^{+/+}$ and *Atoh1-Brd4*$^{-/-}$ mice. When stained for Carboxy-terminal Binding Protein 2 (CtBP2), which labeled presynaptic ribbons found in IHC, and for GluR2/3, an AMPA receptor subunit that labeled postsynaptic glutamate receptors on afferent nerve terminals, reduced numbers of intact synapses in IHC were observed (**Figure 3B**).

## Severe HC Loss Is Observed in Brd4 Conditional Knock-Out Mice

We then examined whether HC loss occurred in the auditory epithelium of the *Atoh1-Brd4*$^{-/-}$ mice. Confocal images of *Atoh1-Brd4*$^{-/-}$ whole-mount specimen immunostained using HC marker Myo7a and DAPI to the stain the nuclei showed severe HC loss at P21 (**Figure 4A**). A schematic representation of HC death is shown in **Figure 4B**. Quantification of the total number of OHCs and IHCs was done through different postnatal developmental stages. No significant HC loss at P8 was detected. By P14, there was occasional OHC loss along the length of the cochlea, although the IHCs appeared largely intact. Beginning at P16, both the OHCs and IHCs underwent rapid cell death,

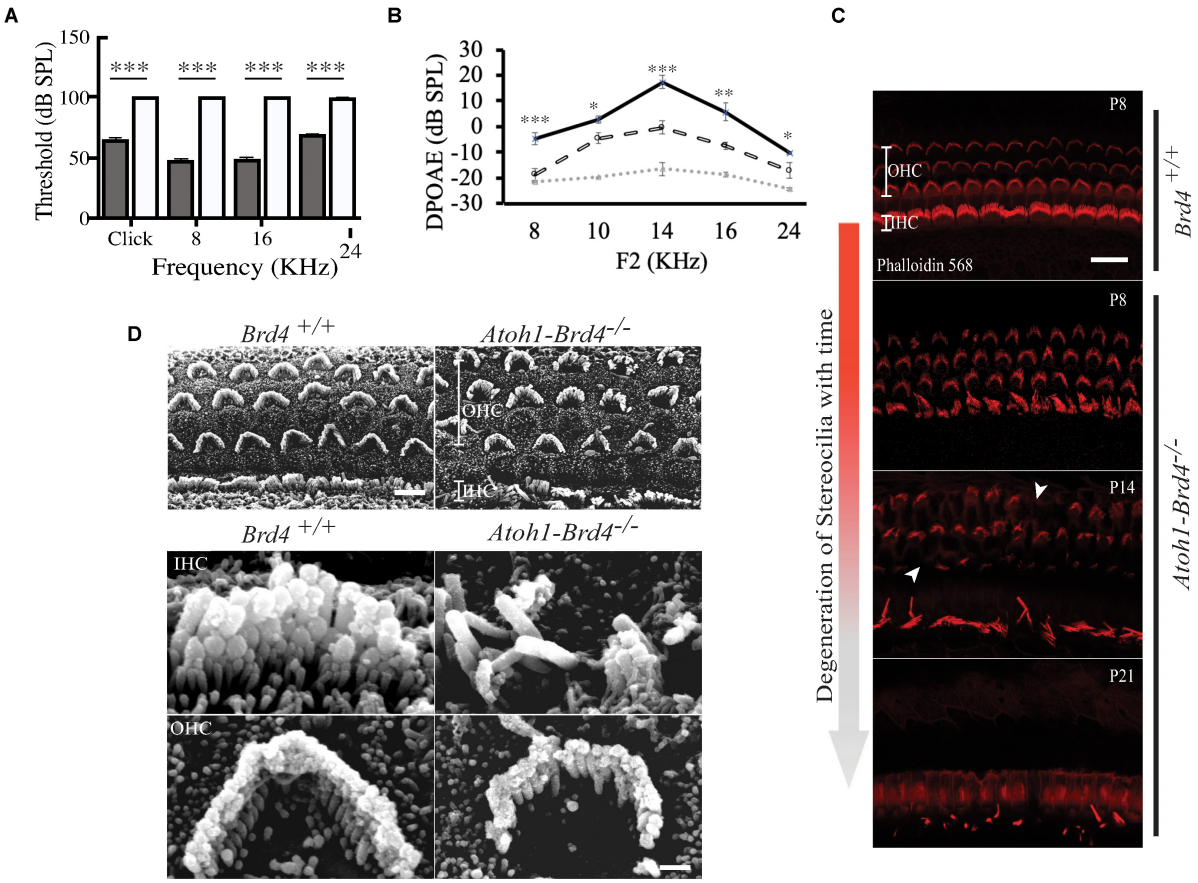


**FIGURE 2 |** Auditory Neuropathy and Stereocilia degeneration. **(A)** The ABR thresholds for click response in (gray) *Brd4*$^{+/+}$ mice ($n$ = 4) were ∼65 dB SPL and ∼100 dB SPL in (white) *Atoh1-Brd4*$^{-/-}$ ($n$ = 5). Similarly, for the pure-tone frequencies, *Atoh1-Brd4*$^{-/-}$ mice had significantly elevated ABR thresholds (∼100 dB SPL) compared with control mice. **(B)** The DPOAE recordings of (dashed white line) *Atoh1-Brd4*$^{-/-}$ ($n$ = 5) mice showed reduced amplitudes, from low to high frequencies (8–24 KHz) compared to (black line) *Brd4*$^{+/+}$ group ($n$ = 5). Noise floor is indicated with a dotted gray line. (Standard $T$-test was performed to determine the significance of the experiment, *$p < 0.05$, **$p < 0.01$, ***$p < 0.001$, ns-not significant). **(C)** Z-stack of mouse cochleae (P8, $n$ = 3; P14, $n$ = 1; P21, $n$ = 3) counterstained for actin filaments (red) (scale: 20 μm) showed degeneration of stereocilia over time between P8 and P21 in *Atoh1-Brd4*$^{-/-}$. The white arrow heads represent the missing bundles of stereocilia. **(D)** SEM images of P8 ($n$ = 2) mouse cochleae processed using the O-T-O-T-O showed show the difference in the structural integrity of the stereocilia between *Brd4*$^{+/+}$ and *Atoh1-Brd4*$^{-/-}$ (Scale: 10 μm upper panel; 2 μM lower panel).

OHCs more than IHC. By P21, there were very few OHCs in the cochlear epithelium. Although a majority of the OHCs were lost by P21 (∼90%; $p$-value $< 0.01$), a considerable number of IHCs remained (75%; $p$-value $< 0.01$). The quantification of the HC loss is shown in **Figure 4C**.

The loss of OHCs and IHCs across the different regions of the cochlea at P21 (base, middle, and apex) has been shown in **Supplementary Figure 3**.

## DISCUSSION

An emerging paradigm in hearing biology is the role of transcriptional regulators in the structure and function of the inner ear. Increasing evidence suggests that epigenetic mechanisms are essential for establishing distinct chromatin states and cell-type specific gene expression patterns that play an important role in the development, function and maintenance of the inner ear. The inner ear sensory organ and the sensory neurons that innervate it, develop from the otic placode through a complex series of differentiation events that depend on the interplay of inductive signals and transcriptional activity. For example, the homeodomain transcription factors Otx2 and Gbx2 are critical for otic placode specification (Steventon et al., 2012). Epigenetic regulation of *GBX2* by *DNMT3A*, a *de novo* DNA methyltransferase (Roellig and Bronner, 2016) supports the involvement of epigenetic processes in normal development of the inner ear. Further, the histone demethylase KDM4B plays a critical role in regulating the expression of *Dlx3*, a member of the vertebrate Distal-less related (*Dlx*) homeodomain genes, required for otic invagination (Uribe et al., 2015). Haploinsufficiency in a member of the chromodomain helicase DNA-binding (CHD) family of ATP-dependent chromatin remodeling enzymes (*Chd7*), causes CHARGE Syndrome, which presents with inner ear defects (Vissers et al., 2004). Analysis of *Chd7* knockout mice revealed that CHD7 regulates the expression of vestibular

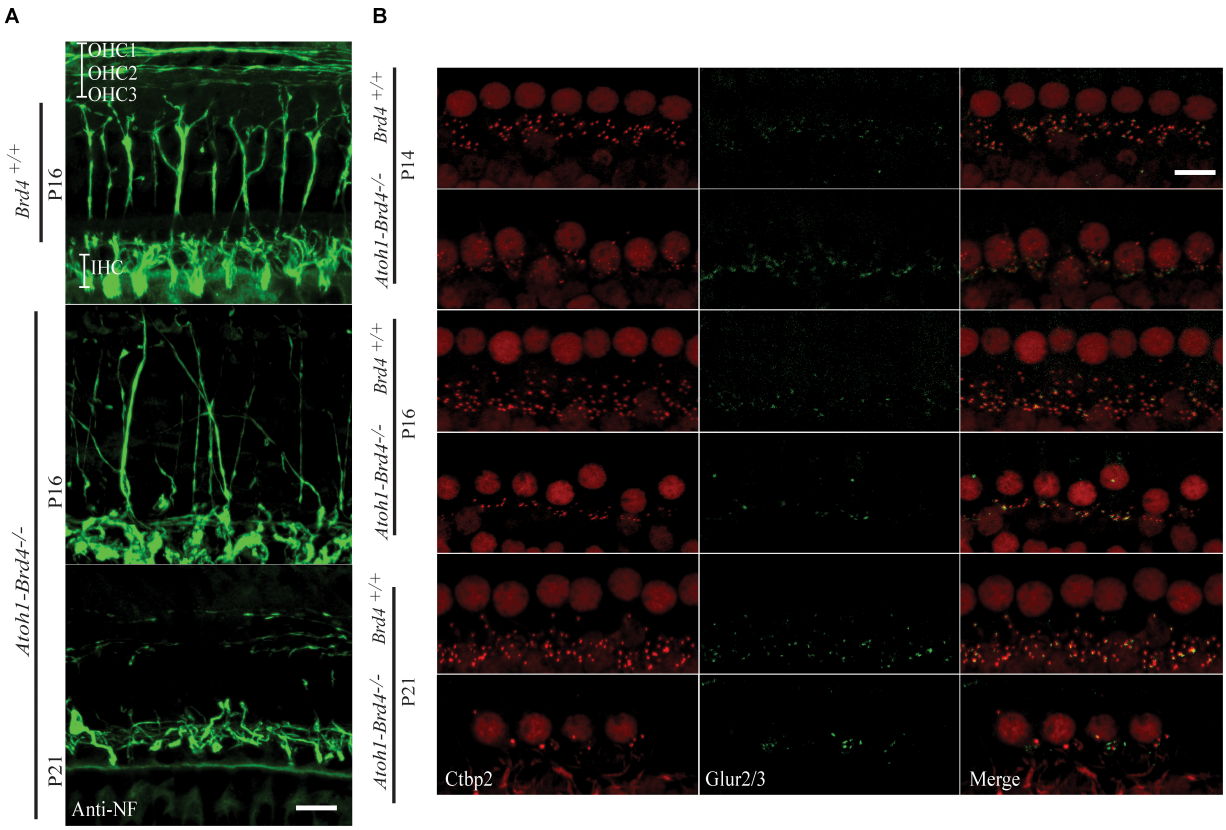


**FIGURE 3 |** Innervation defects and degeneration of ribbon synapses. **(A)** Z-stack projections showing neurofilament fiber bundles with improper fasciculation and eventual degeneration in whole mount mouse cochleae *Atoh1-Brd4*$^{-/-}$. Nerve fibers were immunolabeled with an antibody against neurofilament heavy chain (green) (bar scale: 20 μm). **(B)** Z-stack projections of mice IHCs stained for anti-RIBEYE/CtBP2 (red) and GluR2/3 (green). Reduced numbers of IHC paired CtBP2-GluR2/3 ribbons were observed starting at P14 and severe loss in synaptic ribbon formation was observed by P21 (bar scale: 10 μm).

regulatory genes in a gene dosage dependent manner (Hurd et al., 2010). In neuronal stem cells, it directly interacts with HMG-box transcription factor SOX2 and cooperatively regulates the expression of key developmental regulators including the Notch ligand Jagged1 (JAG1) and the transcription factor GLI3 (Engelen et al., 2011). JAG1 is an essential regulator of inner ear neuro-sensory development and is required for semicircular canal formation (Kiernan et al., 2001). Gli3 is necessary for the correct development of the apical region of the cochlea and its mutation causes Pallister-Hall syndrome which shows a prevalence of low-frequency HL (Driver et al., 2008). Interestingly, most CHD7 binding sites show features of gene enhancer elements. Atonal homolog 1 (Atoh1) is a transcription factor crucial for the generation of HCs and neurons in the inner ear. Dynamic changes in histone modifications at the *Atoh1* locus correlating with *Atoh1* expression reveal an epigenetic mechanism of *Atoh1* regulation underlying HC differentiation and subsequent maturation (Stojanova et al., 2015). Despite all this knowledge, the role of epigenetic regulation in the differentiation, maturation, and maintenance of auditory HCs still remains unclear.

Here we studied the role of BRD4, a member of the BET protein family that interacts with acetylated lysines on chromatin. BRD4 binds to hyperacetylated genomic regions that encompass promoters and enhancers and regulates transcription elongation by paused RNA polymerase II (Pol II). Regions of H3K27ac bound by BRD4 and mediator complex subunit 1 (MED1) have been defined as super-enhancers important to determine cell identity (Hnisz et al., 2013). Several lines of evidence suggested a role for *BRD4* in HL. It has been reported that haploinsufficiency of *BRD4* is associated with Cornelia de Lange syndrome (CdLS), a severe multisystem neurodevelopmental disorder presenting with HL as one of the clinical phenotypes (Olley et al., 2018). Similarly, a novel 2.52 Mb microdeletion at 19p13.12 that includes *BRD4* was also reported in a patient presenting with HL, using high resolution chromosomal microarray analysis (de Souza et al., 2018). In addition, BRD4 and P-TEFb were identified as WHSC1 interacting partners, and together they facilitate transcriptional elongation (Sarai et al., 2013) WHSC1-deficient mice fail to develop normal stereocilia hair bundles required for sound perception. The BET family is a distinct group of bromodomain proteins that in mammals includes BRD2, BRD3, BRD4 (ubiquitously expressed), and BRDT (testis specific). Brd2 and Brd4 have been extensively studied in the context of cell-cycle control and transcription elongation and activation and are known to be overexpressed in multiple tumor types. BET proteins

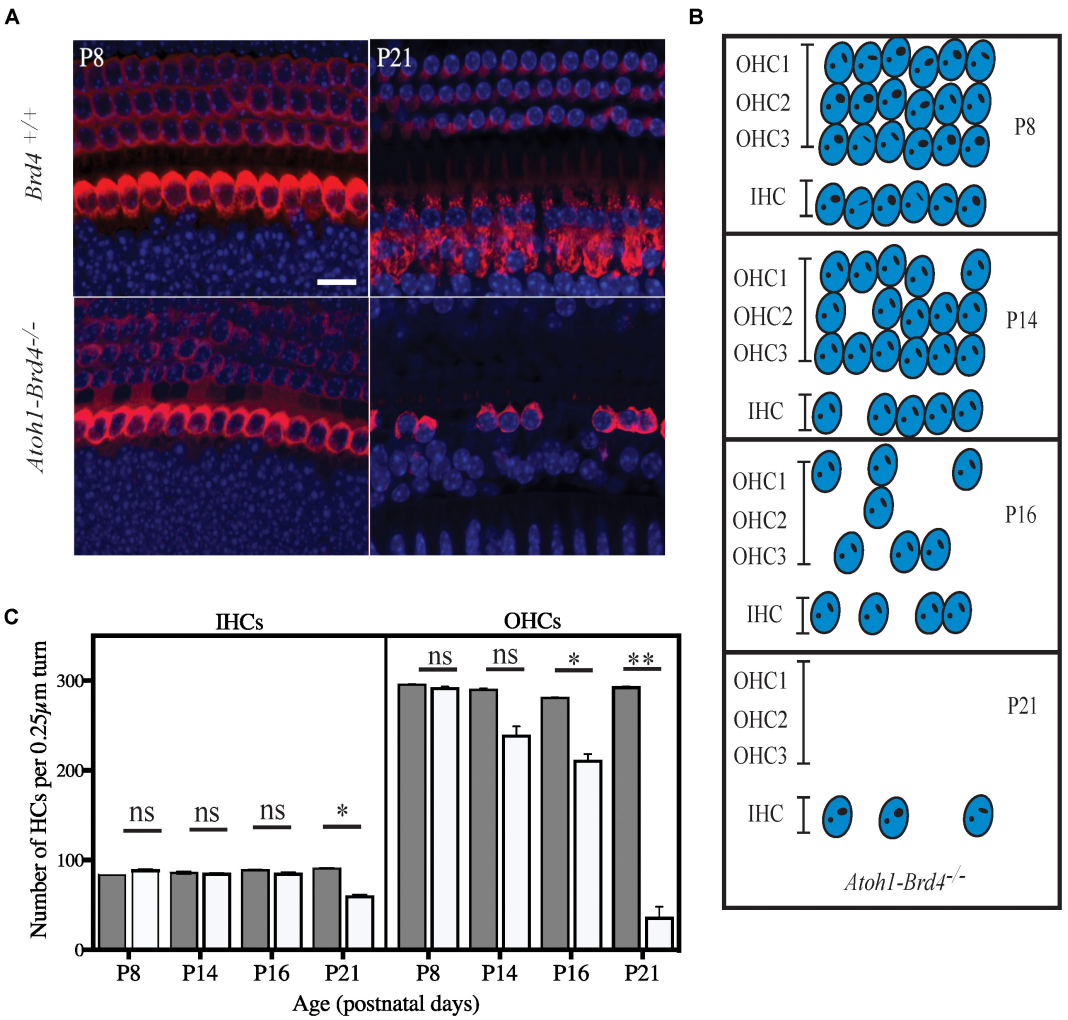


**FIGURE 4 |** Severe hair cell loss. **(A)** Z-stack of *Atoh1-Brd4*$^{-/-}$ mouse cochleae immunolabeled with HC marker Myo7a (red) and DAPI (blue) (scale: 10 μm) showed severe HC loss at P21 with more OHC death compared to IHCs. **(B)** A schematic representation of HC loss at different ages. **(C)** Graphical representation of the quantification of the number of OHCs and IHCs (per 0.25 μm turn of cochlea) of the cochlea at different developmental stages (white, *Atoh1-Brd4*$^{-/-}$; gray, *Brd4*$^{+/+}$). The error bars indicate the SEM (Standard *T*-test was performed to determine the significance of the experiment, *$p < 0.05$, **$p < 0.01$, ***$p < 0.001$, ns-not significant).

promote the expression of oncogenes such as MYC, promoting tumorigenesis. The anti-proliferative effect of inhibiting BET prompted clinical trials for small molecule inhibitors of BET bromodomain proteins in cancer. JQ1 (thienodiazepine) is the one of the first published small molecules that binds competitively to bromodomains (Filippakopoulos et al., 2010). JQ1, along with other BET inhibitors, has been shown to have inhibitory effects in various human cancers and xenograft models (Doroshow et al., 2017). Although the therapeutic success of BET inhibition in clinical trials and animal studies generates enthusiasm, the potential toxicities at the effective doses remain indefinite at this time. Studies in mice have shown that *Brd4* binds to acetylated histone residues which are often modified in embryonic stem cells (ESCs) (Markowetz et al., 2010). In pluripotent cells, the *Brd4* and acetyltransferase complex regulate chromatin structure and mesoderm formation (Wu et al., 2018) and maintain pluripotency of ESCs (Gonzales-Cope et al., 2016; Fernandez-Alonso et al., 2017). *Brd4* has also been shown to have a role in learning and memory *in vivo* in adult animals (Korb et al., 2015; Sartor et al., 2015; Benito et al., 2017) by controlling the expression of these genes as well as synaptic receptor proteins related to memory formation (Korb et al., 2015). *Brd4* also plays a role in adipogenesis and myogenesis by specifically recruiting transcription elongation factors necessary to transcribe genes for brown adipocyte differentiation as well as myogenesis (Lee et al., 2017; Brown et al., 2018), and inducing differentiation in immune and epithelial cells in mice (Zhang et al., 2012; Devaiah et al., 2016).

In our study, we uncovered that deletion of *Brd4* in HCs of mice resulted in profound deafness, ultimately related with cellular death, supporting an important role for *Brd4* in the maintenance/function of HCs. Since *BRD4* has emerged as an

attractive anticancer therapeutic target and its inhibition entered the clinical practice, this finding of BRD4 as a key molecule for the function of the inner ear prompts the study of potential effects of BET inhibition in audition and balance. The *Brd4* conditional knockout developed physiological as well a variety of morphological changes that occur in the cochlea. DPOAEs are used to evoke responses from the OHCs and based on the recordings or lack thereof, it is determined if OHCs are functional. As expected, the OHCs of the mutant mice in our studies were not functional as early as P21. ABRs are another type of hearing evaluation (tested across various frequencies) that specifically tests for the normal innervation of the ear. In this study, the mutants had a threshold of $>100$ dB, indicating that they did not hear at any frequency. This shows that the innervation in the mutant mice has possibly been damaged. The stereocilia bundles form the apical part of the HCs which are terminally differentiated and specialized (Raphael and Altschuler, 2003) and are extremely sensitive to mechanical displacement (sound). The stereocilia respond to sound by opening ion channels and depolarizing HCs, subsequently transferring the signal to the afferent neurons. This study revealed a progressive pattern of degeneration of these bundles, starting with a milder phenotype expressed at P8 and eventually complete loss of the cilia by P21. Integrity of spiral ganglion neurons and HC interactions are crucial for the mechanostransduction process in the inner ear. Upon investigation of the patterns of innervation and synapse formation, there was rapid degeneration of neuronal fibers and a gross reduction in the numbers of intact synapses. The innervation pattern appeared normal in $Brd4^{+/+}$ as the fibers project toward their IHC and OHC targets and they cross the tunnel of Corti (TC) and fasciculate to form three discrete bundles. However, in the *Atoh1-*$Brd4^{-/-}$, it can be observed that the fibers not only fail to fasciculate their target IHC and OHCs, they form loose or improper bundles and eventually degenerate. In the case of synapses, the number of CtBP2 puncta, GluR2/3-labeled terminals, and paired CtBP2-GluR2/3 ribbons were reduced starting at P14. By P16, a significant decrease in the synapse formation was observed and by P21 synapse formation was completely lost in IHCs. This indicates that Brd4 might play a role in regulating the synaptic ribbon formation and communication between SGNs and HCs, necessary for hearing. Finally, severe HC loss occurred in the auditory epithelium. In conclusion, we demonstrate with our study, a strong role for *Brd4* in the inner ear.

## DATA AVAILABILITY STATEMENT

All datasets presented in this study are included in the article/**Supplementary Material**.

## ETHICS STATEMENT

The animal study was reviewed and approved by University of Miami Institutional Animal Care and the National Research Council (US) Guide for the Care and Use of Laboratory Animals.

## AUTHOR CONTRIBUTIONS

AK-S was the primary author of this manuscript and has participated in the design of the study, acquisition, data generation and analysis, interpretation, and validation; also responsible for the preparation of this original manuscript. CA participated in the design and execution of the study and in revising the manuscript critically for important intellectual content. MM and NA participated in revising the manuscript. JY participated in the study design and revision of the manuscript. XL and KW were co-corresponding authors and participated in the supporting and supervising the study as well as critical revision of the manuscript. All authors contributed to the article and approved the submitted version.

## FUNDING

This study was supported by NIH grants of R01DC005575 and R01DC012115 to XL.

## SUPPLEMENTARY MATERIAL

The Supplementary Material for this article can be found online at: https://www.frontiersin.org/articles/10.3389/fcell.2020.576654/full#supplementary-material

## REFERENCES

Benito, E., Ramachandran, B., Schroeder, H., Schmidt, G., Urbanke, H., Burkhardt, S., et al. (2017). The BET/BRD inhibitor JQ1 improves brain plasticity in WT and APP mice. *Transl. Psychiatry* 7:e1239. doi: 10.1038/tp.2017.202

Brown, J. D., Feldman, Z. B., Doherty, S. P., Reyes, J. M., Rahl, P. B., Lin, C. Y., et al. (2018). BET bromodomain proteins regulate enhancer function during adipogenesis. *Proc. Natl. Acad. Sci. U.S.A.* 115, 2144–2149. doi: 10.1073/pnas.1711155115

de Souza, L. C., Sgardioli, I. C., Gil-da-Silva-Lopes, V. L., and Vieira, T. P. (2018). A recognizable phenotype related to 19p13.12 microdeletion. *Am. J. Med. Genet. A* 176, 1753–1759. doi: 10.1002/ajmg.a.38842

Devaiah, B. N., Case-Borden, C., Gegonne, A., Hsu, C. H., Chen, Q., Meerzaman, D., et al. (2016). BRD4 is a histone acetyltransferase that evicts nucleosomes from chromatin. *Nat. Struct. Mol. Biol.* 23, 540–548. doi: 10.1038/nsmb.3228

Doetzlhofer, A., and Avraham, K. B. (2017). Insights into inner ear-specific gene regulation: epigenetics and non-coding RNAs in inner ear development and regeneration. *Semin. Cell Dev. Biol.* 65, 69–79. doi: 10.1016/j.semcdb.2016.11.002

Doroshow, D. B., Eder, J. P., and LoRusso, P. M. (2017). BET inhibitors: a novel epigenetic approach. *Ann. Oncol. Off. J. Eur. Soc. Med. Oncol.* 28, 1776–1787. doi: 10.1093/annonc/mdx157

Driver, E. C., Pryor, S. P., Hill, P., Turner, J., Rüther, U., Biesecker, L. G., et al. (2008). Hedgehog signaling regulates sensory cell formation and auditory

function in mice and humans. *J. Neurosci.* 28, 7350–7358. doi: 10.1523/jneurosci.0312-08.2008

Engelen, E., Akinci, U., Bryne, J. C., Hou, J., Gontan, C., Moen, M., et al. (2011). Sox2 cooperates with Chd7 to regulate genes that are mutated in human syndromes. *Nat. Genet.* 43, 607–611. doi: 10.1038/ng.825

Fernandez-Alonso, R., Davidson, L., Hukelmann, J., Zengerle, M., Prescott, A. R., Lamond, A., et al. (2017). Brd4-Brd2 isoform switching coordinates pluripotent exit and Smad2-dependent lineage specification. *EMBO Rep.* 18, 1108–1122. doi: 10.15252/embr.201643534

Filippakopoulos, P., Qi, J., Picaud, S., Shen, Y., Smith, W. B., Fedorov, O., et al. (2010). Selective inhibition of BET bromodomains. *Nature* 468, 1067–1073. doi: 10.1038/nature09504

Gonzales-Cope, M., Sidoli, S., Bhanu, N. V., Won, K.-J., and Garcia, B. A. (2016). Histone H4 acetylation and the epigenetic reader Brd4 are critical regulators of pluripotency in embryonic stem cells. *BMC Genomics* 17:95. doi: 10.1186/s12864-016-2414-y

Hnisz, D., Abraham, B. J., Lee, T. I., Lau, A., Saint-André, V., Sigova, A. A., et al. (2013). Super-enhancers in the control of cell identity and disease. *Cell* 155, 934–947. doi: 10.1016/j.cell.2013.09.053

Houzelstein, D., Bullock, S. L., Lynch, D. E., Grigorieva, E. F., Wilson, V. A., and Beddington, R. S. P. (2002). Growth and early postimplantation defects in mice deficient for the bromodomain-containing protein Brd4. *Mol. Cell. Biol.* 22, 3794–3802. doi: 10.1128/MCB.22.11.3794-3802.2002

Hurd, E. A., Poucher, H. K., Cheng, K., Raphael, Y., and Martin, D. M. (2010). The ATP-dependent chromatin remodeling enzyme CHD7 regulates pro-neural gene expression and neurogenesis in the inner ear. *Development* 137, 3139–3150. doi: 10.1242/dev.047894

Kiernan, A. E., Ahituv, N., Fuchs, H., Balling, R., Avraham, K. B., Steel, K. P., et al. (2001). The Notch ligand *Jagged1* is required for inner ear sensory development. *Proc. Natl. Acad. Sci. U.S.A.* 98, 3873–3878. doi: 10.1073/pnas.071496998

Korb, E., Herre, M., Zucker-Scharff, I., Darnell, R. B., and Allis, C. D. (2015). BET protein Brd4 activates transcription in neurons and BET inhibitor Jq1 blocks memory in mice. *Nat. Neurosci.* 18, 1464–1473. doi: 10.1038/nn.4095

Layman, W. S., Williams, D. M., Dearman, J. A., Sauceda, M. A., and Zuo, J. (2015). Histone deacetylase inhibition protects hearing against acute ototoxicity by activating the Nf-κB pathway. *Cell Death Discov.* 1: 15012. doi: 10.1038/cddiscovery.2015.12

Lee, J. E., Park, Y. K., Park, S., Jang, Y., Waring, N., Dey, A., et al. (2017). Brd4 binds to active enhancers to control cell identity gene induction in adipogenesis and myogenesis. *Nat. Commun.* 8:2217. doi: 10.1038/s41467-017-02403-5

Markowetz, F., Mulder, K. W., Airoldi, E. M., Lemischka, I. R., and Troyanskaya, O. G. (2010). Mapping dynamic histone acetylation patterns to gene expression in nanog-depleted murine embryonic stem cells. *PLoS Comput. Biol.* 6:e1001034. doi: 10.1371/journal.pcbi.1001034

Olley, G., Ansari, M., Bengani, H., Grimes, G. R., Rhodes, J., von Kriegsheim, A., et al. (2018). BRD4 interacts with NIPBL and BRD4 is mutated in a Cornelia de Lange–like syndrome. *Nat. Genet.* 50, 329–332. doi: 10.1038/s41588-018-0042-y

Ong, C. T., and Corces, V. G. (2014). CTCF: an architectural protein bridging genome topology and function. *Nat. Rev. Genet.* 15, 234–246. doi: 10.1038/nrg3663

Penas, C., Maloof, M. E., Stathias, V., Long, J., Tan, S. K., Mier, J., et al. (2019). Time series modeling of cell cycle exit identifies Brd4 dependent regulation of cerebellar neurogenesis. *Nat. Commun.* 10:3028. doi: 10.1038/s41467-019-10799-5

Raphael, Y., and Altschuler, R. A. (2003). Structure and innervation of the cochlea. *Brain Res. Bull.* 60, 397–422. doi: 10.1016/S0361-9230(03)00047-9

Roellig, D., and Bronner, M. E. (2016). The epigenetic modifier DNMT3A is necessary for proper otic placode formation. *Dev. Biol.* 411, 294–300. doi: 10.1016/j.ydbio.2016.01.034

Sanchez, R., and Zhou, M. M. (2009). The role of human bromodomains in chromatin biology and gene transcription. *Curr. Opin. Drug Discov. Dev.* 12, 659–665.

Sarai, N., Nimura, K., Tamura, T., Kanno, T., Patel, M. C., Heightman, T. D., et al. (2013). WHSC1 links transcription elongation to HIRA-mediated histone H3.3 deposition. *EMBO J.* 32, 2392–2406. doi: 10.1038/emboj.2013.176

Sartor, G. C., Powell, S. K., Brothers, S. P., and Wahlestedt, C. (2015). Epigenetic readers of lysine acetylation regulate cocaine-induced plasticity. *J. Neurosci.* 35, 15062–15072. doi: 10.1523/JNEUROSCI.0826-15.2015

Steventon, B., Mayor, R., and Streit, A. (2012). Mutual repression between Gbx2 and Otx2 in sensory placodes reveals a general mechanism for ectodermal patterning. *Dev. Biol.* 367, 55–65. doi: 10.1016/j.ydbio.2012.04.025

Stojanova, Z. P., Kwan, T., and Segil, N. (2015). Epigenetic regulation of atoh1 guides hair cell development in the mammalian cochlea. *Development* 142, 3529–3536. doi: 10.1242/dev.126763

Taniguchi, Y. (2016). The bromodomain and extra-terminal domain (BET) family: functional anatomy of BET paralogous proteins. *Int. J. Mol. Sci.* 17:1849. doi: 10.3390/ijms17111849

Tekin, M., Arnos, K. S., and Pandya, A. (2001). Advances in hereditary deafness. *Lancet* 358, 1082–1090. doi: 10.1016/S0140-6736(01)06186-4

Uribe, R. A., Buzzi, A. L., Bronner, M. E., and Strobl-Mazzulla, P. H. (2015). Histone demethylase KDM4B regulates otic vesicle invagination via epigenetic control of Dlx3 expression. *J. Cell Biol.* 211, 815–827. doi: 10.1083/jcb.201503071

Vissers, L. E. L. M., van Ravenswaaij, C. M. A., Admiraal, R., Hurst, J. A., de Vries, B. B. A., Janssen, I. M., et al. (2004). Mutations in a new member of the chromodomain gene family cause CHARGE syndrome. *Nat. Genet.* 36, 955–957. doi: 10.1038/ng1407

Wang, C. Y., and Filippakopoulos, P. (2015). Beating the odds: BETs in disease. *Trends Biochem. Sci.* 40, 468–479. doi: 10.1016/j.tibs.2015.06.002

Woods, C., Montcouquiol, M., and Kelley, M. W. (2004). Math1 regulates development of the sensory epithelium in the mammalian cochlea. *Nat. Neurosci.* 7, 1310–1318. doi: 10.1038/nn1349

Wu, D. K., and Kelley, M. W. (2012). Molecular mechanisms of inner ear development. *Cold Spring Harb. Perspect. Biol.* 4:a008409. doi: 10.1101/cshperspect.a008409

Wu, S.-Y., and Chiang, C.-M. (2007). The double bromodomain-containing chromatin adaptor Brd4 and transcriptional regulation. *J. Biol. Chem.* 282, 13141–13145. doi: 10.1074/jbc.R700001200

Wu, T., Kamikawa, Y. F., and Donohoe, M. E. (2018). Brd4's bromodomains mediate histone H3 acetylation and chromatin remodeling in pluripotent cells through P300 and Brg1. *Cell Rep.* 25, 1756–1771. doi: 10.1016/J.CELREP.2018.10.003 doi: 10.1016/j.celrep.2018.10.003

Zhang, W., Prakash, C., Sum, C., Gong, Y., Li, Y., Kwok, J. J. T., et al. (2012). Bromodomain-containing protein 4 (BRD4) regulates RNA polymerase II serine 2 phosphorylation in human $CD4^+$ T cells. *J. Biol. Chem.* 287, 43137–43155. doi: 10.1074/jbc.M112.413047

**Conflict of Interest:** The authors declare that the research was conducted in the absence of any commercial or financial relationships that could be construed as a potential conflict of interest.

*Copyright © 2020 Kannan-Sundhari, Abad, Maloof, Ayad, Young, Liu and Walz. This is an open-access article distributed under the terms of the Creative Commons Attribution License (CC BY). The use, distribution or reproduction in other forums is permitted, provided the original author(s) and the copyright owner(s) are credited and that the original publication in this journal is cited, in accordance with accepted academic practice. No use, distribution or reproduction is permitted which does not comply with these terms.*

frontiers in Cell and Developmental Biology

ORIGINAL RESEARCH
published: 17 December 2020
doi: 10.3389/fcell.2020.604026

# Rbm24a Is Necessary for Hair Cell Development Through Regulating mRNA Stability in Zebrafish

*Yan Zhang[1], Yanfei Wang[1], Xuebo Yao[1], Changquan Wang[2], Fangyi Chen[2], Dong Liu[3], Ming Shao[1]* and Zhigang Xu[1,4]**

*[1] Shandong Provincial Key Laboratory of Animal Cells and Developmental Biology, School of Life Sciences, Shandong University, Qingdao, China, [2] Department of Biomedical Engineering, Southern University of Science and Technology, Shenzhen, China, [3] Key Laboratory of Neuroregeneration of Jiangsu and Ministry of Education, Co-Innovation Center of Neuroregeneration, School of Life Sciences, Nantong University, Nantong, China, [4] Shandong Provincial Collaborative Innovation Center of Cell Biology, Shandong Normal University, Jinan, China*

OPEN ACCESS

**Edited by:**
*Qingyin Zheng,*
*Case Western Reserve University, United States*

**Reviewed by:**
*Artur A. Indzhykulian, Massachusetts Eye and Ear Infirmary, Harvard Medical School, United States*
*Suk-Won Jin, Gwangju Institute of Science and Technology, South Korea*
*Shan Sun, Fudan University, China*

***Correspondence:**
*Ming Shao*
*shaoming@sdu.edu.cn*
*Zhigang Xu*
*xuzg@sdu.edu.cn*

**Specialty section:**
*This article was submitted to Cell Growth and Division, a section of the journal Frontiers in Cell and Developmental Biology*

**Received:** *08 September 2020*
**Accepted:** *01 December 2020*
**Published:** *17 December 2020*

**Citation:**
*Zhang Y, Wang Y, Yao X, Wang C, Chen F, Liu D, Shao M and Xu Z (2020) Rbm24a Is Necessary for Hair Cell Development Through Regulating mRNA Stability in Zebrafish. Front. Cell Dev. Biol. 8:604026. doi: 10.3389/fcell.2020.604026*

Hair cells in the inner ear and lateral lines are mechanosensitive receptor cells whose development and function are tightly regulated. Several transcription factors as well as splicing factors have been identified to play important roles in hair cell development, whereas the role of RNA stability in this process is poorly understood. In the present work, we report that RNA-binding motif protein 24a (Rbm24a) is indispensable for hair cell development in zebrafish. *Rbm24a* expression is detected in the inner ear as well as lateral line neuromasts. Albeit *rbm24a* deficient zebrafish do not survive beyond 9 days post fertilization (dpf) due to effects outside of the inner ear, *rbm24a* deficiency does not affect the early development of inner ear except for delayed otolith formation and semicircular canal fusion. However, hair cell development is severely affected and hair bundle is disorganized in *rbm24a* mutants. As a result, the auditory and vestibular function of *rbm24a* mutants are compromised. RNAseq analyses identified several Rbm24a-target mRNAs that are directly bound by Rbm24a and are dysregulated in *rbm24a* mutants. Among the identified Rbm24a-target genes, *lrrc23*, *dfna5b*, and *smpx* are particularly interesting as their dysregulation might contribute to the inner ear phenotypes in *rbm24a* mutants. In conclusion, our data suggest that Rbm24a affects hair cell development in zebrafish through regulating mRNA stability.

**Keywords: Rbm24a, hair cells, inner ear, lateral line, mRNA stability**

## INTRODUCTION

Hair cells are mechanosensitive sensory receptor cells in the inner ear and fish lateral line, characterized by the hairy-looking protrusions called hair bundles on their apical surface. The hair bundle of each hair cell consists of dozens to hundreds of actin-based stereocilia and one tubulin-based kinocilium. The stereocilia are organized into several rows of increasing height, with the mechano-electrical transduction (MET) channels localized at the tips of shorter row stereocilia (Beurg et al., 2009). The kinocilium is juxtaposed next to the tallest row stereocilia and plays an essential role in the development of hair bundle (Jones et al., 2008). As highly differentiated sensory

receptor cells, hair cells are very sensitive to genetic mutations and environmental assaults, and deficits in hair cell development or function are the main reasons for hearing loss (Müller and Barr-Gillespie, 2015). Several key transcription factors such as Atoh1, Pou4f3, Gfi1, and Rfxs have been identified to play important roles in hair cell development (Erkman et al., 1996; Bermingham et al., 1999; Wallis et al., 2003; Elkon et al., 2015). At the post-transcriptional level, alternative splicing regulated by Srrm4, Sfswap, and Esrp1 has been shown to be involved in hair cell development (Nakano et al., 2012; Moayedi et al., 2014; Rohacek et al., 2017). However, the role of RNA stability regulation in hair cell development/function is less understood.

RNA-binding proteins (RBPs) play pivotal roles in post-transcriptional RNA processing, from pre-mRNA alternative splicing to mRNA stability, localization and translation (Hentze et al., 2018). Dysfunction of RBPs is associated with various types of developmental diseases (Brinegar and Cooper, 2016). RBPs usually bind to target RNAs through their so-called RNA-recognition motifs (RRMs). RNA-binding motif protein 24 (Rbm24) is an RBP that contains a single RRM and an alanine-rich low-complexity region (Fetka et al., 2000). It regulates alternative splicing through binding to the intronic splicing enhancer (ISE) sites in its target pre-mRNAs (Yang et al., 2014; Ito et al., 2016; Zhang et al., 2016; Lin et al., 2018; van den Hoogenhof et al., 2018; Liu et al., 2019). Moreover, Rbm24 regulates the stability or translation of its target mRNAs through binding to AU/U-rich elements (AREs; Jiang Y. et al., 2014; Xu et al., 2014; Zhang et al., 2018).

*In situ* hybridization results reveal that *Rbm24* is expressed in the otic vesicle during early embryonic development in zebrafish, frog, chick, and mouse (Fetka et al., 2000; Poon et al., 2012; Grifone et al., 2014; Maragh et al., 2014). Rbm24 is also expressed during later developmental stages of mouse inner ear (Cai et al., 2015; Grifone et al., 2018). Immunostaining and *in situ* hybridization reveal that Rbm24 is specifically expressed in the hair cells of embryonic and neonatal mice (Cai et al., 2015; Grifone et al., 2018). *Rbm24* expression in the developing mouse hair cells is further supported by the transcriptome data (Scheffer et al., 2015; Shen et al., 2015). The specific expression of Rbm24 in the otic vesicle during early development as well as in the hair cells at a later developmental stage suggests that Rbm24 might play important roles in the inner ear.

In the present work, we investigate the role of Rbm24 in hair cells using the zebrafish as a model. Zebrafish sensory hair cells are located in the five sensory epithelia (two maculae and three cristae) of the otic vesicle and the two lateral line systems (anterior lateral lines (aLL) and posterior lateral lines (pLL)) at the body surface (Nicolson, 2005). Each of the anterior and posterior macula is associated with a calcium carbonate-based otolith, and their hair cells sense sound and linear acceleration. Hair cells in the anterior, lateral and posterior cristae sense angular acceleration, whereas the lateral line hair cells sense water movement. Our present data suggest that inactivation of the *rbm24a* gene affects the development of hair cells in both the otic vesicle and the lateral line systems. Further investigations show that Rbm24a affects hair cell development through regulating the stability of its target mRNAs.

# MATERIALS AND METHODS

## Zebrafish

All zebrafish animal procedures were carried out following the institutional guidelines approved by the Animal Ethics Committee of Shandong University School of Life Sciences. The *rbm24a* mutant zebrafish was generated using TALENs (transcription activator-like effector nucleases) as described previously (Shao et al., 2020). The *brn3c*:GFP transgenic zebrafish were generated as described previously (He et al., 2017).

## *In situ* Hybridization

Whole-mount *in situ* hybridization was carried out according to a standard protocol (Thisse and Thisse, 2008). For each target gene, a corresponding cDNA fragment was cloned into a pEASY Blunt Zero Cloning vector (Tiangen) and used as DNA template for synthesis of antisense RNA probe. The probes were labeled with digoxygenin-labeled rNTP mix (Roche Diagnostics), and NBT/BCIP was used as substrate. The probes for *dlx3*, *pax2a*, and *lrrc23* are the same as reported previously (Han et al., 2018; Xing et al., 2018). Primers for other probes are listed in **Supplementary Table 1**.

## Startle Response Measurement

Startle response was measured as described previously (Wang et al., 2017). Briefly, 10–20 zebrafish larvae at 5 dpf were maintained in an 8-cm Petri dish containing a thin layer (2 mm) of water. Tone bursts of 400 Hz at different sound intensity were delivered to the Petri dish through a mini vibrator (QY50R-Z). The movement of each larva was recorded using a digital camera (Basler acA1300–200 μm) at 120-frame per second (fps) and analyzed using a customized software developed in MATLAB (MathWorks, MA, United States). The distance of larvae's C-shape movement upon sound stimulation was used as a measure of its auditory startle response.

## Vestibular Head Tilt Response Measurement

Vestibular head tilt response was measured as described previously (Sun et al., 2018). Briefly, individual zebrafish larva at 5 dpf was placed in a customized holder, where its tail was glued to immobilize the fish. The head of the fish was merged in the water for comfortable accommodation. The holder was then placed on a rotary platform with the fish head-up. The rotary platform was driven by a stepper motor (model TSM17Q-3AG, MOONS', Shanghai, China) running in a sinusoidal profile of ±75 degrees around the vertical location. Larval eye movement stimulated by rotation was recorded using a monochrome IR camera (Point Gray, Richmond, Canada) at 30 fps and analyzed using a customized imaging analysis program written in MATLAB (Mathworks). The ratio of the maximum projection area change during eye movement to the maximum projection area of the eye

in the larval frontal plane was used as a measure of the vestibular head tilt response.

## FM1-43FX Uptake Assay

Zebrafish larvae at 3 dpf were treated with 1.2 μM FM1-43FX (Molecular Probes, Invitrogen) in embryo medium for 30 s. After rinsing three times in fresh embryo medium, the larvae were anesthetized with 0.17 mg/mL$^{-1}$ Tricaine (MS-222, Sigma) and the labeled lateral line hair cells were visualized using a florescent microscope (Olympus IX53).

## Paraffin Section and HE Staining

Embryos were anesthetized with 0.17 mg/mL$^{-1}$ Tricaine (MS-222, Sigma), then fixed in 4% paraformaldehyde (PFA) at 4°C overnight. After that, embryos were embedded in paraffin and sliced into 5 μm-thick sections. Hematoxylin (Solarbio, H8070) and Eosin Y (Solarbio, G1100) staining was performed subsequently according to the manufacturer's user guide. Images were taken using a light microscope (Leica DM2000).

## Confocal Microscopy

Embryos in *brn3c*:GFP transgenic background were anesthetized with 0.17 mg/mL$^{-1}$ Tricaine (MS-222, Sigma), followed by fixation in 4% PFA at 4°C overnight. After washing with phosphate-buffered saline with Tween-20 (PBST), the samples were incubated with phalloidin (4 μg/ml, YEASEN, 40734ES80) at 37°C for 15 min. The samples were washed with PBST again, then mounted in 1% low-melting agarose. Images were taken using a confocal microscope (Zeiss, LSM700), and Z-stack projections were obtained by using the z-projection function. Image volumes were acquired at 0.5-μm intervals along the *z*-axis. Crista hair cells were imaged with a 0.95NA/20× Kort M27 objective lens. Neuromast hair cells were imaged with a 0.95NA/40× Kort M27 objective lens. Higher resolution images of crista and macula hair cells were taken with a 0.95NA/63× Kort M27 objective lens. The *x-y* pixel size is 1024 × 1024 for all images.

## Scanning Electronic Microscopy

Scanning electronic microscopy (SEM) was performed as previously described with modifications (Du et al., 2020). Briefly, embryos after 100% epiboly were treated with 0.06–0.08 g/L PTU (P110661, Aladdin Industrial Corporation, China) to block pigment synthesis. Then larvae at 72 hpf were anesthetized with 0.17 mg/mL$^{-1}$ Tricaine (MS-222, Sigma) for 30 s and fixed with 2.5% glutaraldehyde at 4°C over night, followed by post-fixation with 1% osmium tetroxide at 4°C for 2 h. After dehydration in ethanol, samples were critically point dried using a Leica EM CPD300 (Leica, Germany), then mounted and sputter coated with 10-nm platinum using a Cressington 108 sputter coater (Cressington, United Kingdom). Images were taken using a Quanta250 field-emission scanning electron microscope (FEI, Netherlands) with a beam strength of 3 kV.

## RNAseq and RT-PCR

RNAseq analysis was performed by Genewiz (Suzhou, China) following the manufacturer's protocols. Briefly, total RNAs were extracted from the otic vesicles of zebrafish larvae at 34 hpf (3 samples from wild-type and 3 samples from *rbm24a* mutants) using TRIzol reagent (Invitrogen), then mRNAs were enriched using the Poly(A) mRNA Magnetic Isolation Module (NEB). After mRNA fragmentation and cDNA synthesis, cDNA libraries were constructed using Ultra RNA Library Prep Kit for Illumina (NEB), followed by purification using Agencourt AMPure XP beads (Beckman) and quantification using Agilent 2100 (Agilent Technologies). The libraries were then multiplexed and clustered, and 150 bp paired-end sequencing was performed on Illumina HiSeq 2000. The sequencing results were filtered using Cutadapt and aligned with reference genome using Hisat2. Differential expression was analyzed using Htseq and DESeq2, and differential alternative splicing was analyzed using ASprofile and String Tie. RT-PCR and qPCR were then performed to confirm the sequencing results using primers specific for candidate genes (**Supplementary Table 2**).

## RNA Immunoprecipitation

RNA immunoprecipitation (RIP) analysis was performed as described previously (Li et al., 2020). Briefly, HEK293T cells were transfected with expression vectors using LipoMax transfection reagents (Sudgen, Cat. No. 32012) to express Rbm24a-Myc together with its target mRNAs. The transfected cells were lysed in lysis buffer containing 100 mM KCl, 5 mM $MgCl_2$, 10 mM HEPES-NaOH, 0.5% NP-40, 1 mM DTT, 200 units/mL RNase inhibitor (Takara, Cat. No. 2313A), and EDTA-free protease inhibitor cocktail (Sigma-Aldrich, Cat. No. S8830). After centrifugation, the supernatant was collected and incubated with immobilized anti-Myc antibody (Sigma-Aldrich, Cat. No. E6654). The immunoprecipitated RNA was used as template for RT-PCR analysis using specific primers for Rbm24a-target mRNAs (**Supplementary Table 3**).

## Western Blot

The coding sequence (CDS) of *rbm24a* with or without the 8-bp deletion was inserted into modified pEGFP-N2 vector with EGFP-CDS replaced by Myc-CDS. HEK293T cells were transfected with expression vectors using LipoMax transfection reagents (Sudgen, Cat. No. 32012). 24 h after transfection, cells were lysed in ice-cold lysis buffer containing 150 mM NaCl, 50 mM Tris at pH 7.5, 1% (vol/vol) Triton X-100, 1 mM PMSF, and 1 × protease inhibitor cocktail (Roche). The supernatant was then collected after centrifugation and separated by polyacrylamide gel electrophoresis (PAGE), then transferred to PVDF membrane. After blocking in TBS (20 mM Tris–HCl, 150 mM NaCl) containing 5% non-fat dry milk and 0.05% Tween-20, the membrane was incubated with anti-Myc antibody (Abclonal, Cat. No. AE010) or anti β-Actin antibody (Abmart, Cat. No. P30002) at 4°C overnight, followed by incubation with HRP-conjugated secondary antibody (Bio-Rad, Cat. No. 170-6515 and 170-6516) at room temperature for an hour. The signals were detected with the ECL system (Thermo Fisher Scientific).

## Statistical Analysis

Each experiment was repeated at least three times. Student's *t*-test was used to determine the statistical significance, and $p < 0.05$ was considered statistically significant. Data were shown as means ± SEM.

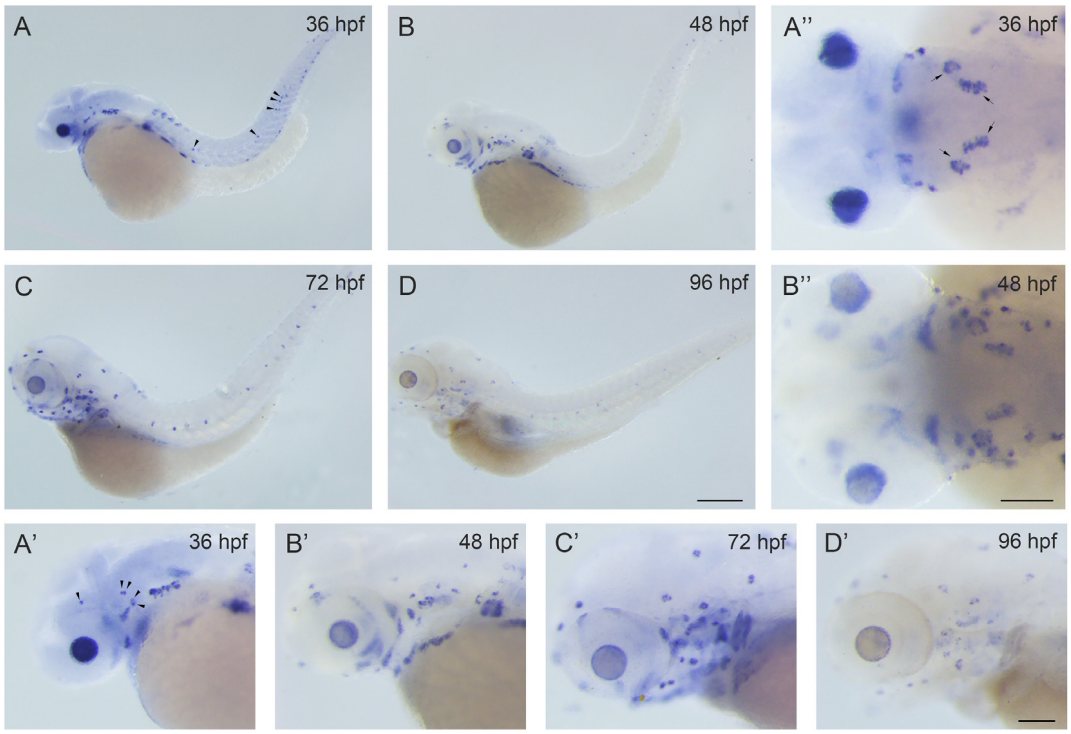


**FIGURE 1 |** *Rbm24a* is expressed in the otic vesicles and lateral line neuromasts of the zebrafish. Expression pattern of *rbm24a* during development was examined by performing *in situ* hybridization of zebrafish embryos at 36 hpf **(A–A")**, 48 hpf **(B–B")**, 72 hpf **(C,C')**, and 96 hpf **(D,D')**. Otic vesicles are indicated with arrows, and lateral line neuromasts are indicated with arrowheads. Scale bars, 0.25 mm in **(A–D)**, 0.1 mm in **(A'–D')** and **(A",B")**.

# RESULTS

## *Rbm24a* Is Expressed in the Inner Ear and Lateral Line Neuromasts

There are two *rbm24* homologs in the zebrafish, *rbm24a* and *rbm24b*. *Rbm24a* shows higher sequence homology with mammalian *Rbm24* compared to *rbm24b*. At the protein level, the similarity of mouse Rbm24 to zebrafish Rbm24a and Rbm24b is 87% and 72%, respectively. Meanwhile, *rbm24a* has been detected in the otic vesicles, whereas *rbm24b* has not (Poon et al., 2012; Maragh et al., 2014). Hence we focus on *rbm24a* in the present study. We first examined the spatial-temporal expression pattern of *rbm24a* by performing *in situ* hybridization. The results show that *rbm24a* transcripts could be readily detected in the otic vesicle and lateral line neuromasts at 36 hours post fertilization (hpf; **Figures 1A,A',A"**). *Rbm24a* expression persists at 48 hpf and 72 hpf (**Figures 1B–C'**). By 96 hpf, *rbm24a* expression is still present in the otic vesicle and lateral lines (**Figures 1D,D'**). This specific expression pattern suggests that *rbm24a* might play an important role in the development of inner ear and lateral line neuromasts.

## *Rbm24a* Deficiency Affects Hair Cell Function

We investigated the function of *rbm24a* in hair cells using a *rbm24a* mutant zebrafish line, which contains a deletion of 8 base pairs (bp) in exon 1 of the *rbm24a* gene (Shao et al., 2020; **Supplementary Figure 1A**). The 8 bp-deletion will result in premature translational termination, giving rise to a truncated Rbm24a protein of only 28 amino acids (aa) instead of the full-length 230 aa (**Supplementary Figure 1B**). RT-PCR and *in situ* hybridization results show that *rbm24a* mRNA is still present in the homozygous *rbm24a* mutants (*rbm24a*$^{-/-}$; **Supplementary Figures 1C,D**). There are several downstream AUG codons in *rbm24a* CDS, among which M59 is the first one (**Supplementary Figure 1B**). Translation started from these AUG codons in the mutant *rbm24a* mRNA might produce truncated Rbm24a proteins. Because Rbm24a-specific antibodies are not available, we expressed wild type or mutant Rbm24a with a Myc tag at the C-terminus in cultured HEK293T cells and examined their expression by performing western blot with anti-Myc antibody. From the cells expressing wild-type Rbm24a, we detected a band with a molecular weight of around 30 kDa. However, from the cells expressing mutant Rbm24a, we detected a band with a molecular weight of lower than 25 kDa, possibly corresponding to a truncated Rbm24a protein started from M59 (**Supplementary Figure 1E**). This mutant Rbm24a lacks most part of the RRM domain, suggesting that it is not functional. Consistent with this hypothesis, heterozygous *rbm24a* mutants are morphologically and behaviorally indistinguishable from wild type zebrafish, whereas homozygous *rbm24a* mutants suffer from severe heart defects and do not survive beyond 9 days post fertilization (dpf; **Supplementary Figure 1F**). Moreover, the body length of

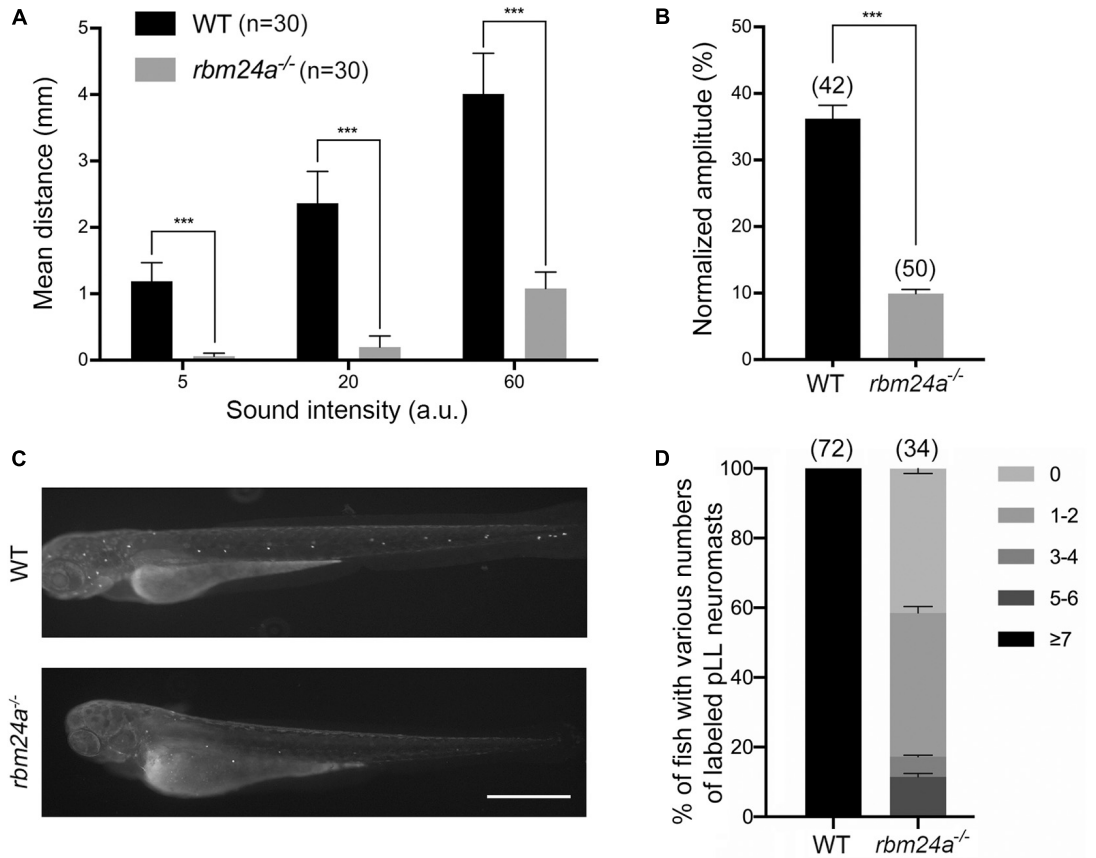


**FIGURE 2 |** Hair cell function is affected in *rbm24a* mutants. **(A)** The auditory function of zebrafish larvae at 5 dpf is evaluated by examining the startle response to various sound intensity. ***$p < 0.001$. **(B)** The vestibular function of zebrafish larvae at 5 dpf is evaluated by vestibular head tilt response measurement. ***$p < 0.001$. **(C)** The function of hair cells is evaluated by performing FM1-43FX uptake experiment at 3 dpf. Scale bar, 0.5 mm. **(D)** The numbers of labeled pLL neuromasts per larvae are calculated according to the results from **(C)**. *P* value < 0.001. The numbers of larvae for each group are indicated in brackets.

*rbm24a* mutants is slightly shorter than that of wild type (wild type at 48 hpf, 3.19 ± 0.02 mm; *rbm24a* mutant at 48 hpf, 2.85 ± 0.01 mm; wild type at 96 hpf, 3.55 ± 0.03 mm; *rbm24a* mutant at 96 hpf, 3.17 ± 0.02 mm. For each genotype, $n = 18$. *P* value < 0.000001).

We first evaluated the auditory function of mutant zebrafish larvae by measuring startle response (Kimmel et al., 1974; Zeddies and Fay, 2005). Various levels of sound stimulus were given to the fish larvae at 5 dpf, and the moving distance in a characteristic C-shape motion of the larvae was used as a measure of its auditory startle response. Compared to control wild-type larvae, *rbm24a* mutants show significant reduced startle response at each sound level, suggesting that *rbm24a* deficiency affects the auditory function of zebrafish (**Figure 2A**). We also evaluated the vestibular function of the mutants by measuring vestibular head tilt response (Mo et al., 2010). In this experiment, eye movement of 5 dpf larvae evoked by the rotational motion was used as a measure of the vestibular function. The results show that compared to wild-type control, *rbm24a* mutants show significantly reduced vestibular head tilt response, suggesting that *rbm24a* deficiency affects the vestibular function of zebrafish (**Figure 2B**).

Considering that *rbm24a* deficiency might affect muscle function, which could in turn affect the performance of the larvae in startle response and vestibular head tilt response, we then directly examined the functional integrity of hair cells by performing FM1-43FX uptake experiment. Florescent dye FM1-43 or its fixable analog FM1-43FX can enter hair cells through the MET channels, which provides an indicator of the functional integrity of hair cells (Gale et al., 2001; Meyers et al., 2003). The results show that FM1-43FX uptake by both aLL and pLL neuromasts is significantly decreased in 3 dpf *rbm24a* mutant larvae (**Figures 2C,D**). Taken together, our data suggest that hair cell function is severely affected in *rbm24a* mutant zebrafish.

## Early Inner Ear Development Is Largely Unaffected by *rbm24a* Deficiency

Given the expression of *rbm24a* in the otic vesicles during early embryonic development, we wonder whether *rbm24a* deficiency affects early inner ear development. The morphology of otic vesicles was examined by performing hematoxylin-eosin (HE) staining, which does not reveal any significant difference between wild-type control and *rbm24a* mutants

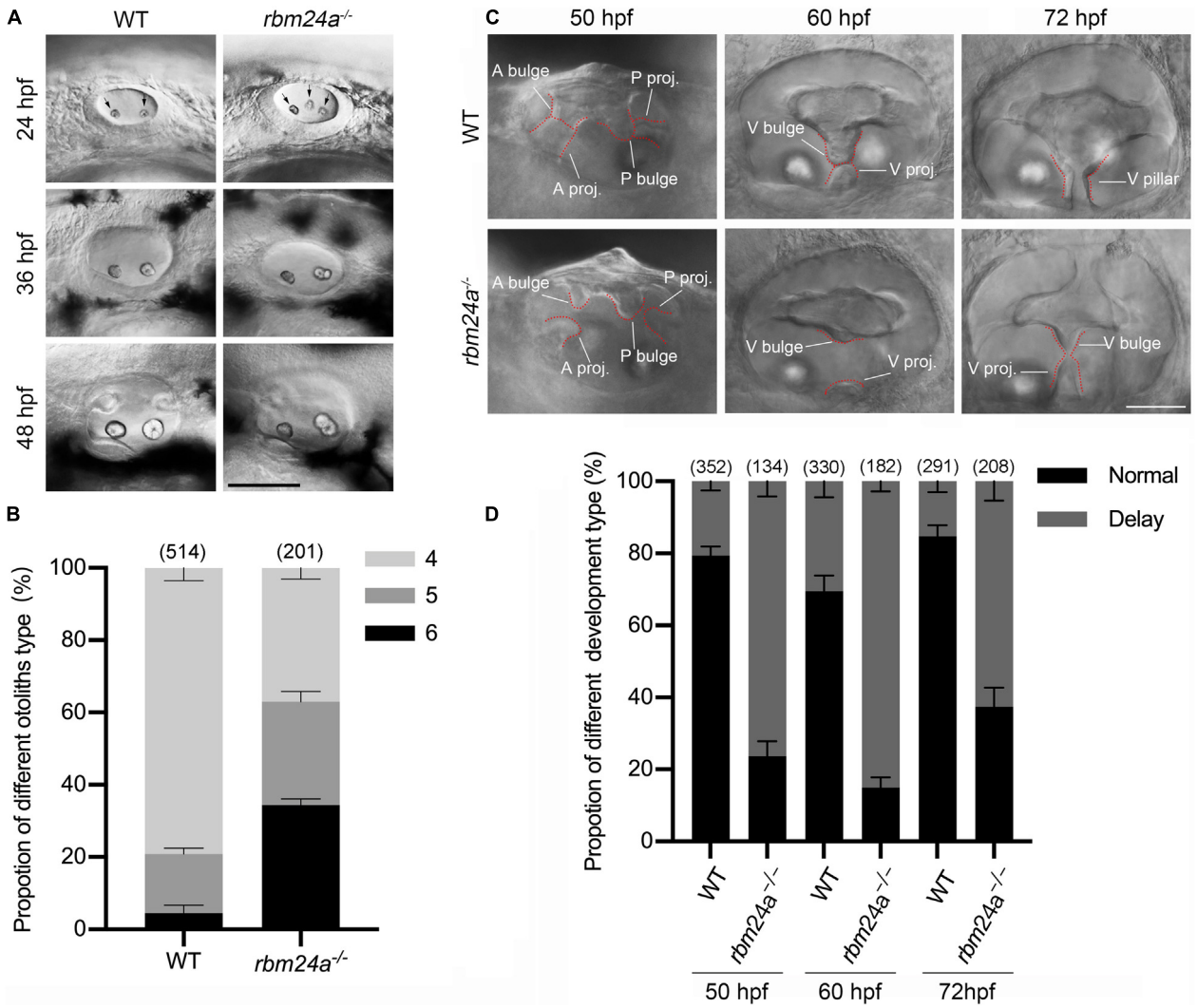


**FIGURE 3 |** Otolith formation and semicircular canal fusion are delayed in *rbm24a* mutants. **(A)** Otolith formation in zebrafish larvae is examined using a light microscope at 24, 36, and 48 hpf as indicated. Otoliths are indicated with arrows. Scale bar, 0.1 mm. **(B)** The numbers of otic vesicles per larvae at 24 hpf are calculated according to the results from **(A)**. *P* values are 0.000833 (larvae with 4 otoliths), 0.020678 (larvae with 5 otoliths), and 0.00044 (larvae with 6 otoliths). **(C)** Fusion of the semicircular canals is examined using a light microscope at 50, 60, and 72 hpf as indicated. Scale bar, 50 μm. **(D)** The numbers of larvae with normal or delayed semicircular canal fusion are calculated according to the results from **(C)**. *P* values are 0.000001 (50 hpf), 0.00005 (60 hpf), and 0.000034 (72 hpf). The numbers of larvae for each genotype are indicated in brackets. A bulge, anterior bulge; A proj., anterior projection; P bulge, posterior bulge; P proj., posterior projection; V bulge, ventral bulge; V proj., ventral projection; and V pillar, ventral pillar.

(**Supplementary Figures 2A–C**). However, examination with a light microscope shows that otolith formation in *rbm24a* mutants is delayed during early development. In each otic vesicle of early zebrafish embryo, otolith precursor particles are first distributed throughout the otic vesicle lumen, then tethered to form two otoliths at the otic vesicle poles, which are readily detectable by 24 hpf (Riley et al., 1997). Consistently, our data show that at 24 hpf, most wild-type embryos contain 4 otoliths (2 for each otic vesicle). In contrast, less than 40% of *rbm24a* mutants contain 4 otoliths, and all the others contain 5 or 6 otoliths (**Figures 3A,B**). The ectopic otolith gradually fuses to the regular posterior otolith, and there is no visible difference between the otoliths of the mutant and control larvae after 48 hpf (**Figure 3A**).

Moreover, delayed fusion of the semicircular canals is observed in *rbm24a* mutant larvae. The development of semicircular canals begins with the formation of three protrusions (the anterior, posterior, and lateral projections) from the otic vesicle between 42 and 48 hpf (Waterman and Bell, 1984). Afterward, the lateral projection bifurcates into the anterior and posterior bulges, which then fuse with the anterior and posterior projections to form the anterior and posterior pillars, respectively. Finally, the lateral projection gives rise to a ventral bulge, which then fuses with the newly developed ventral projection to form the ventral pillar by 72 hpf (Waterman and Bell, 1984). We found that in most wild-type larvae at 50 hpf, the anterior and posterior projections fuse with the anterior and

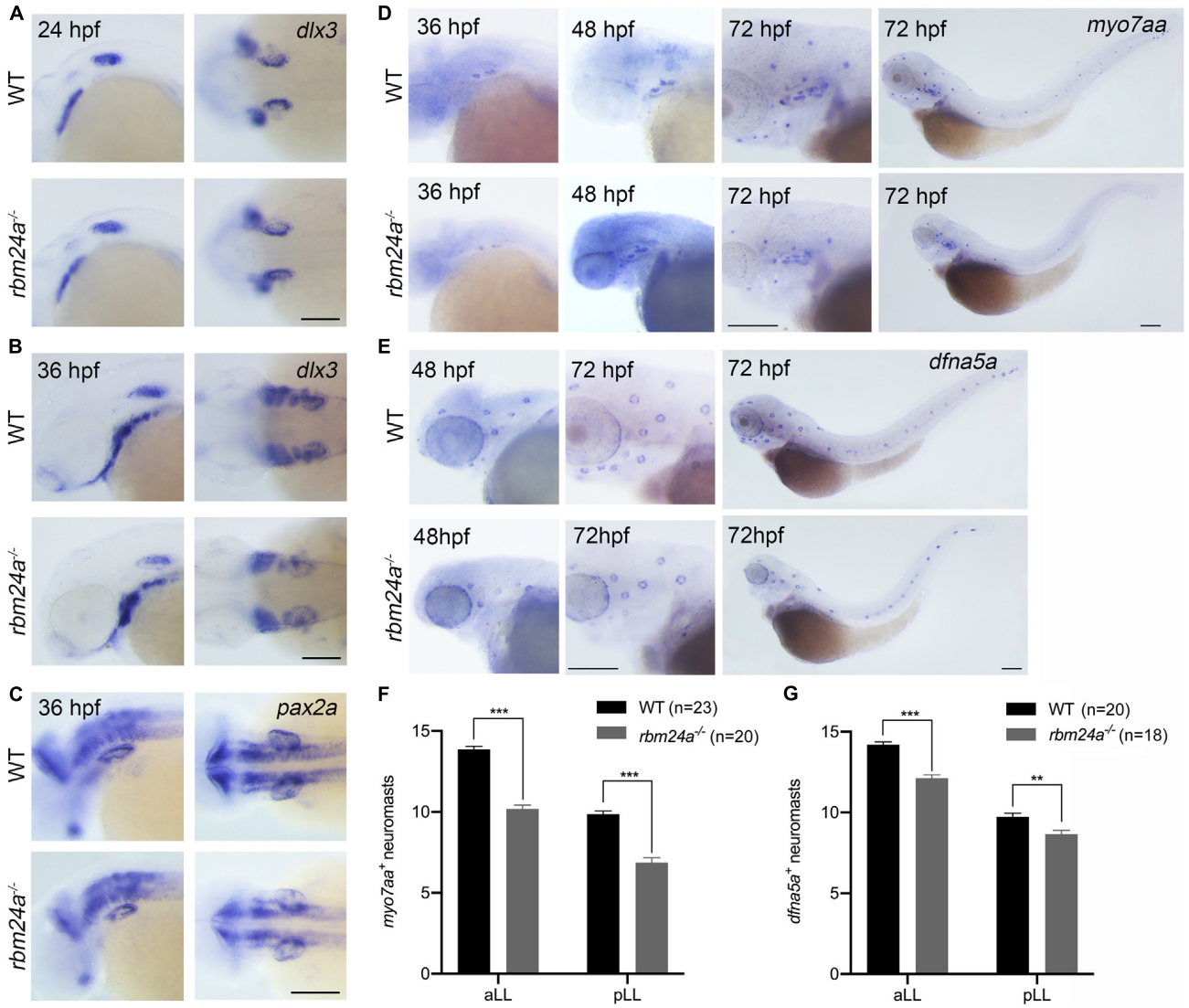


**FIGURE 4 |** Early inner ear development is largely unaffected in *rbm24a* mutants. Inner ear development is examined by performing *in situ* hybridization of *dlx3* **(A,B)**, *pax2a* **(C)**, *myo7aa* **(D)**, and *dfna5a* **(E)** at different developmental stages as indicated. **(F)** The numbers of *myo7aa*$^{+}$ neuromasts are calculated according to the results from **(D)**. **(G)** The numbers of *dfna5a*$^{+}$ neuromasts are calculated according to the results from **(E)**. The numbers of larvae for each group are indicated in brackets. Scale bars, 0.2 mm. $^{**}p < 0.01$; $^{***}p < 0.001$.

posterior bulges, respectively, which is not observed in most *rbm24a* mutant larvae until 60 hpf (**Figures 3C,D**). Similarly, the ventral projection is fused with the ventral bulge in most wild-type larvae at 60 hpf, but not in most *rbm24a* mutant larvae until 72 hpf (**Figures 3C,D**).

We then performed *in situ* hybridization to examine the expression of early otic vesicle markers in *rbm24a* mutants. *Dlx3* is expressed in the otic vesicle at an early developmental stage (Ekker et al., 1992). Our results show that *dlx3* expression in the otic vesicles of *rbm24a* mutant larvae is comparable to that of control at 24 and 36 hpf (**Figures 4A,B**). Similar results were obtained for another early otic vesicle marker, *pax2a* (Pfeffer et al., 1998; **Figure 4C**). Taken together, our present data suggest that early inner ear development is largely unaffected by *rbm24a* deficiency except for delayed otolith formation and semicircular canal fusion.

## *Rbm24a* Deficiency Leads to Reduced Hair Cell Number and Disorganized Hair Bundle

We moved on to examine the hair cells in *rbm24a* mutants by performing *in situ* hybridization of a hair cell marker *myo7aa* (Ernest et al., 2000). At 36 and 48 hpf, *myo7aa* is expressed in the otic vesicles of *rbm24a* mutant larvae similarly to that in controls (**Figure 4D**). By 72 hpf, robust expression of *myo7aa* in aLL and pLL neuromasts is detected in wild-type larvae; however, the number of *myo7aa*$^{+}$ neuromasts is significantly

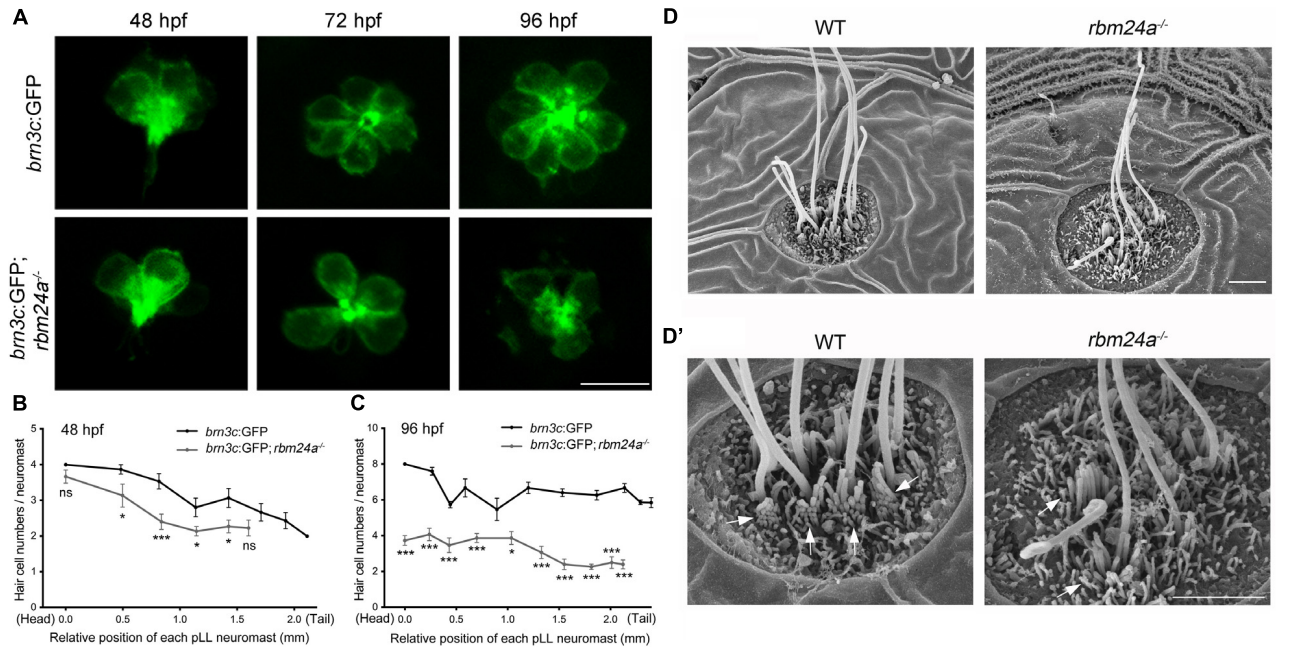


**FIGURE 5 |** Development of pLL hair cells is affected in *rbm24a* mutants. **(A)** Confocal microscopic imaging analysis of pLL neuromasts in wild-type or *rbm24a* mutant *brn3c*:GFP line at different developmental stages as indicated. **(B,C)** The numbers of GFP-positive hair cells of each pLL neuromasts at 48 and 96 hpf are calculated according to the results from **(A)**. The numbers of larvae for each group is 15. **(D,D')** Hair bundles of pLL neuromasts at 72 hpf are examined using SEM. Stereocilia are indicated with arrows. Scale bars, 10 μm in **(A)**, 2 μm in **(D,D')**. ns, not significant; $^{*}p < 0.05$; and $^{***}p < 0.001$.

decreased in *rbm24a* mutants (**Figures 4D,F**). The reduced expression of *myo7aa* in lateral lines of *rbm24a* mutants suggest that hair cell development is affected by *rbm24a* deficiency. We also performed *in situ* hybridization of *dfna5a*, a gene that is specifically expressed in the lateral line neuromasts (Jiang L. et al., 2014). The results show that the number of *dfna5a*$^{+}$ neuromasts is slightly reduced in *rbm24a* mutants (**Figures 4E,G**), which could be explained by the shortened body length.

To visualize the hair cells directly, we crossed *rbm24a* mutant zebrafish with *brn3c*:GFP transgenic zebrafish, which express GFP in the hair cells of both inner ear and lateral lines. The numbers of GFP-positive hair cells in each pLL neuromast are similar in *rbm24a* mutants and wild-type controls at 48 hpf (**Figures 5A,B**). However, by 72 hpf, the hair cell numbers per pLL neuromast in *rbm24a* mutants are less than that in controls, which becomes more obvious at 96 hpf (**Figures 5A,C**). At 96 hpf, there are 6–8 hair cells per pLL neuromast in wild-type controls, whereas no more than 4 hair cells per neuromast could be found in *rbm24a* mutants (**Figures 5A,C**). Meanwhile, similar to the *in situ* hybridization results of *dfna5a*, the total numbers of pLL neuromasts in *rbm24a* mutants are slightly less than that in controls (**Figures 5B,C**). Decreased hair cell numbers are also observed in the maculae and the cristae of the inner ear in *rbm24a* mutants (**Supplementary Figures 3**, **4**).

Scanning electrical microscopy was then employed to examine the morphology of hair bundles of the mutants. The results show that the stereocilia of pLL hair cells in wild type zebrafish are organized into a nice staircase pattern, which is largely lost in *rbm24a* mutants (**Figures 5D,D'**). To examine the hair bundles of inner ear hair cells, we used phalloidin to stain the F-actin core of stereocilia. Meanwhile, stereocilia and kinocilia could also be visualized by the strong GFP fluorescence in *brn3c*:GFP zebrafish. The results show that at 72 hpf, the length of hair cell stereocilia in *rbm24a* mutant crista is decreased to about half of that in wild-type control (**Figures 6A,B**). The length of kinocilia is also decreased in *rbm24a* mutants although to a lesser extent (**Figure 6C**). This phenotype remains in *rbm24a* mutants at 96 hpf (**Figures 6D–F**). Similar results are also observed in the macula (**Supplementary Figures 5A–D**). Taken together, our data suggest that *rbm24a* deficiency leads to reduced hair cell number and disorganized hair bundle.

## *Rbm24a* Deficiency Leads to Dysregulated Expression of Several Inner Ear-Expressed Genes

Previously, we performed RNA sequencing (RNAseq) of *rbm24a* mutant embryos to analyze the Rbm24a-regulated mRNAs (Shao et al., 2020). In the present work, we also prepared polyadenylated mRNA samples from the otic vesicle of *rbm24a* mutants at 34 hpf and performed RNAseq analysis. Neither of the analyses reveals meaningful differences in alternative splicing events between *rbm24a* mutants and controls. However, the RNAseq results reveal that the mRNA level of several genes such as *lrrc23*, *smpx*, *casp6a*, and *dfna5b* is significantly decreased in the *rbm24a* mutants (**Figure 7A**). On the other hand, the mRNA level of a few genes such as *cyp2aa7* and *dnah7* is upregulated in the *rbm24a* mutants (**Figure 7A**). The dysregulation was further validated

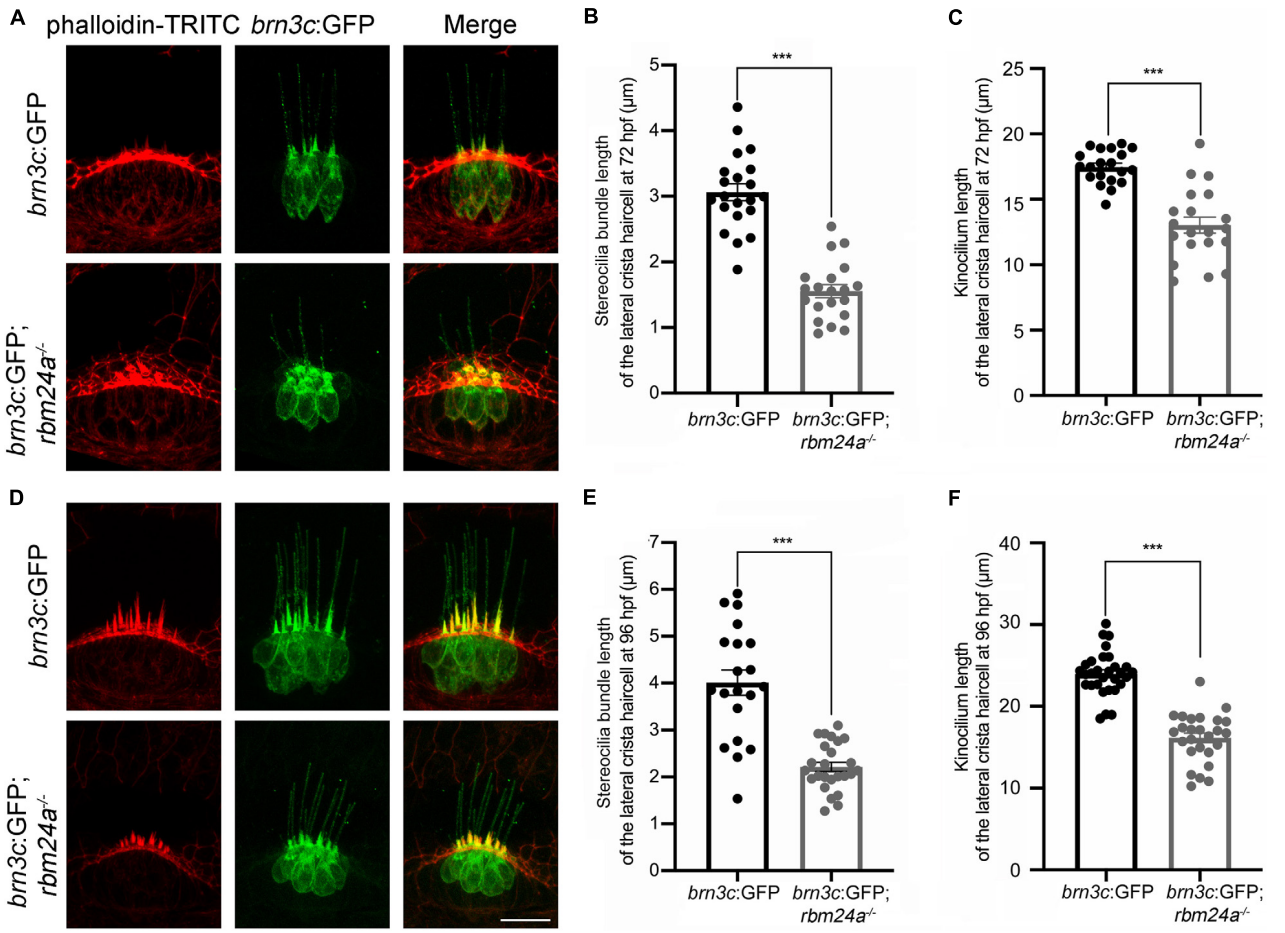


**FIGURE 6 |** Development of lateral crista hair cells is affected in *rbm24a* mutants. Confocal microscopic imaging analysis of *rbm24a* mutant *brn3c*:GFP line at 72 hpf **(A)** and 96 hpf **(D)**. **(B,E)** Stereocilia length is calculated according to the results from **(A,D)**, respectively. **(C,F)** Kinocilia length is calculated according to the results from **(A,D)**, respectively. For stereocilia length measurement at 72 hpf, *brn3c*:GFP, $n = 21$ (from 3 larvae); *brn3c*:GFP;*rbm24a*$^{-/-}$, $n = 20$ (from 4 larvae). For stereocilia length measurement at 96 hpf, *brn3c*:GFP, $n = 20$ (from 3 larvae); *brn3c*:GFP;*rbm24a*$^{-/-}$, $n = 25$ (from 4 larvae). For kinocilia length measurement at 72 hpf, *brn3c*:GFP, $n = 20$ (from 3 larvae); *brn3c*:GFP;*rbm24a*$^{-/-}$, $n = 20$ (from 4 larvae). For kinocilia length measurement at 96 hpf, *brn3c*:GFP, $n = 30$ (from 3 larvae); *brn3c*:GFP;*rbm24a*$^{-/-}$, $n = 26$ (from 3 larvae). Scale bar, 10 μm. ***$p < 0.001$.

by performing RT-PCR and qPCR (**Figures 7B,C**). Furthermore, RNA immunoprecipitation (RIP) experiments confirm that Rbm24a directly binds to these target mRNAs (**Figure 7D**).

We then performed *in situ* hybridization to analyze the expression pattern of these Rbm24a-target mRNAs. The results show that the examined mRNAs are all expressed in the otic vesicles of wild-type controls (**Figures 8A,B**). Meanwhile, the expression of *dfna5b*, *epcam*, *casp6a*, *lrrc23*, *enosf1*, and *smpx* is decreased in the *rbm24a* mutants, whereas the expression of *dnah7* is increased in the mutants, which is consistent with the RNAseq, RT-PCR, and qPCR results (**Figures 8A,B**).

## DISCUSSION

The physiological role of Rbm24 has been intensively investigated in the heart and skeletal muscles. *Rbm24* knockdown in C2C12 cells, *Xenopus*, or chick somatic myogenic progenitor cells affects myogenic differentiation (Miyamoto et al., 2009; Li et al., 2010; Grifone et al., 2014). *Rbm24* knockdown in zebrafish leads to deficits in cardiovascular development and somitogenesis (Maragh et al., 2011, 2014; Poon et al., 2012). Furthermore, inactivation of *Rbm24* in mice disrupts cardiac development through activating aberrant p53-dependent apoptosis (Yang et al., 2014; Zhang et al., 2018). Recently, we and others reported that Rbm24a plays pivotal roles in eye development of zebrafish through regulating mRNA stability and translation efficiency (Dash et al., 2020; Shao et al., 2020). In the present work, we report that Rbm24a is indispensable for hair cell development through regulating mRNA stability in zebrafish.

Expression of *rbm24a* could be detected in the otic visicles during early embryonic development. However, the morphology of otic visicle is largely unaffected in *rbm24a* mutants, suggesting that Rbm24a is dispensable for early inner ear development in the zebrafish. Nevertheless, otolith formation and semicircular

**A**

**Dysregulated genes in the inner ear of *rbm24a* mutants identified from RNAseq**

| | |
|---|---|
| Downregulated | *casp6a* |
| | *dfna5b* |
| | *epcam* |
| | *enosf1* |
| | *gfpt1* |
| | *lrrc23* |
| | *ptprc* |
| | *si:ch211-108d22.2* |
| | *si:dkey-271j15.3* |
| | *smpx** |
| Upregulated | *cyp2aa7* |
| | *dnah7* |

*Identified from RNAseq of whole embryos

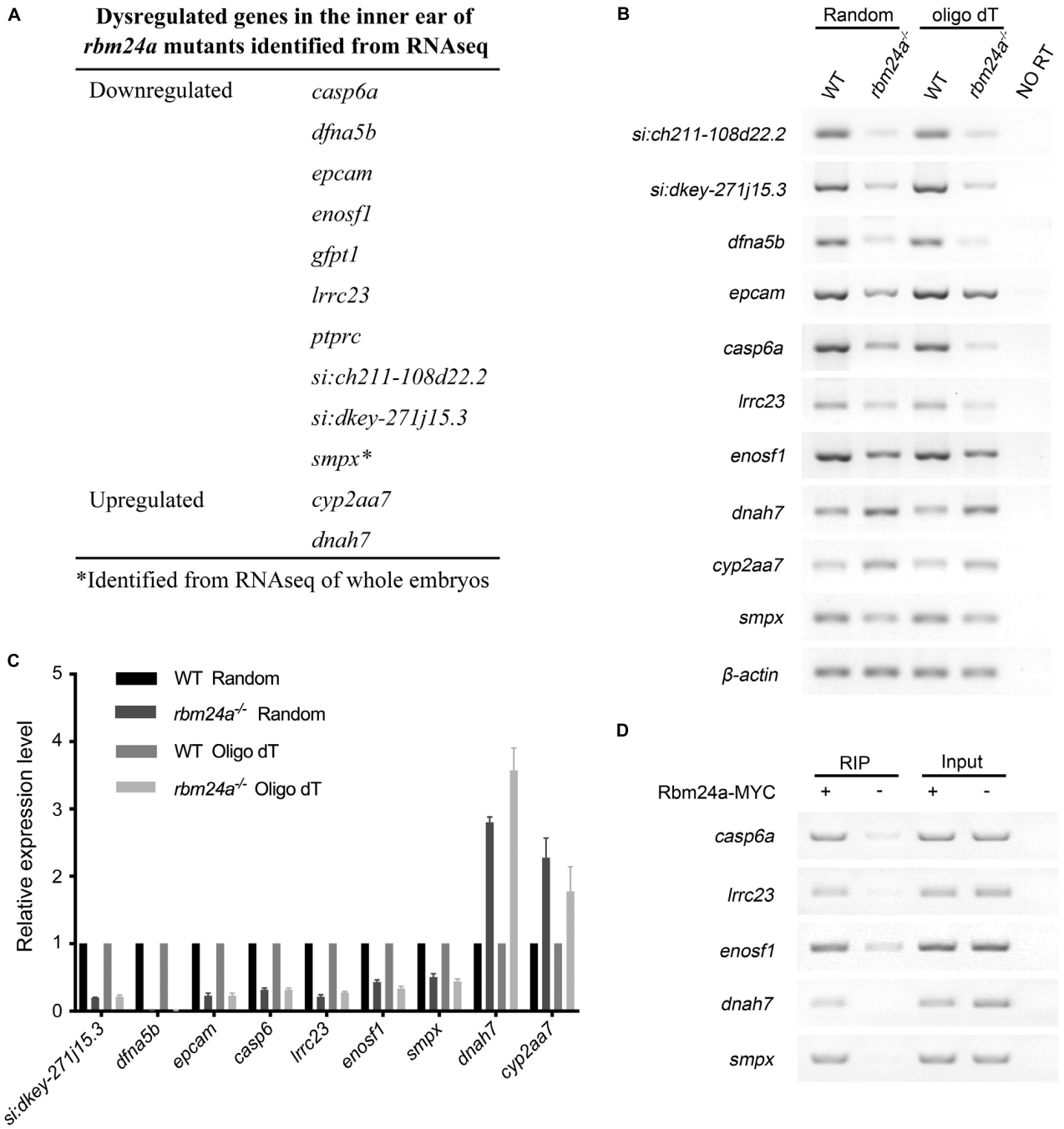


**FIGURE 7 |** Dysregulated genes in the inner ear of *rbm24a* mutants. **(A)** Dysregulated genes in the inner ear of *rbm24a* mutants identified from RNAseq analysis. RT-PCR **(B)** and qPCR **(C)** were performed to confirm the RNAseq results. Random primers or oligo dT were used as primers for reverse transcription as indicated. **(D)** RIP experiments were performed to examine the binding of Rbm24a with its target mRNAs. Statistical analysis of the qPCR results shows that the expression difference is significant (*P* value $< 0.000001$, except that *P* value of *cyp2aa7* is 0.001315).

canal fusion are delayed in *rbm24a* mutants. Otoliths are biomineralized aggregates of calcium carbonate and proteins sitting over hair cells in the maculae, embedded in the otolithic membrane (Schulz-Mirbach et al., 2019). Otolith formation in the zebrafish requires kinocilia and motile cilia, and defects in otolith formation is a characteristic phenotype of ciliary mutants (Stooke-Vaughan et al., 2012; Whitfield, 2020). For example, otolith formation is delayed in zebrafish deficient for *lrrc23* gene that encodes a radial spoke protein of the cilia (Han et al., 2018). Our data show that *lrrc23* mRNA is bound with Rbm24a and its level is decreased in *rbm24a* mutants, suggesting that Rbm24a might affect otolith formation through regulating *lrrc23* mRNA

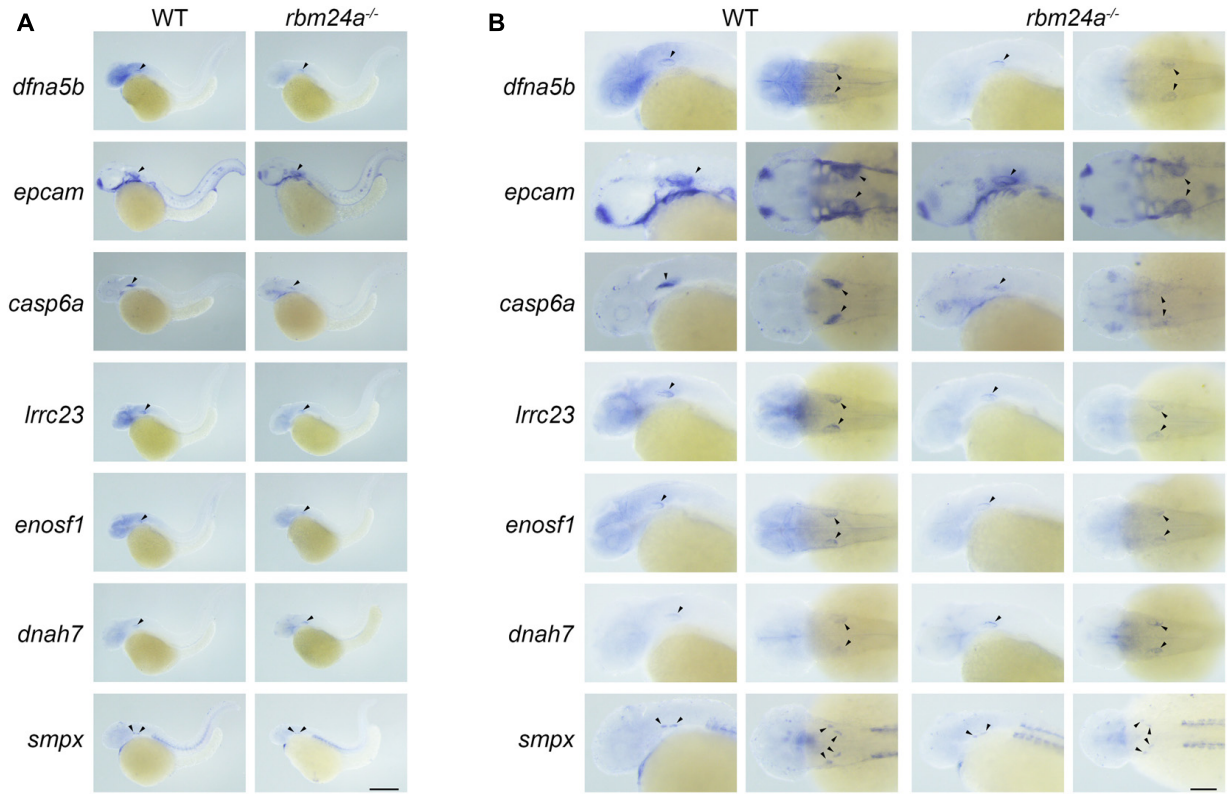


**FIGURE 8 |** Expression pattern of important Rbm24a target mRNAs in the zebrafish. *In situ* hybridization of zebrafish embryos at 34 hpf was performed to examine the expression of *dfna5b*, *epcam*, *casp6a*, *lrrc23*, *enosf1*, *dnah7*, and *smpx*. **(A)** Lower magnification images. **(B)** Higher magnification images. Scale bars, 0.25 mm in **(A)** and 0.1 mm in **(B)**.

stability. Another potential Rbm24a-target that might contribute to the otolith phenotype is *dnah7*, which encodes dynein heavy chain 7, an inner arm component of cilia (Zhang et al., 2002). Interestingly, *dnah7* is one of the few genes whose expression is upregulated in *rbm24a* mutants.

Another important Rbm24a-target is *dfna5b*. Mutations in human *DFNA5* gene are associated with nonsyndromic hearing loss (Van Laer et al., 1998). There are two *DFNA5* orthologs in the zebrafish genome, *dfna5a* and *dfna5b*, among which *dfna5b* shows higher homology with human *DFNA5*. *Dfna5b* is expressed in the inner ear, and *dfna5b* knockdown leads to malformation of the semicircular canals (Busch-Nentwich et al., 2004). Given that both *rbm24a* mutation and *dfna5b* knockdown affect the development of semicircular canals, and that *dfna5b* expression is downregulated in *rbm24a* mutant larvae, we hypothesize that Rbm24a regulates semicircular canal development through affecting the stability of *dfna5b* mRNA. Meantime, *dfna5a* shows different expression pattern from *dfna5b*. Our *in situ* hybridization results show that *dfna5a* is expressed in a circular pattern at the lateral line neuromasts, and its expression level is largely unaffected in *rbm24a* mutants.

*Rbm24a* is also expressed in the hair cells of the inner ear and the lateral line neuromasts. Our data show that *rbm24a* deficiency results in decreased hair cell numbers and disorganized hair bundle, suggesting that Rbm24a is indispensable for hair cell development. Consistently, the MET function of hair cells is compromised in *rbm24a* mutants. As a result, both the auditory and vestibular function are affected in *rbm24a* mutants. RNAseq reveals that many inner ear-expressed genes are dysregulated in *rbm24a* mutants, which might contribute to the hair cell phenotypes. An interesting candidate is *smpx*, which is highly expressed in the hair cells of both mice and zebrafish (Yoon et al., 2011; Ghilardi et al., 2020). *SMPX* gene mutations are associated with nonsyndromic hearing loss DFNX4 (Huebner et al., 2011; Schraders et al., 2011). Smpx protein has been localized at the actin-based cuticular plate, a specialized structure at the apical surface of hair cells (Ghilardi et al., 2020). The cuticular plate is important for stabilizing the stereocilia, and its deficits could lead to stereocilia abnormalities (Pollock and McDermott, 2015; Du et al., 2019). Our present data suggest that Rbm24a might affect stereocilia development through regulating the stability of *smpx* mRNA. Further investigations are warranted to learn more about the underlying mechanism.

Our *in situ* hybridization results show that the number of *dfna5a*$^{+}$ neuromasts is slightly decreased in *rbm24a* mutants. Similar pattern is also observed when GFP-positive neuromast hair cells are examined in *brn3c*:GFP background zebrafish. The slightly decreased pLL neuromast number could be explained by the shortened body length of *rbm24a* mutants. Rbm24a is indispensable for heart development, and *rbm24a* mutants suffer

from severe heart defects and do not survive beyond 9 dpf (Shao et al., 2020). The severe overall sickness of *rbm24a* mutants might lead to the shortened body length before their eventual death. *In situ* hybridization results also reveal more significant decrease of *myo7aa*$^{+}$ neuromast number in *rbm24a* mutants, which might be a result of reduced *myo7aa*$^{+}$ hair cell numbers in each neuromast.

Rbm24 has been shown to be a major regulator of alternative splicing (Yang et al., 2014). Recently we showed that Rbm24 regulates the alternative splicing of *Cdh23* exon 68 in mice (Li et al., 2020). CDH23 forms the upper part of tip links that play a pivotal role in hair cell MET (Assad et al., 1991; Siemens et al., 2004; Kazmierczak et al., 2007). Mutations in *CDH23* gene have been associated with hearing loss in human, mice and zebrafish (Bolz et al., 2001; Bork et al., 2001; Di Palma et al., 2001; Sollner et al., 2004). However, our RNAseq analyses do not reveal any significant changes of alternative splicing in *rbm24a* mutants. We therefore performed RT-PCR experiments to examine the alternative splicing of *cdh23* gene in *rbm24a* mutants. The results show that the inclusion of *cdh23* exon 68 in *rbm24a* mutants is indeed decreased than that in wild type zebrafish (**Supplementary Figures 6A,B**). However, the remained *cdh23* exon 68 inclusion suggests that altered splicing of *cdh23* gene is not a main contributor to the auditory and vestibular phenotypes in *rbm24a* mutants.

In conclusion, our present work reveal that Rbm24a is an important post-transcriptional regulator in the hair cells, and that Rbm24a deficiency affects hair cell development in zebrafish through regulating RNA stability.

## DATA AVAILABILITY STATEMENT

The original contributions presented in the study are included in the article/**Supplementary Material**, further inquiries can be directed to the corresponding author/s.

## ETHICS STATEMENT

The animal study was reviewed and approved by Animal Ethics Committee of Shandong University School of Life Sciences.

## AUTHOR CONTRIBUTIONS

ZX: study concept and design. YZ, YW, XY, and CW: acquisition of data. YZ, FC, DL, MS, and ZX: analysis and interpretation of data. YZ and ZX: drafting the manuscript. MS and ZX: study supervision. All authors contributed to the article and approved the submitted version.

## FUNDING

This work was supported by grants from the National Key Basic Research Program of China (2018YFC1003600), the National Natural Science Foundation of China (81771001), and the Fundamental Research Funds of Shandong University (2018JC025).

## ACKNOWLEDGMENTS

We would like to thank Sen Wang, Xiaomin Zhao, and Haiyan Yu from the core facilities for life and environmental sciences, Shandong University for the technical support in SEM and confocal microscopy.

## SUPPLEMENTARY MATERIAL

The Supplementary Material for this article can be found online at: https://www.frontiersin.org/articles/10.3389/fcell.2020.604026/full#supplementary-material

## REFERENCES

Assad, J. A., Shepherd, G. M. G., and Corey, D. P. (1991). Tip-link integrity and mechanical transduction in vertebrate hair-cells. *Neuron* 7, 985–994. doi: 10.1016/0896-6273(91)90343-x

Bermingham, N. A., Hassan, B. A., Price, S. D., Vollrath, M. A., Ben-Arie, N., Eatock, R. A., et al. (1999). Math1: an essential gene for the generation of inner ear hair cells. *Science* 284, 1837–1841. doi: 10.1126/science.284.5421.1837

Beurg, M., Fettiplace, R., Nam, J. H., and Ricci, A. J. (2009). Localization of inner hair cell mechanotransducer channels using high-speed calcium imaging. *Nat. Neurosci.* 12, 553–558. doi: 10.1038/nn.2295

Bolz, H., von Brederlow, B., Ramirez, A., Bryda, E. C., Kutsche, K., Nothwang, H. G., et al. (2001). Mutation of CDH23, encoding a new member of the cadherin gene family, causes Usher syndrome type 1D. *Nat. Genet.* 27, 108–112. doi: 10.1038/83667

Bork, J. M., Peters, L. M., Riazuddin, S., Bernstein, S. L., Ahmed, Z. M., Ness, S. L., et al. (2001). Usher syndrome 1D and nonsyndromic autosomal recessive deafness DFNB12 are caused by allelic mutations of the novel cadherin-like gene CDH23. *Am. J. Hum. Genet.* 68, 26–37. doi: 10.1086/316954

Brinegar, A. E., and Cooper, T. A. (2016). Roles for RNA-binding proteins in development and disease. *Brain Res.* 1647, 1–8. doi: 10.1016/j.brainres.2016.02.050

Busch-Nentwich, E., Sollner, C., Roehl, H., and Nicolson, T. (2004). The deafness gene dfna5 is crucial for ugdh expression and HA production in the developing ear in zebrafish. *Development* 131, 943–951. doi: 10.1242/dev.00961

Cai, T., Jen, H. I., Kang, H., Klisch, T. J., Zoghbi, H. Y., and Groves, A. K. (2015). Characterization of the transcriptome of nascent hair cells and identification of direct targets of the Atoh1 transcription factor. *J. Neurosci.* 35, 5870–5883. doi: 10.1523/jneurosci.5083-14.2015

Dash, S., Brastrom, L. K., Patel, S. D., Scott, C. A., Slusarski, D. C., and Lachke, S. A. (2020). The master transcription factor SOX2, mutated in anophthalmia/microphthalmia, is post-transcriptionally regulated by the conserved RNA-binding protein RBM24 in vertebrate eye development. *Hum. Mol. Genet.* 29, 591–604. doi: 10.1093/hmg/ddz278

Di Palma, F., Holme, R. H., Bryda, E. C., Belyantseva, I. A., Pellegrino, R., Kachar, B., et al. (2001). Mutations in Cdh23, encoding a new type of cadherin, cause stereocilia disorganization in waltzer, the mouse model for Usher syndrome type 1D. *Nat. Genet.* 27, 103–107. doi: 10.1038/83660

Du, H., Zou, L., Ren, R., Li, N., Li, J., Wang, Y., et al. (2020). Lack of PDZD7 long isoform disrupts ankle-link complex and causes hearing loss in mice. *FASEB J.* 34, 1136–1149. doi: 10.1096/fj.201901657rr

Du, T. T., Dewey, J. B., Wagner, E. L., Cui, R., Heo, J., Park, J. J., et al. (2019). LMO7 deficiency reveals the significance of the cuticular plate for hearing function. *Nat. Commun.* 10:1117.

Ekker, M., Akimenko, M. A., Bremiller, R., and Westerfield, M. (1992). Regional expression of three homeobox transcripts in the inner ear of zebrafish embryos. *Neuron* 9, 27–35. doi: 10.1016/0896-6273(92)90217-2

Elkon, R., Milon, B., Morrison, L., Shah, M., Vijayakumar, S., Racherla, M., et al. (2015). RFX transcription factors are essential for hearing in mice. *Nat. Commun.* 6:8549.

Erkman, L., McEvilly, R. J., Luo, L., Ryan, A. K., Hooshmand, F., O'Connell, S. M., et al. (1996). Role of transcription factors Brn-3.1 and Brn-3.2 in auditory and visual system development. *Nature* 381, 603–606. doi: 10.1038/381603a0

Ernest, S., Rauch, G. J., Haffter, P., Geisler, R., Petit, C., and Nicolson, T. (2000). Mariner is defective in myosin VIIA: a zebrafish model for human hereditary deafness. *Hum. Mol. Genet.* 9, 2189–2196. doi: 10.1093/hmg/9.14.2189

Fetka, I., Radeghieri, A., and Bouwmeester, T. (2000). Expression of the RNA recognition motif-containing protein SEB-4 during Xenopus embryonic development. *Mech. Dev.* 94, 283–286. doi: 10.1016/s0925-4773(00)00284-7

Gale, J. E., Marcotti, W., Kennedy, H. J., Kros, C. J., and Richardson, G. P. (2001). FM1-43 dye behaves as a permeant blocker of the hair-cell mechanotransducer channel. *J. Neurosci.* 21, 7013–7025. doi: 10.1523/jneurosci.21-18-07013.2001

Ghilardi, A., Diana, A., Prosperi, L., and Del Giacco, L. (2020). Expression pattern of the small muscle protein, X-linked (smpx) gene during zebrafish embryonic and larval developmental stages. *Gene Expr. Patterns* 36:119110. doi: 10.1016/j.gep.2020.119110

Grifone, R., Saquet, A., Xu, Z., and Shi, D. L. (2018). Expression patterns of Rbm24 in lens, nasal epithelium, and inner ear during mouse embryonic development. *Dev. Dyn.* 247, 1160–1169. doi: 10.1002/dvdy.24666

Grifone, R., Xie, X., Bourgeois, A., Saquet, A., Duprez, D., and Shi, D. L. (2014). The RNA-binding protein Rbm24 is transiently expressed in myoblasts and is required for myogenic differentiation during vertebrate development. *Mech. Dev.* 134, 1–15. doi: 10.1016/j.mod.2014.08.003

Han, X., Xie, H., Wang, Y., and Zhao, C. (2018). Radial spoke proteins regulate otolith formation during early zebrafish development. *FASEB J.* 32, 3984–3992. doi: 10.1096/fj.201701359r

He, Y. Z., Lu, X. L., Qian, F. P., Liu, D., Chai, R. J., and Li, H. W. (2017). Insm1a is required for zebrafish posterior lateral line development. *Front. Mol. Neurosci.* 10:241. doi: 10.3389/fnmol.2017.00241

Hentze, M. W., Castello, A., Schwarzl, T., and Preiss, T. (2018). A brave new world of RNA-binding proteins. *Nat. Rev. Mol. Cell Biol.* 19, 327–341. doi: 10.1038/nrm.2017.130

Huebner, A. K., Gandia, M., Frommolt, P., Maak, A., Wicklein, E. M., Thiele, H., et al. (2011). Nonsense mutations in SMPX, encoding a protein responsive to physical force, result in X-chromosomal hearing loss. *Am. J. Hum. Genet.* 88, 621–627. doi: 10.1016/j.ajhg.2011.04.007

Ito, J., Iijima, M., Yoshimoto, N., Niimi, T., Kuroda, S., and Maturana, A. D. (2016). RBM20 and RBM24 cooperatively promote the expression of short enh splice variants. *FEBS Lett.* 590, 2262–2274. doi: 10.1002/1873-3468.12251

Jiang, L., Romero-Carvajal, A., Haug, J. S., Seidel, C. W., and Piotrowski, T. (2014). Gene-expression analysis of hair cell regeneration in the zebrafish lateral line. *Proc. Natl. Acad. Sci. U.S.A.* 111, E1383–E1392.

Jiang, Y., Zhang, M., Qian, Y., Xu, E., Zhang, J., and Chen, X. (2014). Rbm24, an RNA-binding protein and a target of p53, regulates p21 expression via mRNA stability. *J. Biol. Chem.* 289, 3164–3175. doi: 10.1074/jbc.m113.524413

Jones, C., Roper, V. C., Foucher, I., Qian, D., Banizs, B., Petit, C., et al. (2008). Ciliary proteins link basal body polarization to planar cell polarity regulation. *Nat. Genet.* 40, 69–77. doi: 10.1038/ng.2007.54

Kazmierczak, P., Sakaguchi, H., Tokita, J., Wilson-Kubalek, E. M., Milligan, R. A., Muller, U., et al. (2007). Cadherin 23 and protocadherin 15 interact to form tip-link filaments in sensory hair cells. *Nature* 449, 87–91. doi: 10.1038/nature06091

Kimmel, C. B., Patterson, J., and Kimmel, R. O. (1974). The development and behavioral characteristics of the startle response in the zebra fish. *Dev. Psychobiol.* 7, 47–60. doi: 10.1002/dev.420070109

Li, H. Y., Bourdelas, A., Carron, C., and Shi, D. L. (2010). The RNA-binding protein Seb4/RBM24 is a direct target of MyoD and is required for myogenesis during Xenopus early development. *Mech. Dev.* 127, 281–291. doi: 10.1016/j.mod.2010.03.002

Li, N., Du, H., Ren, R., Wang, Y., and Xu, Z. (2020). Alternative splicing of Cdh23 exon 68 is regulated by RBM24, RBM38, and PTBP1. *Neural Plast.* 2020:8898811.

Lin, Y., Tan, K. T., Liu, J., Kong, X., Huang, Z., and Xu, X. Q. (2018). Global profiling of Rbm24 bound RNAs uncovers a multi-tasking RNA binding protein. *Int. J. Biochem. Cell Biol.* 94, 10–21. doi: 10.1016/j.biocel.2017.11.002

Liu, J., Kong, X., Zhang, M., Yang, X., and Xu, X. (2019). RNA binding protein 24 deletion disrupts global alternative splicing and causes dilated cardiomyopathy. *Protein Cell* 10, 405–416. doi: 10.1007/s13238-018-0578-8

Maragh, S., Miller, R. A., Bessling, S. L., McGaughey, D. M., Wessels, M. W., de Graaf, B., et al. (2011). Identification of RNA binding motif proteins essential for cardiovascular development. *BMC Dev. Biol.* 11:62. doi: 10.1186/1471-213X-11-62

Maragh, S., Miller, R. A., Bessling, S. L., Wang, G., Hook, P. W., and McCallion, A. S. (2014). Rbm24a and Rbm24b are required for normal somitogenesis. *PLoS One* 9:e105460. doi: 10.1371/journal.pone.0105460

Meyers, J. R., MacDonald, R. B., Duggan, A., Lenzi, D., Standaert, D. G., Corwin, J. T., et al. (2003). Lighting up the senses: FM1-43 loading of sensory cells through nonselective ion channels. *J. Neurosci.* 23, 4054–4065. doi: 10.1523/jneurosci.23-10-04054.2003

Miyamoto, S., Hidaka, K., Jin, D., and Morisaki, T. (2009). RNA-binding proteins Rbm38 and Rbm24 regulate myogenic differentiation via p21-dependent and -independent regulatory pathways. *Genes Cells* 14, 1241–1252. doi: 10.1111/j.1365-2443.2009.01347.x

Mo, W., Chen, F., Nechiporuk, A., and Nicolson, T. (2010). Quantification of vestibular-induced eye movements in zebrafish larvae. *BMC Neurosci.* 11:110. doi: 10.1186/1471-2202-11-110

Moayedi, Y., Basch, M. L., Pacheco, N. L., Gao, S. S., Wang, R., Harrison, W., et al. (2014). The candidate splicing factor Sfswap regulates growth and patterning of inner ear sensory organs. *PLoS Genet.* 10:e1004055. doi: 10.1371/journal.pgen.1004055

Müller, U., and Barr-Gillespie, P. G. (2015). New treatment options for hearing loss. *Nat. Rev. Drug Discov.* 14, 346–365. doi: 10.1038/nrd4533

Nakano, Y., Jahan, I., Bonde, G., Sun, X., Hildebrand, M. S., Engelhardt, J. F., et al. (2012). A mutation in the Srrm4 gene causes alternative splicing defects and deafness in the Bronx waltzer mouse. *PLoS Genet.* 8:e1002966. doi: 10.1371/journal.pgen.1002966

Nicolson, T. (2005). The genetics of hearing and balance in zebrafish. *Ann. Rev. Genet.* 39, 9–22. doi: 10.1146/annurev.genet.39.073003.105049

Pfeffer, P. L., Gerster, T., Lun, K., Brand, M., and Busslinger, M. (1998). Characterization of three novel members of the zebrafish Pax2/5/8 family: dependency of Pax5 and Pax8 expression on the Pax2.1 (noi) function. *Development* 125, 3063–3074.

Pollock, L. M., and McDermott, B. M. Jr. (2015). The cuticular plate: a riddle, wrapped in a mystery, inside a hair cell. *Birth Defects Res. C. Embryo Today* 105, 126–139. doi: 10.1002/bdrc.21098

Poon, K. L., Tan, K. T., Wei, Y. Y., Ng, C. P., Colman, A., Korzh, V., et al. (2012). RNA-binding protein RBM24 is required for sarcomere assembly and heart contractility. *Cardiovasc. Res.* 94, 418–427. doi: 10.1093/cvr/cvs095

Riley, B. B., Zhu, C., Janetopoulos, C., and Aufderheide, K. J. (1997). A critical period of ear development controlled by distinct populations of ciliated cells in the zebrafish. *Dev. Biol.* 191, 191–201. doi: 10.1006/dbio.1997.8736

Rohacek, A. M., Bebee, T. W., Tilton, R. K., Radens, C. M., McDermott-Roe, C., Peart, N., et al. (2017). ESRP1 mutations cause hearing loss due to defects in alternative splicing that disrupt cochlear development. *Dev. Cell* 43, 318–331. doi: 10.1016/j.devcel.2017.09.026

Scheffer, D. I., Shen, J., Corey, D. P., and Chen, Z. Y. (2015). Gene expression by mouse inner ear hair cells during development. *J. Neurosci.* 35, 6366–6380. doi: 10.1523/jneurosci.5126-14.2015

Schraders, M., Haas, S. A., Weegerink, N. J., Oostrik, J., Hu, H., Hoefsloot, L. H., et al. (2011). Next-generation sequencing identifies mutations of SMPX, which encodes the small muscle protein, X-linked, as a cause of progressive hearing impairment. *Am. J. Hum. Genet.* 88, 628–634. doi: 10.1016/j.ajhg.2011.04.012

Schulz-Mirbach, T., Ladich, F., Plath, M., and Hess, M. (2019). Enigmatic ear stones: what we know about the functional role and evolution of fish otoliths. *Biol. Rev. Camb. Philos. Soc.* 94, 457–482. doi: 10.1111/brv.12463

Shao, M., Lu, T., Zhang, C., Zhang, Y. Z., Kong, S. H., and Shi, D. L. (2020). Rbm24 controls poly(A) tail length and translation efficiency of crystallin mRNAs in the lens via cytoplasmic polyadenylation. *Proc. Natl. Acad. Sci. U.S.A.* 117, 7245–7254. doi: 10.1073/pnas.1917922117

Shen, J., Scheffer, D. I., Kwan, K. Y., and Corey, D. P. (2015). SHIELD: an integrative gene expression database for inner ear research. *Database Oxford* 2015:bav071. doi: 10.1093/database/bav071

Siemens, J., Lillo, C., Dumont, R. A., Reynolds, A., Williams, D. S., Gillespie, P. G., et al. (2004). Cadherin 23 is a component of the tip link in hair-cell stereocilia. *Nature* 428, 950–955. doi: 10.1038/nature02483

Sollner, C., Rauch, G. J., Siemens, J., Geisler, R., Schuster, S. C., Muller, U., et al. (2004). Mutations in cadherin 23 affect tip links in zebrafish sensory hair cells. *Nature* 428, 955–959. doi: 10.1038/nature02484

Stooke-Vaughan, G. A., Huang, P., Hammond, K. L., Schier, A. F., and Whitfield, T. T. (2012). The role of hair cells, cilia and ciliary motility in otolith formation in the zebrafish otic vesicle. *Development* 139, 1777–1787. doi: 10.1242/dev.079947

Sun, P., Zhang, Y., Zhao, F., Wu, J. P., Pun, S. H., Peng, C., et al. (2018). An assay for systematically quantifying the vestibulo-ocular reflex to assess vestibular function in zebrafish larvae. *Front. Cell. Neurosci.* 12:257. doi: 10.3389/fncel.2018.00257

Thisse, C., and Thisse, B. (2008). High-resolution in situ hybridization to whole-mount zebrafish embryos. *Nat. Protoc.* 3, 59–69. doi: 10.1038/nprot.2007.514

van den Hoogenhof, M. M. G., van der Made, I., de Groot, N. E., Damanafshan, A., van Amersfoorth, S. C. M., Zentilin, L., et al. (2018). AAV9-mediated Rbm24 overexpression induces fibrosis in the mouse heart. *Sci. Rep.* 8:11696.

Van Laer, L., Huizing, E. H., Verstreken, M., van Zuijlen, D., Wauters, J. G., Bossuyt, P. J., et al. (1998). Nonsyndromic hearing impairment is associated with a mutation in DFNA5. *Nat. Genet.* 20, 194–197. doi: 10.1038/2503

Wallis, D., Hamblen, M., Zhou, Y., Venken, K. J., Schumacher, A., Grimes, H. L., et al. (2003). The zinc finger transcription factor Gfi1, implicated in lymphomagenesis, is required for inner ear hair cell differentiation and survival. *Development* 130, 221–232. doi: 10.1242/dev.00190

Wang, C., Zhong, Z., Sun, P., Zhong, H., Li, H., and Chen, F. (2017). Evaluation of the hair cell regeneration in zebrafish larvae by measuring and quantifying the startle responses. *Neural Plast.* 2017:8283075.

Waterman, R. E., and Bell, D. H. (1984). Epithelial fusion during early semicircular canal formation in the embryonic zebrafish, Brachydanio rerio. *Anat. Rec.* 210, 101–114. doi: 10.1002/ar.1092100113

Whitfield, T. T. (2020). Cilia in the developing zebrafish ear. *Philos. Trans. R. Soc. Lond. B. Biol. Sci.* 375:20190163. doi: 10.1098/rstb.2019.0163

Xing, Y. Y., Cheng, X. N., Li, Y. L., Zhang, C., Saquet, A., Liu, Y. Y., et al. (2018). Mutational analysis of dishevelled genes in zebrafish reveals distinct functions in embryonic patterning and gastrulation cell movements. *PLoS Genet.* 14:e1007551. doi: 10.1371/journal.pgen.1007551

Xu, E., Zhang, J., Zhang, M., Jiang, Y., Cho, S. J., and Chen, X. (2014). RNA-binding protein RBM24 regulates p63 expression via mRNA stability. *Mol. Cancer Res.* 12, 359–369. doi: 10.1158/1541-7786.mcr-13-0526

Yang, J., Hung, L. H., Licht, T., Kostin, S., Looso, M., Khrameeva, E., et al. (2014). RBM24 is a major regulator of muscle-specific alternative splicing. *Dev. Cell* 31, 87–99. doi: 10.1016/j.devcel.2014.08.025

Yoon, H., Lee, D. J., Kim, M. H., and Bok, J. (2011). Identification of genes concordantly expressed with Atoh1 during inner ear development. *Anat. Cell Biol.* 44, 69–78. doi: 10.5115/acb.2011.44.1.69

Zeddies, D. G., and Fay, R. R. (2005). Development of the acoustically evoked behavioral response in zebrafish to pure tones. *J. Exp. Biol.* 208, 1363–1372. doi: 10.1242/jeb.01534

Zhang, M., Zhang, Y., Xu, E., Mohibi, S., de Anda, D. M., Jiang, Y., et al. (2018). Rbm24, a target of p53, is necessary for proper expression of p53 and heart development. *Cell Death Differ.* 25, 1118–1130. doi: 10.1038/s41418-017-0029-8

Zhang, T., Lin, Y., Liu, J., Zhang, Z. G., Fu, W., Guo, L. Y., et al. (2016). Rbm24 regulates alternative splicing switch in embryonic stem cell cardiac lineage differentiation. *Stem Cells* 34, 1776–1789. doi: 10.1002/stem.2366

Zhang, Y. J., O'Neal, W. K., Randell, S. H., Blackburn, K., Moyer, M. B., Boucher, R. C., et al. (2002). Identification of dynein heavy chain 7 as an inner arm component of human cilia that is synthesized but not assembled in a case of primary ciliary dyskinesia. *J. Biol. Chem.* 277, 17906–17915. doi: 10.1074/jbc.m200348200

**Conflict of Interest:** The authors declare that the research was conducted in the absence of any commercial or financial relationships that could be construed as a potential conflict of interest.

*Copyright © 2020 Zhang, Wang, Yao, Wang, Chen, Liu, Shao and Xu. This is an open-access article distributed under the terms of the Creative Commons Attribution License (CC BY). The use, distribution or reproduction in other forums is permitted, provided the original author(s) and the copyright owner(s) are credited and that the original publication in this journal is cited, in accordance with accepted academic practice. No use, distribution or reproduction is permitted which does not comply with these terms.*

frontiers in Cell and Developmental Biology

BRIEF RESEARCH REPORT
published: 07 January 2021
doi: 10.3389/fcell.2020.570486

# Tmc Reliance Is Biased by the Hair Cell Subtype and Position Within the Ear

*Shaoyuan Zhu[1,2†], Zongwei Chen[1,2†], Haoming Wang[1,2] and Brian M. McDermott Jr.[1,2,3,4*]*

[1] Department of Otolaryngology–Head and Neck Surgery, School of Medicine, Case Western Reserve University, Cleveland, OH, United States, [2] Department of Biology, Case Western Reserve University, Cleveland, OH, United States, [3] Department of Genetics and Genome Sciences, School of Medicine, Case Western Reserve University, Cleveland, OH, United States, [4] Department of Neurosciences, School of Medicine, Case Western Reserve University, Cleveland, OH, United States

Hair cells are heterogenous, enabling varied roles in sensory systems. An emerging hypothesis is that the transmembrane channel-like (Tmc) proteins of the hair cell's mechanotransduction apparatus vary within and between organs to permit encoding of different mechanical stimuli. Five anatomical variables that may coincide with different Tmc use by a hair cell within the ear are the containing organ, cell morphology, cell position within an organ, axis of best sensitivity for the cell, and the hair bundle's orientation within this axis. Here, we test this hypothesis in the organs of the zebrafish ear using a suite of genetic mutations. Transgenesis and quantitative measurements demonstrate two morphologically distinct hair cell types in the central thickness of a vestibular organ, the lateral crista: short and tall. In contrast to what has been observed, we find that tall hair cells that lack Tmc1 generally have substantial reductions in mechanosensitivity. In short hair cells that lack Tmc2 isoforms, mechanotransduction is largely abated. However, hair cell Tmc dependencies are not absolute, and an exceptional class of short hair cell that depends on Tmc1 is present, termed a short hair cell erratic. To further test anatomical variables that may influence Tmc use, we map Tmc1 function in the saccule of mutant larvae that depend just on this Tmc protein to hear. We demonstrate that hair cells that use Tmc1 are found in the posterior region of the saccule, within a single axis of best sensitivity, and hair bundles with opposite orientations retain function. Overall, we determine that Tmc reliance in the ear is dependent on the organ, subtype of hair cell, position within the ear, and axis of best sensitivity.

**Keywords: hair cell, hearing, balance, mechanotransduction, Tmc, zebrafish**

OPEN ACCESS

***Edited by:***
*Anthony Wei Peng, University of Colorado Anschutz Medical Campus, United States*

***Reviewed by:***
*Bo Zhao, Indiana University, United States*
*Allison B. Coffin, Washington State University, United States*

***Correspondence:**
*Brian M. McDermott Jr.*
*bmm30@case.edu*

*[†] These authors have contributed equally to this work*

***Specialty section:***
*This article was submitted to Cell Growth and Division, a section of the journal Frontiers in Cell and Developmental Biology*

***Received:*** *08 June 2020*
***Accepted:*** *21 October 2020*
***Published:*** *07 January 2021*

***Citation:***
*Zhu S, Chen Z, Wang H and McDermott BM Jr (2021) Tmc Reliance Is Biased by the Hair Cell Subtype and Position Within the Ear. Front. Cell Dev. Biol. 8:570486. doi: 10.3389/fcell.2020.570486*

## INTRODUCTION

In the ear, hair cells transduce mechanical stimuli for two senses: hearing and balance (Hudspeth, 1989). The soma of each of these epithelial cells presents a mechanosensitive hair bundle at its apical surface. Consisting of an array of stereocilia of graded lengths, the hair bundle is asymmetrical and is most sensitive along a single axis of best sensitivity (Shotwell et al., 1981). Both hearing and balance depend on hair cell heterogeneity (Eatock and Hurley, 2003; Kandel, 2013). The larval zebrafish ear contains three cristae, which have hair cells that encode accelerations from head rotations (Haddon and Lewis, 1996; Nicolson, 2005). In addition, the anterior (utricle) and posterior (saccule) maculae house hair cells to detect both linear accelerations for the sense of balance and vibrational stimuli for hearing.

Hair cells vary anatomically to accommodate an array of mechanical stimuli for hearing and balance. Hair cell variables include – but are not limited to – the organ that holds it, the morphology of the cell body (Sugihara and Furukawa, 1989), the position of the cell within the organ, and the axis of best sensitivity for the cell (Popper and Lu, 2000). Within the anamniotes, there are a few subtypes of hair cells that can differ in their morphologies and electrophysiological properties depending on the species and organ. The goldfish (*Carassius auratus*) saccule contains two differently sized hair cells: tall or gourd-like and short or eggplant shaped (Sugihara and Furukawa, 1989). In addition to shape differences, these cells contrast in their electrophysiological characteristics. The distribution of these differently sized cells is not homogenous: short hair cells tend to be found in the rostral saccule and both tall and short hair cells are found in the caudal saccule. Zebrafish saccular hair cells also have a stereotyped pattern in the direction their hair bundles face (Inoue et al., 2013). A similar pattern is seen in the mammalian saccule wherein hair cells are divided between two populations that have opposite hair bundle orientations (Deans, 2013). These hair cell populations are separated by a figurative boundary line, the line of polarity reversal. In the frog crista (*Rana pipiens*), there are morphologically distinct hair cells that are shaped like a club, cigar, or pear (Guth et al., 1994). These differently sized and shaped cells are distributed unevenly along the length and width of the crista. In contrast to the maculae, the hair bundles of the cristae are aligned in a single direction with the fluid motion of the semicircular cannels.

Transmembrane channel-like (Tmc) proteins have emerged as critical components of the hair cell's mechanotransduction channel. In mammals, hearing and balance depend on TMC1 and TMC2 (Kawashima et al., 2011). In zebrafish, hearing uses Tmc1, Tmc2a, and Tmc2b (Chen et al., 2020). *Tmc2a* and *tmc2b* paralogs are the result of a whole-genome duplication that occurred in teleost fish between 300 and 450 million years ago (Taylor et al., 2001). Tmcs have several properties indicating that they are components of the mechanotransduction channel. In mammals and fish, Tmc proteins localize to the tips of stereocilia, the site of mechanotransduction (Kawashima et al., 2011; Maeda et al., 2014; Kurima et al., 2015; Chou et al., 2017; Mahendrasingam and Furness, 2019). There they are closely associated with other members of the mechanotransduction apparatus (Gleason et al., 2009; Maeda et al., 2014; Zhao et al., 2014; Erickson et al., 2017; Giese et al., 2017; Ge et al., 2018; Cunningham and Muller, 2019; Li et al., 2019; Pacentine and Nicolson, 2019; Cunningham et al., 2020). Finally, mutational, structural, and liposome-reconstitution studies support the hypothesis that TMCs are pore-forming subunits (Ballesteros et al., 2018; Pan et al., 2018; Jia et al., 2019).

Recently, we demonstrated that the zebrafish lateral line and maculae depend on different sets of Tmc proteins (Chou et al., 2017; Chen et al., 2020). In addition, we showed that hair bundle orientation can correlate with different Tmc use in a neuromast organ. Here, we examine the lateral cristae and posterior maculae of larval zebrafish to determine if five anatomical variables coincide with different Tmc use within the ear: organ, position within the organ, morphology, axis of hair bundle sensitivity, and hair bundle orientation within this axis.

# RESULTS AND DISCUSSION

## Zebrafish Have Two Predominant Hair Cell Subtypes in the Central Thickness of the Lateral Crista: Tall and Short

Since the sensory epithelia of goldfish and amphibians have hair cells with different morphologies, we examined the contours and dimensions of crista hair cells to quantitatively determine if these organs have differently shaped and sized hair cells or whether they are homogenous. To examine the crista for multiple hair cell subtypes based on morphology, we created somatic F0 mosaic transgenic zebrafish that express the fluorescent protein Cerulean under the control of the hair cell promoter *myosin 6b* (Cruz et al., 2015). This allowed us to identify sporadically labeled hair cells. Zebrafish at the larval stage were examined because they are optically clear, permitting scrutinization of hair cells *in vivo*. Using a confocal microscope, we imaged optical slices of the central thickness of the lateral crista because it is known that the lateral hair cells are developing in larvae (Haddon and Lewis, 1996), and the central region may contain the most mature population. Micrographs revealed two prevalent hair cell types: Tall hair cells with an elongated thin neck region and a nucleus close to the basal area of the cell and short hair cells that are stunted in comparison (**Figures 1A,C**). To quantitate length differences and determine spatial relationships between these cells, we generated a stable transgenic line, *Tg*(*myo6b:Cerulean*). In this section of the crista, tall and short hair cells are interdigitated (**Figures 1B,C**). Plots of hair cell lengths reveal two discernable populations (**Figures 1D,E**). The mean somata lengths of the short and tall hair cells are $11.0 \pm 0.2$ (mean $\pm$ SEM) $\mu$m and $17.1 \pm 0.3$ $\mu$m, respectively.

## Tall Hair Cells That Lack Tmc1 Display Defects in Mechanotransduction

Since hair cells between the lateral line and the maculae of fish and between the maculae and the cochleae of mice (Kawashima et al., 2011) depend on different complements of Tmc proteins, we queried if these distinct hair cell subtypes rely on the same Tmc proteins or if their morphologies correlate with particular Tmc dependencies. To address this question, we implemented a genetic strategy using *tmc1* mutant zebrafish, *tmc1*$^{cwr5}$, which lack the Tmc1 protein (**Supplementary Tables S1, S2**; Chen et al., 2020). To visually identify normal mechanosensitive hair cells versus those that may have lost or experienced a reduction in this defining property, we imaged the uptake of cationic fluorescent molecule 4-Di-2-ASP (**Figure 2A**), which passes through the hair cell's mechanotransduction channel to act as an indicator of channel function (Gleason et al., 2009; Owens et al., 2009). After direct injection of 4-Di-2-ASP into the otocyst and subsequent confocal imaging, micrographs demonstrated that most hair cells in controls have functional mechanotransduction channels. However, in the *tmc1*$^{cwr5}$ mutant, tall hair cells (length

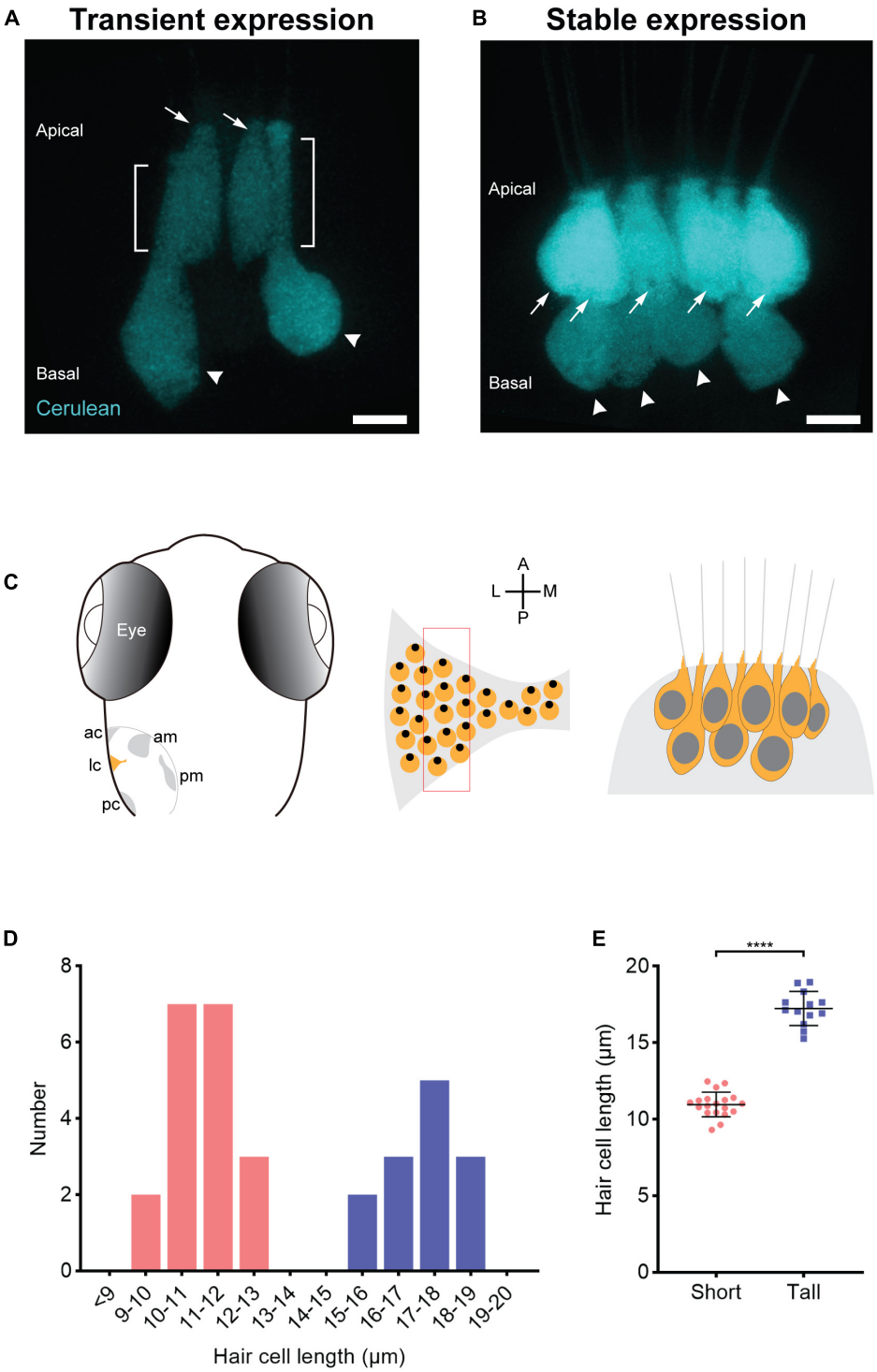


**FIGURE 1 |** Two populations of morphologically distinct hair cells in the central thickness of the lateral crista of larval zebrafish. **(A,B)** Transient **(A)** and stable **(B)** transgenic expression of Cerulean fluorescent protein in the lateral crista reveals two morphologically distinct hair cells: short (arrows) and tall (arrowheads). The brackets mark the neck regions of tall hair cells. Scale bar = 5 μm. **(C)** Left panel, schematic of a dorsal view of a 7-dpf zebrafish ear, illustrating the five mechanosensory patches: the anterior crista (ac), lateral crista (lc), posterior crista (pc), anterior macula (am), and posterior macula (pm). Middle panel, enlarged view schematizing the hair cell arrangement in the lateral crista highlighted in yellow in the left panel. Each yellow circle represents a single hair cell, and the black dot within represents the position of the kinocilium (fonticulus). The red rectangle marks the section from which the hair cells are imaged and characterized. A, anterior; P, posterior; M, medial; L, lateral. Right panel, schematic of the two populations of hair cells (short and tall) in this section of the lateral crista based on imaging results. **(D)** The distribution of somata lengths of the lateral crista hair cells from 7-dpf zebrafish. $n = 4$. Pink bars represent short hair cells. Blue bars represent tall hair cells. **(E)** The somata lengths (mean ± SD) of the two groups of hair cells shown in panel **(D)**. $^{****}P < 0.0001$, unpaired $t$-test.

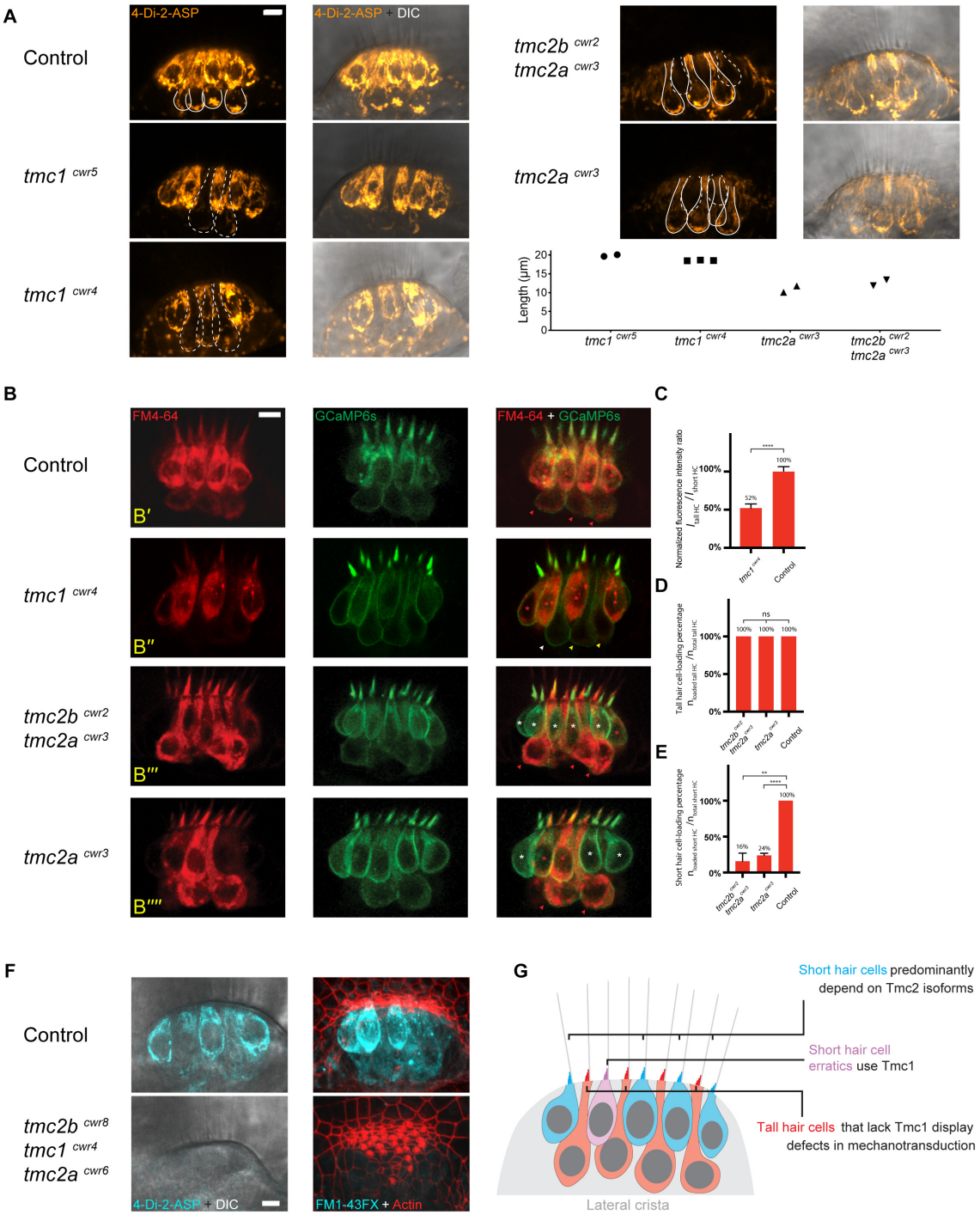


**FIGURE 2 |** Tall and short hair cells of the lateral crista display biases for Tmc proteins in mechanotransduction. **(A)** Representative confocal images of 4-Di-2-ASP (orange) dye uptake assays showing differential dependencies of tall and short hair cells on Tmc proteins in the lateral cristae of 7-dpf larvae. Solid lines outline tall hair cells with 4-Di-2-ASP uptake in a wild-type sibling, a *tmc2a*$^{cwr3}$ single mutant, and a *tmc2b*$^{cwr2}$ *tmc2a*$^{cwr3}$ double mutant. In each wild-type tall hair cell, there is an accumulation of dye near the cell's base. The dashed lines outline tall hair cells with diminished 4-Di-2-ASP uptake in the *tmc1*$^{cwr5}$ single mutant and the *tmc1*$^{cwr4}$ single mutant or short hair cells with no or little 4-Di-2-ASP uptake in the *tmc2b*$^{cwr2}$ *tmc2a*$^{cwr3}$ double mutant and the *tmc2a*$^{cwr3}$ single mutant. Graph of lengths of hair cells that have diminished 4-Di-2-ASP uptake. Each data point represents a single cell's length and associated genotype. Cells associated with each data point are shown in confocal images with dashed outlines. **(B)** Representative confocal images of FM 4–64 (red) uptake assays for a heterozygous sibling control (*tmc2b*$^{cwr2/+}$ *tmc2a*$^{cwr3/+}$, **B′**), a *tmc1*$^{cwr4}$ single mutant **(B″)**, a *tmc2b*$^{cwr2}$ *tmc2a*$^{cwr3}$ double mutant **(B‴)**, and a *tmc2a*$^{cwr3}$ single mutant **(B⁗)**, each at 7-dpf. The lateral crista hair cells express GCaMP6s-CAAX (green), making each cell apparent. The red or white asterisks mark the short hair cells with or without FM4-64 loading, respectively. Red, yellow, or white arrowheads mark tall hair cells with normal, reduced, or no apparent FM4-64 dye loading, respectively. Red asterisk in

*(Continued)*

**FIGURE 2 |** Continued
panel **(B”’)** marks a short hair cell erratic that permits FM4-64 entry in the absence of Tmc2a and Tmc2b. **(C–E)** Graphs of normalized hair cell fluorescence intensity ratios ($I_{\text{Tall HCs (hair cells)}}/I_{\text{Short HCs}}$, **C**) and the percentages of hair cells that loaded with FM4-64 ($n_{\text{loaded HCs}}/n_{\text{total HCs}}$, **D,E**). **(C)** Two-tailed unpaired student's *t*-test, $^{****}P < 0.0001$. **(D)** One-way ANOVA, $P = 0.6076$. **(E)** Two-tailed unpaired student's *t*-test, $^{****}P < 0.0001$, $^{**}P = 0.0017$. For the *tmc1*$^{cwr4}$ single mutant, $n_{\text{Tall HCs}} = 23$, $n_{\text{crista}} = 4$. For the *tmc2b*$^{cwr2}$ *tmc2a*$^{cwr3}$ double mutant, $n_{\text{Tall HCs}} = 15$, $n_{\text{short HCs}} = 28$, $n_{\text{crista}} = 3$. For the *tmc2a*$^{cwr3}$ single mutant, $n_{\text{Tall HCs}} = 21$, $n_{\text{short HCs}} = 30$, $n_{\text{crista}} = 3$. For the controls, $n_{\text{Tall HCs}} = 27$, $n_{\text{short HCs}} = 40$, $n_{\text{crista}} = 4$. **(F)** 4-Di-2-ASP (left, live) and FM1-43FX (right, fixed with hair bundles labeled by phalloidin) uptake assays demonstrate that mechanotransduction of lateral crista hair cells is absent in the *tmc2b*$^{cwr8}$ *tmc1*$^{cwr4}$ *tmc2a*$^{cwr6}$ triple mutant, regardless of hair cell subtype. Control, *tmc2b*$^{cwr8/+}$ *tmc1*$^{cwr4/+}$ *tmc2a*$^{cwr6/+}$. **(A,B,F)** Scale bar = 5 μm. **(G)** Model of Tmc dependencies in the central thickness of the lateral crista.

∼19 μm) had significantly reduced labeling with 4-Di-2-ASP in the central thickness of the lateral crista, indicating that mechanotransduction is greatly diminished in these cells.

Because these outcomes disagree with recent findings by Smith et al. (2020), who stated that Tmc1 and Tmc2b are individually sufficient for MET function in tall hair cells and did not note a difference in uptake of FM dye in their *tmc1* mutant, we verified our findings using a second *tmc1* mutant strain, *tmc1*$^{cwr4}$ (**Supplementary Tables S1, S2**; Chen et al., 2020). In the *tmc1*$^{cwr4}$ mutant, tall hair cells in the central thickness of the lateral crista displayed a substantial reduction in uptake after 4-Di-2-ASP presentation (**Figure 2A**).

To further analyze the relationship between Tmc1 reliance and hair cell morphology, we applied a double-labeling scheme. Specifically, we generated *tmc1*$^{cwr4}$ mutant larvae that express GCaMP6s-CAAX by outcrossing, injected their ears with fluorescent molecule FM4-64, and then imaged the hair cells of their cristae. GCaMP6s-CAAX is a fluorescent protein that labels the plasma membrane, defining the outline of each hair cell through illumination (Lukasz and Kindt, 2018). FM4-64 is a fluorescent molecule that passes through the transduction channel similarly to 4-Di-2-ASP (Meyers et al., 2003), and its emission spectra is distinguishable from that of GCaMP6s-CAAX. This semi-quantitative method detecting FM4-64 demonstrated that the *tmc1*$^{cwr4}$ mutant that expressed GCaMP6s-CAAX contained tall hair cells with reduced mechanotransduction capacity. The flawed mechanotransduction was manifested by a reduction of ∼48% in the normalized fluorescence intensity ratio in the tall hair cell population (**Figures 2B’,B”,C**).

A potential explanation for the discrepancy between our findings and those of Smith et al. (2020) could be genetic in origin. Smith et al. (2020) used a zebrafish strain with a mutation in exon 3 of the *tmc1* gene. In our work, the *tmc1*$^{cwr4}$ and *tmc1*$^{cwr5}$ mutations are on exon 7 and exon 5, respectively. It is possible that exon skipping plays a role (Anderson et al., 2017), and exon 3 of *tmc1* is not as critical for the protein's function in tall hair cells. Alternatively, Smith et al. (2020) may be imaging another region of the crista than the present study where hair cell Tmc dependencies are different. Nevertheless, tall hair cells in the central thickness of the lateral crista depend heavily on Tmc1 (**Figure 2G**).

## Short Hair Cells Predominantly Depend on Tmc2 Isoforms

Since tall hair cells are heavily dependent on Tmc1 for mechanotransduction, where short hair cells display no such reliance, we considered the possibility that short hair cells use Tmc2 isoforms, who are encoded by *tmc2a* and *tmc2b*. After injecting the larval ears of *tmc2b*$^{cwr2}$ *tmc2a*$^{cwr3}$ double mutants (**Supplementary Tables S1, S2**) with 4-Di-2-ASP and imaging optical sections of the central thicknesses of lateral cristae, we noted that most short hair cells (∼11 μm) do not permit passage of the fluorescent molecule, indicating that short hair cells require Tmc2 isoforms for mechanotransduction (**Figures 2A,G**). In contrast, in this double mutant, tall hair cell 4-Di-2-ASP labeling revealed no apparent phenotype.

Next, we looked to confirm the presence of unlabeled short hair cells using GCaMP6s-CAAX as a counter label in the double mutant. Specifically, we generated *tmc2b*$^{cwr2}$ *tmc2a*$^{cwr3}$ animals that express GCaMP6s-CAAX, and then imaged uptake of FM4-64 by hair cells of the lateral cristae. Similar to labeling with 4-Di-2-ASP, most short hair cells do not take up the FM4-64, contrasting with the tall hair cells, which permit entry of the fluorescent molecule (**Figures 2B”’,D,E**). Although most short hair cells lacking Tmc2 isoforms did not take up FM4-64, on occasion a short hair cell did permit entry of this fluorescent molecule. As these cells seemed out of place, we termed them short hair cell erratics (**Figure 2B”’**, bottom, red asterisk), borrowing from the geology term for rocks that appear incongruous with the local bedrock.

Because *tmc2a* mRNA is detectable in the crista by *in situ* hybridization, where *tmc2b* mRNA is not (Maeda et al., 2014), we aimed to determine if removal of Tmc2a alone could perturb mechanotransduction by short hair cells. Thus, we carried out 4-Di-2-ASP uptake studies on hair cells in *tmc2a*$^{cwr3}$ single mutant zebrafish. Similar to the double mutant, the *tmc2a*$^{cwr3}$ single mutant predominantly lacked 4-Di-2-ASP uptake by short hair cells (**Figure 2A**). Comparable results were obtained with FM4-64 injections into the ears of the *tmc2a*$^{cwr3}$ single mutant that expresses GCaMP6s-CAAX (**Figures 2B””,D,E**). These findings confirm that short hair cells mainly depend on Tmc2 isoforms, and Tmc2a plays a significant role in these cells.

We hypothesized that the short hair cell erratics, who permit mechanotransduction despite being devoid of Tmc2 isoforms, are in fact dependent on Tmc1. To test this, we carried out 4-Di-2-ASP uptake studies on the *tmc2b*$^{cwr8}$ *tmc1*$^{cwr4}$ *tmc2a*$^{cwr6}$ triple mutant (Chen et al., 2020; **Supplementary Tables S1, S2**). None of the lateral crista hair cells permitted 4-Di-2-ASP entry, indicating that short hair cell erratics of the lateral crista are dependent on Tmc1 (**Figure 2F**). We confirmed these results using FM1-43FX, a fluorescent molecule that enters through the mechanotransduction channel (Gale et al., 2001; Meyers et al., 2003; Chou et al., 2017; **Figure 2F**). In all, these findings show

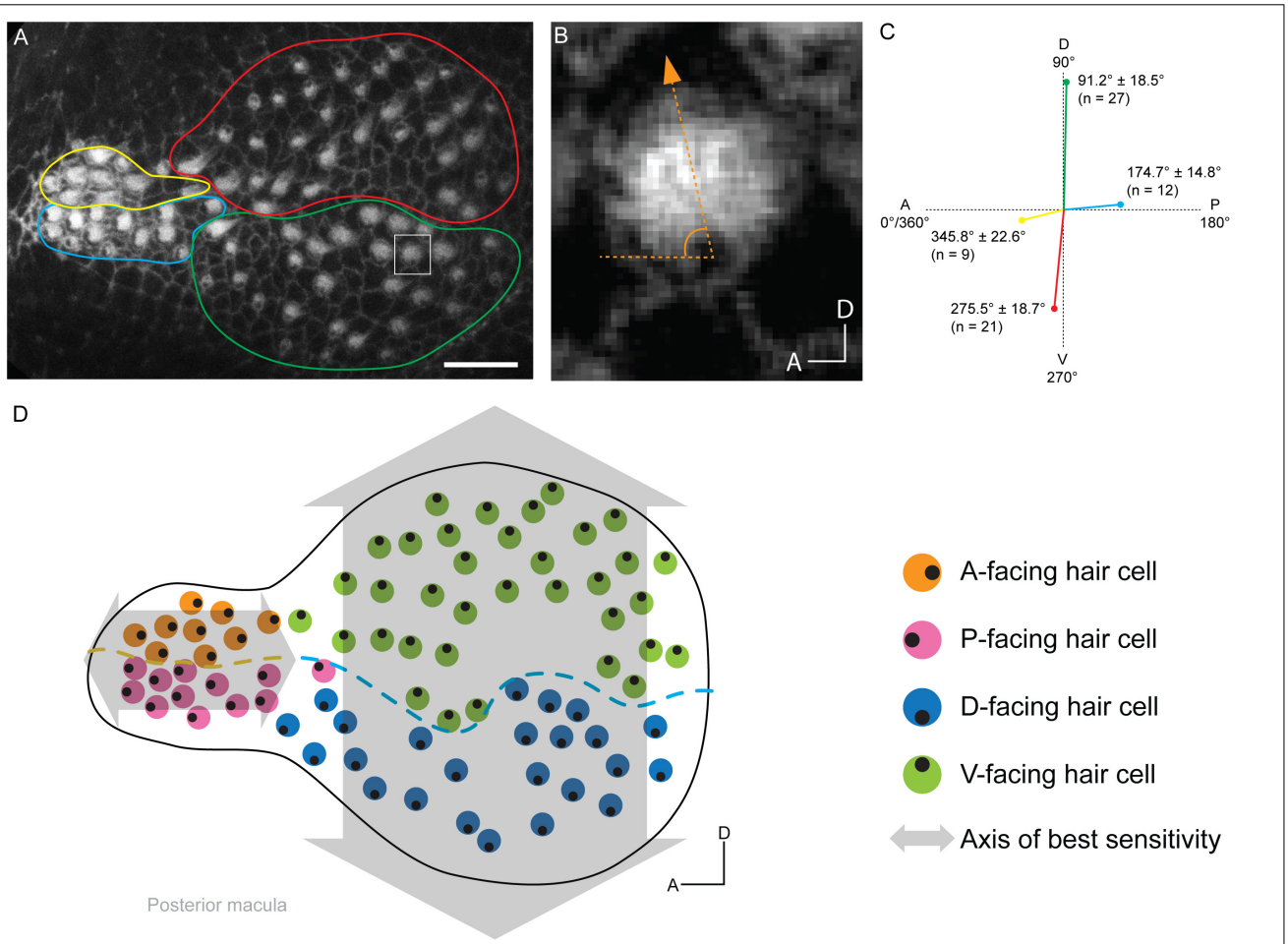


**FIGURE 3 |** Map of hair bundle polarities in the posterior macula of a 7-dpf larva. **(A)** Confocal image of a single posterior macula labeled with phalloidin. Circumscribed regions contain groups of hair cells with particular hair bundle polarities: yellow – anterior, blue – posterior, red – ventral, and green – dorsal. **(B)** Enlarged view of a hair bundle in square in panel **(A)**. The hair bundles angle of deviation from the A-P axis is depicted. **(C)** Posterior macula hair bundle polarities and associated hair cell numbers. Each colored line length represents the number of hair cells with that orientation in each group from panel **(A)**. Each line orientation is the mean deviation from the A-P axis ± SD. **(D)** Map of hair bundle polarities in the posterior macula from panel **(A)**. Each color circle represents an individual hair cell, and the black dot within represents the position of the kinocilium, which reflects bundle polarity. Lines of polarity reversal are shown in the bulbus (blue dashed line) and narrow region (yellow dashed line) for D-V-facing and A-P-facing hair cells, respectively. Axes of best sensitivity are depicted by gray arrows.

that hair cell morphology coincides with a bias for specific Tmc use within the ear, but the relationship of a particular Tmc to a morphology need not be absolute.

## Hair Cell Position and Axis of Best Sensitivity Coincide With Tmc Dependencies in the Saccule

Next, we considered whether four hair cell anatomical variables – as they relate to Tmc dependencies – play a role in hearing: organ, position within an organ, axis of best sensitivity in which the hair bundle responds, and the hair bundle's orientation within this axis. More specifically, a hair cell's dependency on a particular Tmc may be restricted to one hair bundle orientation within an axis of best sensitivity (asymmetric model), or it may be free of this constraint (symmetric model) (**Supplementary Figure S1**). We explored Tmc dependencies in the saccule, which is considered the major hearing organ in the larval zebrafish ear (Inoue et al., 2013) and offers a sensory epithelium where the hair bundle orientations can be mapped and correlated to function.

To explore these four hair cell anatomical variables and their relationship to Tmc dependencies in the saccule, we took a two-step approach. We mapped the hair bundle orientations of the 7-dpf saccule of the wild-type *Tübingen* (*Tü*) strain by labeling with fluorophore-coupled phalloidin and then overlaid hair cell Tmc dependencies onto this organ. The first step was done in quadruplicate and a representative map is displayed in **Figure 3**. The map of the posterior macula revealed a stereotyped organization of hair bundles similar to those of 5-dpf animals (Inoue et al., 2013), showing that during this developmental time period the hair bundle orientations are not greatly altered. Overall, the organ is light bulb shaped (**Figures 3A,D**). There is an anterior narrowing where the dorsal hair cells tend to face

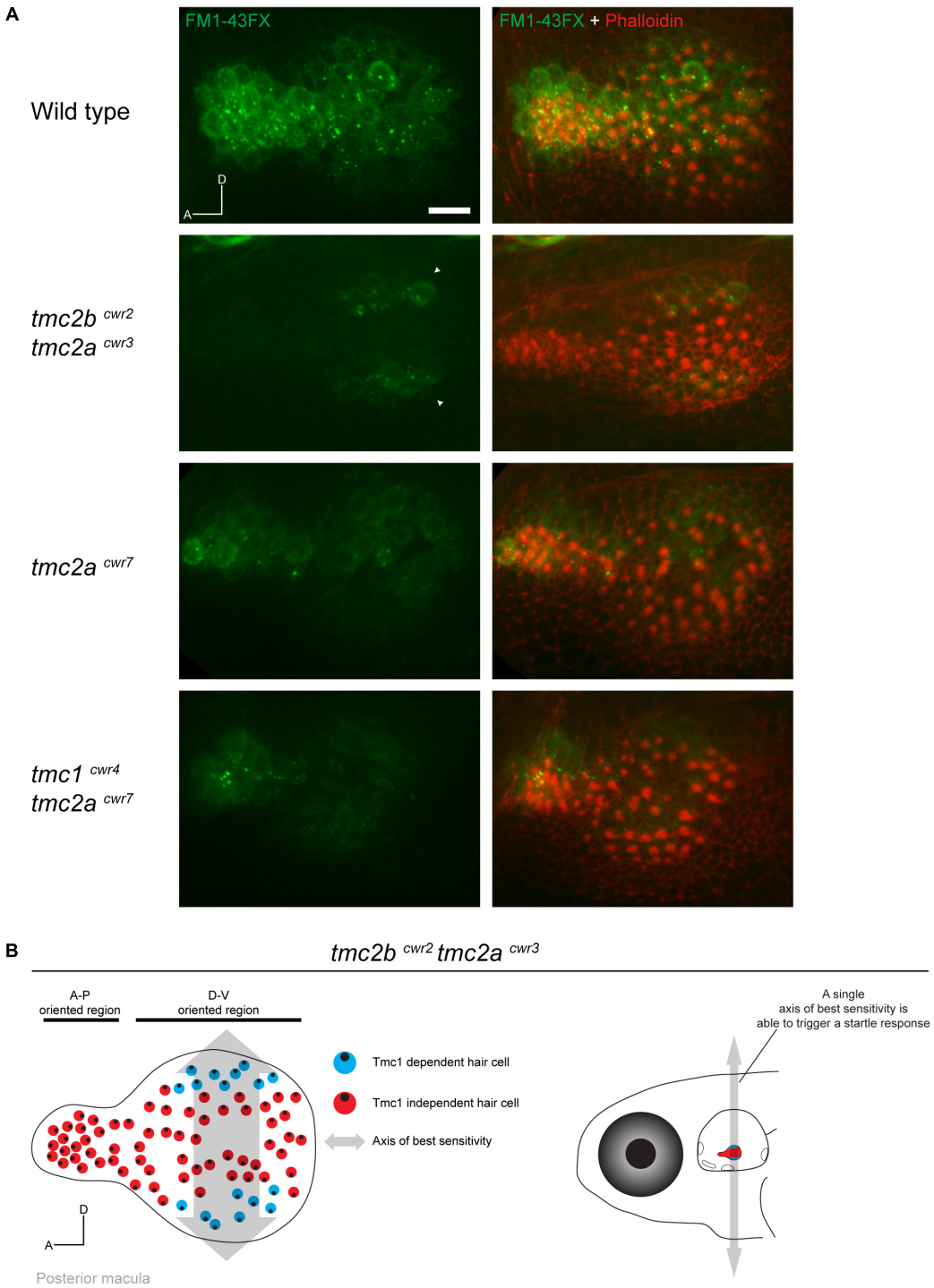


**FIGURE 4 |** Hair cells of the posterior macula are differentially dependent on Tmc proteins. **(A)** Representative images of FM1-43FX (green) uptake in posterior maculae of wild-type and mutant larvae at 7 dpf. Hair bundles are labeled with phalloidin (red). In a wild-type macula, passage of FM1-43FX is observed in all hair cells. In the *tmc2b*$^{cwr2}$ *tmc2a*$^{cwr3}$ double mutant, FM1-43FX uptake is limited to two symmetrical stripes of hair cells located toward the posterior of the macula at the dorsal and ventral poles (arrowheads). In contrast, the *tmc2a*$^{cwr7}$ single mutant or *tmc1*$^{cwr4}$ *tmc2a*$^{cwr7}$ double mutant hair cells do not reveal a pattern similar to the *tmc2b*$^{cwr2}$ *tmc2a*$^{cwr3}$ double mutant. A, anterior; D, dorsal. Scale bar = 10 μm. Similar patterns of saccular uptake were observed for five larvae for each mutant type and control. **(B)** (Left) Map of hair cell positions and hair bundle polarities in relation to Tmc1 use within the posterior macula based on the *tmc2b*$^{cwr2}$ *tmc2a*$^{cwr3}$ double mutant. Each color circle (red or blue) represents an individual hair cell, and the black dot within represents the position of the kinocilium, which reflects bundle polarity. Double-headed arrow indicates axis of best sensitivity preserved in the *tmc2b*$^{cwr2}$ *tmc2a*$^{cwr3}$ double mutant. (Right) Schematized zebrafish head depicting just one axis of best sensitivity (dorsal-ventral) able to elicit a startle response.

anteriorly, but the ventral cells face posteriorly – establishing a single anterior–posterior axis of best sensitivity (**Figures 3A,D**). Hair bundles in the bulbous region have two orientations: the dorsal hair cells face ventrally, and the ventral hair cells face dorsally, yielding a single dorsal-ventral axis of best sensitivity (**Figures 3B–D**). There seems to be a transition area between the narrow region and the bulbous region that has hair bundles that may be in the process of orienting to the major axes of best sensitivity (**Figure 3A,D**). Overall, we show that 7-dpf larvae have two major axes of best sensitivity that are perpendicular to each other, and run parallel to those of the lateral line (Lopez-Schier et al., 2004; Chou et al., 2017), suggesting the paramount importance of detecting these directions for larval survival. Interestingly, the adult zebrafish saccule and those of goldfish and carp have just one axis of best sensitivity (Platt, 1993), contrasting with those of otophysan fishes who have two (Popper and Lu, 2000). Thus, the larval zebrafish saccular architecture – with respect to hair bundle orientations – is more similar to that of the latter superorder than it is to adult zebrafish.

Using this map, we explored if hair cell anatomical variables – either position of the hair cell, axis of best sensitivity, or a hair bundle's orientation within this axis – play a role in Tmc dependencies in the ear. Alternatively, these variables may not be relevant and Tmc dependencies in the maculae may be organized by a different set of criteria or even randomly. To address this question, we used the *tmc2b*$^{cwr2}$ *tmc2a*$^{cwr3}$ double mutant larvae for a number of favorable properties that it offers. One, hair cell mechanotransduction in this fish strain is dependent on just one Tmc protein, Tmc1, eliminating the chances of complex Tmc interactions that could complicate the interpretation of results. Two, the hair cells that still function are in the posterior macula, but functional hair cells have not been mapped with high resolution (Chen et al., 2020; Smith et al., 2020). Three, this mutant can hear. Its capacity to do so is limited, but the presence of Tmc1 is able to mediate a C-start response to vibrational stimuli (Chen et al., 2020).

To evaluate the potential roles of the anatomical variables, we injected FM1-43FX into the ears of mutant zebrafish and labeled the animals with phalloidin to reveal hair bundle orientations and FM1-43FX uptake. High-resolution confocal images revealed that Tmc1-dependent transduction in the larval saccule is limited to just ∼10–18 hair cells. These Tmc1-dependent hair cells were highly constrained, located in the bulged end of the lightbulb-shaped organ in two symmetrical stripes (**Figures 4A,B**). The Tmc1-dependent stripes are located at opposite poles of the organ, dorsal and ventral. Each stripe is approximately two hair cells in thickness. All Tmc1-dependent hair cells fall within a unitary axis of best sensitivity, dorsal-ventral, and face both directions, preserving symmetry. This pattern of uptake is not observed in the *tmc2a*$^{cwr7}$ single mutant or *tmc1*$^{cwr4}$ *tmc2a*$^{cwr7}$ double mutant, indicating it is a pattern specific to Tmc1 (**Figure 4A**). These findings reveal a number of rules about the geometrical nature of Tmc1 dependencies. One, position is a major factor in determining Tmc1 dependence because only cells in the peripherally positioned stripes use this protein. Two, Tmc1-dependence falls within a single axis of best sensitivity, dorsal-ventral. Three, not all hair cells depend on Tmc1 in this axis, so it cannot be the only determining factor of Tmc1 dependence. Four, since Tmc1-dependent hair cells have opposite hair bundle orientations, a single hair bundle direction does not govern Tmc1 reliance, thus, satisfying the symmetric model of Tmc1 dependence (**Supplementary Figure S1**).

## CONCLUSION

Tmc proteins have emerged as mechanotransduction channel components of hair cells. The fundamental rules of how members of this small family of proteins are paired with hair cells within the crista and saccule for the inception of hearing and balance are poorly understood. We have investigated which, if any, of five hair cell anatomical variables coincide with different Tmc use within the ear: organ, position within the organ, morphology, axis of hair bundle sensitivity, and hair bundle orientation within this axis. First, we demonstrated that the zebrafish lateral crista has tall and short hair cells that have mean lengths of ∼17 and ∼11 μm, respectively. This finding demonstrates that fish have more than one hair cell type in the crista to detect head rotations. Moreover, using a suite of genetic mutations, we showed that tall hair cells that lack Tmc1 display defects in mechanotransduction, and short hair cells predominately depend on Tmc2 isoforms. However, there are rare short hair cells that do not follow these rules. Termed short hair cell erratics, these less frequently observed cells of the central thickness of the lateral crista use Tmc1. In all, these findings suggest that there are functional differences between the tall and short hair cells at the level of mechanotransduction.

The role of short hair cell erratics is unclear. They may be maturing hair cells that are transitioning between different Tmcs during the course of development, similar to what has been observed in mice (Kawashima et al., 2011). On the other hand, short hair cell erratics may be mature, functional hair cells that need to have a different Tmc complement than the similarly sized majority and contribute specifically to detecting rotational accelerations by adding diversity to the mechanotransduction response of the whole crista. The particular differences that may be instilled into mechanotransduction by each Tmc or each Tmc combination is yet unknown. However, it is clear that TMC1 and TMC2 are not wholly equivalent in mammals (Nakanishi et al., 2018), and this may be true for zebrafish Tmc protein isoforms as well.

To examine the fundamentals of Tmc function in hearing, we used the saccule, the primary hearing organ of the larval zebrafish ear, and the *tmc2b*$^{cwr2}$ *tmc2a*$^{cwr3}$ double mutant zebrafish, which has just a handful of hair cells that permit attenuated hearing. This simplified genetic *tmc* background has a single Tmc protein, Tmc1, that enables inconsistent hearing as we described in Chen et al. (2020). More precisely, in *tmc2b*$^{cwr2}$ *tmc2a*$^{cwr3}$ double mutants, when presented with vibrational stimuli, just 39% were reacted to with a C-start reflex; in contrast, controls reacted to 100% of stimuli (Chen et al., 2020). The variability in responsiveness occurred within individual fish. By mapping hair cell position, hair bundle orientation, and the functional hair cells

of the saccule, we identify a set of succinct rules for Tmc1 function and ultimately hearing. One, hair cell location is a key factor that correlates with Tmc1 dependence. Two, Tmc1-dependent hair cells occupy a single axis of best sensitivity. Three, not all hair cells depend on Tmc1 in this axis. Four, hair bundles that depend on Tmc1 face both directions within the axis of best sensitivity and are equally distributed along a mirror plane of symmetry (**Supplementary Figure S1**). Other factors that may correlate with hair cell Tmc dependency, such as hair cell innervation pattern and the ultimate destination within the central nervous system the mechanical information derived from a particular Tmc is sent, are potential areas that may reveal the significance of Tmc diversity.

Finally, these data suggest minimal parameters for hearing in a vertebrate. This is because *tmc2b*$^{cwr2}$ *tmc2a*$^{cwr3}$ double mutant zebrafish can hear (Chen et al., 2020), and the saccule is the major hearing organ of larvae (Inoue et al., 2013). Hearing can occur with just 10–18 hair cells functional in each saccule. These cells need to only express Tmc1 and lay within a single (dorsal-ventral) axis of best sensitivity (**Figure 4B**). Therefore, hair cells within the anterior–posterior axis of best sensitivity are not required to elicit a startle response. In summary, by investigating Tmc1's role in the saccule, we have established minimal anatomical and molecular genetic requirements and relationships for hearing.

# METHODS

## Zebrafish

Protocols for housing and handling of zebrafish were approved by Case Western Reserve University's Institutional Animal Care and Use Committee. Wild-type *Tübingen* (*Tü*), *Tg(myo6b:GCaMP6s-caax)* transgenic (Lukasz and Kindt, 2018), *tmc1*$^{cwr5}$ mutant, *tmc2a*$^{cwr3}$ mutant, *tmc2b*$^{cwr2}$ *tmc2a*$^{cwr3}$ double mutant, and *tmc2b*$^{cwr8}$ *tmc1*$^{cwr4}$ *tmc2a*$^{cwr6}$ triple mutant fish (Chen et al., 2020) were used in this study.

## Mutation of *tmc1* and *tmc2a* With CRISPR/Cas9

CRISPR gene editing was performed as described previously (Chen et al., 2020). *Tmc1* (ENSDARG00000056386) was targeted with an sgRNA complementary to exon 7 (5′-TGGGCTG GTCATGGTTCCAG-3′). *Tmc2a* (ENSDARG00000033104) was targeted with an sgRNA complementary to exon 9 (5′-AGGTC CCAATGCCCACCATG-3′). The mutations in each gene carried by founder fish and F1 fish were identified using sequencing primers described previously (Chen et al., 2020). *Tmc1*$^{cwr4}$ mutant fish with an 8-bp deletion and *tmc2a*$^{cwr7}$ mutant fish with a 1-bp indel were used for assays in this work. The *tmc2a*$^{cwr7}$ single mutant fish was isolated from a crossover recombination event after mating *tmc1*$^{cwr4/+}$ *tmc2a*$^{cwr7/+}$ fish with wild-type animals and subsequent incrossing.

## Transgenesis

To generate *Tg(myo6b:Cerulean)* zebrafish, DNA plasmid, pMT/myo6b/cerulean, at 100 ng/μl and *Tol*2 RNA at 62.5 ng/μl were mixed with phenol red and 0.125 mM KCl solution and then coinjected into *Tü* zebrafish embryos at the one-cell stage to create somatic transgenics. To generate a stable transgenic line, positive founder fish were outcrossed with *Tü* zebrafish.

To generate *Tg(myo6b:GCaMP6s-CAAX)*; *tmc2b*$^{cwr2}$ *tmc2a*$^{cwr3}$ zebrafish, we crossed *tmc2b*$^{cwr2/+}$ *tmc2a*$^{cwr3}$ fish with stable transgenic *Tg(myo6b:GCaMP6s-CAAX)* fish. We then crossed *Tg(myo6b:GCaMP6s-CAAX)*; *tmc2b*$^{cwr2/+}$ *tmc2a*$^{cwr3/+}$ fish with *tmc2b*$^{cwr2/+}$ *tmc2a*$^{cwr3}$ fish to obtain *Tg(myo6b:GCaMP6s-CAAX)*; *tmc2b*$^{cwr2}$ *tmc2a*$^{cwr3}$ zebrafish. Crossing was used to generate *Tg(myo6b:GCaMP6s-CAAX)*; *tmc1*$^{cwr4}$ zebrafish.

## Fixed and Live Imaging

Fixation and FM1-43FX imaging were performed as described previously (Chou et al., 2017). For live imaging, the larvae were anesthetized in 0.612 mM ethyl 3-aminobenzoate methanesulfonic acid (Sigma-Aldrich) in fish water and mounted laterally on glass-bottom dishes (MatTek) in 1.0% (wt/vol) low-melting-point agarose (Promega). Z-stack images of the entire lateral crista were collected on a confocal microscope (TCS SP8, Leica) with a 40 × /1.3 NA oil-immersion objective. A laser wavelength of 405 nm was used for Cerulean excitation. A laser wavelength of 488 nm was used for 4-Di-2-ASP excitation. Laser wavelengths of 545 and 488 nm were used for FM4-64 and GCaMP6s excitation, respectively. For the identification of hair bundle orientations, Alexa Fluor 633 phalloidin at 1:50 dilution was used to label actin filaments (Chou et al., 2017; Chen et al., 2020). For Alexa Fluor 633, an excitation wavelength of 633 nm was used.

## Image Processing and Quantification

Confocal images were imported to and analyzed in ImageJ (NIH). A Gaussian blur filter (radius = 1.00) was applied to all images to reduce random noise. For Cerulean, GCaMP6s, and phalloidin channels, the brightness/contrast were adjusted automatically to enhance the morphological appearance of hair cells or hair bundles. For the styryl dye (4-Di-2-ASP, FM4-64, and FM1-43FX) emission channels, raw data are presented. Images of partial Z-stack maximum projections are shown for the lateral crista to minimize hair cell overlap. For mapping, images of whole Z-stack maximum projections are shown for the posterior macula.

Due to the densely overlapping nature of crista hair cells, cell length measurements or enumeration was performed manually by scanning the Z-stack series of Cerulean-labeled or FM4-64/GCaMP6s double-labeled hair cells, respectively. Graphs were generated in GraphPad Prism version 8 (GraphPad Software).

## Statistics

All statistics were performed by GraphPad Prism version 8. Data are reported as mean ± SEM or SD. Comparisons between groups were tested by one-way ANOVA or Student's *t*-test. Short hair cells were judged to be positive for mechanotransduction if their fluorescence intensity was 2.33 standard deviations greater than the background intensity (Honegger et al., 2011).

## Quantification of FM4-64 Intensity

To quantitate FM4-64 uptake in the lateral crista hair cells, a 0.75 $\mu m^2$ square region of interest (ROI) was defined manually within the hair cell, not overlapping with other hair cells, using the GCaMP6s-CAAX images taken simultaneously (LAS X, Leica). Each ROI selected for quantitation was from the optical slice with the maximum fluorescence intensity of that hair cell's Z-stack. After background subtraction, the average of the FM4-64 intensities of individual hair cells in the lateral crista were normalized to the average of the intensity of the corresponding control group (**Figure 2C**).

## DATA AVAILABILITY STATEMENT

The raw data supporting the conclusions of this article will be made available by the authors, without undue reservation.

## ETHICS STATEMENT

The animal study was reviewed and approved by IACUC.

## AUTHOR CONTRIBUTIONS

SZ carried out gene editing. SZ and HW performed the dye injection. ZC and SZ performed the imaging. BM wrote the manuscript. All authors developed the experimental plans and commented on and contributed to the final version of the manuscript.

## FUNDING

This work was supported by NIH grants DC009437 (BM) and the Center for Clinical Research and Technology at University Hospitals Cleveland Medical Center (BM).

## ACKNOWLEDGMENTS

We are grateful to Drs. K. Kindt and D. Rabile for the *Tg*(*myo6b:GCaMP6s-CAAX*) transgenic line and the *myosin6b* promoter plasmid, respectively. We acknowledge H. Nguyen and Y. McDermott for zebrafish husbandry and the members of our laboratory who provided discussion and comments on this manuscript.

## SUPPLEMENTARY MATERIAL

The Supplementary Material for this article can be found online at: https://www.frontiersin.org/articles/10.3389/fcell.2020.570486/full#supplementary-material

**Supplementary Figure 1 |** Symmetric and asymmetric models of Tmc dependencies within the ear.

## REFERENCES

Anderson, J. L., Mulligan, T. S., Shen, M. C., Wang, H., Scahill, C. M., Tan, F. J., et al. (2017). mRNA processing in mutant zebrafish lines generated by chemical and CRISPR-mediated mutagenesis produces unexpected transcripts that escape nonsense-mediated decay. *PLoS Genet.* 13:e1007105. doi: 10.1371/journal.pgen.1007105

Ballesteros, A., Fenollar-Ferrer, C., and Swartz, K. J. (2018). Structural relationship between the putative hair cell mechanotransduction channel TMC1 and TMEM16 proteins. *eLife* 7:e38433. doi: 10.7554/eLife.38433.039

Chen, Z., Zhu, S., Kindig, K., Wang, S., Chou, S. W., Davis, R. W., et al. (2020). Tmc proteins are essential for zebrafish hearing where Tmc1 is not obligatory. *Hum. Mol. Genet.* 29, 2004–2021. doi: 10.1093/hmg/ddaa045

Chou, S. W., Chen, Z., Zhu, S., Davis, R. W., Hu, J., Liu, L., et al. (2017). A molecular basis for water motion detection by the mechanosensory lateral line of zebrafish. *Nat. Commun.* 8:2234. doi: 10.1038/s41467-017-01604-2

Cruz, I. A., Kappedal, R., Mackenzie, S. M., Hailey, D. W., Hoffman, T. L., Schilling, T. F., et al. (2015). Robust regeneration of adult zebrafish lateral line hair cells reflects continued precursor pool maintenance. *Dev. Biol.* 402, 229–238. doi: 10.1016/j.ydbio.2015.03.019

Cunningham, C. L., and Muller, U. (2019). Molecular structure of the hair cell mechanoelectrical transduction complex. *Cold Spring Harb. Perspect. Med.* 9:a033167. doi: 10.1101/cshperspect.a033167

Cunningham, C. L., Qiu, X., Wu, Z., Zhao, B., Peng, G., Kim, Y. H., et al. (2020). TMIE defines pore and gating properties of the mechanotransduction channel of mammalian cochlear hair cells. *Neuron* 107, 126–143.e8. doi: 10.1016/j.neuron.2020.03.033

Deans, M. R. (2013). A balance of form and function: planar polarity and development of the vestibular maculae. *Semin. Cell Dev. Biol.* 24, 490–498. doi: 10.1016/j.semcdb.2013.03.001

Eatock, R. A., and Hurley, K. M. (2003). Functional development of hair cells. *Curr. Top. Dev. Biol.* 57, 389–448. doi: 10.1016/s0070-2153(03)57013-2

Erickson, T., Morgan, C. P., Olt, J., Hardy, K., Busch-Nentwich, E., Maeda, R., et al. (2017). Integration of Tmc1/2 into the mechanotransduction complex in zebrafish hair cells is regulated by Transmembrane O-methyltransferase (Tomt). *eLife* 6:e28474. doi: 10.7554/eLife.28474.020

Gale, J. E., Marcotti, W., Kennedy, H. J., Kros, C. J., and Richardson, G. P. (2001). FM1-43 dye behaves as a permeant blocker of the hair-cell mechanotransducer channel. *J. Neurosci.* 21, 7013–7025. doi: 10.1523/jneurosci.21-18-07013.2001

Ge, J., Elferich, J., Goehring, A., Zhao, H., Schuck, P., and Gouaux, E. (2018). Structure of mouse protocadherin 15 of the stereocilia tip link in complex with LHFPL5. *eLife* 7:e38770. doi: 10.7554/eLife.38770

Giese, A. P. J., Tang, Y. Q., Sinha, G. P., Bowl, M. R., Goldring, A. C., Parker, A., et al. (2017). CIB2 interacts with TMC1 and TMC2 and is essential for mechanotransduction in auditory hair cells. *Nat. Commun.* 8:43. doi: 10.1038/s41467-017-00061-1

Gleason, M. R., Nagiel, A., Jamet, S., Vologodskaia, M., Lopez-Schier, H., and Hudspeth, A. J. (2009). The transmembrane inner ear (Tmie) protein is essential for normal hearing and balance in the zebrafish. *Proc. Natl. Acad. Sci. U.S.A.* 106, 21347–21352. doi: 10.1073/pnas.0911632106

Guth, P. S., Fermin, C. D., Pantoja, M., Edwards, R., and Norris, C. (1994). Hair cells of different shapes and their placement along the frog crista ampullaris. *Hear. Res.* 73, 109–115. doi: 10.1016/0378-5955(94)90288-7

Haddon, C., and Lewis, J. (1996). Early ear development in the embryo of the zebrafish, *Danio rerio*. *J. Comp. Neurol.* 365, 113–128. doi: 10.1002/(sici)1096-9861(19960129)365:1<113::aid-cne9>3.0.co;2-6

Honegger, K. S., Campbell, R. A., and Turner, G. C. (2011). Cellular-resolution population imaging reveals robust sparse coding in the *Drosophila* mushroom body. *J. Neurosci.* 31, 11772–11785. doi: 10.1523/jneurosci.1099-11.2011

Hudspeth, A. J. (1989). How the ear's works work. *Nature* 341, 397–404. doi: 10.1038/341397a0

Inoue, M., Tanimoto, M., and Oda, Y. (2013). The role of ear stone size in hair cell acoustic sensory transduction. *Sci. Rep.* 3:2114. doi: 10.1038/srep02114

Jia, Y., Zhao, Y., Kusakizako, T., Wang, Y., Pan, C., Zhang, Y., et al. (2019). TMC1 and TMC2 proteins are pore-forming subunits of mechanosensitive ion channels. *Neuron* 105, 310–321. doi: 10.1016/j.neuron.2019.10.017

Kandel, E. R. (2013). *Principles of Neural Science*, 5th Edn, New York, NY: McGraw-Hill.

Kawashima, Y., Geleoc, G. S., Kurima, K., Labay, V., Lelli, A., Asai, Y., et al. (2011). Mechanotransduction in mouse inner ear hair cells requires transmembrane channel-like genes. *J. Clin. Invest.* 121, 4796–4809. doi: 10.1172/jci60405

Kurima, K., Ebrahim, S., Pan, B., Sedlacek, M., Sengupta, P., Millis, B. A., et al. (2015). TMC1 and TMC2 localize at the site of mechanotransduction in mammalian inner ear hair cell *Stereocilia*. *Cell Rep.* 12, 1606–1617. doi: 10.1016/j.celrep.2015.07.058

Li, X., Yu, X., Chen, X., Liu, Z., Wang, G., Li, C., et al. (2019). Localization of TMC1 and LHFPL5 in auditory hair cells in neonatal and adult mice. *FASEB J.* 33, 6838–6851. doi: 10.1096/fj.201802155rr

Lopez-Schier, H., Starr, C. J., Kappler, J. A., Kollmar, R., and Hudspeth, A. J. (2004). Directional cell migration establishes the axes of planar polarity in the posterior lateral-line organ of the zebrafish. *Dev. Cell* 7, 401–412. doi: 10.1016/j.devcel.2004.07.018

Lukasz, D., and Kindt, K. S. (2018). In vivo calcium imaging of lateral-line hair cells in larval Zebrafish. *J. Vis. Exp.* 141, 10.3791/58794. doi: 10.3791/58794

Maeda, R., Kindt, K. S., Mo, W., Morgan, C. P., Erickson, T., Zhao, H., et al. (2014). Tip-link protein protocadherin 15 interacts with transmembrane channel-like proteins TMC1 and TMC2. *Proc. Natl. Acad. Sci. U.S.A.* 111, 12907–12912. doi: 10.1073/pnas.1402152111

Mahendrasingam, S., and Furness, D. N. (2019). Ultrastructural localization of the likely mechanoelectrical transduction channel protein, transmembrane-like channel 1 (TMC1) during development of cochlear hair cells. *Sci. Rep.* 9:1274. doi: 10.1038/s41598-018-37563-x

Meyers, J. R., MacDonald, R. B., Duggan, A., Lenzi, D., Standaert, D. G., Corwin, J. T., et al. (2003). Lighting up the senses: FM1-43 loading of sensory cells through nonselective ion channels. *J. Neurosci.* 23, 4054–4065. doi: 10.1523/jneurosci.23-10-04054.2003

Nakanishi, H., Kurima, K., Pan, B., Wangemann, P., Fitzgerald, T. S., Geleoc, G. S., et al. (2018). Tmc2 expression partially restores auditory function in a mouse model of DFNB7/B11 deafness caused by loss of Tmc1 function. *Sci. Rep.* 8:12125. doi: 10.1038/s41598-018-29709-8

Nicolson, T. (2005). The genetics of hearing and balance in zebrafish. *Annu. Rev. Genet.* 39, 9–22. doi: 10.1146/annurev.genet.39.073003.105049

Owens, K. N., Coffin, A. B., Hong, L. S., Bennett, K. O., Rubel, E. W., and Raible, D. W. (2009). Response of mechanosensory hair cells of the zebrafish lateral line to aminoglycosides reveals distinct cell death pathways. *Hear. Res.* 253, 32–41. doi: 10.1016/j.heares.2009.03.001

Pacentine, I. V., and Nicolson, T. (2019). Subunits of the mechano-electrical transduction channel, Tmc1/2b, require Tmie to localize in zebrafish sensory hair cells. *PLoS Genet.* 15:e1007635. doi: 10.1371/journal.pgen.1007635

Pan, B., Akyuz, N., Liu, X. P., Asai, Y., Nist-Lund, C., Kurima, K., et al. (2018). TMC1 forms the pore of mechanosensory transduction channels in vertebrate inner ear hair cells. *Neuron* 99, 736–753.e736. doi: 10.1016/j.neuron.2018.07.033

Platt, C. (1993). Zebrafish inner ear sensory surfaces are similar to those in goldfish. *Hear. Res.* 65, 133–140. doi: 10.1016/0378-5955(93)90208-i

Popper, A. N., and Lu, Z. (2000). Structure-function relationships in fish otolith organs. *Fish. Res.* 46, 15–25. doi: 10.1016/s0165-7836(00)00129-6

Shotwell, S. L., Jacobs, R., and Hudspeth, A. J. (1981). Directional sensitivity of individual vertebrate hair cells to controlled deflection of their hair bundles. *Ann. N. Y. Acad. Sci.* 374, 1–10. doi: 10.1111/j.1749-6632.1981.tb30854.x

Smith, E. T., Pacentine, I., Shipman, A., Hill, M., and Nicolson, T. (2020). Disruption of tmc1/2a/2b genes in zebrafish reveals subunit requirements in subtypes of inner ear hair cells. *J. Neurosci.* 40, 4457–4468. doi: 10.1523/jneurosci.0163-20.2020

Sugihara, I., and Furukawa, T. (1989). Morphological and functional aspects of two different types of hair cells in the goldfish sacculus. *J. Neurophysiol.* 62, 1330–1343. doi: 10.1152/jn.1989.62.6.1330

Taylor, J. S., Van de Peer, Y., Braasch, I., and Meyer, A. (2001). Comparative genomics provides evidence for an ancient genome duplication event in fish. *Philos. Trans. R. Soc. Lond. B* 356, 1661–1679. doi: 10.1098/rstb.2001.0975

Zhao, B., Wu, Z., Grillet, N., Yan, L., Xiong, W., Harkins-Perry, S., et al. (2014). TMIE is an essential component of the mechanotransduction machinery of cochlear hair cells. *Neuron* 84, 954–967. doi: 10.1016/j.neuron.2014.10.041

**Conflict of Interest:** The authors declare that the research was conducted in the absence of any commercial or financial relationships that could be construed as a potential conflict of interest.

*Copyright © 2021 Zhu, Chen, Wang and McDermott. This is an open-access article distributed under the terms of the Creative Commons Attribution License (CC BY). The use, distribution or reproduction in other forums is permitted, provided the original author(s) and the copyright owner(s) are credited and that the original publication in this journal is cited, in accordance with accepted academic practice. No use, distribution or reproduction is permitted which does not comply with these terms.*

frontiers in Cell and Developmental Biology

REVIEW
published: 25 February 2021
doi: 10.3389/fcell.2021.643856

# Functional Role of Class III Myosins in Hair Cells

*Joseph A. Cirilo Jr., Laura K. Gunther and Christopher M. Yengo**

*Department of Cellular and Molecular Physiology, College of Medicine, Pennsylvania State University, Hershey, PA, United States*

Cytoskeletal motors produce force and motion using the energy from ATP hydrolysis and function in a variety of mechanical roles in cells including muscle contraction, cargo transport, and cell division. Actin-based myosin motors have been shown to play crucial roles in the development and function of the stereocilia of auditory and vestibular inner ear hair cells. Hair cells can contain hundreds of stereocilia, which rely on myosin motors to elongate, organize, and stabilize their structure. Mutations in many stereocilia-associated myosins have been shown to cause hearing loss in both humans and animal models suggesting that each myosin isoform has a specific function in these unique parallel actin bundle-based protrusions. Here we review what is known about the classes of myosins that function in the stereocilia, with a special focus on class III myosins that harbor point mutations associated with delayed onset hearing loss. Much has been learned about the role of the two class III myosin isoforms, MYO3A and MYO3B, in maintaining the precise stereocilia lengths required for normal hearing. We propose a model for how class III myosins play a key role in regulating stereocilia lengths and demonstrate how their motor and regulatory properties are particularly well suited for this function. We conclude that ongoing studies on class III myosins and other stereocilia-associated myosins are extremely important and may lead to novel therapeutic strategies for the treatment of hearing loss due to stereocilia degeneration.

**Keywords: actin, myosin, ATPase, stereocilia, MYO3A, MYO3B, force generation**

OPEN ACCESS

***Edited by:***
*Zhigang Xu,*
*Shandong University, China*

***Reviewed by:***
*Jonathan Bird,*
*University of Florida, United States*
*Benjamin Perrin,*
*Purdue University Indianapolis, United States*

***Correspondence:**
*Christopher M. Yengo*
*cmy11@psu.edu*

***Specialty section:***
*This article was submitted to Cell Growth and Division, a section of the journal Frontiers in Cell and Developmental Biology*

***Received:*** *18 December 2020*
***Accepted:*** *01 February 2021*
***Published:*** *25 February 2021*

***Citation:***
*Cirilo JA Jr, Gunther LK and Yengo CM (2021) Functional Role of Class III Myosins in Hair Cells. Front. Cell Dev. Biol. 9:643856. doi: 10.3389/fcell.2021.643856*

## INTRODUCTION

Hearing is a complex physiological processes that ultimately requires the conversion of a mechanical signal, in the form of sound waves, into an electrical signal that can be recognized by the auditory cortex in the brain. Unfortunately, when this tightly regulated process is disrupted, various forms of hearing loss can occur. In general, hearing loss affects 2 out of every 1,000 infants, with half of those cases having a genetic origin (DiStefano et al., 2019). In total, mutations in over 100 genes have been proposed to be associated with non-syndromic hearing loss and another 400 associated with syndromic hearing loss. The high prevalence of genetic forms of hearing loss highlights the importance of understanding the molecular causes and mechanisms of disease pathogenesis. Auditory and vestibular inner ear hair cells are the sensory cells of the inner ear that contain mechanosensitive cellular protrusions called stereocilia (White et al., 2020). In the organ of Corti, which houses the auditory inner ear hair cells, the stereocilia form a defined staircase-like pattern comprised of three rows of ascending lengths (**Figure 1A**). Each stereocilia is

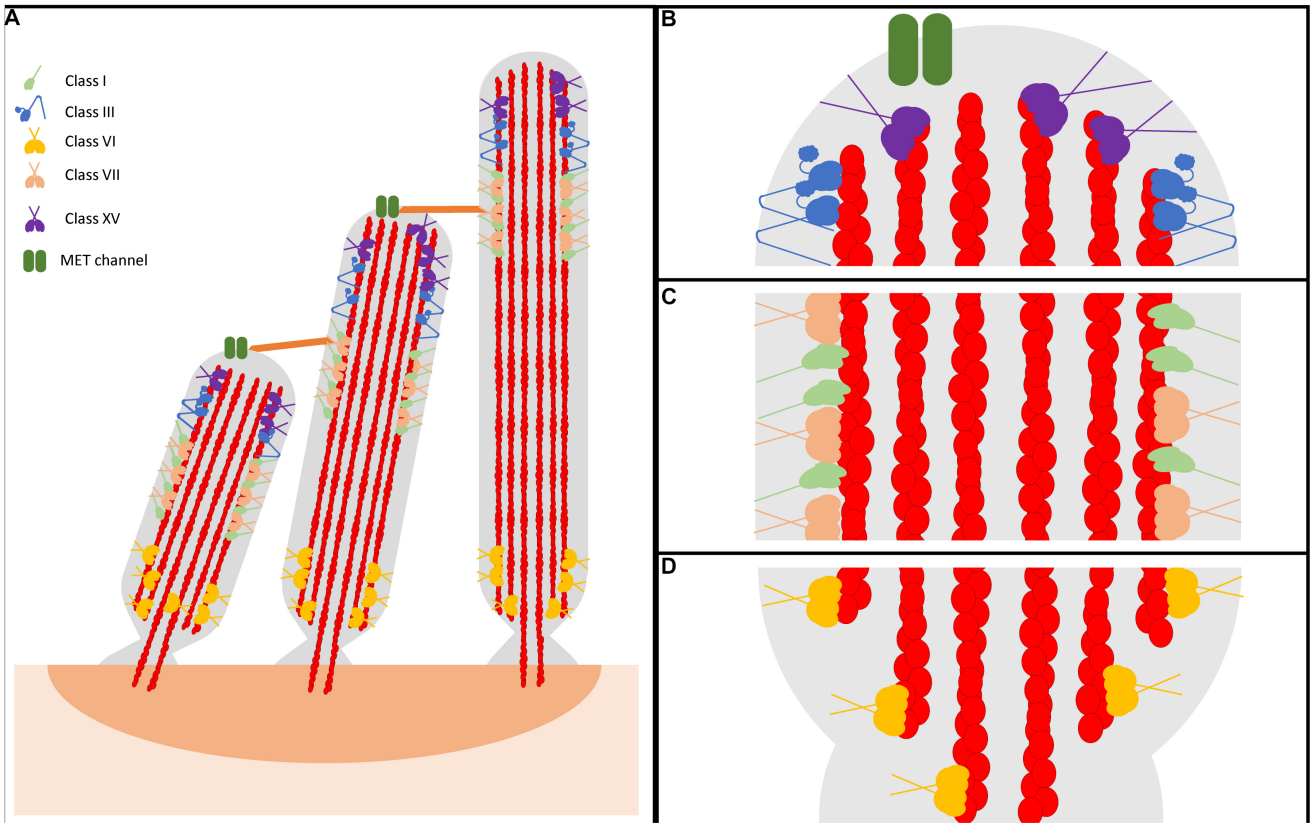


**FIGURE 1 |** Representative model of myosin motor localization in inner ear hair cell stereocilia. **(A)** Three rows of stereocilia form a staircase-like pattern, tethered together by various tip links, that is maintained through an organism's lifetime. In an individual stereocilium, there are three main regions where myosins localize: **(B)** the stereocilia tips, also known as the lower tip link density, containing class III myosins and class XV myosins, as well as MET channels, **(C)** the lower tip link density, containing class I and class VII myosins, and **(D)** the anklet, containing class VI myosins. MYO7A has been shown to localize throughout the entire length of the stereocilia, however since its proposed function as a tensioning myosin occurs at the UTLD it is shown only here for simplicity. Apart from class III myosins, all stereocilia myosins have direct evidence of membrane binding. However, class III myosins are hypothesized to interact with the membrane, potentially modulated via its binding partner MORN4. Lastly, both MYO7A and MYO15A have not been directly shown to form dimers on their own, however MYO7A can form dimers via a cargo-mediated mechanism and MYO15A was proposed to oligmerize in a complex with cargo. For simplicity, both are represented as dimers.

connected to its smaller/larger neighbor via a tip link, consisting of cadherin-23 and protcadherin-15 (Siemens et al., 2002; Kazmierczak et al., 2007; Grati et al., 2016). Also found at the tip are mechanoelectrical transduction, or MET, channels that respond to mechanical changes in the stereocilia, and ultimately trigger the electrophysiological response produced by the inner ear hair cell (Corey et al., 2019). Recent work has identified two subunits of the MET complex found at stereocilia tips, TMC1 and TMC2, which likely function as the mechanosenstive channels in stereocilia (Kurima et al., 2015; Yue et al., 2019; Jia et al., 2020). Specifically, as stereocilia are displaced by sound waves, the increased tension on MET channels increases their open probability and allows for the influx of cations into the hair cell, which causes a graded electrophysiological response relative to the degree of stereocilia displacement (Fettiplace, 2017). The stereocilia then can undergo a process known as adaptation, whereby they rapidly reset, leading to channel closing in preparation for the next stimulus. Depolarization of hair cells leads to an increase in synaptic release onto the afferent auditory neurons. Stereocilia length and morphology are critical for normal mechanotransduction, and therefore disruption of either of these properties results in hearing loss (Tilney and Saunders, 1983; Vélez-Ortega and Frolenkov, 2019).

Stereocilia are composed of a cytoskeleton actin core that is tightly bundled and crosslinked, providing a strong scaffold for the cellular protrusion (Tilney et al., 1980; Rzadzinska et al., 2005; **Figure 1**). The crosslinked actin filaments in the stereocilia are aligned parallel to each other with their plus (barbed) ends orientated at the tips. There are three main regions within the stereocilia: the tip, the tip-link, and the anklet. At the stereocilia tips, the actin cytoskeleton is thought to be more dynamic, undergoing regular turnover, while the remaining actin at the shaft and base is extremely stable (Zhang et al., 2012; McGrath et al., 2017; Vélez-Ortega and Frolenkov, 2019). The upper tip link density, located along the stereocilia shaft, contains complexes of proteins responsible for maintaining the link between adjacent stereocilia (Grati and Kachar, 2011; He et al., 2019). Lastly, the anklet contains strong links between the actin

cytoskeleton, which is tapered at the base, and the membrane and helps maintain stereocilia morphology at the base (Grati et al., 2012). Though the tips are dynamic, stereocilia length must be precisely maintained throughout an organism's lifetime. A key question in the field is how stereocilia length is maintained both throughout development, as well as in a mature organism. In addressing this question, recent studies have determined that the turnover of actin at the tips in adult hair cells is restricted only to the tip region and requires actin severing proteins, suggesting a unique mechanism of actin turnover separate from what is observed in more dynamic actin protrusions (Zhang et al., 2012; Drummond et al., 2015; Narayanan et al., 2015). For example, filopodia and microvilli are known to renew their actin bundles by an actin treadmilling mechanism, a process by which new actin monomers are added to the protrusion tips and travel to the base as they cycle through the filament (Tyska and Mooseker, 2002; Loomis et al., 2003; Craig et al., 2012). In addition, researchers have identified many different stereocilia-associated proteins found to play essential roles in formation, morphology, and maintenance. Amongst these proteins are various myosin motors, including the tip localizing MYO3A/B and MYO15A (**Figure 1B**), the tip-link associated MYO7A and MYO1C (**Figure 1C**), and the ankle tethering MYO6 (**Figure 1D**; Peng et al., 2011). Each motor is proposed to be important for different aspects of stereocilia morphology/function and thus loss of any individual myosin motor leads to stereocilia degeneration and hearing loss (Lin et al., 2011; Rehman et al., 2016; Dantas et al., 2018; Calabro et al., 2019; Wang et al., 2019). Therefore, numerous studies have examined stereocilia-associated myosins providing crucial insight into their role in the hearing process.

Photoreceptors contain actin-based protrusions called the calyceal processes, though their function is currently unknown (Nagle et al., 1986; Dosé et al., 2003). Both MYO7A and MYO3A/B, as well as the stereocilia-associated proteins protocadherin-15, cadherin-23, whirlin, sans, and harmonin were all found to be localized to the calyceal processes (Hasson et al., 1995; Dosé et al., 2003; Kremer et al., 2006; Lelli et al., 2016). Mutations in any of these proteins, with the exception of MYO3A/B, cause a form of deafness and blindness called Usher syndrome (Hasson et al., 1995; Kremer et al., 2006). Overall, the structure of stereocilia and calyceal processes is similar, however the stereocilia are maintained throughout a lifetime while the calyceal processes are renewed regularly (1–6 weeks) (Young, 1967; Schietroma et al., 2017). Thus, myosins may have a parallel function in these similar actin-based structures that are found in two critically important sensory cells.

## THE MYOSIN SUPERFAMILY

The typical domain structure of myosins is composed of an N-terminal conserved motor domain (head), a light chain binding region (neck), and a class specific C-terminal region domain (tail) (**Figure 2**; Heissler and Sellers, 2016). The motor domain contains the ATP and actin binding regions, which is allosterically connected to the light chain binding neck referred to as the lever arm. When myosin is strongly bound to actin the lever arm tilts to allow force generation or translocation along actin (Houdusse and Sweeney, 2016). The light chain binding neck is comprised of a variable number of IQ (consensus sequence: [IVL]QXXXRXXXX[RK]XX[FILVWY]) motifs that bind to calmodulin or calmodulin like proteins (Rhoads and Friedberg, 1997). The tail domain is the most variable region of myosins. For example, the tail domain can contain a coiled-coil for dimerization, a filament forming region, or cargo/membrane binding motifs (Heissler and Sellers, 2016). Myosins such as MYO3A/B and MYO15A contain unique N-terminal extensions that have been proposed to alter motor activity (Dosé et al., 2008). Thus, it is postulated that all myosins utilize their conserved motor domain to produce mechanical work, while the variable tail domain allows myosins to localize to specific regions of the cell, carry specific cargo, or assemble into contractile filaments.

In general, myosins are P-loop associated ATPases with structural similarities to G-proteins and kinesins (Kull et al., 1998). The acto-myosin ATPase cycle is well conserved within the myosin superfamily, while the rate and equilibrium constants that control the cycle are unique to each myosin which allows them to perform specific cellular functions (**Figure 3**; De La Cruz and Ostap, 2004; Geeves, 2016; Heissler and Sellers, 2016). Myosin binds tightly to actin in the absence of nucleotide. ATP binds to the nucleotide binding region via several conserved nucleotide-binding elements: P-loop, switch I, and switch II (Kull et al., 1998). Once ATP binds, there is a dramatic weakening of the affinity of myosin for actin. The hydrolysis of ATP occurs while myosin is detached from actin and allows the lever arm to be positioned in a pre-power stroke conformation (recovery stroke). When myosin with the hydrolyzed products in the active site binds to actin there is a transition into the strongly bound actomyosin state and a shift from a pre-power stroke to a post-power stroke state that is key to force generation (power stroke) as well as the acceleration of phosphate release (Trivedi et al., 2015; Gunther et al., 2020). The release of ADP from actomyosin is required before another ATP cycle can occur. Individual steps of the ATPase cycle (e.g., ATP binding, ATP hydrolysis, ADP release etc.) can be analyzed via transient kinetic stopped-flow analysis (De La Cruz and Ostap, 2009). An important parameter that can be determined from kinetic analysis is the myosin duty ratio, or the fraction of the ATPase cycle that myosin spends tightly bound to actin (De La Cruz and Ostap, 2004; O'Connell et al., 2007). Myosins that demonstrate a high duty ratio ($\geq$0.5) can function as a processive dimeric motor, capable of taking multiple steps along actin without diffusing away from the track, and thus are well suited to function as cargo transporters (Moore et al., 2001). On the other hand, low duty ratio motors typically function in teams to generate ensemble force and motion by interacting with actin filaments.

Myosins have been the subject of biomedical research for quite some time, with various members of the superfamily being associated with a wide array of disease conditions (Trivedi et al., 2020). For example, mutations in *MYH7,* the gene that encodes beta-cardiac myosin, have been shown to lead to various types of cardiomyopathies, including hypertrophic and dilated cardiomyopathy (Yotti et al., 2019). Similarly, mutations in the *MYO5A* gene, that encodes the cargo-transporting MYO5A,

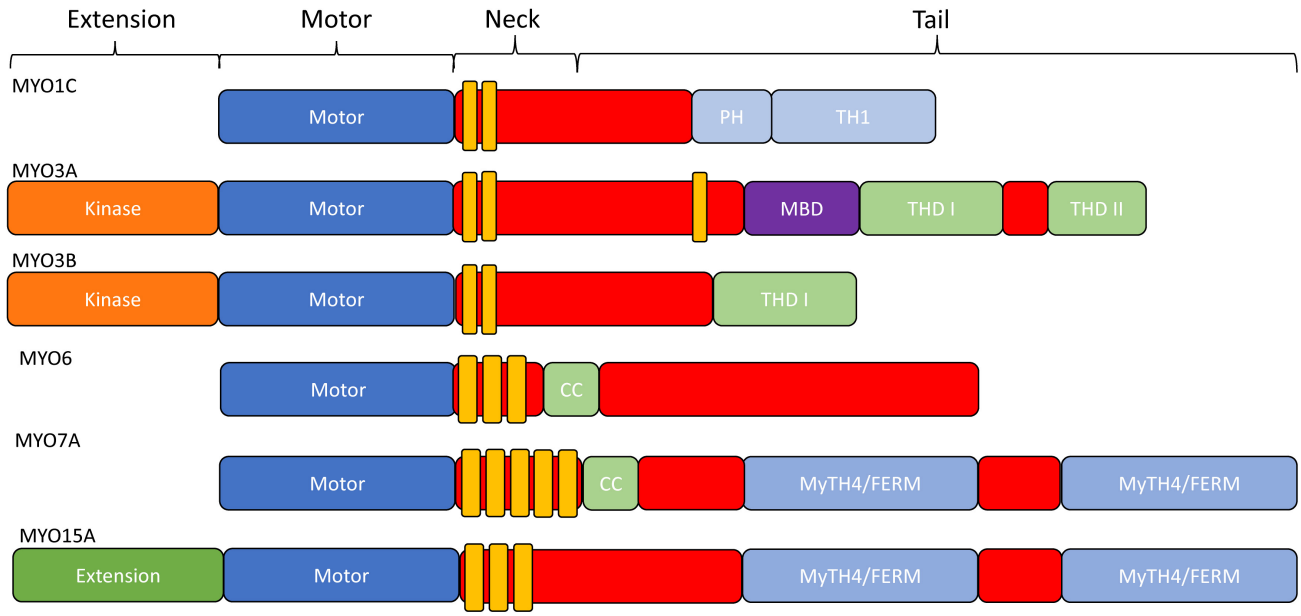


**FIGURE 2 |** Domain structure of stereocilia-associated myosins. In general, all myosins contain a conserved N-terminal motor domain (head), light chain binding region (neck), and a variable C-terminal domain (tail) which allows specialized functions (e.g., dimerization, filament formation, membrane binding, and cargo/adapter protein binding). Additionally, MYO1C has a membrane binding Pleckstrin-Homology domain, as well as a membrane binding tail homology domain. MYO3A/MYO3B, MYO6, and MYO15A all contain an N-terminal extension domain, with the MYO3A/MYO3B extension being a protein kinase. MYO6 and MYO7A have dimerizing coiled-coil domains, and MYO7A and MYO15A each contain two membrane binding MyTH4/FERM domains.

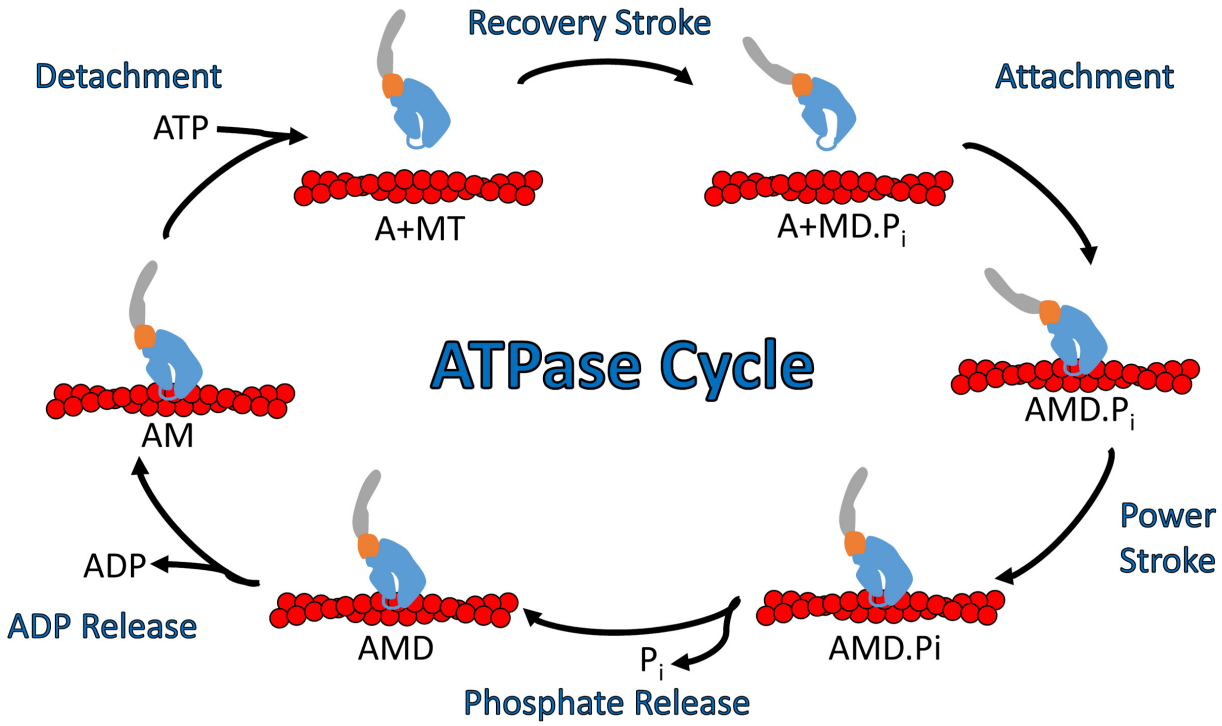


**FIGURE 3 |** Diagram of the actomyosin ATPase cycle. Myosin cycles between "weak" actin binding and "strong" actin binding states and while strongly bound generates a power stroke that drives filament sliding or walking along actin. Specifically, ATP binding to myosin dissociates it from actin which is followed by ATP hydrolysis and a transition into the pre-power stroke state (recovery stroke). Myosin binding to actin with the hydrolyzed products in its active site leads to strong actin binding, the myosin power stroke, and the release of phosphate. After the power stroke, ADP is released from the nucleotide pocket in a strong actin binding state, which allows for another ATP molecule to bind and start a new ATPase cycle. Abbreviations for actin, myosin, ATP, ADP, ADP.Pi are A, M, T, D, D.Pi, respectively.

have been associated with Griscelli's Syndrome, a debilitating neurological disorder (Emanuel et al., 2007). It is important to understand how these mutations alter the conserved mechanism of force generation in myosins. Recently, small molecule allosteric regulators of myosin have been successfully developed to treat heart disease, suggesting this strategy may be successful for treating other myosin-associated disease conditions (Malik et al., 2011; Green et al., 2016; Alsulami and Marston, 2020).

## Myosins and Deafness

Various classes of myosin have been found to localize to different parts of the stereocilia and be involved in the hearing process. Class I myosins are small monomeric myosin motors that share a typical function of linking the membrane and actin cytoskeleton (McIntosh and Ostap, 2016). Two class I myosins have been described to play potential roles in the hearing process, MYO1A and MYO1C. Although originally found expressed in the inner ear, MYO1A was later ruled out as a candidate hearing loss gene (Patton et al., 2016). Therefore, much research has focused on MYO1C as the predominant hearing-associated class I myosin (Adamek et al., 2011; Lin et al., 2011; Pyrpassopoulos et al., 2012). MYO1C, first described as the adaptation motor, localizes near the MET channels in the upper tip link density as well as at stereocilia tips (Dumont et al., 2002; Phillips et al., 2006). Within its tail domain, it contains two membrane binding domains; a Pleckstrin homology (PH) domain, and a tail homology (TH) domain (**Figure 2**; Hokanson et al., 2006; Chung et al., 2019). Although its role has yet to be fully elucidated, researchers have demonstrated that class I myosins have a unique strain-sensitive ADP-release mechanism (Laakso et al., 2008), which could make MYO1C ideally suited to sense the membrane tension associated with stereocilia movement (Batters et al., 2004; Laakso et al., 2008). Indeed, MYO1C was found to be crucial in MET channel adaptation, a process by which the MET channel gating is reset between stimuli (Holt et al., 2002). The adaptation process was originally thought to be regulated via MYO1C alone, though further research has suggested other myosin motors may play a role (Caprara et al., 2020).

The *MYO6* gene, found on chromosome 6, encodes for a unique unconventional myosin that walks toward the minus end of actin filaments (Avraham et al., 1997). All myosins characterized thus far, with the exception of MYO6, move toward the plus end of actin filaments (Wells et al., 1999). MYO6 contains an N-terminal canonical myosin motor followed by a single calmodulin-binding IQ motif, resulting in a short lever arm (**Figure 2**). However, one study suggests that there may be another calmodulin binding site found within the motor domain, affecting motor activity (Chevreux et al., 2005). Following the IQ motif, there is a three-helix bundle and a single alpha-helical (SAH) domain, both of which are predicted to contribute to cargo binding abilities (**Figure 2**). There is a unique 53aa insertion in the motor that is not seen in other members of the myosin superfamily. This insertion is proposed to function as the "reverse gear" and responsible for facilitating movement of the lever arm during the power stroke in the opposite direction as canonical myosins (Ménétrey et al., 2005). Also, MYO6 has been shown to bind $PIP_2$ lipids in the cell membrane through an R/K rich domain in its cargo binding tail domain (Buss and Kendrick-Jones, 2008).

Within the stereocilia, MYO6 localizes at the base of the actin protrusion near the rootlet region (Seki et al., 2017), where the minus (pointed) ends of actin filaments are located (Tilney et al., 1980). Mutations in *MYO6* have been shown to be associated with both an autosomal dominant and an autosomal recessive form of hearing loss, DFNA22 and DFNB37, respectively (Melchionda et al., 2001; Ahmed et al., 2003). A mouse model that displays loss of MYO6, known as Snell's waltzer, demonstrates a phenotype associated with balance and hearing defects including circling, head tossing, and deafness (Avraham et al., 1995; Self et al., 1999). Stereocilia lacking MYO6 were found to develop abnormally, specifically by fusing at their base and forming large stereocilia, suggesting a role for MYO6 in anchoring the stereocilia membrane to the actin core. Another study suggested that the loss of MYO6 was associated with increased levels of hair cell death (Avraham et al., 1995). Mutations in *MYO6* associated with autosomal dominant non-syndromic hearing loss (ADNSHL) have also been identified (Melchionda et al., 2001). One common mutation, R205Q, occurs in the motor domain and slows both actin-activated ATPase activity and *in vitro* motility (Kwon et al., 2014). The R205Q mutation results in a progressive hearing loss phenotype that starts within the first decade of life (Kwon et al., 2014). Other mutations that affect cargo binding, such as the truncation mutant R1166X, affect MYO6 cellular localization (Arden et al., 2016).

*MYO7A* is one of two class VII myosins within the human genome. Found on chromosome 11, the *MYO7A* gene encodes for a 250 kDa unconventional myosin that contains an N-terminal canonical myosin motor domain with a high duty ratio, five light-chain binding IQ motifs, and two MyTH4/FERM domains in its tail region, separated by an SH3 domain (**Figure 2**; El-Amraoui et al., 2008; Heissler and Manstein, 2012). Due to its expression in both the calyceal processes and stereocilia, MYO7A mutations have been associated with both vision and hearing loss (Calabro et al., 2019). Two distinct modes of hearing loss are commonly associated with *MYO7A* mutations, known as DFNA11 and DFNB2. DFNA11 is characterized by a progressive form of hearing loss and DFNB2 is an autosomal recessive form of hearing loss (Bakhchane et al., 2017; Yamamoto et al., 2020) that develops as early as 7 months (Riazuddin et al., 2008; Hildebrand et al., 2010). Usher syndrome type B, or USH1B, is the most common disease resulting from *MYO7A* mutations, which is characterized by both loss of vision and profound deafness. A mouse model of USH1B, known as shaker-1, contains a mutation in the *MYO7A* gene and displays both vision and hearing loss phenotypes (Eudy and Sumegi, 1999). Interestingly, $MYO7A^{(-/-)}$ mice with no MYO7A expression have profound hearing and vision loss, displaying a loss of both inner and outer hair cells, though no loss in calyceal process structure or photoreceptor cells (Calabro et al., 2019).

Within the stereocilia, MYO7A can be found localized to the plasma membrane along the shaft of the protrusion, with high localization near the UTLD (Sakai et al., 2011). It is here

that MYO7A associates with the tip link complex, composed of cadherin-23, protocadherin-15, sans, and harmonin. MYO7A cargo binding is proposed to trigger MYO7A dimerization and translocation to the tips of stereocilia. The tip localized MYO7A may also function by pulling on the tip-link complex, thus creating tension that has been proposed to both help regulate MET channel gating, as well as provide a strong parallel link between adjacent stereocilia (Siemens et al., 2002; Bahloul et al., 2010; Grati and Kachar, 2011; Yu et al., 2017). Interestingly, this function correlates with the role that MYO7B plays within microvilli of the intestine, where MYO7B both links the actin cytoskeleton to the membrane via its MyTH4/FERM domains as well as links adjacent villi together via its interaction with USH1C and ANKS4B (He et al., 2019). MYO7B was found to have a high duty ratio and kinetic properties that make it well suited to function as a transporter and/or mechanosensitive motor important for sensing tension on tip-link complexes that connect adjacent actin protrusions (Henn and De La Cruz, 2005; He et al., 2019). However, its slow ensemble and single molecule motility (16 and 11 nm/s, respectively) suggest it may not be well suiting for long range transport (Inoue and Ikebe, 2003; Sato et al., 2017). Two recent studies which studied the role of myosin motors in the MET channel adaptation reported that MYO7A is a good candidate to maintain resting tension on the MET channel, but its slow motility speed likely precludes it from functioning in adaptation (Caprara et al., 2020; Li et al., 2020). Thus, future studies are crucial for specifically examining the role of MYO7A in maintaining tip-link tension and MET channel gating.

MYO15A and MYO15B are two class XV myosins found on chromosome 17 (Friedman et al., 1995; Boger et al., 2001). MYO15B, was long believed to be a pseudo gene due to the absence of conserved residues known to be crucial for myosin motor domain function (Boger et al., 2001). Interestingly, proteomic analysis from this same study revealed expression of MYO15B in the stomach, kidney, and colon, though its function is yet to be elucidated. MYO15A, is unique in that it contains an N-terminal extension that is followed by a functional canonical myosin motor domain and 3 IQ motifs in the neck region (**Figure 2**). Similar to other unconventional myosins, MYO15A also contains two MyTH4/FERMs, allowing it to interact with the cell membrane. Mutations in both the motor domain, as well as the MyTH4/FERM domain, have been shown to cause non-syndromic hearing loss (DFNB3) (Zhang et al., 2019). Mouse models that lack MYO15A expression, including the shaker-2 mouse, show defects in both stereocilia elongation, as well as morphology (e.g., thickness), demonstrating MYO15A is required for stereocilia formation (Probst et al., 1998).

Early studies of MYO15A found that it localizes to the extreme tip of stereocilia, leading to the initial hypothesis that it was involved in the stereocilia elongation process (Belyantseva et al., 2003). Further data has shown that MYO15A also acts as a transporter, bringing the protein whirlin to the tips of stereocilia (Belyantseva et al., 2005; Delprat et al., 2005). Interestingly, whirler mice that lack a functional whirlin protein demonstrate short stereocilia and a deafness phenotype, mirroring that of shaker-2 mice. In addition, a study of transfected MYO15A in shaker-2 mouse hair cells showed both restoration of normal hair bundle morphology, as well as proper whirlin localization, further suggesting that both MYO15A and whirlin localization are critical for actin protrusion elongation (Belyantseva et al., 2005). Furthermore, studies that utilized a MYO15A isoform specific KO mouse showed that stereocilia bundles that expressed only the short isoform of MYO15A, which lacks the N-terminal extension, would initially develop normally, but they would retract as early as P11, with a near full retraction occurring by P50 (Fang et al., 2015). However, the long MYO15A isoform is able to traffic to these bundles and prevent disassembly, suggesting a role in stereocilia architecture and maintenance. Recent kinetic analysis of the MYO15A motor demonstrated a moderate duty ratio (∼0.5) and relatively high affinity for actin (Jiang et al., 2021). *In vitro* motility experiments demonstrated that MYO15A can move actin filaments at rate of ∼300–400 nm/s and confocal microscopy showed localization of MYO15A at protrusion tips of live cells (Belyantseva et al., 2005; Bird et al., 2014). There are two possible models for MYO15A that can explain its ability to act as a transporter within stereocilia. One such model suggests that MYO15A functions as a dimer or oligomer, perhaps as a complex with cargo, to move processively toward the actin protrusion tips (Jiang et al., 2021).The second model suggests a membrane binding mediated movement, whereby monomeric MYO15A associates with both the actin cytoskeleton and the plasma membrane, moving via a diffusive sliding mechanism (Bird et al., 2014). Overall, the current results suggest MYO15A functions as a tip-directed cargo transporter and/or elongation regulator.

## Class III Myosins

Class III myosins exist in two different isoforms, MYO3A and MYO3B, found on chromosomes 10 and 2, respectively (Dosé et al., 2003). Both MYO3A and MYO3B have been shown to be localized to the calyceal processes of photoreceptors as well as in the stereocilia of vestibular and auditory inner ear hair cells (Dosé et al., 2003; Schneider et al., 2006). Similar to MYO15A, both MYO3A and MYO3B localize to the tips of stereocilia. However, MYO3A and MYO3B show a "thimble-like" localization at the tips (Schneider et al., 2006), whereas MYO15A localizes at the extreme tips (Belyantseva et al., 2003). MYO3A has been shown to be associated with a form of non-syndromic hearing loss known as DFNB30 (Walsh et al., 2002, 2011). DFNB30 is a late onset form of hearing loss, with the average onset in the third or fourth decade. The localization of class III myosins at the tips of filopodia in heterologous cell culture systems correlates with the *in vivo* localization within stereocilia, which has allowed researchers to investigate binding partners and requirements for tip localization (Les Erickson, 2003; Schneider et al., 2006; Salles et al., 2009; Quintero et al., 2010; Mecklenburg et al., 2015). The overall structure of MYO3A and MYO3B are similar. Both MYO3A and MYO3B have an N-terminal kinase domain located before their canonical myosin motor and a 2-IQ neck region (**Figure 2**; Dosé et al., 2003). Also, both share a domain in their tail region, known as tail homology domain I (THDI) that binds the actin crosslinking protein espin (ESPN-1 and ESPN-L) via the ankyrin repeat domains (ARD) (Salles et al., 2009; Merritt et al., 2012; Ebrahim et al., 2016; Liu et al., 2016). MYO3A contains a

second tail homology domain, THDII, which contains an actin binding motif known to be required for MYO3A associated tip localization (Dosé et al., 2003; Les Erickson, 2003). MYO3B lacks THDII and is thus unable to localize to protrusion tips, while fusing THDII to the MYO3B tail rescues tip localization (Merritt et al., 2012; Raval et al., 2016). Interestingly, MYO3B is thought to utilize the actin binding motif of ESPN (associated with the tail of MYO3B) to provide a second actin binding site and localization to the protrusion tips. ESPN is important for the maintenance of structures that contain tightly packed, parallel actin bundles such as microvilli and stereocilia (Loomis et al., 2003). In a cell culture model, it was shown that both MYO3A and MYO3B have the capability to transport ESPN to the tips of filopodia, though ESPN itself is necessary for MYO3B tip localization (Salles et al., 2009; Merritt et al., 2012).

MYO3A also contains a region in its tail capable of binding the membrane occupation and recognition nexus repeat containing protein, MORN4 (Mecklenburg et al., 2015; Li et al., 2019), a protein with no known function in inner ear hair cells. Similarly, cell biological studies have shown that MYO3A can co-localize with MORN4 at filopodia tips (Mecklenburg et al., 2015) while MYO3A is not necessary for MORN4 localization at stereocilia tips (Lelli et al., 2016). MORN4 is the human homolog of the *Drosophila* protein retinophilin (RTP), which can co-localize to actin-based structures in photoreceptors in *Drosophila* and directly bind to NINAC, the Drosophila homologue of class III myosins (Hicks and Williams, 1992; Porter et al., 1992; Venkatachalam et al., 2010). MYO3A contains a region in its tail between its third IQ domain and THDI where MORN4 binds (Mecklenburg et al., 2015; Li et al., 2019). The function of this interaction is still unknown, however RTP helps stabilize NINAC in *Drosophila* rhabdomeres and MORN repeat containing proteins are known to both stabilize proteins, as well as contribute to protein-membrane interactions (Mecklenburg et al., 2015). Thus, it is interesting to speculate that MORN4 serves to tether MYO3A to the plasma membrane at the tips of stereocilia and calyceal processes, while future studies in inner ear hair cells and photoreceptors are required to investigate this interesting possibility.

Studies have examined class III myosin function using a variety of approaches, including performing biochemical analysis with purified proteins and examining cellular function in heterologous cell culture systems (Dosé et al., 2007; Merritt et al., 2012; Raval et al., 2016). The motor properties of MYO3A and MYO3B are relatively well defined, with MYO3B demonstrating a twofold slower maximum ATPase rate and much weaker actin binding affinity compared to MYO3A (Merritt et al., 2012; Raval et al., 2016). Early studies of MYO3A analyzed the motor properties in a construct that contained the MYO3A kinase, motor, and neck region (including 2IQ domains), but lacking the entire tail (Dosé et al., 2007). These studies found MYO3A to have a relatively slow maximum ATPase rate ($\sim$1 $s^{-1}$). In addition, the same study found MYO3A to have a relatively high affinity for actin in co-sedimentation assays, as well as fast phosphate release and slow ADP release, suggesting a moderately high duty ratio for MYO3A (Dosé et al., 2007). Many of the studies that have investigated the biochemical and cell biological properties of class III myosins were performed with the kinase domain deleted ($\Delta$K) to prevent autophosphorylation of the motor (see kinase regulation below). However, removal of the kinase domain in MYO3A enhances the maximum ATPase activity twofold ($\sim$2 $s^{-1}$) and increases actin affinity, which suggests the kinase domain does alter MYO3A motor properties (Dosé et al., 2008). In addition, the rate-limiting step in the MYO3A $\Delta$K 2IQ construct was proposed to be ATP hydrolysis, but determining the actual ATP hydrolysis rate constant was challenging since ATP-binding to the MYO3A motor is extremely slow. Thus, our current kinetic simulations that assume rate limiting ATP hydrolysis suggest that the duty ratio of MYO3A $\Delta$K 2IQ is $\sim$0.25, while further measurements are necessary in the kinase-containing construct. Interestingly, MYO3A $\Delta$K 2IQ can slide filaments in the *in vitro* motility assay twofold faster than MYO3B $\Delta$K 2IQ (71 and 31 nm/s, respectively), demonstrating it not only has faster ATPase kinetics but faster motile activity (Raval et al., 2016).

A unique property of class III myosins is their N-terminal kinase domain. Both the MYO3A and MYO3B kinase domain belong to the STE20 class of protein kinases (Quintero et al., 2013). Studies of MYO3A found two threonines in the motor domain and two in the kinase domain that are targets for intermolecular kinase domain phosphorylation (Quintero et al., 2013). Phosphorylation of the kinase domain increases kinase activity and phosphorylation of the motor domain decreases motor activity (Quintero et al., 2010, 2013). This contributes to the concentration-dependent regulation by autophosphorylation mechanism of MYO3A. In short, MYO3A is able to walk toward the tips of actin protrusions. However, once MYO3A begins to accumulate at the tip, there is an increased probability that the kinase domain of these tip localized MYO3A molecules will phosphorylate both the motor and kinase domain of other MYO3A molecules. Phosphorylation of the kinase domain increases kinase activity and phosphorylation of the motor domain decreases MYO3A motor ATPase activity and actin affinity, resulting in a higher probability of being recycled back to the cell body (Quintero et al., 2010, 2013).Therefore, the proposed auto-regulatory mechanism precisely controls MYO3A concentration at the protrusions tips which may be crucial for regulating actin protrusion lengths.

*In vivo* models of class III myosins have demonstrated their essential function within inner ear hair cells, especially during development. Specifically, previous work has shown that co-localization of MYO3A/B with ESPN at the protrusion tips may be important for elongation and to maintain the ultrastructure of stereocilia (Rzadzinska et al., 2005; Salles et al., 2009; Merritt et al., 2012; Mecklenburg et al., 2015; Ebrahim et al., 2016; Liu et al., 2016). Loss of both MYO3A and MYO3B in mice resulted in a severe deafness phenotype, as well as disrupted stereocilia structure and morphology (Lelli et al., 2016). In these studies, stereocilia were abnormally long and displayed an increase spacing between rows. When MYO3B alone was absent, there was little to no overall change in stereocilia structure (Ebrahim et al., 2016). Conversely, loss of MYO3A caused age-dependent hearing loss similar to the DFNB30 phenotype found in humans (Ebrahim et al., 2016;

Lelli et al., 2016). Interestingly, in mice that were MYO3B$^{-/-}$, MYO3A-PNcKO (i.e., contained MYO3A expression during post-natal development, but eliminated upon maturation), there was no deficit seen in stereocilia structure or function, suggesting class III myosins are crucial during development (Lelli et al., 2016). This same study found that both ESPN and MORN4 were able localize at stereocilia tips in the absence of MYO3A/B, suggesting that class III myosins are not required to transport these proteins to the tips. Overall, MYO3B appears to be able to partially compensate for the loss of MYO3A in

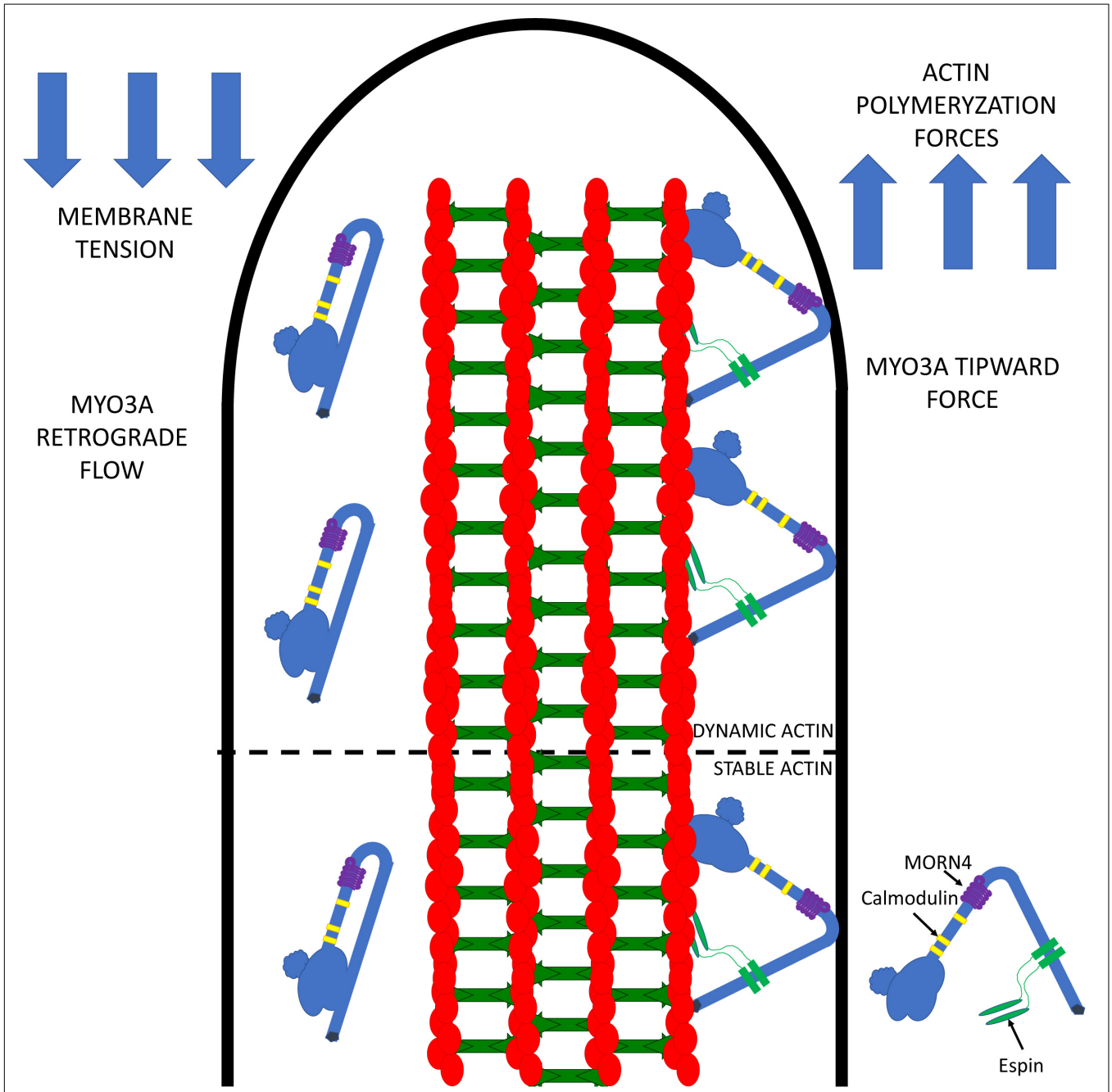


**FIGURE 4 |** Working model for MYO3A function in inner ear hair cell stereocilia. MYO3A walks toward the plus end of actin protrusions utilizing its motor and actin binding tail domains and can dock at the tips by an unknown mechanism. The tip localized MYO3A can produce an ensemble force that works together with the actin polymerization forces to combat membrane tension, which can result in protrusion elongation or retraction (depending on the balance of forces). The amount of tip-directed force produced by MYO3A motors at the protrusion tips is impacted by the number of motors present, as well as their duty ratio and intrinsic force producing abilities. Examining how MYO3A motor-based forces are altered by physiological factors (e.g., phosphorylation and protein-protein interactions) or disease associated mutations (e.g., deafness mutations) will be the focus of future investigations that will further test this model.

DFNB30, while class III myosins appear to be most important during development.

Many MYO3A hearing loss mutations have been identified via genetic screens, while two dominant mutations, G488E and L697W, have been studied in depth (Grati et al., 2016; Dantas et al., 2018). G488E was shown to reduce ATPase activity but increase the *in vitro* motility of MYO3A (Grati et al., 2016). Interestingly, G488E failed to tip localize in the filopodia of COS-7 cells, though it did tip localize to stereocilia tips in organotypic inner ear hair cell cultures. We speculated that the G488E mutant may be unable to walk to the filopodia tips because of its disrupted ATPase cycle and or duty ratio, but in the stereocilia interactions with other binding partners may allow the mutant to translocate to the tips (e.g., as a complex with endogenous WT MYO3A). The L697W mutant was found to decrease both ATPase activity and *in vitro* motility, however, it did not have a defect in tip localization in COS-7 cells (Dantas et al., 2018). Interestingly, L697W was able to outcompete WT MYO3A for localization to protrusion tips in the presence of ESPN-1, while filopodia were overall shorter and fewer in number in the presence of the mutant. We proposed that L697W may be effective at localizing to the protrusion tips, and even more efficiently in the presence of ESPN-1, but its disrupted motor may prevent it from performing its tip associated functions important for length regulation. Further studies of the detailed ATPase mechanism of the G488E and L697 mutants will be extremely important as we attempt to relate the specific motor properties (e.g., duty ratio and attached lifetime) of MYO3A to its function in actin protrusions.

Our current model for the role of MYO3A in actin protrusions is summarized in **Figure 4**. We propose that MYO3A walks toward the plus-ended actin protrusion tips and docks at the tips by some unknown mechanism (e.g., membrane binding and/or protein-protein interactions). The steady-state concentration of MYO3A at the tips is at least partially dependent on autoregulation by the kinase domain. We propose that the tip localized MYO3A can produce a plus-end directed force that along with actin polymerization forces can elongate the actin protrusion. The plus-end directed forces can combat the membrane tension to result in a net elongation of the protrusion in a mechanism similar to that proposed for myosin I and myosin X, whereby the motor is able to link the plasma membrane and actin cytoskeleton while exerting force (Nambiar et al., 2010; Watanabe et al., 2010; He et al., 2017). We predict that the turnover of MYO3A at the tips is at least partially controlled by the myosin duty ratio and steady-state actin affinity, since the higher actin affinity of MYO3A compared to MYO3B correlates with its more efficient tip localization (Raval et al., 2016). We also predict that the rate of elongation may be controlled by MYO3A motor activity, and likely correlates with *in vitro* actin gliding velocity since multiple MYO3A motors likely work together at the protrusion tips to generate force. The balance of forces at the tips likely controls the average length of the actin protrusion. For example, if membrane tension becomes greater than the motor and actin polymerization forces, the protrusion will undergo a net retraction. Overall, we hypothesize that the motor properties of MYO3A are critical for its role in protrusion length maintenance, and thus deafness mutations that alter the duty ratio, force production, or actin gliding properties will specifically disrupt the length regulation function of MYO3A.

Does MYO3A work together with MYO15 to regulate stereocilia length? We predict that MYO15 may perform a similar function by generating a protrusive force at the stereocilia tips to combat membrane tension and since it is a faster motor it may dominate the protrusion elongation rate. MYO3A is a slower motor that may function as a brake to prevent over-elongation of the stereocilia. This hypothesis is consistent with the mouse model results that demonstrate shorter stereocilia in the absence of MYO15 (Probst et al., 1998) but over-elongated stereocilia in the absence of MYO3A (Lelli et al., 2016). Although we have focused on the more well characterized MYO3A our model is also likely consistent with MYO3B playing a similar role at the protrusion tips.

## SUMMARY AND DISCUSSION

There are several open questions related to the function of myosin motors in the stereocilia and other similar actin-based protrusions. One question is related to cargo transport within the stereocilia and the requirement for myosin motors to be processive to function as cargo transporters. Stereocilia-associated myosins were found to have a wide range of duty ratios and motility speeds and direct measurements of processive motion in single molecule motility assays with myosins thought to function in transport (e.g., MYO3A and MYO15A) are lacking. Nearly all of the stereocilia-associated myosins were found to have membrane binding motifs, which could be crucial for localization within a specific region of the stereocilia. Membrane binding could also be important for docking at the stereocilia tips and forming a link between the membrane and actin bundle that is necessary for elongation. Finally, it is unclear how different classes of myosin motors work together to function in the stereocilia. For example, MYO3A and MYO15A may work together to elongate the stereocilia and if so, how does this impact the overall rate of elongation since MYO3A slides actin filaments fivefold slower than MYO15A in the *in vitro* motility assay. In addition, MY07A and MYO1C may work together to mediate tension of the MET channel during adaptation. Future studies that will examine the motor properties of stereocilia-associated myosins both with *in vitro* biophysical approaches, cell biological studies, and *in vivo* transgenic mouse models will provide a clearer picture of the role of each myosin motor in the stereocilia.

## AUTHOR CONTRIBUTIONS

JC and CY wrote the manuscript. LG provided the editorial input. All authors contributed to the article and approved the submitted version.

## FUNDING

This work was supported by the PA Lions Hearing Research Foundation Grant to CY and an NIH F32 DC016788 to LG.

## REFERENCES


Adamek, N., Geeves, M. A., and Coluccio, L. M. (2011). Myo1c mutations associated with hearing loss cause defects in the interaction with nucleotide and actin. *Cell. Mol. Life Sci.* 68, 139–150. doi: 10.1007/s00018-010-0448-x

Ahmed, Z. M., Morell, R. J., Riazuddin, S., Gropman, A., Shaukat, S., and Ahmad, M. M. (2003). Mutations of MYO6 are associated with recessive deafness, DFNB37. *Am. J. Hum. Genet.* 72, 1315–1322. doi: 10.1086/375122

Alsulami, K., and Marston, S. (2020). Small molecules acting on myofilaments as treatments for heart and skeletal muscle diseases. *Int. J. Mol. Sci.* 21:9599. doi: 10.3390/ijms21249599

Arden, S. D., Tumbarello, D. A., Butt, T., Kendrick-Jones, J., and Buss, F. (2016). Loss of cargo binding in the human myosin VI deafness mutant (R1166X) leads to increased actin filament binding. *Biochem. J.* 473, 3307–3319. doi: 10.1042/BCJ20160571

Avraham, K. B., Hasson, T., Sobe, T., Balsara, B., Testa, J. R., Skvorak, A. B., et al. (1997). Characterization of unconventional MYO6, the human homologue of the gene responsible for deafness in Snell's waltzer mice. *Hum. Mol. Genet.* 6, 1225–1231. doi: 10.1093/hmg/6.8.1225

Avraham, K. B., Hasson, T., Steel, K. P., Kingsley, D. M., Russell, L. B., Mooseker, M. S., et al. (1995). The mouse Snell's waltzer deafness gene encodes an unconventional myosin required for structural integrity of inner ear hair cells. *Nat. Genet.* 11, 369–375. doi: 10.1038/ng1295-369

Bahloul, A., Michel, V., Hardelin, J. P., Nouaille, S., Hoos, S., Houdusse, A., et al. (2010). Cadherin-23, myosin VIIa and harmonin, encoded by Usher syndrome type I genes, form a ternary complex and interact with membrane phospholipids. *Hum. Mol. Genet.* 19, 3557–3565. doi: 10.1093/hmg/ddq271

Bakhchane, A., Charif, M., Bousfiha, A., Boulouiz, R., Nahili, H., Rouba, H., et al. (2017). Novel compound heterozygous MYO7A mutations in Moroccan families with autosomal recessive non-syndromic hearing loss. *PLoS One* 12:e0176516. doi: 10.1371/journal.pone.0176516

Batters, C., Arthur, C. P., Lin, A., Porter, J., Geeves, M. A., Milligan, R. A., et al. (2004). Myo1c is designed for the adaptation response in the inner ear. *EMBO J.* 23, 1433–1440. doi: 10.1038/sj.emboj.7600169

Belyantseva, I. A., Boger, E. T., and Friedman, T. B. (2003). Myosin XVa localizes to the tips of inner ear sensory cell stereocilia and is essential for staircase formation of the hair bundle. *Proc. Natl. Acad. Sci. U.S.A.* 100, 13958–13963. doi: 10.1073/pnas.2334417100

Belyantseva, I. A., Boger, E. T., Naz, S., Frolenkov, G. I., Sellers, J. R., Ahmed, Z. M., et al. (2005). Myosin-XVa is required for tip localization of whirlin and differential elongation of hair-cell stereocilia. *Nat. Cell Biol.* 7, 148–156. doi: 10.1038/ncb1219

Bird, J. E., Takagi, Y., Billington, N., Strub, M. P., Sellers, J. R., and Friedman, T. B. (2014). Chaperone-enhanced purification of unconventional myosin 15, a molecular motor specialized for stereocilia protein trafficking. *Proc. Natl. Acad. Sci. U.S.A.* 111, 12390–12395. doi: 10.1073/pnas.1409459111

Boger, E. T., Sellers, J. R., and Friedman, T. B. (2001). Human myosin XVBP is a transcribed pseudogene. *J. Muscle Res. Cell Motil.* 22, 477–483. doi: 10.1023/A:1014507705858

Buss, F., and Kendrick-Jones, J. (2008). How are the cellular functions of myosin VI regulated within the cell? *Biochem. Biophys. Res. Commun.* 369, 165–175. doi: 10.1016/j.bbrc.2007.11.150

Calabro, K. R., Boye, S. L., Choudhury, S., Fajardo, D., Peterson, J. J., Li, W., et al. (2019). A novel mouse model of MYO7A USH1B reveals auditory and visual system Haploinsufficiencies. *Front. Neurosci.* 13:1255. doi: 10.3389/fnins.2019.01255

Caprara, G. A., Mecca, A. A., and Peng, A. W. (2020). Decades-old model of slow adaptation in sensory hair cells is not supported in mammals. *Sci. Adv.* 6:eabb4922. doi: 10.1126/sciadv.abb4922

Chevreux, G., Potier, N., Van Dorsselaer, A., Bahloul, A., Houdusse, A., Wells, A., et al. (2005). Electrospray ionization mass spectrometry studies of noncovalent myosin VI complexes reveal a new specific calmodulin binding site. *J. Am. Soc. Mass Spectrom* 16, 1367–1376. doi: 10.1016/j.jasms.2005.03.023

Chung, C.-L., Tai, S. B., Hu, T. H., Chen, J.-J., and Chen, C. L. (2019). Roles of myosin-mediated membrane trafficking in TGF-β signaling. *Int. J. Mol. Sci.* 20:3913. doi: 10.3390/ijms20163913

Corey, D. P., Akyuz, N., and Holt, J. R. (2019). Function and dysfunction of TMC channels in inner ear hair cells. *Cold Spring Harb. Perspect. Med.* 9:a033506. doi: 10.1101/cshperspect.a033506

Craig, E. M., Van Goor, D., Forscher, P., and Mogilner, A. (2012). Membrane tension, myosin force, and actin turnover maintain actin treadmill in the nerve growth cone. *Biophys. J.* 102, 1503–1513. doi: 10.1016/j.bpj.2012.03.003

Dantas, V. G. L., Raval, M. H., Ballesteros, A., Cui, R., Gunther, L. K., Yamamoto, G. L., et al. (2018). Characterization of a novel MYO3A missense mutation associated with a dominant form of late onset hearing loss. *Sci. Rep.* 8:8706. doi: 10.1038/s41598-018-26818-2

De La Cruz, E. M., and Ostap, E. M. (2009). Kinetic and equilibrium analysis of the myosin ATPase. *Methods Enzymol.* 455, 157–192. doi: 10.1016/S0076-6879(08)04206-7

De La Cruz, E. M., and Ostap, E. M. (2004). Relating biochemistry and function in the myosin superfamily. *Curr. Opin. Cell Biol.* 16, 61–67. doi: 10.1016/j.ceb.2003.11.011

Delprat, B., Michel, V., Goodyear, R., Yamasaki, Y., Michalski, N., and El-Amraoui, A. (2005). Myosin XVa and whirlin, two deafness gene products required for hair bundle growth, are located at the stereocilia tips and interact directly. *Hum. Mol. Genet.* 14, 401–410. doi: 10.1093/hmg/ddi036

DiStefano, M. T., Hemphill, S. E., Oza, A. M., Siegert, R. K., Grant, A. R., Hughes, M. Y., et al. (2019). ClinGen expert clinical validity curation of 164 hearing loss gene–disease pairs. *Genet. Med.* 21, 2239–2247. doi: 10.1038/s41436-019-0487-0

Dosé, A. C., Ananthanarayanan, S., Moore, J. E., Burnside, B., and Yengo, C. M. (2007). Kinetic mechanism of human myosin IIIA. *J. Biol. Chem.* 282, 216–231. doi: 10.1074/jbc.M605964200

Dosé, A. C., Ananthanarayanan, S., Moore, J. E., Corsa, A. C., Burnside, B., and Yengo, C. M. (2008). The kinase domain alters the kinetic properties of the myosin IIIA motor. *Biochemistry* 47, 2485–2496. doi: 10.1021/bi7021574

Dosé, A. C., Hillman, D. W., Wong, C., Sohlberg, L., Lin-Jones, J., Burnside, B., et al. (2003). Myo3A, one of two class III myosin genes expressed in vertebrate retina, is localized to the calycal processes of rod and cone photoreceptors and is expressed in the sacculus. *Mol. Biol. Cell* 14, 1058–1073. doi: 10.1091/mbc.e02-06-0317

Drummond, M. C., Barzik, M., Bird, J. E., Zhang, D. S., Lechene, C. P., Corey, D. P., et al. (2015). Live-cell imaging of actin dynamics reveals mechanisms of stereocilia length regulation in the inner ear. *Nat. Commun.* 6:6873. doi: 10.1038/ncomms7873

Dumont, R. A., Zhao, Y. D., Holt, J. R., Bähler, M., and Gillespie, P. G. (2002). Myosin-I isozymes in neonatal rodent auditory and vestibular epithelia. *J. Assoc. Res. Otolaryngol.* 3, 375–389. doi: 10.1007/s101620020049

Ebrahim, S., Avenarius, M. R., Grati, M., Krey, J. F., Windsor, A. M., Sousa, A. D., et al. (2016). Stereocilia-staircase spacing is influenced by myosin III motors and their cargos espin-1 and espin-like. *Nat. Commun.* 7:10833. doi: 10.1038/ncomms10833

El-Amraoui, A., Amel, B., and Christine, P. (2008). "'Myosin VII.," in *Myosins: A Superfamily of Molecular Motors*, ed. L. M. Coluccio (Dordrecht: Springer Netherlands).

Emanuel, P. O., Sternberg, L. J., and Phelps, R. G. (2007). Griscelli syndrome. *Skinmed* 6, 147–149. doi: 10.1111/j.1540-9740.2007.05783.x

Eudy, J. D., and Sumegi, J. (1999). Molecular genetics of Usher syndrome. *Cell. Mol. Life Sci.* 56, 258–267.

Fang, Q., Indzhykulian, A. A., Mustapha, M., Riordan, G. P., Dolan, D. F., Friedman, T. B., et al. (2015). The 133-kDa N-terminal domain enables myosin 15 to maintain mechanotransducing stereocilia and is essential for hearing. *eLife* 4:e08627.

Fettiplace, R. (2017). Hair cell transduction, tuning, and synaptic transmission in the mammalian Cochlea. *Compr Physiol* 7, 1197–1227. doi: 10.1002/cphy.c160049

Friedman, T. B., Liang, Y., Weber, J. L., Hinnant, J. T., Barber, T. D., and Winata, S. (1995). A gene for congenital, recessive deafness DFNB3 maps to the pericentromeric region of chromosome 17. *Nat. Genet.* 9, 86–91. doi: 10.1038/ng0195-86

Geeves, M. A. (2016). Review: the ATPase mechanism of myosin and actomyosin. *Biopolymers* 105, 483–491. doi: 10.1002/bip.22853

Grati, M., and Kachar, B. (2011). Myosin VIIa and sans localization at stereocilia upper tip-link density implicates these Usher syndrome proteins in mechanotransduction. *Proc. Natl. Acad. Sci. U.S.A.* 108, 11476–11481. doi: 10.1073/pnas.1104161108

Grati, M., Shin, J. B., Weston, M. D., Green, J., Bhat, M. A., Gillespie, P. G., et al. (2012). Localization of PDZD7 to the stereocilia ankle-link associates this scaffolding protein with the Usher syndrome protein network. *J. Neurosci.* 32, 14288–14293. doi: 10.1523/jneurosci.3071-12.2012

Grati, M., Yan, D., Raval, M. H., Walsh, T., Ma, Q., and Chakchouk, I. (2016). MYO3A causes human dominant deafness and interacts with Protocadherin 15-CD2 Isoform. *Hum. Mutat.* 37, 481–487. doi: 10.1002/humu.22961

Green, E. M., Wakimoto, H., Anderson, R. L., Evanchik, M. J., Gorham, J. M., and Harrison, B. C. (2016). A small-molecule inhibitor of sarcomere contractility suppresses hypertrophic cardiomyopathy in mice. *Science* 351, 617–621. doi: 10.1126/science.aad3456

Gunther, L. K., Rohde, J. A., Tang, W., Cirilo, J. A. Jr., Marang, C. P., and Scott, B. D. (2020). FRET and optical trapping reveal mechanisms of actin-activation of the power stroke and phosphate-release in myosin V. *J. Biol. Chem.* 295, 17383–17397.

Hasson, T., Heintzelman, M. B., Santos-Sacchi, J., Corey, D. P., and Mooseker, M. S. (1995). Expression in cochlea and retina of myosin VIIa, the gene product defective in Usher syndrome type 1B. *Proc. Natl. Acad. Sci. U.S.A.* 92, 9815–9819. doi: 10.1073/pnas.92.21.9815

He, K., Sakai, T., Tsukasaki, Y., Watanabe, T. M., and Ikebe, M. (2017). Myosin X is recruited to nascent focal adhesions at the leading edge and induces multi-cycle filopodial elongation. *Sci. Rep.* 7:13685.

He, Y., Li, J., and Zhang, M. (2019). Myosin VII, USH1C, and ANKS4B or USH1G together form condensed molecular assembly via liquid-liquid phase separation. *Cell Rep.* 29, 974–986.e4.

Heissler, S. M., and Manstein, D. J. (2012). Functional characterization of the human myosin-7a motor domain. *Cell. Mol. Life Sci.* 69, 299–311. doi: 10.1007/s00018-011-0749-8

Heissler, S. M., and Sellers, J. R. (2016). Kinetic adaptations of myosins for their diverse cellular functions. *Traffic* 17, 839–859. doi: 10.1111/tra.12388

Henn, A., and De La Cruz, E. M. (2005). Vertebrate myosin VIIb is a high duty ratio motor adapted for generating and maintaining tension. *J. Biol. Chem.* 280, 39665–39676. doi: 10.1074/jbc.m507667200

Hicks, J. L., and Williams, D. S. (1992). Distribution of the myosin I-like ninaC proteins in the *Drosophila* retina and ultrastructural analysis of mutant phenotypes. *J. Cell Sci.* 101(Pt 1), 247–254.

Hildebrand, M. S., Thorne, N. P., Bromhead, C. J., Kahrizi, K., Webster, J. A., Fattahi, Z., et al. (2010). Variable hearing impairment in a DFNB2 family with a novel MYO7A missense mutation. *Clin. Genet.* 77, 563–571. doi: 10.1111/j.1399-0004.2009.01344.x

Hokanson, D. E., Laakso, J. M., Lin, T., Sept, D., and Ostap, E. M. (2006). Myo1c binds phosphoinositides through a putative pleckstrin homology domain. *Mol. Biol. Cell* 17, 4856–4865. doi: 10.1091/mbc.e06-05-0449

Holt, J. R., Gillespie, S. K., Provance, D. W., Shah, K., Shokat, K. M., Corey, D. P., et al. (2002). A chemical-genetic strategy implicates myosin-1c in adaptation by hair cells. *Cell* 108, 371–381. doi: 10.1016/s0092-8674(02)00629-3

Houdusse, A., and Sweeney, H. L. (2016). How myosin generates force on actin filaments. *Trends Biochem. Sci.* 41, 989–997. doi: 10.1016/j.tibs.2016.09.006

Inoue, A., and Ikebe, M. (2003). Characterization of the motor activity of mammalian myosin VIIA. *J. Biol. Chem.* 278, 5478–5487. doi: 10.1074/jbc.m210489200

Jia, Y., Zhao, Y., Kusakizako, T., Wang, Y., Pan, C., Zhang, Y., et al. (2020). TMC1 and TMC2 proteins are pore-forming subunits of mechanosensitive ion channels. *Neuron* 105, 310–321.e3.

Jiang, F., Takagi, Y., Shams, A., Heissler, S. M., Friedman, T. B., Sellers, J. R., et al. (2021). The ATPase mechanism of myosin 15, the molecular motor mutated in DFNB3 human deafness. *J. Biol. Chem.* 100243. doi: 10.1074/jbc.ra120.014903 [Epub ahead of print].

Kazmierczak, P., Sakaguchi, H., Tokita, J., Wilson-Kubalek, E. M., Milligan, R. A., Müller, U., et al. (2007). Cadherin 23 and protocadherin 15 interact to form tip-link filaments in sensory hair cells. *Nature* 449, 87–91. doi: 10.1038/nature06091

Kremer, H., van Wijk, E., Märker, T., Wolfrum, U., and Roepman, R. (2006). Usher syndrome: molecular links of pathogenesis, proteins and pathways. *Hum. Mol. Genet.* 15, R262–R270.

Kull, F. J., Vale, R. D., and Fletterick, R. J. (1998). The case for a common ancestor: kinesin and myosin motor proteins and G proteins. *J. Muscle Res. Cell Motil.* 19, 877–886.

Kurima, K., Ebrahim, S., Pan, B., Sedlacek, M., Sengupta, P., Millis, B. A., et al. (2015). TMC1 and TMC2 localize at the site of mechanotransduction in mammalian inner ear hair cell Stereocilia. *Cell Rep.* 12, 1606–1617. doi: 10.1016/j.celrep.2015.07.058

Kwon, T. J., Oh, S. K., Park, H. J., Sato, O., Venselaar, H., and Choi, S. Y. (2014). The effect of novel mutations on the structure and enzymatic activity of unconventional myosins associated with autosomal dominant non-syndromic hearing loss. *Open Biol.* 4:140107. doi: 10.1098/rsob.140107

Laakso, J. M, Lewis, J. H., Henry, S., and Ostap, E. M. (2008). Myosin I can act as a molecular force sensor. *Science* 321, 133–136. doi: 10.1126/science.1159419

Lelli, A., Michel, V., Boutet de Monvel, J., Cortese, M., Bosch-Grau, M., and Aghaie, A. (2016). Class III myosins shape the auditory hair bundles by limiting microvilli and stereocilia growth. *J. Cell Biol.* 212, 231–244. doi: 10.1083/jcb.201509017

Les Erickson, F. (2003). Localization of a class III myosin to filopodia tips in transfected HeLa cells requires an actin-binding site in its tail domain. *Mol. Biol. Cell.* 14, 4173–4180. doi: 10.1091/mbc.e02-10-0656

Li, J., Haiyang, L., Raval, M. H., Jun, W., Christopher, M. Y., Liu, W., et al. (2019). Structure of the MORN4/Myo3a tail complex reveals MORN repeats as protein binding modules. *Structure* 27, 1366–1374.e3.

Li, S., Mecca, A., Kim, J., Caprara, G. A., Wagner, E. L., Du, T. T., et al. (2020). Myosin-VIIa is expressed in multiple isoforms and essential for tensioning the hair cell mechanotransduction complex. *Nat. Commun.* 11:2066.

Lin, T., Greenberg, M. J., Moore, J. R., and Ostap, E. M. (2011). A hearing loss-associated myo1c mutation (R156W) decreases the myosin duty ratio and force sensitivity. *Biochemistry* 50, 1831–1838. doi: 10.1021/bi1016777

Liu, H., Li, J., Raval, M. H., Yao, N., Deng, X., and Lu, Q. (2016). Myosin III-mediated cross-linking and stimulation of actin bundling activity of Espin. *eLife* 5:e12856.

Loomis, P. A., Zheng, L., Sekerková, G., Changyaleket, B., Mugnaini, E., and Bartles, J. R. (2003). Espin cross-links cause the elongation of microvillus-type parallel actin bundles in vivo. *J. Cell Biol.* 163, 1045–1055. doi: 10.1083/jcb.200309093

Malik, F. I., Hartman, J. J., Elias, K. A., Morgan, B. P., Rodriguez, H., and Brejc, K. (2011). Cardiac myosin activation: a potential therapeutic approach for systolic heart failure. *Science* 331, 1439–1443.

McGrath, J., Roy, P., and Perrin, B. J. (2017). Stereocilia morphogenesis and maintenance through regulation of actin stability. *Semin. Cell Dev. Biol.* 65, 88–95. doi: 10.1016/j.semcdb.2016.08.017

McIntosh, B. B., and Ostap, E. M. (2016). Myosin-I molecular motors at a glance. *J. Cell Sci.* 129, 2689–2695. doi: 10.1242/jcs.186403

Mecklenburg, K. L., Freed, S. A., Raval, M., Quintero, O. A., Yengo, C. M., and O'Tousa, J. E. (2015). Invertebrate and vertebrate class III myosins interact with MORN repeat-containing adaptor proteins. *PLoS One* 10:e0122502. doi: 10.1371/journal.pone.0122502

Melchionda, S., Ahituv, N., Bisceglia, L., Sobe, T., Glaser, F., Rabionet, R., et al. (2001). MYO6, the human homologue of the gene responsible for deafness in Snell's waltzer mice, is mutated in autosomal dominant nonsyndromic hearing loss. *Am. J. Hum. Genet.* 69, 635–640. doi: 10.1086/323156

Ménétrey, J., Bahloul, A., Wells, A. L., Yengo, C. M., Morris, C. A., Sweeney, H. L., et al. (2005). The structure of the myosin VI motor reveals the mechanism of directionality reversal. *Nature* 435, 779–785. doi: 10.1038/nature03592

Merritt, R. C., Manor, U., Salles, F. T., Grati, M., Dose, A. C., and Unrath, W. C. (2012). Myosin IIIB uses an actin-binding motif in Its Espin-1 cargo to reach the tips of actin protrusions. *Curr. Biol.* 22, 320–325. doi: 10.1016/j.cub.2011.12.053

Moore, J. R., Krementsova, E. B., Trybus, K. M., and Warshaw, D. M. (2001). Myosin V exhibits a high duty cycle and large unitary displacement. *J. Cell Biol.* 155, 625–635. doi: 10.1083/jcb.200103128

Nagle, B. W., Okamoto, C., Taggart, B., and Burnside, B. (1986). The teleost cone cytoskeleton. localization of actin, microtubules, and intermediate filaments. *Invest. Ophthalmol. Vis. Sci.* 27, 689–701.

Nambiar, R., McConnell, R. E., and Tyska, M. J. (2010). Myosin motor function: the ins and outs of actin-based membrane protrusions. *Cell. Mol. Life Sci.* 67, 1239–1254. doi: 10.1007/s00018-009-0254-5

Narayanan, P., Chatterton, P., Ikeda, A., Ikeda, S., Corey, D. P., Ervasti, J. M., et al. (2015). Length regulation of mechanosensitive stereocilia depends on very slow actin dynamics and filament-severing proteins. *Nat. Commun.* 6:6855.

O'Connell, C. B., Tyska, M. J., and Mooseker, M. S. (2007). Myosin at work: motor adaptations for a variety of cellular functions. *Biochim. Biophys. Acta* 1773, 615–630. doi: 10.1016/j.bbamcr.2006.06.012

Patton, J., Brewer, C., Chien, W., Johnston, J. J., Griffith, A. J., and Biesecker, L. G. (2016). A genotypic ascertainment approach to refute the association of MYO1A variants with non-syndromic deafness. *Eur. J. Hum. Genet.* 25, 147–149. doi: 10.1038/ejhg.2016.140

Peng, A. W., Salles, F. T., Pan, B., and Ricci, A. J. (2011). Integrating the biophysical and molecular mechanisms of auditory hair cell mechanotransduction. *Nat. Commun.* 2:523.

Phillips, K. R., Tong, S., Goodyear, R., Richardson, G. P., and Cyr, J. L. (2006). Stereociliary myosin-1c receptors are sensitive to calcium chelation and absent from cadherin 23 mutant mice. *J. Neurosci.* 26, 10777–10788. doi: 10.1523/jneurosci.1847-06.2006

Porter, J. A., Hicks, J. L., Williams, D. S., and Montell, C. (1992). Differential localizations of and requirements for the two *Drosophila* ninaC kinase/myosins in photoreceptor cells. *J. Cell Biol.* 116, 683–693. doi: 10.1083/jcb.116.3.683

Probst, F. J., Fridell, R. A., Raphael, Y., Saunders, T. L., Wang, A., Liang, Y., et al. (1998). Correction of deafness in shaker-2 mice by an unconventional myosin in a BAC transgene. *Science* 280, 1444–1447. doi: 10.1126/science.280.5368.1444

Pyrpassopoulos, S., Feeser, E. A., Mazerik, J. N., Tyska, M. J., and Ostap, E. M. (2012). Membrane-bound Myo1c powers asymmetric motility of actin filaments. *Curr. Biol.* 22, 1688–1692. doi: 10.1016/j.cub.2012.06.069

Quintero, O. A., Moore, J. E., Unrath, W. C., Manor, U., Salles, F. T., Grati, M., et al. (2010). Intermolecular autophosphorylation regulates myosin IIIa activity and localization in parallel actin bundles. *J. Biol. Chem.* 285, 35770–35782. doi: 10.1074/jbc.m110.144360

Quintero, O. A., Unrath, W. C., Stevens, S. M. Jr., Manor, U., Kachar, B., and Yengo, C. M. (2013). Myosin 3A kinase activity is regulated by phosphorylation of the kinase domain activation loop. *J. Biol. Chem.* 288, 37126–37137. doi: 10.1074/jbc.m113.511014

Raval, M. H., Quintero, O. A., Weck, M. L., Unrath, W. C., Gallagher, J. W., and Cui, R. (2016). Impact of the motor and tail domains of class III myosins on regulating the formation and elongation of actin protrusions. *J. Biol. Chem.* 291, 22781–22792. doi: 10.1074/jbc.m116.733741

Rehman, A. U., Bird, J. E., Faridi, R., Shahzad, M., Shah, S., and Lee, K. (2016). Mutational spectrum ofMYO15Aand the molecular mechanisms of DFNB3 human deafness. *Hum. Mutat.* 37, 991–1003. doi: 10.1002/humu.23042

Rhoads, A. R., and Friedberg, F. (1997). Sequence motifs for calmodulin recognition. *FASEB J.* 11, 331–340. doi: 10.1096/fasebj.11.5.9141499

Riazuddin, S., Nazli, S., Ahmed, Z. M., Yang, Y., Zulfiqar, F., and Shaikh, R. S. (2008). Mutation spectrum of MYO7A and evaluation of a novel nonsyndromic deafness DFNB2 allele with residual function. *Hum. Mutat.* 29, 502–511. doi: 10.1002/humu.20677

Rzadzinska, A., Schneider, M., Noben-Trauth, K., Bartles, J. R., and Kachar, B. (2005). Balanced levels of Espin are critical for stereociliary growth and length maintenance. *Cell Motil. Cytoskeleton* 62, 157–165. doi: 10.1002/cm.20094

Sakai, T., Nobuhisa, U., Ikebe, R., and Ikebe, M. (2011). Cargo binding activates myosin VIIA motor function in cells. *Proc. Natl. Acad. Sci. U.S.A.* 108, 7028–7033. doi: 10.1073/pnas.1009188108

Salles, F. T., Merritt, R. C. Jr., Manor, U., Dougherty, G. W., Sousa, A. D., and Moore, J. E. (2009). Myosin IIIa boosts elongation of stereocilia by transporting espin 1 to the plus ends of actin filaments. *Nat. Cell Biol.* 11, 443–450. doi: 10.1038/ncb1851

Sato, O., Komatsu, S., Sakai, T., Tsukasaki, Y., Tanaka, R., Mizutani, T., et al. (2017). Human myosin VIIa is a very slow processive motor protein on various cellular actin structures. *J. Biol. Chem.* 292, 10950–10960. doi: 10.1074/jbc.m116.765966

Schietroma, C., Parain, K., Estivalet, A., Aghaie, A., Boutet de Monvel, J., Picaud, S., et al. (2017). Usher syndrome type 1-associated cadherins shape the photoreceptor outer segment. *J. Cell Biol.* 216, 1849–1864. doi: 10.1083/jcb.201612030

Schneider, M. E., Dose, A. C., Salles, F. T., Chang, W., Erickson, F. L., Burnside, B., et al. (2006). A new compartment at stereocilia tips defined by spatial and temporal patterns of myosin IIIa expression. *J. Neurosci.* 26, 10243–10252. doi: 10.1523/jneurosci.2812-06.2006

Seki, Y., Miyasaka, Y., Suzuki, S., Wada, K., Yasuda, S. P., and Matsuoka, K. (2017). A novel splice site mutation of myosin VI in mice leads to stereociliary fusion caused by disruption of actin networks in the apical region of inner ear hair cells. *PLoS One* 12:e0183477. doi: 10.1371/journal.pone.0183477

Self, T., Sobe, T., Copeland, N. G., Jenkins, N. A., Avraham, K. B., and Steel, K. P. (1999). Role of myosin VI in the differentiation of cochlear hair cells. *Dev. Biol.* 214, 331–341. doi: 10.1006/dbio.1999.9424

Siemens, J., Kazmierczak, P., Reynolds, A., Sticker, M., Littlewood-Evans, A., and Muller, U. (2002). The Usher syndrome proteins cadherin 23 and harmonin form a complex by means of PDZ-domain interactions. *Proc. Natl. Acad. Sci. U.S.A.* 99, 14946–14951. doi: 10.1073/pnas.232579599

Tilney, L. G., Derosier, D. J., and Mulroy, M. J. (1980). The organization of actin filaments in the stereocilia of cochlear hair cells. *J. Cell Biol.* 86, 244–259. doi: 10.1083/jcb.86.1.244

Tilney, L. G., and Saunders, J. C. (1983). Actin filaments, stereocilia, and hair cells of the bird cochlea. I. Length, number, width, and distribution of stereocilia of each hair cell are related to the position of the hair cell on the cochlea. *J. Cell Biol.* 96, 807–821. doi: 10.1083/jcb.96.3.807

Trivedi, D. V., Muretta, J. M., Swenson, A. M., Davis, J. P., Thomas, D. D., and Yengo, C. M. (2015). Direct measurements of the coordination of lever arm swing and the catalytic cycle in myosin V. *Proc. Natl. Acad. Sci. U.S.A.* 112, 14593–14598. doi: 10.1073/pnas.1517566112

Trivedi, D. V., Nag, S., Spudich, A., Ruppel, K. M., and Spudich, J. A. (2020). The myosin family of Mechanoenzymes: from mechanisms to therapeutic approaches. *Annu. Rev. Biochem.* 89, 667–693. doi: 10.1146/annurev-biochem-011520-105234

Tyska, M. J., and Mooseker, M. S. (2002). MYO1A (brush border myosin I) dynamics in the brush border of LLC-PK1-CL4 cells. *Biophys. J.* 82, 1869–1883. doi: 10.1016/s0006-3495(02)75537-9

Vélez-Ortega, A. C., and Frolenkov, G. I. (2019). Building and repairing the stereocilia cytoskeleton in mammalian auditory hair cells. *Hear. Res.* 376, 47–57. doi: 10.1016/j.heares.2018.12.012

Venkatachalam, K., Wasserman, D., Wang, X., Li, R., Mills, E., and Elsaesser, R. (2010). Dependence on a Retinophilin/Myosin complex for stability of PKC and INAD and termination of phototransduction. *J. Neurosci.* 30, 11337–11345. doi: 10.1523/jneurosci.2709-10.2010

Walsh, T., Walsh, V., Vreugde, S., Hertzano, R., Shahin, H., and Haika, S. (2002). From flies' eyes to our ears: mutations in a human class III myosin cause progressive nonsyndromic hearing loss DFNB30. *Proc. Natl. Acad. Sci. U.S.A.* 99, 7518–7523. doi: 10.1073/pnas.102091699

Walsh, V. L., Raviv, D., Dror, A. A., Shahin, H., Walsh, T., and Kanaan, M. N. (2011). A mouse model for human hearing loss DFNB30 due to loss of function of myosin IIIA. *Mamm. Genome* 22, 170–177. doi: 10.1007/s00335-010-9310-6

Wang, J., Shen, J., Guo, L., Cheng, C., Chai, R., Shu, Y., et al. (2019). A humanized mouse model, demonstrating progressive hearing loss caused by MYO6 p.C442Y, is inherited in a semi-dominant pattern. *Hear. Res.* 379, 79–88. doi: 10.1016/j.heares.2019.04.014

Watanabe, T. M., Tokuo, H., Gonda, K., Higuchi, H., and Ikebe, M. (2010). Myosin-X induces filopodia by multiple elongation mechanism. *J. Biol. Chem.* 285, 19605–19614. doi: 10.1074/jbc.m109.093864

Wells, A. L., Lin, A. W., Chen, L. Q., Safer, D., Cain, S. M., Hasson, T., et al. (1999). Myosin VI is an actin-based motor that moves backwards. *Nature* 401, 505–508. doi: 10.1038/46835

White, H. J., Helwany, M., and Peterson, D. C. (2020). *Anatomy, Head and Neck, Ear Organ of Corti*. Treasure Island, FL: StatPearls Publishing LLC

Yamamoto, N., Mutai, H., Namba, K., Goto, F., Ogawa, K., and Matsunaga, T. (2020). Clinical Profiles of DFNA11 at diverse stages of development and aging in a large family identified by linkage analysis. *Otol. Neurotol.* 41, e663–e673.

Yotti, R., Seidman, C. E., and Seidman, J. G. (2019). Advances in the genetic basis and pathogenesis of sarcomere cardiomyopathies. *Annu. Rev. Genomics Hum. Genet.* 20, 129–153. doi: 10.1146/annurev-genom-083118-015306

Young, R. W. (1967). The renewal of photoreceptor cell outer segments. *J. Cell Biol.* 33, 61–72. doi: 10.1083/jcb.33.1.61

Yu, I. M., Planelles-Herrero, V. J., Sourigues, Y., Moussaoui, D., Sirkia, H., and Kikuti, C. (2017). Myosin 7 and its adaptors link cadherins to actin. *Nat. Commun.* 8:15864. doi: 10.1038/ncomms15864

Yue, X., Sheng, Y., Kang, L., and Xiao, R. (2019). Distinct functions of TMC channels: a comparative overview. *Cell. Mol. Life Sci.* 76, 4221–4232. doi: 10.1007/s00018-019-03214-1

Zhang, D. S., Piazza, V., Perrin, B. J., Rzadzinska, A. K., Poczatek, J. C., and Wang, M. (2012). Multi-isotope imaging mass spectrometry reveals slow protein turnover in hair-cell stereocilia. *Nature* 481, 520–524. doi: 10.1038/nature10745

Zhang, J., Guan, J., Wang, H., Yin, L., Wang, D., Zhao, L., et al. (2019). Genotype-phenotype correlation analysis of MYO15A variants in autosomal recessive non-syndromic hearing loss. *BMC Med. Genet.* 20:60. doi: 10.1186/s12881-019-0790-2

**Conflict of Interest:** The authors declare that the research was conducted in the absence of any commercial or financial relationships that could be construed as a potential conflict of interest.

*Copyright © 2021 Cirilo, Gunther and Yengo. This is an open-access article distributed under the terms of the Creative Commons Attribution License (CC BY). The use, distribution or reproduction in other forums is permitted, provided the original author(s) and the copyright owner(s) are credited and that the original publication in this journal is cited, in accordance with accepted academic practice. No use, distribution or reproduction is permitted which does not comply with these terms.*

frontiers in Cell and Developmental Biology

ORIGINAL RESEARCH
published: 15 April 2021
doi: 10.3389/fcell.2021.642666

# Structure and Membrane Targeting of the PDZD7 Harmonin Homology Domain (HHD) Associated With Hearing Loss

*Lin Lin[1*†], Huang Wang[1†], Decheng Ren[1†], Yitian Xia[2], Guang He[1*] and Qing Lu[3,4*]*

[1] Key Laboratory for the Genetics of Developmental and Neuropsychiatric Disorders, Ministry of Education, Bio-X Institutes, Shanghai Jiao Tong University, Shanghai, China, [2] State Key Laboratory of Molecular Biology, Shanghai Institute of Biochemistry and Cell Biology, Center for Excellence in Molecular Cell Science, Chinese Academy of Sciences, Shanghai, China, [3] Key Laboratory for the Genetics of Developmental and Neuropsychiatric Disorders, Ministry of Education, Bio-X Institutes, Shanghai Jiao Tong University, Shanghai, China, [4] Bio-X-Renji Hospital Research Center, School of Medicine, Renji Hospital, Shanghai Jiao Tong University, Shanghai, China

OPEN ACCESS

**Edited by:**
*Zhigang Xu,*
*Shandong University, China*

**Reviewed by:**
*Nicolas Wolff,*
*Institut Pasteur, France*
*William Crawley,*
*University of Toledo, United States*

***Correspondence:**
*Lin Lin*
*linlin_8626@sjtu.edu.cn*
*Guang He*
*heguang@sjtu.edu.cn*
*Qing Lu*
*luqing67@sjtu.edu.cn*

*† These authors have contributed equally to this work*

**Specialty section:**
*This article was submitted to Cell Growth and Division, a section of the journal Frontiers in Cell and Developmental Biology*

**Received:** *16 December 2020*
**Accepted:** *15 March 2021*
**Published:** *15 April 2021*

**Citation:**
*Lin L, Wang H, Ren D, Xia Y, He G and Lu Q (2021) Structure and Membrane Targeting of the PDZD7 Harmonin Homology Domain (HHD) Associated With Hearing Loss. Front. Cell Dev. Biol. 9:642666. doi: 10.3389/fcell.2021.642666*

Usher syndrome (USH) is the leading cause of hereditary hearing–vision loss in humans. PDZ domain-containing 7 (PDZD7) has been reported to be a modifier of and contributor to USH. PDZD7 co-localizes with USH2 proteins in the inner ear hair cells and is essential for ankle-link formation and stereocilia development. PDZD7 contains three PDZ domains and a low-complexity region between the last two PDZ domains, which has been overlooked in the previous studies. Here we characterized a well-folded harmonin homology domain (HHD) from the middle region and solved the PDZD7 HHD structure at the resolution of 1.49 Å. PDZD7 HHD adopts the same five-helix fold as other HHDs found in Harmonin and Whirlin; however, in PDZD7 HHD, a unique α1N helix occupies the canonical binding pocket, suggesting a distinct binding mode. Moreover, we found that the PDZD7 HHD domain can bind lipid and mediate the localization of PDZD7 to the plasma membrane in HEK293T cells. Intriguingly, a hearing-loss mutation at the N-terminal extension region of the HHD can disrupt the lipid-binding ability of PDZD7 HHD, suggesting that HHD-mediated membrane targeting is required for the hearing process. This structural and biochemical characterization of the PDZD7 HHD region provides mechanistic explanations for human deafness-causing mutations in PDZD7. Furthermore, this structure will also facilitate biochemical and functional studies of other HHDs.

**Keywords: usher syndrome, PDZD7, lipid binding, structure, deafness**

## INTRODUCTION

Usher syndrome (USH) is the most common hereditary disease affecting both the visual and auditory systems in humans (Boughman et al., 1983; Keats and Corey, 1999; El-Amraoui and Petit, 2005). Based on the severity and progression of hearing loss, retinitis pigmentosa, and vestibular dysfunction, USH can be classified into three types: USH1, USH2, and USH3 (Gillespie and Müller, 2009; Friedman et al., 2011; Richardson et al., 2011; Pan and Zhang, 2012;

Barr-Gillespie, 2015). USH2 is characterized by moderate-to-severe hearing impairment, progressive retinitis pigmentosa, and preserved vestibular function (Kimberling et al., 2010). Variants in the *USH2A*, *ADGRV1*, *WHRN*, and *PDZD7* genes are associated with USH2 in human (Weston et al., 2004; van Wijk et al., 2006; Ebermann et al., 2010). Stereocilia are actin-based protrusions on the apical surface of inner ear hair cells, essential for mechano-transduction in the cochlea. Stereocilia are organized in a staircase-like pattern and connected by several extracellular links, including tip link, ankle link, and basal link. USH2 proteins were reported to localize at the ankle link of hair cell stereocilia, but the molecular mechanisms governing ankle-link formation are not well characterized.

PDZ domain-containing 7 (PDZD7) is part of the ankle-link complex, playing a vital role in the development of cochlear hair cells (Grati et al., 2012; Chen et al., 2014; Hu et al., 2014; Zou et al., 2014; Du et al., 2020). *Pdzd7* knockout mice exhibit stereocilia disorganization, mechano-transduction reduction, and congenital deafness (Zou et al., 2014). At the molecular level, localization of USH2 proteins (USH2A, VLGR1, and Whirlin) at the ankle region is disrupted in *Pdzd7* knockout mice, suggesting that PDZD7 determines the localization of the USH2 complex. PDZD7 also interacts with USH1 proteins (USH1B, USH1C, and USH1G) (Schneider et al., 2009; Chen et al., 2014; Morgan et al., 2016). Mutations in PDZD7 are associated with non-syndromic hearing loss and contribute to digenic USH (Schneider et al., 2009; Ebermann et al., 2010). Recently, a novel mutation in *PDZD7*, p.525_533delDQERGRALLinsV was reported to be associated with non-syndromic hearing loss in the Chinese population (Wu et al., 2020).

The long isoform of PDZD7, which is indispensable for hair cell development (Du et al., 2020), contains tandem PDZ domains (PDZ1-2), an HHD (harmonin homology domain), a PR (proline-rich) region, and a third PDZ domain (PDZ3). The PDZ domains are responsible for interacting with USH2 proteins to form the ankle-link complex (Chen et al., 2014). However, the function of the PDZD7 HHD remains unknown. Due to the low similarity of the primary sequence, the HHD family was only recently classified and has been barely characterized (Faure et al., 2014). The first solved HHD structure was Harmonin HHD (Pan et al., 2009), with 80 amino acids folded into a compact five alpha-helix bundle. Interestingly, three hearing loss-related proteins (Harmonin, Whirlin, and PDZD7) contain this HHD, but the molecular mechanism of these HHDs is largely unknown. In previous studies of PDZD7, the region containing the HHD has been widely overlooked due to the low complexity of this region. Noticeably, the human deafness mutation mentioned above (p.525_533delDQERGRALLinsV in *PDZD7*) locates adjacent to the HHD region, implying its involvement with hearing loss.

In this study, we characterized the HHD region of PDZD7 and found it responsible for targeting PDZD7 to the plasma membrane. First, we designed two HHD constructs (a.a. 546–646 and a.a. 508–646), both of which form homogeneous and stable monomers in solution. Further, we solved the PDZD7 HHD structure at a resolution of 1.49 Å. PDZD7 HHD adopts a canonical five-helix fold and exists as a monomer. Intriguingly, PDZD7 has a unique extended helix at the N-terminus of the HHD domain (referred to as α1N), which is not observed in other HHD structures. α1N blocks the common pocket, which allows the Harmonin HHD to bind with SANS, suggesting a distinct structure feature of target recognition for PDZD7. Moreover, we discovered a lipid-binding property of the PDZD7 HHD domain *in vitro* and found that the HHD region is required for PDZD7 to localize to the plasma membrane in HEK293T cells. Furthermore, we found that a hearing-loss mutation of *PDZD7*, located in the N-terminal extension region of the HHD, can disrupt the lipid-binding ability of the PDZD7 HHD. Together with biochemical and structural characterization of the PDZD7 HHD region, we propose that PDZD7 HHD-mediated lipid binding is required for the hearing process. Our findings will also expand our knowledge on the action mode of HHDs.

# MATERIALS AND METHODS

## Constructs, Protein Expression, and Purification

For PDZD7 (UniProtKB: E9Q9W7), HHD (HHD, a.a. 546–646) and HHD-Long (HHD-L, a.a. 508–646) were amplified by standard PCR (Vazyme, Nanjing, China) and inserted into pET.M.3C or pET.32M.3C through homologous recombination (Yeasen, Shanghai, China). For Whirlin, HHD2 (a.a. 410–510) was cloned into pET.M.3C. Mutants were created by PCR-based mutagenesis. All the plasmids were confirmed by DNA sequencing (GENEWIZ, Suzhou, China).

Proteins were expressed in BL21 (DE3) *E. coli* cells in LB medium at 16°C. Protein purifications were conducted using $Ni^{2+}$-NTA affinity chromatography followed by size-exclusion chromatography (SEC) using a Superdex 200 column (GE Healthcare) in a buffer of 50 mM Tris–HCl, 1 mM DTT, 1 mM EDTA, pH 7.8, and 100 mM NaCl. Protein tags were cleaved using 3C protease and then removed by another step of size-exclusion chromatography.

## Crystallization, Data Collection, and Structure Determination

Crystals of PDZD7 HHD (∼10 mg/mL) were obtained at 16°C by the sitting-drop vapor diffusion method, in 0.1 M Bis–Tris pH 6.5 and 45% polypropylene glycol P400. Crystals were cryoprotected in reservoir solution with 20% glycerol. Diffraction data were collected at BL19U1 at Shanghai Synchrotron Radiation Facility (SSRF, Shanghai, China) and were processed with XDS.

The structure was solved by molecular replacement using the structure of Whirlin HHD2 (PDB code: 6FDD) as the search model by Phaser. Jelly-body refinement was performed with the obtained solutions using REFMAC in CCP4 (Murshudov et al., 2011), and the density maps were examined in Coot (Emsley and Cowtan, 2004). Further refinement was performed using Coot and REFMAC (Winn et al., 2011) iteratively. The final refinement statistics of the structure are listed in **Table 1**. Structural diagrams were prepared using PyMOL[1].

[1]http://www.pymol.org

**TABLE 1 |** Data collection and refinement statistics.

| **Data collection and processing** | |
|---|---|
| Crystal | PDZD7 HHD |
| Source | SSRF-BL19U1 |
| Wavelength (Å) | 0.97891 |
| Space group | $P2_1$ |
| Unit cell (a, b, c, Å) | 32.8, 75.0, 42.9 |
| Unit cell (α, β, γ, °) | 90, 103.1, 90 |
| Resolution range (Å) | 50–1.49 (1.55–1.49) |
| No. of unique reflections | 32,592 (3,159) |
| Redundancy | 6.7 (6.6) |
| I/σ (I) | 13.5 (1.4) |
| Completeness (%) | 99.5 (97.4) |
| $R_{merge}$ (%)[a] | 8.4 (13.5) |
| CC1/2 | 99.9 (71.1) |
| **Structure refinement** | |
| Resolution (Å) | 37.50–1.49 |
| $R_{work}$[b]/$R_{free}$[c] (%) | 17.71/19.40 |
| rmsd bonds (Å)/angles (°) | 0.013/1.280 |
| **Number of reflections** | |
| Working set | 30,582 (2,963) |
| Test set | 1,998 (194) |
| Number of protein atoms | 1,523 |
| Number of solvent atoms | 151 |
| Average B factor (Å$^2$) (Protein/solvent) | 21.71/33.80 |
| **Ramachandran plot (%)** | |
| Most favored regions | 98.9 |
| Additionally allowed | 1.1 |
| Outlier | 0 |

*Numbers in parentheses represent the value for the highest-resolution shell.*
*[a] Rmerge = Σ| Ii–Im| /ΣIi, where Ii is the intensity of the measured reflection and Im is the mean intensity of all symmetry-related reflections.*
*[b] Rwork = Σ| | Fobs| –| Fcalc| | /Σ| Fobs|, where Fobs and Fcalc are observed and calculated structure factors.*
*[c] Rfree = Σ T| | Fobs| –| Fcalc| | /Σ T| Fobs|, where T is a test data set of about 5% of the total reflections randomly chosen and set aside prior to refinement.*

## SEC Coupled With Multi-Angle Static Light Scattering (SEC-MALS)

A pre-equilibrated Superose 12 10/300 GL column (GE Healthcare) was coupled to the AKTA FPLC system, a multi-angle static light scattering detector (miniDAWN, Wyatt), and a differential refractive index detector (Optilab, Wyatt). Protein samples were prepared for loading at 300 μl and 50 μM. Data were analyzed using ASTRA 6 (Wyatt).

## Circular Dichroism (CD)

Purified proteins cleaved from their tags were prepared. CD spectra were collected with a thermostated cell holder on a J-1500 spectropolarimeter (Jasco, Tokyo) at different temperatures (20–100°C). A quartz cell with a 1 cm path length was used for measurements in the far-UV region from 200 to 240 nm. The spectra of buffer alone were used to correct the sample spectra. Results were analyzed using Excel (Microsoft) and GraphPad Prism (GraphPad Software).

## Lipid-Binding Assay

A liposome stock was prepared by resuspending bovine brain lipid extracts (Folch fraction I, Sigma B1502) with HEPES buffer (20 mM HEPES, 100 mM NaCl, 1 mM DTT, pH 7.0). The stock at 5 mg/mL was dissolved by ultrasonication on ice. Protein samples at 0.3 mg/mL (without tags) were incubated with liposomes at room temperature for 15 min and then centrifuged at 100,000 × g for 40 min at 4°C in a Beckman TLA100.1 rotor. After centrifugation, the supernatants were collected to determine the unbound proteins. The pellets were washed and resuspended with loading buffer to determine the bound proteins. Both the supernatant and pellet proteins were subjected to sodium dodecyl sulfate-polyacrylamide gel electrophoresis (SDS-PAGE) and visualized by Coomassie blue staining.

## Cellular Localization

PDZD7-FL was cloned into pEGFP-C3, and the mutants ΔHHD-L, ΔHHD, Δ525–533, and L610DI613D were created. 293T cells were seeded into 12-well plates at the density of 2 × $10^5$ cells per well. The cells were cultured at 37°C in DMEM containing 10% fetal bovine serum (FBS) in 5% $CO_2$. All the plasmids (3.3 μg each, the DNA concentration was in the range from 800 to 1,000 ng/μl) were transiently transfected into HEK293T cells via lipofection using the FuGENE HD kit (Promega, United States). After transfection, the cells were cultured for another 24 h before fixation. Cells were imaged with a TCS SP8 STED 3X Super-resolution Multiphoton Confocal Microscope (Leica, Germany). Fluorescence intensities of the plasma membrane and cytosolic regions were quantified by ImageJ software (National Institutes of Health, United States). Data were analyzed using unpaired *t*-test. Values (means ± SE) were calculated from three independent experiments (15 cells counted for each experiments).

# RESULTS

## Structural Characterization of the PDZD7 HHD Domain

To elucidate the molecular mechanism of PDZD7 for ankle-link formation and stereocilia development, we carried out sequence analysis and found out a highly conserved helical region (HHD) between PDZ2 and PDZ3 (**Figure 1A**). Based on sequence alignment and secondary structure prediction, we designed two PDZD7 constructs containing the HHD domain (a.a. 546–646 and a.a. 508–646, namely, HHD and HHD-L, respectively). HHD-L contains an N-terminal extension region (a.a. 508–545), which is highly conserved among species (**Figure 1B**) but not found in Harmonin HHD or other HHDs.

To obtain structural information, we performed crystallization screening on HHD and HHD-L; however, only HHD successfully crystallized. HHD shows good homogeneity and exists as monomer in solution (**Figure 1E**). We then determined the HHD structure at 1.49-Å resolution. The HHD adopts a canonical five-helix fold (α1–α5) (**Figure 1C**). In the structure, α1–α5 are aligned anti-parallel to one another, making a five-helix bundle with multiple

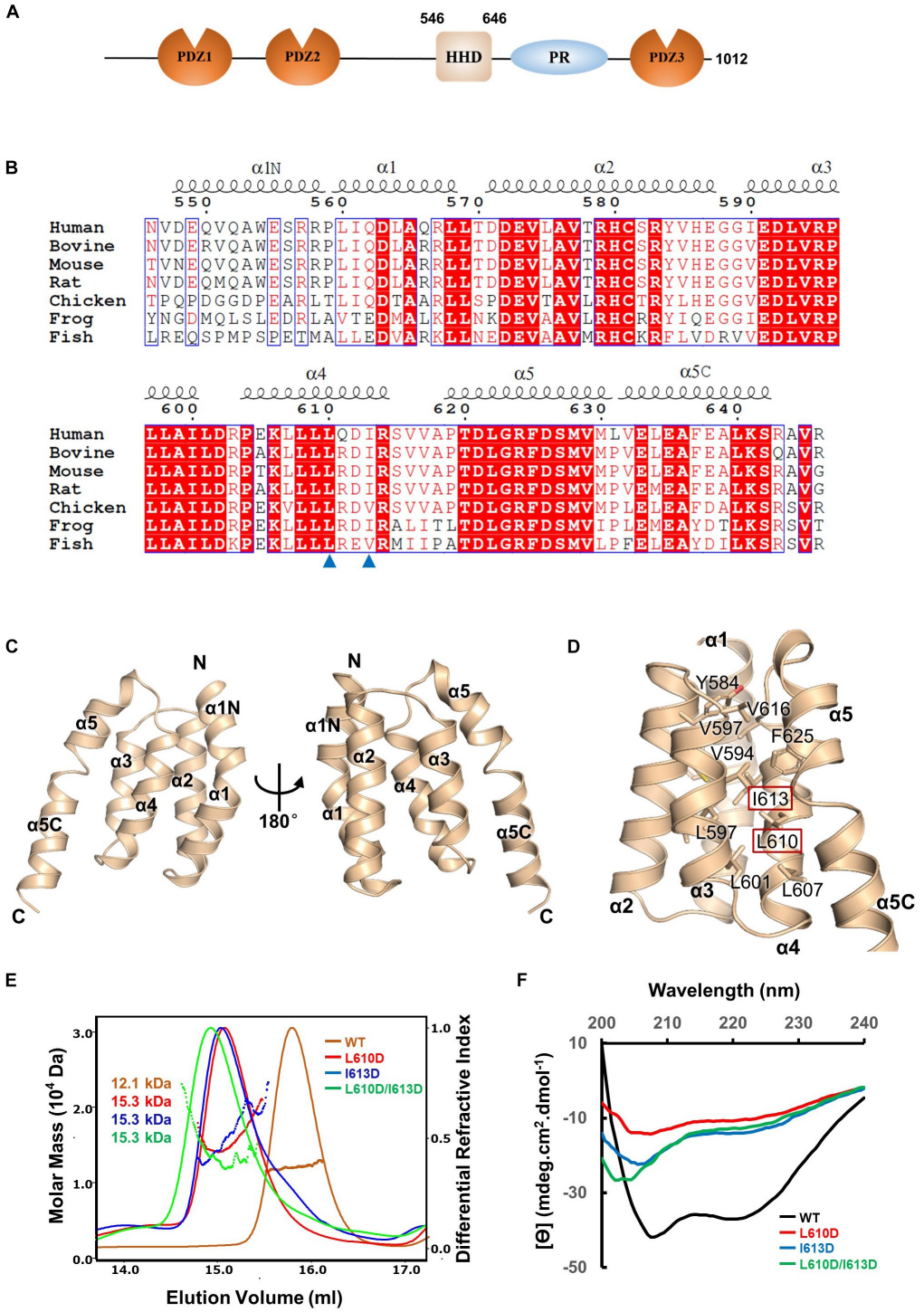


**FIGURE 1 |** Crystal structure of the PDZD7 HHD domain. **(A)** Schematic diagrams showing the domain organization of PDZD7 long isoform. **(B)** Multiple-sequence alignment of PDZD7 HHD among different species. The secondary structural elements are indicated above the alignment. The identical residues are highlighted with red boxes, and the conserved residues are colored in red. Residues Leu610 and Ile613 are indicated by blue triangles. **(C)** Ribbon diagram representation of the PDZD7 HHD structure as viewed from the front (left) and the back (right). Secondary structure elements are labeled. **(D)** Residues involved in hydrophobic core formation are shown with the stick model. Residues Leu610 and Ile613 are highlighted with the red box. **(E)** FPLC coupled with static light scattering of wild-type HHD and its mutants, L610D, I613D, and L610D/I613D. **(F)** Circular dichroism spectrum of wild-type HHD, L610D, I613D, and L610D/I613D.

hydrophobic interactions inside the bundle (**Figure 1D**). Interestingly, both α1 and α5 helices turn bend, and the extended bend regions were named as α1N (a.a. 547–559) and α5C (a.a. 631–643). α1N and α5C flank the cleft of α2/α4 and α3/α4, respectively, to contribute to the hydrophobic core formation.

To further elucidate the effect of the hydrophobic-interaction network, we designed two single mutations (L610D and I613D

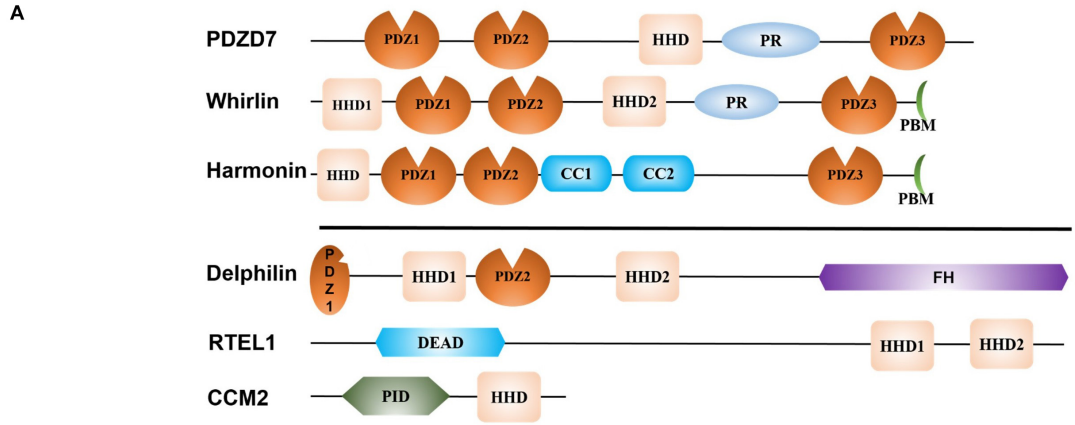


B

```
                 α1N          α1                 α2
PDZD7
PDZD7      .TVNEQVQAWESRRPLIQDLARRLLTD..DEVLAVTRHCSRYV.HEGGVEDL
Harmonin   .......MDRKVAR.EFRHKVDFLIEN.DAEKDYLYDVLRMYH.QTMDVAVL
Whirlin_1  GGGAGLRLLSANVR.QLHQALTALLSE..PEREQFTHCLNAYH.ARRNVFDL
Whirlin_2  .SQVTLSSLGNQTRALLDDQARHLLTE..QERATMMYYLAQYRGGTISVEAM
CCM2       .SESELSTSATELLQDYMLTLRTKLSS..QEIQQFAALLHEYR.NGASIHEF
Delphilin_1 RPDAVHRERRRKAQ.EFSCQVDDILGDRLTAKEQVFTALKQFA.AEQRVDEL
Delphilin_2 VADILPSSIRVQGR.TFSQQLDHLLTP..PERYGVCRALERFF.QHRNIDTL
RTEL_1     PEEPMAGTQAG.RAKMFMVAVKQALSQ..ANFDTFTQALQHYK.SSDDFEAL
RTEL_2     .VGCAVEKPGQPAVSDYLSDVHKALGS..ASCNQLTAALRAYK.QDDDLDKV

                 α3          α4          α5          α5C
PDZD7
PDZD7      VRPLLAIL.DRPTKLLLLRDIRSVVAPTDLGRFDSMVMPVELEAFEALKSRA
Harmonin   VGDLKLVI.NEPNRLPLFDAIRPLIPLKHQVEYDQLTPRRSRKLKEVRLDRL
Whirlin_1  VRTLRVLL.DSPVKRRLLPMLRLVIPRSDQLLFDQYTAEGLYLPATTPYRQP
Whirlin_2  VMALFELL.NTHAKFSLLSEVRSIISPQDLDRFDHLVLRREIESMKARQPPG
CCM2       CISLRQLY.GDSRKF.LLLGLRPFIPEKDSQHFENFLETIGVKDGRGIITDS
Delphilin_1 VWTLTLVL.PSEAQGPVLDNLRIFIPKKHRARFDEVVSQGLLGKLCRARRAQ
Delphilin_2 IVDVYPVL.DTPAKQVLWQFLYQLLTYEEQELCQEKIACFLGYTAMTEPESS
RTEL_1     VASLTCLFAEDPKKHTLLKGFYQFVRPHHKQQFEDICFQLTGQRCGYQPGKR
RTEL_2     VAVVAALTTAKPEHLPLLQRFGMFVRRHHKPQFLQTCADLMGLPTTGKDLEL
```

| Sequence identity with PDZD7 (%) | |
|---|---|
| Harmonin | 15.38 |
| Whirlin_1 | 26.04 |
| Whirlin_2 | 30.30 |
| CCM2 | 15.79 |
| Delphilin_1 | 18.56 |
| Delphilin_2 | 14.43 |
| RTEL_1 | 17.58 |
| RTEL_2 | 15.12 |

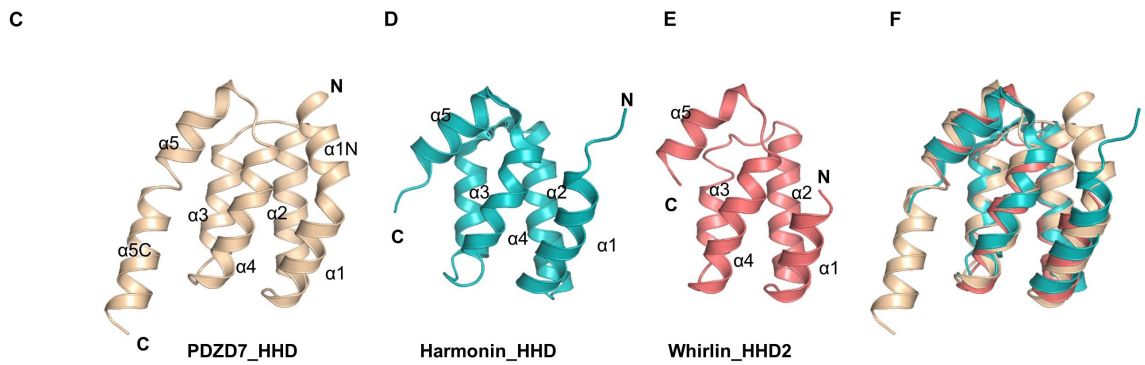


**FIGURE 2 |** Conservation of HHD-containing proteins. **(A)** Schematic diagrams showing the domain organization of the six known HHD-containing proteins. **(B)** Sequence alignment of the nine known HHDs from *Mus musculus*. The conserved residues are colored in red. The sequence identity of other eight HHDs with PDZD7 is indicated. **(C–F)** Ribbon diagram representations of the PDZD7 HHD **(C)**, Harmonin HHD **(D)**, and Whirlin HHD2 **(E)** from the same view. **(F)** Structural superimposition of PDZD7, Harmonin, and Whirlin HHD2.

at the α4 helix) and one double mutation (L610D/I613D) to destabilize the hydrophobic interactions in the HHD (**Figure 1D**). SEC-MALS was carried out to characterize the protein behavior of these mutants (**Figure 1E**). The experimental MW of wild-type (WT) PDZD7 (12.1 kDa) matches its theoretical MW of 11.4 kDa, confirming that the PDZD7 HHD is monomeric in solution. Compared with the WT protein, the peaks of the mutants shifted forward, suggesting that the homogeneity of the mutants was disturbed (**Figure 1E**). CD spectroscopy data also showed that these mutations disrupted protein folding (**Figure 1F**). Taking these results together, hydrophobic interactions inside the five-helix bundle are important for the folding of the PDZD7 HHD.

## PDZD7 HHD Contains Unique α1N and α5C Regions

Until now, the HHD has only been identified in six proteins: PDZD7, Whirlin, Harmonin, Delphilin, regulator of telomere elongation helicase 1 (RTEL1), and cerebral cavernous malformation 2 (CCM2) (**Figure 2A**). Although these HHDs share a similar folding topology, the sequence similarities are very low and limited to residues forming the hydrophobic core (**Figure 2B**). Interestingly, three of the identified HHD-containing proteins are paralog USH scaffold proteins, namely, Harmonin, Whirlin, and PDZD7. Harmonin has an HHD at the N-terminal region coupled with its first PDZ domain, PDZ1, while Whirlin has one HHD (HHD1) in the N-terminal region and another HHD in the middle region(HHD2). PDZD7 HHD shares 26 and 30% sequence identity with HHD1 and HHD2 of Whirlin, respectively, and shares 15% identity with Harmonin. Superposition of PDZD7 HHD (**Figure 2C**) with Harmonin HHD (PDB: 2KBQ; **Figure 2D**) and Whirlin HHD2 (PDB: 6FDD; **Figure 2E**) indicates that they are well aligned and the overall folding is quite similar, with the RMSD on Cα of 1.81 and 1.37 Å, respectively. However, the extended regions, α1N and α5C, are not seen in Harmonin and Whirlin, suggesting that α1N and α5C are unique to PDZD7 (**Figure 2F**).

## PDZD7 HHD May Take a Distinct Target-Binding Mode

A unique feature of the PDZD7 HHD structure is that the α1N helix turns back and contacts with the pocket formed between α1, α2, and α4. Val547, Val616, and Trp554 from α1N form extensive hydrophobic interactions with Val577, Cys581, and Val585 from α2, and Ile613 and Val616 from α4 (**Figure 3A**). Interestingly, this hydrophobic cleft between α1 and α2 is a common site in HHDs, such as in Harmonin and CCM2, and is required to recognize an isolated amphipathic helix on their binding targets.

In the typical target recognition mode of the HHD domain, such as in the structure of the Harmonin HHD/cadherin23 complex (PDB: 2KBR), the α1/α2 hairpin of Harmonin forms a hydrophobic cleft (composed of residues Val6, Phe9, and Val13 from α1, and Tyr27, Leu30, and Tyr33 from α2) to accommodate the cadherin23 helix (involving residues Tyr104, Leu105, Ile109, and Tyr112), resulting in a tight interaction between the two proteins (**Figure 3B**). Similarly, in the CCM2 HHD/CT structure (PDB: 4YKC), the isolated amphipathic C-helix of CCM2 (involving residues Met424,

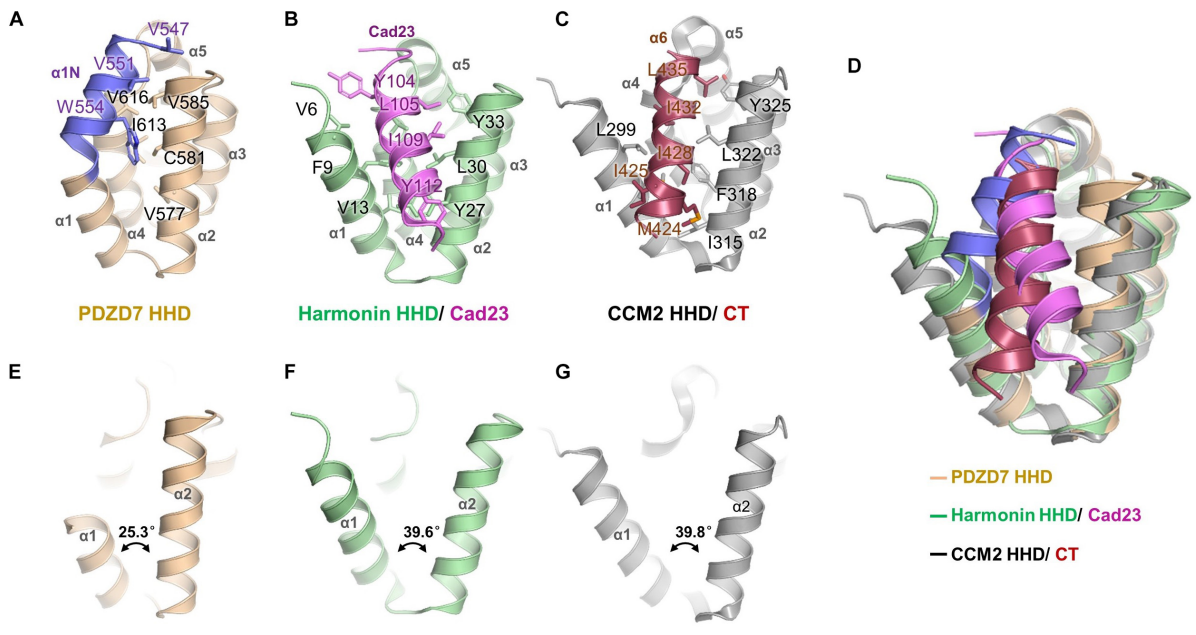


**FIGURE 3 |** Structure comparison of PDZD7 HHD and other HHD complex structures. **(A)** Intramolecular interaction of PDZD7 HHD. The hydrophobic residues on the α1N helix and residues forming the α1/α2 cleft are labeled and shown as stick models. **(B)** Intermolecular interaction of Harmonin HHD and Cad23. The involved residues are labeled and shown as stick models. **(C)** Intramolecular interaction of CCM2 HHD and its C-terminal helix (CT). **(D)** Structural superimposition of PDZD7, Harmonin/Cad23, and CCM2/CT. **(E–G)** Structural scheme of the variability of α1/α2 cleft of PDZD7 **(E)**, Harmonin **(F)**, and CCM2 **(G)**.

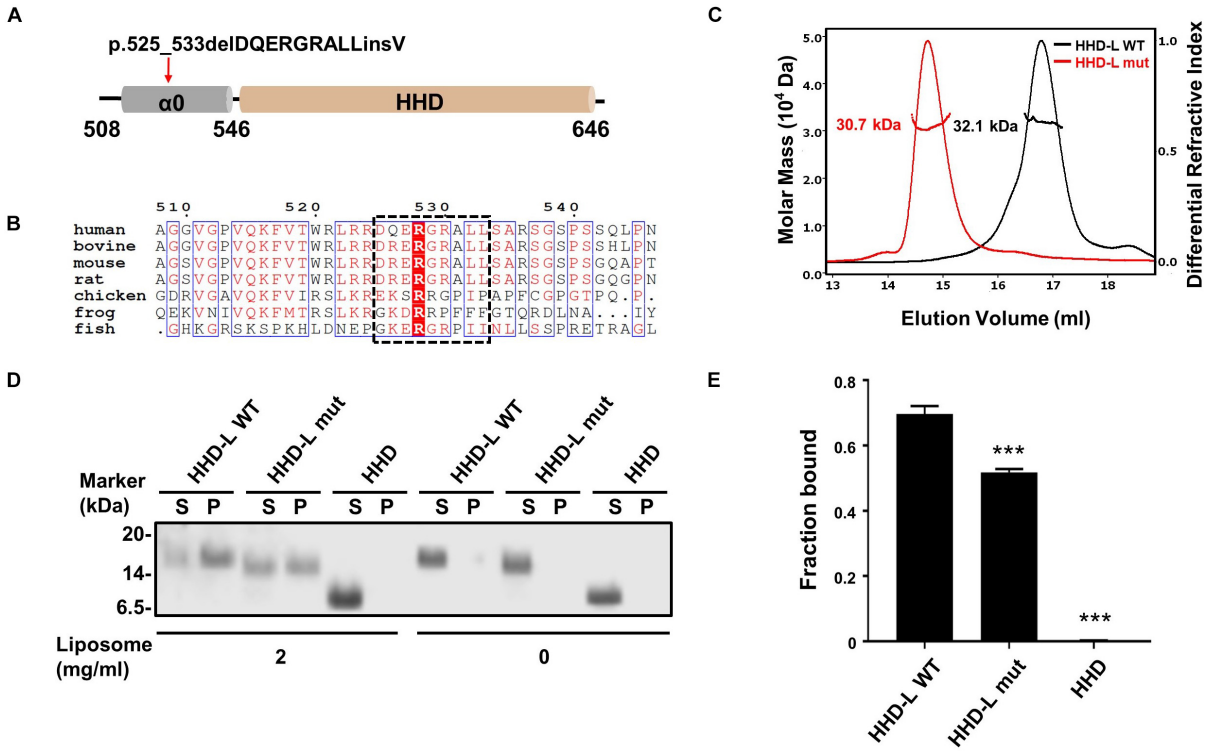


**FIGURE 4 |** The N terminal extension region of HHD; α0 plays a role in lipid binding. **(A)** Schematic diagram of PDZD7 HHD-L (residues 508–646) to show the deafness-associated mutation, p.525_533delPQERGRALLinsV located at the α0 ahead of HHD. **(B)** Sequence alignment of the α0 region in different species. The deletion region in the deafness mutation is highlighted in black box. **(C)** FPLC coupled with static light scattering of two Trx-tagged proteins, wild-type HHD-L, and its mutation, Δ525–533 (HHD-L mut). **(D)** Co-sedimentation-based assay of tag-cut HHD-L WT, HHD-L mut, and HHD bindings to liposomes prepared from bovine brain lipid extract. After centrifugation, fractions labeled with S represent proteins in supernatants and fractions labeled with P represent proteins in pellets in the assays. **(E)** The bar graph represents the fraction of the protein recovered in the liposome-bound pellet in each sedimentation assay. Values are mean ± SD of three independent experiments. ***$p < 0.001$, using one-way ANOVA with Tukey's multiple-comparison test.

Ile425, Ile428, Ile432, and Leu435) packs with the groove formed between α1/α2 (involving residues Leu299, Met303, Ile315, Phe318, Leu322, and Tyr325) to form a hydrophobic interaction (**Figure 3C**).

Structural superimposition of the three structures of PDZD7, harmonin, and CCM2 shows that the PDZD7 HHD is well-aligned onto Harmonin and CCM2, and the α1/α2 cleft of the PDZD7 HHD domain is occupied by α1N and is not available for canonical target recognition (**Figure 3D**). Besides, a deviation of the α1/α2 V-shaped cleft was observed (**Figures 3E–G**). In the Harmonin/Cad23 and the CCM2/CT structures, the α1/α2 angle is about 39.6° and 39.8°, respectively. However, the α1/α2 angle in the PDZD7 HHD structure is 25.3°, suggesting that it adopts a more compact conformation. These unique structural features suggest that the PDZD7 HHD may take a distinct binding or regulation mode for target recognition. However, our crystal structure reveals a static view of PDZD7 HHD, so future work is needed to understand the conformational dynamics of the α1N helix in solution. Clearly, additional structures of the PDZD7 HHD in complex with its binding target will be helpful in understanding the underlying mechanism, although no binding targets of PDZD7 HHD have been reported yet. Our structure provides a starting point for dissecting the target recognition mechanism of PDZD7 HHD.

## The N-Terminal Extension Region of HHD Is Responsible for Lipid Binding

*PDZD7* is a deafness-causing gene, and a previous report has associated PDZD7 mutations with USH, DFNB57, and autosomal recessive non-syndromic hearing loss (ARNSHL). Recently, a novel mutation in PDZD7, p.525_533delDQERGRALLinsV, has been shown to be associated with ARNSHL in the Chinese population. Notably, the eliminated nine residues ($^{525}$DQERGRALL$^{533}$) in this mutation are located adjacently to the N-terminus of the HHD (**Figure 4A**). Sequence alignment of the N-terminal extension region of the HHD (a.a. 508–545, named as α0 according to its secondary structure prediction) indicates that it contains a group of positively charged residues and is highly conserved among species (**Figure 4B**). To understand whether the deletion mutation affects the protein properties of the PDZD7 HHD, we performed SEC-MALS of WT Trx-tagged HHD$^{508-646}$ (HHD-L WT) and Trx-tagged HHD$^{508-646}$ Δ525–533 (HHD-L mut). The measured MWs of both HHD-L WT and HHD-L mut proteins (32.1 and

30.7 kDa, respectively) fit their theoretical MWs (30.0 and 29.1 kDa, respectively), indicating that they are monomeric in solution. Compared with HHD-L WT, the peak of HHD-L mut shifts forward, and the mutation affects the overall conformation of HHD-L mut and impairs the homogeneity of the protein (**Figure 4C**).

Considering that the N-terminal extension region of the HHD contains many conserved positively charged residues (Arg521, Arg523, Arg524, Arg526, Arg528, Arg530, and Arg536), we hypothesized that HHD-L might possess a putative lipid membrane-binding ability. We carried out a co-sedimentation-based liposome-binding assay to determine the lipid-binding ability of HHD-L WT, HHD-L mut, and HHD *in vitro*. Satisfyingly, approximately 72% of the purified HHD-L WT proteins bound to the liposome prepared from total bovine brain lipid extracts. In contrast, the liposome-bound pellet fraction of HHD-L mut decreased to ∼50%, possibly due to its loss of partial basic residues (Arg526, Arg528, and Arg530). Consistently, HHD, lacking the positively charged clusters, almost eliminated the lipid-binding capacity (**Figures 4D,E**). These results indicate that the N-terminal extension region is required for the lipid-binding ability of the PDZD7 HHD.

## HHD-L Is Essential for PDZD7 to Localize to the Plasma Membrane in HEK293T Cells

Next, we assessed the lipid-binding properties of PDZD7 under cellular conditions. When overexpressed in HEK293T cells, some of the full-length PDZD7 localizes to the plasma membrane (**Figure 5A**), suggesting that PDZD7 possesses lipid membrane-binding ability in cells. To show whether membrane targeting of PDZD7 is mediated by the HHD-L region, we designed a construct named as PDZD7 ΔHHD-L by deleting the HHD-L region from the full-length PDZD7 sequence. As expected, deletion of HHD-L dramatically decreased the membrane localization of PDZD7 with most of PDZD7 diffused into the cytosol (**Figure 5B**), revealing that the HHD-L region plays an essential role in the membrane localization of PDZD7 in HEK293T cells. Intriguingly, ΔHHD alone also weakens the membrane localization of PDZD7 so that PDZD7 presents as a diffused distribution in the cytosol (**Figure 5C**), suggesting that the HHD domain and its N-terminal extension region are both required for facilitating PDZD7 membrane binding. Consistent with this hypothesis, substitution of two hydrophobic core residues in the HHD, Leu610 and Ile613 with Asp, also eliminates the membrane localization of PDZD7 (**Figure 5E**). These data suggest that the positive-charged N-terminal extension region and the core helical bundle may work together for membrane targeting.

More importantly, the hearing-loss mutation (Δ525–533) disrupts the plasma membrane-binding ability of PDZD7 (**Figure 5D**). This disease-causing mutation may affect the human hearing process by preventing PDZD7 from localizing to the membrane. It is also suggested that HHD-mediated membrane targeting is required for the hearing process.

To further verify if the membrane-targeting ability of PDZD7 is mediated by HHD-L, we overexpressed GFP-tagged PDZD7 HHD-L, HHD, HHD-L mut (Δ525–533), 1–507, and 508-end in 293T cells, respectively. As expected, a small part of HHD-L proteins localize at the plasma membrane, indicating its membrane association ability. HHD, HHD-L mut, and 508-end all present diffused distribution in cells, whereas 1–507 proteins form punctate enrichment in cytosol (**Supplementary Figure 1**). The results further confirmed that the N-terminal extension region is critical for the membrane targeting of PDZD7.

## Implications of the Hearing-Loss Mutations in the HHD Domain of Whirlin and PDZD7

The structural and biochemical characterization on the HHD domain can provide mechanistic explanations for human deafness mutations in both PDZD7 and Whirlin. As shown in **Figures 4**, **5D**, the hearing-loss mutation at the α0 of PDZD7 HHD disrupts the lipid-binding ability of PDZD7 HHD *in vitro* and in HEK293T cells. Sequence analysis showed that two deafness-associated mutation sites in Whirlin (V460 and R490, NCBI Clinvar database, VCV000364688, and VCV000156029) are conserved between Whirlin and PDZD7, which are corresponding to V594 and R624 in PDZD7 (**Supplementary Figures 2A,B**). Interestingly, although these two sites are conserved, only mutants of Whirlin proteins present decreased homogeneity and stability (**Supplementary Figures 2E,F**) and PDZD7 mutant proteins have no impact (**Supplementary Figures 2C,D**). Our data suggest that these two disease mutations on Whirlin may disturb hearing by affecting the overall protein folding. Considering that three hearing-related proteins (Harmonin, Whirlin, and PDZD7) contain four HHD domains, our study not only provides mechanistic explanations to currently known disease-causing mutations, but also will be valuable in understanding functions of HHD domains in the hearing system.

# DISCUSSION

PDZD7 is essential for ankle-link formation and stereocilia development; however, the structural and biochemical mechanisms of PDZD7 remain unclear. Here, we have characterized the HHD domain located in the middle region of PDZD7 and solved its crystal structure at high resolution. For the first time, we have reported the lipid-binding ability of PDZD7 in this study and found that the HHD region is responsible for targeting PDZD7 to the plasma membrane in HEK293T cells. Further, we have shown that a hearing-loss mutation in humans, located at the HHD N-terminal extension region, can disrupt the lipid-binding ability of the PDZ7 HHD, suggesting that the HHD-mediated membrane targeting is required for the hearing process. PDZD7 constitutes the ankle-link complex together with Whirlin, USH2A, and VLGR1 at the ankle region of stereocilia. Noticeably, localization of all three USH2 proteins at the ankle region is disrupted in *Pdzd7* knockout

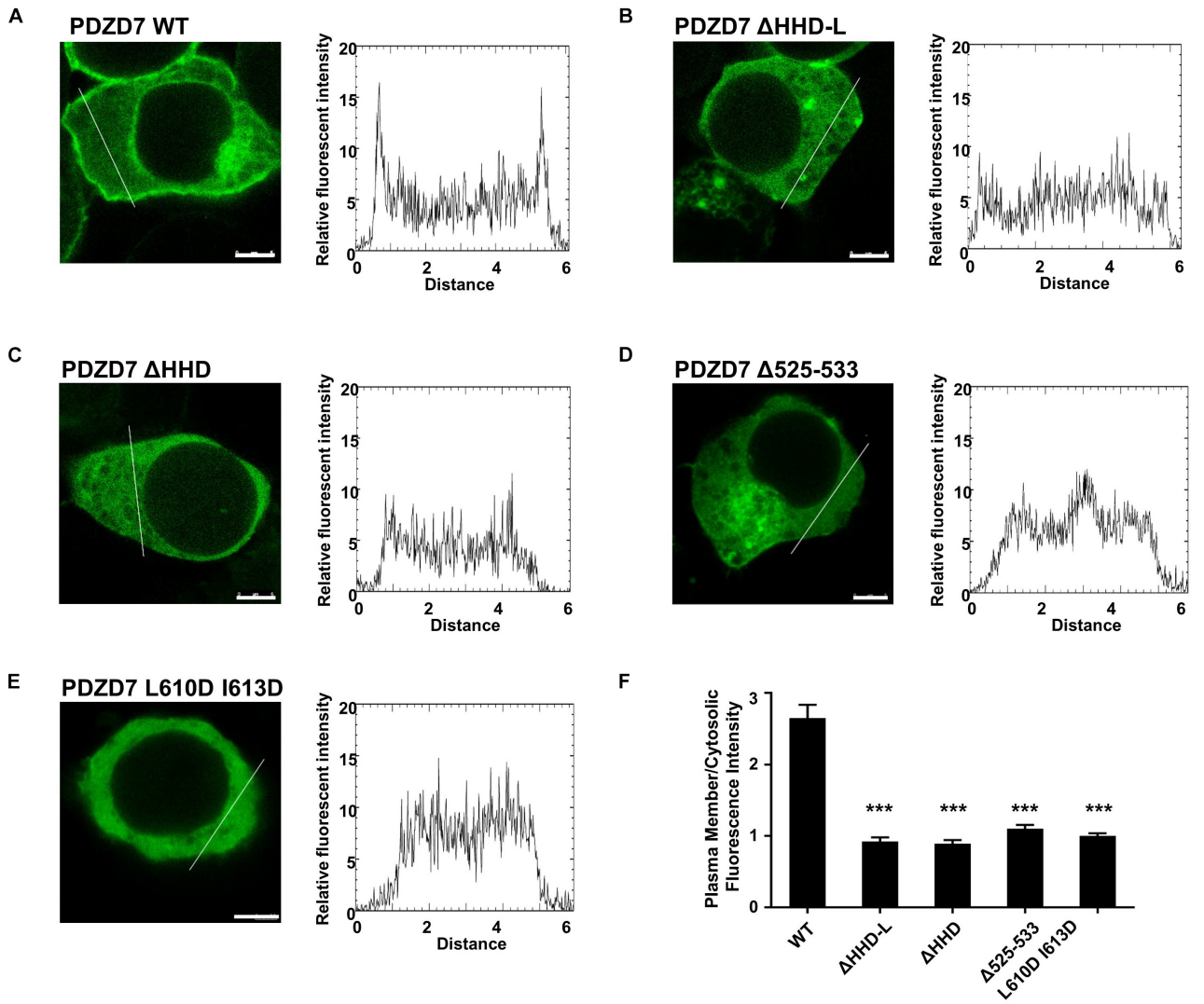


**FIGURE 5 |** The subcellular localization of the PDZD7 FL wild type and mutants in HEK 293T cells. **(A–E)** Confocal image and elative fluorescence intensity in the membrane and cytosolic distributions of HEK293T cells transfected with GFP-tagged PDZD7 FL **(A)**, PDZD7 ΔHHD-L **(B)**, PDZD7 ΔHHD **(C)**, PDZD7 Δ525–533 **(D)**, and PDZD7 L610D I613D **(E)**, respectively. Scale bar: 5 μm. Fluorescence-intensity profiles represent the area marked by the white lines in **(A–E)**. **(F)** Quantitative analysis of membrane and cytosolic distributions of GFP-tagged PDZD7 FL, PDZD7 ΔHHD-L, PDZD7 ΔHHD, PDZD7 Δ525–533, and PDZD7 L610D I613D. Values are means ± SE from three independent experiments (15 cells per time), analyzed with unpaired *t*-test; ***$p < 0.001$.

mice, suggesting that PDZD7 determines the localization of the USH2 proteins and is essential for organizing the ankle-link complex in developing cochlear hair cells. Our results indicate that HHD-mediated membrane targeting of PDZD7 may be important for regulating its interactions with membrane proteins USH2A and VLGR1. Further work is needed to verify this hypothesis.

The structure and lipid-binding property of the PDZD7 HHD reported in our work will also facilitate biochemical and functional studies of other HHD domains. As shown in the structure (**Figures 1C**, **2E**), PDZD7 HHD adopts the same five-helix fold as the other HHDs, but the canonical binding pocket of PDZD7 is blocked by a unique α1N helix. We speculate that PDZD7 may adopt a distinct binding mode for membrane targeting via its HHD region. Both the HHD and its N-terminal extension region are required for membrane binding, suggesting that the extended α0 may couple with the core five-helix bundle (**Figure 5**). These findings expand the knowledge of the HHD family and imply diverse folding and binding capacity of helical domains.

## DATA AVAILABILITY STATEMENT

The datasets presented in this study can be found in online repositories. The names of the repository/repositories and accession number(s) can be found below: http://www.wwpdb.org/, 7DE7.

## AUTHOR CONTRIBUTIONS

LL, HW, and DR performed the experiments. LL, HW, DR, YX, GH, and QL analyzed the data. LL, GH, and QL designed the research. LL and QL drafted the manuscript. QL coordinated the project. All authors commented on the manuscript.

## FUNDING

This work was supported by the National Key Research and Development Program (2020YFA0509700) to QL, National Natural Science Foundation of China (19Z103150073) to QL, Shanghai Sailing Program (18YF1410600) to QL, and the National Key Research and Development Program (2016YFC0906400) to QL and GH.

## ACKNOWLEDGMENTS

We thank Dr. Mingjie Zhang and Dr. Jianchao Li for scientific discussion on this project.

## SUPPLEMENTARY MATERIAL

The Supplementary Material for this article can be found online at: https://www.frontiersin.org/articles/10.3389/fcell.2021.642666/full#supplementary-material

**Supplementary Figure 1 |** The subcellular localization of different PDZD7 constructs in HEK 293T cells. **(A–E)** Confocal image and elative fluorescence intensity in membrane and cytosolic of HEK293T cells transfected with GFP-tagged PDZD7 HHD-L **(A)**, PDZD7 HHD **(B)**, PDZD7 HHD-L mut **(C)**, PDZD7 1–507 **(D)** and PDZD7 648-end **(E)**, respectively. Scale bar: 5 μm. Fluorescence-intensity profiles represent the area marked by the white lines in **(A–E)**.

**Supplementary Figure 2 |** The effects of deafness-associated mutations on Whirlin and PDZD7 HHD proteins. **(A)** Sequence alignment of Whirlin and PDZD7 HHD domains from different species. The totally conserved residues are highlighted with red box, and conserved residues are colored in red. Two deafness-associated mutation sites in Whirlin, V460 and R490 (V594 and R624 in PDZD7 correspondingly) are annotated below as black triangles. **(B)** The combined ribbon and stick representations showing V594 and R624 in PDZD7 HHD structures. **(C)** FPLC coupled with static light scattering of PDZD7 HHD WT, V594, and R490H. **(D)** Circular dichroism spectrum of PDZD7 HHD WT, V594, and R490H at 208 nm. **(E)** FPLC coupled with static light scattering of Whirlin HHD WT, V460I, and R490H. **(F)** Circular dichroism spectrum of Whirlin HHD WT, V460I, and R490H at 208 nm.

## REFERENCES

Barr-Gillespie, P. G. (2015). Assembly of hair bundles, an amazing problem for cell biology. *Mol. Biol. Cell* 26, 2727–2732. doi: 10.1091/mbc.E14-04-0940

Boughman, J. A., Vernon, M., and Shaver, K. A. (1983). Usher syndrome: definition and estimate of prevalence from two high-risk populations. *J. Chronic. Dis.* 36, 595–603. doi: 10.1016/0021-9681(83)90147-9

Chen, Q., Zou, J., Shen, Z., Zhang, W., and Yang, J. (2014). Whirlin and PDZ domain-containing 7 (PDZD7) proteins are both required to form the quaternary protein complex associated with Usher syndrome type 2. *J. Biol. Chem.* 289, 36070–36088. doi: 10.1074/jbc.M114.610535

Du, H., Zou, L., Ren, R., Li, N., Li, J., Wang, Y., et al. (2020). Lack of PDZD7 long isoform disrupts ankle-link complex and causes hearing loss in mice. *FASEB J.* 34, 1136–1149. doi: 10.1096/fj.201901657RR

Ebermann, I., Phillips, J. B., Liebau, M. C., Koenekoop, R. K., Schermer, B., Lopez, I., et al. (2010). PDZD7 is a modifier of retinal disease and a contributor to digenic Usher syndrome. *J. Clin. Invest.* 120, 1812–1823. doi: 10.1172/jci39715

El-Amraoui, A., and Petit, C. (2005). Usher I syndrome: unravelling the mechanisms that underlie the cohesion of the growing hair bundle in inner ear sensory cells. *J. Cell Sci.* 118(Pt 20), 4593–4603. doi: 10.1242/jcs.02636

Emsley, P., and Cowtan, K. (2004). Coot: model-building tools for molecular graphics. *Acta Crystallogr. D Biol. Crystallogr.* 60(Pt 12 Pt 1), 2126–2132. doi: 10.1107/s0907444904019158

Faure, G., Revy, P., Schertzer, M., Londono-Vallejo, A., and Callebaut, I. (2014). The C-terminal extension of human RTEL1, mutated in Hoyeraal-Hreidarsson syndrome, contains harmonin-N-like domains. *Proteins* 82, 897–903. doi: 10.1002/prot.24438

Friedman, T. B., Schultz, J. M., Ahmed, Z. M., Tsilou, E. T., and Brewer, C. C. (2011). Usher syndrome: hearing loss with vision loss. *Adv. Otorhinolaryngol.* 70, 56–65. doi: 10.1159/000322473

Gillespie, P. G., and Müller, U. (2009). Mechanotransduction by hair cells: models, molecules, and mechanisms. *Cell* 139, 33–44. doi: 10.1016/j.cell.2009.09.010

Grati, M., Shin, J. B., Weston, M. D., Green, J., Bhat, M. A., Gillespie, P. G., et al. (2012). Localization of PDZD7 to the stereocilia ankle-link associates this scaffolding protein with the Usher syndrome protein network. *J. Neurosci.* 32, 14288–14293. doi: 10.1523/JNEUROSCI.3071-12.2012

Hu, Q. X., Dong, J. H., Du, H. B., Zhang, D. L., Ren, H. Z., Ma, M. L., et al. (2014). Constitutive Galphai coupling activity of very large G protein-coupled receptor 1 (VLGR1) and its regulation by PDZD7 protein. *J. Biol. Chem.* 289, 24215–24225. doi: 10.1074/jbc.M114.549816

Keats, B. J., and Corey, D. P. (1999). The usher syndromes. *Am. J. Med. Genet.* 89, 158–166.

Kimberling, W. J., Hildebrand, M. S., Shearer, A. E., Jensen, M. L., Halder, J. A., Trzupek, K., et al. (2010). Frequency of Usher syndrome in two pediatric populations: implications for genetic screening of deaf and hard of hearing children. *Genet. Med.* 12, 512–516. doi: 10.1097/GIM.0b013e3181e5afb8

Morgan, C. P., Krey, J. F., Grati, M., Zhao, B., Fallen, S., Kannan-Sundhari, A., et al. (2016). PDZD7-MYO7A complex identified in enriched stereocilia membranes. *Elife* 5:e18312. doi: 10.7554/eLife.18312

Murshudov, G. N., Skubák, P., Lebedev, A. A., Pannu, N. S., Steiner, R. A., Nicholls, R. A., et al. (2011). REFMAC5 for the refinement of macromolecular crystal structures. *Acta Crystallogr. D Biol. Crystallogr.* 67(Pt 4), 355–367. doi: 10.1107/s0907444911001314

Pan, L., Yan, J., Wu, L., and Zhang, M. (2009). Assembling stable hair cell tip link complex via multidentate interactions between harmonin and cadherin 23. *Proc. Natl. Acad. Sci. U.S.A.* 106, 5575–5580. doi: 10.1073/pnas.0901819106

Pan, L., and Zhang, M. (2012). Structures of usher syndrome 1 proteins and their complexes. *Physiology (Bethesda)* 27, 25–42. doi: 10.1152/physiol.00037.2011

Richardson, G. P., de Monvel, J. B., and Petit, C. (2011). How the genetics of deafness illuminates auditory physiology. *Annu. Rev. Physiol.* 73, 311–334. doi: 10.1146/annurev-physiol-012110-142228

Schneider, E., Marker, T., Daser, A., Frey-Mahn, G., Beyer, V., Farcas, R., et al. (2009). Homozygous disruption of PDZD7 by reciprocal translocation in a consanguineous family: a new member of the Usher syndrome protein interactome causing congenital hearing impairment. *Hum. Mol. Genet.* 18, 655–666. doi: 10.1093/hmg/ddn395

van Wijk, E., van der Zwaag, B., Peters, T., Zimmermann, U., Te Brinke, H., Kersten, F. F., et al. (2006). The DFNB31 gene product whirlin connects to the Usher protein network in the cochlea and retina by direct association with USH2A and VLGR1. *Hum. Mol. Genet.* 15, 751–765. doi: 10.1093/hmg/ddi490

Weston, M. D., Luijendijk, M. W., Humphrey, K. D., Moller, C., and Kimberling, W. J. (2004). Mutations in the VLGR1 gene implicate G-protein signaling in the pathogenesis of Usher syndrome type II. *Am. J. Hum. Genet.* 74, 357–366. doi: 10.1086/381685

Winn, M. D., Ballard, C. C., Cowtan, K. D., Dodson, E. J., Emsley, P., Evans, P. R., et al. (2011). Overview of the CCP4 suite and current developments. *Acta Crystallogr. D Biol. Crystallogr.* 67(Pt 4), 235–242. doi: 10.1107/s0907444910045749

Wu, D., Huang, W., Xu, Z., Li, S., Zhang, J., Chen, X., et al. (2020). Clinical and genetic study of 12 Chinese Han families with nonsyndromic deafness. *Mol. Genet. Genomic Med.* 8:e1177. doi: 10.1002/mgg3.1177

Zou, J., Zheng, T., Ren, C., Askew, C., Liu, X. P., Pan, B., et al. (2014). Deletion of PDZD7 disrupts the Usher syndrome type 2 protein complex in cochlear hair cells and causes hearing loss in mice. *Hum. Mol. Genet.* 23, 2374–2390. doi: 10.1093/hmg/ddt629

**Conflict of Interest:** The authors declare that the research was conducted in the absence of any commercial or financial relationships that could be construed as a potential conflict of interest.

*Copyright © 2021 Lin, Wang, Ren, Xia, He and Lu. This is an open-access article distributed under the terms of the Creative Commons Attribution License (CC BY). The use, distribution or reproduction in other forums is permitted, provided the original author(s) and the copyright owner(s) are credited and that the original publication in this journal is cited, in accordance with accepted academic practice. No use, distribution or reproduction is permitted which does not comply with these terms.*

frontiers in Cell and Developmental Biology

ORIGINAL RESEARCH
published: 16 April 2021
doi: 10.3389/fcell.2021.649830

# Non-Canonical Wnt Signaling Regulates Cochlear Outgrowth and Planar Cell Polarity via Gsk3β Inhibition

*Andre Landin Malt, Shaylyn Clancy, Diane Hwang, Alice Liu, Connor Smith, Margaret Smith, Maya Hatley, Christopher Clemens and Xiaowei Lu**

*Department of Cell Biology, University of Virginia Health System, Charlottesville, VA, United States*

During development, sensory hair cells (HCs) in the cochlea assemble a stereociliary hair bundle on their apical surface with planar polarized structure and orientation. We have recently identified a non-canonical, Wnt/G-protein/PI3K signaling pathway that promotes cochlear outgrowth and coordinates planar polarization of the HC apical cytoskeleton and alignment of HC orientation across the cochlear epithelium. Here, we determined the involvement of the kinase Gsk3β and the small GTPase Rac1 in non-canonical Wnt signaling and its regulation of the planar cell polarity (PCP) pathway in the cochlea. We provided the first *in vivo* evidence for Wnt regulation of Gsk3β activity via inhibitory Ser9 phosphorylation. Furthermore, we carried out genetic rescue experiments of cochlear defects caused by blocking Wnt secretion. We showed that cochlear outgrowth was partially rescued by genetic ablation of Gsk3β but not by expression of stabilized β-catenin; while PCP defects, including hair bundle polarity and junctional localization of the core PCP proteins Fzd6 and Dvl2, were partially rescued by either Gsk3β ablation or constitutive activation of Rac1. Our results identify Gsk3β and likely Rac1 as downstream components of non-canonical Wnt signaling and mediators of cochlear outgrowth, HC planar polarity, and localization of a subset of core PCP proteins in the cochlea.

**Keywords: non-canonical Wnt, Gsk3β, Rac1, planar cell polarity, hair bundle, kinocilium, cochlea**

OPEN ACCESS

***Edited by:***
*Zhigang Xu,*
*Shandong University, China*

***Reviewed by:***
*Mireille Montcouquiol,*
*Institut National de la Santé et de la Recherche Médicale (INSERM), France*
*Bo Gao,*
*The University of Hong Kong, Hong Kong*

****Correspondence:***
*Xiaowei Lu*
*xl6f@virginia.edu*

***Specialty section:***
*This article was submitted to Cell Growth and Division, a section of the journal Frontiers in Cell and Developmental Biology*

***Received:*** *05 January 2021*
***Accepted:*** *17 March 2021*
***Published:*** *16 April 2021*

***Citation:***
*Landin Malt A, Clancy S, Hwang D, Liu A, Smith C, Smith M, Hatley M, Clemens C and Lu X (2021) Non-Canonical Wnt Signaling Regulates Cochlear Outgrowth and Planar Cell Polarity via Gsk3β Inhibition. Front. Cell Dev. Biol. 9:649830. doi: 10.3389/fcell.2021.649830*

## INTRODUCTION

Wnt signaling regulates a plethora of developmental processes through the canonical β-catenin-dependent pathway and the non-canonical β-catenin-independent pathway (Komiya and Habas, 2008; Wiese et al., 2018). Upon Wnt ligand binding to the Frizzled receptor, non-canonical Wnt signaling controls cell polarity and morphogenetic movements through the Rho family small GTPases or heterotrimeric G-proteins. In addition, the evolutionarily conserved planar cell polarity (PCP) pathway is a key regulator of tissue morphogenesis, whereby asymmetric localized core PCP protein complexes orient cell polarity and drive polarized cell behaviors within the plane of the tissue (Devenport, 2014). Specifically, two opposing asymmetric protein complexes, one consisting of homologs of Frizzled (Fzd) and Dishevelled (Dvl), and the other Van Gogh and Prickle, bridged across cell membranes by Flamingo (homolog of Celsr1-3), generate a polarity vector across the

tissue plane (Butler and Wallingford, 2017). Because the non-canonical Wnt and PCP pathways share many components, including the Fzd receptor, as well as the effectors Dvl and Rho GTPases, the PCP pathway is often considered to be a branch of non-canonical Wnt signaling. However, emerging evidence suggests divergence of, and crosstalk between, the mammalian non-canonical Wnt and PCP pathways. The mammalian genome encodes 19 Wnt, 10 Fzd, and 3 Dvl genes. Fzd3/6 are components of the mammalian PCP pathway (Wang et al., 2006; Chang et al., 2016); however, to date, their specific Wnt ligands have not been identified (Sato et al., 2010; Yu et al., 2012; Voloshanenko et al., 2017). On the other hand, we and others have recently demonstrated that secreted Wnts are required for asymmetric localizations of a subset of PCP proteins in inner ear sensory epithelia, including Fzd3/6 and Dvl2 (Landin Malt et al., 2020; Najarro et al., 2020). Importantly, we have shown that asymmetric localization of Fzd6 is controlled by a Wnt/G-protein/PI3K signaling pathway (Landin Malt et al., 2020). In this study, we leverage the inner ear sensory epithelium and genetic tools available to further illuminate the precise relationship between the mammalian non-canonical Wnt and PCP pathways.

The mouse cochlear sensory epithelium, or the organ of Corti (OC), is a well-established system for studying PCP signaling (Tarchini and Lu, 2019). Crucial for their function as sound receptors, hair cells (HCs) in the OC project on their apical surface a V-shaped hair bundle consisting of rows of actin-based stereocilia organized in a staircase pattern. The vertices of all hair bundles are uniformly aligned along the medial-lateral axis of the cochlear duct. The polarized structure of hair bundles and other apical cytoskeletal elements define cell-intrinsic PCP (iPCP), while uniform hair bundle orientation is a hallmark of tissue-level PCP. Hair bundle formation is coincident with the migration of the microtubule-based kinocilium, which migrates to, and anchors at, the lateral edge of the HC and is tethered to the nascent hair bundle at its vertex. Thus, kinocilium positioning is crucial for hair bundle polarity and orientation. This process is coordinately controlled by intercellular PCP signaling, several iPCP signaling modules, and a novel, non-canonical Wnt/G-protein/PI3K signaling pathway (Tarchini and Lu, 2019; Landin Malt et al., 2020). To shed light on the crosstalk and integration of these signaling pathways, we sought to identify cochlear effectors of non-canonical Wnt signaling. Specifically, we focused on two candidates: the small GTPase Rac1 and the kinase Gsk3β. Rac1 has been shown to be activated by non-canonical Wnt signaling in cultured cells and mediate one of the iPCP signaling modules in the OC (Grimsley-Myers et al., 2009; Sato et al., 2010; Landin Malt et al., 2019). On the other hand, Gsk3β activity is inhibited by both canonical Wnt and PI3K/Akt signaling (Metcalfe and Bienz, 2011; Beurel et al., 2015). Here, we report that epithelium-secreted Wnts promote inhibitory phosphorylation of Gsk3β at Ser9 (S9) in the OC *in vivo*. We further show that cochlear growth, hair bundle polarity, and core PCP protein localization defects caused by blocking Wnt secretion are partially rescued by genetic ablation of Gsk3β in the cochlear epithelium, and to a lesser extent, constitutive activation of Rac1. Together, these findings identify both Gsk3β and Rac1 as effectors of non-canonical Wnt signaling crucial for hair bundle morphogenesis and cross-regulation of the PCP pathway.

# RESULTS

## Wnt Signaling Regulates Gsk3β Activity via Serine 9 Phosphorylation in the Cochlea

Conditional deletion of *Wntless* (*Wls*) driven by $Emx2^{Cre}$ ($Wls^{cKO}$) blocked Wnt secretion from the cochlear epithelium, resulting in stunted cochlear outgrowth and both PCP and iPCP defects. We have identified PI3K as a key effector of non-canonical Wnt signaling in the OC; PI3K activity was decreased in the $Wls^{cKO}$ OC, and importantly, PI3K activation rescued most of the $Wls^{cKO}$ cochlear phenotypes (Landin Malt et al., 2020). However, the downstream targets of PI3K crucial for cochlear morphogenesis remain unknown. Because PI3K activation of Akt leads to inhibitory phosphorylation of Gsk3β at S9 (Beurel et al., 2015), we examined the localization of pS9-Gsk3β as well as total Gsk3β in $Wls^{cKO}$ cochleae, using commercial knockout (KO)-validated anti-pS9-Gsk3β and anti-Gsk3β antibodies. In the control cochlea at embryonic day (E)18.5, pS9-Gsk3β was enriched in the pericentriolar region (**Figures 1A–F**, open arrowheads), the tip of the kinocilium (**Figures 1A–F**, arrowheads), and the hair bundle in both inner and outer hair cells (IHCs and OHCs) (**Figures 1A–F**). In addition, diffused cytoplasmic staining of pS9-Gsk3β was detected in HCs, neighboring supporting cells (SCs), and non-sensory cells surrounding the OC (**Figures 1M,N**). In contrast, pS9-Gsk3β staining was greatly diminished at all subcellular locations in $Wls^{cKO}$ cochleae (**Figures 1G–L,O,P**). On the other hand, total Gsk3β localization in $Wls^{cKO}$ cochleae was similar to the control; Gsk3β was localized to the hair bundle (**Figures 2A–H**), at the adherens junctions in the OC and in the cytoplasm of both sensory and non-sensory cells (**Figures 2I–L**). The specificity of the observed staining patterns of pS9-Gsk3β and total Gsk3β was confirmed by their absence in the $Gsk3\beta^{cKO}$ cochleae driven by $Emx2^{Cre}$ (**Supplementary Figures 1**, **2**). Thus, we conclude that epithelium-secreted Wnts regulate Gsk3β activity by promoting S9 phosphorylation in the developing cochlea.

## Wnts Regulate Cochlear Outgrowth in Part Through Gsk3β Inhibition

Activation of Rac1 by non-canonical Wnt signaling has been well established in cultured cells; therefore, we hypothesized that Rac1 mediates non-canonical Wnt signaling in the cochlea. To test this, we asked whether constitutive activation of Rac1 was able to rescue cochlear defects of $Wls^{cKO}$ mutants. Specifically, we crossed a Cre-inducible, constitutively active Rac1-G12V transgene (*R26-LSL-Rac1DA*) into $Wls^{cKO}$ embryos. We first measured the length of $Wls^{cKO}$; *Rac1DA*/+ compound mutant cochleae

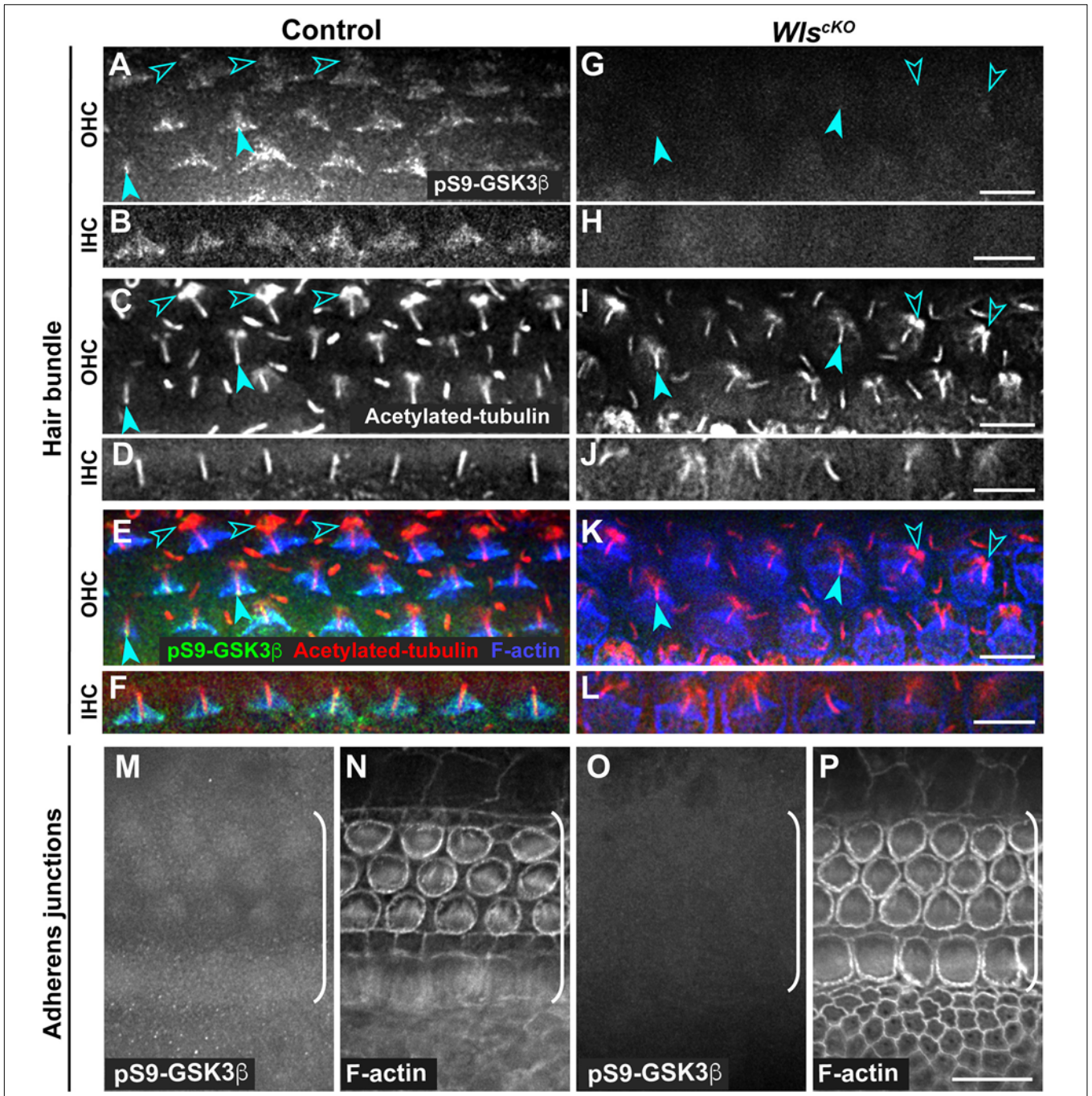


**FIGURE 1 |** Wnts promote inhibitory phosphorylation of Gsk3β at Ser9 in the cochlea. **(A–L)** pS9-Gsk3β (green), acetylated-tubulin (red), and phalloidin (blue) staining at the level of the hair bundle in control **(A–F)** and *Wls*$^{cKO}$ **(G–L)** OC at E18.5. Open arrowheads indicate the pericentriolar region. Arrowheads indicate the tip of the kinocilium. **(M–P)** pS9-Gsk3β and phalloidin staining at the level of adherens junctions in control **(M,N)** and *Wls*$^{cKO}$ **(O,P)** OC and surrounding regions. Brackets indicate the OC. Lateral is up. Scale bars: **(A–L)**, 6 μm; **(M–P)**, 10 μm.

at E18.5. As a control, expression of Rac1-G12V in the cochlear epithelium driven by *Emx2*$^{Cre}$ (*Rac1DA*/+) did not significantly alter cochlear length, width, or OC patterning (**Figures 3A,B,G,H,M,N**). Moreover, Rac1-G12V expression in *Wls*-deficient cochlear epithelia did not rescue the cochlear length (**Figures 3D,E,J,K,M**).

Next, we analyzed the *Gsk3β*$^{cKO}$ cochleae to determine the role of Gsk3β in Wnt-mediated cochlear outgrowth. At E18.5, *Gsk3β*$^{cKO}$ cochleae had largely normal length and OC patterning (**Figures 3A,C,G,I,M–O**), suggesting that the function of Gsk3 in cell fate regulation at earlier stages was spared in *Gsk3β*$^{cKO}$ mutants (Ellis et al., 2019). In contrast to Rac1 activation, the

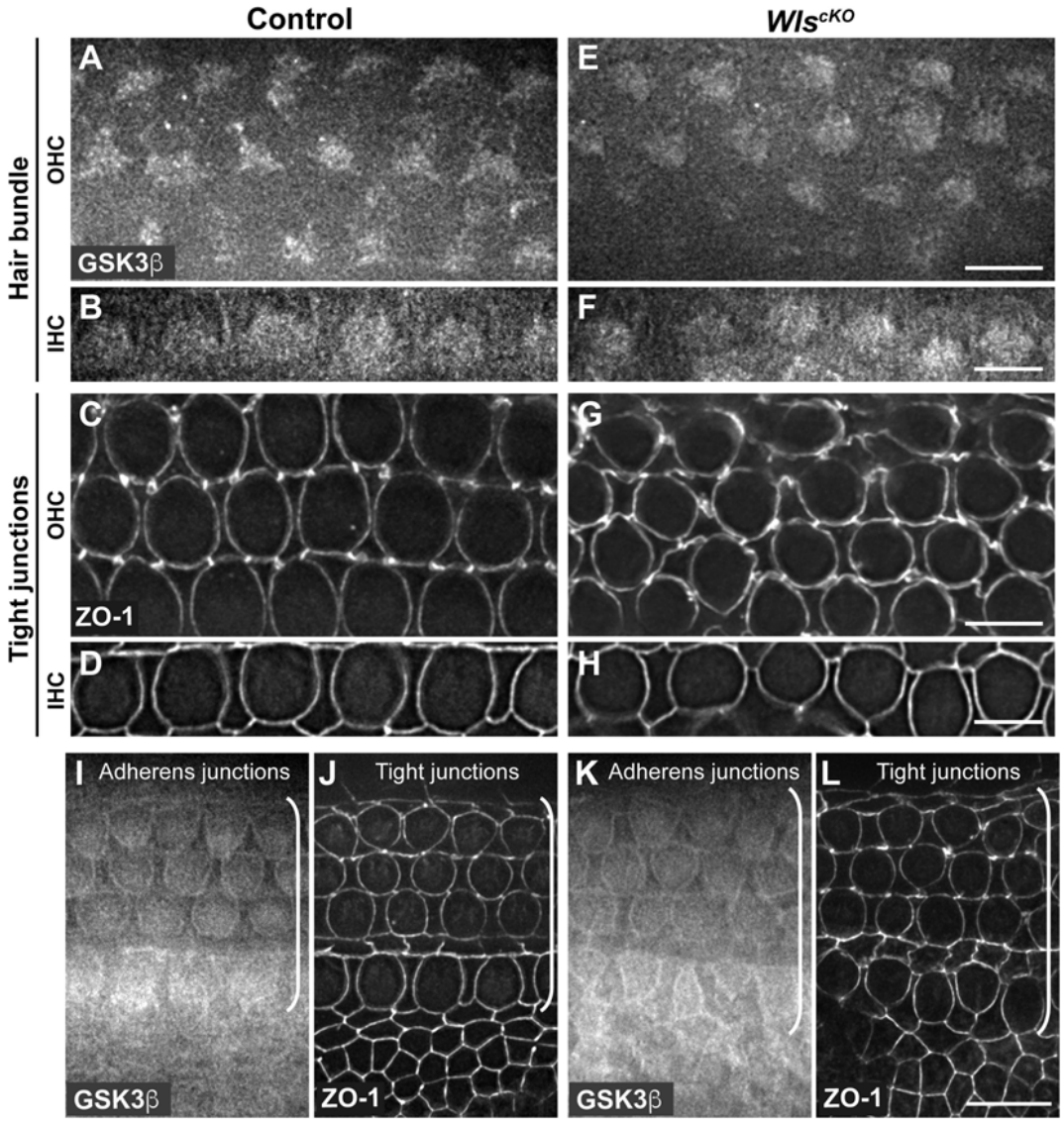


**FIGURE 2 |** Similar Gsk3β localizations in control and *Wls*$^{cKO}$ cochleae. **(A–H)** Gsk3β staining at the level of hair bundle and ZO-1 staining at the level of tight junctions in control **(A–D)** and *Wls*$^{cKO}$ **(E–H)** OC at E18.5. **(I–L)** Gsk3β staining at the level of adherens junctions and ZO-1 staining at the level of tight junctions in control **(I,J)** and *Wls*$^{cKO}$ **(K,L)** OC and surrounding regions. Brackets indicate the OC. Lateral is up. Scale bars: **(A–L)**, 6 μm; **(M–P)**, 10 μm.

length of the *Wls*$^{cKO}$; *Gsk3*β$^{cKO}$ compound mutant cochleae was partially but significantly rescued, and an intermittent extra OHC row was present along ∼60% of the total cochlear length (**Figures 3D,F,J,L–O**). As Gsk3β inactivation, but not Rac1 activation, partially rescued cochlear outgrowth defects of *Wls*$^{cKO}$ mutants, we conclude that Wnt signaling promotes cochlear outgrowth in part through Gsk3β inhibition.

## Expression of Stabilized β-Catenin Failed to Rescue Outgrowth Defects of *Wls*$^{cKO}$ Cochleae

Gsk3 inhibition is a key step in canonical Wnt signaling; sequestration of Gsk3 prevents phosphorylation of β-catenin, thereby stabilizing β-catenin, which translocates into the nucleus and partners with TCF transcription factors to activate Wnt target gene expression (Wiese et al., 2018). During cochlear development, canonical Wnt signaling promotes cell proliferation of otic precursors in the prosensory domain (Jacques et al., 2012). To determine whether the partial rescue of cochlear outgrowth observed in *Wls*$^{cKO}$; *Gsk3*β$^{cKO}$ mutants was due to activation of canonical Wnt signaling, we induced the expression of a stabilized β-catenin mutant in the cochlear epithelium by crossing an exon3-floxed β-catenin (*Ctnnb1*$^{flox(ex3)}$) allele into *Wls*$^{cKO}$ mutants. Deletion of exon3 driven by *Emx2*$^{Cre}$ generated a mutant form of β-catenin refractory to inhibitory phosphorylation by Gsk3. Surprisingly, expression of stabilized β-catenin by itself resulted

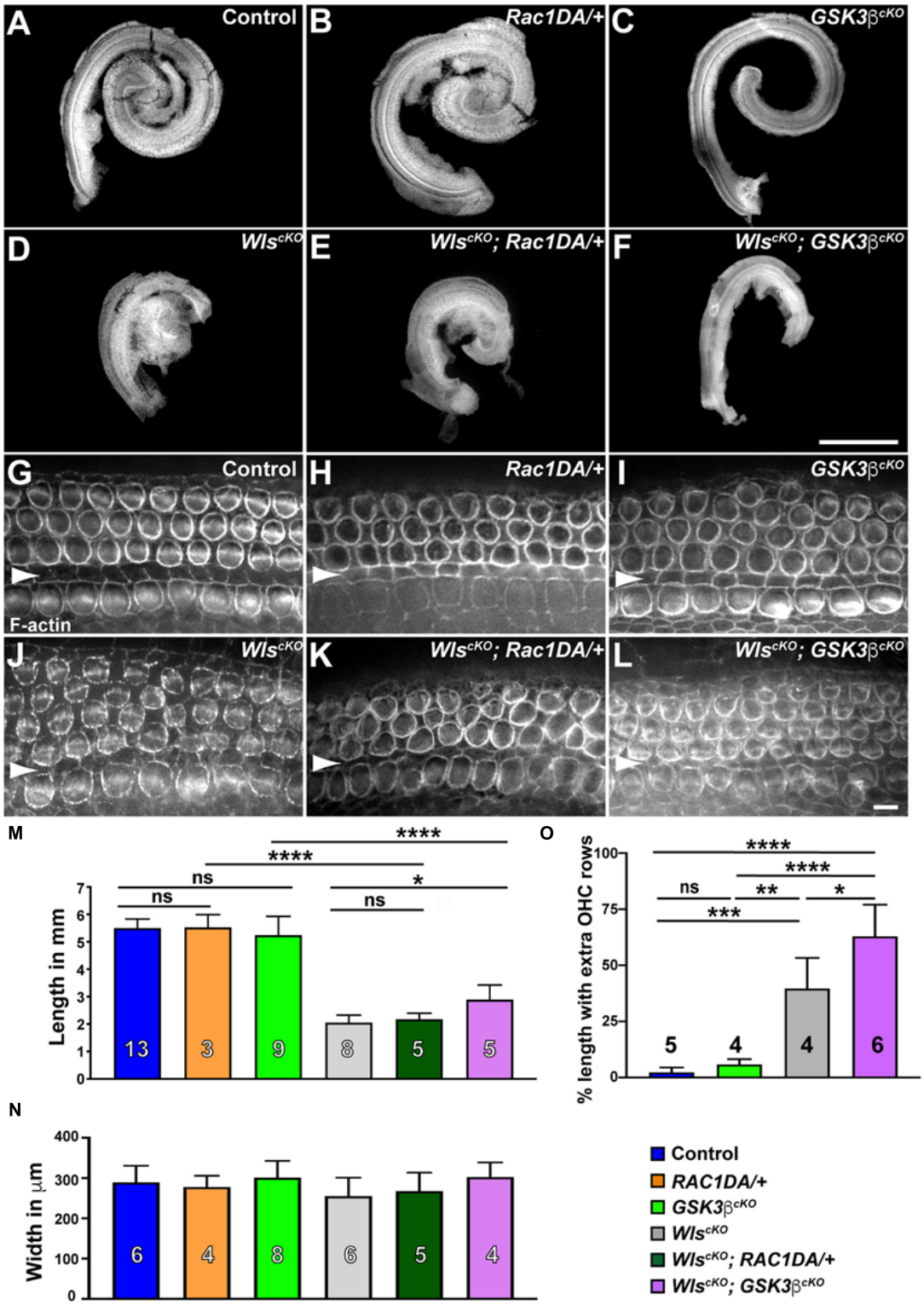


**FIGURE 3 |** Gsk3β inactivation but not Rac1 activation partially rescued cochlear outgrowth of $Wls^{cKO}$ mutant. **(A–F)** Dissected cochlear ducts from E18.5 wild-type control (**A**), *Rac1DA/+* **(B)**, $Gsk3\beta^{cKO}$ **(C)**, $Wls^{cKO}$ **(D)**, $Wls^{cKO}$; *Rac1DA/+* **(E)**, and $Wls^{cKO}$; $Gsk3\beta^{cKO}$ **(F)** mutants. **(G–L)** Flat-mounted OC from the middle region (40–60% cochlear length) of wild-type control **(G)**, *Rac1DA/+* **(H)**, $Gsk3\beta^{cKO}$ **(I)**, $Wls^{cKO}$ **(J)**, $Wls^{cKO}$; *Rac1DA/+* **(K)**, and $Wls^{cKO}$; $Gsk3\beta^{cKO}$ **(L)** cochleae stained by phalloidin. Arrowheads indicate the inner pillar cell row. Lateral is up. Scale bars: **(A–F)**, 1 mm; **(G–L)**, 6 μm. **(M–O)** Quantifications of cochlear length **(M)**, cochlear duct width **(N)**, and presence of extra OHC rows **(O)** in genotypes indicated by the color keys. Cochlear duct width **(N)** was not significantly different in all pair-wise comparisons. The number of cochleae analyzed is indicated. Ns, not significant.

in a shortened cochlea, and cochlear outgrowth was severely stunted in the *Wls*$^{cKO}$*; Ctnnb1*$^{\Delta\ ex3/+}$ compound mutants (**Supplementary Figures 3C,D**), precluding dissection and assessment of the OC. These results suggest that Gsk3β regulation of cochlear outgrowth is not mediated by stabilization of β -catenin.

## Effects of Rac1 Activation on Hair Bundle Defects of *Wls*$^{cKO}$ Mutants

Similar iPCP defects were observed in *Wls*$^{cKO}$ and *Rac1*-deficient cochleae, including misoriented and misshapen hair bundles with an off-center kinocilium (Grimsley-Myers et al., 2009; Landin Malt et al., 2020), consistent with Rac1 being a downstream effector of Wnt-regulated hair bundle polarity. To test this, we examined hair bundle orientation and kinocilium positioning in *Wls*$^{cKO}$*; Rac1DA/+* cochleae at E18.5. Compared with the wild-type control, *Rac1DA/+* had mild but significant hair bundle misorientation (**Figures 4A,B,J** and **Supplementary Figure 4**), consistent with the crucial role of localized Rac1 activity in hair bundle orientation (Grimsley-Myers et al., 2009). Interestingly, hair bundle misorientation in *Wls*$^{cKO}$; *Rac1DA/+* cochleae was more severe than the *Wls*$^{cKO}$ mutants (**Figures 4E,H,J** and **Supplementary Figure 4**), particularly toward the cochlear apex where many supernumerary, disorganized OHC rows were present (**Figures 4G,H**).

We next assessed the effect of Rac1 activation on kinocilium positioning within the hair bundle by measuring the kinocilium index (Landin Malt et al., 2020). In the wild type at E18.5, the kinocilium is found at the vertex of the V-shaped hair bundle, with a mean kinocilium index (KI) of 1.16, whereas many hair bundles in *Wls*$^{cKO}$ cochleae had an off-center kinocilium, as shown previously (**Figures 4A,D**, arrows). Rac1 activation by itself had negligible effect on the KI (mean = 1.24; **Figures 4B,K**). In the *Wls*$^{cKO}$; *Rac1DA/+* cochleae, kinocilium positioning was partially but significantly rescued compared with *Wls*$^{cKO}$ mutants (**Figures 4E,K**). Thus, partial rescue of kinocilium positioning but not hair bundle orientation defects of *Wls*$^{cKO}$ mutants by Rac1 activation supports the proposed role of Rac1 as a downstream effector of Wnt-mediated hair bundle polarity.

## The Role of Gsk3β in Hair Bundle Orientation and Kinocilium Positioning

To determine the role of Gsk3β in hair bundle morphogenesis, we first analyzed hair bundle orientation and kinocilium positioning in *Gsk3*β$^{cKO}$ cochleae at E18.5. Interestingly, *Gsk3*β$^{cKO}$ mutants had mild but significant hair bundle misorientation, indicating a requirement of Gsk3β for normal hair bundle orientation (**Figures 4C,L** and **Supplementary Figure 4**). On the other hand, the normal V-shape of the hair bundle and kinocilium positioning at the hair bundle vertex were largely intact in *Gsk3*β$^{cKO}$ cochleae (**Figures 4C,M**).

Next, we assessed the effect of Gsk3β inactivation on hair bundle defects in *Wls*$^{cKO}$ mutants. Interestingly, in *Wls*$^{cKO}$*; Gsk3*β$^{cKO}$ OC at E18.5, hair bundle misorientation was worse than in either single mutant (**Figures 4F,I,L** and **Supplementary Figure 4**). However, kinocilium positioning at the vertex of the hair bundle was significantly rescued compared with *Wls*$^{cKO}$ mutants (**Figures 4F,I,M**). Taken together, these results indicate that a normal level of Gsk3β signaling is required for hair bundle orientation and that Wnts control hair bundle morphogenesis in part through inhibition of Gsk3β.

## Rac1 Activation and Gsk3β Inactivation Partially Restored Fzd6 and Dvl2 Junctional Localization in the Absence of Secreted Wnt Ligands

Our results so far suggest that both Rac1 and Gsk3β are downstream effectors of non-canonical Wnt signaling crucial for HC PCP. To further elucidate their roles in PCP establishment in the OC, we sought to determine whether Rac1 and Gsk3β also play a role in Wnt-dependent asymmetric localization of core PCP proteins.

We and others previously uncovered a requirement of secreted Wnt ligands in asymmetric junctional localization of a subset of core PCP proteins (Landin Malt et al., 2020; Najarro et al., 2020). Specifically, Fzd6 is normally enriched along the medial border of HCs (**Figures 5A,B**, arrows, **7A**), and this localization was abolished in the *Wls*$^{cKO}$ cochleae (**Figures 5G,H**, **7D**). Similar to the control, we found that Fzd6 was enriched along medial HC junctions in both the *Rac1DA/+* and *Gsk3*β$^{cKO}$ cochleae (**Figures 5C–F**, **7B,C**). Interestingly, junctional Fzd6 localization was significantly recovered in both *Wls*$^{cKO}$; *Rac1DA/+* and *Wls*$^{cKO}$; *Gsk3*β$^{cKO}$ cochleae; however, Fzd6 planar asymmetry along the medial-lateral axis was not restored in *Wls*$^{cKO}$; *Rac1DA/+* and only partially restored in *Wls*$^{cKO}$; *Gsk3*β$^{cKO}$ cochleae (**Figures 5I–M**, **7E,F**).

Another Wnt-dependent core PCP protein, Dvl2, is normally enriched along the lateral border of HCs (**Figures 6A,B**, arrows, **7A**) and lost its junctional localization in the *Wls*$^{cKO}$ cochleae (**Figures 6G,H**, **7D**). In both the *Rac1DA/+* and *Gsk3*β$^{cKO}$ cochleae, enrichment of Dvl2 on the lateral HC junctions was largely intact (**Figures 6C–F**, arrows, **7B,C**). In *Wls*$^{cKO}$*; Rac1DA/+* and *Wls*$^{cKO}$; *Gsk3*β$^{cKO}$ OC, junctional Dvl2 localization was partially recovered (**Figures 6I–L**, arrows, **7E,F**). However, Dvl2 planar asymmetry was not restored in either compound mutant (**Figure 6M**). Together, these results indicate that both Rac1 and Gsk3β are involved in Wnt-mediated junctional localization of a subset of core PCP proteins; however, neither Rac1 activation nor Gsk3β inactivation was sufficient for generating planar asymmetry of core PCP proteins.

# DISCUSSION

## The Non-canonical Wnt Pathway Signals Through Multiple Effectors to Control Different Aspects of Cochlear Morphogenesis

In this study, we have further delineated the non-canonical, Wnt/G-protein/PI3K pathway for cochlear outgrowth and establishment of iPCP and PCP in the cochlea (**Figure 8A**). Our

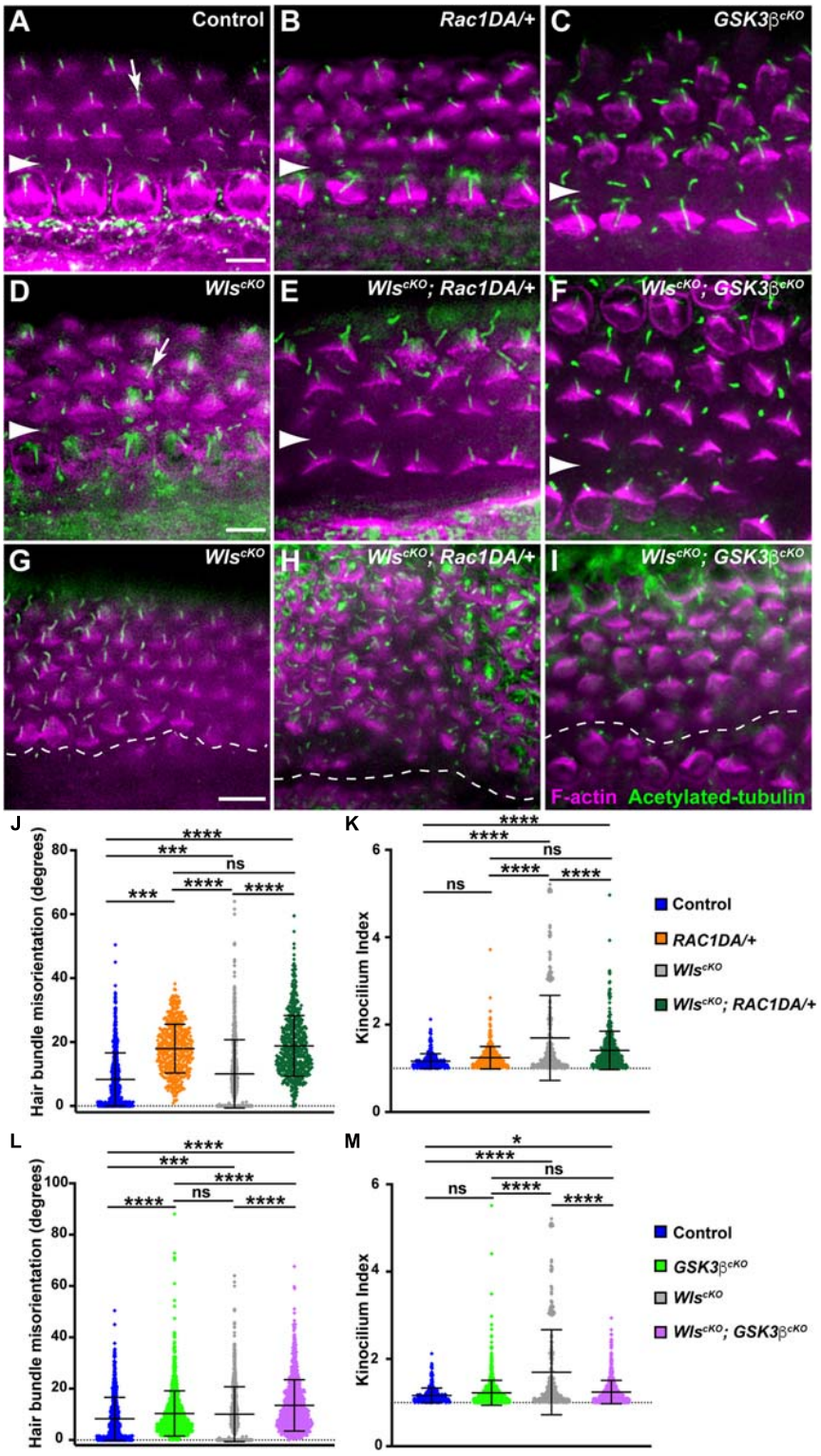


**FIGURE 4 |** Partial rescue of hair bundle defects of *Wls*-deficient mutants by Rac1 activation and Gsk3β inactivation. **(A–I)** Flat-mounted E18.5 OC stained for acetylated tubulin (green) and F-actin (magenta). **(A–F)** Basal or mid-basal regions of wild-type control **(A)**, *Rac1DA/+* **(B)**, *Gsk3β*$^{cKO}$ **(C)**, *Wls*$^{cKO}$ **(D)**, *Wls*$^{cKO}$*; Rac1DA/+* **(E)**, and *Wls*$^{cKO}$; *Gsk3β*$^{cKO}$ OC **(F)**. Arrows in panels **(A,D)** indicate normal kinocilium position at the hair bundle vertex and an off-center kinocilium, respectively. **(G–I)** Apical regions of *Wls*$^{cKO}$ **(G)**, *Wls*$^{cKO}$; *Rac1DA/+* **(H)**, and *Wls*$^{cKO}$; *Gsk3β*$^{cKO}$ **(I)** OC. Arrowheads and the dashed line indicate the inner pillar cell row. Lateral is up. Scale bars: 6 μm. **(J–M)** Quantifications of hair bundle orientation **(J,L)** and kinocilium positioning **(K,M)**. Color keys for genotypes are indicated on the right. Ns, not significant.

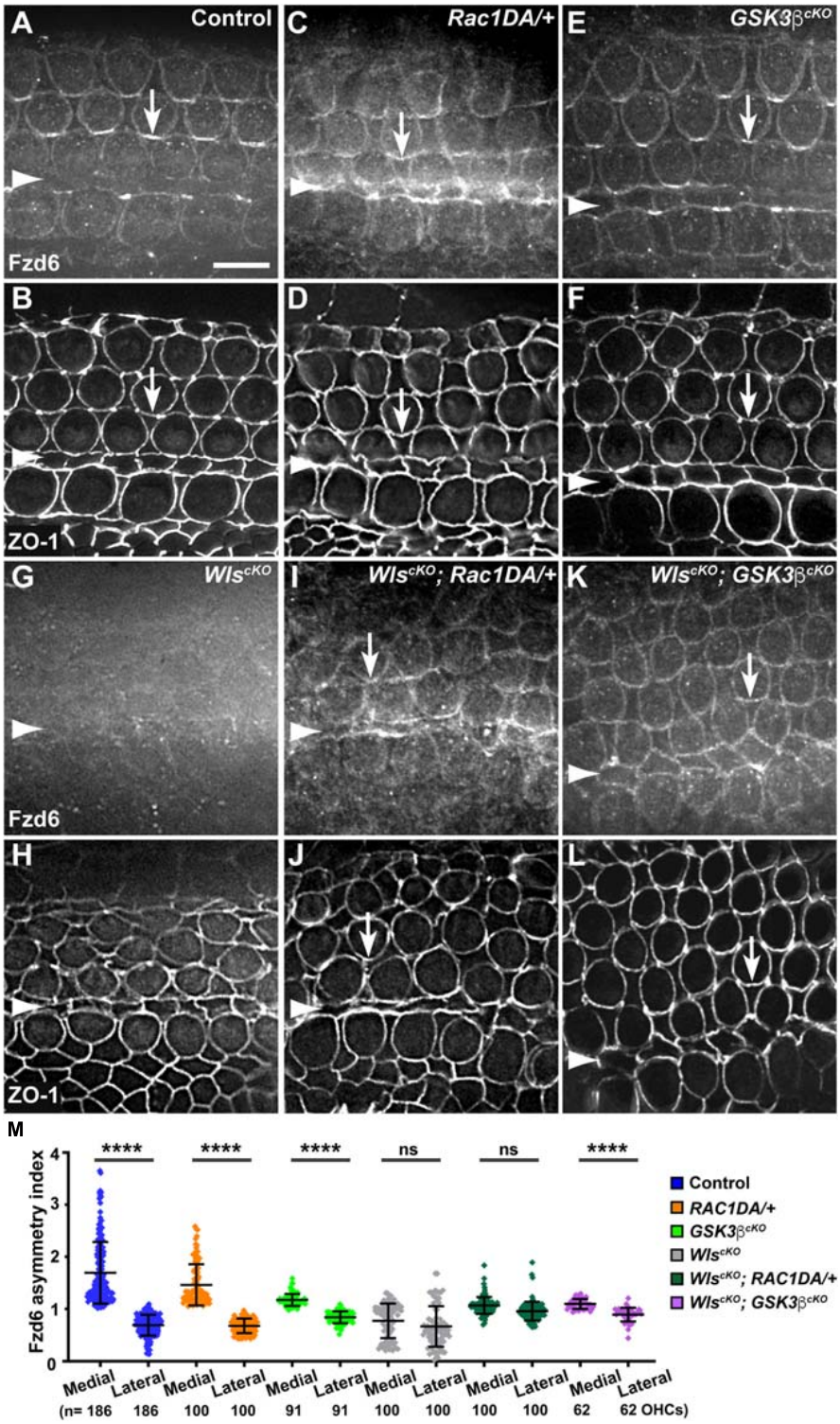


**FIGURE 5 |** Rac1 activation and Gsk3β inactivation recovered Fzd6 junctional localization but not planar asymmetry in Wls-deficient OC. **(A–L)** Flat-mounted E18.5 wild-type control **(A,B)**, *Rac1DA/+* **(C,D)**, *Gsk3β*$^{cKO}$ **(E,F)**, *Wls*$^{cKO}$ **(G,H)**, *Wls*$^{cKO}$; *Rac1DA/+* **(I,J)**, and *Wls*$^{cKO}$; *Gsk3β*$^{cKO}$ **(K,L)** OC stained for Fzd6 and ZO-1 as indicated. Arrows indicate Fzd6 crescents along the medial borders of OHCs. Arrowheads indicate the inner pillar cell row. Lateral is up. Scale bar: 6 μm. **(M)** Quantifications of Fzd6 staining along the medial and lateral junctions of OHCs. Numbers of OHCs scored are indicated on the bottom. Color keys for genotypes are indicated on the right. Ns, not significant.

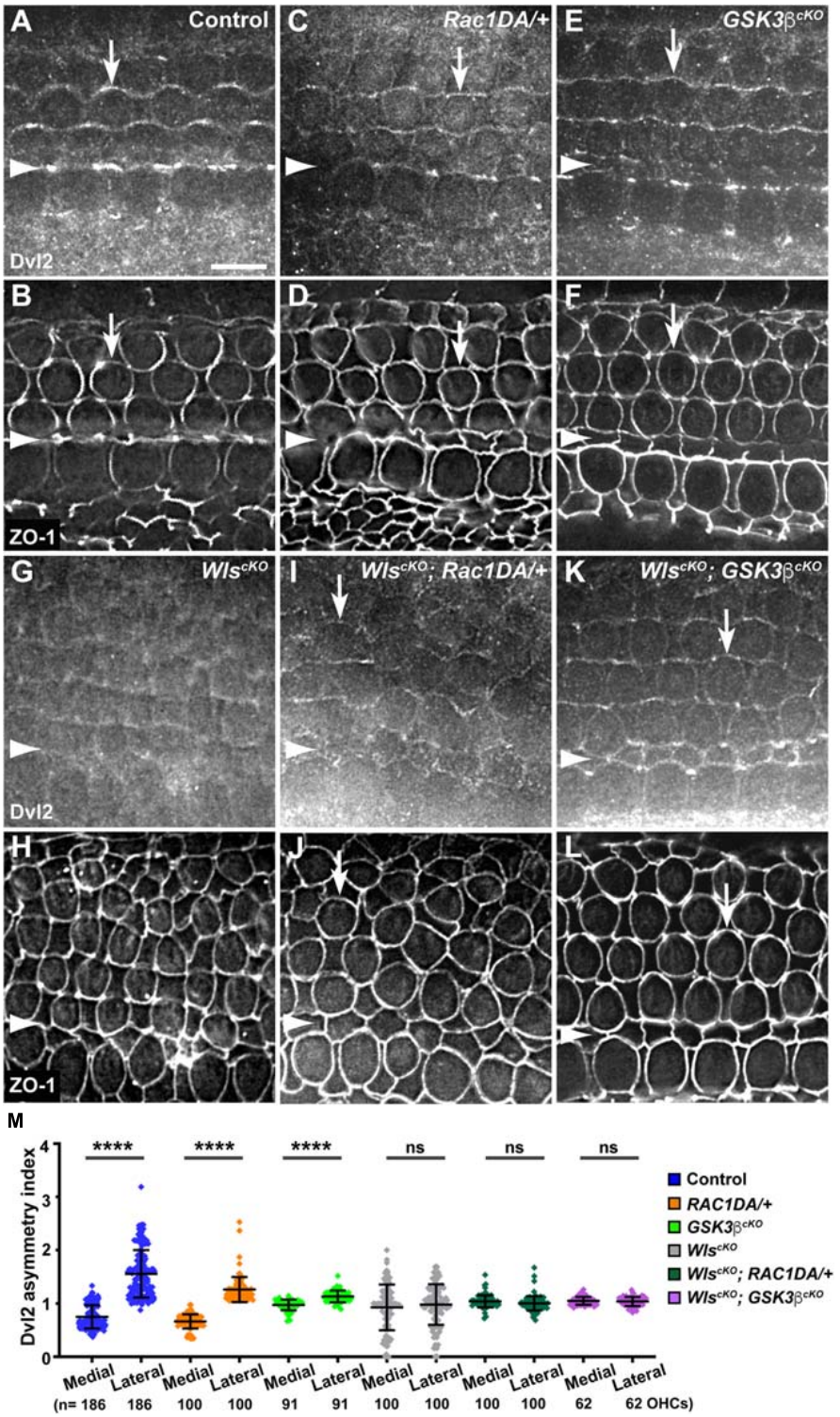


**FIGURE 6 |** Effects of Rac1 activation and Gsk3β inactivation on Dvl2 localization in Wls-deficient OC. **(A–L)** Flat-mounted E18.5 wild-type control **(A,B)**, *Rac1DA/+* **(C,D)**, *Gsk3β*$^{cKO}$ **(E,F)**, *Wls*$^{cKO}$ **(G,H)**, *Wls*$^{cKO}$; *Rac1DA/+* **(I,J)**, and *Wls*$^{cKO}$; *Gsk3β*$^{cKO}$ **(K,L)** OC stained for Dvl2 and ZO-1 as indicated. Arrows indicate Dvl2 crescents along the lateral borders of OHCs. Arrowheads indicate the inner pillar cell row. Lateral is up. Scale bar: 6 μm. **(M)** Quantifications of Dvl2 staining along the medial and lateral junctions of OHCs. Numbers of OHCs scored are indicated on the bottom. Color keys for genotypes are indicated on the right. Ns, not significant.

genetic rescue experiments have provided strong evidence that PI3K, Gsk3β, and Rac1 are all downstream effectors of non-canonical Wnt signaling in the cochlea. The extent to which the cochlear defects of $Wls^{cKO}$ mutants were rescued varied among the effectors. Thus, these effectors likely act in parallel and have non-overlapping functions to mediate non-canonical Wnt signaling in the cochlea.

Cochlear elongation is regulated by multiple developmental signals from the epithelium and surrounding mesenchyme and spiral ganglion (Bok et al., 2013; Huh et al., 2015), suggesting integration of multiple molecular pathways. Within the epithelium, while PCP signaling is thought to mediate convergent extension of the OC (Mao et al., 2011; Montcouquiol and Kelley, 2019), the mechanisms underlying Wnt-mediated cochlear elongation remain incompletely understood. We showed that outgrowth of $Wls^{cKO}$ cochleae was rescued fully by PI3K activation and partially by Gsk3β inactivation but not rescued by Rac1 activation or expression of stabilized β-catenin, suggesting that Wnt/G-protein/PI3K signaling engages Gsk3β and additional regulators ("X"; **Figure 8A**) to promote cell proliferation and/or cell survival during cochlear outgrowth.

## Epithelium-Secreted Wnts Act in Parallel to and Cross-Regulates the PCP Pathway in the Cochlea

Our findings suggest that Wnts secreted by the cochlear epithelium act in parallel and crosstalk with the PCP pathway in the mammalian cochlea. Of note, $Wls^{cKO}$ and core PCP mutants have distinct hair bundle phenotypes: hair bundle misorientation in $Wls^{cKO}$ cochleae was milder than core PCP mutants; moreover, $Wls^{cKO}$ but not PCP mutants were defective in kinocilium positioning at the hair bundle vertex (**Figure 8B**). Epithelium-secreted Wnt ligands likely act in concert with additional tissue polarity cues, including non-epithelial Wnts, to specify the PCP vector and align HC orientation (**Figure 8A**). Epithelium-secreted Wnt5a, a prototype non-canonical Wnt, is dispensable for cochlear PCP (Najarro et al., 2020), suggesting involvement of other Wnt ligands. In the future, identification of the relevant Wnt ligands in the cochlea will help determine permissive versus instructive roles of Wnt signaling in HC PCP. Importantly, we have uncovered a non-canonical Wnt pathway that signals through PI3K, Rac1, and Gsk3β to promote junctional localization of a subset of core PCP proteins, including Fzd6 and Dvl2, thereby cross-regulating the PCP pathway. This is in stark contrast to the *Drosophila* PCP pathway, which operates independently of Wnt ligands (Bartscherer et al., 2006; Chen et al., 2008; Ewen-Campen et al., 2020; Yu et al., 2020). Wnt signaling may regulate the trafficking of PCP proteins or HC–SC junctional dynamics, which in turn influences asymmetric PCP protein localization (see below).

## Rac1 Integrates Multiple Developmental Signals During Hair Cell Planar Polarization

Although Rac1 is activated by non-canonical Wnt signaling in cultured cells, it remains to be determined whether Wnt signaling stimulates Rac1 activity in the cochlea. At present, we have been unable to address this question, as our attempts to evaluate the localization and levels of active Rac1 by immunostaining or Western blot using a commercially sourced Rac1-GTP-specific antibody were unsuccessful. Thus, more sensitive and specific tools are needed to detect active Rac1 *in vivo*. PCP defects caused by modest overexpression of Rac1-G12V expression were mild, likely due to the presence of wild-type Rac proteins undergoing the normal GTPase cycle. In the $Wls^{cKO}$*; Rac1DA/+* OC, Fzd6 and Dvl2 junctional localization was partially rescued, consistent with Rac1 being a downstream effector of non-canonical Wnt signaling. Rac1 may promote Fzd6 and Dvl2 junctional localization through regulation of junctional and cytoskeletal dynamics (de Curtis and Meldolesi, 2012). In previous studies, we have shown that the activity of p21-activated kinases (PAKs), which are downstream effectors of both Rac1 and Cdc42, are regulated in the OC by multiple mechanisms, including intercellular PCP signaling, plus- and minus-end-directed microtubule motors and the cell polarity protein Par3 (Grimsley-Myers et al., 2009; Sipe and Lu, 2011; Sipe et al., 2013; Landin Malt et al., 2019). Therefore, multiple signaling pathways, including the non-canonical Wnt pathway, likely converge on Rac1 to tightly control its activity in space and time during HC planar polarization.

## Gsk3β Inhibition Is a Key Step of the Non-canonical Wnt Pathway in the Cochlea

We show, for the first time, that Wnts secreted by the cochlear epithelium promote inhibitory Ser9 phosphorylation of Gsk3β *in vivo*. This is different from the mode of Gsk3β inhibition by canonical Wnt signaling, which is thought to occur through sequestration of Gsk3β and dissociation of the disruption complex (Metcalfe and Bienz, 2011; Beurel et al., 2015). Previous studies using pharmacological inhibitors have shown that Gsk3 signaling regulates OC progenitor cell proliferation and fate decision (Jacques et al., 2012; Ellis et al., 2019). Our genetic analyses further reveal multi-faceted roles of Gsk3β in PCP and iPCP regulation *in vivo*. First, Gsk3β is required for uniform hair bundle orientation. Second, Gsk3β inhibition is crucial for Wnt-dependent kinocilium positioning and junctional localization of Fzd6 and Dvl2. Interestingly, both too little (in $Gsk3\beta^{cKO}$ mutants) and too much Gsk3β activity (in $Wls^{cKO}$ mutants) led to hair bundle orientation defects, suggesting that levels of Gsk3β need to be precisely controlled to achieve uniform HC orientation. In the future, it would be interesting to assess earlier roles of Gsk3β in cochlear patterning *in vivo* by deleting Gsk3β in the otocyst.

Gsk3β is a promiscuous kinase with numerous known substrates. The crucial Gsk3β targets that mediate kinocilium positioning and PCP protein localization remain to be identified. Gsk3β has a well-established role in regulating neuronal cytoskeletal dynamics through phosphorylation of microtubule-associated proteins (MAPs) including collapsin response mediator proteins (CRMPs), APC, Tau, MAP1B, and doublecortin (Hur and Zhou, 2010; Morgan-Smith et al., 2014). In the OC, microtubules and microtubule-based motors have

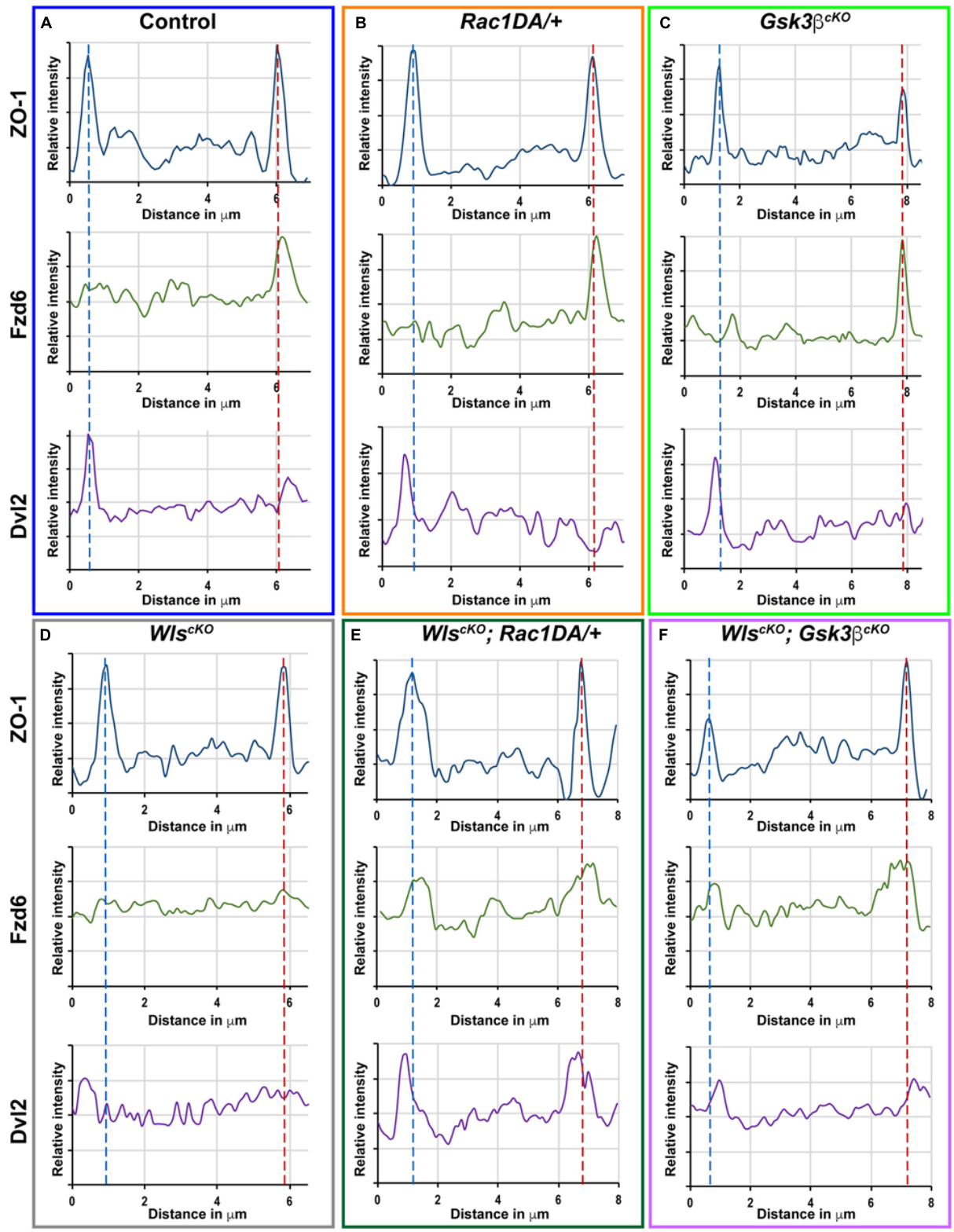


**FIGURE 7 |** Linescan analysis of junctional localization of Fzd6 and Dvl2 in outer hair cells. **(A–F)** Representative linescans of individual OHCs from E18.5 wild-type control **(A)**, *Rac1DA/+* **(B)**, *Gsk3β*$^{cKO}$ **(C)**, *Wls*$^{cKO}$ **(D)**, *Wls*$^{cKO}$*; Rac1DA/+* **(E)**, and *Wls*$^{cKO}$; *Gsk3β*$^{cKO}$ **(F)** OC stained for ZO-1, Fzd6, and Dvl2. For each genotype, a line was drawn parallel to the medial–lateral axis bisecting the OHC. Intensity profiles of each image channel were aligned along the distance axis. The lateral and medial junctions of the OHC were identified by peaks of ZO-1 staining and indicated by the blue and red dashed lines, respectively. Junctional Fzd6 and Dvl2 staining was defined by peaks in close proximity to the lateral or medial borders of the OHC.

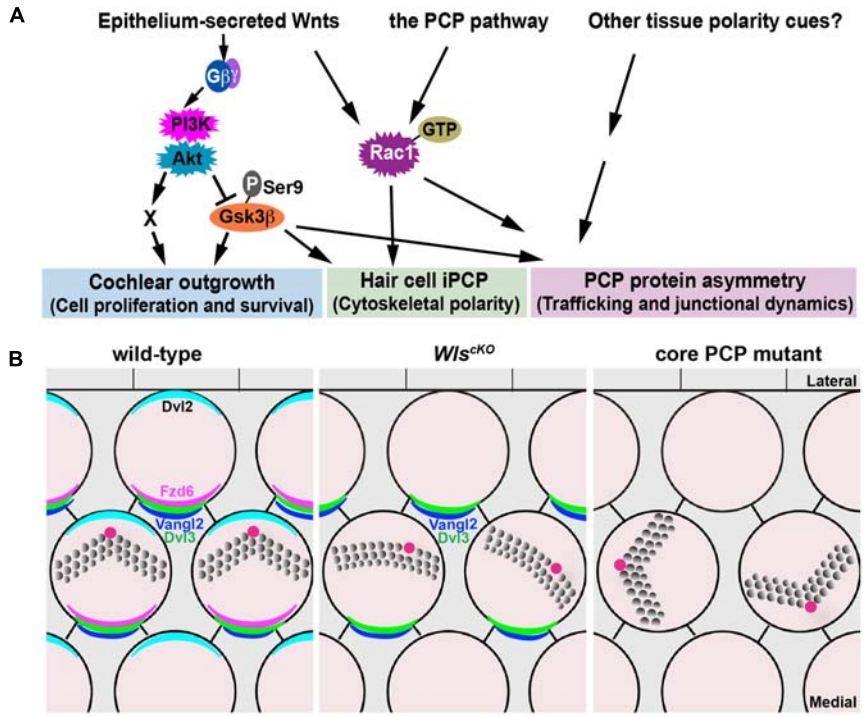


**FIGURE 8 |** Non-canonical Wnt and PCP pathways act in concert to regulate cochlear morphogenesis. **(A)** A working model for the concerted actions of the non-canonical Wnt and PCP pathways in regulating different aspects of cochlear morphogenesis. **(B)** Schematic diagrams comparing PCP defects in the *Wls*$^{cKO}$ and core PCP mutant OC. Kinocilium (the red dot) positioning at the hair bundle vertex was disrupted in *Wls*$^{cKO}$ but not core PCP mutants.

been implicated in hair bundle orientation and kinocilium positioning (Sipe and Lu, 2011; Ezan et al., 2013; Sipe et al., 2013). In addition, cytoskeletal molecules disrupted in Usher syndrome and ciliopathies also play a role in hair bundle polarity (Lefevre et al., 2008; Jagger et al., 2011). Thus, HC microtubule and other cytoskeletal regulators are potential targets of Gsk3β during hair bundle morphogenesis.

In other systems, microtubules are also involved in polarized trafficking of core PCP proteins (Vladar et al., 2012; Matis et al., 2014). However, asymmetric PCP protein localization was normal in several mutants affecting HC microtubule organization or transport (Sipe and Lu, 2011; Kirjavainen et al., 2015; Siletti et al., 2017), suggesting alternative mechanisms by which Gsk3β regulates PCP protein localization/trafficking. Interestingly, Gsk3β has been shown to regulate endocytosis/recycling of membrane cargos in different cell types (Roberts et al., 2004; Clayton et al., 2010; Reis et al., 2015; Ferreira et al., 2020). Future investigations will shed light on the mechanisms by which Gsk3β influences HC polarity and core PCP protein trafficking in the OC.

# MATERIALS AND METHODS

## Mice

Animal care and use was performed in compliance with the NIH guidelines and the Institutional Animal Care and Use Committee at the University of Virginia. *Wls*$^{flox}$ (Fu et al., 2011), *Gsk3β*$^{flox}$ (Patel et al., 2008), and *R26-LSL-Rac1DA* (Srinivasan et al., 2009) mice were obtained from the Jackson Laboratories (Stock #012888, #029592, and #012361, respectively). *Ctnnb1*$^{flox(ex3)}$ and *Emx2*$^{Cre}$ mice have been described (Harada et al., 1999; Ono et al., 2014). All mice were maintained on a mixed genetic background. To generate *Wls* conditional and compound mutants, *Wls*$^{flox/+}$; *Emx2*$^{Cre/+}$ males were mated with *Wls*$^{flox/flox}$, *Wls*$^{flox/flox}$; *R26-LSL-Rac1DA/+*, or *Wls*$^{flox/flox}$; *Ctnnb1*$^{flox(ex3)/+}$ females, and *Wls*$^{flox/+}$; *Gsk3β*$^{flox/+}$; *Emx2*$^{Cre/+}$ males with *Wls*$^{flox/flox}$; *Gsk3β*$^{flox/flox}$ females. For timed pregnancies, the morning of the plug was designated as embryonic day 0.5 (E0.5), and the day of birth postnatal day 0 (P0).

## Immunohistochemistry

Mouse skulls were dissected and fixed in 4% paraformaldehyde (PFA) for 45 min at room temperature (RT) or in 10% TCA for 1 h on ice, then washed three times in PBS. Dissected cochleae were blocked in PBS containing 0.1% Triton X-100, 5% heat-inactivated horse serum, and 0.02% NaN3 for 1 h at RT, then incubated with primary antibodies for 16–32 h at 4°C. After three washes in PBS/0.1% Triton X-100, samples were incubated with secondary antibodies and phalloidin for 2 h at RT, washed twice in PBS 0.1% Triton X-100, post-fixed for 15 min at RT in 4% paraformaldehyde and then washed two more times. Stained samples are flat mounted in

| Antibody | Concentration | Vendor | Catalog No. |
|---|---|---|---|
| Alexa-conjugated phalloidin | 1:200 | Thermo Fisher Scientific | A12379, A12380, A12381, A22287 |
| Alexa-conjugated secondary antibodies | 1:500 | Thermo Fisher Scientific | A11036, A11029, A11057, A11077 |
| Anti-acetylated tubulin | 1:1,000 | Sigma-Aldrich | T6793 |
| Anti-Dvl2 | 1:100 (TCA) | Proteintech | 12037-1-AP |
| Anti-Fzd6 | 1:100 (TCA) | R & D Systems | AF1526-SP |
| Anti-S9-Gsk3β (D85E12) | 1:100 | Cell Signaling | 5558 |
| Anti-Gsk3β (D5C5Z) | 1:100 (TCA) | Cell Signaling | 12456 |
| Anti-myosin VI | 1:500 | PROTEUS | 25-6791 |
| Anti-ZO-1 | 1:100 (TCA) | DSHB | R26.4C-c |

Mowiol with 5% N-propyl gallate. The table above lists the antibodies used.

## Microscopy and Image Analysis

Control and mutant samples were imaged under identical conditions. For hair bundle and PCP protein localization, images were collected using a Deltavision deconvolution microscope with a 60×/1.35 NA oil-immersion objective controlled by SoftWoRx software (Applied Precision). Whole-mount cochlear ducts were imaged using a Leica MZ16F stereomicroscope. Images were processed using Fiji (National Institutes of Health) and Photoshop (Adobe).

## Quantification of Hair Bundle Phenotypes

Hair bundle orientation and kinocilium position within the hair bundle along the entire cochlear length were quantified as previously described (Landin Malt et al., 2020). In brief, the hair bundle is labeled by phalloidin staining and the kinocilium by anti-acetylated tubulin staining. A hair bundle with its vertex pointing to the lateral or medial edge of the cochlear duct has a misorientation of 0° and 180°, respectively. The kinocilium index is the length ratio of the long and short hair bundle "halves" as bisected by the kinocilium.

## Quantification of Protein Localization

Fzd6 and Dvl2 immunostaining along OHC-Deiters cell junctions from the basal to mid-apical regions was quantified using Fiji, as previously described (Landin Malt et al., 2020). The cochlear apex, where HC–SC junctions were more irregular/less mature, was excluded. In brief, single optic sections with the strongest junctional staining intensity were chosen for each imaging channel. In general, lateral Dvl2 crescents are localized at the level of the tight junction, while medial Fzd6 crescents are localized at a level about 1 μm below the tight junction. Cell junctions were identified using ZO-1 staining. A 30 × 10—, 20 × 10—, and 30 × 5-pixel region of interest (ROI) centered around the medial, lateral, and orthogonal OHC junctions, respectively, was then selected. Following background subtraction, mean fluorescence intensity of Fzd6 or Dvl2 staining for the medial or lateral ROI was normalized to that of the orthogonal ROI of the same OHC and plotted as the asymmetry index.

Line scan analysis was performed using Fiji and Excel to demonstrate the localization of Fzd6 and Dvl2 staining relative to cell junctions. Specifically, a diametral line was drawn intersecting the lateral and medial OHC junctions as marked by ZO-1 immunostaining. Following background subtraction, fluorescence intensity of each imaging channel was plotted in the lateral to medial direction of the line.

# STATISTICS

Statistical analysis of at least three cochleae from three different litters was performed using GraphPad Prism. Data were analyzed using one-way analysis of variance (ANOVA) followed by a *post hoc* Tukey's test. *p*-Values for statistical significance are defined as follows: $^{*}p \leq 0.0332$; $^{**}p \leq 0.0021$; $^{***}p \leq 0.0002$, and $^{****}p \leq 0.0001$. Data were presented as mean ± standard deviation.

# DATA AVAILABILITY STATEMENT

The original contributions presented in the study are included in the article/**Supplementary Material**, further inquiries can be directed to the corresponding author.

# ETHICS STATEMENT

The animal study was reviewed and approved by the Animal Care and Use Committee at the University of Virginia.

# AUTHOR CONTRIBUTIONS

ALM and XL designed the research, performed the experiments, analyzed the data, and wrote the manuscript. SC performed the experiments and analyzed the data. DH, AL, CS, MS, MH, and CC analyzed the data. All authors contributed to the article and approved the submitted version.

# FUNDING

This study was supported by NIH grant R01DC013773 (XL).

## ACKNOWLEDGMENTS

We thank Wenxia Li for the technical assistance and Dr. Jeremy Nathans (the Johns Hopkins University) for the reagents.

## SUPPLEMENTARY MATERIAL

The Supplementary Material for this article can be found online at: https://www.frontiersin.org/articles/10.3389/fcell.2021.649830/full#supplementary-material

## REFERENCES

Bartscherer, K., Pelte, N., Ingelfinger, D., and Boutros, M. (2006). Secretion of Wnt ligands requires Evi, a conserved transmembrane protein. *Cell* 125, 523–533. doi: 10.1016/j.cell.2006.04.009

Beurel, E., Grieco, S. F., and Jope, R. S. (2015). Glycogen synthase kinase-3 (GSK3): regulation, actions, and diseases. *Pharmacol. Ther.* 148, 114–131. doi: 10.1016/j.pharmthera.2014.11.016

Bok, J., Zenczak, C., Hwang, C. H., and Wu, D. K. (2013). Auditory ganglion source of Sonic hedgehog regulates timing of cell cycle exit and differentiation of mammalian cochlear hair cells. *Proc. Natl. Acad. Sci. U.S.A.* 110:13869. doi: 10.1073/pnas.1222341110

Butler, M. T., and Wallingford, J. B. (2017). Planar cell polarity in development and disease. *Nat. Rev. Mol. Cell Biol.* 18, 375–388.

Chang, H., Smallwood, P. M., Williams, J., and Nathans, J. (2016). The spatio-temporal domains of Frizzled6 action in planar polarity control of hair follicle orientation. *Dev. Biol.* 409, 181–193. doi: 10.1016/j.ydbio.2015.10.027

Chen, W. S., Antic, D., Matis, M., Logan, C. Y., Povelones, M., Anderson, G. A., et al. (2008). Asymmetric homotypic interactions of the atypical cadherin flamingo mediate intercellular polarity signaling. *Cell* 133, 1093–1105. doi: 10.1016/j.cell.2008.04.048

Clayton, E. L., Sue, N., Smillie, K. J., O'Leary, T., Bache, N., Cheung, G., et al. (2010). Dynamin I phosphorylation by GSK3 controls activity-dependent bulk endocytosis of synaptic vesicles. *Nat. Neurosci.* 13, 845–851. doi: 10.1038/nn.2571

de Curtis, I., and Meldolesi, J. (2012). Cell surface dynamics – how Rho GTPases orchestrate the interplay between the plasma membrane and the cortical cytoskeleton. *J. Cell Sci.* 125, 4435. doi: 10.1242/jcs.108266

Devenport, D. (2014). The cell biology of planar cell polarity. *J. Cell Biol.* 207, 171–179. doi: 10.1083/jcb.201408039

Ellis, K., Driver, E. C., Okano, T., Lemons, A., and Kelley, M. W. (2019). GSK3 regulates hair cell fate in the developing mammalian cochlea. *Dev. Biol.* 453, 191–205. doi: 10.1016/j.ydbio.2019.06.003

Ewen-Campen, B., Comyn, T., Vogt, E., and Perrimon, N. (2020). No evidence that Wnt ligands are required for planar cell polarity in *Drosophila*. *Cell Rep.* 32:108121. doi: 10.1016/j.celrep.2020.108121

Ezan, J., Lasvaux, L., Gezer, A., Novakovic, A., May-Simera, H., Belotti, E., et al. (2013). Primary cilium migration depends on G-protein signalling control of subapical cytoskeleton. *Nat. Cell Biol.* 15, 1107–1115. doi: 10.1038/ncb2819

Ferreira, A. P. A., Casamento, A., Roas, S. C., Panambalana, J., Subramaniam, S., Schützenhofer, K., et al. (2020). Cdk5 and GSK3β inhibit fast Endophilin-mediated endocytosis. *bioRxiv* [Preprint]. doi: 10.1101/2020.04.11.036863

Fu, J., Ivy Yu, H. M., Maruyama, T., Mirando, A. J., and Hsu, W. (2011). Gpr177/mouse Wntless is essential for Wnt-mediated craniofacial and brain development. *Dev. Dyn.* 240, 365–371. doi: 10.1002/dvdy.22541

Grimsley-Myers, C. M., Sipe, C. W., Geleoc, G. S., and Lu, X. (2009). The small GTPase Rac1 regulates auditory hair cell morphogenesis. *J. Neurosci.* 29, 15859–15869. doi: 10.1523/jneurosci.3998-09.2009

Harada, N., Tamai, Y., Ishikawa, T., Sauer, B., Takaku, K., Oshima, M., et al. (1999). Intestinal polyposis in mice with a dominant stable mutation of the beta-catenin gene. *EMBO J.* 18, 5931–5942. doi: 10.1093/emboj/18.21.5931

Huh, S. H., Warchol, M. E., and Ornitz, D. M. (2015). Cochlear progenitor number is controlled through mesenchymal FGF receptor signaling. *Elife* 4:e05921.

Hur, E. M., and Zhou, F. Q. (2010). GSK3 signalling in neural development. *Nat. Rev. Neurosci.* 11, 539–551. doi: 10.1038/nrn2870

Jacques, B. E., Puligilla, C., Weichert, R. M., Ferrer-Vaquer, A., Hadjantonakis, A.-K., Kelley, M. W., et al. (2012). A dual function for canonical Wnt/β-catenin signaling in the developing mammalian cochlea. *Development* 139, 4395. doi: 10.1242/dev.080358

Jagger, D., Collin, G., Kelly, J., Towers, E., Nevill, G., Longo-Guess, C., et al. (2011). Alstrom syndrome protein ALMS1 localizes to basal bodies of cochlear hair cells and regulates cilium-dependent planar cell polarity. *Hum. Mol. Genet.* 20, 466–481. doi: 10.1093/hmg/ddq493

Kirjavainen, A., Laos, M., Anttonen, T., and Pirvola, U. (2015). The Rho GTPase Cdc42 regulates hair cell planar polarity and cellular patterning in the developing cochlea. *Biol. Open.* 4, 516–526. doi: 10.1242/bio.20149753

Komiya, Y., and Habas, R. (2008). Wnt signal transduction pathways. *Organogenesis* 4, 68–75. doi: 10.4161/org.4.2.5851

Landin Malt, A., Dailey, Z., Holbrook-Rasmussen, J., Zheng, Y., Hogan, A., Du, Q., et al. (2019). Par3 is essential for the establishment of planar cell polarity of inner ear hair cells. *Proc. Natl. Acad. Sci. U.S.A.* 116, 4999–5008. doi: 10.1073/pnas.1816333116

Landin Malt, A., Hogan, A. K., Smith, C. D., Madani, M. S., and Lu, X. (2020). Wnts regulate planar cell polarity via heterotrimeric G protein and PI3K signaling. *J. Cell Biol.* 219:e201912071.

Lefevre, G., Michel, V., Weil, D., Lepelletier, L., Bizard, E., Wolfrum, U., et al. (2008). A core cochlear phenotype in USH1 mouse mutants implicates fibrous links of the hair bundle in its cohesion, orientation and differential growth. *Development* 135, 1427–1437. doi: 10.1242/dev.012922

Mao, Y., Mulvaney, J., Zakaria, S., Yu, T., Morgan, K. M., Allen, S., et al. (2011). Characterization of a ⁢em>Dchs1⁢/em> mutant mouse reveals requirements for Dchs1-Fat4 signaling during mammalian development. *Development* 138:947.

Matis, M., Russler-Germain, D. A., Hu, Q., Tomlin, C. J., and Axelrod, J. D. (2014). Microtubules provide directional information for core PCP function. *Elife* 3:e02893.

Metcalfe, C., and Bienz, M. (2011). Inhibition of GSK3 by Wnt signalling–two contrasting models. *J. Cell Sci.* 124, 3537–3544. doi: 10.1242/jcs.091991

Montcouquiol, M., and Kelley, M. W. (2019). Development and patterning of the cochlea: from convergent extension to planar polarity. *Cold Spring Harb. Perspect. Med.* 10:a033266. doi: 10.1101/cshperspect.a033266

Morgan-Smith, M., Wu, Y., Zhu, X., Pringle, J., and Snider, W. D. (2014). GSK-3 signaling in developing cortical neurons is essential for radial migration and dendritic orientation. *Elife* 3:e02663.

Najarro, E. H., Huang, J., Jacobo, A., Quiruz, L. A., Grillet, N., and Cheng, A. G. (2020). Dual regulation of planar polarization by secreted Wnts and Vangl2 in the developing mouse cochlea. *Development* 147:dev191981. doi: 10.1242/dev.191981

Ono, K., Kita, T., Sato, S., O'Neill, P., Mak, S.-S., Paschaki, M., et al. (2014). FGFR1-Frs2/3 signalling maintains sensory progenitors during inner ear hair cell formation. *PLoS Genet.* 10:e1004118. doi: 10.1371/journal.pgen.1004118

Patel, S., Doble, B. W., MacAulay, K., Sinclair, E. M., Drucker, D. J., and Woodgett, J. R. (2008). Tissue-specific role of glycogen synthase kinase 3beta in glucose homeostasis and insulin action. *Mol. Cell. Biol.* 28, 6314–6328. doi: 10.1128/mcb.00763-08

Reis, C. R., Chen, P. H., Srinivasan, S., Aguet, F., Mettlen, M., and Schmid, S. L. (2015). Crosstalk between Akt/GSK3beta signaling and dynamin-1 regulates clathrin-mediated endocytosis. *EMBO J.* 34, 2132–2146. doi: 10.15252/embj.201591518

Roberts, M. S., Woods, A. J., Dale, T. C., van der Sluijs, P., and Norman, J. C. (2004). Protein kinase B/Akt acts via glycogen synthase kinase 3 to regulate recycling of αvβ3 and α5β1 integrins. *Mol. Cell. Biol.* 24:1505. doi: 10.1128/mcb.24.4.1505-1515.2004

Sato, A., Yamamoto, H., Sakane, H., Koyama, H., and Kikuchi, A. (2010). Wnt5a regulates distinct signalling pathways by binding to Frizzled2. *EMBO J.* 29, 41–54. doi: 10.1038/emboj.2009.322

Siletti, K., Tarchini, B., and Hudspeth, A. J. (2017). Daple coordinates organ-wide and cell-intrinsic polarity to pattern inner-ear hair bundles. *Proc. Natl. Acad. Sci. U.S.A.* 114, E11170–E11179.

Sipe, C. W., Liu, L., Lee, J., Grimsley-Myers, C., and Lu, X. (2013). Lis1 mediates planar polarity of auditory hair cells through regulation of microtubule organization. *Development* 140, 1785–1795. doi: 10.1242/dev.089763

Sipe, C. W., and Lu, X. (2011). Kif3a regulates planar polarization of auditory hair cells through both ciliary and non-ciliary mechanisms. *Development* 138, 3441–3449. doi: 10.1242/dev.065961

Srinivasan, L., Sasaki, Y., Calado, D. P., Zhang, B., Paik, J. H., and DePinho, R. A. (2009). PI3 kinase signals BCR-dependent mature B cell survival. *Cell* 139, 573–586. doi: 10.1016/j.cell.2009.08.041

Tarchini, B., and Lu, X. (2019). New insights into regulation and function of planar polarity in the inner ear. *Neurosci. Lett*. 709:134373. doi: 10.1016/j.neulet.2019.134373

Vladar, E. K., Bayly, R. D., Sangoram, A. M., Scott, M. P., and Axelrod, J. D. (2012). Microtubules enable the planar cell polarity of airway cilia. *Curr. Biol*. 22, 2203–2212. doi: 10.1016/j.cub.2012.09.046

Voloshanenko, O., Gmach, P., Winter, J., Kranz, D., and Boutros, M. (2017). Mapping of Wnt-Frizzled interactions by multiplex CRISPR targeting of receptor gene families. *FASEB J*. 31, 4832–4844. doi: 10.1096/fj.201700144r

Wang, Y., Guo, N., and Nathans, J. (2006). The role of Frizzled3 and Frizzled6 in neural tube closure and in the planar polarity of inner-ear sensory hair cells. *J. Neurosci*. 26, 2147–2156. doi: 10.1523/jneurosci.4698-05.2005

Wiese, K. E., Nusse, R., and van Amerongen, R. (2018). Wnt signalling: conquering complexity. *Development* 145:dev165902. doi: 10.1242/dev.165902

Yu, H., Ye, X., Guo, N., and Nathans, J. (2012). Frizzled 2 and frizzled 7 function redundantly in convergent extension and closure of the ventricular septum and palate: evidence for a network of interacting genes. *Development* 139, 4383–4394. doi: 10.1242/dev.083352

Yu, J. J. S., Maugarny-Calès, A., Pelletier, S., Alexandre, C., Bellaiche, Y., Vincent, J.-P., et al. (2020). Frizzled-dependent planar cell polarity without secreted Wnt ligands. *Dev. Cell* 54, 583–592.e5.

**Conflict of Interest:** The authors declare that the research was conducted in the absence of any commercial or financial relationships that could be construed as a potential conflict of interest.

*Copyright © 2021 Landin Malt, Clancy, Hwang, Liu, Smith, Smith, Hatley, Clemens and Lu. This is an open-access article distributed under the terms of the Creative Commons Attribution License (CC BY). The use, distribution or reproduction in other forums is permitted, provided the original author(s) and the copyright owner(s) are credited and that the original publication in this journal is cited, in accordance with accepted academic practice. No use, distribution or reproduction is permitted which does not comply with these terms.*

frontiers in Cell and Developmental Biology

BRIEF RESEARCH REPORT
published: 05 May 2021
doi: 10.3389/fcell.2021.671364

# N-Terminus of GRXCR2 Interacts With CLIC5 and Is Essential for Auditory Perception

*Jinan Li†, Chang Liu† and Bo Zhao**

*Department of Otolaryngology-Head and Neck Surgery, Indiana University School of Medicine, Indianapolis, IN, United States*

Stereocilia of cochlear hair cells are specialized mechanosensing organelles that convert sound-induced vibration to electrical signals. Glutaredoxin domain-containing cysteine-rich protein 2 (GRXCR2) is localized at the base of stereocilia and is necessary for stereocilia morphogenesis and auditory perception. However, the detailed functions of GRXCR2 in hair cells are still largely unknown. Here, we report that GRXCR2 interacts with chloride intracellular channel protein 5 (CLIC5) which is also localized at the base of stereocilia and required for normal hearing in human and mouse. Immunolocalization analyses suggest that GRXCR2 is not required for the localization of CLIC5 to the stereociliary base during development, or vice versa. Using clustered regularly interspaced short palindromic repeats (CRISPR)/Cas9 system, we deleted 60 amino acids near the N-terminus of GRXCR2 essential for its interaction with CLIC5. Interestingly, mice harboring this in-frame deletion in *Grxcr2* exhibit moderate hearing loss at lower frequencies and severe hearing loss at higher frequencies although the morphogenesis of stereocilia is minimally affected. Thus, our findings reveal that the interaction between GRXCR2 and CLIC5 is crucial for normal hearing.

**Keywords: hearing loss, hair cell, stereocilia, CLIC5, GRXCR2**

OPEN ACCESS

***Edited by:***
*Wei Xiong,*
*Tsinghua University, China*

***Reviewed by:***
*Jocelyn Krey,*
*Oregon Health & Science University, United States*
*Gregory I. Frolenkov,*
*University of Kentucky, United States*

***Correspondence:**
*Bo Zhao*
*zhaozb@iu.edu*

*† These authors have contributed equally to this work and share first authorship*

***Specialty section:***
*This article was submitted to Cell Growth and Division, a section of the journal Frontiers in Cell and Developmental Biology*

***Received:*** *23 February 2021*
***Accepted:*** *13 April 2021*
***Published:*** *05 May 2021*

***Citation:***
*Li J, Liu C and Zhao B (2021) N-Terminus of GRXCR2 Interacts With CLIC5 and Is Essential for Auditory Perception. Front. Cell Dev. Biol. 9:671364. doi: 10.3389/fcell.2021.671364*

## INTRODUCTION

Hearing loss is the fourth leading cause of disability in the world, affecting 6–8% of the population (Brown et al., 2018). The most common form is sensorineural hearing loss, frequently caused by morphogenetic defects of cochlear hair cells, the sensors in the mammalian inner ear. Hair cells convert mechanical sound stimuli into electrical signals transmitted to the nervous system (Gillespie and Muller, 2009; Pacentine et al., 2020). Mutations that cause deafness frequently are linked to defects of the stereociliary hair bundle, the staircase-shaped cellular organelles that protrude from the apical surface of hair cells (Frolenkov et al., 2004).

The base of stereocilia, the site of stereocilia pivoting, shows a striking structural organization, including the formation of a taper, as well as cytoskeletal specializations, including rootlet filaments (**Figure 1A**; Frolenkov et al., 2004; Pacentine et al., 2020). Genetic and immunolocalization studies have identified several proteins linked to hearing loss in humans that are concentrated at or near the basal region of stereocilia (Pacentine et al., 2020). TRIOBP bundles actin filament and forms rootlet which provides the durability and rigidity for mechanosensitive of stereocilia (Kitajiri et al., 2010; Katsuno et al., 2019). VLGR1 interacts with USH2A, whirlin and PDZD7 and makes up the ankle links that connect the stereocilia at their base during development (Michalski et al., 2007; Grati et al., 2012; Chen et al., 2014; Morgan et al., 2016). Taperin, an actin regulatory protein

(Rehman et al., 2010; Liu et al., 2018), forms a dense-core-like structure which is encircled by a circumferential ring structure formed by RIPOR2 (previously named as Fam65b) oligomers at the taper region of stereocilia (Zhao et al., 2016). Chloride intracellular channel protein 5 (CLIC5), a ∼28 kDa highly conserved protein in vertebrates, associates with taperin, radixin and myosin 6 and stabilizes membrane-actin filament linkages (Salles et al., 2014). Although mutations of CLIC5 leads to hearing loss in humans and mice (Gagnon et al., 2006; Seco et al., 2015), the underlying molecular mechanism is unknown.

Glutaredoxin domain-containing cysteine-rich protein 2 (GRXCR2), mutations of which lead to hearing loss in humans and mice (Imtiaz et al., 2014; Avenarius et al., 2018; Liu et al., 2018; Wonkam et al., 2021), also localizes at the base of stereocilia (Liu et al., 2018). Loss of GRXCR2 leads to the mislocalization of taperin and disorganization of stereocilia, which result in profound hearing loss in mice. Remarkably, reducing taperin expression level by depleting one allele of taperin in the genome rescues the morphological defects of stereocilia but only partially restores the hearing of null *Grxcr2*-mutant mice, suggesting that GRXCR2 interacts with additional protein(s) which are also required for normal hearing (Liu et al., 2018).

In this study, we found that GRXCR2 interacts with CLIC5. The localization of these two proteins at the stereociliary base is independent of each other. Disrupting the interaction between GRXCR2 and CLIC5 *in vivo* has minimal effects on stereocilia morphogenesis but leads to hearing loss in mice. Thus, the interaction between GRXCR2 and CLIC5 is crucial for normal hearing.

# MATERIALS AND METHODS

## Yeast Two-Hybrid Screening

Cochlear specific yeast two-hybrid cDNA library constructed from mRNA isolated from P3-P7 mouse organ of Corti was constructed previously (Zhao et al., 2014) and yeast two-hybrid screening was performed following the manufacturer's instruction (Dualsystems Biotech). In brief, *Clic5* cDNA (NM_172621) was cloned into a yeast two-hybrid bait vector and introduced into yeast by transformation. Self-activation of the bait was tested and screening stringency was optimized. Yeast libraries were then transformed into yeast expressing the bait. Putative interactors were selected from among ∼1 million transformants. Positive clones were picked and re-tested for bait dependency. Plasmids from positive clones were isolated and the identity of interacting partners was determined by DNA sequencing.

## Cell Culture

HEK293 cell line was obtained from ATCC. Cells were maintained in the DMEM medium (Cat# 11965118, Thermo Fisher Scientific) supplemented with 10% heat-inactivated fetal bovine serum (Fisher Scientific), 100 U/ml penicillin and 100 μg/ml streptomycin (Fisher Scientific). Cells were grown at 37°C in a 5% $CO_2$ humidified atmosphere.

## cDNA Constructions, Immunoprecipitations and Western Blots

The coding sequence of *Clic5*, *Clic4*, *Grxcr2*, and *taperin* were amplified from mouse cochlear cDNA library. Expression of the constructs, immunoprecipitations, and western blots were carried out as described (Senften et al., 2006; Zhao et al., 2016; Liu et al., 2018). Immunoprecipitation experiments were carried out at least three times to verify the reproducibility of the data. The following antibodies were used for the experiments: anti-HA (Cat# 2367S, Cell signaling); anti-Myc (Cat# 2278S, Cell signaling); anti-Myc (Cat# sc-40, Santa Cruz); anti-GFP (Cat# sc-9996, Santa Cruz).

## Animal Models and Animal Care

*Grxcr2*$^{-/-}$ mouse (previously named as *Grxcr2*$^{D46/D46}$ mouse) has been described previously (Liu et al., 2018). *Clic5*$^{-/-}$ mouse (also named as *Clic5*$^{jbg/jbg}$ mouse) was purchased from Jackson lab (Gagnon et al., 2006). Using clustered regularly interspaced short palindromic repeats (CRISPR)/Cas9 technology, 180 bp nucleotides in exon 1 of *Grxcr2* were deleted from the genome of C57BL/6J mouse, resulting in a change of amino acid sequence after residue 35, a loss of 60 amino acids and remains in frame. In brief, two sgRNAs (5′-GGATGGCGTTTATGGGTCTGGGG-3′ and 5′-CAGCGGCGCCTACACTCTGGCGG-3′) were synthesized by *in vitro* transcription and microinjected into one-cell embryos. Genomic DNA was then collected from the offspring obtained by the embryo injections, screened using PCR and then sequenced to confirm in-frame deletion. The founder mice were then back-crossed with C57BL/6J mice for two generations. To genotype the *Grxcr2*$^{D180/D180}$ mice, the following primers were used: 5′-TCTTCCTACAGTGGCCGAGT-3′ and 5′-TGAATGTGAGCGAGATACCG-3′. All animal experiments were approved by Institutional Animal Care and Use Committee of The Scripps Research Institute and Indiana University School of Medicine. Both male and female mice were used in our experiment, and we did not find any sex-based differences.

## Whole Mount Immunostaining

Cochlear whole mount staining was carried out as described (Zhao et al., 2016; Liu et al., 2018). In brief, organ of Corti tissue was dissected and fixed in 4% PFA in Hank's Balanced Salt Solution (HBSS) for 20 min. Samples were blocked for 20 min at room temperature in HBSS containing 5% bovine serum albumin (BSA), 1% goat serum and 0.5% Triton X-100, and then incubated overnight at 4°C with primary antibodies in HBSS containing 1% BSA and 0.1% Triton X-100. Samples were washed in HBSS and incubated 2 h at room temperature with secondary antibodies. Tissues were mounted in ProLong® Antifade Reagents (Invitrogen). Stacked images (Z step, ∼0.17 μm; pixel size, 0.04 μm) were then captured by deconvolution microscope (Leica) using a 100 X objective (HCX PL APO 100×/1.40–0.70 OIL). Images were then deconvoluted using blind deconvolution method. Primary antibodies were as follows: anti-GRXCR2 (Cat# HPA059421, Sigma); anti-taperin (Cat# HPA020899, Sigma); anti-CLIC5 (Cat# ACL-025, Alomone

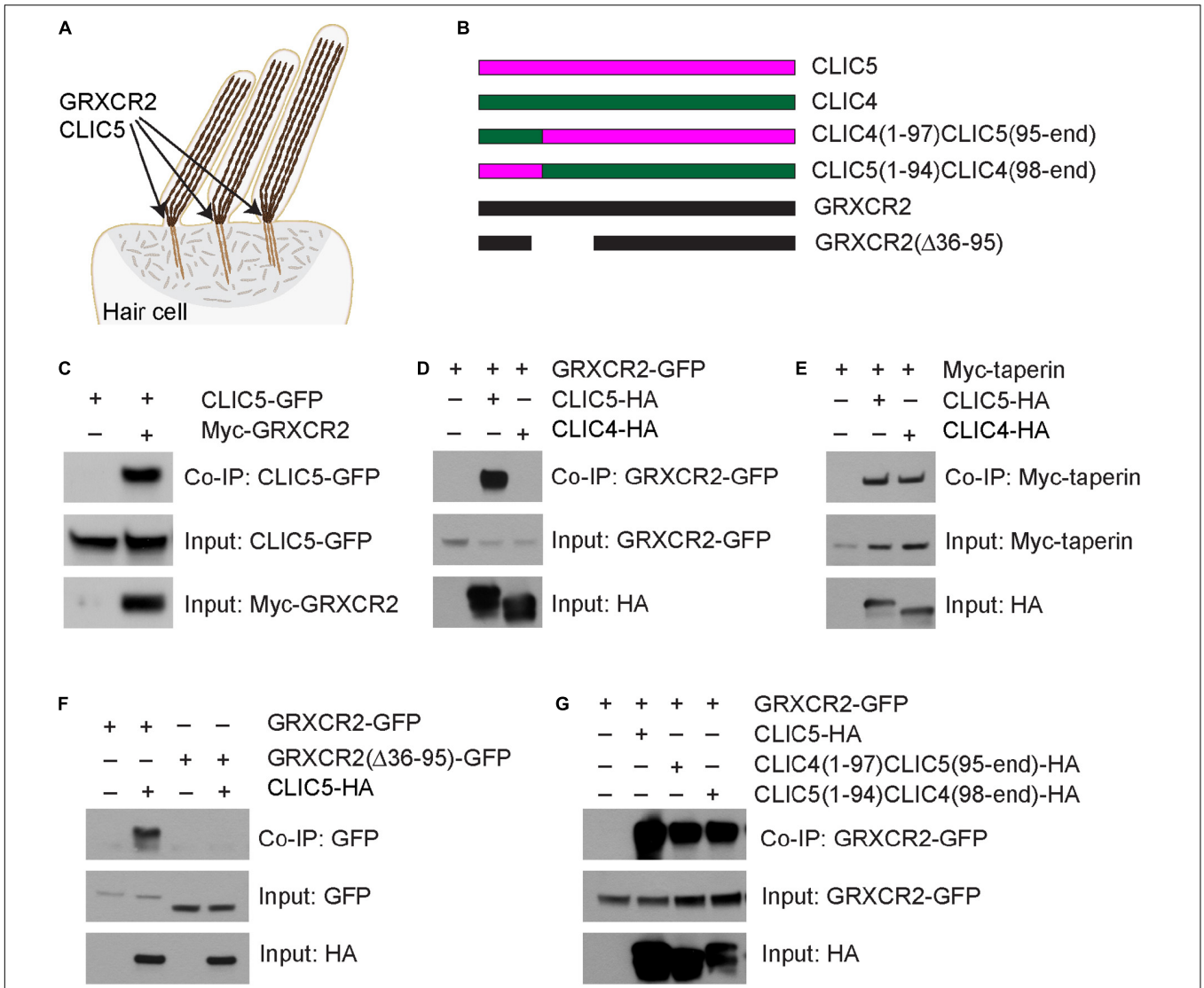


**FIGURE 1 |** Glutaredoxin domain-containing cysteine-rich protein 2 (GRXCR2) interacts with CLIC5. **(A)** Diagram of cochlear hair cell showing the staircase-shaped hair bundle. Inside the stereocilia, the tightly cross-linked actin filaments provide the stiffness of stereocilia. GRXCR2 and CLIC5 are concentrated at the base of stereocilia, the site of stereocilia pivoting. **(B)** Diagram of the constructs used for biochemical experiments. **(C–G)** HEK293 cells were transfected with the constructs indicated on the top of each panel. Immunoprecipitations were carried out with Myc-antibody **(C)** or HA-antibody **(D–G)** followed by western blotting to detect co-expressed proteins. The upper rows show Co-IP results and lower rows show input proteins.

labs). Additional reagents were: Alexa Fluor 488-phalloidin (Thermo Fisher Scientific), Alexa Fluor 568-phalloidin (Thermo Fisher Scientific), Alexa Fluor 647-phalloidin (Thermo Fisher Scientific), Alexa Fluor 488 goat anti-rabbit (Thermo Fisher Scientific), and Alexa Fluor 546 goat anti-rabbit (Thermo Fisher Scientific).

## Scanning Electron Microscopy

The experiments were performed as described (Zhao et al., 2016; Liu et al., 2018). In brief, inner ears were dissected in fixative (2.5% glutaraldehyde; 4% formaldehyde; 0.05 mM Hepes Buffer pH 7.2; 10 mM $CaCl_2$; 5 mM $MgCl_2$; 0.9% NaCl) and fixed for 1 h at RT. Samples were then dissected to remove the stria vascularis, Reissner's membrane and tectorial membrane. Samples were post-fixed by immersion in for 1 day in the same fixative at 4°C. After fixation in 1% $OsO_4$ for 1 h, samples were serially dehydrated in ethanol, dried in a critical point drier (Autosamdri-815A, Tousimis), finely dissected and mounted on aluminum stubs. Samples were then coated by gold and viewed on a JEOL 7800F scanning electron microscope. At least three animals representative of each experimental paradigm were analyzed.

## Auditory Brainstem Response Measurement

Auditory brainstem responses (ABRs) of mice were recorded as described (Zhao et al., 2016; Liu et al., 2018) using TDT

Bioacoustic system 3 and BioSigRZ software. In brief, mice were anesthetized using the mixture of 100 mg/kg ketamine and 10 mg/kg xylazine. Electrodes were inserted under the skin at the vertex and ipsilateral ear, while a ground was inserted under the skin near the tail. The speaker was placed 5 cm away from the mouse ear. Tone stimulus is presented 21 times per second. Band-pass filtered from 300 to 3000 Hz. Averaging window was 10 ms. A total of 512 responses were averaged at each frequency and level combination. The intensity of sound stimulus was started at 90 dB SPL and decreased in 10 dB SPL stepwise to a sub-threshold level. ABR thresholds were analyzed for both ears and for a range of frequencies (for Pure Tone, 4–28 kHz). If no ABR wave was detected at maximum intensity stimulation, a nominal threshold of 90 dB was assigned.

## Quantification and Statistical Analysis

All data are mean ± standard error of the mean. Student's two-tailed unpaired *t* test or Two-way ANOVA were used to determine statistical significance (*, $p < 0.05$, **, $p < 0.01$, ***, $p < 0.001$).

# RESULTS

## GRXCR2 Interacts With CLIC5

Chloride intracellular channel protein 5 has been linked to sensorineural hearing loss in humans and mice (Gagnon et al., 2006; Salles et al., 2014; Seco et al., 2015). However, the molecular functions of CLIC5 in hair cells are still unknown. To identify binding partners for CLIC5, an unbiased yeast-two-hybrid screening was performed using full length CLIC5 as bait. By screening a yeast-two-hybrid library constructed using RNA extracted from organ of Corti, we identified 30 positive clones from ∼1 million transformants. One positive clone expresses taperin, consistent with the previous finding that CLIC5 interacts with taperin (Salles et al., 2014; Bird et al., 2017). Interestingly, 23 positive clones express GRXCR2, suggesting a strong interaction between CLIC5 and GRXCR2. To confirm the yeast-two-hybrid data, we carried out co-immunoprecipitation (co-IP) experiments with extracts from HEK293 cells that were transfected with GFP-tagged CLIC5 and Myc-tagged GRXCR2. CLIC5-GFP was co-immunoprecipitated with Myc-GRXCR2 (**Figure 1C**). Correspondingly, GFP tagged GRXCR2 was co-immunoprecipitated with HA-tagged CLIC5 (**Figure 1D**).

Chloride intracellular channel protein 5 shows an overall 75% similarity to its paralog CLIC4. CLIC5 and CLIC4 are both highly expressed in the cochlear hair cells and concentrated at the base of stereocilia (Shen et al., 2015; Bird et al., 2016). Although both of them interact with taperin (**Figure 1E** and Bird et al., 2017), only CLIC5 is known to be essential for the morphogenesis of stereocilia and auditory perception (Bird et al., 2016), suggesting that in addition to TPRN, CLIC5, and CLIC4 have different binding partners and functions. Interestingly, our data shows that only CLIC5 binds strongly to GRXCR2 (**Figure 1D**), suggesting that the specific interaction between CLIC5 and GRXCR2 might be important for the auditory perception. To identify region(s) in GRXCR2 critical for the interaction with CLIC5, we next generated several truncated GRXCR2 constructs and their interactions with CLIC5 were evaluated by co-IP (**Supplementary Figure 1A**). Finally, we found that 60 amino acids from 36 to 95 in GRXCR2, which are highly conserved in mammals, are essential for its interaction with CLIC5 (**Figure 1F**). A previous study reported that amino acids from 121 to 140 in GRXCR2 mediate the interaction with taperin (Liu et al., 2018). Deleting 60 amino acids from 36 to 95 in GRXCR2 did not affect its binding with taperin (**Supplementary Figure 1B**), further confirming that CLIC5 and taperin bind to different regions of GRXCR2. To identify region(s) in CLIC5 mediating the interaction with GRXCR2, we generated domain-swapped CLIC5 and CLIC4 proteins by exchanging their N terminal 94 aa motifs (**Figure 1B** and **Supplementary Figure 1C**). Interesting, both chimeric proteins interacted with GRXCR2 (**Figure 1G**), suggesting that at least two regions in CLIC5 are essential for its interaction with GRXCR2.

## Independent Localization of CLIC5 and GRXCR2 in Hair Cells During Development

Previous studies found that GRXCR2 is essential for the localization of taperin to the basal region of stereocilia (Liu et al., 2018). CLIC5 is also localized at the base of stereocilia and forms a complex with taperin (Gagnon et al., 2006; Salles et al., 2014). To investigate the extent to which the interaction between GRXCR2 and CLIC5 is required for their proper localization in the stereocilia, immunohistochemistry experiments were performed. To confirm the immunostaining signals obtained are specific, antibodies used in this study were validated using samples from null mutant mice. In the wild-type hair cells, we observed expression in outer hair cells (OHCs) and inner hair cells (IHCs) where CLIC5 and GRXCR2 immunostaining signals concentrated at the base of each stereocilium, outlining the shape of stereociliary bundle (**Figures 2A,B**). In the hair cells from $Clic5^{jbg/jbg}$ mouse (referred as $Clic5^{-/-}$ mouse hereafter), in which a 97 bp deletion introduces a translational frameshift and premature stop codon in *Clic5* (Gagnon et al., 2006), no immunostaining signal of CLIC5 was observed, suggesting that the immunostaining signals obtained using CLIC5 antibody are specific (**Figure 2A**). Similarly, the GRXCR2 antibody used in this study is also specific as no immunostaining signal was observed in the hair cells from $Grxcr2^{D46/D46}$ mouse (Liu et al., 2018, referred as $Grxcr2^{-/-}$ mouse hereafter), in which a 46 bp frameshift deletion creates a premature stop codon in *Grxcr2* (**Figure 2B**).

At higher magnifications, CLIC5 localized at the base of stereocilia in wild-type OHCs and IHCs, consistent with previous results (Gagnon et al., 2006; Salles et al., 2014). In $Grxcr2^{-/-}$ hair cells, CLIC5 was still concentrated at the base of stereocilia, suggesting that GRXCR2 is not essential for the localization of CLIC5 to the basal region of stereocilia during development (**Figure 2C**). Our previous study found that taperin is diffused along the stereocilia length and sometimes accumulated toward the distal end of the stereocilia in the $Grxcr2^{-/-}$ hair cells (Liu et al., 2018). Although taperin interacts with CLIC5 at the base of stereocilia (Salles et al., 2014; Bird et al., 2016, 2017), mislocalized

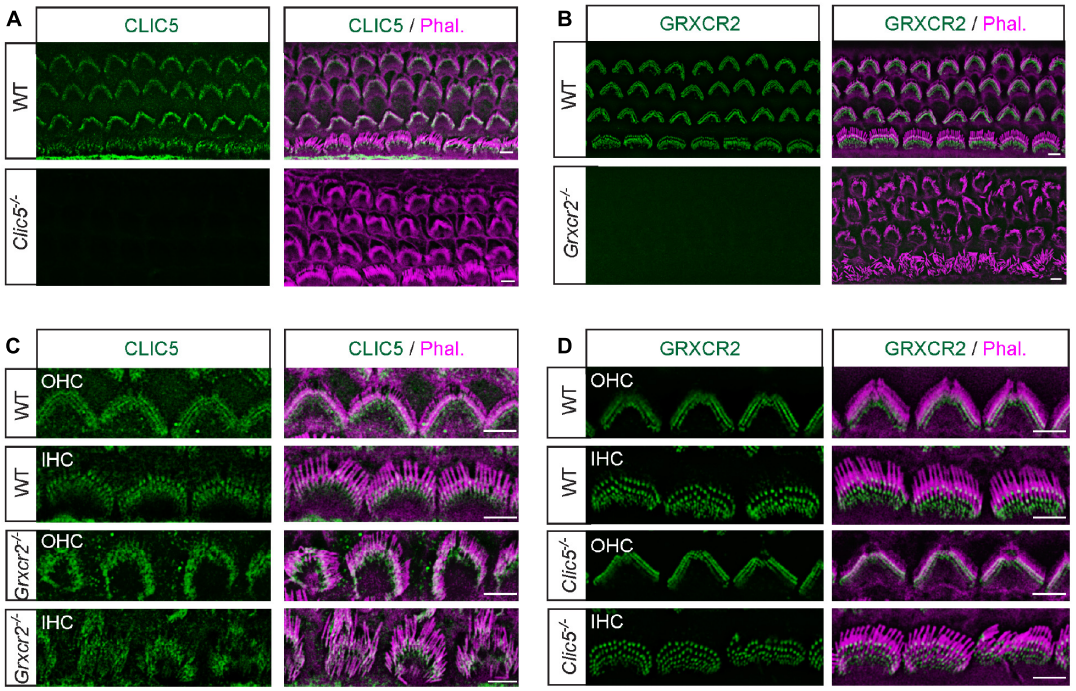


**FIGURE 2 |** Independent localization of CLIC5 and GRXCR2 in hair cells during development. **(A)** Costaining of cochlear whole mounts from wild-type and *Clic5*$^{-/-}$ mice at postnatal day 4 (P4) with CLIC5-antibody (green) and phalloidin (red) to reveal stereocilia. Note, no immunostaining signal in *Clic5*$^{-/-}$ hair cells, suggesting that the CLIC5-antibody is specific. **(B)** Costaining of cochlear whole mounts from wild-type and *Grxcr2*$^{-/-}$ mice with GRXCR2-antibody and phalloidin. Note, no immunostaining signal in *Grxcr2*$^{-/-}$ hair cells, suggesting that the GRXCR2-antibody is specific. **(C)** Co-staining of P4 cochlear whole mounts from wild-type and *Grxcr2*$^{-/-}$ mice with CLIC5-antibody and phalloidin. Note, CLIC5 was concentrated at the base of stereocilia in outer hair cells (OHCs) and inner hair cell (IHCs) of wild-type and *Grxcr2*$^{-/-}$ mice. **(D)** Co-staining of P5 cochlear whole mounts from wild-type and *Clic5*$^{-/-}$ mice with GRXCR2-antibody and phalloidin. Note, GRXCR2 was concentrated at the base of stereocilia in wild-type and *Clic5*$^{-/-}$ hair cells. Scale bars: 5 μm.

taperin in the *Grxcr2*$^{-/-}$ hair cells did not affect the localization of CLIC5 in stereocilia. Similarly, GRXCR2 localized at the base of stereocilia in both wild-type and *Clic5*$^{-/-}$ hair cells, suggesting that CLIC5 is not required for the GRXCR2 localization in hair cells during development either (**Figure 2D**).

## Disrupting the Interaction Between GRXCR2 and CLIC5 Has Minimal Effects on Stereocilia Morphogenesis

The 60 amino acids from 36 to 95 in GRXCR2, the binding site with CLIC5, are highly conserved in mammals (**Figure 3A**). To investigate the extent to which the interaction between GRXCR2 and CLIC5 is involved in auditory perception, 180 bp nucleotides coding these 60 amino acids were deleted from the exon 1 of *Grxcr2* using the CRISPR/Cas9 system. Founder mouse was back-crossed with wild-type C57BL/6J mice for two generations to reduce potential off-target effects of CRISPR. Finally, we obtained a new *Grxcr2*-mutant mouse line, which will be referred as *Grxcr2*$^{D180/D180}$ mouse (**Figure 3B**). To confirm whether the 180 bp is deleted from the mRNA of *Grxcr2*, mRNA was extracted from the inner ear of *Grxcr2*$^{D180/D180}$ mice. Then cDNA of *Grxcr2* was amplified and sequenced. Indeed, the 180 bp nucleotides were deleted from *Grxcr2*. The GRXCR2 antibody used for immunostaining does not recognize GRXCR2 (Δ36–95) as the immunogen of the antibody is located within the first 80 amino acids of GRXCR2. To investigate whether GRXCR2 (Δ36–95) is also concentrated at the base of stereocilia, injectoporation (Xiong et al., 2014) was performed to express Myc-tagged GRXCR2 (Δ36–95) in P3 hair cells. Two days after injectoporation, hair cells were fixed and Myc-antibody was used to detect Myc-GRXCR2 (Δ36–95). Similar to the full-length GRXCR2, GRXCR2 (Δ36–95) was also concentrated near the base of the stereocilia (**Figure 3C**).

To analyze the stereocilia morphology in *Grxcr2*$^{D180/D180}$ mice, scanning electron microscopy (SEM) was performed. In *Grxcr2*$^{-/-}$ mice, most of the hair cell bundles were disorganized and had lost their characteristic V-shapes, which is consistent with the previous results (**Figure 3D**; Liu et al., 2018). Interestingly, in *Grxcr2*$^{D180/D180}$ mice, both IHC and OHC bundles were minimally affected at P14, suggesting that the interaction between GRXCR2 and CLIC5 is not essential for the stereocilia morphogenesis (**Figure 3D**).

To investigate the localization of CLIC5 in the *Grxcr2*$^{D180/D180}$ hair cells, whole mount immunostaining was performed. Similar to that in wild-type and *Grxcr2*$^{-/-}$ hair cells, CLIC5 was also concentrated at the base of stereocilia in *Grxcr2*$^{D180/D180}$ hair cells at P7 (**Figure 3E**). In the 6-week-old wild-type hair cells, some CLIC5 entered stereocilia shaft. The immunostaining signals of CLIC5 had no significant difference

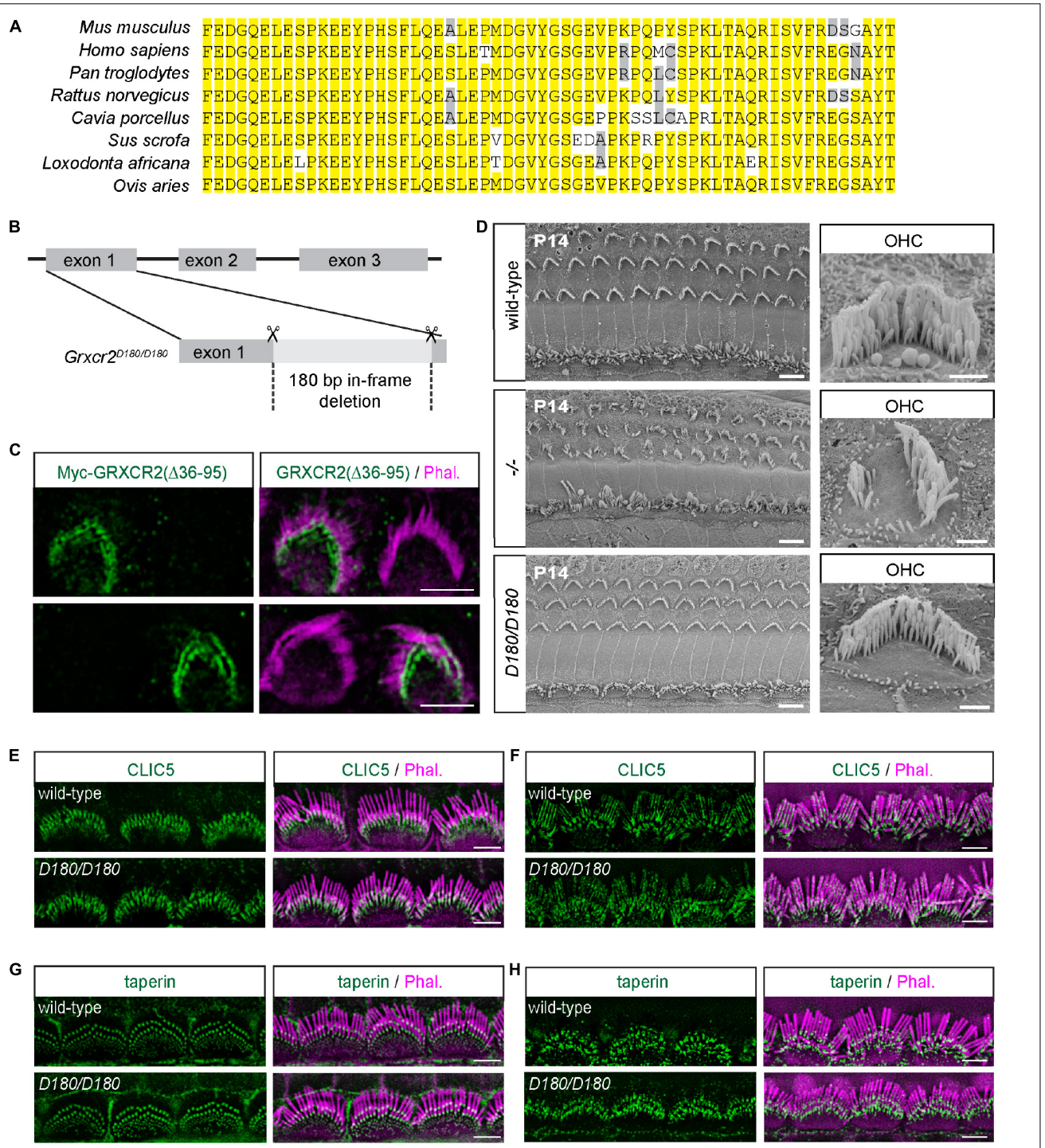


**FIGURE 3 |** Disrupting the interaction between GRXCR2 and CLIC5 has minimal effects on stereocilia morphogenesis. **(A)** Amino acids from 36 to 95 in GRXCR2 are highly conserved in mammals. **(B)** Diagram of the strategy to generate *Grxcr2*$^{D180/D180}$ mice. sgRNAs targeting exon 1 of *Grxcr2* induced a 180-bp in-frame deletion, which was confirmed by sanger sequencing. **(C)** P3 cochlear explants were injectoporated to express Myc-GRXCR2 (Δ36–95). Two days later, tissues were fixed and stained with the Myc-antibody. Note Myc-GRXCR2 (Δ36–95) was concentrated at the base of the stereocilia. **(D)** Scanning electron microscope images showing auditory sensory epithelia of wild-type (upper panel), *Grxcr2*$^{-/-}$ (middle panel), and *Grxcr2*$^{D180/D180}$ (lower panel) mice at the age of P14. Note, stereocilia of *Grxcr2*$^{-/-}$ mice were disorganized while the stereocilia were fairly normal in *Grxcr2*$^{D180/D180}$ mice. Scale bars: left panel 5 μm, right panel 1 μm. **(E,F)** Cochlear whole mounts from wild-type and *Grxcr2*$^{D180/D180}$ mice at the age of P7 **(E)** and 6 weeks **(F)** were stained for CLIC5. Stereocilia were visualized by staining with phalloidin (red). Note, CLIC5 staining did not show any significant change in *Grxcr2*$^{D180/D180}$ hair cells. **(G,H)** Cochlear whole mounts from wild-type and *Grxcr2*$^{D180/D180}$ mice at the age of P7 **(G)** and 6 weeks **(H)** were stained for taperin. Note, taperin was still concentrated at the base of stereocilia in *Grxcr2*$^{D180/D180}$ hair cells. Scale bars: 5 μm.

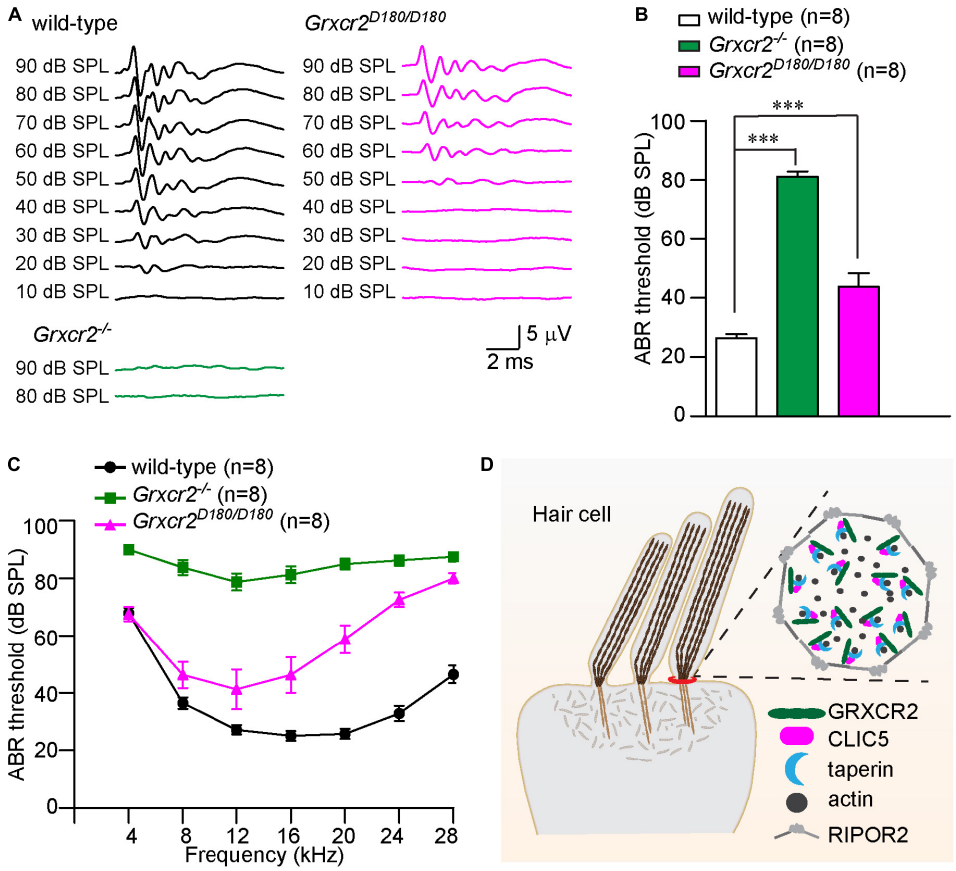


**FIGURE 4 |** Disrupting the interaction between GRXCR2 and CLIC5 leads to hearing loss in mice. **(A)** Representative ABR traces to click stimuli in wild-type (black traces), *Grxcr2*$^{-/-}$ (green traces), and *Grxcr2*$^{D180/D180}$ mice (red traces). Note, *Grxcr2*$^{-/-}$ mice had profound hearing loss while *Grxcr2*$^{D180/D180}$ mice have moderate hearing loss. **(B)** ABR thresholds for click stimuli in 6-week-old wild-type, *Grxcr2*$^{-/-}$ and *Grxcr2*$^{D180/D180}$ mice. All values are represented as the mean ± SEM. ***$p < 0.001$, Student's *t* test. **(C)** ABR thresholds for pure tones in 6-week-old wild-type, *Grxcr2*$^{-/-}$ and *Grxcr2*$^{D180/D180}$ mice. $P < 0.001$ between wild-type and *Grxcr2*$^{-/-}$ mice, wild-type and *Grxcr2*$^{D180/D180}$ mice, *Grxcr2*$^{-/-}$ and *Grxcr2*$^{D180/D180}$ mice (two-way ANOVA). **(D)** Model of GRXCR2 protein complex at the base of stereocilia. In our model, GRXCR2 forms a protein complex with CLIC5 and taperin, which is surrounded by a circumferential ring structure formed by RIPOR2 (previously named as Fam65b) oligomers. GRXCR2 and CLIC5 regulate the localization of taperin, which is an actin cytoskeleton regulatory protein located at the base of stereocilia.

between wild-type and *Grxcr2*$^{D180/D180}$ hair cells (**Figure 3F**). These results further suggest that GRXCR2 is not required for the localization of CLIC5 to the stereociliary base. Deleting 60 amino acids from 36 to 95 in GRXCR2 does not affect the binding of GRXCR2 with taperin. Consistently, in the *Grxcr2*$^{D180/D180}$ hair cells, taperin was still concentrated at the base of stereocilia in both P7 and adult hair cells (**Figures 3G,H**).

## Disrupting the Interaction Between GRXCR2 and CLIC5 Leads to Hearing Loss in Mice

To investigate whether the interaction between GRXCR2 and CLIC5 is required for auditory perception, brain stem response (ABR) to broadband click stimuli in 6-week-old animals was measured. The *Grxcr2*$^{-/-}$ mice had profound hearing loss. Interestingly, although the *Grxcr2*$^{D180/D180}$ has fairly normal V-shaped hair bundles, they had a moderate hearing loss with ∼20 dB hearing threshold elevation compared with wild-type mice (**Figures 4A,B**). Measurements of responses to pure tones revealed that *Grxcr2*$^{D180/D180}$ had moderate hearing loss at lower frequencies (∼10–15 dB hearing thresholds elevation at 8 and 12 kHz) and more severe hearing loss at higher frequencies (∼40 dB hearing thresholds elevation at 24 and 28 kHz) (**Figure 4C**). These results suggest that the interaction between GRXCR2 and CLIC5 is required for normal hearing especially for hearing at high frequencies (**Figure 4D**).

# DISCUSSION

The basal region of stereocilia is critical for hair cell function and many deafness-related proteins are concentrated at this region. Here, we revealed an interaction between GRXCR2 and CLIC5, two proteins linked to hearing loss in humans (Imtiaz et al., 2014;

Seco et al., 2015; Wonkam et al., 2021). In our previous studies, we found that GRXCR2 forms a complex with taperin at the base of stereocilia. Depleting GRXCR2 expression leads to profound hearing loss which is partially caused by the mislocalization of taperin in the hair cells, as reducing taperin expression level only partially restores the hearing in null *Grxcr2*-mutant mice (Liu et al., 2018). Hearing thresholds are still significantly elevated especially at high frequencies after the morphological defects of stereocilia are rescued in the $Grxcr2^{-/-}$ mice, suggesting that GRXCR2 interacts with additional proteins required for normal hearing (Liu et al., 2018). Indeed, here we revealed an interaction between GRXCR2 and CLIC5, which is also essential for normal hearing.

Glutaredoxin domain-containing cysteine-rich protein 2, CLIC5, and taperin form a protein complex at the base of stereocilia (Salles et al., 2014; Bird et al., 2016, 2017; Liu et al., 2018). By mapping their binding domains, we found that different regions of GRXCR2 mediate the interaction with CLIC5 and taperin, respectively. Although the interaction between GRXCR2 with CLIC5 is not critical for the stereocilia morphogenesis, loss of this interaction might affect the stability of the protein complex formed by GRXCR2, CLIC5, and taperin, and results in moderate hearing loss.

Chloride intracellular channel protein 5 has been linked to hearing loss in humans and mice but its functions in hair cells are still unknown (Gagnon et al., 2006; Seco et al., 2015). Structure analysis found that CLIC5 belongs to the glutathione S-transferase (GST) fold superfamily, however, evidences are still lacking to demonstrate a putative enzymatic function (Littler et al., 2010). Although some CLIC proteins could form integral membrane ion channels *in vitro* (Littler et al., 2010), studies have found that CLIC5 is tightly associated with the cytoskeleton, rather than functioning as an ion channel in hair cells (Salles et al., 2014). In line with that, taperin, an actin cytoskeleton regulatory protein in stereocilia (Rehman et al., 2010; Liu et al., 2018), directly binds to CLIC5 (Salles et al., 2014; Bird et al., 2017). Here, we revealed a novel interaction between CLIC5 and GRXCR2. Similar to the $Grxcr2^{-/-}$ mice, *Clic5*-deficient mice have disorganized stereocilia, in which taperin is also diffused along the stereocilia (Salles et al., 2014). Since the mislocalized taperin causes the morphological defects of stereocilia in the $Grxcr2^{-/-}$ mice (Liu et al., 2018), the morphological defects of stereocilia and hearing loss in *Clic5*-deficient mice might be also caused by or partially caused by the mislocalization of taperin. To test this hypothesis, further studies to investigate whether reducing taperin expression level could rescue or partially rescue the stereociliary morphological defects and/or hearing loss in *Clic5*-deficient mouse would be informative.

Glutaredoxin domain-containing cysteine-rich protein 2 is concentrated at the base of stereocilia. Although it interacts with taperin and CLIC5, depleting taperin or CLIC5 alone in hair cells does not affect the localization of GRXCR2 in hair cells. One possibility is that depleting taperin or CLIC5 alone is not enough to affect the localization of GRXCR2 in hair cells. We are currently crossing *Clic5* and *taperin* null mice and will investigate the localization of GRXCR2 in the *Clic5* and *taperin* double knockout mice. Another possibility is that some other protein(s) at the base of stereocilia determines the localization of GRXCR2. It will be of interest to screen additional GRXCR2 interacting proteins and investigate the extent to which they are required for GRXCR2 localization in hair cells.

## DATA AVAILABILITY STATEMENT

The original contributions presented in the study are included in the article/**Supplementary Material**, further inquiries can be directed to the corresponding author/s.

## ETHICS STATEMENT

The animal study was reviewed and approved by Institutional Animal Care and Use Committee of The Scripps Research Institute and Indiana University School of Medicine.

## AUTHOR CONTRIBUTIONS

All authors contributed to the methodology and investigation. JL and BZ: writing. BZ: conceptualization and supervision.

## FUNDING

This work was supported by National Institute on Deafness and Other Communication Disorders (NIDCD) grant DC017147 (BZ), International Research Grant from Royal National Institute for Deaf People (BZ), and Indiana University School of Medicine startup funding (BZ).

## ACKNOWLEDGMENTS

We thank Drs. Thomas B. Friedman and Inna Belyantseva for their valuable comments and suggestions on the manuscript.

## SUPPLEMENTARY MATERIAL

The Supplementary Material for this article can be found online at: https://www.frontiersin.org/articles/10.3389/fcell.2021.671364/full#supplementary-material

## REFERENCES

Avenarius, M. R., Jung, J. Y., Askew, C., Jones, S. M., Hunker, K. L., Azaiez, H., et al. (2018). Grxcr2 is required for stereocilia morphogenesis in the cochlea. *PLoS One* 13:e0201713. doi: 10.1371/journal.pone.0201713

Bird, J. E., Barzik, M., Drummond, M. C., Sutton, D. C., Goodman, S. M., Morozko, E. L., et al. (2016). Harnessing molecular motors for

nanoscale pulldown in live cells. *bioRxiv [preprint]* doi: 10.1101/053744, 053744

Bird, J. E., Barzik, M., Drummond, M. C., Sutton, D. C., Goodman, S. M., Morozko, E. L., et al. (2017). Harnessing molecular motors for nanoscale pulldown in live cells. *Mol. Biol. Cell* 28, 463–475. doi: 10.1091/mbc.e16-08-0583

Brown, C. S., Emmett, S. D., Robler, S. K., and Tucci, D. L. (2018). Global hearing loss prevention. *Otolaryngol. Clin. North Am.* 51, 575–592.

Chen, Q., Zou, J., Shen, Z., Zhang, W., and Yang, J. (2014). Whirlin and PDZ domain-containing 7 (PDZD7) proteins are both required to form the quaternary protein complex associated with usher syndrome type 2. *J. Biol. Chem.* 289, 36070–36088. doi: 10.1074/jbc.m114.610535

Frolenkov, G. I., Belyantseva, I. A., Friedman, T. B., and Griffith, A. J. (2004). Genetic insights into the morphogenesis of inner ear hair cells. *Nat. Rev. Genet.* 5, 489–498. doi: 10.1038/nrg1377

Gagnon, L. H., Longo-Guess, C. M., Berryman, M., Shin, J. B., Saylor, K. W., Yu, H., et al. (2006). The chloride intracellular channel protein CLIC5 is expressed at high levels in hair cell stereocilia and is essential for normal inner ear function. *J. Neurosci.* 26, 10188–10198. doi: 10.1523/jneurosci.2166-06.2006

Gillespie, P. G., and Muller, U. (2009). Mechanotransduction by hair cells: models, molecules, and mechanisms. *Cell* 139, 33–44. doi: 10.1016/j.cell.2009.09.010

Grati, M., Shin, J. B., Weston, M. D., Green, J., Bhat, M. A., Gillespie, P. G., et al. (2012). Localization of PDZD7 to the stereocilia ankle-link associates this scaffolding protein with the Usher syndrome protein network. *J. Neurosci.* 32, 14288–14293. doi: 10.1523/jneurosci.3071-12.2012

Imtiaz, A., Kohrman, D. C., and Naz, S. (2014). A frameshift mutation in GRXCR2 causes recessively inherited hearing loss. *Hum. Mutat.* 35, 618–624. doi: 10.1002/humu.22545

Katsuno, T., Belyantseva, I. A., Cartagena-Rivera, A. X., Ohta, K., Crump, S. M., Petralia, R. S., et al. (2019). TRIOBP-5 sculpts stereocilia rootlets and stiffens supporting cells enabling hearing. *JCI Insight* 4:e128561.

Kitajiri, S., Sakamoto, T., Belyantseva, I. A., Goodyear, R. J., Stepanyan, R., Fujiwara, I., et al. (2010). Actin-bundling protein TRIOBP forms resilient rootlets of hair cell stereocilia essential for hearing. *Cell* 141, 786–798. doi: 10.1016/j.cell.2010.03.049

Littler, D. R., Harrop, S. J., Goodchild, S. C., Phang, J. M., Mynott, A. V., Jiang, L., et al. (2010). The enigma of the CLIC proteins: ion channels, redox proteins, enzymes, scaffolding proteins? *FEBS Lett.* 584, 2093–2101. doi: 10.1016/j.febslet.2010.01.027

Liu, C., Luo, N., Tung, C. Y., Perrin, B. J., and Zhao, B. (2018). GRXCR2 regulates taperin localization critical for stereocilia morphology and hearing. *Cell Rep.* 25, 1268–1280.e4.

Michalski, N., Michel, V., Bahloul, A., Lefevre, G., Barral, J., Yagi, H., et al. (2007). Molecular characterization of the ankle-link complex in cochlear hair cells and its role in the hair bundle functioning. *J. Neurosci.* 27, 6478–6488. doi: 10.1523/jneurosci.0342-07.2007

Morgan, C. P., Krey, J. F., Grati, M., Zhao, B., Fallen, S., Kannan-Sundhari, A., et al. (2016). PDZD7-MYO7A complex identified in enriched stereocilia membranes. *eLife* 5:e18312.

Pacentine, I., Chatterjee, P., and Barr-Gillespie, P. G. (2020). Stereocilia rootlets: actin-based structures that are essential for structural stability of the hair bundle. *Int. J. Mol. Sci.* 21:324. doi: 10.3390/ijms21010324

Rehman, A. U., Morell, R. J., Belyantseva, I. A., Khan, S. Y., Boger, E. T., Shahzad, M., et al. (2010). Targeted capture and next-generation sequencing identifies C9orf75, encoding taperin, as the mutated gene in nonsyndromic deafness DFNB79. *Am. J. Hum. Genet.* 86, 378–388. doi: 10.1016/j.ajhg.2010.01.030

Salles, F. T., Andrade, L. R., Tanda, S., Grati, M., Plona, K. L., Gagnon, L. H., et al. (2014). CLIC5 stabilizes membrane-actin filament linkages at the base of hair cell stereocilia in a molecular complex with radixin, taperin, and myosin VI. *Cytoskeleton (Hoboken)* 71, 61–78. doi: 10.1002/cm.21159

Seco, C. Z., Oonk, A. M., Dominguez-Ruiz, M., Draaisma, J. M., Gandia, M., Oostrik, J., et al. (2015). Progressive hearing loss and vestibular dysfunction caused by a homozygous nonsense mutation in CLIC5. *Eur. J. Hum. Genet.* 23, 189–194. doi: 10.1038/ejhg.2014.83

Senften, M., Schwander, M., Kazmierczak, P., Lillo, C., Shin, J. B., Hasson, T., et al. (2006). Physical and functional interaction between protocadherin 15 and myosin VIIa in mechanosensory hair cells. *J. Neurosci.* 26, 2060–2071. doi: 10.1523/jneurosci.4251-05.2006

Shen, J., Scheffer, D. I., Kwan, K. Y., and Corey, D. P. (2015). SHIELD: an integrative gene expression database for inner ear research. *Database (Oxford)* 2015:bav071. doi: 10.1093/database/bav071

Wonkam, A., Lebeko, K., Mowla, S., Noubiap, J. J., Chong, M., and Pare, G. (2021). Whole exome sequencing reveals a biallelic frameshift mutation in GRXCR2 in hearing impairment in Cameroon. *Mol. Genet. Genomic Med.* Online ahead of print.

Xiong, W., Wagner, T., Yan, L., Grillet, N., and Muller, U. (2014). Using injectoporation to deliver genes to mechanosensory hair cells. *Nat. Protoc.* 9, 2438–2449. doi: 10.1038/nprot.2014.168

Zhao, B., Wu, Z., and Muller, U. (2016). Murine Fam65b forms ring-like structures at the base of stereocilia critical for mechanosensory hair cell function. *eLife* 5:e14222.

Zhao, B., Wu, Z., Grillet, N., Yan, L., Xiong, W., Harkins-Perry, S., et al. (2014). TMIE is an essential component of the mechanotransduction machinery of cochlear hair cells. *Neuron* 84, 954–967. doi: 10.1016/j.neuron.2014.10.041

**Conflict of Interest:** The authors declare that the research was conducted in the absence of any commercial or financial relationships that could be construed as a potential conflict of interest.

*Copyright © 2021 Li, Liu and Zhao. This is an open-access article distributed under the terms of the Creative Commons Attribution License (CC BY). The use, distribution or reproduction in other forums is permitted, provided the original author(s) and the copyright owner(s) are credited and that the original publication in this journal is cited, in accordance with accepted academic practice. No use, distribution or reproduction is permitted which does not comply with these terms.*

frontiers in Cell and Developmental Biology

BRIEF RESEARCH REPORT
published: 03 June 2021
doi: 10.3389/fcell.2021.680155

# Annexin A4 Is Dispensable for Hair Cell Development and Function

*Nana Li[1], Yuehui Xi[1], Haibo Du[1], Hao Zhou[1] and Zhigang Xu[1,2]**

*[1] Shandong Provincial Key Laboratory of Animal Cell and Developmental Biology, School of Life Sciences, Shandong University, Qingdao, China, [2] Shandong Provincial Collaborative Innovation Center of Cell Biology, Shandong Normal University, Jinan, China*

Annexin A4 (ANXA4) is a $Ca^{2+}$-dependent phospholipid-binding protein that is specifically expressed in the cochlear and vestibular hair cells, but its function in the hair cells remains unknown. In the present study, we show that besides localizing on the plasma membrane, ANXA4 immunoreactivity is also localized at the tips of stereocilia in the hair cells. In order to investigate the role of ANXA4 in the hair cells, we established *Anxa4* knockout mice using CRISPR/Cas9 technique. Unexpectedly, the development of both cochlear and vestibular hair cells is normal in *Anxa4* knockout mice. Moreover, stereocilia morphology of *Anxa4* knockout mice is normal, so is the mechano-electrical transduction (MET) function. Consistently, the auditory and vestibular functions are normal in the knockout mice. In conclusion, we show here that ANXA4 is dispensable for the development and function of hair cells, which might result from functional redundancy between ANXA4 and other annexin(s) in the hair cells.

**Keywords: *Anxa4*, inner ear, hair cells, stereocilia, knockout mice**

OPEN ACCESS

***Edited by:***
*Junmin Pan,*
*Tsinghua University, China*

***Reviewed by:***
*Paris Alexander Skourides,*
*University of Cyprus, Cyprus*
*Bo Zhao,*
*Indiana University, United States*

***Correspondence:**
*Zhigang Xu*
*xuzg@sdu.edu.cn*

***Specialty section:***
*This article was submitted to Cell Growth and Division, a section of the journal Frontiers in Cell and Developmental Biology*

***Received:*** *13 March 2021*
***Accepted:*** *06 May 2021*
***Published:*** *03 June 2021*

***Citation:***
*Li N, Xi Y, Du H, Zhou H and Xu Z (2021) Annexin A4 Is Dispensable for Hair Cell Development and Function. Front. Cell Dev. Biol. 9:680155. doi: 10.3389/fcell.2021.680155*

## INTRODUCTION

Hair cells are mechanosensitive sensory receptor cells in the cochlea and vestibular organs, characterized by their hairy-looking, actin-based stereocilia on the apical surface. The stereocilia are organized into several rows of increasing height, forming a staircase-like pattern. Mechanical stimuli causes deflection of the stereocilia, which changes the opening probability of the mechano-electrical transduction (MET) channels localized at the tips of shorter row stereocilia, resulting in influx of cations into the hair cells (Hudspeth and Jacobs, 1979; Beurg et al., 2009; Schwander et al., 2010). The development and function of hair cells are tightly regulated, and deficits in this process are the main reasons for hearing loss and balancing dysfunction (Müller and Barr-Gillespie, 2015).

Genetic, transcriptomic and proteomic analysis have identified several proteins that are essential for hair cell development and/or function (Richardson et al., 2011; Cai et al., 2015; Scheffer et al., 2015; Krey et al., 2018). Some of the identified proteins are specifically expressed in the hair cells, such as ATOH1, a famous transcription factor that plays pivotal roles in hair cells. *Atoh1*-deficient mice fail to generate hair cells, and overexpression of *Atoh1* in immature rodent inner ears induce ectopic hair cells, suggesting that ATOH1 is important for hair cell formation during development (Bermingham et al., 1999; Zheng and Gao, 2000; Woods et al., 2004). Several ATOH1-regulated genes have been identified through transcriptomic analysis, such as *Anxa4*, *Rbm24*, *Srrm4*, et al. (Cai et al., 2015). Previously, we and others showed that RBM24 and SRRM4 are important for hair cell development and/or function through regulating mRNA splicing or stability (Nakano et al., 2012; Zhang et al., 2020; Zheng et al., 2020).

*Anxa4* encodes annexin A4 (ANXA4), a $Ca^{2+}$-dependent phospholipid-binding protein that is predominantly expressed in the epithelial cells (Kaetzel et al., 1989, 1994). Upon $Ca^{2+}$ binding, ANXA4 undergoes oligomerization and translocates to the plasma membrane (Crosby et al., 2013). ANXA4 binding increases the rigidity of plasma membrane, induces membrane curvature, and reduces the permeability of water, $H^+$, and $Cl^-$ (Kaetzel et al., 1994, 2001; Hill et al., 2003; Boye et al., 2017). Moreover, ANXA4 was suggested to be a direct regulator of adenylyl cyclase type 5 (AC5) (Heinick et al., 2015). In the mouse cochlea, *in situ* hybridization reveals that *Anxa4* is expressed in the outer hair cells (OHCs) and inner hair cells (IHCs) (Cai et al., 2015). In the mouse vestibular organs, immunostaining suggests that ANXA4 is expressed at the plasma membrane of type II vestibular hair cells (VHCs) (McInturff et al., 2018). The hair cell-specific expression of *Anxa4* is further supported by the transcriptome data (Scheffer et al., 2015; Shen et al., 2015). However, despite of the specific expression pattern, little is known about the function of ANXA4 in the hair cells.

Three *Anxa4* transcripts have been identified in mice, which have different 5′ untranslated regions (5′UTR) but encode an identical ANXA4 protein (Li et al., 2003). An *Anxa4* gene trap mouse line was created through inserting a retrovirus-based trapping cassette into the first intron of *Anxa4* gene, which disrupts the expression of one *Anxa4* transcript but leaves the other two unaffected (Li et al., 2003). In the present work, we establish *Anxa4* knockout mice by deleting exons 3–6 of *Anxa4* gene that are common to all three *Anxa4* transcripts. Using this knockout mouse model, we investigate the role of ANXA4 in the development and function of hair cells.

# MATERIALS AND METHODS

## Mice

*Anxa4* knockout mice were generated using clustered regularly interspaced short palindromic repeats (CRISPR)/Cas9 technique by Cyagen Biosciences Inc. (Suzhou, China) on a C57BL/6N background. Briefly, genomic DNA sequences 5′-TGTTATAAATATAACGCACAAGG-3′ and 5′-AGCCTGAGCCTACACCTCGAGGG-3′ were chosen as the guide RNA (gRNA) targets. *In vitro* transcribed gRNAs and *Cas9* mRNA were injected into the cytoplasm of zygotes, followed by culturing for 24 h *in vitro*. The injected zygotes were transferred into the oviduct of a pseudopregnant ICR female mouse at 0.5 day post coitus (dpc) to give rise to F0 mice, which were then crossed to wild type C57BL/6N mice to give rise to heterozygous F1 mice. The following genotyping primers were used for examination of the knockout allele: F1, 5′-AGATCCCCATCCAAATAAGGTTTG-3′; R1, 5′-ATCACTTTACAGAGTTTCGA-3′ (436 bp). The following genotyping primers were used for examination of the wild type allele: F2, 5′-CTTAGGACTGACTTCCTGTGTCAT-3′; R2, 5′-TTGTCCATACAGCAATGAAGGGAT-3′ (620 bp). *Atoh1-GFP* transgenic mice and *Cdh23-V*$^{2J}$ mice were maintained and genotyped as described previously (Di Palma et al., 2001; Lumpkin et al., 2003).

## Reverse Transcription-Polymerase Chain Reaction (RT-PCR)

Total RNA of mouse inner ear was extracted using TRIzol reagent (Invitrogen) according to the manufacturer's protocol. Afterward, 1 μg total RNA was used for reverse transcription (RT) using PrimeScript RT Reagent Kit with gDNA Eraser (Takara, RR047A). Polymerase chain reaction (PCR) was then performed using the RT product as template with the following primers: *Anxa1*-F, 5′-ATGTATCCTCGGATGTTGCTGC-3′; *Anxa1*-R, 5′-TGAGCATTGGTCCTCTTGGTA-3′; *Anxa2*-F, 5′-ATGTCTACTGTCCACGAAATCCT-3′; *Anxa2*-R, 5′-CGAAG TTGGTGTAGGGTTTGACT-3′; *Anxa4*-F, 5′-TGTGACTGAA CTCTGAACGTGA-3′; *Anxa4*-R, 5′-TTTCACCTCGTCTGTC CCCC-3′; *Anxa5*-F, 5′-ATCCTGAACCTGTTGACATCCC-3′; *Anxa5*-R, 5′-AGTCGTGAGGGCTTCATCATA-3′; *Anxa6*-F, 5′-CCTATTGTGACGCCAAAGAGAT-3′; *Anxa6*-R, 5′-GCCGG AAGTGTCTCCAATGA-3′; *Anxa7*-F, 5′-AGGATTGTGGTCA CTCGAAGT-3′; *Anxa7*-R, 5′-TGTAATCTCCACTCGTG TCACT-3′; β-*actin*-F, 5,-CGTTGACATCCGTAAAGACC-3′; β-*actin*-R, 5′-AACAGTCCGCCTAGAAGCAC-3′. Annealing temperatures were adjusted between 58 and 62°C to obtain the optimal sensitivity and specificity.

## Western Blot

Mouse tissues were dissected and lysed in ice-cold lysis buffer containing 150 mM NaCl, 50 mM Tris at pH 7.5, 1% (vol/vol) Triton X-100, 1 mM PMSF, and 1 × protease inhibitor cocktail (Sigma-Aldrich, Cat. No. S8830). After centrifugation, the supernatant was separated by polyacrylamide gel electrophoresis (PAGE), followed by transferring to PVDF membrane. The membrane was blocked in PBS with 5% BSA and 0.1% Tween-20, followed by incubation with primary antibody at 4℃ overnight and corresponding secondary antibody at room temperature for an hour. The signals were detected using the ECL system (Thermo Fisher Scientific). Antibodies used in the present study are as follows: rabbit anti-ANXA4 antibody (ABclonal, Cat. No. A13466); mouse anti-GAPDH antibody (Millipore, Cat. No. MAB374); HRP-conjugated goat anti-mouse antibody (Bio-Rad, Cat. No. 170-6516); HRP-conjugated goat anti-rabbit antibody (Bio-Rad, Cat. No. 170-6515).

## Whole-Mount Immunostaining

Whole-mount immunostaining was performed as previously described (Du et al., 2020). Briefly, dissected sensory epithelia were fixed with 4% paraformaldehyde (PFA) in PBS for 30 min, then permeabilized and blocked with PBT1 (0.1% Triton X-100, 1% BSA, and 5% heat-inactivated goat serum in PBS, pH 7.3) for an hour. The samples were then incubated with primary antibody in PBT1 overnight at 4°C, followed by incubation with secondary antibody in PBT2 (0.1% Triton X-100 and 0.1% BSA in PBS) for an hour. For stereocilia visualization, samples were additionally treated with TRITC-conjugated phalloidin (Sigma-Aldrich, Cat. No. P1951) in PBS for 30 min. The samples were mounted in PBS/glycerol (1:1) and imaged with confocal microscope (LSM 700 and 900, Zeiss, Germany). Antibodies used in the present study are as follows: goat anti-ANXA4 antibody (R&D Systems,

Cat. No. AF4146); rabbit anti-ANXA4 antibody (ABclonal, Cat. No. A13466); rabbit anti-MYO7A antibody (Proteus Biosciences, Cat. No. 25-6790); Alexa Fluor 488-conjugated donkey anti-rabbit IgG (Thermo Fisher Scientific, Cat. No. A21206); Alexa Fluor 488-conjugated donkey anti-goat IgG (Thermo Fisher Scientific, Cat. No. A11055); Cy3 rabbit anti-goat IgG (H + L) (ABclonal, Cat. No. AS015).

## Scanning Electron Microscopy (SEM)

The temporal bone were fixed with 2.5% glutaraldehyde in 0.1 M phosphate buffer overnight at 4°C, then the cochlea were dissected out and post-fixed with 1% osmium tetroxide in 0.1 M phosphate buffer at 4°C for 2 h. After that, samples were dehydrated in ethanol and critically point dried using a Leica EM CPD300 (Leica, Germany). Samples were then mounted and sputter coated with platinum (15 nm) using a Cressington 108 sputter coater (Cressington, United Kingdom), and images were taken using a Quanta250 field-emission scanning electron microscope (FEI, Netherlands) with a beam strength of 3 kV.

## Auditory Brainstem Response (ABR) Measurement

RZ6 workstation and BioSig software (Tucker-Davis Technologies, Alachua, FL, United States) were used to measure and analyze ABR. Mice were anesthetized by intraperitoneally injecting Pentobarbital (8.4 mg/100 g body weight) and placed on an isothermal pad to keep the body temperature during the experiment. Acoustic stimuli (clicks or pure-tone bursts) of decreasing sound level from 90 dB SPL in 10 dB SPL steps were delivered to the mouse ear through a loudspeaker (MF1, Tucker-Davis Technologies). A total of 512 responses were sampled and averaged at each sound level. Hearing threshold was determined as the lowest sound level at which the ABR waves were recognizable.

## Vestibular Function Examination

Vestibular function of mice was evaluated as described previously (Fasquelle et al., 2011). Briefly, six different tests were performed as follows: (1) Head bobbing was counted to record abnormal intermittent backward extension of the neck; (2) Retropulsion was counted to record typical backward walk due to vestibular disturbance; (3) Circling stereotyped movement was counted to record compulsive circles around the animal's hips; (4) Swimming test was performed to observe swimming behavior ranging from normal swimming to drowning; (5) Tail-hanging reflex was tested to examine the normal forelimb extension to reach the ground; (6) Rotarod test was performed to evaluate the falling latency on rotating rod. For tests of head bobbing, retropulsion and circling stereotyped movement, mice were placed in a 45 × 30 cm cube for 1 min and the frequency of corresponding behaviors was recorded. Swimming test scores were defined as follows: 0, normal swimming; 1, irregular swimming; 2, immobile floating; and 3, underwater tumbling. For tail hanging reflex test, mice were scored 0–4 corresponding to normal to severe vestibular defect. For rotarod test, the rod apparatus (HB-600, Ruanlong, China) was set to accelerate from 0 to 50 rpm over a 3-min period. Mice were placed on the rod and the time before dropping from the rod was measured automatically. Mice were trained for four consecutive days and testing data was recorded on day 2, 3, and 4. Each day consisted of four trials and the second, third and fourth one was measured with the first one as a training trial.

## FM1-43FX Uptake Experiment

Mouse auditory or vestibular sensory epithelia were dissected out and incubated with 3 μM FM 1-43FX (Thermo Fisher, Cat. No. F35355) in PBS for 30 s, followed by washing three times with PBS. The samples were then fixed with 4% PFA at room temperature for 20 min, and mounted in PBS-glycerol (1:1). Images were taken using a confocal microscope (LSM 700, Zeiss, Germany).

## Statistical Analysis

All experiments were performed at least three times independently. Data were shown as means ± standard error of mean (SEM). Student's two-tailed unpaired *t*-test was used to determine statistical significance, and $P < 0.05$ was considered statistically significant.

# RESULTS

## ANXA4 Is Localized at the Stereociliary Tips and Plasma Membrane of Cochlear Hair Cells

We first examined the localization of ANXA4 in the cochlear hair cells by performing whole-mount immunostaining using a commercial anti-ANXA4 antibody. The results reveal robust ANXA4 immunoreacivity in the stereocilia of both OHCs and IHCs (**Figure 1A**). Further examination at higher resolution shows that ANXA4 immunoreacivity is enriched at the stereociliary tips of OHCs and IHCs (**Figure 1B**). Similar results were obtained using another commercial anti-ANXA4 antibody (**Supplementary Figures 1A–C**). The specificity of the antibodies were confirmed using *Anxa4* knockout mice (see below) (**Figures 1A,B** and **Supplementary Figures 1A–C**). Moreover, ANXA4 immunoreactivity is also detected on the plasma membrane of OHCs and IHCs (**Figure 2A**). Taken together, our present data suggest that ANXA4 is localized at the stereociliary tips and plasma membrane of cochlear hair cells.

## Generation of *Anxa4* Knockout Mice

Mouse *Anxa4* gene contains 13 exons, with the start codon ATG localized in exon 2 and stop codon TAA localized in exon 13 (**Supplementary Figure 2A**). Transcription could start from exon 1 or exon 2, or an alternative exon 1 (exon 1'), giving rise to three different transcripts encoding an identical ANXA4 protein (Li et al., 2003) (**Supplementary Figure 2A**). Two gRNAs were used to delete exons 3–6, which are common for all three *Anxa4* transcripts (**Supplementary Figure 2A**). This deletion is expected to cause a premature translational

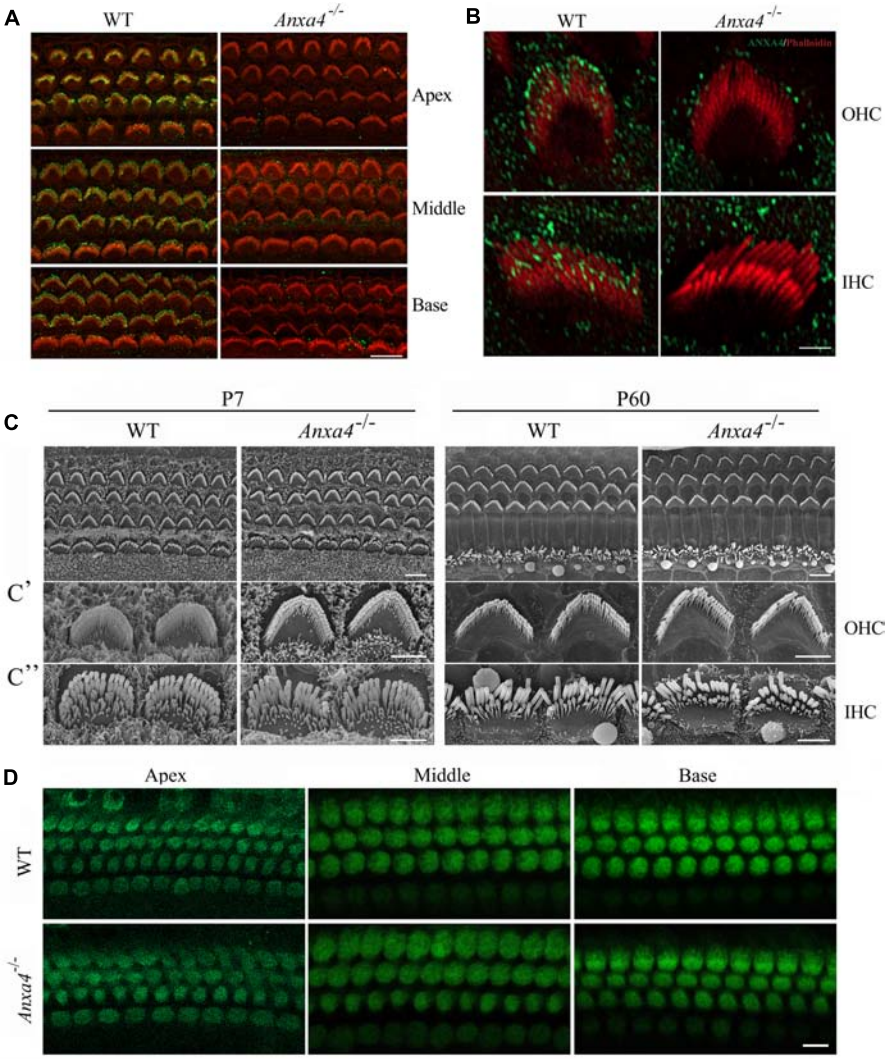


**FIGURE 1 |** Stereocilia morphology and MET function of cochlear hair cells are unaffected in *Anxa4*$^{-/-}$ mice. **(A)** Cochlear hair cell stereocilia of P5 wild type or *Anxa4*$^{-/-}$ mice were stained with anti-ANXA4 antibody (ABclonal) and imaged using confocal microscope. Stereocilia F-actin core was visualized by staining with TRITC-conjugated phalloidin. **(B)** Higher resolution confocal microscopy images show stereociliary tip localization of ANXA4 in P7 OHC and IHC. **(C)** Examination of hair bundle morphology of wild type or *Anxa4*$^{-/-}$ mice at P7 or P60 using SEM. **(C',C")** Higher resolution SEM images of OHCs and IHCs, respectively. **(D)** FM1-43FX uptake by OHCs and IHCs of P7 wild type or *Anxa4*$^{-/-}$ mice was examined using confocal microscope. Shown are images taken from the middle turn unless otherwise indicated. Scale bars, 10 μm in **(A,D)**, 2 μm in **(B,C',C")**, 5 μm in **(C)**.

stop and give rise to a potentially truncated ANXA4 protein (**Supplementary Figure 2B**).

RT-PCR was performed to examine the expression of *Anxa4* transcript using primers flanking the deleted region, which gives rise to two PCR products in *Anxa4*$^{-/-}$ mice (**Supplementary Figure 2C**). Sanger sequencing reveals that the smaller band represents the expected *Anxa4* transcript with exon 3–6 deleted, whereas the larger band represents a similar transcript with additional 43 nucleotide acids corresponding to sequences from intron 2 (**Supplementary Figure 2D**). The smaller knockout transcript will generate a peptide of 41 amino acids (aa) unrelated to ANXA4, while the larger knockout transcript might produce a truncated ANXA4 protein containing the last two ANX domains (**Supplementary Figure 2B**). Nevertheless, the expression level of these two knockout transcripts is much lower than that of the wild type *Anxa4* transcript, suggesting that they undergo non-specific mRNA decay (NMD) (**Supplementary Figure 2C**).

ANXA4 has been reported to have a molecular weight of 35 kDa (Kaetzel et al., 1994; Li et al., 2003). Consistently, western blot detects a band of 35 kDa from *Anxa4*$^{+/-}$ mice but not *Anxa4*$^{-/-}$ mice, suggesting that ANXA4 expression is completely disrupted in the *Anxa4* knockout mice (**Supplementary Figure 2E**). *Anxa4*$^{-/-}$ mice are morphologically and behaviorally indistinguishable from *Anxa4*$^{+/-}$ or wild type mice. Moreover, interbreeding of *Anxa4*$^{+/-}$ mice gives rise to offspring in the expected

Mendelian ratio (21% wild-type, 49% *Anxa4*$^{+/-}$, and 30% *Anxa4*$^{-/-}$; n = 86; $\chi^2$-test *P*-value = 0.68) with normal viability. These results suggest that ANXA4 is dispensable for general development in mice.

## Stereocilia Development and MET Function Are Unaffected in *Anxa4* Knockout Mice

Phalloidin staining shows that stereocilia morphology is normal in *Anxa4*$^{-/-}$ mice (**Figures 1A,B** and **Supplementary Figures 1A–C**). Stereocilia morphology was further examined by performing scanning electron microscopy (SEM), which shows that the stereocilia in both OHCs and IHCs of *Anxa4*$^{-/-}$ mice are indistinguishable from that of wild type mice up to postnatal day 60 (P60) (**Figures 1C–C**"). Therefore, our present data suggest that *Anxa4* disruption does not affect the development or maintenance of stereocilia.

It has long been known that stereocilia play a pivotal role in MET of hair cells (Hudspeth and Jacobs, 1979). The normal morphology of stereocilia suggest that MET function might also be unaffected in *Anxa4*$^{-/-}$ mice. MET function was then examined by performing FM1-43FX uptake experiment. FM1-43FX is a fluorescent dye that enters hair cells through

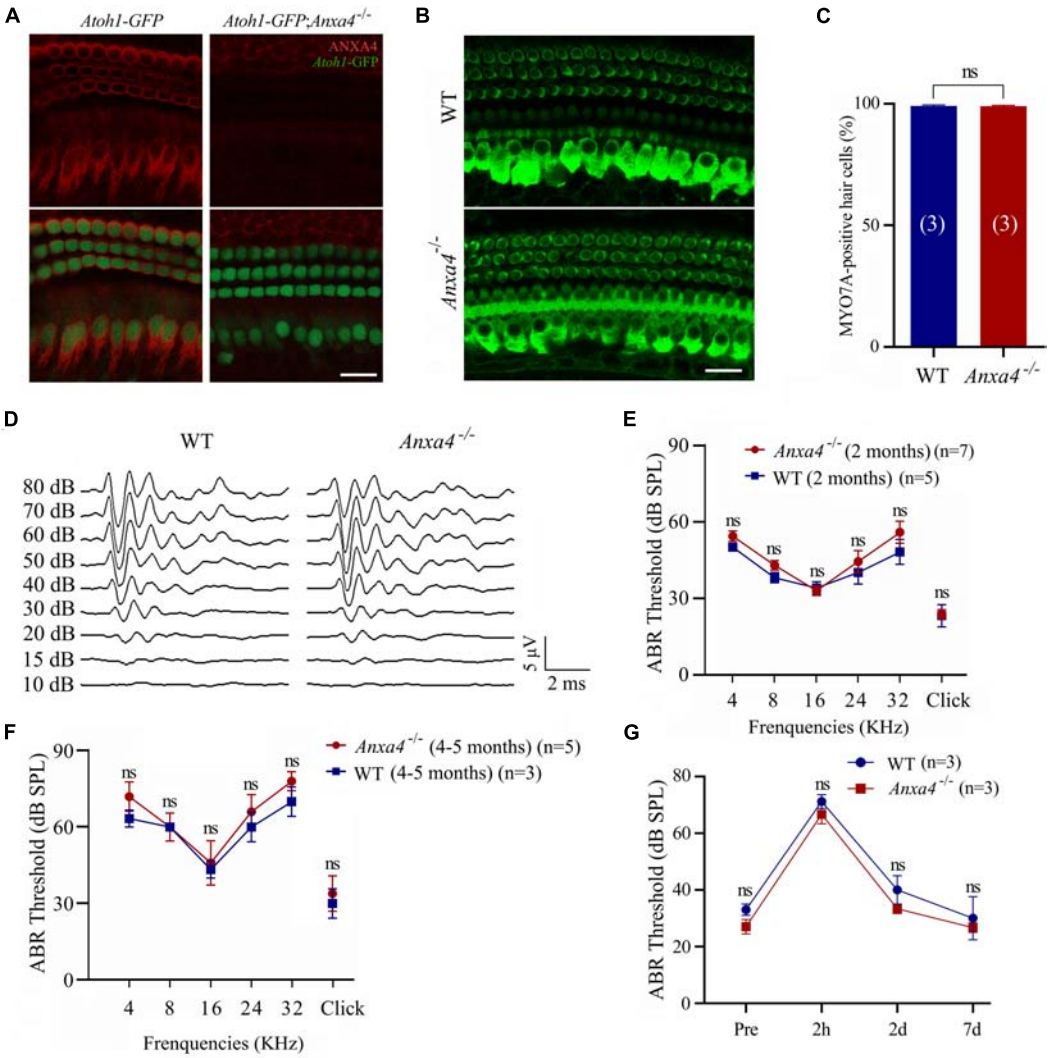


**FIGURE 2 |** Cochlear hair cells and auditory function are unaffected in *Anxa4*$^{-/-}$ mice. **(A)** Cochlear hair cells of P7 *Atoh1-GFP* or *Atoh1-GFP*; *Anxa4*$^{-/-}$ mice were stained with anti-ANXA4 antibody (R&D Systems) and imaged using confocal microscope. Hair cells were labeled by nuclear GFP. **(B)** Cochlear hair cells of P60 wild type or *Anxa4*$^{-/-}$ mice were stained with anti-MYO7A antibody and imaged using confocal microscope. Shown are images taken from the middle turn. **(C)** Numbers of MYO7A-positive hair cells from different genotypes as indicated were calculated according to the results from **(B)**. **(D)** Raw traces of ABR responses to click stimuli in 2-month-old wild type or *Anxa4*$^{-/-}$ mice. **(E)** The ABR thresholds for pure tone and click stimuli in 2-month-old wild type or *Anxa4*$^{-/-}$ mice. **(F)** The ABR thresholds for pure tone and click stimuli in 4–5-month-old wild type or *Anxa4*$^{-/-}$ mice. **(G)** Two-month-old wild type or *Anxa4*$^{-/-}$ mice were subjected to 2–20 kHz noise at 110 dB DSL for 2 hours, and ABR thresholds were measured pre-exposure and at different post-exposure time points as indicated. The numbers of animals used in each experiments are indicated in brackets. Scale bars, 20 μm in **(A,B)**. ns, not significant.

the MET channels when applied briefly, hence is used as an indicator of MET function of hair cells (Gale et al., 2001; Meyers et al., 2003). Consistent with the normal stereocilia morphology, FM1-43FX uptake is normal in neonatal *Anxa4*$^{-/-}$ cochlear hair cells, suggesting that MET is unaffected by *Anxa4* disruption (**Figure 1D**).

## Cochlear Hair Cells and Auditory Function Are Unaffected in *Anxa4* Knockout Mice

To facilitate examination of the inner ear hair cells, we crossed *Anxa4* knockout mice with *Atoh1-GFP* transgenic mice that express a nuclear GFP driven by *Atoh1* enhancer (Lumpkin et al., 2003). As previously reported, GFP strongly labels the nuclei of cochlear hair cells in this transgenic line (**Figure 2A**). Immunostaining shows robust ANXA4 immunoreactivity on the plasma membrane of IHCs and OHCs in *Atoh1-GFP* mice but not *Atoh1-GFP*; *Anxa4*$^{-/-}$ mice at P7 (**Figure 2A**). However, no loss of GFP-positive cochlear hair cells is observed in *Atoh1-GFP*; *Anxa4*$^{-/-}$ mice at this age (**Figure 2A**). Cochlear hair cells were further examined in 2-month-old mice by immunostaining of Myosin 7A (MYO7A), a hair cell marker, which again does not reveal any hair cell loss in *Anxa4*$^{-/-}$ mice (**Figures 2B,C**). Taken together, our present data suggest that the development

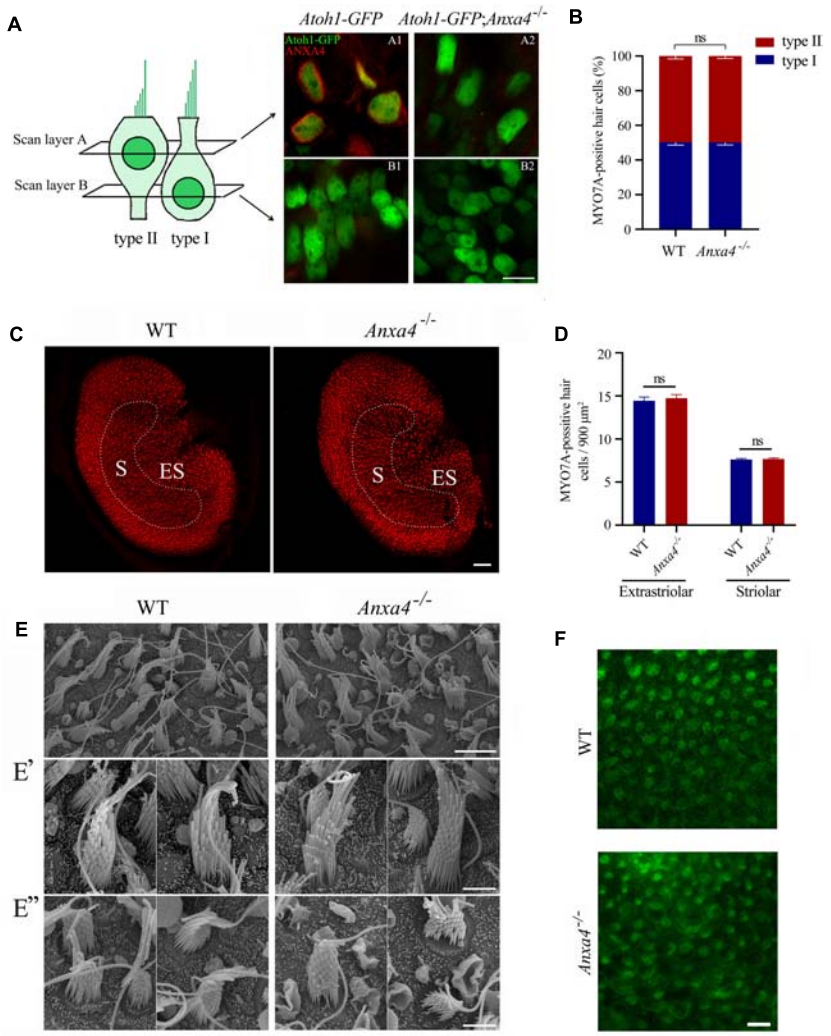


**FIGURE 3 |** VHCs are unaffected in *Anxa4*$^{-/-}$ mice. **(A)** VHCs in the utricle of P60 *Atoh1-GFP* or *Atoh1-GFP*; *Anxa4*$^{-/-}$ mice were stained with anti-ANXA4 antibody (R&D Systems). Hair cells were labeled by nuclear GFP. Confocal microscopy images were taken at different levels as indicated. **(B)** VHCs in the utricle of P60 wild type or *Anxa4*$^{-/-}$ mice were stained with anti-MYO7A antibody, and numbers of type I and type II MYO7A-positive VHCs were calculated. **(C)** VHCs in the utricle of P60 wild type or *Anxa4*$^{-/-}$ mice were stained with TRITC-conjugated phalloidin and imaged with confocal microscope. **(D)** Numbers of striolar or extrastriolar phalloidin-positive VHCs were calculated according to the results from **(C)**. **(E)** Examination of utricle hair bundles of P60 wild type or *Anxa4*$^{-/-}$ mice using SEM. **(E',E")** Higher resolution SEM images of type I and type II VHCs, respectively. **(F)** FM1-43FX uptake by VHCs of utricle in P7 wild type or *Anxa4*$^{-/-}$ mice was examined using confocal microscope. The numbers of animals used in each groups in **(B,D)** are 3. Scale bars, 10 μm in **(A,F)**, 5 μm in **(E)**, 2 μm in **(E',E")**, 50 μm in **(C)**. ns, not significant.

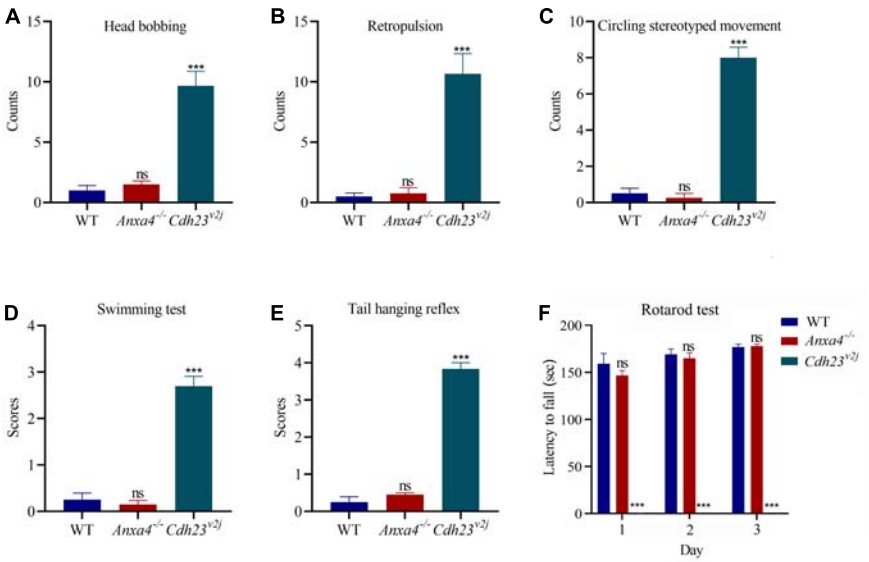


**FIGURE 4 |** Vestibular function is unaffected in *Anxa4*$^{-/-}$ mice. The vestibular function of 2-month-old *Anxa4*$^{-/-}$ and wild type mice ($n$ = 4) was evaluated by performing **(A)** head bobbing, **(B)** retropulsion, **(C)** circling stereotyped movement, **(D)** swimming, **(E)** tail hanging reflex, and **(F)** rotarod test. Five-month-old *Cdh23* mutant mice ($V^{2J}$) ($n$ = 3) were included as positive control. ns, not significant; ***$P$ < 0.001.

and maintenance of cochlear hair cells are unaffected in *Anxa4*$^{-/-}$ mice.

The auditory function of *Anxa4*$^{-/-}$ mice was then evaluated by performing auditory brainstem response (ABR) measurements. No significant differences in ABR thresholds to either click or pure-tune stimuli were found between 2-month-old wild type and *Anxa4*$^{-/-}$ mice (**Figures 2D,E**). Similar results were obtained in *Anxa4*$^{-/-}$ mice up to age of 5 months (**Figure 2F**). To investigate whether *Anxa4*$^{-/-}$ mice show increased acoustic vulnerability, we exposed 2-month-old mice to 2–20 kHz noise at 110 dB SPL for 2 hours. ABR thresholds were measured before and after the noise exposure, which does not reveal any significant difference between wild type and *Anxa4*$^{-/-}$ mice (**Figure 2G**). Taken together, our data suggest that the auditory function is not affected in *Anxa4*$^{-/-}$ mice.

## VHCs and Vestibular Function Are Unaffected in *Anxa4* Knockout Mice

Mammalian VHCs are divided into type I and type II according to their morphology, physiology and innervation patterns (Eatock et al., 1998; Deans, 2013). Morphologically, type I VHCs have flask-shaped cell bodies with nuclei above the supporting cell nuclei, whereas type II VHCs have cylindrical, goblet-like, or dumb-bell shaped cell bodies with nuclei close to the lumen (Pujol et al., 2014). Moreover, the stereocilia of type II VHCs are shorter than that of type I (Li et al., 2008). ANXA4 has been reported to be specifically expressed in type II VHCs (McInturff et al., 2018). By performing whole-mount immunostaining, we confirm that ANXA4 is expressed on the plasma membrane of type II VHCs in neonatal *Atoh1-GFP* mice but not *Atoh1-GFP*; *Anxa4*$^{-/-}$ mice (**Figure 3A**). However, the numbers of either VHC type are largely unaffected in *Atoh1-GFP*; *Anxa4*$^{-/-}$ mice (**Figure 3A**). Immunostaining using anti-MYO7A antibody and phalloidin staining further confirms that the percentage of different VHC types as well as the density of VHCs are not significantly different between wild type and *Anxa4*$^{-/-}$ mice at P60 (**Figures 3B–D**), suggesting that VHC development and maintenance is not affected by *Anxa4* disruption.

SEM was then employed to examine the morphology of VHC hair bundles of adult *Anxa4*$^{-/-}$ mice. The results show that in the utricle of P60 *Anxa4*$^{-/-}$ mice, hair bundles are morphologically normal compared with that of wild type mice (**Figures 3E–E**”). Furthermore, FM1-43FX uptake results show that MET function remains normal in *Anxa4*$^{-/-}$ VHCs (**Figure 3F**).

The vestibular function of *Anxa4*$^{-/-}$ mice was evaluated by performing a series of examinations including head bobbing, retropulsion, circling stereotyped movement, swimming, tail hanging reflex, and rotarod test. *Cdh23* mutant mice ($V^{2J}$) have been reported to show profound vestibular abnormalities (Di Palma et al., 2001), hence were included as a control to confirm the validity of the tests. The results do not reveal any significant difference between 2-month-old *Anxa4*$^{-/-}$ mice and wild type mice, suggesting that the vestibular function of *Anxa4*$^{-/-}$ mice is normal (**Figures 4A–F**).

## Other Annexin Family Members Are Expressed in Mouse Inner Ear

So far, our data show that ANXA4 is specifically expressed in inner ear hair cells, and is dispensable for hair cell development and function. ANXA4 belongs to the annexin protein family, which consists of 12 proteins (ANXA1-11, ANXA13) in vertebrates (Moss and Morgan, 2004). We wonder whether the lack of phenotype in *Anxa4*$^{-/-}$ mice is because of the expression

of other annexins in the hair cells. RT-PCR was then performed to examine the expression of annexin family members, which shows that *Anxa1*, *Anxa2*, *Anxa5*, *Anxa6*, and *Anxa7* are all expressed in the inner ear of wild type mice (**Supplementary Figure 3A**). However, the expression of these annexin genes are not altered in *Anxa4*$^{-/-}$ mice, which is further confirmed by qPCR (**Supplementary Figures 3A,B**).

## DISCUSSION

*Anxa4* has been shown to be specifically expressed in the cochlear and vestibular hair cells, suggesting that it might play an important role in the development and/or function of hair cells (Cai et al., 2015; McInturff et al., 2018). In the present work, we established *Anxa4* knockout mice to explore the role of ANXA4 in hair cells. Exon 3-6 of *Anxa4* gene is deleted in the knockout mice, which will disrupt the expression of ANXA4 protein. Furthermore, RT-PCR results reveal that this deletion results in degradation of *Anxa4* mRNA. Western blot and immunostaining using two different anti-ANXA4 antibodies confirm that ANXA4 protein is not present in the homozygous knockout mice.

Unexpectedly, our present data show that *Anxa4* gene disruption does not affect hair cell development and function. The morphology and MET function of both cochlear and vestibular hair cells are largely normal in *Anxa4* knockout mice. As a result, no abnormalities are detected by standard auditory and vestibular function tests in *Anxa4* knockout mice. One possibility is that ANXA4 is required for the function of hair cells under some specific conditions that are not examined in our present study. Alternatively, the function of ANXA4 might be compensated or substituted by other proteins such as other annexins.

Among all the annexin members, ANXA4 and Annexin A5 (ANXA5) are evolutionally closest to each other, and differ from most of the other annexins in their self-assembly ability on membranes with negatively charged phospholipids as well as the membrane curvature they induce (Concha et al., 1992; Kaetzel et al., 2001; Bouter et al., 2011; Crosby et al., 2013; Boye et al., 2018). ANXA5 has recently been shown to be highly expressed in the stereocilia as well as cell body of hair cells (Krey et al., 2016). Interestingly, similar to *Anxa4*$^{-/-}$ mice, *Anxa5*$^{-/-}$ mice are viable, fertile, and do not show any auditory and vestibular deficits (Brachvogel et al., 2003; Krey et al., 2016). No upregulation of *Anxa5* or *Anxa4* were detected in *Anxa4*$^{-/-}$ or *Anxa5*$^{-/-}$ mice, respectively, suggesting that there is no compensation between these two genes (Krey et al., 2016) (and the present study). However, this does not rule out the possibility of functional redundancy between ANXA4 and ANXA5 in the hair cells. Analysis of *Anxa4* and *Anxa5* double knockout mice will certainly help to address this question.

Interestingly, our present data show that ANXA4 is enriched at the tips of stereocilia besides localizing on the plasma membrane in cochlear hair cells. Similar stereocilia localization has also been reported for ANXA5 (Krey et al., 2016). The underlying mechanism of their transportation and function at the tips of stereocilia remain elusive. In the intestine, annexin A13 (ANXA13) is localized at the tips of microvilli, the actin-based cell protrusions similar to stereocilia (McCulloch et al., 2019). The function of ANXA13 at the tips of microvilli is still unknown, but this localization is consistent with a possible role in lumenal vesicle formation (McConnell et al., 2009). Identification of ANXA4/5-binding partners in the stereocilia as well as examination of the stereocilia phenotypes of *Anax4*/*Anxa5* double knockout mice will help us to learn more about their roles in the stereocilia.

## DATA AVAILABILITY STATEMENT

The original contributions presented in the study are included in the article/**Supplementary Material**, further inquiries can be directed to the corresponding author/s.

## ETHICS STATEMENT

The animal study was reviewed and approved by the Animal Ethics Committee of Shandong University School of Life Sciences.

## AUTHOR CONTRIBUTIONS

ZX: study concept and design. NL, YX, HD, and HZ: acquisition of data. NL, YX, HD, HZ, and ZX: analysis and interpretation of data. NL and ZX: drafting the manuscript. All the authors contributed to the article and approved the submitted version.

## FUNDING

This work was supported by grants from the National Natural Science Foundation of China (82071051 and 81771001), Major Basic Research Project of Shandong Provincial Natural Science Foundation (ZR2020ZD39), and the Fundamental Research Funds of Shandong University (2018JC025).

## ACKNOWLEDGMENTS

We thank Sen Wang, Xiaomin Zhao, and Haiyan Yu from the core facilities for life and environmental sciences, Shandong University for the technical support in SEM and confocal microscopy.

## SUPPLEMENTARY MATERIAL

The Supplementary Material for this article can be found online at: https://www.frontiersin.org/articles/10.3389/fcell.2021.680155/full#supplementary-material

## REFERENCES


Bermingham, N. A., Hassan, B. A., Price, S. D., Vollrath, M. A., Ben-Arie, N., Eatock, R. A., et al. (1999). Math1: an essential gene for the generation of inner ear hair cells. *Science* 284, 1837–1841. doi: 10.1126/science.284.5421.1837

Beurg, M., Fettiplace, R., Nam, J. H., and Ricci, A. J. (2009). Localization of inner hair cell mechanotransducer channels using high-speed calcium imaging. *Nat. Neurosci.* 12, 553–558. doi: 10.1038/nn.2295

Bouter, A., Gounou, C., Berat, R., Tan, S., Gallois, B., Granier, T., et al. (2011). Annexin-A5 assembled into two-dimensional arrays promotes cell membrane repair. *Nat. Commun.* 2:270. doi: 10.1038/ncomms1270

Boye, T. L., Jeppesen, J. C., Maeda, K., Pezeshkian, W., Solovyeva, V., Nylandsted, J., et al. (2018). Annexins induce curvature on free-edge membranes displaying distinct morphologies. *Sci. Rep.* 8:10309. doi: 10.1038/s41598-018-28481-z

Boye, T. L., Maeda, K., Pezeshkian, W., Sonder, S. L., Haeger, S. C., Gerke, V., et al. (2017). Annexin A4 and A6 induce membrane curvature and constriction during cell membrane repair. *Nat. Commun.* 8:1623. doi: 10.1038/s41467-017-01743-6

Brachvogel, B., Dikschas, J., Moch, H., Welzel, H., von der Mark, K., Hofmann, C., et al. (2003). Annexin A5 is not essential for skeletal development. *Mol. Cell. Biol.* 23, 2907–2913. doi: 10.1128/Mcb.23.8.2907-2913.2003

Cai, T., Jen, H. I., Kang, H., Klisch, T. J., Zoghbi, H. Y., and Groves, A. K. (2015). Characterization of the transcriptome of nascent hair cells and identification of direct targets of the Atoh1 transcription factor. *J. Neurosci.* 35, 5870–5883. doi: 10.1523/JNEUROSCI.5083-14.2015

Concha, N. O., Head, J. F., Kaetzel, M. A., Dedman, J. R., and Seaton, B. A. (1992). Annexin V forms calcium-dependent trimeric units on phospholipid vesicles. *FEBS Lett.* 314, 159–162. doi: 10.1016/0014-5793(92)80964-i

Crosby, K. C., Postma, M., Hink, M. A., Zeelenberg, C. H. C., Adjobo-Hermans, M. J. W., and Gadella, T. W. J. (2013). Quantitative analysis of self-association and mobility of annexin A4 at the plasma membrane. *Biophys. J.* 104, 1875–1885. doi: 10.1016/j.bpj.2013.02.057

Deans, M. R. (2013). A balance of form and function: planar polarity and development of the vestibular maculae. *Semin. Cell. Dev. Biol.* 24, 490–498. doi: 10.1016/j.semcdb.2013.03.001

Di Palma, F., Holme, R. H., Bryda, E. C., Belyantseva, I. A., Pellegrino, R., Kachar, B., et al. (2001). Mutations in Cdh23, encoding a new type of cadherin, cause stereocilia disorganization in waltzer, the mouse model for Usher syndrome type 1D. *Nat. Genet.* 27, 103–107. doi: 10.1038/83660

Du, H., Zou, L., Ren, R., Li, N., Li, J., Wang, Y., et al. (2020). Lack of PDZD7 long isoform disrupts ankle-link complex and causes hearing loss in mice. *FASEB J.* 34, 1136–1149. doi: 10.1096/fj.201901657RR

Eatock, R. A., Rusch, A., Lysakowski, A., and Saeki, M. (1998). Hair cells in mammalian utricles. *Otolaryngol. Head Neck Surg.* 119, 172–181. doi: 10.1016/S0194-5998(98)70052-X

Fasquelle, L., Scott, H. S., Lenoir, M., Wang, J., Rebillard, G., Gaboyard, S., et al. (2011). Tmprss3, a transmembrane serine protease deficient in human DFNB8/10 deafness, is critical for cochlear hair cell survival at the onset of hearing. *J. Biol. Chem.* 286, 17383–17397. doi: 10.1074/jbc.M110.190652

Gale, J. E., Marcotti, W., Kennedy, H. J., Kros, C. J., and Richardson, G. P. (2001). FM1-43 dye behaves as a permeant blocker of the hair-cell mechanotransducer channel. *J. Neurosci.* 21, 7013–7025. doi: 10.1523/jneurosci.21-18-07013.2001

Heinick, A., Husser, X., Himmler, K., Kirchhefer, U., Nunes, F., Schulte, J. S., et al. (2015). Annexin A4 is a novel direct regulator of adenylyl cyclase type 5. *FASEB J.* 29, 3773–3787. doi: 10.1096/fj.14-269837

Hill, W. G., Kaetzel, M. A., Kishore, B. K., Dedman, J. R., and Zeidel, M. L. (2003). Annexin A4 reduces water and proton permeability of model membranes but does not alter aquaporin 2-mediated water transport in isolated endosomes. *J. Gen. Physiol.* 121, 413–425. doi: 10.1085/jgp.200308803

Hudspeth, A. J., and Jacobs, R. (1979). Stereocilia mediate transduction in vertebrate hair cells (auditory system/cilium/vestibular system). *Proc. Natl. Acad. Sci. U.S.A.* 76, 1506–1509. doi: 10.1073/pnas.76.3.1506

Kaetzel, M. A., Chan, H. C., Dubinsky, W. P., Dedman, J. R., and Nelson, D. J. (1994). A role for annexin IV in epithelial cell function. Inhibition of calcium-activated chloride conductance. *J. Biol. Chem.* 269, 5297–5302. doi: 10.1016/s0021-9258(17)37687-1

Kaetzel, M. A., Hazarika, P., and Dedman, J. R. (1989). Differential tissue expression of three 35-kDa annexin calcium-dependent phospholipid-binding proteins. *J. Biol. Chem.* 264, 14463–14470. doi: 10.1016/s0021-9258(18)71701-8

Kaetzel, M. A., Mo, Y. D., Mealy, T. R., Campos, B., Bergsma-Schutter, W., Brisson, A., et al. (2001). Phosphorylation mutants elucidate the mechanism of annexin IV-mediated membrane aggregation. *Biochemistry* 40, 4192–4199. doi: 10.1021/bi002507s

Krey, J. F., Drummond, M., Foster, S., Porsov, E., Vijayakumar, S., Choi, D., et al. (2016). Annexin A5 is the most abundant membrane-associated protein in stereocilia but is dispensable for hair-bundle development and function. *Sci. Rep.* 6:27221. doi: 10.1038/srep27221

Krey, J. F., Scheffer, D. I., Choi, D., Reddy, A., David, L. L., Corey, D. P., et al. (2018). Mass spectrometry quantitation of proteins from small pools of developing auditory and vestibular cells. *Sci. Data* 5:180128. doi: 10.1038/sdata.2018.128

Li, A., Xue, J., and Peterson, E. H. (2008). Architecture of the mouse utricle: macular organization and hair bundle heights. *J. Neurophysiol.* 99, 718–733. doi: 10.1152/jn.00831.2007

Li, B., Dedman, J. R., and Kaetzel, M. A. (2003). Intron disruption of the annexin IV gene reveals novel transcripts. *J. Biol. Chem.* 278, 43276–43283. doi: 10.1074/jbc.M306361200

Lumpkin, E. A., Collisson, T., Parab, P., Omer-Abdalla, A., Haeberle, H., Chen, P., et al. (2003). Math1-driven GFP expression in the developing nervous system of transgenic mice. *Gene Expr. Patterns* 3, 389–395. doi: 10.1016/s1567-133x(03)00089-9

McConnell, R. E., Higginbotham, J. N., Shifrin, D. A., Tabb, D. L., Coffey, R. J., and Tyska, M. J. (2009). The enterocyte microvillus is a vesicle-generating organelle. *J. Cell Biol.* 185, 1285–1298. doi: 10.1083/jcb.200902147

McCulloch, K. M., Yamakawa, I., Shifrin, D. A. Jr., McConnell, R. E., Foegeding, N. J., Singh, P. K., et al. (2019). An alternative N-terminal fold of the intestine-specific annexin A13a induces dimerization and regulates membrane-binding. *J. Biol. Chem.* 294, 3454–3463. doi: 10.1074/jbc.RA118.004571

McInturff, S., Burns, J. C., and Kelley, M. W. (2018). Characterization of spatial and temporal development of Type I and Type II hair cells in the mouse utricle using new cell-type-specific markers. *Biol. Open* 7:bio038083. doi: 10.1242/bio.038083

Meyers, J. R., MacDonald, R. B., Duggan, A., Lenzi, D., Standaert, D. G., Corwin, J. T., et al. (2003). Lighting up the senses: FM1-43 loading of sensory cells through nonselective ion channels. *J. Neurosci.* 23, 4054–4065. doi: 10.1523/jneurosci.23-10-04054.2003

Moss, S. E., and Morgan, R. O. (2004). The annexins. *Genome Biol.* 5:219. doi: 10.1186/gb-2004-5-4-219

Müller, U., and Barr-Gillespie, P. G. (2015). New treatment options for hearing loss. *Nat. Rev. Drug Discov.* 14, 346–365. doi: 10.1038/nrd4533

Nakano, Y., Jahan, I., Bonde, G., Sun, X., Hildebrand, M. S., Engelhardt, J. F., et al. (2012). A mutation in the Srrm4 gene causes alternative splicing defects and deafness in the Bronx waltzer mouse. *PLoS Genet.* 8:e1002966. doi: 10.1371/journal.pgen.1002966

Pujol, R., Pickett, S. B., Nguyen, T. B., and Stone, J. S. (2014). Large basolateral processes on type II hair cells are novel processing units in mammalian vestibular organs. *J. Comp. Neurol.* 522, 3141–3159. doi: 10.1002/cne.23625

Richardson, G. P., de Monvel, J. B., and Petit, C. (2011). How the genetics of deafness illuminates auditory physiology. *Annu. Rev. Physiol.* 73, 311–334. doi: 10.1146/annurev-physiol-012110-142228

Scheffer, D. I., Shen, J., Corey, D. P., and Chen, Z. Y. (2015). Gene expression by mouse inner ear hair cells during development. *J. Neurosci.* 35, 6366–6380. doi: 10.1523/Jneurosci.5126-14.2015

Schwander, M., Kachar, B., and Muller, U. (2010). Review series: the cell biology of hearing. *J. Cell Biol.* 190, 9–20. doi: 10.1083/jcb.201001138

Shen, J., Scheffer, D. I., Kwan, K. Y., and Corey, D. P. (2015). SHIELD: an integrative gene expression database for inner ear research. *Database (Oxford)* 2015:bav071. doi: 10.1093/database/bav071

Woods, C., Montcouquiol, M., and Kelley, M. W. (2004). Math1 regulates development of the sensory epithelium in the mammalian cochlea. *Nat. Neurosci.* 7, 1310–1318. doi: 10.1038/nn1349

Zhang, Y., Wang, Y., Yao, X., Wang, C., Chen, F., Liu, D., et al. (2020). Rbm24a is necessary for hair cell development through regulating mRNA stability in zebrafish. *Front. Cell. Dev. Biol.* 8:604026. doi: 10.3389/fcell.2020.604026

Zheng, J. L., and Gao, W. Q. (2000). Overexpression of Math1 induces robust production of extra hair cells in postnatal rat inner ears. *Nat. Neurosci.* 3, 580–586. doi: 10.1038/75753

Zheng, L., Yuan, H., Zhang, M., Wang, C., Cai, X., Liu, J., et al. (2020). Rbm24 regulates inner-ear-specific alternative splicing and is essential for maintaining auditory and motor coordination. *RNA Biol.* 18, 468–480. doi: 10.1080/15476286.2020.1817265

**Conflict of Interest:** The authors declare that the research was conducted in the absence of any commercial or financial relationships that could be construed as a potential conflict of interest.

*Copyright © 2021 Li, Xi, Du, Zhou and Xu. This is an open-access article distributed under the terms of the Creative Commons Attribution License (CC BY). The use, distribution or reproduction in other forums is permitted, provided the original author(s) and the copyright owner(s) are credited and that the original publication in this journal is cited, in accordance with accepted academic practice. No use, distribution or reproduction is permitted which does not comply with these terms.*

frontiers in Cell and Developmental Biology

ORIGINAL RESEARCH
published: 04 June 2021
doi: 10.3389/fcell.2021.683495

# Targeted Deletion of Loxl3 by Col2a1-Cre Leads to Progressive Hearing Loss

*Ziyi Liu, Xinfeng Bai, Peifeng Wan, Fan Mo, Ge Chen, Jian Zhang* and Jiangang Gao**

*School of Life Science and Key Laboratory of the Ministry of Education for Experimental Teratology, Shandong University, Jinan, China*

Collagens are major constituents of the extracellular matrix (ECM) that play an essential role in the structure of the inner ear and provide elasticity and rigidity when the signals of sound are received and transformed into electrical signals. LOXL3 is a member of the lysyl oxidase (LOX) family that are copper-dependent amine oxidases, generating covalent cross-links to stabilize polymeric elastin and collagen fibers in the ECM. Biallelic missense variant of LOXL3 was found in Stickler syndrome with mild conductive hearing loss. However, available information regarding the specific roles of LOXL3 in auditory function is limited. In this study, we showed that the Col2a1-Cre-mediated ablation of Loxl3 in the inner ear can cause progressive hearing loss, degeneration of hair cells and secondary degeneration of spiral ganglion neurons. The abnormal distribution of type II collagen in the spiral ligament and increased inflammatory responses were also found in *Col2a1–Loxl3*$^{-/-}$ mice. Amino oxidase activity exerts an effect on collagen; thus, Loxl3 deficiency was expected to result in the instability of collagen in the spiral ligament and the basilar membrane, which may interfere with the mechanical properties of the organ of Corti and induce the inflammatory responses that are responsible for the hearing loss. Overall, our findings suggest that Loxl3 may play an essential role in maintaining hearing function.

**Keywords: Loxl3, hearing loss, spiral ligament, extracellular matrix, mouse model**

OPEN ACCESS

***Edited by:***
*Wei Xiong,*
*Tsinghua University, China*

***Reviewed by:***
*Jeremy Duncan,*
*Western Michigan University, United States*
*Shan Sun,*
*Fudan University, China*

****Correspondence:***
*Jian Zhang*
*zhj8226@sdu.edu.cn*
*Jiangang Gao*
*jggao@sdu.edu.cn*

***Specialty section:***
*This article was submitted to Cell Growth and Division, a section of the journal Frontiers in Cell and Developmental Biology*

***Received:*** *21 March 2021*
***Accepted:*** *11 May 2021*
***Published:*** *04 June 2021*

***Citation:***
*Liu Z, Bai X, Wan P, Mo F, Chen G, Zhang J and Gao J (2021) Targeted Deletion of Loxl3 by Col2a1-Cre Leads to Progressive Hearing Loss. Front. Cell Dev. Biol. 9:683495. doi: 10.3389/fcell.2021.683495*

## INTRODUCTION

Collagens are major constituents of the extracellular matrix (ECM) and play an essential role in the structure of the inner ear, providing elasticity, and rigidity when the signals of sound are received and transformed into electrical signals. Several types of collagen have been reported in the inner ear, including types I, II, III, IV, V, IX, and XI (Cosgrove et al., 1996; Tsuprun and Santi, 1997). Among these, type II collagen was expressed in the spiral limbus, tectorial membrane (TM), and basilar membrane and was the most abundant component of the spiral ligament (Thalmann, 1993; Dreiling et al., 2002; Husar-Memmer et al., 2013). Furthermore, the TM is composed mostly of the parallel arrangement of type II collagen bundles and associated with other fibrillar and

nonfibrillar types of collagen, such as Collagen V, IX, and XI (Richardson et al., 1987; Legan et al., 1997; Gavara et al., 2011; Andrade et al., 2016). Both type V collagen and type IV collagen were identified in the strial capillary basement membrane (Cosgrove et al., 1996; Meyer zum Gottesberge and Felix, 2005). More and more mutations of different types of collagen have been identified in both syndromic and non-syndromic hearing loss, such as Stickler syndrome (Vikkula et al., 1995; Richards et al., 1996; Williams et al., 1996), Spondyloepiphyseal dysplasia congenita (Mark et al., 2011; Veeravagu et al., 2013; Xu et al., 2014), Marshall syndrome (Griffith et al., 2000), and Alport syndrome (Mochizuki et al., 1994).

Apart from mutations in genes encoding collagen, a homozygous missense variant in LOXL3 (c.2027G>A, p.Cys676Tyr) was found in two siblings with an autosomal recessive Stickler syndrome, one of the siblings exhibited mild conductive hearing loss (Alzahrani et al., 2015). Stickler syndrome is mostly an autosomal dominant human collagenophathy caused by monoallelic mutations in *COL2A1*, *COL11A2*, or *COL11A1* (Robin et al., 1993). Stickler syndrome is also inherited in an autosomal recessive manner caused by pathogenic variants in *COL9A1*, *COL9A2*, or *COL9A3*. The symptoms of Stickler syndrome include retinal detachment, auditory dysfunction, hypermobile tympanic membrane, and joint laxity (McAlinden et al., 2008; Acke et al., 2012). LOXL3 is a member of the LOX family that are copper-dependent amine oxidases. All the members can catalyze the oxidative deamination of lysine and hydroxylysine residues, generating covalent cross-links to convert soluble collagen and elastin chains into the insoluble form and stabilize polymeric elastin and collagen fibers in the ECM (Lucero and Kagan, 2006). In the amine oxidase assay, LOXL3 presents amine oxidase activity toward different types of collagen (types I, II, III, IV, VI, VIII, and X). Additionally, the amino oxidase activity of LOXL3 could be suppressed by β-aminopropionitrile (β-APN), with the inhibition of the formation of covalent cross-links *in vivo* (Lee and Kim, 2006; Jeong and Kim, 2017). Further studies were performed using several animal models to understand the importance of LOXL3 in development. A zebrafish model with the lack of Loxl3b presented craniofacial defects (van Boxtel et al., 2011). These results were consistent with our previous finding. Our results showed that Loxl3-deficient mice ($Loxl3^{-/-}$) exhibited perinatal lethality and severe craniofacial defects, containing palatal cleft and shortened mandible. Additionally, the $Loxl3^{-/-}$ mice showed abnormalities in the cartilage primordia of the thoracic vertebrae (Zhang et al., 2015). Both craniofacial defects and spinal cord deformities are related to the decrease of mature collagen cross-links. However, thus far, the effect of LOXL3 on auditory function has not been studied.

Considering the amino oxidase activity of LOXL3 on collagen, Loxl3 conditional knockout mice in the inner ear were generated by crossing homozygous floxed-*Loxl3* mice ($Loxl3^{f/f}$) (Zhang et al., 2015) with Col2a1-Cre mice that specifically expressed the Cre recombinase under the Col2a1 promoter (Sakai et al., 2001). In Col2a1-Cre transgenic mice, the Cre recombinase was first detected at E9-E9.5 in the otic vesicle and notochord (Sakai et al., 2001). Using the Col2a1–*Loxl3* conditional knockout mice, we explored the roles of the *Loxl3* gene in the maintenance of auditory function.

# RESULTS

## Col2a1-Cre-Mediated Ablation of the *Loxl3* Gene and *Loxl3* Gene Expression in the Inner Ear

To investigate the role of Loxl3 in inner ear development, Loxl3 conditional knockout mice were generated with the Cre-loxP system. Homozygous mice ($Loxl3^{f/f}$) carrying the floxed *Loxl3* allele were crossed with Col2a1-Cre mice (**Figure 1A**). The genotypes of the pups were identified by PCR (**Figure 1B**). We analyzed the expression pattern of Cre recombinase under Col2a1 using the *Rosa26-tdTomato* reporter mouse strain (Madisen et al., 2010). At P30, immunofluorescence was performed with sections of the cochlea of the Col2a1-Cre and *Rosa26-tdTomato* doubly transgenic mice (**Figures 1C–J**). The Cre recombinase under the Col2a1 promoter was expressed in the most of spiral limbus (white arrow), all types of fibrocytes in spiral ligament (yellow triangle), basilar membrane (white triangle), and hair cells (blue triangle). The Cre recombinase was expressed sparsely in spiral ganglion cells (yellow arrow) and not expressed in stria vascularis completely. The result of immunofluorescence staining showed that Loxl3 had been inactivated in the spiral limbus (white arrow), basilar membrane (white triangle), outer hair cells (blue triangle), and spiral ligament (yellow triangle). Loxl3 was still expressed in TM (red arrow), part of inner hair cells and spiral ganglion cells (yellow arrow) (**Figures 1K–R**).

## Targeted Inactivation of Loxl3 in the Cochlea by Col2a1-Cre Leads to Progressive Hearing Loss and Degeneration of OHCs and IHCs

To assess the hearing function of *Col2a1–*$Loxl3^{-/-}$ mice, auditory brainstem response (ABR) measurements were performed from P30. In broadband click, adult *Col2a1–*$Loxl3^{-/-}$ mice exhibited no obvious difference in the ABR thresholds at P30. Moreover, the ABR thresholds of the *Col2a1–*$Loxl3^{-/-}$ mice were increased at P90 with a sound pressure level (SPL) of averaged 35 dB, whereas the $Loxl3^{f/f}$ mice showed hearing thresholds of 10–20 dB SPL (**Figure 2A**). And the data showed a statistically significant increase in the ABR thresholds of the *Col2a1–*$Loxl3^{-/-}$ mice. At P150, the *Col2a1–*$Loxl3^{-/-}$ mice exhibited variation of ABR thresholds of 30–70 dB SPL, and the average of ABR thresholds for broadband click was significantly elevated to approximately 50 dB compared to 20 dB in $Loxl3^{f/f}$ mice.

The ABR measurements with frequency-specific pure tone stimuli also showed a progressive increase in the ABR thresholds of *Col2a1–*$Loxl3^{-/-}$ mice that were 20–40 dB higher than those in $Loxl3^{f/f}$ mice until P150 (**Figures 2B–D**). The results indicate that the targeted inactivation of Loxl3 under Col2a1-Cre leads to progressive hearing loss.

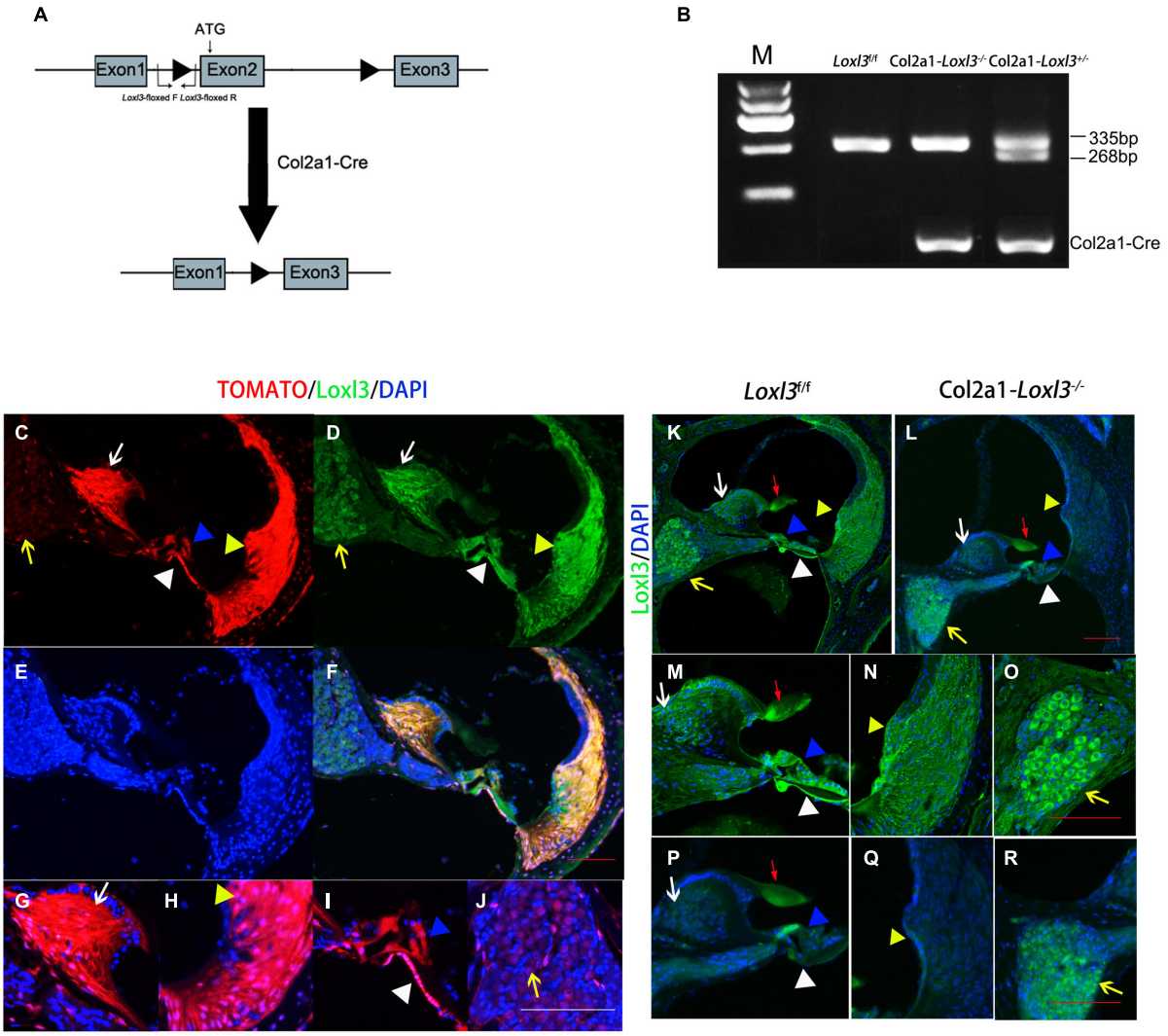


**FIGURE 1 |** Analysis of Cre recombinase expression in the cochlea of Col2a1-Cre transgenic mice and conditional Loxl3 inactivation in the cochlea of the mice. **(A)** Schematic diagram of the mice containing floxed Loxl3 alleles crossed with Col2a1-Cre transgenic mice. The deletion of Loxl3 exon 2 leads to deleted ATG start codon for protein translation. **(B)** Mouse genotyping using PCR analysis. *Lane1* wild-type (*Loxl3*$^{f/f}$) *Lane2* homozygous (Col2a1–*Loxl3*$^{-/-}$) *Lane3* heterozygous (Col2a1–*Loxl3*$^{+/-}$) mice. **(C–F)** The Cre recombinase expression under the Col2a1 promoter and expression pattern of Loxl3 in mouse cochlea. The expression of Loxl3 and Cre recombinase was overlapped in the spiral limbus (white arrow), spiral ligament (yellow triangle), basilar membrane (white triangle), and hair cells (blue triangle) The Cre recombinase was expressed sparsely in spiral ganglion cells (yellow arrow). Scale bars: 100 μm. **(G–J)** The high magnification of the Cre recombinase expression under the Col2a1 promoter. The expression of Col2a1-Cre recombinase was observed in the most cells of spiral limbus (white arrow), all types of fibrocytes in spiral ligament (yellow triangle), basilar membrane (white triangle), and hair cells (blue triangle). The Cre recombinase was expressed sparsely in spiral ganglion cells (yellow arrow) and not expressed in stria vascularis completely. Scale bars: 100 μm. **(K–L)** The targeted inactivation of Loxl3 in Col2a1–*Loxl3*$^{-/-}$ mice. The targeted inactivation of Loxl3 was observed in the spiral limbus (white arrow), spiral ligament (yellow triangle), basilar membrane (white triangle), and hair cells (blue triangle), except spiral ganglion cells (yellow arrow) and tectorial membrane (red arrow). Scale bars: 100 μm. **(M–O)** The high magnification of the Loxl3 expression. The expression of Loxl3 was observed in the spiral limbus (white arrow), basilar membrane (white triangle), hair cells (blue triangle), tectorial membrane (red arrow), spiral ligament (yellow triangle), and spiral ganglion cells (yellow arrow). **(P–R)** The high magnification of the targeted inactivation of Loxl3 in Col2a1–*Loxl3*$^{-/-}$ mice. The targeted inactivation of Loxl3 was observed in the spiral limbus (white arrow), basilar membrane (white triangle), outer hair cells (blue triangle), and spiral ligament (yellow triangle). Loxl3 was still expressed in tectorial membrane (red arrow), part of inner hair cells and spiral ganglion cells (yellow arrow). Scale bars: 100 μm.

To examine the morphology of hair cells in *Col2a1–Loxl3*$^{-/-}$ mice, immunofluorescence assay of cochlear whole mounts was performed and was labeled with phalloidin (green) for stereociliary bundles and Moy7a (red) for hair cell body. Consistent with the results of ABR measurement, few loss of outer hair cells (OHCs) were found at P30 (**Figures 3A–F**) and approximately 19% OHC loss was observed in the cochlea basal turn of *Col2a1–Loxl3*$^{-/-}$ mice at P90 (**Figures 3G–L**). Until P150, significant OHC degeneration was observed in the cochlea basal turn (40%)

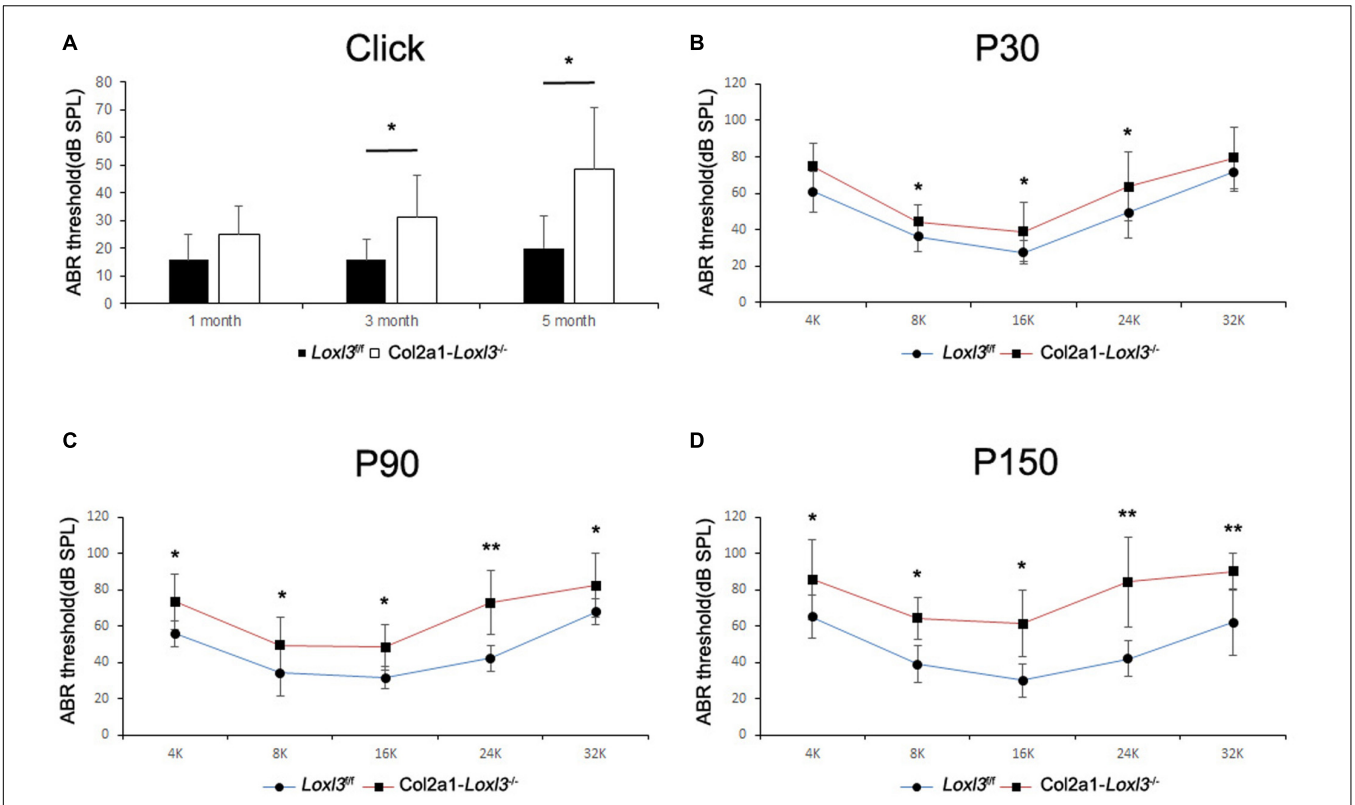


**FIGURE 2 |** ABR analysis between *Loxl3*$^{f/f}$ and *Col2a1–Loxl3*$^{-/-}$ mice. **(A)** ABR thresholds with a broadband click between *Loxl3*$^{f/f}$ and *Col2a1–Loxl3*$^{-/-}$ mice ($n$ = 10). No obvious difference was observed at P30, and the ABR thresholds were increased significantly at P90 and P150, indicating progressive hearing loss. **(B–D)** ABR thresholds with frequency-specific pure tone stimuli (containing 4, 8, 16, 24, and 32 k) ($n$ = 10). The ABR thresholds were increased significantly from P30 to P150. *$p < 0.05$; **$p < 0.01$ by two-tailed Student's $t$ test.

with spotty loss of OHCs in the cochlea middle turn (6%) of *Col2a1–Loxl3*$^{-/-}$ mice (**Figures 3M–R**). The data showed statistically significant differences (**Figure 3S**). And a small amount of IHCs was also absent in the cochlea basal turn (white asterisk).

## Loss of Loxl3 Leads to Impaired Stereocilia of the OHCs and IHCs in the Cochlea

To examine the stereocilia of the IHCs and OHCs, scanning electron micrography was performed from the apical turn to the basal turn of the cochlea. At P30, the shape and arrangement of the stereocilia were normal in the *Col2a1–Loxl3*$^{-/-}$ mice (**Figures 4A,C**), consistent with the results of ABR measurement and immunofluorescence. However, the high magnification of the OHCs in the basal turn of the *Col2a1–Loxl3*$^{-/-}$ mice cochlea showed partly stereocilia fusion (**Figures 4B,D**). Until P150, the stereocilia of the OHCs in the basal turn of the *Col2a1–Loxl3*$^{-/-}$ mice cochlea showed serious impairment and complete fusion, (**Figures 4F,H**) along with loss of OHCs (**Figures 4E,G**). The stereocilia of IHCs in *Col2a1–Loxl3*$^{-/-}$ mice also showed spotty loss (red asterisk). The high magnification of the TM in scanning electron micrograph of *Col2a1–Loxl3*$^{-/-}$ mice showed normal morphology at P150 (**Figures 4I–L**).

## *Col2a1–Loxl3*$^{-/-}$ Mice Showed Progressive Degeneration of SGNs

The morphology of the cochlea in the inner ear was investigated by hematoxylin and eosin (H&E) staining. There was no apparent abnormal cochlear morphology in *Col2a1–Loxl3*$^{-/-}$ mice at P90 (**Figures 5A–H**), even in the spiral limbus and spiral ligament, where the Loxl3 was inactivated at P150 (**Figures 5I–P**). The TM of *Col2a1–Loxl3*$^{-/-}$ mice was also normal at P90 and P150 (**Figures 5H,P**). However, the spiral ganglion neurons (SGNs) of *Col2a1–Loxl3*$^{-/-}$ mice appeared degenerated at P150; this may be due to the loss of OHCs (**Figure 5O**). The immunofluorescence microscopy of Tubulin β3 (Tuj1), a marker for both types I and II SGNs, was performed (**Figures 6A–H**). The SGNs data by the serial sections showed that the density of SGNs decreased significantly in *Col2a1–Loxl3*$^{-/-}$ mice at P150 (**Figure 6I**).

## *Col2a1–Loxl3*$^{-/-}$ Mice Showed Abnormal Distribution of Type II Collagen in Spiral Ligament and Increased Inflammatory Responses

The primary function of Loxl3 is to catalyze the covalent cross-links of collagen, and type II collagen is the most abundant

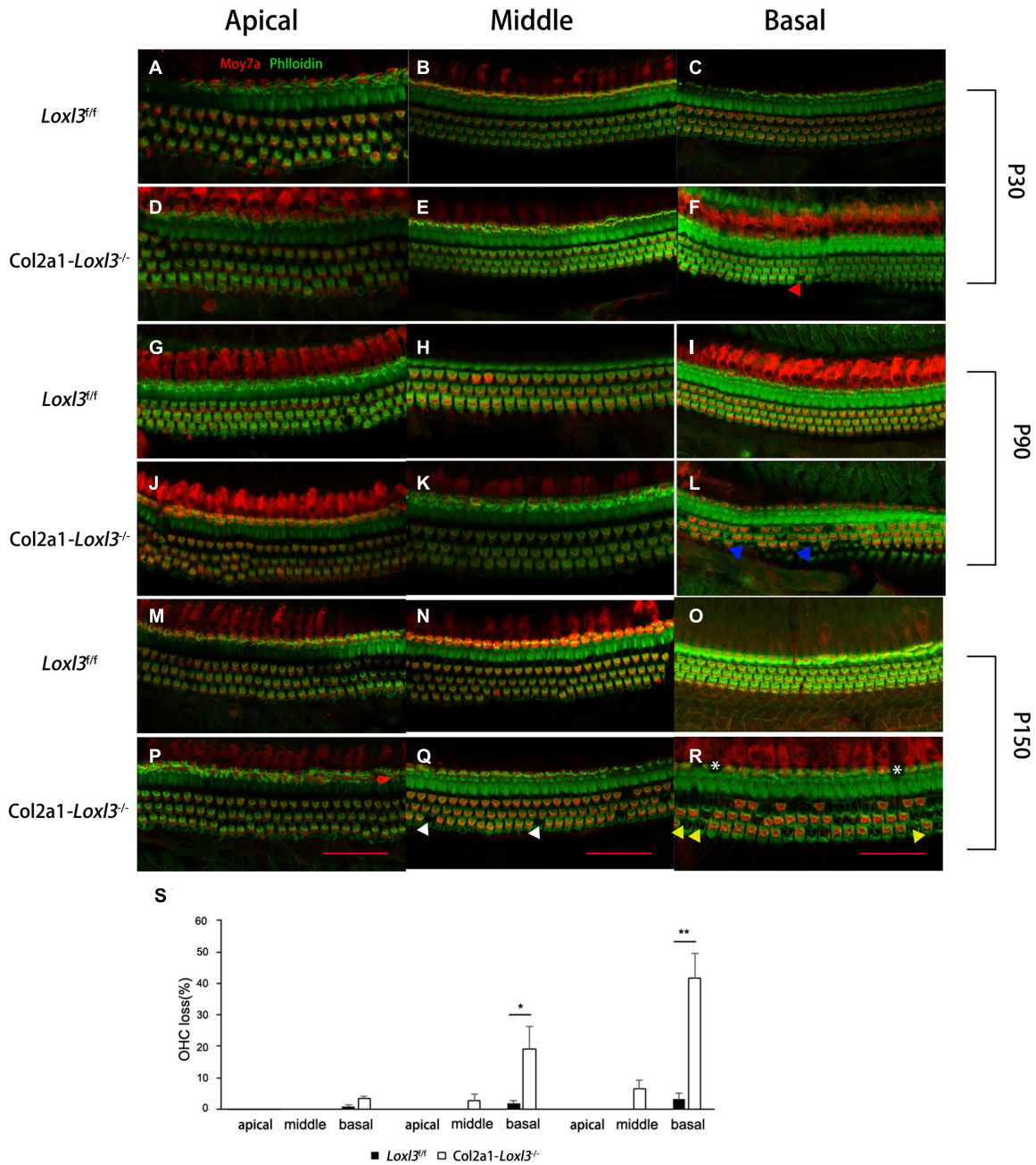


**FIGURE 3 |** Progressive degeneration of OHCs and IHCs in *Col2a1–Loxl3*$^{-/-}$ mice. **(A–F)** Confocal images of cochlea hair cells in *Loxl3*$^{f/f}$ and *Col2a1–Loxl3*$^{-/-}$ mice at P30. Spotty loss of OHCs was observed in the cochlea basal turn (red triangle). **(G–L)** Confocal images of cochlea hair cells in *Loxl3*$^{f/f}$ and *Col2a1–Loxl3*$^{-/-}$ mice at P90. Approximately 19% OHCs loss was observed in the cochlea basal turn. (blue triangle). **(M–R)** Confocal images of cochlea hair cells in *Loxl3*$^{f/f}$ and *Col2a1–Loxl3*$^{-/-}$ mice at P150. Significant OHCs degeneration was observed in the cochlea basal turn (yellow triangle), with spotty loss of OHCs in the cochlea middle turn (white triangle). And a little loss of IHCs was also observed in the cochlea basal turn (white asterisk) Scale bars: 100 μm. OHCs, outer hair cells; IHCs, inner hair cells. **(S)** Quantifications of OHC loss at specific locations of the cochlea in *Loxl3*$^{f/f}$ and *Col2a1–Loxl3*$^{-/-}$ mice ($n = 10$). *$p < 0.05$; **$p < 0.01$ by two-tailed Student's *t* test.

in the whole cochlea (Husar-Memmer et al., 2013). Thus, the distribution of type II collagen was examined in the inner ear. Immunofluorescence staining revealed that the distribution of type II collagen was normal in the TM and spiral limbus of *Col2a1–Loxl3*$^{-/-}$ mice as compared with that in *Loxl3*$^{f/f}$ mice (**Figures 7A,C**). However, the type II collagen fibrils were slightly abnormal in the spiral ligament of *Col2a1–Loxl3*$^{-/-}$ mice than in those of *Loxl3*$^{f/f}$ mice. Sparse and curved type II collagen fibrils were observed (**Figures 7B,D**). Type II collagen plays an essential role in the spiral ligament; thus, the function of the

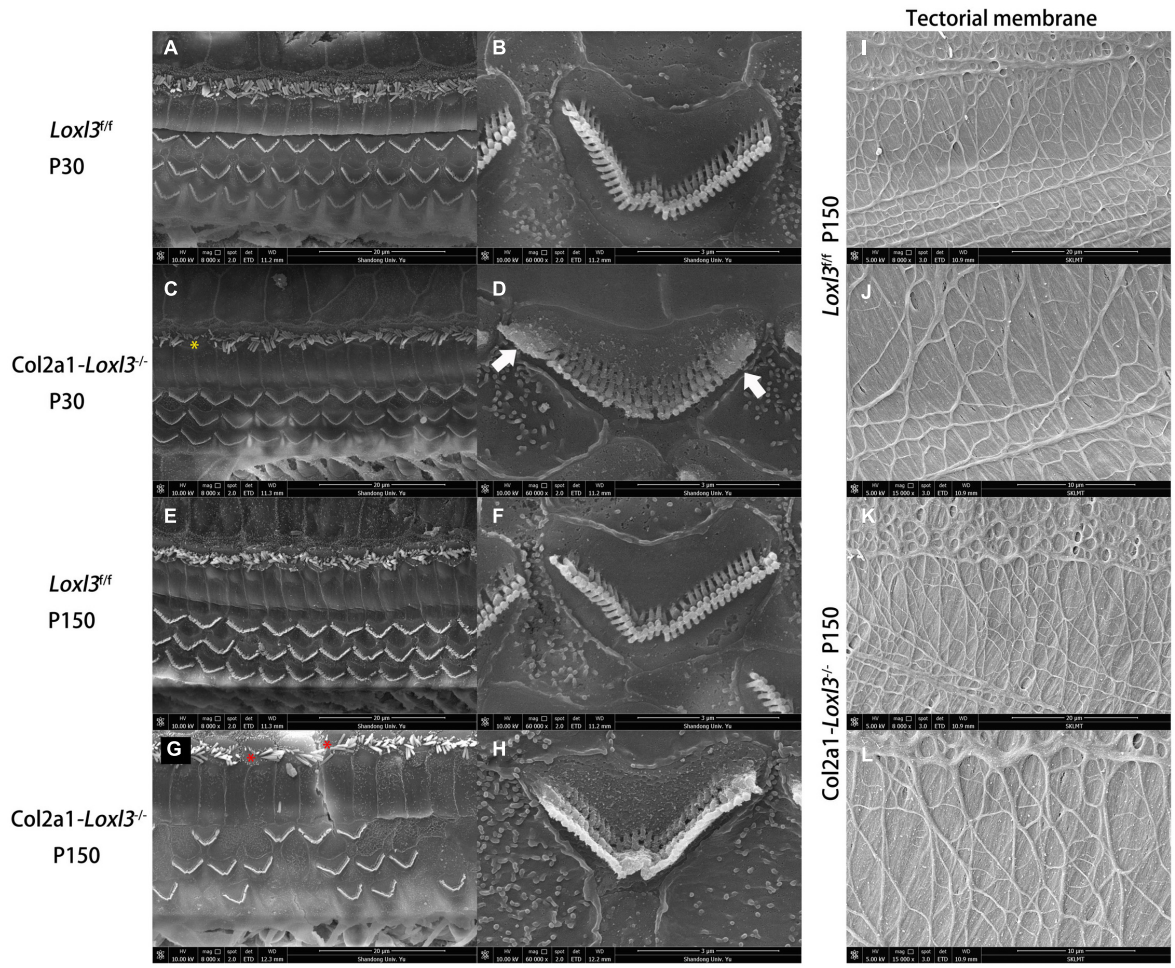


**FIGURE 4 |** The impaired stereocilia of the outer hair cells and inner hair cells and normal tectorial membrane in *Col2a1–Loxl3*$^{-/-}$ mice. **(A–D)** Scanning electron micrograph of hair cell stereocilia in the basal turn of the *Loxl3*$^{f/f}$ and *Col2a1–Loxl3*$^{-/-}$ cochlea at P30. The magnification of the outer hair cells (OHC) in *Col2a1–Loxl3*$^{-/-}$ mice showed partial stereocilia fusion (white arrow). And the stereocilia of inner hair cells in *Col2a1–Loxl3*$^{-/-}$ mice showed spotty loss (yellow asterisk). **(E–H)** Scanning electron micrograph of hair cell stereocilia in the basal turn of the *Loxl3*$^{f/f}$ and *Col2a1–Loxl3*$^{-/-}$ cochlea at P150. The stereocilia of the outer hair cells (OHCs) in *Col2a1–Loxl3*$^{-/-}$ mice showed serious impairment and complete stereocilia fusion, along with loss of OHCs. And the stereocilia of inner hair cells in *Col2a1–Loxl3*$^{-/-}$ mice showed spotty loss (red asterisk). **(I–L)** Scanning electron micrograph of tectorial membrane in the basal turn of the *Loxl3*$^{f/f}$ and *Col2a1–Loxl3*$^{-/-}$ cochlea at P150. The magnification of the tectorial membrane $^{TM}$ in *Col2a1–Loxl3*$^{-/-}$ mice showed normal.

spiral ligament fibrocytes may be affected, which are proposed to be associated with the mediation of inflammatory responses to trauma. To detect the inflammatory responses in the cochlea of *Col2a1–Loxl3*$^{-/-}$ mice and *Loxl3*$^{f/f}$ mice, vascular endothelial growth factor (VEGF), a marker of the inflammatory responses, was analyzed using western blot. The results of western blot analysis showed that the VEGF expression in the cochlea of *Col2a1–Loxl3*$^{-/-}$ mice was significantly higher than in those of *Loxl3*$^{f/f}$ mice at P30–P150, implying the inflammatory responses in the cochlea of *Col2a1–Loxl3*$^{-/-}$ mice (**Figure 7E**).

## DISCUSSION

As demonstrated by the perinatal lethality of the Loxl3-null mice (Zhang et al., 2015), Lox3 plays an critical role in embryonic development. Although a variety novel functions of Loxl3 have been described, the most important biological function of LOXL3 is related to the amino oxidase activity for the crosslinking of collagen.

In this study, we showed that Col2a1-Cre-mediated *Loxl3* ablation in the inner ear can cause progressive hearing loss and degeneration of OHCs and IHCs. At P150, the average of ABR thresholds for broadband click in Col2a1–*Loxl3*$^{-/-}$ mice was significantly elevated to approximately 50 dB compared with 20 dB in *Loxl3*$^{f/f}$ mice. Moreover, no apparent morphologic abnormality was found at the light microscopic level in whole mounts and cross-sections of inner ears. However, the SGNs in *Col2a1–Loxl3*$^{-/-}$ mice appeared degenerated at P150; this may be caused by the loss of OHCs. An irreversible damage to cochlear hair cells is often followed by secondary degeneration of SGNs (Dodson and Mohuiddin, 2000; Xu et al., 2021). The

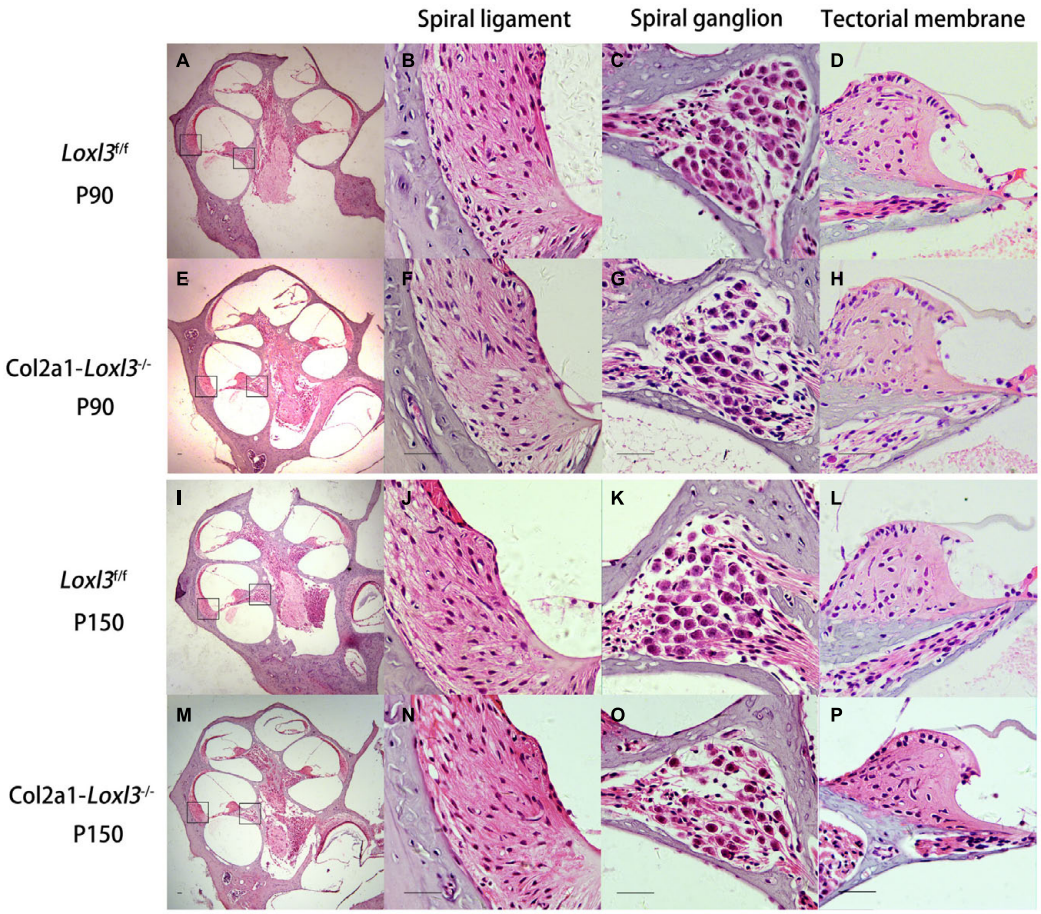


**FIGURE 5 |** Normal cochlear morphology and progressive degeneration of spiral ganglion neurons (SGNs) in *Col2a1–Loxl3*$^{-/-}$ mice. **(A–H)** Hematoxylin and eosin (H&E) staining of sections of *Loxl3*$^{f/f}$ and *Col2a1–Loxl3*$^{-/-}$ mice at P90. No significant abnormality was observed in the spiral ligament, where Loxl3 was conditionally inactivated. **(I–P)** Hematoxylin and eosin staining of sections of *Loxl3*$^{f/f}$ and *Col2a1–Loxl3*$^{-/-}$ mice at P150. The progressive degeneration of the SGNs appeared in the cochlea basal turn of *Col2a1–Loxl3*$^{-/-}$ mice at P150. Scale bars: 200 μm.

degeneration of SGNs usually starts with the loss of synaptic terminals followed by the disintegration of cell bodies (Pan et al., 2011; Shibata et al., 2011).

In the previous study, we crossed the *Loxl3*$^{f/f}$ mice with Atoh1-Cre mice that primarily express the Cre recombinase in hair cells, and the mice with deletion of Loxl3 mediated by Atoh1 promotor did not show hearing loss and degeneration of OHCs (data not shown), suggesting that the precise ablation of Loxl3 in hair cells was not able to affect the function of OHCs. The results of this study showed that the expression of Cre recombinase in Col2a1-Cre transgenic mice overlapped with the expression pattern of Loxl3, including the spiral limbus, basilar membrane, and spiral ligament; hence, the primary function of Loxl3 in the inner ear may be to catalyze the cross-links of collagen. Moreover, the deficiency of Loxl3 was expected to result in collagen instability that leads to the semblable phenotypes in *Col2a1–Loxl3*$^{-/-}$ mice and several mouse models with mutations of collagen, such as progressive hearing loss in type IX collagen knockout mice (Suzuki et al., 2005).

Among the several types of collagen expressed in the inner ear, type II collagen is the most abundant throughout the cochlea; it is encoded by Col2a1 and comprises three identical alpha-1(II) chains (Husar-Memmer et al., 2013). The results of Type II collagen immunofluorescence showed that the deposition of type II collagen was basically in the TM, spiral limbus and spiral ligament. The type II collagen fibrils were regular in the TM and spiral limbus, consistent with the results of H&E staining. However, the type II collagen fibrils were sparse and curved in the spiral ligament of *Col2a1–Loxl3*$^{-/-}$ mice compared with those in *Loxl3*$^{f/f}$ mice. Type II collagen is produced by spiral ligament fibrocytes, and the abnormal staining could be a sign of pathology (Tsuprun and Santi, 1999; Buckiova et al., 2006). Type II collagen is also the main component of the spiral ligament where collagen fibrils provide stability and strength to the ECM and maintain the integrity of the ion transport systems (Spicer and Schulte, 1991). As shown by the results, the expression of Loxl3 was basically deleted in the spiral ligament; which might affect the crosslink of collagen and led to abnormal type II collagen fibrils. Then the function of spiral ligament was affected.

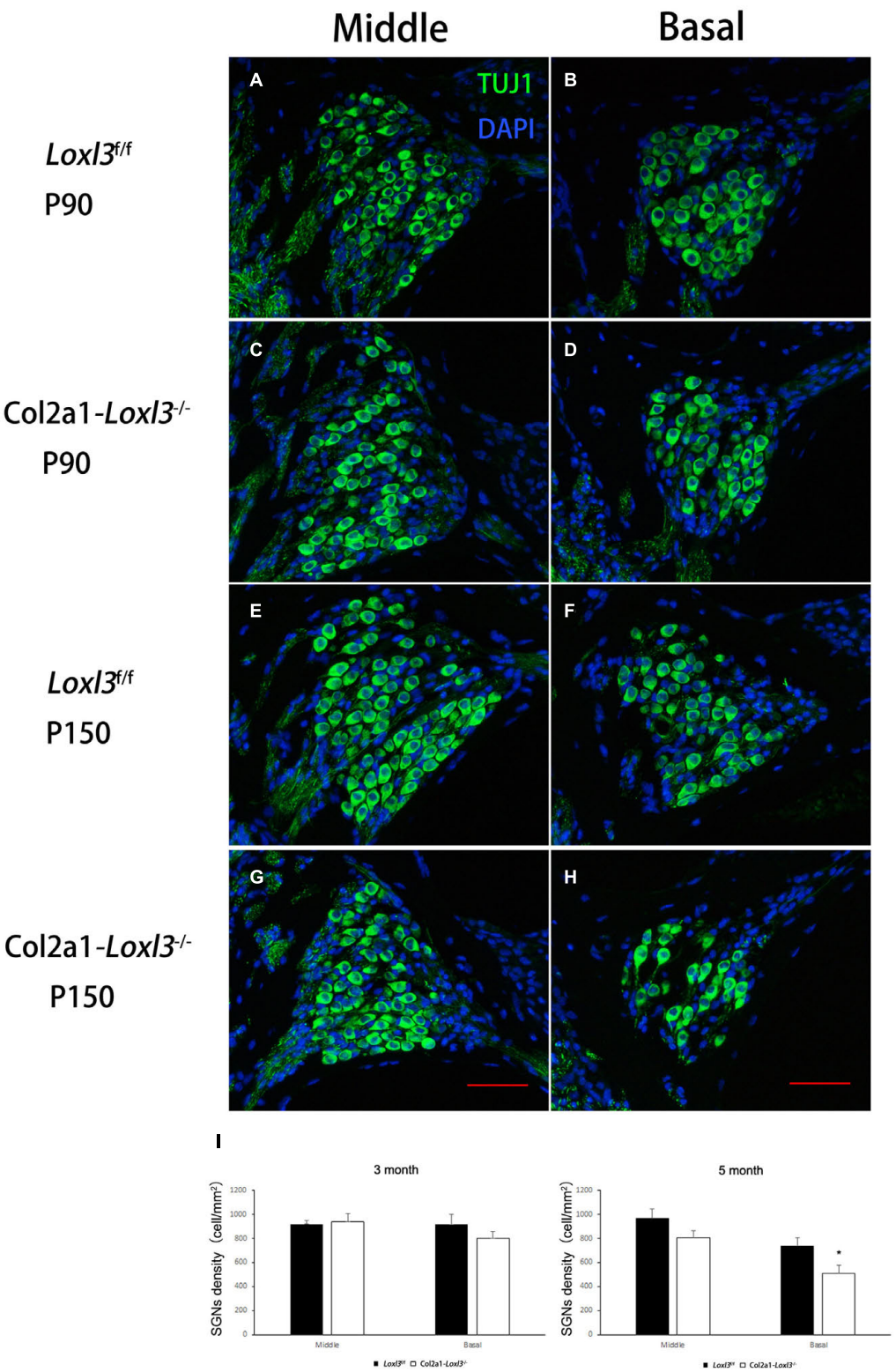


**FIGURE 6 |** Images of SGNs in *Loxl3*$^{f/f}$ and *Col2a1–Loxl3*$^{-/-}$ mice. **(A–D)** Representative image of Tuj1 (green) immunofluorescence in the spiral ganglion cells of *Loxl3*$^{f/f}$ and *Col2a1–Loxl3*$^{-/-}$ mice at P90. Tuj1 is a marker of types I and II neurons; no significant difference was observed between the *Col2a1–Loxl3*$^{-/-}$ and *Loxl3*$^{f/f}$ mice. **(E–H)** Representative image of Tuj1 (green) immunofluorescence in the spiral ganglion cells of *Loxl3*$^{f/f}$ and *Col2a1–Loxl3*$^{-/-}$ mice at P150. Scale bars: 100 μm. **(I)** Counting of the SGNs in the serial sections showed a significant decrease in the density of the SGNs in *Col2a1–Loxl3*$^{-/-}$ mice at P150 ($n = 5$). *$p < 0.05$ by two-tailed Student's $t$ test.

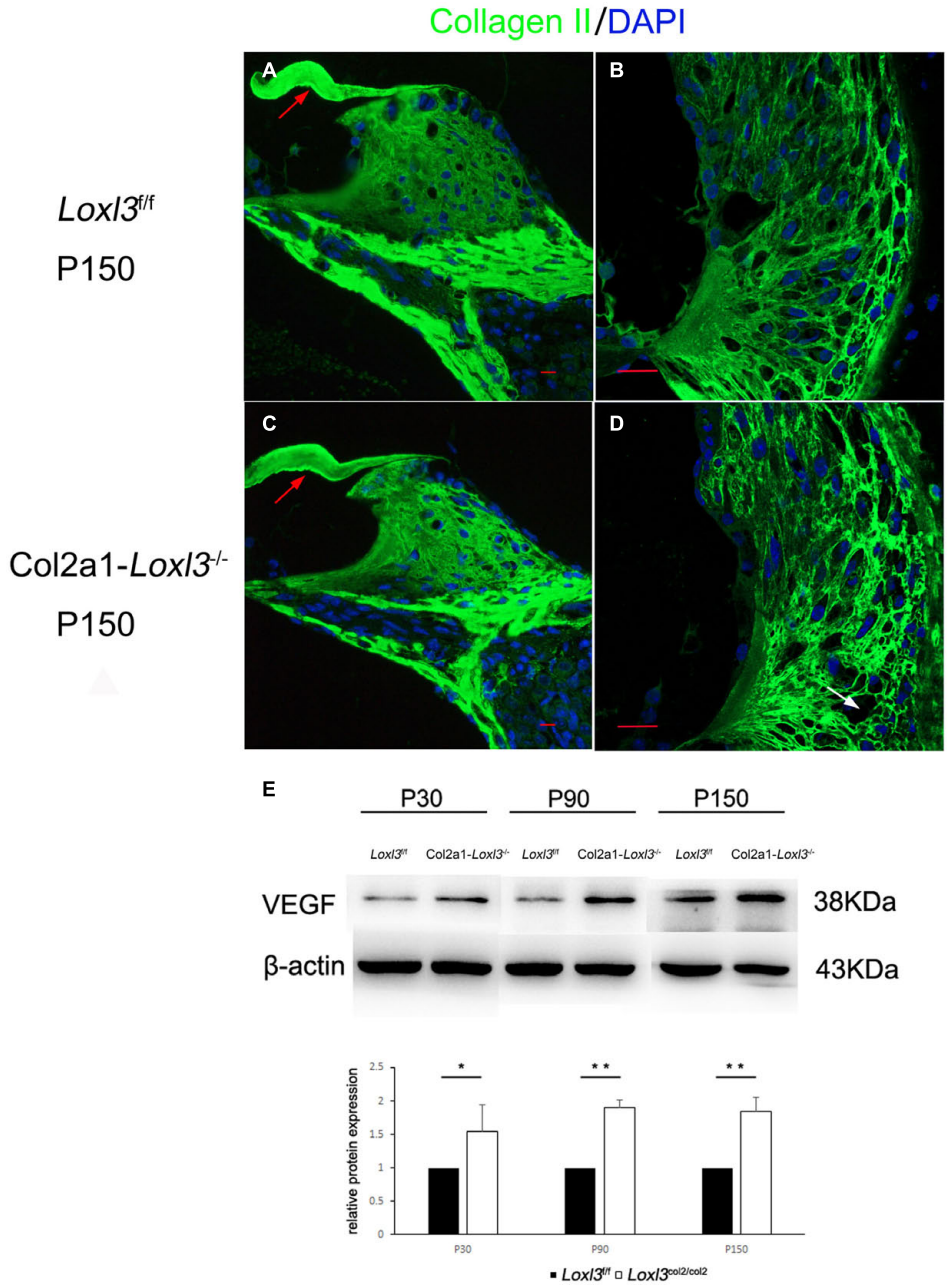


**FIGURE 7 |** Distribution of Type II collagen in the spiral ligament and the expression of vascular endothelial growth factor (VEGF) in the cochlea of *Loxl3*$^{f/f}$ and *Col2a1–Loxl3*$^{-/-}$ mice. **(A,C)** Representative image of type II collagen (green) immunofluorescence in the spiral limbus and the tectorial membrane of *Loxl3*$^{f/f}$ and *Col2a1–Loxl3*$^{-/-}$ mice at P150. The deposition of type II collagen was normal in the tectorial membrane of *Col2a1–Loxl3*$^{-/-}$ mice than in those of *Loxl3*$^{f/f}$ mice (red arrow). **(B,D)** Representative image of type II collagen (green) immunofluorescence in the spiral ligament of *Loxl3*$^{f/f}$ and *Col2a1–Loxl3*$^{-/-}$mice at P150. The deposition of type II collagen was slightly abnormal in the spiral ligament of *Col2a1–Loxl3*$^{-/-}$ mice than in those of *Loxl3*$^{f/f}$ mice (white arrow). Scale bars: 20 μm. **(E)** Western blot analysis of VEGF expression in the cochlea of *Col2a1–Loxl3*$^{-/-}$ and *Loxl3*$^{f/f}$ mice at P30–P150. The results of western blot analysis showed that the VEGF expression was significantly increased in the cochlea of *Col2a1–Loxl3*$^{-/-}$ mice than in those of *Loxl3*$^{f/f}$ mice at P30–P150 ($n = 5$; $^{*}p < 0.05$; $^{**}p < 0.01$).

Western blot analysis showed that the VEGF expression was significantly increased in the cochlea of *Col2a1–Loxl3*$^{-/-}$ mice than in those of *Loxl3*$^{f/f}$ mice at P30–P150. It had been reported that VEGF expression was upregulated at the onset of cochlear noise-induced damage. The VEGF upregulation was observed in the stria vascularis, spiral ligament and spiral ganglion and the expression of VEGF-receptors was normal (Picciotti et al., 2006). Therefore, these pathological phenotypes of *Col2a1–Loxl3*$^{-/-}$ mice were similar to the cochlear damage induced by noise or ototoxic antibiotics (Jiang et al., 2017; Sha and Schacht, 2017).

Moreover, the death of hair cells and SGNs induced by noise or ototoxic antibiotics was mostly associated with macrophage recruitment and cochlear inflammation (Kaur et al., 2018; He et al., 2020). In noise-induced hearing loss, the damage to fibrocytes of the spiral ligament is likely to lead to changes in cytokines or chemokines such as TNF-a, IL-1b, IL-6, and Icam-1 (Fujioka et al., 2006, 2014; Tornabene et al., 2006). The cochlear spiral ligament is a connective tissue that is suggested to play an essential role in the pathophysiology of different etiologies of hearing loss. The spiral ligament is composed of several specialized fibrocytes that are proposed to play different roles in fluid homeostasis, the mediation of inflammatory responses to trauma, and the fine tuning of cochlear mechanics (Hequembourg and Liberman, 2001; Wangemann, 2006; Ohlemiller, 2009). VEGF could induce vascular neogenesis and was produced by spiral ligament fibrocytes stimulated by IL-1L or TNF-K. These inflammatory response mediators together might induce inflammatory cell movement that would prolong the inflammatory response and impair hair cells (Yoshida et al., 1999). Thus, the abnormal type II collagen fibrils caused by inactivated Loxl3 may affect the function of spiral ligament and lead to inflammatory response in inner ear of Col2a1–*Loxl3*$^{-/-}$ mice, resulting in the loss of hair cells and secondary degeneration of SGNs. Then the Col2a1–*Loxl3*$^{-/-}$ mice showed progressive hearing loss.

Type II collagen has also been detected in the basilar membrane, overlapping with the deletion of Loxl3 in *Col2a1–Loxl3*$^{-/-}$ mice. Both sensory hair cells and supporting cells are localized on the basilar membrane; Deiters' and pillar cells are essential for constituting a cochlear amplifier, providing necessary structural support for the hair cells (Cosgrove et al., 1996; Meyer zum Gottesberge and Felix, 2005). It has been discovered that the deficiency of one collagen-binding receptor (DDR1) in mice leads to both the abnormal morphology of the supporting cells and the alteration of OHCs. It is noteworthy that the DDR1-null mice also showed ABR thresholds shift at P60, explaining that the variation in intracellular electron density of Deiters' cells led to the reduced anchorage to the basilar membrane and impairment in OHCs (Meyer zum Gottesberge et al., 2008). In *Col2a1–Loxl3*$^{-/-}$ mice, the structural abnormality of the basilar membrane and Deiters' cells lead to the degeneration of OHCs, and the ultrastructural features of the basilar membrane are expected to be observed in further investigation.

In conclusion, we have demonstrated that Loxl3 plays an essential role in the maintenance of the inner ear function; the results may provide more explanation for the pathology of Stickler syndrome caused by homozygous mutations in LOXL3.

# MATERIALS AND METHODS

## Animals

*Rosa26-tdTomato* (No. 007914) and Col2a1-Cre (No. 003554) mice were obtained from the Jackson Laboratory. Mice homozygous for floxed Loxl3 exon2 were crossed with Col2a1-Cre mice. The following primers were used for mouse genotyping: *Loxl3*-floxed F (5′-CCCTTCCTGTCACA TCCTGT-3′) and *Loxl3*-floxed R (5′-AACAGGCACAGCCCT AGAGA-3′) for the floxed Loxl3 allele and Cre-F (5′-GCATC GACCGGTAATGCAGGC-3′) and Cre-R (5′-AGGGTCCAG CCCGAGCTACTT-3′) for specific Col2a1-Cre.

## Auditory Brainstem Response Measurement

Auditory brainstem response was performed in a soundproof room. The mice were anesthetized with pentobarbital sodium (50 mg/kg body weight) via intraperitoneal injection. Three electrodes were inserted subcutaneously in the mice through the cranial vertex, the external ear, and the back near the tail. Brand click and tone burst stimuli of 4, 8, 16, 24, and 32 kHz were generated, and signals of responses were recorded using a Tucker Davis Technologies (TDT, United States) workstation running SigGen32 software (TDT, United States). The ABR thresholds were determined using the lowest sound intensity at which the first wave could be elicited clearly.

## Immunostaining Analysis

The cochlea was fixed in 4% formaldehyde at 4°C overnight and decalcified in 10% EDTA at room temperature for at least 24 h. For sectioning, the cochleae were dehydrated with 15% sucrose for 2 h and later in 30% sucrose overnight at 4°C. Samples were embedded in Tissue-Tek OCT compound and frozen at −20°C and then sectioned into 9-μm-thick slices. For whole-mount immunostaining, the sensory epithelium in the cochlea was isolated and divided into several parts of apical, middle, and basal turns. Then, the sections or whole cochlea samples were permeabilized with 0.5% Triton X-100 in PBS at room temperature for 15 min, washed in PBS thrice, and then blocked in 10% goat serum in PBS at 374°C for 30 min. The samples were incubated with a primary antibody at 4°C overnight. After washing with PBS, further incubation with a secondary antibody (goat anti-rabbit Alexa-488 or Alexa-568, 1:500; Invitrogen) diluted in PBS at 37°C for 1 h was performed, followed by Alexa Fluor 488-conjugated phalloidin (Sigma-Aldrich, United States) at 37°C for 30 min and DAPI at RT for 5 min. Immunofluorescence images were collected using an LSM 880 confocal microscope (Zeiss). The primary antibodies included rabbit anti-LOXL3 (1:200, American Research Products, United States), rabbit anti-myosin VIIa (1:200, Cell Signaling, United States), and rabbit anti-Tuj1 (1:400, Cell Signaling, United States).

## Scanning Electron Microscopy

The inner ears of the mice were dissected and fixed with 2.5% glutaraldehyde overnight at 4°C and decalcified in 10% EDTA at room temperature for at least 24 h. The sensory epithelium in the cochlea was isolated and post-fixed in 1% osmium tetroxide for 2 h. The samples were dehydrated through a graded ethanol series and critically point dried. The samples were then mounted and sputter-coated with gold. Thereafter, stereociliary bundles

and TM were examined using a Hitachi S-4800 Field Emission scanning electron microscope.

### Histology Analysis

The cochlea samples were fixed and decalcified using a similar procedure as described in the immunostaining assay; then, they were dehydrated with an ethanol series ranging from 30 to 100% and embedded in paraffin to then be sectioned at a thickness of 5 μm and stained using H&E.

### Western Blot

*Loxl3*$^{f/f}$ and *Col2a1–Loxl3*$^{-/-}$ mice were sacrificed via cervical dislocation, and their cochleae were dissected. Cochleae proteins were incubated in cell lysis buffer (P0013, Beyotime) and extracted using a homogenizer. Western blot analyses were performed as described previously (Hou et al., 2014). The following primary antibodies were used: anti-VEGFA polyclonal antibody (rabbit, 1:400, ABclonal) and anti-β-actin polyclonal antibody (rabbit, 1:3,000, Proteintech). All data are presented as mean ± standard error of the mean, and data analyses were performed using the Image J software. Student's *t* test was used for single-factor experiments involving two groups. The significance level was set to $p < 0.05$ for all statistical analyses.

### Statistical Analysis

Data were expressed as the mean ± SD and indicated from at least three independent experiments. Statistical analysis of the data was performed using a two-tailed-distribution Student's *t* test or one-way ANOVA using GraphPad Software. For all tests, a value of $p < 0.05$ was considered to be statistically significant.

## DATA AVAILABILITY STATEMENT

The original contributions presented in the study are included in the article/supplementary material, further inquiries can be directed to the corresponding authors.

## ETHICS STATEMENT

The animal study was reviewed and approved by Ethics Committee of Shandong University. All experimental procedures about animals were approved by Ethics Committee of Shandong University. Animal management was performed strictly in accordance with the standards of the Animal Ethics Committee of Shandong University (Permit Number: ECAESDUSM 20123004).

## AUTHOR CONTRIBUTIONS

ZL: writing–original draft, investigation, software, and writing–review and editing. XB: writing–original draft, investigation, and software. PW, FM and GC: investigation. JZ: funding acquisition and writing–review and editing. JG: writing–review and editing, funding acquisition, supervision, resources, project, and administration. All authors contributed to the article and approved the submitted version.

## FUNDING

This work was supported by grants from the Natural Science Foundation of China (No. 81670943), the National Basic Research Program of China (No. 2014CB541703), the Fundamental Research Fund of Shandong University (Grant No. 2017JC038), the Shandong Provincial Natural Science Foundation of China (Grant No. ZR2017MC028), and the National Key Research and Developmental Program of China (Grant No. 2018YFC1003602-3).

## ACKNOWLEDGMENTS

We thank Sen Wang, Haiyan Yu, Xiaomin Zhao, and Yuyu Guo from State Key Laboratory of Microbial Technology, Shandong University for assistance in microimaging of SEM analysis.

## REFERENCES

Acke, F. R., Dhooge, I. J., Malfait, F., and De Leenheer, E. M. (2012). Hearing impairment in Stickler syndrome: a systematic review. *Orphanet J. Rare Dis.* 7:84. doi: 10.1186/1750-1172-7-84

Alzahrani, F., Al Hazzaa, S. A., Tayeb, H., and Alkuraya, F. S. (2015). LOXL3, encoding lysyl oxidase-like 3, is mutated in a family with autosomal recessive Stickler syndrome. *Hum. Genet.* 134, 451–453. doi: 10.1007/s00439-015-1531-z

Andrade, L. R., Salles, F. T., Grati, M., Manor, U., and Kachar, B. (2016). Tectorins crosslink type II collagen fibrils and connect the tectorial membrane to the spiral limbus. *J. Struct. Biol.* 194, 139–146. doi: 10.1016/j.jsb.2016.01.006

Buckiova, D., Popelar, J., and Syka, J. (2006). Collagen changes in the cochlea of aged Fischer 344 rats. *Exp. Gerontol.* 41, 296–302. doi: 10.1016/j.exger.2005.11.010

Cosgrove, D., Samuelson, G., and Pinnt, J. (1996). Immunohistochemical localization of basement membrane collagens and associated proteins in the murine cochlea. *Hear. Res.* 97, 54–65. doi: 10.1016/s0378-5955(96)80007-4

Dodson, H. C., and Mohuiddin, A. (2000). Response of spiral ganglion neurones to cochlear hair cell destruction in the guinea pig. *J. Neurocytol.* 29, 525–537.

Dreiling, F. J., Henson, M. M., and Henson, O. W. Jr. (2002). The presence and arrangement of type II collagen in the basilar membrane. *Hear. Res.* 166, 166–180. doi: 10.1016/s0378-5955(02)00314-3

Fujioka, M., Kanzaki, S., Okano, H. J., Masuda, M., Ogawa, K., and Okano, H. (2006). Proinflammatory cytokines expression in noise-induced damaged cochlea. *J. Neurosci. Res.* 83, 575–583. doi: 10.1002/jnr.20764

Fujioka, M., Okamoto, Y., Shinden, S., Okano, H. J., Okano, H., Ogawa, K., et al. (2014). Pharmacological inhibition of cochlear mitochondrial respiratory chain induces secondary inflammation in the lateral wall: a potential therapeutic target for sensorineural hearing loss. *PLoS One* 9:e90089. doi: 10.1371/journal.pone.0090089

Gavara, N., Manoussaki, D., and Chadwick, R. S. (2011). Auditory mechanics of the tectorial membrane and the cochlear spiral. *Curr. Opin. Otolaryngol. Head Neck Surg.* 19, 382–387. doi: 10.1097/moo.0b013e32834a5bc9

Griffith, A. J., Gebarski, S. S., Shepard, N. T., and Kileny, P. R. (2000). Audiovestibular phenotype associated with a COL11A1 mutation in Marshall syndrome. *Arch. Otolaryngol. Head Neck Surg.* 126, 891–894. doi: 10.1001/archotol.126.7.891

He, W., Yu, J., Sun, Y., and Kong, W. (2020). Macrophages in noise-exposed cochlea: changes, regulation and the potential role. *Aging Dis.* 11, 191–199. doi: 10.14336/ad.2019.0723

Hequembourg, S., and Liberman, M. C. (2001). Spiral ligament pathology: a major aspect of age-related cochlear degeneration in C57BL/6 mice. *J. Assoc. Res. Otolaryngol.* 2, 118–129. doi: 10.1007/s101620010075

Hou, C., Ding, L., Zhang, J., Jin, Y., Sun, C., Li, Z., et al. (2014). Abnormal cerebellar development and Purkinje cell defects in Lgl1-Pax2 conditional knockout mice. *Dev. Biol.* 395, 167–181. doi: 10.1016/j.ydbio.2014.07.007

Husar-Memmer, E., Ekici, A., Al Kaissi, A., Sticht, H., Manger, B., Schett, G., et al. (2013). Premature osteoarthritis as presenting sign of Type II collagenopathy: a Case report and literature review. *Semin. Arthritis Rheu.* 42, 355–360. doi: 10.1016/j.semarthrit.2012.05.002

Jeong, C., and Kim, Y. (2017). LOXL3-sv2, a novel variant of human lysyl oxidase-like 3 (LOXL3), functions as an amine oxidase. *Int. J. Mol. Med.* 39, 719–724. doi: 10.3892/ijmm.2017.2862

Jiang, M. Y., Karasawa, T., and Steyger, P. S. (2017). Aminoglycoside-induced cochleotoxicity: a review. *Front. Cell Neurosci.* 11:308. doi: 10.3389/fncel.2017.00308

Kaur, T., Ohlemiller, K. K., and Warchol, M. E. (2018). Genetic disruption of fractalkine signaling leads to enhanced loss of cochlear afferents following ototoxic or acoustic injury. *J. Comp. Neurol.* 526, 824–835. doi: 10.1002/cne.24369

Lee, J. E., and Kim, Y. (2006). A tissue-specific variant of the human lysyl oxidase-like protein 3 (LOXL3) functions as an amine oxidase with substrate specificity. *J. Biol. Chem.* 281, 37282–37290. doi: 10.1074/jbc.m600977200

Legan, P. K., Rau, A., Keen, J. N., and Richardson, G. P. (1997). The mouse tectorins. modular matrix proteins of the inner ear homologous to components of the sperm-egg adhesion system. *J. Biol. Chem.* 272, 8791–8801.

Lucero, H. A., and Kagan, H. M. (2006). Lysyl oxidase: an oxidative enzyme and effector of cell function. *Cell Mol. Life Sci.* 63, 2304–2316. doi: 10.1007/s00018-006-6149-9

Madisen, L., Zwingman, T. A., Sunkin, S. M., Oh, S. W., Zariwala, H. A., Gu, H., et al. (2010). A robust and high-throughput Cre reporting and characterization system for the whole mouse brain. *Nat. Neurosci.* 13, 133–140. doi: 10.1038/nn.2467

Mark, P. R., Torres-Martinez, W., Lachman, R. S., and Weaver, D. D. (2011). Association of a p.Pro786Leu variant in COL2A1 with mild spondyloepiphyseal dysplasia congenita in a three-generation family. *Am. J. Med. Genet. A.* 155A, 174–179. doi: 10.1002/ajmg.a.33762

McAlinden, A., Majava, M., Bishop, P. N., Perveen, R., Black, G. C., Pierpont, M. E., et al. (2008). Missense and nonsense mutations in the alternatively-spliced exon 2 of COL2A1 cause the ocular variant of Stickler syndrome. *Hum. Mutat.* 29, 83–90. doi: 10.1002/humu.20603

Meyer zum Gottesberge, A. M., and Felix, H. (2005). Abnormal basement membrane in the inner ear and the kidney of the Mpv17-/- mouse strain: ultrastructural and immunohistochemical investigations. *Histochem. Cell Biol.* 124, 507–516. doi: 10.1007/s00418-005-0027-7

Meyer zum Gottesberge, A. M., Gross, O., Becker-Lendzian, U., Massing, T., and Vogel, W. F. (2008). Inner ear defects and hearing loss in mice lacking the collagen receptor DDR1. *Lab. Invest.* 88, 27–37. doi: 10.1038/labinvest.3700692

Mochizuki, T., Lemmink, H. H., Mariyama, M., Antignac, C., Gubler, M. C., Pirson, Y., et al. (1994). Identification of mutations in the alpha 3(IV) and alpha 4(IV) collagen genes in autosomal recessive Alport syndrome. *Nat. Genet.* 8, 77–81. doi: 10.1038/ng0994-77

Ohlemiller, K. K. (2009). Mechanisms and genes in human strial presbycusis from animal models. *Brain Res.* 1277, 70–83. doi: 10.1016/j.brainres.2009.02.079

Pan, N., Jahan, I., Kersigo, J., Kopecky, B., Santi, P., Johnson, S., et al. (2011). Conditional deletion of Atoh1 using Pax2-Cre results in viable mice without differentiated cochlear hair cells that have lost most of the organ of Corti. *Hear. Res.* 275, 66–80. doi: 10.1016/j.heares.2010.12.002

Picciotti, P. M., Fetoni, A. R., Paludetti, G., Wolf, F. I., Torsello, A., Troiani, D., et al. (2006). Vascular endothelial growth factor (VEGF) expression in noise-induced hearing loss. *Hear. Res.* 214, 76–83. doi: 10.1016/j.heares.2006.02.004

Richards, A. J., Yates, J. R. W., Williams, R., Payne, S. J., Pope, F. M., Scott, J. D., et al. (1996). A family with Stickler syndrome type 2 has a mutation in the COL11A1 gene resulting in the substitution of glycine 97 by valine in alpha 1(XI) collagen. *Hum. Mol. Genet.* 5, 1339–1343. doi: 10.1093/hmg/5.9.1339

Richardson, G. P., Russell, I. J., Duance, V. C., and Bailey, A. J. (1987). Polypeptide composition of the mammalian tectorial membrane. *Hear. Res.* 25, 45–60. doi: 10.1016/0378-5955(87)90078-5

Robin, N. H., Moran, R. T., and Ala-Kokko, L. (1993). "Stickler syndrome," in *GeneReviews [Internet]*, Edn, eds M. P. Adam, H. H. Ardinger, R. A. Pagon, S. E. Wallace, L. J. H. Bean, and K. Stephens et al. (Seattle (WA): University of Washington, Seattle.).

Sakai, K., Hiripi, L., Glumoff, V., Brandau, O., Eerola, R., Vuorio, E., et al. (2001). Stage-and tissue-specific expression of a Col2a1-Cre fusion gene in transgenic mice. *Matrix Biol.* 19, 761–767. doi: 10.1016/s0945-053x(00)00122-0

Sha, S. H., and Schacht, J. (2017). Emerging therapeutic interventions against noise-induced hearing loss. *Expert Opin. Investig. Drugs* 26, 85–96. doi: 10.1080/13543784.2017.1269171

Shibata, S. B., Budenz, C. L., Bowling, S. A., Pfingst, B. E., and Raphael, Y. (2011). Nerve maintenance and regeneration in the damaged cochlea. *Hear. Res.* 281, 56–64. doi: 10.1016/j.heares.2011.04.019

Spicer, S. S., and Schulte, B. A. (1991). Differentiation of inner-ear fibrocytes according to their iron-transport related activity. *Hear. Res.* 56, 53–64. doi: 10.1016/0378-5955(91)90153-z

Suzuki, N., Asamura, K., Kikuchi, Y., Takumi, Y., Abe, S., Imamura, Y., et al. (2005). Type IX collagen knock-out mouse shows progressive hearing loss. *Neurosci. Res.* 51, 293–298. doi: 10.1016/j.neures.2004.12.001

Thalmann, I. (1993). Collagen of accessory structures of organ of Corti. *Connect. Tissue Res.* 29, 191–201. doi: 10.3109/03008209309016826

Tornabene, S. V., Sato, K., Pham, L., Billings, P., and Keithley, E. M. (2006). Immune cell recruitment following acoustic trauma. *Hear. Res.* 222, 115–124. doi: 10.1016/j.heares.2006.09.004

Tsuprun, V., and Santi, P. (1997). Ultrastructural organization of proteoglycans and fibrillar matrix of the tectorial membrane. *Hear. Res.* 110, 107–118. doi: 10.1016/s0378-5955(97)00068-3

Tsuprun, V., and Santi, P. (1999). Ultrastructure and immunohistochemical identification of the extracellular matrix of the chinchilla cochlea. *Hear. Res.* 129, 35–49. doi: 10.1016/s0378-5955(98)00219-6

van Boxtel, A. L., Gansner, J. M., Hakvoort, H. W. J., Snell, H., Legler, J., and Gitlin, J. D. (2011). Lysyl oxidase-like 3b is critical for cartilage maturation during zebrafish craniofacial development. *Matrix Biol.* 30, 178–187. doi: 10.1016/j.matbio.2010.12.002

Veeravagu, A., Lad, S. P., Camara-Quintana, J. Q., Jiang, B., and Shuer, L. (2013). Neurosurgical interventions for spondyloepiphyseal dysplasia congenita: clinical presentation and assessment of the literature. *World Neurosurg.* 80, e1–e8.

Vikkula, M., Mariman, E. C., Lui, V. C., Zhidkova, N. I., Tiller, G. E., Goldring, M. B., et al. (1995). Autosomal dominant and recessive osteochondrodysplasias associated with the COL11A2 locus. *Cell* 80, 431–437. doi: 10.1016/0092-8674(95)90493-x

Wangemann, P. (2006). Supporting sensory transduction: cochlear fluid homeostasis and the endocochlear potential. *J. Physiol.* 576(Pt 1), 11–21. doi: 10.1113/jphysiol.2006.112888

Williams, C. J., Ganguly, A., Considine, E., McCarron, S., Prockop, D. J., Walsh-Vockley, C., et al. (1996). A-2–>G transition at the 3′ acceptor splice site of IVS17 characterizes the COL2A1 gene mutation in the original Stickler syndrome kindred. *Am. J. Med. Genet.* 63, 461–467. doi: 10.1002/(sici)1096-8628(19960614)63:3<461::aid-ajmg9>3.0.co;2-u

Xu, K., Chen, S., Xie, L., Qiu, Y., Bai, X., Liu, X. Z., et al. (2021). Local Macrophage-Related Immune Response Is Involved in Cochlear Epithelial Damage in Distinct Gjb2-Related Hereditary Deafness Models. *Front. Cell Dev. Biol.* 8:597769. doi: 10.3389/fcell.2020.597769

Xu, L., Qiu, X., Zhu, Z., Yi, L., and Qiu, Y. (2014). A novel mutation in COL2A1 leading to spondyloepiphyseal dysplasia congenita in a three-generation family. *Eur. Spine J.* 23(Suppl. 2), 271–277. doi: 10.1007/s00586-014-3292-0

Yoshida, K., Ichimiya, I., Suzuki, M., and Mogi, G. (1999). Effect of proinflammatory cytokines on cultured spiral ligament fibrocytes. *Hear. Res.* 137, 155–159. doi: 10.1016/s0378-5955(99)00134-3

Zhang, J., Yang, R., Liu, Z., Hou, C., Zong, W., Zhang, A., et al. (2015). Loss of lysyl oxidase-like 3 causes cleft palate and spinal deformity in mice. *Hum. Mol. Genet.* 24, 6174–6185. doi: 10.1093/hmg/ddv333

**Conflict of Interest:** The authors declare that the research was conducted in the absence of any commercial or financial relationships that could be construed as a potential conflict of interest.

*Copyright © 2021 Liu, Bai, Wan, Mo, Chen, Zhang and Gao. This is an open-access article distributed under the terms of the Creative Commons Attribution License (CC BY). The use, distribution or reproduction in other forums is permitted, provided the original author(s) and the copyright owner(s) are credited and that the original publication in this journal is cited, in accordance with accepted academic practice. No use, distribution or reproduction is permitted which does not comply with these terms.*

frontiers in Cell and Developmental Biology

MINI REVIEW
published: 05 August 2021
doi: 10.3389/fcell.2021.715037

# The Kinocilia of Cochlear Hair Cells: Structures, Functions, and Diseases

*Difei Wang*[1] *and Jun Zhou*[1,2]*

[1] State Key Laboratory of Medicinal Chemical Biology, College of Life Sciences, Nankai University, Tianjin, China, [2] Shandong Provincial Key Laboratory of Animal Resistance Biology, Collaborative Innovation Center of Cell Biology in Universities of Shandong, Institute of Biomedical Sciences, College of Life Sciences, Shandong Normal University, Jinan, China

Primary cilia are evolutionarily conserved and highly specialized organelles that protrude from cell membranes. Mutations in genes encoding ciliary proteins can cause structural and functional ciliary defects and consequently multiple diseases, collectively termed ciliopathies. The mammalian auditory system is responsible for perceiving external sound stimuli that are ultimately processed in the brain through a series of physical and biochemical reactions. Here we review the structure and function of the specialized primary cilia of hair cells, termed kinocilia, found in the mammalian auditory system. We also discuss areas that might prove amenable for therapeutic management of auditory ciliopathies.

**Keywords: primary cilia, ciliopathy, auditory system, hair cell, kinocilia**

OPEN ACCESS

***Edited by:***
*Zhigang Xu,*
*Shandong University, China*

***Reviewed by:***
*Bo Zhao,*
*Indiana University, United States*
*Katie Kindt,*
*National Institutes of Health (NIH), United States*
*Daisuke Takao,*
*The University of Tokyo, Japan*

****Correspondence:***
*Jun Zhou*
*junzhou@nankai.edu.cn*

***Specialty section:***
*This article was submitted to Cell Growth and Division, a section of the journal Frontiers in Cell and Developmental Biology*

***Received:*** *26 May 2021*
***Accepted:*** *14 July 2021*
***Published:*** *05 August 2021*

***Citation:***
*Wang D and Zhou J (2021) The Kinocilia of Cochlear Hair Cells: Structures, Functions, and Diseases. Front. Cell Dev. Biol. 9:715037. doi: 10.3389/fcell.2021.715037*

## INTRODUCTION

Primary cilia are non-motile, highly specialized, and evolutionarily well-conserved organelles that project from the cell surface, which are essential throughout biological development and maturation. As analytical technologies have developed over the last few decades, our understanding of primary cilia has gradually changed from regarding them neglected "degenerate organelles" to well-appreciated "cellular antennas" (Singla and Reiter, 2006). There is only one primary cilium per cell (Satir and Christensen, 2007). The ciliary membrane of primary cilia harbors a variety of receptors and ion channels, including components of the Notch, Hedgehog, Wnt, G protein-coupled receptor, receptor tyrosine kinase, transforming growth factor β/bone morphogenetic protein signaling pathways, and $Ca^{2+}$ channel-associated proteins such as polycystin 1 and 2 (Delling et al., 2013; Christensen et al., 2017; Anvarian et al., 2019; Ta et al., 2020). Through these cilium-dependent signaling pathways, primary cilia play key roles in the regulation of cell division, proliferation, and signal transduction and are thus crucial in tissue and organ development and normal mammalian physiology (Lancaster and Gleeson, 2009; Goetz and Anderson, 2010; Joukov and De Nicolo, 2019; Nachury and Mick, 2019). Moreover, primary cilia can act as a portal connecting the organism to the environment (Falk et al., 2015; Bujakowska et al., 2017; Uytingco et al., 2019; Ran and Zhou, 2020).

Some primary cilia with specialized structures and functions have been characterized in sensory cells, which can transduce external physical or chemical signals, such as smell and visual signals, to electrical signals in mammalian olfactory and vision systems (Falk et al., 2015). Kinocilia are specialized primary cilia present in auditory hair cells (HCs) in the inner ear. These cilia do not directly mediate auditory mechano-electrical transduction (MET), but partially retain the characteristics of motility responsible for the response of HCs to sound stimuli. Although showing

a traditional 9 + 2 axoneme pattern of "motile cilia," they lack the inner dynein arms and only directionally "move" after the cells sense sound, i.e., passive motion (Kikuchi et al., 1989). Besides, kinocilia are essential for HCs morphogenesis and planar cell polarity (PCP), and further auditory integrity (Sipe and Lu, 2011; Kazmierczak and Muller, 2012; Elliott et al., 2018). Genetic mutations affecting ciliary proteins can lead to diseases in multiple organs, collectively known as ciliopathies. Therefore, maintaining stable morphology and structure of kinocilia is essential to normal physiology and their dysfunction results in corresponding sensory ciliopathies. In this review, we describe the structure, function, and degeneration of kinocilia present in the mammalian auditory system and discuss if they are promising therapeutic targets for hearing deficits.

## COCHLEAR HAIR CELLS

The mammalian ear consists of the outer, middle, and inner ears, the latter consisting of the vestibular system and the cochlea. The former is sensitive to position signals mainly caused by linear acceleration and head rotation, and the latter mediates the conversion of vibrations into nerve impulses in response to sound (Liu et al., 2016). Both of these two systems have their own sensory epithelium, on which exist a large number of HCs that underpin both balance sensation and hearing. In the vestibular system, the sensory epithelium organizes as a repeating mosaic which consists of supporting cells and type I and type II HCs that differ in morphology and physiology (Warchol et al., 2019). However, the cochlea, a structure unique to mammals, has a more delicate sensory epithelium, also known as the organ of Corti.

In the organ of Corti, HCs are categorized as inner hair cells (IHCs) and outer hair cells (OHCs) (**Figure 1**; Atkinson et al., 2015). Every HC is supported by several highly specialized cells, such as Deiters' cells, pillar cells, inner border cells, and Hensen's cells. All of the HCs are highly differentiated and polarized, and each acts as a mechano-electrical transducer that turns physical signals into electrical signals. External sensory stimuli physically open MET channels leading to an influx of $K^+$ ions that depolarizes the HC. HC depolarization activates $Ca^{2+}$ channels at the plasma membrane resulting in neurotransmission onto spiral ganglion neurons via the cochlear nerve. Finally, physical signals turn into electrical signals, which then pass through spiral ganglion neurons via the cochlear nerve, and the sensory signal ultimately reaches the cortex via the auditory pathway (Fettiplace, 2017; Ashmore, 2020). The apical surface of HCs are arranged as a unique subset by a single row of IHCs and a triple row of OHCs, each of which is surrounded by a variety of non-sensory support cells based on their location relative to the spiral ganglion (Elliott et al., 2018; Tarchini and Lu, 2019). The OHCs are located on the lateral (non-neural) side and are mainly responsible for amplifying acoustic vibrations through periodic contraction and elongation of the cell body driven by changes in membrane potential. The IHCs are located on the medial (neural) side, where they integrate and transmit sound signals to neurons. Synergy between these two types of cells greatly improves the resolution and sensitivity of sound signal processing (Fettiplace, 2017).

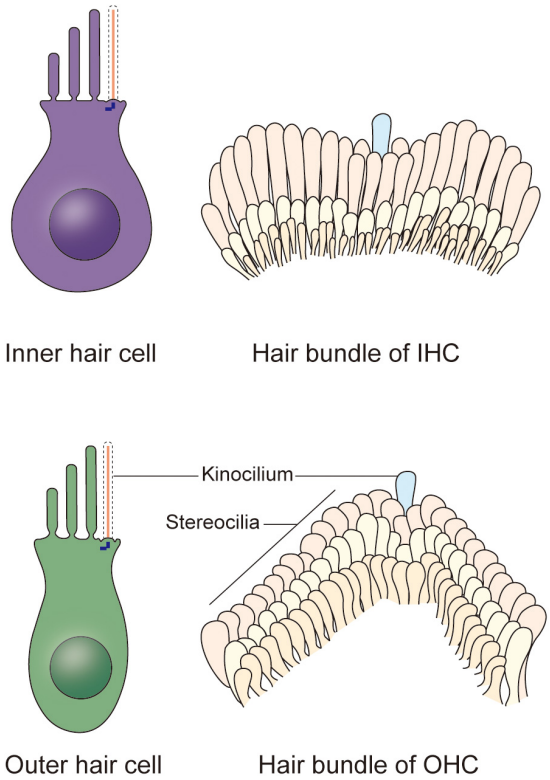


**FIGURE 1 |** Schematic representation of the cochlear hair cells and hair bundles. Two types of hair cells responsible for mechano-electrical transduction and auditory sensing are present in the cochlea. The stair-like W or V-shaped hair bundle appears on the apical plasma membrane of each inner hair cell and outer hair cell, collectively. Each hair bundle contains plenty of stereocilia and a kinocilium near the corner of them, and the kinocilium degenerates after maturation of hair cells, indicating the acquisition of hearing.

## THE KINOCILIA OF COCHLEAR HAIR CELLS

In newborn mice, the top of each HC possesses dozens to hundreds of actin filament-based stereocilia of increasing height arranged in a stepped V or W shape (**Figure 1**). A true microtubule-based cilium that is about the same height as the tallest row of stereocilia, called the kinocilium, is found near the corner of this arrangement, i.e., on the non-neural side (Flock and Duvall, 1965; Sobkowicz et al., 1995). The stereocilia and kinocilium of each HC are collectively termed the hair bundle (**Figure 1**). Adjacent stereocilia are connected by several types of connecting protein including tip links, horizontal top connectors, shaft connectors, and ankle links (Goodyear et al., 2005). Similarly, the kinocilium and adjacent stereocilia are connected by kinocilial links, while in some HCs, the kinocilia are physically separated from stereocilia (Avan et al., 2019). This cilium seems to exhibit a traditional 9 + 2 axoneme pattern in most cases,

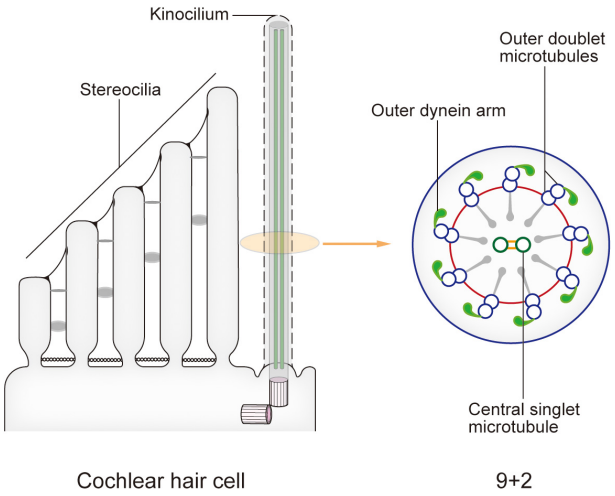


**FIGURE 2 |** Model of the kinocilium and its cross section. The kinocilium shows a 9 + 2 axoneme pattern with typical motile cilium structures such as outer dynein arms and radial spokes. However, a lack of inner dynein arms renders the lack of motor function. After the kinocilium degenerates, stereocilia mediate the entire mechano-electrical transduction (MET) process. When sound waves are transmitted to the cochlea, the shearing motion caused by lymph flow drives the passive swing of the hair bundle and sound signal processing.

hence its name (Sobkowicz et al., 1995). However, although it has outer dynein arms and radial spokes, it does not have inner dynein arms (**Figure 2**; Kikuchi et al., 1989). Therefore, the outer dynein arms allow the kinocilia retaining some motor function to passively swing with the rhythmic vibration rather than through autonomous movement that requires inner dynein arms (Spoon and Grant, 2013).

Mammalian kinocilia mediate HC morphogenesis and PCP, and the latter dictates the proper arrangement of stereocilia that is required for hearing. In mouse cochlear HCs, kinocilium development is complete around embryonic day 15 (E15), after which time they move to the non-neural side of the cell with the basal body. Meanwhile, nearby stereocilia gradually grow to form the three rows of stair-like and V-shaped stereocilia of different heights around E17, together forming the hair bundle (Williams et al., 2017). Kinocilium develops before stereocilia, finally leading the hair bundle facing toward the non-neural side. Accordingly, the HCs also acquire PCP in readiness for hearing and receiving external stimuli. In this way, the kinocilia play vital roles in the maturation of HCs.

The MET apparatuses are located at the top of stereocilia. The hair bundle tilts toward the longer stereocilia when receiving the sound stimulus, and the tip links are stretched, leading to the opening of MET channels and the subsequent depolarization of HCs. Therefore, the stereocilia completely determine the MET activity of mature HCs, so the kinocilium, which dictates the proper arrangement of stereocilia that is required for hearing, must form correctly during the initial stages of HC differentiation. Some typical ciliopathies including Bardet-Biedl syndrome (BBS), Alstrom syndrome (ALMS), Usher syndrome (US) are characterized by hearing dysfunction (Cosgrove and Zallocchi, 2014; Tsang et al., 2018; Hearn, 2019). Mutations in some ciliary genes encoding important intraflagellar transport (IFT) proteins such as *Ift88* can also cause hearing defects. *Ift88* conditional knockout mice exhibit shortened cochlear ducts with multiple extra rows of HCs at the apex, severe hair bundle polarity defects, and premature differentiation of HCs (Moon et al., 2020). Other studies have shown that the phenotypes of these knockout mice all include kinocilium loss, disorderly arrangement of stereocilia of different lengths, short and collapsed structural defects, and mislocation of centrosomes (Tarchini and Lu, 2019). Furthermore, some genes such as *Alms1* encoding proteins associated with centrosomes and ciliogenesis also show abnormal phenotypes in knockout mice, especially the mass loss of OHCs (Jagger et al., 2011). These data indicate that kinocilia play key roles in the correct orientation of stereocilia and consequently the normal function of HCs. Moreover, some ciliopathy related genes encoding connecting proteins can cause hearing dysfunction. Mutation of *Dcdc2a*, which is related to the autosomal recessive deafness-66 and encodes a protein located in the kinocilium, shows deficiency in the regulation of kinocilial ciliogenesis and length, and abnormal cohesion of the kinocilial microtubule core (Grati et al., 2015). Depletion of Usher syndrome 1 (Ush1) proteins, such as CDH23 and PCDH15, which are responsible for tip links and kinocilial links, significantly shortens stereocilia (Cosgrove and Zallocchi, 2014; Richardson and Petit, 2019).

## DEGENERATION OF THE KINOCILIA

Although kinocilia can be observed in newborn mouse cochlea HCs, they gradually degenerate in HCs from the bottom to the top of the cochlea after mice gain hearing at about postnatal day 8 (P8) and completely disappear at about P12, but the basal body still remains in mature HCs (Leibovici et al., 2005). In contrast, the kinocilia of HCs in the vestibular system persist throughout an animal's life (Guinan, 2012). The physiological significance of this cochlear degeneration is still not fully understood, but we can gain insights through comparison of cochlear kinocilia with those in the vestibular system.

Kinocilia on the surfaces of the two types of HCs in the vestibular system are anchored in "otolith," a kind of biomineralized aggregate of calcium and protein (Day and Fitzpatrick, 2005; Ramosdemiguel et al., 2020). When the head inclines or the body accelerates, the otolith shifts due to the effects of gravity, thereby moving kinocilia to one side through kinociliary links (Day and Fitzpatrick, 2005). Coupled with various connections between different parts of stereocilia, the whole hair bundle then leans toward the kinocilium's bending direction. At that time, as MET channels open, a large amount of $K^+$ flows into the hair cells, depolarizing the cell membrane and finally processing the signal of the head position. When the vestibular stimulus disappears, the stereocilia pull the kinocilium in the opposite direction, restoring the cell membrane to its resting potential (Jacobo and Hudspeth, 2014). Surprisingly, although kinocilia are not present in the HCs of the mature cochlea, the stereocilia

bundle, after being mechanically stimulated, still oscillates toward the original position of the kinocilium, consistent with the behavior of HCs in the vestibular system (Fettiplace, 2017). Similar to the kinocilium and otolith, the tip of the longest stereocilium in the cochlear HC is anchored to the tectorial membrane above. Structurally, it appears that these stereocilia are substitutes for the vestibular kinocilium. So, do the longest stereocilium and tectorial membrane also have a similar pull-in pattern?

The role of the tectorial membrane in the cochlea helps us to understand this pattern. This membrane links the longest stereocilium of each OHC via otogelin, otogelin-like, and stereocilin proteins (Avan et al., 2019). When sound waves transmit from the perilymph to endolymph, they pass through the basilar membrane as traveling waves, converting vibration to the tectorial membrane via periodic compression at the top of the HC protein network. The relative displacement of both leads to radial fluid flow in a narrow space, a shearing motion, which results in stereocilia movement in the horizontal direction and finally causing stereocilia to tilt (Guinan, 2012). The tectorial membrane acts as a calcium reservoir storing a large amount of $Ca^{2+}$, and HCs can rapidly process signals by directly utilizing the $Ca^{2+}$ released by it instead of relying on endolymph when MET channels open, which may also be the reason why the endolymphatic fluid and the intracellular $Ca^{2+}$ ionic environment are almost the same (Strimbu et al., 2019).

Presumably, kinocilia are not needed for auditory signal processing in the cochlea, since the longest stereocilia play a very similar role. As mentioned above, the cochlea is unique to mammals, and its internal mechanical receptors have correspondingly evolved in structure and function. Primitive vertebrates such as fish only have an inner ear, which is mainly used for balance. Moreover, although they have a complete vestibular system, auditory functions must be taken into account (Whitfield, 2020). Amphibians such as frogs have evolved a middle ear with an eardrum (Mason et al., 2015). In most reptiles, the ear develops further with an internal eardrum, giving rise to a prototypic external auditory canal (Schwab et al., 2020). While the ears of birds and mammals differ greatly, they still have highly developed outer, middle, and inner ears. The cochlea of mammals provides a single organ responsible for hearing that can cooperate with the other sensory functions of the ear. The longest stereocilia and related structures have a very close interrelationship, so the complete degradation of cochlear HC kinocilia will not have a profound physiological effect. This process therefore is probably best regarded a result of evolution.

## CONCLUDING REMARKS

Mammalian sensory systems are vital for the interactions between organisms and their environment. Among them, the auditory system is mediated through ion channels and receptors present on the actin filament-based microvilli called stereocilia, in line with the tactile and taste systems. However, unlike the specialized primary cilia present in visual and olfactory systems, the kinocilia are not involved in signal transduction, but play vital roles in mediating precise directional arrangement of stereocilia and the unique distribution of HCs in the cochlea, both of which are crucial for auditory integrity.

Kinocilia have their own unique characteristics that defy their classification into simply "motile" or "primary," which represents one of the higher evolutionary characteristics of mammals. Unfortunately, evolution can be a double-edged sword. Unlike in some species (such as birds and amphibians) with the capacity for spontaneous regeneration, mammalian cochlear HCs lack the ability to actively regenerate in adults. The irreversible reduction in the number of these sensory cells in some congenital or hereditary genetic diseases or acquired through aging or disease define neurodegenerative pathology. Although perhaps a product of higher evolution of mammals, the physiological significance of kinocilia degeneration is still incompletely understood and further research is necessary to understand the relationship–if any–between kinocilium degeneration and neurodegenerative diseases such as congenital sensorineural hearing loss.

Transplanting sensory cells artificially induced *in vitro* might be one way to restore sensation, and attempts are now underway to generate and then transplant these "simulated cells" to save the loss of HCs. There has been promising progress in using embryonic stem cells and hiPSCs to produce 3D organoids (Liu et al., 2016; Koehler et al., 2017; Jeong et al., 2018). Besides, although various types of cells can be obtained *in vitro* using these tools, their structure, function, and physiological indicators still do not completely replicate *in vivo* conditions. Therefore, artificially generating sensory cells with mature structures and physiological functions for translational use remains an ongoing area of research. With respect to other sensory cells like olfactory sensory neurons, AAV adenoviral -meditated ciliary restoration have shown promise in proof-of-principle preclinical studies (Green et al., 2018; Uytingco et al., 2019). Thus, together with gene editing, *in vitro* gene therapy and stem cell transplantation could become promising therapeutic approaches for overcoming sensorineural loss in the long term, provided that common barriers such as efficacy, safety, and immunorejection are overcome. However, it is still unclear whether kinocilia are present in these organoids. It is also interesting to explore whether mammalian HC regeneration is related to or even regulated by kinocilia. Thus, although kinocilia are promising therapeutic targets for genetic and acquired diseases, further studies are warranted to develop the treatment strategies.

## AUTHOR CONTRIBUTIONS

DW wrote the manuscript and drew the figures. JZ conceived the study and revised the manuscript. Both authors read and approved the final version of the manuscript.

## FUNDING

This work was supported by grants from the National Natural Science Foundation of China (31991193).

## REFERENCES


Anvarian, Z., Mykytyn, K., Mukhopadhyay, S., Pedersen, L. B., and Christensen, S. T. (2019). Cellular signalling by primary cilia in development, organ function and disease. *Nat. Rev. Nephrol.* 15, 199–219. doi: 10.1038/s41581-019-0116-9

Ashmore, J. (2020). A maturing view of cochlear calcium. *J. Physiol.* 598, 7–8. doi: 10.1113/jp279215

Atkinson, P. J., Huarcaya Najarro, E., Sayyid, Z. N., and Cheng, A. G. (2015). Sensory hair cell development and regeneration: similarities and differences. *Development* 142, 1561–1571. doi: 10.1242/dev.114926

Avan, P., Le Gal, S., Michel, V., Dupont, T., Hardelin, J. P., Petit, C., et al. (2019). Otogelin, otogelin-like, and stereocilin form links connecting outer hair cell stereocilia to each other and the tectorial membrane. *Proc. Natl. Acad. Sci. U. S. A.* 116, 25948–25957. doi: 10.1073/pnas.1902781116

Bujakowska, K. M., Liu, Q., and Pierce, E. A. (2017). Photoreceptor Cilia and Retinal Ciliopathies. *Cold Spring Harb. Perspect. Biol.* 9:a028274. doi: 10.1101/cshperspect.a028274

Christensen, S. T., Morthorst, S. K., Mogensen, J. B., and Pedersen, L. B. (2017). Primary Cilia and Coordination of Receptor Tyrosine Kinase (RTK) and Transforming Growth Factor beta (TGF-beta) Signaling. *Cold Spring Harb. Perspect. Biol.* 9:a028167. doi: 10.1101/cshperspect.a028167

Cosgrove, D., and Zallocchi, M. (2014). Usher protein functions in hair cells and photoreceptors. *Int. J. Biochem. Cell Biol.* 46, 80–89. doi: 10.1016/j.biocel.2013.11.001

Day, B. L., and Fitzpatrick, R. C. (2005). The vestibular system. *Curr. Biol.* 15, R583–R586.

Delling, M., Decaen, P. G., Doerner, J. F., Febvay, S., and Clapham, D. E. (2013). Primary cilia are specialized calcium signalling organelles. *Nature* 504, 311–314. doi: 10.1038/nature12833

Elliott, K. L., Fritzsch, B., and Duncan, J. S. (2018). Evolutionary and Developmental Biology Provide Insights Into the Regeneration of Organ of Corti Hair Cells. *Front. Cell Neurosci.* 12:252. doi: 10.3389/fncel.2018.00252

Falk, N., Losl, M., Schroder, N., and Giessl, A. (2015). Specialized Cilia in Mammalian Sensory Systems. *Cells* 4, 500–519. doi: 10.3390/cells4030500

Fettiplace, R. (2017). Hair Cell Transduction, Tuning, and Synaptic Transmission in the Mammalian Cochlea. *Compr. Physiol.* 7, 1197–1227. doi: 10.1002/cphy.c160049

Flock, A., and Duvall, A. J. III (1965). The Ultrastructure of the Kinocilium of the Sensory Cells in the Inner Ear and Lateral Line Organs. *J. Cell Biol.* 25, 1–8. doi: 10.1083/jcb.25.1.1

Goetz, S. C., and Anderson, K. V. (2010). The primary cilium: a signalling centre during vertebrate development. *Nat. Rev. Genet.* 11, 331–344. doi: 10.1038/nrg2774

Goodyear, R. J., Marcotti, W., Kros, C. J., and Richardson, G. P. (2005). Development and properties of stereociliary link types in hair cells of the mouse cochlea. *J. Comp. Neurol.* 485, 75–85. doi: 10.1002/cne.20513

Grati, M., Chakchouk, I., Ma, Q., Bensaid, M., Desmidt, A., Turki, N., et al. (2015). A missense mutation in DCDC2 causes human recessive deafness DFNB66, likely by interfering with sensory hair cell and supporting cell cilia length regulation. *Hum. Mol. Genet.* 24, 2482–2491. doi: 10.1093/hmg/ddv009

Green, W. W., Uytingco, C. R., Ukhanov, K., Kolb, Z., Moretta, J., McIntyre, J. C., et al. (2018). Peripheral Gene Therapeutic Rescue of an Olfactory Ciliopathy Restores Sensory Input, Axonal Pathfinding, and Odor-Guided Behavior. *J. Neurosci.* 38, 7462–7475. doi: 10.1523/jneurosci.0084-18.2018

Guinan, J. J. Jr. (2012). How are inner hair cells stimulated? Evidence for multiple mechanical drives. *Hear. Res.* 292, 35–50. doi: 10.1016/j.heares.2012.08.005

Hearn, T. (2019). ALMS1 and Alström syndrome: a recessive form of metabolic, neurosensory and cardiac deficits. *J. Mol. Med.* 97, 1–17. doi: 10.1007/s00109-018-1714-x

Jacobo, A., and Hudspeth, A. J. (2014). Reaction-diffusion model of hair-bundle morphogenesis. *Proc. Natl. Acad. Sci. U. S. A.* 111, 15444–15449. doi: 10.1073/pnas.1417420111

Jagger, D., Collin, G., Kelly, J., Towers, E., Nevill, G., Longo-Guess, C., et al. (2011). Alström Syndrome protein ALMS1 localizes to basal bodies of cochlear hair cells and regulates cilium-dependent planar cell polarity. *Hum. Mol. Genet.* 20, 466–481. doi: 10.1093/hmg/ddq493

Jeong, M., O'Reilly, M., Kirkwood, N. K., Al-Aama, J., Lako, M., Kros, C. J., et al. (2018). Generating inner ear organoids containing putative cochlear hair cells from human pluripotent stem cells. *Cell Death Dis.* 9:922.

Joukov, V., and De Nicolo, A. (2019). The Centrosome and the Primary Cilium: the Yin and Yang of a Hybrid Organelle. *Cells* 8:701. doi: 10.3390/cells8070701

Kazmierczak, P., and Muller, U. (2012). Sensing sound: molecules that orchestrate mechanotransduction by hair cells. *Trends Neurosci.* 35, 220–229. doi: 10.1016/j.tins.2011.10.007

Kikuchi, T., Takasaka, T., Tonosaki, A., and Watanabe, H. (1989). Fine structure of guinea pig vestibular kinocilium. *Acta Otolaryngol.* 108, 26–30. doi: 10.3109/00016488909107388

Koehler, K. R., Nie, J., Longworth-Mills, E., Liu, X. P., Lee, J., Holt, J. R., et al. (2017). Generation of inner ear organoids containing functional hair cells from human pluripotent stem cells. *Nat. Biotechnol.* 35, 583–589. doi: 10.1038/nbt.3840

Lancaster, M. A., and Gleeson, J. G. (2009). The primary cilium as a cellular signaling center: lessons from disease. *Curr. Opin. Genet. Dev.* 19, 220–229. doi: 10.1016/j.gde.2009.04.008

Leibovici, M., Verpy, E., Goodyear, R. J., Zwaenepoel, I., Blanchard, S., Lainé, S., et al. (2005). Initial characterization of kinocilin, a protein of the hair cell kinocilium. *Hear. Res.* 203, 144–153. doi: 10.1016/j.heares.2004.12.002

Liu, X. P., Koehler, K. R., Mikosz, A. M., Hashino, E., and Holt, J. R. (2016). Functional development of mechanosensitive hair cells in stem cell-derived organoids parallels native vestibular hair cells. *Nat. Commun.* 7:11508.

Mason, M. J., Segenhout, J. M., Cobo-Cuan, A., Quinones, P. M., and van Dijk, P. (2015). The frog inner ear: picture perfect? *J. Assoc. Res. Otolaryngol.* 16, 171–188. doi: 10.1007/s10162-015-0506-z

Moon, K. H., Ma, J. H., Min, H., Koo, H., Kim, H., Ko, H. W., et al. (2020). Dysregulation of sonic hedgehog signaling causes hearing loss in ciliopathy mouse models. *Elife* 9:e56551.

Nachury, M. V., and Mick, D. U. (2019). Establishing and regulating the composition of cilia for signal transduction. *Nat. Rev. Mol. Cell Biol.* 20, 389–405. doi: 10.1038/s41580-019-0116-4

Ramosdemiguel, A., Zarowski, A., Sluydts, M., Ramosmacias, A., and Wuyts, F. (2020). The Superiority of the Otolith System. *Audiol. Neurotol.* 25, 34–40.

Ran, J., and Zhou, J. (2020). Targeting the photoreceptor cilium for the treatment of retinal diseases. *Acta pharmacol. Sin.* 41, 1410–1415. doi: 10.1038/s41401-020-0486-3

Richardson, G. P., and Petit, C. (2019). Hair-Bundle Links: genetics as the Gateway to Function. *Cold Spring Harb. Perspect. Med.* 9:a033142. doi: 10.1101/cshperspect.a033142

Satir, P., and Christensen, S. T. (2007). Overview of structure and function of mammalian cilia. *Annu. Rev. Physiol.* 69, 377–400. doi: 10.1146/annurev.physiol.69.040705.141236

Schwab, J. A., Young, M. T., Neenan, J. M., Walsh, S. A., Witmer, L. M., Herrera, Y., et al. (2020). Inner ear sensory system changes as extinct crocodylomorphs transitioned from land to water. *Proc. Natl. Acad. Sci. U. S. A.* 117, 10422–10428. doi: 10.1073/pnas.2002146117

Singla, V., and Reiter, J. F. (2006). The primary cilium as the cell's antenna: signaling at a sensory organelle. *Science* 313, 629–633. doi: 10.1126/science.1124534

Sipe, C. W., and Lu, X. (2011). Kif3a regulates planar polarization of auditory hair cells through both ciliary and non-ciliary mechanisms. *Development* 138, 3441–3449. doi: 10.1242/dev.065961

Sobkowicz, H. M., Slapnick, S. M., and August, B. K. (1995). The kinocilium of auditory hair cells and evidence for its morphogenetic role during the regeneration of stereocilia and cuticular plates. *J. Neurocytol.* 24, 633–653.

Spoon, C., and Grant, W. (2013). Biomechanical measurement of kinocilium. *Methods Enzymol.* 525, 21–43.

Strimbu, C. E., Prasad, S., Hakizimana, P., and Fridberger, A. (2019). Control of hearing sensitivity by tectorial membrane calcium. *Proc. Natl. Acad. Sci. U. S. A.* 116, 5756–5764.

Ta, C. M., Vien, T. N., Ng, L. C. T., and DeCaen, P. G. (2020). Structure and function of polycystin channels in primary cilia. *Cell. Signal.* 72:109626.

Tarchini, B., and Lu, X. (2019). New insights into regulation and function of planar polarity in the inner ear. *Neurosci. Lett.* 709:134373.

Tsang, S. H., Aycinena, A., and Sharma, T. (2018). Ciliopathy: bardet-Biedl Syndrome. *Adv. Exp. Med. Biol.* 1085, 171–174.

Uytingco, C. R., Green, W. W., and Martens, J. R. (2019). Olfactory Loss and Dysfunction in Ciliopathies: molecular Mechanisms and Potential Therapies. *Curr. Med. Chem.* 26, 3103–3119.

Warchol, M. E., Massoodnia, R., Pujol, R., Cox, B. C., and Stone, J. S. (2019). Development of hair cell phenotype and calyx nerve terminals in the neonatal mouse utricle. *J. Comp. Neurol.* 527, 1913–1928.

Whitfield, T. T. (2020). Cilia in the developing zebrafish ear. *Philos. Trans. R. Soc. Lond. B Biol. Sci.* 375:20190163.

Williams, C. L., Uytingco, C. R., Green, W. W., McIntyre, J. C., Ukhanov, K., Zimmerman, A. D., et al. (2017). Gene Therapeutic Reversal of Peripheral Olfactory Impairment in Bardet-Biedl Syndrome. *Mol. Ther.* 25, 904–916.

**Conflict of Interest:** The authors declare that the research was conducted in the absence of any commercial or financial relationships that could be construed as a potential conflict of interest.

**Publisher's Note:** All claims expressed in this article are solely those of the authors and do not necessarily represent those of their affiliated organizations, or those of the publisher, the editors and the reviewers. Any product that may be evaluated in this article, or claim that may be made by its manufacturer, is not guaranteed or endorsed by the publisher.

*Copyright © 2021 Wang and Zhou. This is an open-access article distributed under the terms of the Creative Commons Attribution License (CC BY). The use, distribution or reproduction in other forums is permitted, provided the original author(s) and the copyright owner(s) are credited and that the original publication in this journal is cited, in accordance with accepted academic practice. No use, distribution or reproduction is permitted which does not comply with these terms.*

frontiers in Cell and Developmental Biology

ORIGINAL RESEARCH
published: 26 August 2021
doi: 10.3389/fcell.2021.725101

# Fluid Jet Stimulation of Auditory Hair Bundles Reveal Spatial Non-uniformities and Two Viscoelastic-Like Mechanisms

*Anthony W. Peng[1]*, Alexandra L. Scharr[2,3], Giusy A. Caprara[1], Dailey Nettles[4], Charles R. Steele[2,5] and Anthony J. Ricci[2,6]*

[1] Department of Physiology and Biophysics, University of Colorado Anschutz Medical Campus, Aurora, CO, United States, [2] Department of Otolaryngology, Head and Neck Surgery, School of Medicine, Stanford University, Stanford, CA, United States, [3] Neuroscience Graduate Program, School of Medicine, Stanford University, Stanford, CA, United States, [4] Neuroscience Graduate Program, University of Colorado Anschutz Medical Campus, Aurora, CO, United States, [5] Department of Mechanical Engineering and Aeronautics and Astronautics, School of Engineering, Stanford University, Stanford, CA, United States, [6] Department of Molecular and Cellular Physiology, School of Medicine, Stanford University, Stanford, CA, United States

OPEN ACCESS

**Edited by:**
*Hongmin Qin, Texas A&M University, United States*

**Reviewed by:**
*Bo Zhao, Indiana University Bloomington, United States*
*Permeen Yusoff, Singapore General Hospital, Singapore*

***Correspondence:**
*Anthony W. Peng*
*anthony.peng@cuanschutz.edu*

**Specialty section:**
*This article was submitted to Cell Growth and Division, a section of the journal Frontiers in Cell and Developmental Biology*

**Received:** *14 June 2021*
**Accepted:** *27 July 2021*
**Published:** *26 August 2021*

**Citation:**
*Peng AW, Scharr AL, Caprara GA, Nettles D, Steele CR and Ricci AJ (2021) Fluid Jet Stimulation of Auditory Hair Bundles Reveal Spatial Non-uniformities and Two Viscoelastic-Like Mechanisms. Front. Cell Dev. Biol. 9:725101. doi: 10.3389/fcell.2021.725101*

Hair cell mechanosensitivity resides in the sensory hair bundle, an apical protrusion of actin-filled stereocilia arranged in a staircase pattern. Hair bundle deflection activates mechano-electric transduction (MET) ion channels located near the tops of the shorter rows of stereocilia. The elicited macroscopic current is shaped by the hair bundle motion so that the mode of stimulation greatly influences the cell's output. We present data quantifying the displacement of the whole outer hair cell bundle using high-speed imaging when stimulated with a fluid jet. We find a spatially non-uniform stimulation that results in splaying, where the hair bundle expands apart. Based on modeling, the splaying is predominantly due to fluid dynamics with a small contribution from hair bundle architecture. Additionally, in response to stimulation, the hair bundle exhibited a rapid motion followed by a slower motion in the same direction (creep) that is described by a double exponential process. The creep is consistent with originating from a linear passive system that can be modeled using two viscoelastic processes. These viscoelastic mechanisms are integral to describing the mechanics of the mammalian hair bundle.

**Keywords: stereocilia bundle, fluid jet, hair cell, modeling, creep, viscoelasticity**

## INTRODUCTION

The auditory system relies on a cochlear amplification process to achieve its high dynamic range and sharp frequency selectivity. The inner ear hair cell hair bundle is comprised of an array of graded length stereocilia organized in a staircase manner. The hair bundle is hypothesized to be an active force generator and integral to cochlear amplification (Howard and Hudspeth, 1987; Kennedy et al., 2005; Beurg et al., 2008; Hudspeth, 2008). Quantifying the mechanical properties of the hair bundle is essential to evaluating its role in cochlear amplification.

Hair bundle arrays in different species and organs vary in height, number of rows, stereocilia thickness, staircase step size, and coherence, defined here as how uniformly and reproducibly stereocilia will move relative to each other in time, direction and distance. Mammalian cochlear hair bundles are unique in having fewer stereocilia rows, typically three, with the lower two rows possessing functional mechano-electric transduction (MET) channels (Beurg et al., 2009). The stereocilia of low-frequency hair bundles are highly synchronous, where individual stereocilia move in unison in time, distance, and direction (Kozlov et al., 2007; Karavitaki and Corey, 2010). Mammalian cochlear bundles lack coherence (Langer et al., 2001; Nam et al., 2015; Scharr and Ricci, 2018). Importantly, this asynchrony of stereocilia motion can alter the macroscopic manifestations of channel gating and adaptation (Nam et al., 2015). Reduced coherence makes hair bundles more susceptible to the mode of stimulation, as the bundles can conform to the temporal and spatial variations in the stimulus. As hair bundles are stimulated in a variety of manners *in vivo,* from free standing to embedded in an overlying membrane and from sinusoidal modulation to static displacement, bundle coherence is important in shaping how these stimulations are translated to a force sensed by the MET channel. Thus, understanding the within bundle and between stereocilia variations in movement is critical to constructing the force sensed by the MET channels which cumulatively generates the receptor current.

Two stimulations methods are most used in *ex vivo* experiments to interrogate the MET process: stiff probes and fluid jets. For mammalian hair bundles, stiff probes are susceptible to uneven stimulation of the hair bundle due to the decreased bundle coherence (Nam et al., 2015). On the other hand, the fluid jet is argued to provide a more uniform hair bundle stimulation (Corns et al., 2014); however, details of the hair bundle motion's spatial uniformity have not been described. Using high-speed imaging of the hair bundle during fluid-jet stimulation, we characterize the motion of the whole outer hair cell hair bundle. We found that hair bundles exhibit a spatial and temporal non-uniformity when stimulated with a fluid jet. The spatial non-uniformity is contributed to by hair bundles acting as a barrier to fluid flow to alter the flow around the bundle and the presence of lateral links that redistribute forces within the hair bundle. We found the temporal non-uniformity, which appears as a slower motion in the direction of the original stimulus (creep), results from linear passive mechanics intrinsic to the hair bundle, which is consistent with two viscoelastic-like mechanisms present in the hair bundle.

# RESULTS

## Spatially Non-uniform Hair Bundle Displacement

The fluid jet is a common technique used to stimulate hair bundles in *ex vivo* hair cell experiments (Kros et al., 2002; Dinklo et al., 2007; Corns et al., 2014). The fluid jet ejects fluid from a pipette tip causing a fluid velocity that exerts a drag force on the hair bundle (Dinklo et al., 2007). Using a force step hair bundle stimulation reveals underlying mechanical properties of the hair bundle (Crawford and Fettiplace, 1985; Howard and Hudspeth, 1987; Ricci et al., 2000; Kros et al., 2002; Kennedy et al., 2005; Beurg et al., 2008). The stereocilia displacement with fluid jet stimulation will vary with both intrinsic hair bundle properties (e.g., individual stereocilia stiffness, the position of the stereocilia with respect to the fluid flow, the stereocilia height, and the hair bundle coherence which describes how well coupled the stereocilia are to each other) and fluid jet construction and position (e.g., the size of the fluid jet pipette tip opening, the shape of the fluid jet pipette taper, the angle of the fluid jet in $z$ with respect to the hair bundle, the lateral and vertical position of the fluid jet relative to the hair bundle, properties of the piezoelectric actuator, and load on the piezoelectric actuator). Previous experiments measured hair bundle movement with a dual photodiode system (Corns et al., 2014, 2016; Beurg et al., 2015; Tobin et al., 2019). This system can only measure the displacement of a portion of the hair bundle in a single direction and its sensitivity will be directly related to the intensity and contrast of the hair bundle image being projected (Crawford and Fettiplace, 1985; Geleoc et al., 1997). The lack of cohesion in mammalian hair bundles (Langer et al., 2001; Nam et al., 2015) makes it necessary to simultaneously monitor motion at multiple positions along the hair bundle to identify spatial non-uniformities. Our high-speed imaging system allowed for these investigations (Caprara et al., 2019).

Stimulated OHC hair bundles consistently showed a spatially non-uniform motion, where the hair bundle edges moved outward and upward more readily than the hair bundle center (**Supplementary Video 1**). Taking advantage of high-speed imaging allowed tracking of nanometer scale deflections of the entire hair bundle. Using techniques of position tracking of the hair bundle with fitting the filtered hair bundle intensity profile with a Gaussian curve developed for particle tracking (Yildiz et al., 2004; Ramunno-Johnson et al., 2009; Isojima et al., 2016), we could achieve sub-pixel and sub-diffraction limit displacement of the hair bundle. To determine how the entire hair bundle moved, we calculated the position of the hair bundle in each column of the hair bundle image for every frame of the stimulation movie. When looking at the vertical motion of the hair bundle (i.e., columns of the image), the sides of the hair bundle moved more than the center (**Figure 1A**). We also observed that the sides moved more laterally than the center. We are not able to track the movement of individual stereocilia in OHC hair bundles due to resolution limitations; therefore, when using a vertical line on the hair bundle contour, the lateral motion can overestimate the displacement measured on the sides of the hair bundle. The overestimate is due to the stationary line where the displacement is measured sliding to more medially positioned stereocilia along the hair bundle between the resting and the stimulated positions when lateral stereocilia movement is present. To diminish the potential artifact and ensure that the spatial non-uniformity was not a function of the measurement, we analyzed the motion in the direction perpendicular to the hair bundle contour (**Figure 1B**). With both analysis techniques, the middle of the hair bundle moved less than the sides (**Figures 1C,D**). Overall, the OHC bundle appeared to broaden

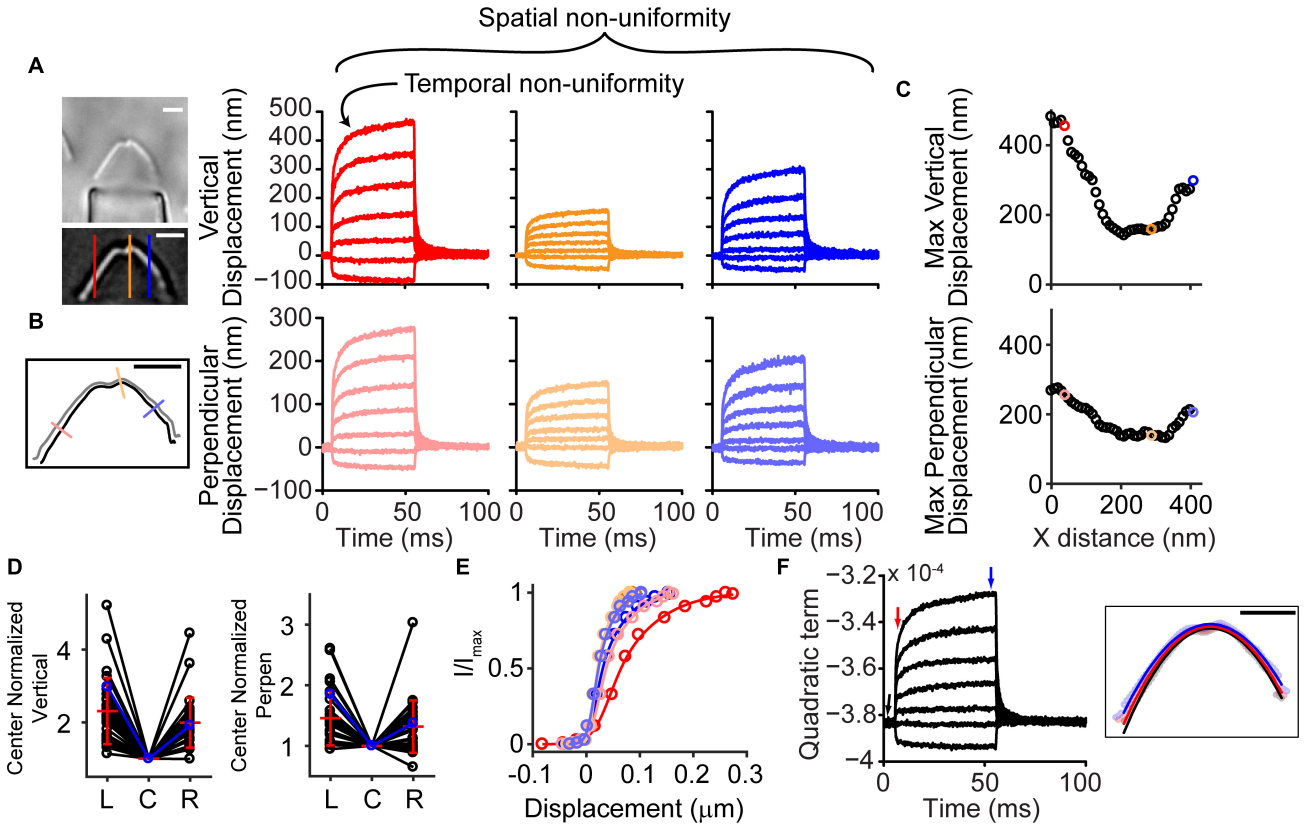


**FIGURE 1 |** Hair bundle motion was not spatially uniform with a fluid jet stimulus. **(A)** Hair bundle images show the raw image (top) and a filtered image used for analysis with colored lines indicating where the vertical motion was measured. Plots of the vertical hair bundle motion at three different positions along the hair bundle indicated differing movement magnitudes demonstrating the spatial non-uniformity. Within each displacement trace there was a temporal non-uniformity exhibited as a creep of the hair bundle. **(B)** Perpendicular hair bundle motion was calculated at different points along the hair bundle (colored lines) and showed different movement magnitudes. The image showed the resting position of the hair bundle in black, with the position at the end of the force step shown in gray. Corresponding displacements along the perpendicular lines are color coded. **(C)** Maximum ending displacements for the cell in panels **(A,B)** as a function of x distance along the hair bundle, indicating that the positions toward the sides of the hair bundle move a greater distance. **(D)** Summary of 29 cells analyzed showing the center normalized movement of the left (L), center (C), and right (R) side of the hair bundle for the vertical and perpendicular directions. The cell in panel **(A–C)** is highlighted in blue. **(E)** The possible resulting activation curves due to the motion at different parts of the hair bundle indicated that the parameters differed more than 2x depending on where and how the motion was measured. Activation curves were generated with the displacement at the time of the peak current. **(F)** Fitting a quadratic equation to the hair bundle position in each frame indicated changes in the hair bundle width that follows a similar time course as the motion in panel **(A,B)** and further confirmed the larger movements toward the hair bundle sides. Right schematic shows the position of the hair bundle at each point along the hair bundle (circles) and the resulting quadratic equation fit (lines). Different colors represent different times when the hair bundle position and quadratic fits were obtained according to the colored arrows in the graph. Scale bars = 2 μm.

the width of its V-shape upon stimulation. Using a third strategy to describe the bundle motion, we fit a quadratic equation to the hair bundle. The quadratic coefficient, which described the steepness of the parabola, indicated a flattening curve over the course of the stimulation (**Figure 1F**), consistent with greater lateral motion at the edges.

The spatially non-uniform motion altered how activation curves were represented. Activation curves generated with the fluid jet tend to be quite steep as compared to those generated with a stiff probe (Fettiplace and Kim, 2014). This discrepancy in part depends on where the bundle motion is measured. Since hair bundle motion magnitude varies with position along the hair bundle, the resulting activation curves can differ by more than two-fold (**Figure 1E**).

Was the spatially non-uniform bundle motion driven by characteristics of the fluid jet or by characteristics of the hair bundle? Fluid flow from the fluid jet pipette center will be greatest with flow velocity decreasing toward the edge of the cone-shaped flow pattern (Tobin et al., 2019). To better understand the fluid flow role in shaping the observed hair bundle motion, the fluid-jet pipette size was varied. For these experiments, we used fixed tissue where only passive hair bundle properties are present, and multiple fluid-jet pipette sizes could easily be tested on the same bundle (**Figure 2**). Examples of small (4 μm), medium (7 μm), and large (21 μm) diameter pipettes showed spatially non-uniform displacement (**Figure 2**). Smaller pipette diameters created more hair bundle edge motion than larger pipettes. Larger pipette diameters resulted in the most spatially

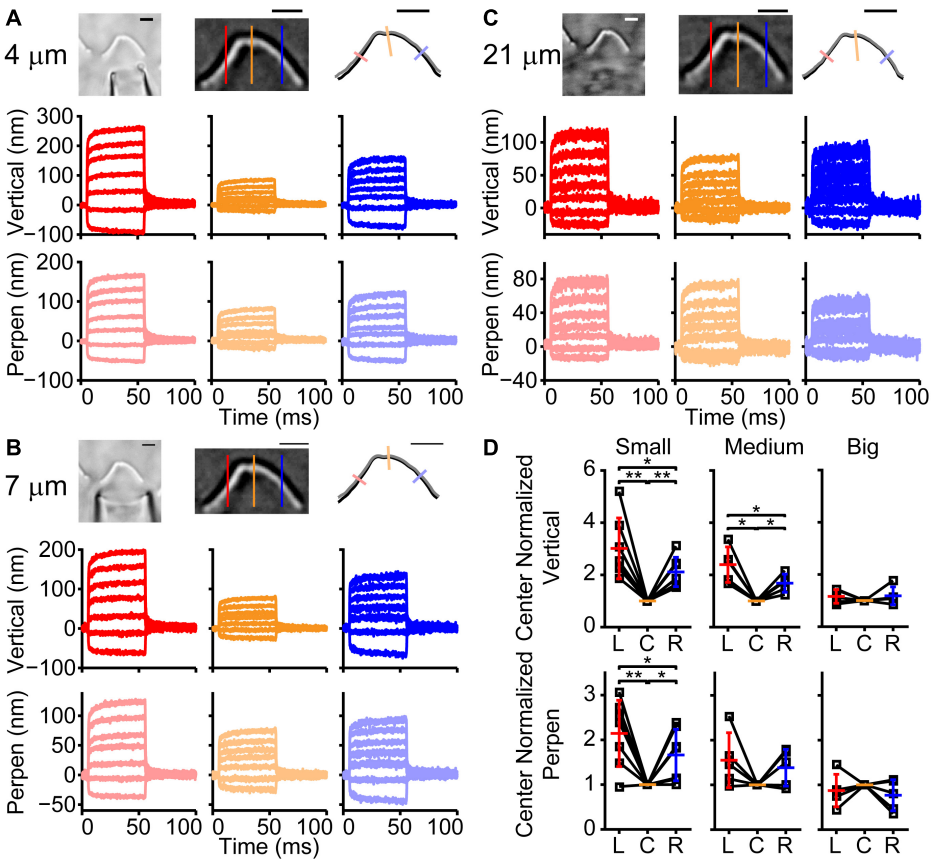


**FIGURE 2 |** Effect of fluid jet size on hair bundle motion on the same fixed hair bundle. **(A)** Raw (left) and filtered (middle) hair bundle images are shown with a small pipette fluid jet (4 μm). The calculated hair bundle position with the corresponding perpendicular lines is shown on the right. Darker lines represent the vertical hair bundle motion at corresponding positions in the filtered image. Lighter lines indicate the perpendicular hair bundle motion along the lines in the right image. **(B,C)** The same analysis as in panel **(A)** is shown, but with a medium-sized pipette (7 μm wide) in **B** and a large fluid jet (21 μm wide) in **C**. Stimulus size was adjusted to yield comparable center bundle motion. **(D)** Summary of hair bundle motion amplitude for the largest step size with left (L) and right (R) side motion normalized to the center (C). Individual cells are shown and demonstrate that the larger pipettes deliver more uniform hair bundle motion when analyzing the vertical or perpendicular hair bundle motion. $n$ = 7, 5, 5 for small, medium, and large pipettes, respectively. Scale bars = 2 μm. $^*p < 0.05$, $^{**}p < 0.01$.

uniform displacement; however, the largest pipettes elicited a visually noticeable movement of the underlying epithelium (data not shown). Increasing pipette size increases the center area with a more uniform fluid velocity (Tobin et al., 2019). Thus, it makes sense that the larger pipette results in more uniform stimulation. However, small pipettes would have lower fluid velocity toward the edge of the hair bundle, which is predicted to result in smaller edge stimulation, but instead, we observed larger displacements suggesting that more than simple uniformity of flow is needed to explain the results.

## Hair Bundle Disrupts the Fluid Flow

To understand the apparent contradiction between the bundle motion and the spatial distribution of fluid velocity, we postulated that the flow disruption by the hair bundle may contribute to the spatially non-uniform motion. To better assess fluid flow from the fluid jet and determine how the hair bundle obstructs and modifies fluid flow, we monitored fluid flow using the fluorescent dye Alexa 594 (1 μM), simulated fluid flow from a pipette using a 3-dimensional (3D) model, and measured fluid flow rates around the hair bundle with a flexible glass fiber.

Imaging fluid flow in the presence of the hair bundle demonstrated that the hair bundle acted as a barrier to fluid flow (**Figures 3A,B**). Fluid flow from the pipette in the absence of the hair bundle resulted in the typical cone-shaped flow (**Figure 3A**). When the hair bundle was present, the flow was disrupted and appeared to create billows of dye (**Figure 3B**). The dye appears to deflect backward and toward the hair bundle sides and move around and over the hair bundle rather than through it. To better assess the hair bundle impact on fluid flow from the fluid jet, a steady-state 3D model was generated where a pipette of medium diameter (8 μm) was placed in front of the 4 μm tall hair bundle (**Figure 3C**). The hair bundle was modeled as panels simply using rootlet stiffness as the primary source of stiffness; top connectors, lateral links, multiple stereocilia rows, and tip links were not included. In the presence of the hair bundle, fluid flowed around and over the hair bundle (**Figures 3D–F**). Fluid flow rates were considerably higher in the region in front of the

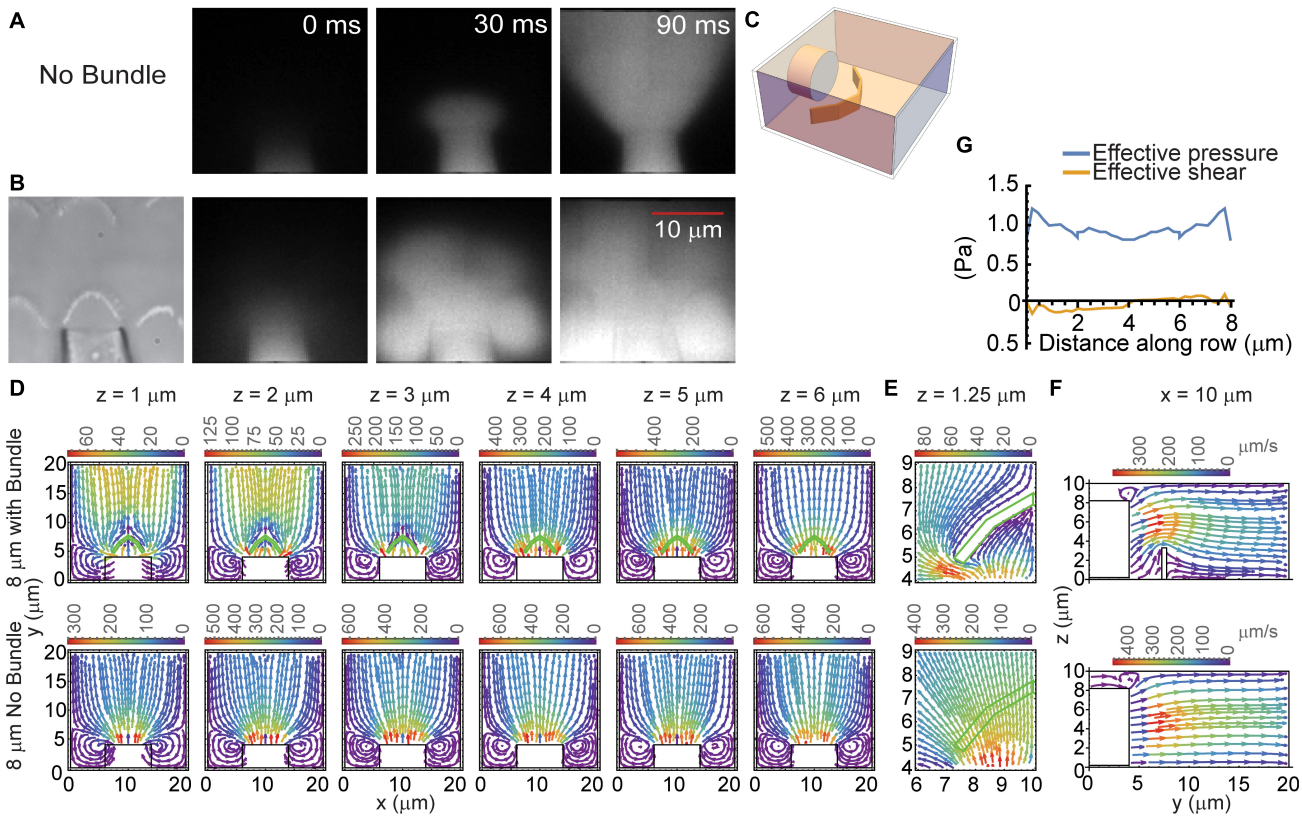


**FIGURE 3 |** Hair bundle effects on fluid flow. **(A,B)** 1 μM Alexa 594 was used to track the flow from the fluid jet pipette. Fluorescent images at three time points corresponding to before the stimulus (0 ms), immediately after stimulus onset (30 ms), and during the stimulus (90 ms) in the absence **(A)** and presence **(B)** of the hair bundle are shown. **(C)** Schematic of the 3D model structure is shown. **(D)** Provides the FEM computed, steady-state fluid flow from a pipette of 8 μm diameter measured at various distances above the apical surface (z) with (top row) and without the hair bundle (bottom row). The hair bundle is depicted in the green outline. The color of flow lines indicates the fluid flow rate according to the color scale above the plot. **(E)** Presents an enlargement of half the bundle to better show how fluid flow was impeded by the hair bundle at $z$ = 1.25 μm. **(F)** Provides a side view of the fluid flow with (top) and without (bottom) the hair bundle at the 10 μm x position from panel **(D)**. **(G)** Presents the effective pressure and the effective shear across the face of the hair bundle. Values are plotted against the distance along the hair bundle contour.

fluid jet when the hair bundle was not present (**Figure 3D**). Fluid flow rates slowed with distance away from the pipette when no bundle was present (**Figure 3D**, bottom row). When the hair bundle is present, flow increased at further distances from the pipette (**Figure 3D**, $z$ = 1–3 μm) due to flow coming from higher $z$ planes as seen in the side views of fluid flow (**Figure 3F**). Zooming in on one half of the bundle (**Figure 3E**) showed how the flow was hindered by the hair bundle presence, such that flow was more outward (lateral) at the bundle edge and more inward (medial) at the bundle center. The effective pressure (force perpendicular to the hair bundle contour) supports the larger displacements measured at the hair bundle edges (**Figure 3G**). The effective shear (forces parallel with the hair bundle contour) was small, indicating the predominant force is perpendicular to the hair bundle contour. This model showed that the interaction between the hair bundle shape and the fluid flow differentially altered the force on the hair bundle with greater forces on the edges of the hair bundle as compared to the center even when the starting fluid flow was uniform when coming out of the stimulating pipette.

To understand the effects of tip links, lateral links, and hair bundle splaying, we used a finite element stereocilia model populated with tip links and lateral links (**Figure 4A**; Nam et al., 2015). We modeled a force step stimulation applied to only the tallest stereocilia row to investigate the effects of links on the hair bundle motion. We found that the presence of lateral links within the hair bundle contributed to a small difference in motion. When lateral links were present in the model (**Figures 4B–D**, blue) the hair bundle exhibited splaying, where the edges of the hair bundle moved a larger distance than when lateral links were absent, indicating that the links redistributed the forces on the stereocilia (**Figures 4B–D**, red). However, the difference in displacement of each stereocilium was small, only differing by 5.5% (**Figure 4C**). The stimulated positions of the hair bundle indicate that the lateral links had a small contribution to the hair bundle splay (**Figure 4D**).

Previously, we found that BAPTA treatment of the hair bundle resulted in changes to the creep behavior (temporal non-uniformity, **Figure 1A**), but the creep remained, implicating a non-BAPTA-sensitive structural contributor

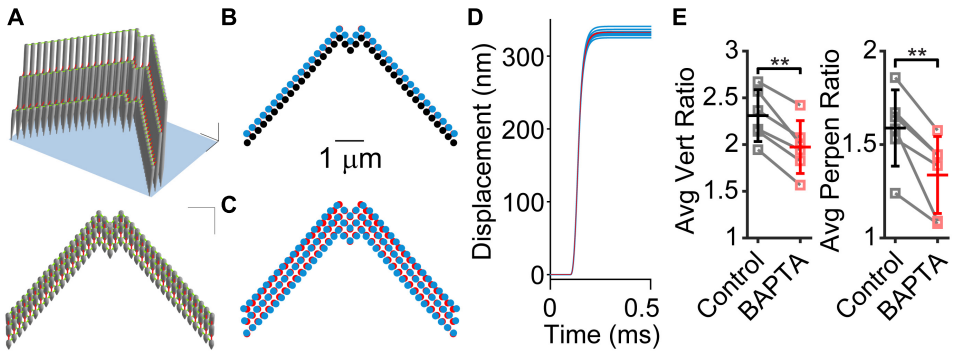


**FIGURE 4 |** Stereocilia displacement non-uniformity is greater when lateral links are present. **(A)** 3D model of stereocilia hair bundle is shown in two perspectives with tip-links shown in red and lateral links in green. **(B)** Movement of the tallest row of stereocilia from the rest position (black) to the final position when tip links are present with (blue) and without (red) lateral links. Note that the blue almost entirely covers the red stereocilia. **(C)** Position of stereocilia in the entire bundle that is multiplied by five times to visualize the difference between the presence (blue) and absence (red) of lateral links. **(D)** Plots of the displacement of individual stereocilia showing that when lateral links are present (blue traces) there is a distribution of displacement sizes, whereas when lateral links are absent, displacement sizes are the same for each stereocilium (red traces). **(E)** Re-analyzing experiments in Caprara et al. (2020) with BAPTA treatment of hair bundles show that after BAPTA treatment, hair bundle non-uniformity is decreased. The center (C) normalized vertical ratios on the left (L) and right (R) side of the hair bundle were averaged for stimulations before (control) and after BAPTA treatment in the same cells. For controls, the largest stimulation was used and after BAPTA treatment, we used the closest matched center displacement stimulation for the calculation. We preformed this analysis using both vertical motion and perpendicular motion like **Figures 1A,B** ($n$ = 6, Vert, $p$ = 0.0011; Perpen, $p$ = 0.0050). $^{**}p < 0.01$.

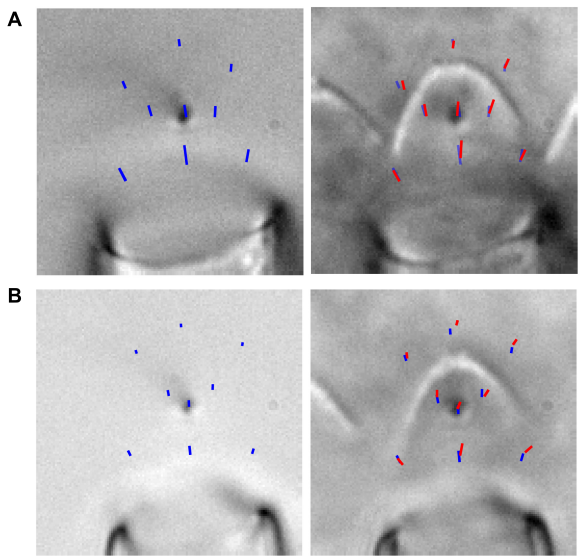


**FIGURE 5 | (A,B)** Two examples of fluid forces with (red) and without (blue) the hair bundle are shown. The images show the trajectories (from rest state to steady-state position) of a flexible fiber bent down toward the tissue such that it appeared as a point in *x-y* and a line in *x-z*. The fiber was moved to various positions, and the trajectory of four presentations of the largest stimulation at each position is overlaid on the image. This demonstrated that the hair bundle presence altered the flow, and the variability between stimulations of a given fiber position was very low. For experiments without the hair bundle, the fluid jet and flexible fiber were moved ∼200 μm above the epithelium.

(Caprara et al., 2020). Using the new analysis method to characterize the motion of the whole hair bundle, we also observed that the spatial non-uniformity was decreased after BAPTA treatment (**Figure 4E**), indicating that the BAPTA-sensitive links had a contribution to the spatial non-uniformity, consistent with the modeling data.

A third approach to determine whether bundle motion reflected stimulus anomalies was to use a flexible fiber to monitor the force delivered by the fluid jet at different positions around the hair bundle (**Figure 5**). To investigate the potential contribution of lateral forces on the hair bundle, we performed experiments with glass fibers bent such that they appeared as a point in the image and extended upward in the *z* direction. This arrangement would provide information about forces in *x-y*, similar to that described with the modeling in **Figure 3F**. The flexible fiber data had a caveat that the total motion observed was due to a weighted sum of the forces along the length of the fiber, with forces at the end of the fiber weighted more heavily. Thus, some of the observed motion was due to fluid-flow forces on the fiber above the bundle. The fluid flow above the hair bundle would lead to an underestimate of the hair bundle effects on the flow, since fluid flow above the hair bundle is largely unchanged by the hair bundle based on the 3D model (**Figure 3D**). Two examples of fluid-jet flow in the absence (blue) and presence (red) of the hair bundle showed that the hair bundle presence altered the fluid flow (**Figure 5**). The length of the plotted lines indicates the distance traveled for a saturating MET stimulus. Four trajectories were plotted for each position corresponding to four presentations of the same stimulus size. Trajectories appeared to be a single line due to the highly reproducible movement of the fiber for each presentation. In these examples, the forces were mainly rotated toward the right due to the hair bundle presence. A significant difference in the fluid drag force is apparent at different distances of the fiber (**Figure 5**, blue). This decrease in drag force is consistent with the results

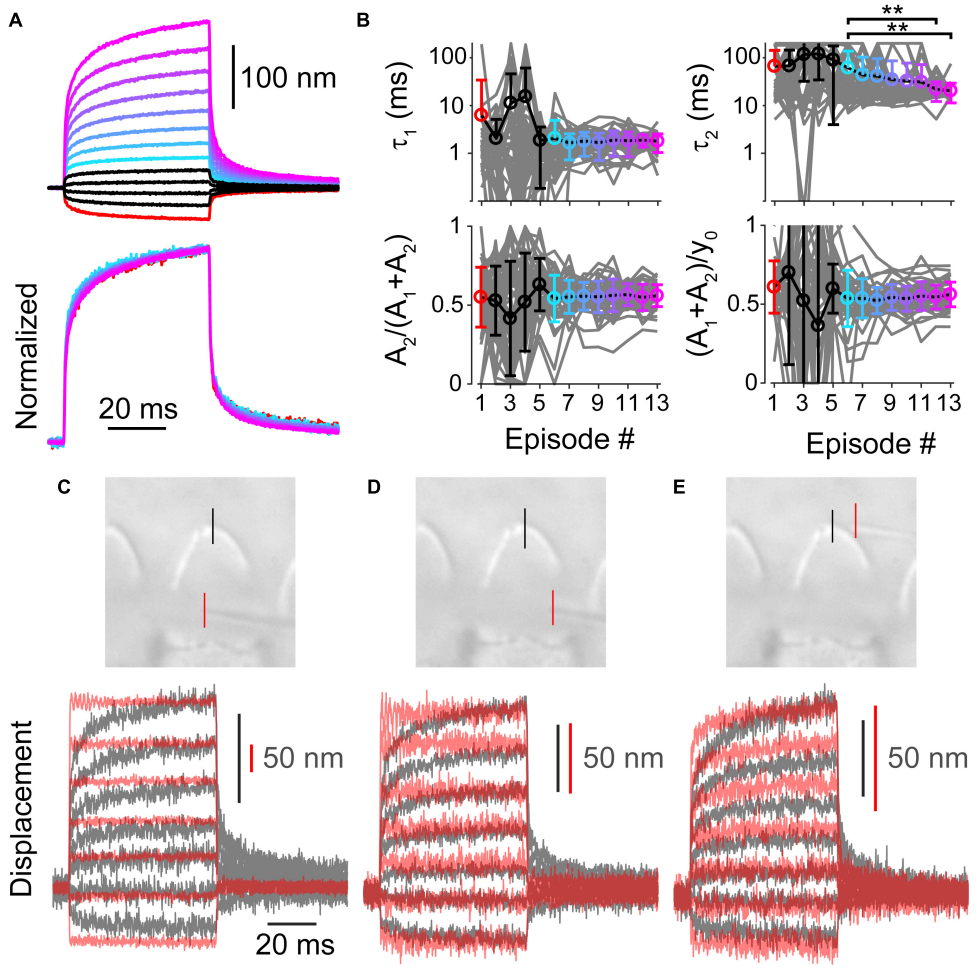


**FIGURE 6 | (A)** Average of all measured displacements and below are those traces normalized to the end of 50 ms force step ($n$ = 47). Episode number color coded according to panel **(B)**. Only episodes 1 and 6–13 are shown for the normalized traces, others are omitted due to low signal to noise. **(B)** Fit parameters for creep vs. stimulation episode number with 1 mM BAPTA intracellular buffer in OHCs. Each cell is plotted in gray with mean ± standard deviation. Tukey-Kramer *post hoc* analysis on $\tau_2$ showed significance for only the comparisons shown; $^{**}p < 0.01$. **(C–E)** Force measurements around the hair bundle indicate that the hair bundle creep is not due to fluid jet anomalies. **(C)** Image of the fiber and hair bundle stimulated by a fluid jet is shown with locations of motion measurement indicated by colored lines. Measured bundle (black) and fiber (red) displacement is plotted below. Resonance observed in the fiber motion was likely due to the vibration of the fluid-jet pipette observed with larger stimulations. **(D)** Shows force out of the fluid jet was square as indicated by the fiber motion in front of the hair bundle toward the side. **(E)** Motion of the of fiber and bundle when the fiber was located behind the hair bundle is shown. When the fiber was behind the hair bundle side, the bundle blocked the flow causing a slower fiber onset similar to the hair bundle creep.

of the 3D model (**Figures 3D,E**) and previous results (Tobin et al., 2019). These data were like the predictions of the model (**Figure 3F**) where the flow was altered in the presence of the hair bundle, but detailed differences in fluid forces may have been caused by hair bundle and fluid jet orientation differences in the experiments. The experimental data further confirmed that the spatially non-uniform hair bundle motion was due to fluid dynamics of the fluid jet with the hair bundle acting as a barrier.

## Mechanical Creep Is Linearly Related to Stimulus Size

Up until now, we have investigated the source of the spatial non-uniformity of the hair bundle stimulation. When using a step-like force stimulation, the hair bundle displacement also exhibits a temporal non-uniformity that is characterized as a mechanical creep (Howard and Hudspeth, 1987; Russell et al., 1992; Kennedy et al., 2005; Beurg et al., 2008; Caprara et al., 2019). For a given hair bundle, the mechanical creep was linearly related to the stimulation voltage, such that the contribution of the creep components $[A_2/(A_1+A_2)]$ and the relative magnitude of the creep to the total displacement of the bundle during the 50 ms force step $[(A_1+A_2)/y_0]$ remained constant with stimulus episode (**Figures 6A,B**). Hair cells were patch-clamped with 1 mM BAPTA as the intracellular calcium buffer and subjected to 13 stimulation intensities ($n$ = 47). We fit the mechanical creep after the force had plateaued (Caprara et al., 2019) with a double exponential equation (see section "Materials and Methods").

Stimulation episode 1 is the largest negative stimulation and 3 is the smallest negative stimulation. Episode 4 is the smallest positive stimulation and 13 is the largest positive stimulation. Looking at the data from episodes 6–13, where variability is lower due to greater signal to noise in the fitting, shows that the relative magnitude of the slow creep $[A_2/(A_1+A_2)]$ and the relative magnitude of the total creep $[(A_1+A_2)/y_0]$ was constant (**Figure 6B**, $p = 0.95$ and $p = 0.76$, respectively). The time constant $\tau_1$ was also constant, but $\tau_2$ was not (1-way ANOVA $p = 0.87$ and $p = 0.0014$, respectively). That the stimulations had comparable relative creep magnitudes supports a linear process underlying the creep.

Even though the creep is a linear process, we wanted to distinguish whether the creep was due to characteristics of the fluid jet or the hair bundle. We measured the kinetics of a flexible fiber motion placed around the hair bundle (**Figures 6C–E**). The flexible fiber allowed us to visualize fluid kinetics that the 3D steady-state model did not provide. Fiber placement in front of the hair bundle indicated a step-like force stimulus across the hair bundle face (**Figures 6C,D**). Even when the fluid drag force due to the fluid jet was step-like, the hair bundle creep was observed, supporting a conclusion that the creep was a result of the hair bundle's mechanical properties. The force on the fiber behind the bundle exhibited a creep similar to that observed by the hair bundle (**Figure 6E**). This indicates that the force kinetics were altered by the hair bundle potentially acting as a barrier to the flow, which slowed the equilibration of force behind the bundle. These data confirmed that the fluid-jet stimulator itself is not responsible for the hair bundle creep.

# DISCUSSION

Fluid jet force stimulation of the mammalian outer hair cell bundle leads to both spatial and temporal non-uniformities. The mammalian hair bundle is incoherent, which allows for different parts of the hair bundle to have different displacement magnitudes with fluid-jet stimulation. Using a combination of experimental manipulations and mathematical modeling, we found that the spatially non-uniform motion have contributions from altered fluid dynamics imparted by the hair bundle acting as a barrier to the fluid flow and by linkages within the hair bundle distributing the fluid forces. For the temporal non-linearity that is exhibited as a creep in the hair bundle, the creep is due to characteristics of the hair bundle and appear to result from a passive linear system.

## Spatially Non-uniform Hair Bundle Motion

Fluid flow from our fluid jet has a typical cone shaped flow and produces a step-like drag force, but the flow is impacted by the apical surface, the hair bundle, and stimulus intensity. This, coupled with a previously documented lack of cohesiveness within the bundle (Langer et al., 2001; Nam et al., 2015), leads to stereocilia motion that is spatially non-uniform. Experimental and modeling data demonstrate that the hair bundle acts as a physical barrier to fluid flow, altering flow around the hair bundle and contributing to the spatial non-uniformity of hair bundle displacement.

OHC bundle motion displays a spatial non-uniformity with a broadening of the bundle shape during stimulation such that the bundle edges are moving laterally as well as forward. This characteristic OHC hair bundle motion is due to the complex fluid dynamics that the hair bundle barrier creates through the inherent shape and architecture of the OHC hair bundle. OHCs are thought to be stimulated by basilar membrane motion shearing the hair bundle embedded in the tectorial membrane, therefore, the motion induced by a fluid jet is unlikely to mimic an *in vivo* response. However, it does suggest that the lack of hair bundle coherence allows the hair bundle to follow the temporal and spatial components of the stimulus more than a coherent bundle would, and this motion would shape the receptor potential. Since the OHC bundles are embedded in the tectorial membrane (Lim, 1972), the stiffness of the tectorial membrane will be critical in determining how the hair bundle moves.

An alternative stimulation mode of the hair bundle could be to "squish" the bundle, which could lead to hair bundle splay like we observe with fluid jet stimulation. This idea is supported by the orientation of tip-links in OHCs that can be more laterally oriented on the sides of the hair bundle when we inspect some scanning electron micrographs of the hair bundle (Velez-Ortega et al., 2017), suggesting that they may be sensitive to hair bundle splay. Additionally, evidence exists for changes in the distance between the tectorial membrane and surface of the epithelium (reticular lamina), which would also be consistent with the "squish" mode of stimulation (Guinan, 2012; Hakizimana et al., 2012; Lee et al., 2015). To be clear, the fluid jet does not replicate *in vivo* stimulation and care must be taken with interpreting these bundle motions as being physiologically relevant. Our data simply points out the need for a better understanding of *in vivo* bundle motion, because the motion will directly shape the receptor current.

## *Ex vivo* Stimulation Methods Are Imperfect

The stiff probe and fluid jet are the predominant methods of *ex vivo* hair bundle stimulation. The stiff probe is fast (as fast as 11 μs rise time) (Peng et al., 2013), mechanically loads the hair bundle (the probe touches multiple stereocilia), does not contact all stereocilia (Nam et al., 2015), and delivers a displacement stimulus that synchronizes a set of stereocilia. The fluid jet is slow (500 μs rise time) (Caprara et al., 2019), does not load the hair bundle (i.e., does not touch the hair bundle), can stimulate all stereocilia (albeit at different axes depending on hair bundle morphology), and delivers a force stimulus. With both stimulus types, we do not know how the second or third stereocilia rows (middle and shortest) are moving, for example the second row stereocilia might be directly pushed into the first row or it could be pulled by the movement of the first row. The differences in stimulus mode shape the MET responses differently (Caprara et al., 2019). It is debated whether stiff probes or fluid jets represent a more physiological stimulation (Corns et al., 2014; Fettiplace and Kim, 2014). Data

presented here identify issues with the fluid jet that make it unlikely to represent a physiological stimulation to either outer or inner hair cells. Problems also exist with the stiff probe (Nam et al., 2015); therefore neither device likely represents a physiological stimulus. However, each has biophysical advantages and disadvantages. Given the major differences in hair bundle response and channel activation associated with the mode of stimulation, it now becomes critically important to develop more physiological stimuli to assess the *in vivo* MET current properties accurately. One strategy is to identify how the hair bundle moves *in situ* and develop a device to mimic that. OHC hair bundles have long been hypothesized to be embedded in the tectorial membrane overlying the hair bundles (Kimura, 1966; Lim, 1972), but old and recent data also indicate that the IHC hair bundle may be attached to the tectorial membrane as well (Hoshino, 1976; Hakizimana and Fridberger, 2021). Knowing there are connections is not enough to mimic stimulation, as the mechanical properties of this coupling will be critical in hair bundles where the stereocilia are not strongly coupled. A better stimulation technique may be to keep the tectorial membrane intact or create an artificial tectorial membrane and stimulate the membrane directly. One potential flaw in these approaches may be that *in vivo,* it is the basilar membrane that is moving. Previous hemi-cochlea techniques achieve basilar membrane stimulation and may represent the most physiological stimulation to date (He et al., 2004).

## Origins of the Temporal Non-uniformity

The bundle displacement shows an initial motion due to the stimulus force onset, followed by a mechanical creep defined as a continued motion in the direction of the stimulus. The mechanical creep was characterized by a fast and slow exponential process and was not due to the motion of the apical surface (Caprara et al., 2019) and is diminished by fixing the tissue (Caprara et al., 2020). BAPTA treatment increased the overall motion and altered the creep kinetics but did not eliminate it (Caprara et al., 2020), suggesting that channel gating or tip-link stretch do not solely underlie the creep but may contribute to it. This result was consistent with Tobin et al. (2019), where the creep was not abolished after BAPTA treatment for the 2 and 4 kHz locations. When calculating the relative softening like Tobin et al. (2019) using time windows of 8–10 ms and 48–50 ms after stimulus onset, the hair bundle observes a relative softening of 17.1 ± 3.6% before and 9.5 ± 4.4% after BAPTA treatment ($n = 6$, $p = 0.0012$), similar to values of Tobin et al. (2019). Since the creep is not lost at other positions indicates that the slow creep is not simply determined by the tip-link and/or MET processes.

We modeled the hair bundle creep using a simple combination of springs and dashpots (**Figure 7A**). Past models of how a fluid jet stimulates the hair bundle suggested a slow creep is manifested through a spring-dashpot series combination (Vollrath and Eatock, 2003). We observe a similar kinetic, except with a double exponential onset, therefore warranting a second spring dashpot series combination. A viscoelastic material can be described by a similar spring-dashpot series combination. This model recapitulates the creep observed by the hair bundle and the effects of tissue fixation (**Figure 7B**). Using the model, we can also predict what would happen during a 2-pulse stimulation (**Figure 7C**). We analyzed our previous data (Caprara et al., 2019), and we found a similar behavior (**Figures 7D–F**). When

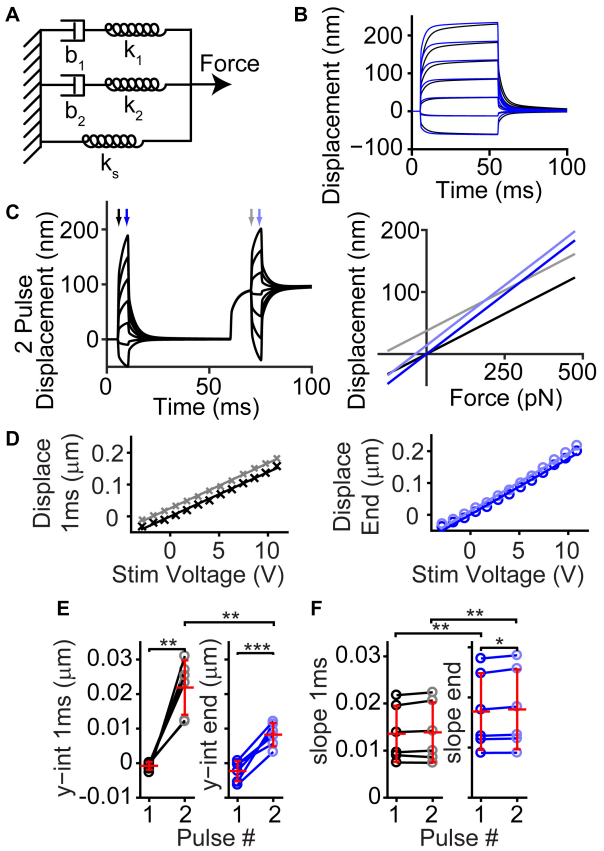


**FIGURE 7 |** Simple passive linear mechanical model explained the general shape of the complex hair bundle motion. **(A)** Passive mechanical model with a combination of springs (k) and dashpots (b) mimicking the classic model of motor adaptation with a second spring-dashpot combination to add the second creep time constant observed in hair bundle motion is shown. **(B)** Black lines are the resulting motion based on the model in panel **(A)** using 100 pN step sizes starting at −125 pN, blue lines indicate the resultant motion when $k_S$ and force applied is increased 2-fold, resulting in a similar effect as seen with fixed tissue (Caprara et al., 2020). **(C)** Using the same linear model, a 2-pulse experiment resulted in similar bundle motions (left) and changes in slope and intercept as observed in panel **(D)**. Displacement vs. force lines were taken at timepoints indicated by arrows in the displacement graph. **(D)** Plots of the bundle displacement at 1 ms and 3.9 ms (near the end of the stimulus) after stimulus onset for –84 mV data (analyzed from Caprara et al. (2019) Figure 3A) show a roughly linear relationship with fluid-jet stimulus voltage. Linear fits of the data indicate the slope (indicator for the effective stiffness of the hair bundle) and y-intercept (indicator of the offset of the hair bundle). **(E)** Summary of the y-intercepts indicated a positive shift in the hair bundle displacement with stimulation size between the first and second activation curves supporting the presence of a mechanical dashpot ($n = 6$, y-int 1 ms, $p = 0.0015$; y-int end, $p = 0.00094$). **(F)** Changes in the slopes of the fit indicated little change between pulses at the same time point, but a clear difference between the beginning and end of the short activation curve pulse indicating a change in effective stiffness ($n = 6$, Pulse 1, $p = 0.0040$, Cohen's $d = 0.53$; Pulse 2, $p = 0.0036$, Cohen's $d = 0.52$). $^*p < 0.05$, $^{**}p < 0.01$, and $^{***}p < 0.001$.

increasing the stereocilia pivot stiffness ($k_s$), we could mimic the changes observed with tissue fixation (Caprara et al., 2020). Since tissue fixation will remove any active processes, the resultant creep arises from a linear passive system. Fluid dynamics are unlikely to account for all of the observed creep, since force out of the pipette is step-like (**Figure 6C,D**), and similar creep is observed with flexible fiber stimulations where fluid dynamics are unlikely to have a role (Russell et al., 1992; Kennedy et al., 2005; Beurg et al., 2008). There are a few potential origins of the viscoelastic-like mechanism. One possibility is that diffusion of the lipid bilayer plays an important role (George et al., 2020), since the spring-dashpot model provides an approximation to the diffusion process. BAPTA insensitive hair bundle links may provide viscoelastic elements that are stretched during bending at the stereocilia base to generate the observed passive mechanics. These viscoelastic elements could also exist in the stereocilia rootlet, where the bending occurs (Furness et al., 2008; Kitajiri et al., 2010). More studies are required to narrow the list of potential origins.

Previously, the slow creep component was thought to originate from the slow adaptation mechanism and was modeled as a viscoelastic type mechanism (Howard and Hudspeth, 1987; Caprara et al., 2020). Even though the model contains only passive components of springs and dashpots, active motor molecules (myosins) were responsible for the dashpot. When using fixed tissue, the active motor molecule cannot be functional, therefore the presence of the creep when the tissue is fixed also argues against the motor model of adaptation underlying the slow creep component in OHCs (Caprara et al., 2020). Although our modeling of increasing the stereocilia pivot stiffness was able to recapitulate features of the fixed tissue motion, we cannot completely rule out that the overall diminished creep with tissue fixation was not just due to decreased function of the myosin motor in the viscoelastic-like element. However, this is rather unlikely, since the system appeared quite linear with negative, positive, small, and large stimulations resulting in similar creep properties in live tissue (**Figures 6A,B**). In the motor model of adaptation, larger stimulations would lead to saturation of slow adaptation and would be correlated with a decrease in the slow creep component, but we do not observe this effect (Howard and Hudspeth, 1987; Hacohen et al., 1989; Assad and Corey, 1992). Thus, the more likely scenario is that the creep is a result of a linear passive system.

### Physiological Relevance of Hair Bundle Motion

There are a few reasons for understanding the hair bundle motion. Since the hair bundle is composed of stereocilia shear detectors all along the hair bundle, if different parts of the hair bundle have different displacement sizes, then the activation curve and hence sensitivity of the hair bundle is broadened (Nam et al., 2015). When trying to understand the sensitivity of the cochlea and the mechanisms that contribute to sensitivity, it is imperative to know how the hair bundle is moving using the different stimulus modalities. This allows the proper biophysical characterization of the MET process itself. The next step is to determine the movement of the hair bundle *in vivo*. How the hair bundle moves in vivo is important for understanding the encoding of stimuli in the cochlea. The mechanical properties of the tectorial membrane and its interaction with the hair bundle as well as how the hair bundle is stimulated (shear vs. squish), can alter the coding of the stimuli. If these mechanical properties suggest a force stimulation on the hair bundle rather than the commonly thought of displacement stimulus, then the mechanical properties of the hair bundle will also alter coding of stimuli. For instance, the mechanical creep exhibited by the hair bundle during force stimuli can prolong the receptor current, which may increase fidelity of stimulus detection.

## CONCLUSION

Hair bundles stimulated with a fluid jet force stimulation exhibit spatial non-uniformities due to the hair bundle modifying the fluid flow and the inherent connections within the hair bundle that redistribute the forces on the stereocilia leading to the sides of the hair bundle exhibiting greater displacements than the center of the hair bundle. The bundle also exhibits a temporal non-uniformity seen as a mechanical creep that can be described by a linear passive system containing two viscoelastic-like mechanisms.

## MATERIALS AND METHODS

### Preparation and Recordings

Animals were euthanized by decapitation using methods approved by the University of Colorado IACUC or the Stanford University Administrative Panel on Laboratory Animal Care. Organs of Corti were dissected from postnatal day (P) 6–9 Sprague-Dawley rats (large majority of experiments used P7-P8) of either sex and placed in recording chambers as previously described (Peng et al., 2013). Tissue was viewed using a 100x (1.0 NA, Olympus, Pittsburg, PA, United States) water-immersion objective with a Phantom Miro 320s (Vision Research, Wayne, NJ, United States) camera on a Slicescope (Scientifica, Clarksburg, NJ, United States) illuminated with a TLED+ 525 nm LED (Sutter Instruments, Novato, CA, United States). Tissue was dissected and perfused with an extracellular solution containing (in mM): 140 NaCl, 2 KCl, 2 $CaCl_2$, 2 $MgCl_2$, 10 HEPES, 2 Creatine monohydrate, 2 Na-pyruvate, 2 ascorbic acid, 6 dextrose, pH = 7.4, 300–310 mOsm. In addition, an apical perfusion, with pipettes tip sizes of 150–300 μm, provided local perfusion to the hair bundles that was often turned off once a giga-ohm seal was achieved. In all preparations, the tectorial membrane was peeled off the tissue. For experiments with fixed tissue, fixation was with a 4% paraformaldehyde in phosphate-buffered saline overnight at 4°C. The solution was prepared from a 16% paraformaldehyde stock (Electron Microscopy Sciences, Hatfield, PA, United States).

### Electrophysiological Recordings

Whole-cell patch-clamp recordings were achieved on first or second row outer hair cells (OHCs) from middle to apical

cochlear turns using an Axon 200B amplifier (Molecular Devices, San Jose, CA, United States) with thick-walled borosilicate patch pipettes (2–6 MΩ) filled with an intracellular solution containing (in mM): 125 CsCl, 3.5 $MgCl_2$, 5 ATP, 5 Creatine Phosphate, 10 HEPES, 1 Cesium BAPTA, 3 ascorbic acid, pH = 7.2, 280–290 mOsm. For 0.1 mM and 10 mM BAPTA internal solution, the BAPTA and CsCl concentrations were adjusted accordingly to reach 280–290 mOsm. Experiments were performed at 18–22°C. Whole-cell currents were filtered at 10 kHz and sampled at 0.05–1 MHz using USB-6356 (National Instruments, Austin, TX, United States) controlled by jClamp (SciSoft Company, Ridgefield, CT, United States). Voltages were corrected offline for liquid junction potentials. All experiments used a −84 mV holding potential unless otherwise noted.

## Hair Bundle Stimulation and Motion Recording

Hair bundles are stimulated with a custom designed fluid jet driven by a piezoelectric disk bender (27 mm 4.6 kHz; Murata Electronics 7BB-27-4L0, Nagaokakyo, Japan). The fluid jet chamber was filled with low viscosity silicone oil (317667, Sigma-Aldrich). Thin wall borosilicate pipettes were pulled to tip diameters of 5–20 micrometers, filled with extracellular solution, and mounted in the fluid jet stimulator. The piezo-disk bender was driven by waveforms generated using jClamp, and the signals were filtered using an 8-pole Bessel filter (L8L 90PF, Frequency Devices Inc., Ottawa, IL, United States) at 1 kHz and variably attenuated (PA5, Tucker Davis, Alachua, FL, United States) before being sent to a high voltage/high current amplifier (Crawford Amplifier) to drive the piezo-disk. During stimulations, hair bundle motion videos were taken at 10,000 frames per second using the Phantom Miro 320s. Videos were saved for each stimulation and analyzed offline. Four stimulus presentations were averaged together at each stimulus level unless otherwise stated. In some experiments, a short flexible fiber that was straight or bent 90° to appear as a point in the high-speed videos was used to monitor local force generated by the fluid jet.

## Hair Bundle Motion Analysis

Custom MATLAB (MathWorks, Natick, MA, United States) scripts were used for extraction and analysis of the hair bundle motion. Movie frames were imported into MATLAB, and the hair bundle position was extracted using the center point of a Gaussian fit to a band-pass filtered hair bundle image (Ramunno-Johnson et al., 2009) for a given vertical row of pixels in the image to yield sub-pixel resolution. To assess whole bundle motion, the motion of all vertical lines along the hair bundle as well as the perpendicular motion was measured. For the perpendicular motion, the initial hair bundle position was generated at each pixel location using a Gaussian fit to the vertical pixel intensity profile, and a spline was created from these positions. Perpendicular lines to each pixel of the resting hair bundle position were calculated. For each frame, the intersection of the hair bundle spline and the perpendicular lines were determined, and the measured displacement was calculated as the displacement from the first frame.

With an incoherent hair bundle, experiments are more susceptible to stimulus artifacts. In one inner hair cell, normal stimulations resulted in MET currents and displacements that we typically observed (**Figure 8A**). In the same cell, upon moving the stimulation pipette further back, a stimulus artifact appeared due to some cellular debris on one side of the hair bundle and was only visible with slow-motion video (**Supplementary Video 2**). The stimulus artifact resulted in a slight hair bundle recoil on the right side of the bundle and resulted in what appeared to be a fast time-dependent current decline (**Figure 8B**). This artifactual motion reinforced the importance of tracking hair bundle motion in every experiment involving the fluid jet to ensure proper stimulation.

## Fluorescent Imaging

Videos of fluorescent dye from fluid jet stimulation, with and without hair cell bundles, using a pipette with a diameter slightly larger than the diameter of the hair bundle, were recorded using a swept-field confocal (Prairie Technologies) on a BX51-WI (Olympus) illuminated with a helium-neon laser at 594 nm. Each pipette was filled with spin-filtered 1 μM Alexa 594 in extracellular solution. Videos were recorded at 1,000 frames per second using a 100x 1.0NA dipping objective (Olympus, Pittsburg, PA, United States).

## Modeling

A MATLAB Simscape model was used to simulate the combination of springs and dashpots. A square force step was used to model the fluid jet step response. The base model used parameters: $b_1$ = 8.3 μN/(m/s) (Shepherd and Corey, 1994), $b_2$ = 3.4 μN/(m/s), $k_1$ = 250 μN/m (Tobin et al., 2019), $k_2$ = 2 mN/m, and $k_s$ = 2 mN/m (Beurg et al., 2008; Tobin et al., 2019). Some parameters were approximated from existing data and others were chosen to generate behavior similar to the hair bundle.

For modeling the fluid flow, we used a 3D computation with the finite element method. The puffer and the tall row of stereocilia in the bundle were configured, as indicated in **Figure 3E**. Flow through the bundle, which can occur for high amplitude stereocilia splaying, and bundle displacement were not considered. The objective was to determine the pressure and shear stress loading of the stereocilia for different puffer sizes and distances from the bundle. The equations for 3D, incompressible fluid flow (Stokes flow) were the following (Batchelor, 1967):

$$\mu\left(u_{,xx}+u_{,yy}+u_{,zz}\right)-p_{,x}=\rho u_{,t}$$

$$\mu\left(v_{,xx}+v_{,yy}+v_{,zz}\right)-p_{,y}=\rho v_{,t}$$

$$\mu\left(w_{,xx}+w_{,yy}+w_{,zz}\right)-p_{,z}=\rho w_{,t}$$

$$u_{,x}+v_{,y}+w_{,z}=0$$

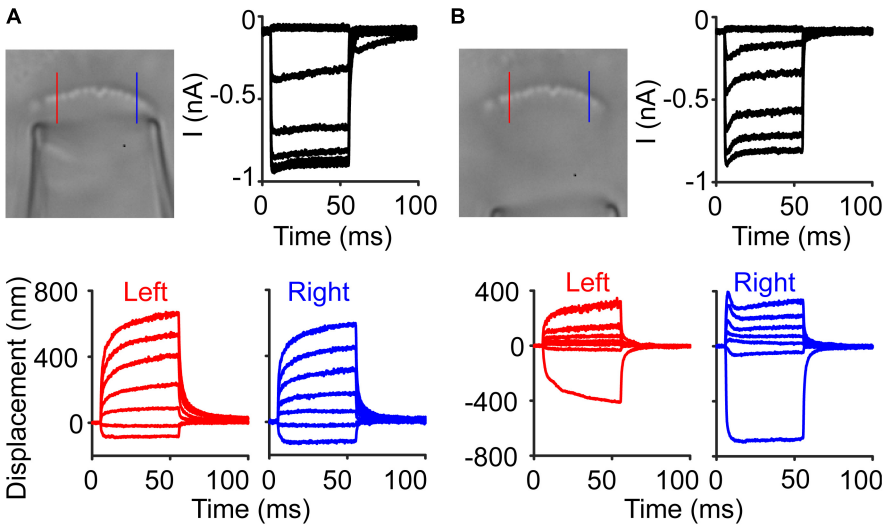


**FIGURE 8 |** Stimulus artifacts lead to the appearance of current adaptation. **(A)** An inner hair cell was stimulated with a fluid jet to elicit a current response with little adaptation observed in the current. Lines indicate locations where the hair bundle motion was taken in the raw image. **(B)** In the same cell, a larger amount of current adaptation was observed, but the hair bundle motion showed that on the right side of the hair bundle, there was a recoil of the hair bundle, causing an artifactual current decline.

where *x, y,* and *z* were the Cartesian coordinates, *t* was time, *u, v,* and *w* were the components of velocity in the *x, y,* and *z* directions, *p* was the pressure, μ was the viscosity, and ρ was the density. Time-dependent solutions are also computed for sinusoidal puffer pressure variation. Because of the small bundle size, the steady-state flow was accurate to well over 10 kHz. These equations were readily solved using the finite element mesh generation and equation solving capability in *Mathematica* (Wolfram, Champaign, IL, United States). The computation required only about 2 min on a laptop (Mac Book Pro, 2.7 GHz). The results were validated by assuring that no significant changes occurred with mesh refinement and that all boundary conditions were satisfied. The differences in the normal and shear stress acting on the front and back surfaces representing the tall row of stereocilia were calculated. This difference multiplied by the distance *z* from the rootlet was then integrated over the height, to obtain the moment acting on each stereocilium about the rootlet. The effective pressure and shear were the values that produce the moment if uniformly distributed.

Parameters for flow calculations: distance puffer face to cilia = 0.47 μm, diameter of puffer = 4.5 and 8 μm, width of cilia row = 5.4 μm, total angle of cilia row = 68.7°, thickness of cilia row = 0.4 μm, length of puffer shown = 4 μm, length of box = 20 μm, height of box = 20 μm (top view), 10 μm (side view), fluid viscosity = 0.7 mPa·s, fluid density = $10^3$ kg/m$^3$. The pressure on the puffer face was uniform with 1 Pa magnitude, while the pressure at the right end of the box was zero. All the other surfaces were no-slip, i.e., with zero velocity components at each point.

For the hair bundle finite element model, we used the model from Nam et al. (2015). Tip-link stiffness was 4 mN/m, lateral link stiffness was 10 mN/m on axis and 5 mN/m off axis, and the damping coefficient of lateral links was 10 μN/(m/s) on axis and 1 μN/(m/s) off axis. Simulations were run with forces applied to the tallest row of stereocilia with and without lateral links, and displacement of the stereocilia were measured.

## Data Analysis

IX plots used the displacement data from the high-speed imaging taking the displacement values at when the peak current occurred for 50 ms step traces. For multi-pulse protocols, displacement and current were taken 1 ms or 3.9 ms after stimulus onset, because

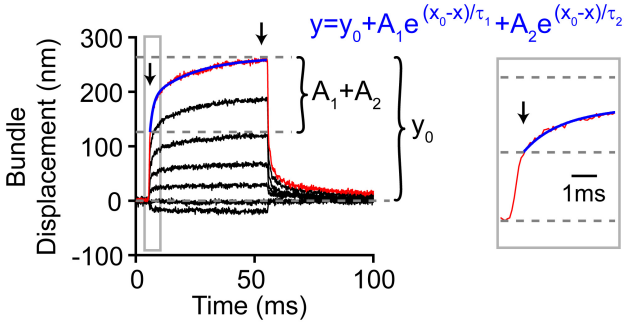


**FIGURE 9 |** Analysis method for hair bundle creep. Red line highlights the measured motion for the largest step, and blue indicates the double exponential fit (equation in blue) to the creep (gray box zooms in on the onset). Not all the bundle motion was included in the blue fit as shown. The zoom-in view shows the part of the onset that was not included in the fit. During this time, the force stimulus itself was still rising and reached a plateau 0.5 ms after force onset. Thus, the creep kinetics were fit after this. Arrows indicate the time points between which the creep was measured.

the steps were short (5 ms), and peak currents were not always reached during this time period. Normalized currents ($I/I_{max}$) were generated by subtracting leak current, which was defined as the smallest remaining current during the negative steps, and normalizing to the peak current. IX plots were fit with a double Boltzmann equation:

$$y = \frac{I_{max}}{1 + e^{Z_2(x_0 - x)}(1 + e^{Z_1(x_0 - x)})}$$

Where $Z_1$ and $Z_2$ were the slope factors and $x_0$ was the set point (Peng et al., 2016; Caprara et al., 2019).

The motion of the hair bundle was also fit with a double exponential equation:

$$y = y_0 + A_1 e^{-(x - x_0)/\tau_1} + A_2 e^{-(x - x_0)/\tau_2}$$

Where $\tau_1$ and $\tau_2$ were the time constants and $A_1$ and $A_2$ were the respective amplitudes (Caprara et al., 2019, 2020). Fits were done after the force of the stimulus plateaued, about 0.5 ms after stimulus onset (Caprara et al., 2019; **Figure 9**). Creep fit parameters were presented as an average of the six largest steps.

In some experiments, the hair bundle's position in each frame was fit using a quadratic equation:

$$y = ax^2 + bx + c$$

Where a was the quadratic coefficient, b was the linear coefficient, and c was a constant. We only used hair bundle positions in the middle parts of the hair bundle approximately from 0.25 to 0.75 of the hair bundle length because the ends of the hair bundle produced artifacts with our position finding algorithm as showcased in **Figure 1D** with gaps and curling at the hair bundle edges.

All sample sizes (n) were biological replicates of individual cells, where generally only one cell was used per animal. The only exception to this was the fixed tissue experiments, where consecutive cells in the same preparation were used. Each data point was the average of four presentations of the same stimulus intensity (technical replicates), unless otherwise noted.

Data were analyzed using jClamp, MATLAB, and Excel (Microsoft, Redmond, WA, United States). Graphs were created using MATLAB, Origin, and Adobe Illustrator. The mechanosensitive current/maximum mechanosensitive current was used as $P_{open}$, where we assumed we observed a $P_{open}$ of 100% when current amplitude was maximum. Maximum MET current was the difference between current values elicited from the maximal negative and maximal positive stimulation.

Statistical analysis used Student two-tailed *t*-tests from MATLAB or Excel unless otherwise stated. Paired tests were used when comparing across data points in the same cell and unpaired-unequal variance tests were used to compare data across cell populations. Significance (*p*-values) were as follows, $^{*}p < 0.05$, $^{**}p < 0.01$, $^{***}p < 0.001$, $^{****}p < 0.0001$. Data were presented as mean ± standard deviation unless otherwise noted. Cohen's d parameters were calculated using pooled variance.

## DATA AVAILABILITY STATEMENT

The raw data supporting the conclusions of this article will be made available by the authors, without undue reservation.

## ETHICS STATEMENT

The animal study was reviewed and approved by the University of Colorado Institutional Animal Care and Use Committee and Stanford University Administrative Panel on Laboratory Animal Care.

## AUTHOR CONTRIBUTIONS

AP and AR designed the research. AS and AR performed imaging and analyzed the data in **Figure 3**. DN performed experiments in **Figure 2**. CS performed the modeling of the 3D fluid flow. GC performed experiments with the flexible fiber in **Figures 5, 6**. AP performed all other experiments and analysis, developed the analysis code with some contribution from AS, and wrote the manuscript. All authors revised the manuscript.

## FUNDING

This work was supported by R00 DC013299 and R01 DC016868 to AP, R01 DC003896 to AR, R01 DC007910-09 to CS. AS was supported by the National Science Foundation Graduate Research Fellowship. DN was supported by T32 NS099042.

## ACKNOWLEDGMENTS

We would like to thank Jong-hoon Nam for providing the code for the FE hair bundle model and assisting in understanding the model and code.

## SUPPLEMENTARY MATERIAL

The Supplementary Material for this article can be found online at: https://www.frontiersin.org/articles/10.3389/fcell.2021.725101/full#supplementary-material

**Supplementary Video 1 |** Video of OHC stimulation from **Figure 1**. Playback is at 50 fps and of the last largest stimulation.

**Supplementary Video 2 |** Video of non-uniform motion of IHC from **Figure 8** showing artifactual relaxation on the right side of the hair bundle. Playback is at 50 fps and of the last largest stimulation.

## REFERENCES


Assad, J. A., and Corey, D. P. (1992). An active motor model for adaptation by vertebrate hair cells . *J. Neurosci.*12, 3291–3309. doi: 10.1523/JNEUROSCI.12-09-03291.1992

Batchelor, G. K. (1967). *An Introduction to Fluid Dynamics*. Cambridge: Cambridge University Press.

Beurg, M., Fettiplace, R., Nam, J. H., and Ricci, A. J. (2009). Localization of inner hair cell mechanotransducer channels using high-speed calcium imaging. *Nat. Neurosci.* 12, 553–558. doi: 10.1038/nn.2295

Beurg, M., Goldring, A. C., and Fettiplace, R. (2015). The effects of Tmc1 Beethoven mutation on mechanotransducer channel function in cochlear hair cells. *J. Gen. Physiol.* 146, 233–243. doi: 10.1085/jgp.201511458

Beurg, M., Nam, J. H., Crawford, A., and Fettiplace, R. (2008). The actions of calcium on hair bundle mechanics in mammalian cochlear hair cells. *Biophys. J.* 94, 2639–2653. doi: 10.1529/biophysj.107.123257

Caprara, G. A., Mecca, A. A., and Peng, A. W. (2020). Decades-old model of slow adaptation in sensory hair cells is not supported in mammals. *Sci. Adv.* 6:eabb4922. doi: 10.1126/sciadv.abb4922

Caprara, G. A., Mecca, A. A., Wang, Y., Ricci, A. J., and Peng, A. W. (2019). Hair bundle stimulation mode modifies manifestations of mechanotransduction adaptation. *J. Neurosci.* 39, 9098–9106. doi: 10.1523/JNEUROSCI.1408-19.2019

Corns, L. F., Johnson, S. L., Kros, C. J., and Marcotti, W. (2014). Calcium entry into stereocilia drives adaptation of the mechanoelectrical transducer current of mammalian cochlear hair cells. *Proc. Natl. Acad. Sci. U.S.A.* 111, 14918–14923. doi: 10.1073/pnas.1409920111

Corns, L. F., Johnson, S. L., Kros, C. J., and Marcotti, W. (2016). Tmc1 point mutation affects Ca2+ sensitivity and block by dihydrostreptomycin of the mechanoelectrical transducer current of mouse outer hair cells. *J. Neurosci.* 36, 336–349. doi: 10.1523/JNEUROSCI.2439-15.2016

Crawford, A. C., and Fettiplace, R. (1985). The mechanical properties of ciliary bundles of turtle cochlear hair cells. *J. Physiol. (Lond)* 364, 359–379. doi: 10.1113/jphysiol.1985.sp015750

Dinklo, T., Meulenberg, C. J., and Van Netten, S. M. (2007). Frequency-dependent properties of a fluid jet stimulus: calibration, modeling, and application to cochlear hair cell bundles. *J. Assoc. Res. Otolaryngol.* 8, 167–182. doi: 10.1007/s10162-007-0080-0

Fettiplace, R., and Kim, K. X. (2014). The physiology of mechanoelectrical transduction channels in hearing. *Physiol. Rev.* 94, 951–986. doi: 10.1152/physrev.00038.2013

Furness, D. N., Mahendrasingam, S., Ohashi, M., Fettiplace, R., and Hackney, C. M. (2008). The dimensions and composition of stereociliary rootlets in mammalian cochlear hair cells: comparison between high- and low-frequency cells and evidence for a connection to the lateral membrane. *J. Neurosci.* 28, 6342–6353. doi: 10.1523/JNEUROSCI.1154-08.2008

Geleoc, G. S., Lennan, G. W., Richardson, G. P., and Kros, C. J. (1997). A quantitative comparison of mechanoelectrical transduction in vestibular and auditory hair cells of neonatal mice. *Proc. R. Soc. Lond. B Biol. Sci.* 264, 611–621. doi: 10.1098/rspb.1997.0087

George, S. S., Steele, C. R., and Ricci, A. J. (2020). Rat auditory inner hair cell mechanotransduction and stereociliary membrane diffusivity are similarly modulated by calcium. *iScience* 23:101773. doi: 10.1016/j.isci.2020.101773

Guinan, J. J. Jr. (2012). How are inner hair cells stimulated? Evidence for multiple mechanical drives. *Hear Res.* 292, 35–50. doi: 10.1016/j.heares.2012.08.005

Hacohen, N., Assad, J. A., Smith, W. J., and Corey, D. P. (1989). Regulation of tension on hair-cell transduction channels: displacement and calcium dependence. *J. Neurosci.* 9, 3988–3997. doi: 10.1523/JNEUROSCI.09-11-03988.1989

Hakizimana, P., Brownell, W. E., Jacob, S., and Fridberger, A. (2012). Sound-induced length changes in outer hair cell stereocilia. *Nat. Commun.* 3:1094. doi: 10.1038/ncomms2100

Hakizimana, P., and Fridberger, A. (2021). Inner hair cell stereocilia are embedded in the tectorial membrane. *Nat. Commun.* 12:2604. doi: 10.1038/s41467-021-22870-1

He, D. Z., Jia, S., and Dallos, P. (2004). Mechanoelectrical transduction of adult outer hair cells studied in a gerbil hemicochlea. *Nature* 429, 766–770. doi: 10.1038/nature02591

Hoshino, T. (1976). Attachment of the inner sensory cell hairs to the tectorial membrane. A scanning electron microscopic study. *ORL J. Otorhinolaryngol. Relat. Spec.* 38, 11–18. doi: 10.1159/000275253

Howard, J., and Hudspeth, A. J. (1987). Mechanical relaxation of the hair bundle mediates adaptation in mechanoelectrical transduction by the bullfrog's saccular hair cell. *Proc. Natl. Acad. Sci. U.S.A.* 84, 3064–3068. doi: 10.1073/pnas.84.9.3064

Hudspeth, A. J. (2008). Making an effort to listen: mechanical amplification in the ear. *Neuron* 59, 530–545. doi: 10.1016/j.neuron.2008.07.012

Isojima, H., Iino, R., Niitani, Y., Noji, H., and Tomishige, M. (2016). Direct observation of intermediate states during the stepping motion of kinesin-1. *Nat. Chem. Biol.* 12, 290–297. doi: 10.1038/nchembio.2028

Karavitaki, K. D., and Corey, D. P. (2010). Sliding adhesion confers coherent motion to hair cell stereocilia and parallel gating to transduction channels. *J. Neurosci.* 30, 9051–9063. doi: 10.1523/JNEUROSCI.4864-09.2010

Kennedy, H. J., Crawford, A. C., and Fettiplace, R. (2005). Force generation by mammalian hair bundles supports a role in cochlear amplification. *Nature* 433, 880–883. doi: 10.1038/nature03367

Kimura, R. S. (1966). Hairs of the cochlear sensory cells and their attachment to the tectorial membrane. *Acta Otolaryngol. (Stockh)* 61, 55–72. doi: 10.3109/00016486609127043

Kitajiri, S., Sakamoto, T., Belyantseva, I. A., Goodyear, R. J., Stepanyan, R., Fujiwara, I., et al. (2010). Actin-bundling protein TRIOBP forms resilient rootlets of hair cell stereocilia essential for hearing. *Cell* 141, 786–798. doi: 10.1016/j.cell.2010.03.049

Kozlov, A. S., Risler, T., and Hudspeth, A. J. (2007). Coherent motion of stereocilia assures the concerted gating of hair-cell transduction channels. *Nat. Neurosci.* 10, 87–92. doi: 10.1038/nn1818

Kros, C. J., Marcotti, W., Van Netten, S. M., Self, T. J., Libby, R. T., Brown, S. D., et al. (2002). Reduced climbing and increased slipping adaptation in cochlear hair cells of mice with Myo7a mutations. *Nat. Neurosci.* 5, 41–47. doi: 10.1038/nn784

Langer, M. G., Fink, S., Koitschev, A., Rexhausen, U., Horber, J. K., and Ruppersberg, J. P. (2001). Lateral mechanical coupling of stereocilia in cochlear hair bundles. *Biophys. J.* 80, 2608–2621. doi: 10.1016/S0006-3495(01)76231-5

Lee, H. Y., Raphael, P. D., Park, J., Ellerbee, A. K., Applegate, B. E., and Oghalai, J. S. (2015). Noninvasive in vivo imaging reveals differences between tectorial membrane and basilar membrane traveling waves in the mouse cochlea. *Proc. Natl. Acad. Sci. U.S.A.* 112, 3128–3133. doi: 10.1073/pnas.1500038112

Lim, D. J. (1972). Fine morphology of the tectorial membrane. Its relationship to the organ of Corti. *Arch. Otolaryngol.* 96, 199–215. doi: 10.1001/archotol.1972.00770090321001

Nam, J. H., Peng, A. W., and Ricci, A. J. (2015). Underestimated sensitivity of mammalian cochlear hair cells due to splay between stereociliary columns. *Biophys. J.* 108, 2633–2647. doi: 10.1016/j.bpj.2015.04.028

Peng, A. W., Effertz, T., and Ricci, A. J. (2013). Adaptation of mammalian auditory hair cell mechanotransduction is independent of calcium entry. *Neuron* 80, 960–972. doi: 10.1016/j.neuron.2013.08.025

Peng, A. W., Gnanasambandam, R., Sachs, F., and Ricci, A. J. (2016). Adaptation independent modulation of auditory hair cell mechanotransduction channel open probability implicates a role for the lipid bilayer. *J. Neurosci.* 36, 2945–2956. doi: 10.1523/JNEUROSCI.3011-15.2016

Ramunno-Johnson, D., Strimbu, C. E., Fredrickson, L., Arisaka, K., and Bozovic, D. (2009). Distribution of frequencies of spontaneous oscillations in hair cells of the bullfrog sacculus. *Biophys. J.* 96, 1159–1168. doi: 10.1016/j.bpj.2008.09.060

Ricci, A. J., Crawford, A. C., and Fettiplace, R. (2000). Active hair bundle motion linked to fast transducer adaptation in auditory hair cells. *J. Neurosci.* 20, 7131–7142. doi: 10.1523/JNEUROSCI.20-19-07131.2000

Russell, I. J., Kossl, M., and Richardson, G. P. (1992). Nonlinear mechanical responses of mouse cochlear hair bundles. *Proc. Biol. Sci.* 250, 217–227. doi: 10.1098/rspb.1992.0152

Scharr, A. L., and Ricci, A. (2018). Stimulus dependent properties of mammalian cochlear hair cell mechanoelectrical transduction. *AIP Conf. Proc.* 1965:060001. doi: 10.1063/1.5038474

Shepherd, G. M., and Corey, D. P. (1994). The extent of adaptation in bullfrog saccular hair cells. *J. Neurosci.* 14, 6217–6229. doi: 10.1523/JNEUROSCI.14-10-06217.1994

Tobin, M., Chaiyasitdhi, A., Michel, V., Michalski, N., and Martin, P. (2019). Stiffness and tension gradients of the hair cell's tip-link complex in the mammalian cochlea. *Elife* 8:e43473. doi: 10.7554/eLife.43473.030

Velez-Ortega, A. C., Freeman, M. J., Indzhykulian, A. A., Grossheim, J. M., and Frolenkov, G. I. (2017). Mechanotransduction current is essential for stability of the transducing stereocilia in mammalian auditory hair cells. *Elife* 6:e24661. doi: 10.7554/eLife.24661.019

Vollrath, M. A., and Eatock, R. A. (2003). Time course and extent of mechanotransducer adaptation in mouse utricular hair cells: comparison with frog saccular hair cells. *J. Neurophysiol.* 90, 2676–2689. doi: 10.1152/jn.00893.2002

Yildiz, A., Tomishige, M., Vale, R. D., and Selvin, P. R. (2004). Kinesin walks hand-over-hand. *Science* 303, 676–678. doi: 10.1126/science.1093753

**Conflict of Interest:** The authors declare that the research was conducted in the absence of any commercial or financial relationships that could be construed as a potential conflict of interest.

**Publisher's Note:** All claims expressed in this article are solely those of the authors and do not necessarily represent those of their affiliated organizations, or those of the publisher, the editors and the reviewers. Any product that may be evaluated in this article, or claim that may be made by its manufacturer, is not guaranteed or endorsed by the publisher.

*Copyright © 2021 Peng, Scharr, Caprara, Nettles, Steele and Ricci. This is an open-access article distributed under the terms of the Creative Commons Attribution License (CC BY). The use, distribution or reproduction in other forums is permitted, provided the original author(s) and the copyright owner(s) are credited and that the original publication in this journal is cited, in accordance with accepted academic practice. No use, distribution or reproduction is permitted which does not comply with these terms.*

frontiers in Cell and Developmental Biology

METHODS
published: 22 October 2021
doi: 10.3389/fcell.2021.744248

# Electron Microscopy Techniques for Investigating Structure and Composition of Hair-Cell Stereociliary Bundles

*Maryna V. Ivanchenko[1]*, Artur A. Indzhykulian[2†] and David P. Corey[1†]*

*[1] Department of Neurobiology, Harvard Medical School, Boston, MA, United States, [2] Department of Otolaryngology, Massachusetts Eye and Ear, Harvard Medical School, Boston, MA, United States*

Hair cells—the sensory cells of the vertebrate inner ear—bear at their apical surfaces a bundle of actin-filled protrusions called stereocilia, which mediate the cells' mechanosensitivity. Hereditary deafness is often associated with morphological disorganization of stereocilia bundles, with the absence or mislocalization within stereocilia of specific proteins. Thus, stereocilia bundles are closely examined to understand most animal models of hereditary hearing loss. Because stereocilia have a diameter less than a wavelength of light, light microscopy is not adequate to reveal subtle changes in morphology or protein localization. Instead, electron microscopy (EM) has proven essential for understanding stereocilia bundle development, maintenance, normal function, and dysfunction in disease. Here we review a set of EM imaging techniques commonly used to study stereocilia, including optimal sample preparation and best imaging practices. These include conventional and immunogold transmission electron microscopy (TEM) and scanning electron microscopy (SEM), as well as focused-ion-beam scanning electron microscopy (FIB-SEM), which enables 3-D serial reconstruction of resin-embedded biological structures at a resolution of a few nanometers. Parameters for optimal sample preparation, fixation, immunogold labeling, metal coating and imaging are discussed. Special attention is given to protein localization in stereocilia using immunogold labeling. Finally, we describe the advantages and limitations of these EM techniques and their suitability for different types of studies.

**Keywords: hair cell, cochlea, stereocilia, electron microscopy, SEM, TEM, FIB-SEM, immunogold**

OPEN ACCESS

***Edited by:***
*Anthony Wei Peng, University of Colorado Anschutz Medical Campus, United States*

***Reviewed by:***
*David Furness, Keele University, United Kingdom*
*Nicolas Grillet, Stanford University, United States*

****Correspondence:***
*Maryna V. Ivanchenko*
*maryna_ivanchenko@hms.harvard.edu*

*† These authors have contributed equally to this work*

***Specialty section:***
*This article was submitted to Cell Growth and Division, a section of the journal Frontiers in Cell and Developmental Biology*

***Received:*** *20 July 2021*
***Accepted:*** *28 September 2021*
***Published:*** *22 October 2021*

***Citation:***
*Ivanchenko MV, Indzhykulian AA and Corey DP (2021) Electron Microscopy Techniques for Investigating Structure and Composition of Hair-Cell Stereociliary Bundles. Front. Cell Dev. Biol. 9:744248. doi: 10.3389/fcell.2021.744248*

## INTRODUCTION

Hair cells of the vertebrate inner ear bear at their apical surfaces a bundle of 30–300 actin-filled protrusions called stereocilia. Stereocilia mediate the hair cells' mechanosensitivity, both by their precise organization in rows of increasing height and with the force-gated ion channel complexes located at their tips (Assad et al., 1991; Gillespie and Walker, 2001; Geleoc and Holt, 2003; Beurg et al., 2009; Zhao and Muller, 2015; Fettiplace, 2017; Velez-Ortega and Frolenkov, 2019). Stereocilia are cross-linked by a variety of transient or permanent links which contribute to the integrity of the bundles—shaping the bundle during the development and keeping the proper stereocilia arrangement thereafter (Pickles et al., 1984; Goodyear et al., 2005).

Mutations in more than 120 genes have been shown to cause deafness in humans, and many more genes remain to be discovered (Van Camp, 2021)[1]. Hereditary deafness is often associated with morphological disorganization of stereocilia bundles, as either a primary or secondary consequence of the gene defect, and is often associated with an absence or mislocalization of specific proteins within stereocilia (Dror and Avraham, 2010; Richardson et al., 2011). Thus, stereocilia bundles are closely examined to understand most animal models of hereditary hearing loss. Because stereocilia have a diameter less than a wavelength of light, light microscopy is not always adequate to reveal subtle changes in morphology or protein localization. Transmitted or confocal light microscopy may hint at stereocilia defects, but electron microscopy is usually needed for full characterization.

For many years, electron microscopy (EM) techniques such as transmission electron microscopy (TEM; Furness and Hackney, 1985; Kachar et al., 2000; Goodyear et al., 2005; Mogensen et al., 2007; Grillet et al., 2009; Karavitaki and Corey, 2010; Mahendrasingam et al., 2017) and scanning electron microscopy (SEM; Furness and Hackney, 1985; Kachar et al., 2000; Mogensen et al., 2007; Grillet et al., 2009; Verpy et al., 2011; Indzhykulian et al., 2013; Fang et al., 2015; Parker et al., 2016; Mahendrasingam et al., 2017; Velez-Ortega et al., 2017; Ivanchenko et al., 2020b, 2021) have been used to study hair-cell bundles, and EM has proven to be essential for understanding stereocilia bundle development, maintenance, normal function, and dysfunction in disease. Immunogold electron microscopy techniques have been increasingly used in hearing research, providing excellent insight into structure-function relationships and protein distribution within the cell (Hasson et al., 1997; Garcia et al., 1998; Siemens et al., 2004; Furness et al., 2005; Michel et al., 2005; Goodyear et al., 2010; Verpy et al., 2011; Chen et al., 2012; Indzhykulian et al., 2013; Fang et al., 2015; Mahendrasingam et al., 2017; Wu et al., 2019; Han et al., 2020; Ivanchenko et al., 2020a).

These methods differ in their underlying physics and sample preparation, and each has advantages for certain experiments. TEM is a method in which a focused beam of electrons passes through an ultrathin 60–100 nm or semithin 250–500 nm section (Furness et al., 2008) specimen placed in an image plane of the electron optics (Bozzolla and Russell, 1998). The sample has been fixed and stained with heavy elements (e.g., osmium tetroxide, potassium ferrocyanide, uranyl acetate, lead citrate) which attach to certain cellular structures, thus enhancing the electron density of some parts of the cell more than others (Glauert and Lewis, 1998). The electrons passing through the samples are scattered more by the denser regions, resulting in dark regions on the projected image. TEM is useful in the analysis of almost all cellular components, including the cytoskeleton, membrane systems, organelles, etc. With new digital TEM cameras, 0.2–0.5 nm resolution in the X-Y plane can be obtained when working with biological samples.

[1]https://hereditaryhearingloss.org

The use of antibodies that are conjugated to 5–25 nm colloidal gold beads, used to localize proteins in cells, has been a major addition to EM (Jones, 2016). As an example, SEM enabled the initial discovery of the tip link (Osborne et al., 1984; Assad et al., 1991; Siemens et al., 2004), which pulls on the force-gated channel complex, but immunogold labeling confirmed its molecular composition (Ahmed et al., 2006; Kazmierczak et al., 2007; Sakaguchi et al., 2009; Goodyear et al., 2010; Indzhykulian et al., 2013). Many different protocols for immunogold TEM (IG-TEM) have been developed. The most commonly used techniques are either immunogold labeling before the sample is embedded in resin (pre-embedding) or immunogold labeling after embedding in resin (post-embedding) (Jones, 2016). In post-embedding immunolabeling, unfixed tissue is high-pressure frozen or fixed with formaldehyde, with or without a small amount of glutaraldehyde, then embedded in acrylic resin, e.g., Lowicryl (low-temperature embedding) or the hydrophilic LR-White resin (room temperature embedding and polymerization). Then blocks are sectioned and ultrathin sections are immunolabeled. The advantage of this method is that it can label proteins regardless of their location (intracellular or extracellular) and offers best ultrastructural preservation when adequate fixation is applied (Boykins et al., 2016; Jones, 2016). Also, a single block of tissue (e.g., a whole mouse cochlea) prepared for TEM yields thousands of sections to label with different antibodies, or alternatively can be used in serial section immunolabeling (Furness et al., 2009). Careful orientation of the sections allows visualization of several turns in cross-section and thus comparisons along the cochlear gradient within the same section. Estimates using calibrated immunogold with post-embedding immunogold labeling have enabled absolute protein densities to be calculated, for instance for PMCA2 in the stereociliary membrane (Chen et al., 2012) and for different calcium buffers in stereocilia compartments vs. the cell cytoplasm (Hackney et al., 2005). In several studies, relative protein concentrations have been compared between cells. Finally, double (or even triple) labeling can be achieved relatively easily with post-embedding immunogold using different-sized gold particles (Mahendrasingam et al., 2011). However, the limitation is that the antibodies have difficulty penetrating into the resin, and as a result, only the antigens that are exposed on the surface of the section can be immunolabeled.

In pre-embedding immunolabeling, the sample is fixed with a "gentle" fixative like formaldehyde, then immunolabeled. The cells are then post-fixed with glutaraldehyde and processed for SEM (Goodyear et al., 2010; Indzhykulian et al., 2013; Wu et al., 2019) or embedded in epoxy resin, blocks are sectioned, and ultrathin sections are imaged with TEM (Jones, 2016; Wu et al., 2019). Double labeling has been achieved with pre-embedding immunolabeling for extracellular epitopes (Goodyear et al., 2010). In contrast to post-embedding, pre-embedding immunolabeling offers better epitope preservation and better antibody binding, and thus a stronger signal. The limitation is that it works best for extracellular proteins where the epitopes are accessible to antibodies, while some intracellular epitopes can be labeled following permeabilization. The labeling procedures require extended incubations in buffers which leads

to reduced ultrastructural preservation since formaldehyde is a weaker fixative than glutaraldehyde. Also, pre-embedding allows a one-off labeling run and is thus more costly in terms of animals, material and time. A protocol in this paper describes a pre-embedding procedure for extracellular proteins that gives reliable results with almost perfect preservation of the ultrastructure.

In contrast to TEM, which allows to image intracellular compartments and organelles on thin sections, SEM is used to visualize surfaces and identify proteins on surfaces (Fischer et al., 2012). With SEM, an electron beam focused to a point scans the surface of a sample coated with a thin layer of conductive material, like platinum, palladium, or gold. In one imaging mode, the incident electrons excite metal atoms of the coating which emit secondary electrons (SE) that are collected by a detector. In another, incident electrons are scattered back, often by heavy metal beads; backscattered electrons (BSE) collected by a different detector. Following a raster scan, an image is created. The result is a two-dimensional (2-D) image of the sample surface; because of shading created from the topology of the specimen's surface and consequently by the angle of incidence of the beam, it appears three-dimensional (3-D). However, the metal sputter coating generates artifactual structures on the surfaces of stereocilia giving some increase in dimensions (e.g., of tip links) that become visible with higher resolution imaging. The use of the OTOTO technique (Heywood and Resnick, 1981; Furness and Hackney, 1985) (osmium tetroxide, followed by thiocarbohydrazide, osmium tetroxide, thiocarbohydrazide, osmium tetroxide) is an advantage in many cases. Thiocarbohydrazide serves as the cross-linking agent and allows more osmium to be taken up by the sample, thus eliminates the need for metal coating. The most common mode in SEM is SE detection, in which the electrons are emitted from the surface or the near-surface areas of the sample, and an image of the surface is created. In contrast, the BSE detection mode provides information about elemental composition of the scattering surface, with high sensitivity to differences in atomic number. Heavier atoms (with a higher atomic number) scatter electrons more strongly than lighter atoms and therefore produce a stronger signal, which appears brighter in the image. Using BSE, imaging can be achieved with nanometer resolution for detection and localization of proteins or other biological molecules immunolabeled with colloidal gold beads on the surface of the cell membrane (IG-SEM).

Serial EM techniques have added a third (Z) dimension, for a more complete representation of biological structure. These methods have become more accessible for use in hearing research, enabling a new body of work using 3-D EM approaches (Vranceanu et al., 2012; Bullen et al., 2015; Katsuno et al., 2019; Wu et al., 2019; Hadi et al., 2020; Ivanchenko et al., 2020a; Hua et al., 2021; Lu et al., 2021; Payne et al., 2021; Wood et al., 2021). The most commonly used 3-D EM techniques are serial section TEM (Harris et al., 2006), focused-ion-beam scanning electron microscopy (FIB-SEM; Kizilyaprak et al., 2014), and serial block-face SEM (SBF-SEM; Denk and Horstmann, 2004). Powerful but less commonly used is electron tomography (Auer et al., 2008).

Serial section TEM was the pioneer among the 3-D EM techniques, used first in the 1950s (Gay and Anderson, 1954). Consecutive thin sections, prepared with a routine ultramicrotome and collected on formvar coated slot or hole grids then are imaged with a conventional TEM and used for 3-D analyses (Miranda et al., 2015). Although technically demanding, it is a very data-rich method. The serial sections, if stored properly and imaged carefully, can be re-investigated many times for different aspects of a structure or to retake the sequence. Some techniques utilize tape-collecting ultramicrotomes to collect serial sections to be imaged with SEM (Goodyear et al., 2010; Baena et al., 2019) or TEM (Bock et al., 2011; Yin et al., 2020), in some cases automatically feeding the tape with EM sections into the microscope (Phelps et al., 2021). Another technique, serial block-face scanning electron microscopy (SBF-SEM), sections the specimen via an ultramicrotome built inside the SEM chamber. Each newly exposed face is imaged, followed by cutting and imaging a new face in an automated fashion (Denk and Horstmann, 2004). Finally, electron tomography consists of acquiring a tilt series of projected images in the electron microscope, followed by a number of image processing and digital reconstruction steps that generate a 3-D volume. It is especially useful for studies at the single protein level, or to avoid serial sectioning (Miranda et al., 2015). All these techniques enable 3-D serial reconstruction of resin-embedded biological structures at a resolution of a few nanometers in the X-Y plane, but vary in their Z step size and the optimal imaging area.

The FIB-SEM instrument is a combination of an SEM, usually equipped with a field-emission source, with a focused ion beam (FIB) of gallium ions that etch a sample embedded in epoxy resin. In FIB-SEM, a 5–20 nm slice is removed with the ion beam, and the newly exposed surface is imaged by the SEM backscatter detector. The process, called "slice and view," is repeated hundreds of times until a volume of cubic micrometers is imaged. The combination of imaging with an electron beam and slicing with the FIB in a dual-beam electron microscope opened new possibilities for serial imaging and 3-D reconstruction with electron microscopic resolution.

Although conventional FIB-SEM can be used to visualize a volume containing several cells in three dimensions with high resolution, it still does not provide information about protein localization. The use of immunogold labeled samples has overcome this limitation. Immunogold FIB-SEM (IG-FIB-SEM) can correlate biomolecular and structural information with high spatial resolution and in large volumes (Gopal et al., 2019; Wu et al., 2019; Ivanchenko et al., 2020a).

These methods vary in their resolution, speed and ability to image different tissues and proteins. Deciding which EM technique is best is sometimes not straightforward, and a combination of EM methods may eventually be chosen to address a single question. Here we describe the specific methods and imaging protocols for each technique. Parameters for optimal sample preparation, fixation, immunogold labeling, metal coating, and imaging are discussed. Special attention is given to protein localization in stereocilia using immunogold labeling. Finally, we describe the advantages and limitations

of these EM techniques and their suitability for different types of studies.

# MATERIALS AND METHODS

## General Instructions

1. Most chemicals used for EM are extremely hazardous, for instance carcinogenic or flammable, so general lab safety rules must be followed. Wear a lab coat, gloves, and protective eyewear whenever working with chemicals. Solutions should be prepared and used in a fume hood. Hazardous material waste must be collected and disposed of in accordance with Hazardous Waste Management guidelines.
2. Because EM sample preparation is a multi-step process, each step affects the final result, extreme fidelity to the protocol is essential. A mistake in any step can compromise the result.
3. An essential factor in EM is the quality of the water used for all the buffers and the solutions. Ultrapure water is recommended.
4. It is important to use a freshly prepared fixative at the same temperature as the tissue itself. Furthermore, it must be applied without delay. The best results are obtained if the fixative reacts with the sample within a few seconds after the removal from the cochlea. The volume of the fixative should exceed the volume of the sample by at least 20 times.
5. It is important to cut samples into pieces no larger than 1–2 mm. This allows rapid penetration of the chemicals, thereby ensuring ultrastructural integrity.
6. Stereocilia are very delicate structures and the integrity of hair cell bundles can be easily disrupted during the washing steps. Never touch the organ of Corti with the pipet tip, and exchange the solutions at a low speed.
7. Large specimens (such as an entire cochlea) must be kept in the dehydration solution for a longer period of time to enable complete removal of water from the specimen. They also require prolonged exposure to osmium tetroxide and extended infiltration in the embedding resin to allow these substances to fully penetrate the sample (Spoendlin and Brun, 1974; Bohne and Harding, 1993).
8. Fixation modifies the structure of antigens, often making them undetectable by specific antibodies. The time and type of fixation should be considered, especially for antibodies that are known to lose their specificity following antigen fixation. Also, antibodies can be made to glutaraldehyde fixed antigens.
9. If possible, previously published antibodies that have been successfully used for immunofluorescence labeling should be considered as a first choice. If using a newly produced antibody, validation experiments should be performed to determine their specificity, selectivity, and reproducibility.

## Tissue Preparation

Animal handling, breeding, and all procedures were performed in compliance with NIH Ethics guidelines and with a protocol approved by the Animal Care Committee of Harvard Medical School (HMS) and Massachusetts Eye and Ear. Mice were housed and bred at the HMS or the Massachusetts Eye and Ear animal facilities.

Neonatal mice (P1–P6) are anesthetized with cryoanesthesia. After the pup no longer responds to painful stimuli it is decapitated at the base of the head (foramen magnum). To access the cochlea, the cranium is opened along the sagittal suture and the caudal forebrain is cut off. Cochleas are isolated from the temporal bones in room temperature Leibovitz's L-15 medium without phenol red (GIBCO, 21083027). The bony labyrinth from each cochlea is removed by careful separation starting from the apex toward the base, using fine forceps. The organ of Corti is unwound from the modiolus. The spiral ligament is then removed from the organ of Corti using fine forceps. Organs then are immediately transferred to the fixative solution using a glass serological pipette with enlarged opening, or a transfer spoon, to prevent the tissue from passing through the water-air interface.

Adult mice (P30 and P90) are anesthetized with isoflurane. After they no longer respond to painful stimuli, they are euthanized by cervical dislocation and decapitated. Cochleas are extracted into a plastic dish filled with a room temperature Leibovitz's L-15 solution. The stapes is removed from the oval window and the round window membrane punctured with fine forceps, to allow fixative to flow through the cochlea. Under a stereomicroscope, a small hole is made in the apex of the cochlea using a 27G needle connected to a 1 ml syringe. Cochleas then are immediately transferred to the fixative solution.

We have found that temperature is not critical and processing on ice is not necessary. All dissection and fixation steps are performed at room temperature.

## Preparation of Solutions

### Solutions for Cochlear Dissection

Leibovitz's L-15 medium, no phenol red (GIBCO, 21083027) is often used. The medium contains amino acids, vitamins, inorganic salts, and other components to maintain cell health and survival in environments without $CO_2$ equilibration. It includes 1.2 mM $Ca^{2+}$, essential to preserve the tip links.

### Solutions for Rinsing

(a) Sodium cacodylate buffer, 0.1 M, pH 7.4, 100 ml is prepared by mixing 50 ml of commercial sodium cacodylate buffer, 0.2 M, pH 7.4 [Electron Microscopy Sciences (EMS), 11652] with 50 ml distilled $H_2O$ ($dH_2O$). This solution can be prepared in advance and stored at 0–5°C. It can be used within 2–3 months. *The sodium cacodylate buffer contains arsenic, which is poisonous and carcinogenic.*

(b) Hank's balanced salt solution (HBSS), with calcium and magnesium, no phenol red, 500 ml (GIBCO, 14025092).

(c) HBSS, with no calcium or magnesium, no phenol red, 500 ml (GIBCO, 14175095).

### Solutions for Fixation

Always use electron microscopy or analytical grade reagents.

(a) 2.5% glutaraldehyde in 0.1 M cacodylate buffer (pH 7.2) supplemented with 2 mM $CaCl_2$ is prepared by adding

10 μl of 2 M $CaCl_2$ stock solution to 10 ml of 2.5% glutaraldehyde in 0.1 M sodium cacodylate buffer, pH 7.4 (EMS, 15960). To make 100 ml of 2 M $CaCl_2$, dissolve 29.4 g of calcium chloride dihydrate (EMS, 12340) in 100 ml of $dH_2O$.

(b) 4% formaldehyde in HBSS with calcium and magnesium, no phenol red (pH 7.2) is prepared by mixing 10 ml of 16% formaldehyde aqueous solution (EMS, 15700) in 30 ml of HBSS with calcium and magnesium, no phenol red (pH 7.2) (GIBCO, 14025092).

(c) 4% formaldehyde/1% glutaraldehyde fixative in 0.1 M sodium cacodylate buffer (100 ml) can be prepared by mixing 25 ml of 16% formaldehyde aqueous solution (EMS, 15700) with 2 ml of 50% glutaraldehyde aqueous solution (EMS, 16300), 50 ml of sodium cacodylate buffer, 0.2 M, pH 7.4 (EMS, 11652), and 23 ml $dH_2O$.

(d) 2.5% glutaraldehyde in 0.1 M cacodylate buffer (pH 7.2) containing 1% (or 5%) tannic acid and supplemented with 2 mM $CaCl_2$ is prepared by dissolving 0.1 g (or 0.5 g) of tannic acid, A.C.S. (EMS, 21710) with 10 ml 2.5% glutaraldehyde in 0.1 M cacodylate buffer (pH 7.2) supplemented with 2 mM $CaCl_2$ (see a).

## Solutions for Staining

(a) 2% aqueous osmium tetroxide is prepared by diluting 5 ml of 4% aqueous osmium tetroxide (EMS, 26604-01) in 5 ml of $dH_2O$. *Osmium tetroxide vapors can cause burns or severe irritation of the skin, respiratory tract, and eyes, and can cause long-term health effects.*

(b) 1% osmium tetroxide/1.5% potassium ferrocyanide in 0.1 M cacodylate buffer, (pH 7.2) is prepared right before use by mixing a solution containing 3% potassium ferrocyanide in 0.2 M cacodylate buffer with 4 mM $CaCl_2$ with an equal volume of 2% aqueous osmium tetroxide.

(c) 3% stock potassium ferrocyanide in 0.2 M cacodylate buffer with 4 mM $CaCl_2$ is prepared by dissolving 0.3 g of potassium ferrocyanide trihydrate (EMS, 26604-01) in 10 ml of 0.2 M sodium cacodylate buffer (EMS, 11652) and supplementing with 20 μl of 2 M $CaCl_2$ stock.

(d) 1% aqueous tannic acid is prepared right before use by dissolving 0.1 g of tannic acid, A.C.S. (EMS, 21710) in 10 ml $dH_2O$.

## Solutions for Dehydration

For the dehydration step, about 50 ml of the following solutions are needed. These solutions can be prepared in advance and stored in tightly closed glass bottles at room temperature for a long time. *Ethanol and propylene oxide are flammable; propylene oxide is carcinogenic.*

(a) 25, 50, 70, 80, and 95% ethanol in $dH_2O$, 50 ml each.

(b) Ethanol, absolute (200 proof, molecular biology grade).

(c) Propylene oxide (EMS, 20401).

(d) Propylene oxide/ethanol (1:1).

## Embedding Resins

(a) Araldite 502/Embed 812 embedding medium without the accelerator (EMS, 13940) can be prepared by pouring measured volumes of Embed-812 (12.5 ml); DDSA (27.5 ml), Araldite 502 (7.5 ml) into a graduated 50 ml polypropylene tube with a tight cap. The best way to accomplish this is to warm components for 15–20 min in the oven (60°C) to reduce their viscosity prior to measuring and mixing the resin. After pouring the warmed resin into the 50 ml polypropylene tube, tighten the cap and keep it on the tube rocker for 10–15 min. For larger batches, the components should be increased proportionally. Unused embedding mix can be stored for up to 6 months at 4–8°C in a tightly closed container. In order to prevent rapid polymerization of the resin during storage, ensure that stored resin mixture does not include an accelerator. However, it is preferable to use a freshly prepared embedding medium. If using a previously stored mixture, it has to be warmed before adding the accelerator. Mix components thoroughly, avoiding bubbles, as they can interfere with the tissue embedding. Plan enough time between mixing the resin and the embedding step for the bubbles to disappear.

(b) 3:1 solution of propylene oxide/Araldite 502/Embed 812 embedding medium can be prepared by mixing 30 ml of propylene oxide (EMS, 20401) with 10 ml of Araldite 502/Embed 812 embedding medium without the accelerator.

(c) 1:1 solution of propylene oxide: Araldite 502/Embed 812 embedding medium can be prepared by mixing 20 ml of propylene oxide (EMS, 20401) with 20 ml of Araldite 502/Embed 812 embedding medium without the accelerator.

(d) 1:3 solution of propylene oxide: Araldite 502/Embed 812 embedding medium can be prepared by mixing 10 ml of propylene oxide (EMS, 20401) with 30 ml of Araldite 502/Embed 812 embedding medium without the accelerator.

(e) Araldite 502/Embed 812 embedding medium with accelerator can be prepared by adding 100 μl of DMP-30 to 5 ml Araldite 502/Embed 812 embedding medium. It has to be prepared just before use to avoid rapid polymerization. The components should be mixed thoroughly using a tube rocker for 10–15 min; avoid creating bubbles.

*Epoxy resin monomers can cause severe contact dermatitis and are carcinogenic. Propylene oxide can carry resins into the skin even through gloves.*

Although our choice of resin is Araldite 502/Embed 812 (low viscosity epoxy resin), other resins such as Epon 812 (Katsuno et al., 2019) (low viscosity epoxy resin), Spurr's resin (Hua et al., 2021; Wang et al., 2021) (less viscous than Epon mixtures), Lowicryl HM-20 (Velez-Ortega et al., 2017) (formulated to provide low viscosity at low temperatures),

LR-White (Furness et al., 2008; Mahendrasingam et al., 2011) (hydrophilic acrylic resin), and Durcupan (Dow et al., 2018) (water-miscible epoxy resin) have been successfully used to study hair cell stereocilia bundles.

### Solutions for Immunogold Labeling

A blocking reagent is used to reduce background from non-specific, conserved sequence and/or Fc receptor binding sites. Normal serum (10%) is diluted in HBSS, with no calcium or magnesium, no phenol red (GIBCO, 14175095). The best results are obtained using the normal serum from the same host as the secondary antibody.

(a) 10% normal goat (or donkey) serum is prepared by diluting 1 ml of stock normal goat (or donkey) serum in 9 ml of HBSS with no calcium or magnesium, no phenol red (GIBCO, 14175095). It has to be prepared freshly and stored at 4°C for use within 48 h. An alternative solution for HBSS is Tris-buffered saline (TBS).

(b) Some vendors provide the serum as a dry, lyophilized powder. In that case, the stock of normal goat (or donkey) serum is prepared by dissolving the serum (Jackson ImmunoResearch, 005-000-121) in 10 ml of $dH_2O$. If the solution is not clear, it is advisable to use centrifugation. The stock product can be aliquoted and stored frozen at −20°C for 1 year; avoid repeated freeze-thaw cycles.

(c) The desired concentrations of solutions for the primary and secondary antibody are prepared in blocking solutions (10% normal serum, see above). The antibody solution must be prepared freshly before use and should be kept cold, on an ice box.

(d) In this work, we used the following antibodies:

- Rabbit anti-PKHD1L1 primary antibody (NovusBio, NBP2-13765), 1:200 dilution in blocking solution.
- Rabbit anti-PCDH15 primary antibody (DC 811), 1:200 dilution in blocking solution. This antibody has been custom made using the same epitope as the previously reported and well-characterized PB811 (Kazmierczak et al., 2007).
- Rabbit anti-STRC primary antibody raised against amino acids 970–985 of the mouse stereocilin protein (Han et al., 2020) 0.12 nm Colloidal Gold AffiniPure Goat Anti-Rabbit IgG (EM Grade) secondary antibody (Jackson ImmunoResearch, 111-205-144), 1:30 dilution in blocking solution.
- Gold Conjugate EM Goat F(ab')2 anti-rabbit IgG: 10 nm gold secondary antibody (BB International #14216), 1:30 dilution in blocking solution.

### Post-staining Solutions

(a) 1% methylene blue/1% sodium borate solution can be prepared by first dissolving 2 g of methylene blue crystals (EMS, 22050) in 100 ml $dH_2O$. The sodium borate solution can then be prepared by dissolving 2 g of sodium borate (EMS, 21130) in 100 ml $dH_2O$. Filter the solutions through a 0.22 μm syringe filter. The two solutions should be mixed 1:1 and stored in a brown bottle.

(b) 5% methanolic uranyl acetate (EMS, 22400) is prepared by dissolving 5 g of uranyl acetate in 48 ml of near-boiling $CO_2$-free double-distilled water. Once the uranyl acetate crystals are fully dissolved, the solution is filtered through a 0.22 μm syringe filter and additionally diluted with 48 ml of acetone-free methanol. The advantage of a methanolic uranyl acetate is that it penetrates more easily into plastic sections giving a higher contrast. Because uranyl acetate is light sensitive, it should be stored in a 100 ml glass brown bottle, or the container should be wrapped with aluminum foil to exclude light, and capped tightly. This stock solution can be stored at 4°C for several months.

(c) Lead citrate is prepared as described by Reynolds (1963) by dissolving 1.33 g of lead nitrate (EMS, 17900) and 1.76 g of sodium citrate (EMS, 21140) in 30 ml of freshly boiled and cooled, deionized, or distilled water in a 50 ml volumetric flask. The milky suspension is shaken vigorously for 1 min, followed by continued intermittent shaking to ensure complete conversion of lead nitrate to lead citrate. After 30 min, 8.0 ml of carbonate-free, 1 N NaOH solution is added, making the solution clear. Carbonate-free, 1 N NaOH solution purchased from a reliable vendor is preferable to freshly prepared solutions made in the laboratory. Dilute the resulting solution to 50 ml with freshly boiled deionized or distilled water. The Reynold's solution may be stored in a glass-stoppered bottle for up to 6 months. The pH of the final solution should be about 12.0. In addition, an improved method for storing stains has been described (Reynolds, 1963). Before use, pass the solution through a microfilter.

An alternative protocol for immediate use is to dissolve lead citrate compound (between 0.1 and 0.4 mg in 10 ml ultrapure water) at high pH by adding 4 N NaOH.

## Step-by-Step Procedures Used in This Study

### Protocol for Conventional Scanning Electron Microscopy

#### *Fixation*

P1–P3 cochlear explants are fixed immediately after dissection, with 2.5% glutaraldehyde in 0.1 M cacodylate buffer (pH 7.2) supplemented with 2 mM $CaCl_2$, for 2 h at room temperature. The samples are rinsed three times in sodium cacodylate buffer, 0.1 M, pH 7.4 for 10 min, and then briefly once in distilled water.

P4–P7 explants are prefixed immediately after dissection with 4% formaldehyde in HBSS with calcium and magnesium, no phenol red (pH 7.2) for 10–15 min, and then transferred to HBSS with calcium and magnesium, no phenol red (pH 7.2). Under a dissecting microscope, the tectorial membrane overlaying the hair cells is pulled away using fine forceps to expose the sensory epithelium. The organ of Corti is postfixed with 2.5% glutaraldehyde in 0.1 M cacodylate buffer (pH 7.2) supplemented with 2 mM $CaCl_2$ for 2 h at room temperature. Samples are rinsed three times in sodium cacodylate buffer, 0.1 M, pH 7.4 for 10 min, and then briefly once in distilled water.

Adult cochleas are prefixed immediately after dissection by immersion in 1% glutaraldehyde/4% formaldehyde in 0.1 M cacodylate buffer (pH 7.2) supplemented with 2 mM $CaCl_2$, for 1 h at room temperature. Additionally, samples are gently and slowly perfused with 1% glutaraldehyde/4% formaldehyde solution via the round and oval windows until the solution is washed out of the small hole at the apex. After the prefixation step, the samples are fixed with 2.5% glutaraldehyde in 0.1 M cacodylate buffer (pH 7.2) supplemented with 2 mM $CaCl_2$, for 1 h at room temperature, rinsed in 0.1 M cacodylate buffer (pH 7.2) and then rinsed in distilled water. The cochlear bone is carefully peeled out with a 27-gauge needle, then the organ of Corti is microdissected and the tectorial membrane is pulled out to expose the sensory epithelium. Next, the samples are immersed in a saturated aqueous solution of 1% osmium tetroxide for 1 h in the dark, washed once with water for 10 min, and postfixed with 1% tannic acid aqueous solution for 1 h in the dark (a modified OTOTO protocol). Finally, the samples are rinsed in distilled water.

### *Dehydration in an ascending series of ethanol*

Glass scintillation vials (20 ml) are prepared and each is filled with 2 ml of $dH_2O$. Each sample is transferred to a vial. The following volumes of absolute ethanol are added to the vial every 10 min: 250 μl, 500 μl, 1000 μl, 2 ml, 4 ml, 8 ml, and 8 ml. Next, the solution is replaced with pure ethanol for 30 min. If samples need to be stored overnight or for extended periods, they have to be kept in 70% ethanol at 4°C to minimize the loss of lipids. However, to achieve the best results we recommend prompt critical point drying.

### *Critical point drying*

The top of the mesh basket (EMS, 70190-01) for the critical point dryer is placed into a 60 mm Petri dish filled with absolute ethanol. The samples are carefully transferred into the basket with a glass pipette or a transfer spoon while they are observed under a dissecting microscope. The bottom part of the basket is screwed onto the top part while ensuring the sample remains submerged in ethanol. The sample should never be exposed to the air as ethanol evaporates very quickly and may cause artifacts. Both the top and the bottom parts of the mesh basket (EMS, 70190-01) are made from a stainless steel mesh, which offers good fluid circulation. The mesh baskets with samples are quickly transferred into the critical point dryer chamber filled with ethanol, minimizing the time the sample is exposed to air. Several automated critical point drying systems are available on the market. We recommend using the manufacturer's protocol for specimen loading and operation. In this work, a Tousimis Autosamdri 815 system was used.

### *Mounting*

The appropriate aluminum specimen stub mount must be securely placed under the dissecting microscope to allow for observation and access. Use the specimen stub mount that is compatible with the SEM specimen holder of the microscope. The ultra-smooth carbon adhesive tab (EMS, 77827-12) is placed on the aluminum specimen stub, and the top protective layer is peeled off. The organ of Corti is carefully picked up with the tip of 27G needle and mounted ∼2 mm from the edge of the specimen stub, oriented with hair cells upward and with the cochlea coil facing the edge. The organ of Corti is extremely fragile and delicate after critical point drying, so very small pressure should be applied with the needle to mount it on the specimen stub. To improve the sample conductivity, a small dot of Silver Conductive Adhesive 503 (EMS, 12686-15) can be placed on the carbon disk around the sample if necessary.

### *Sputter coating*

The samples are sputter coated with platinum to a thickness of 5 nm using the instrument manufacturer's protocol. The coated stubs are then transferred to a suitable holder and stored in a desiccator before imaging. The OTOTO (Heywood and Resnick, 1981; Furness and Hackney, 1985) method eliminates the need for metal coating and avoids sample thickening after coating; as a result, the tip links appear much thinner (Furness and Hackney, 1985).

### *Imaging*

The samples are observed in a field-emission scanning electron microscope with a SE detector using the SEM manufacturer's guidelines. To achieve the best orientation of the hair bundles during the imaging and a high SE signal, a 45° tilting sample holder is used (Ted Pella, 15329-7). The aluminum specimen stub mount is oriented with the organ of Corti located at the highest point (closest to the detector). A flat holder for multiple stubs also can be used (Ted Pella, 15310-6) if compatible with SEM. In this study, SEM images were taken with a Hitachi S-4700 field-emission SEM. During the imaging process, the best signal is obtained using the following parameters of the electron beam: accelerating voltage 3–5 kV, current 10 μA, and working distance 6–8 mm.

## Protocol for Conventional Transmission Electron Microscopy

### *Fixation*

P1–P6 explants are prefixed immediately after dissection with 2.5% glutaraldehyde in 0.1 M cacodylate buffer (pH 7.2) supplemented with 2 mM $CaCl_2$ for 10 min at room temperature; samples are then transferred to 2.5% glutaraldehyde in 0.1 M cacodylate buffer (pH 7.2) supplemented with 1% tannic acid for 1–2 h at room temperature to visualize links, or to 5% tannic acid for 12 h at 4°C to visualize the stereocilia surface coat. Samples are rinsed three times in sodium cacodylate buffer, 0.1 M, pH 7.4 for 10 min, and then once in distilled water.

### *Post-fixation*

For increased contrast, samples are post-fixed with 1% osmium tetroxide/1.5% potassium ferrocyanide in 0.1 M cacodylate buffer for 2 h at room temperature in the dark. Then samples are washed three times in 0.1 cacodylate buffer (pH 7.2), then briefly washed in distilled water.

### *Dehydration*

We find most convenient throughout the dehydration steps to keep each cochlea in the 10 ml glass scintillation vials or 1.5 Eppendorf tubes in which cochleas were fixed and stained. The

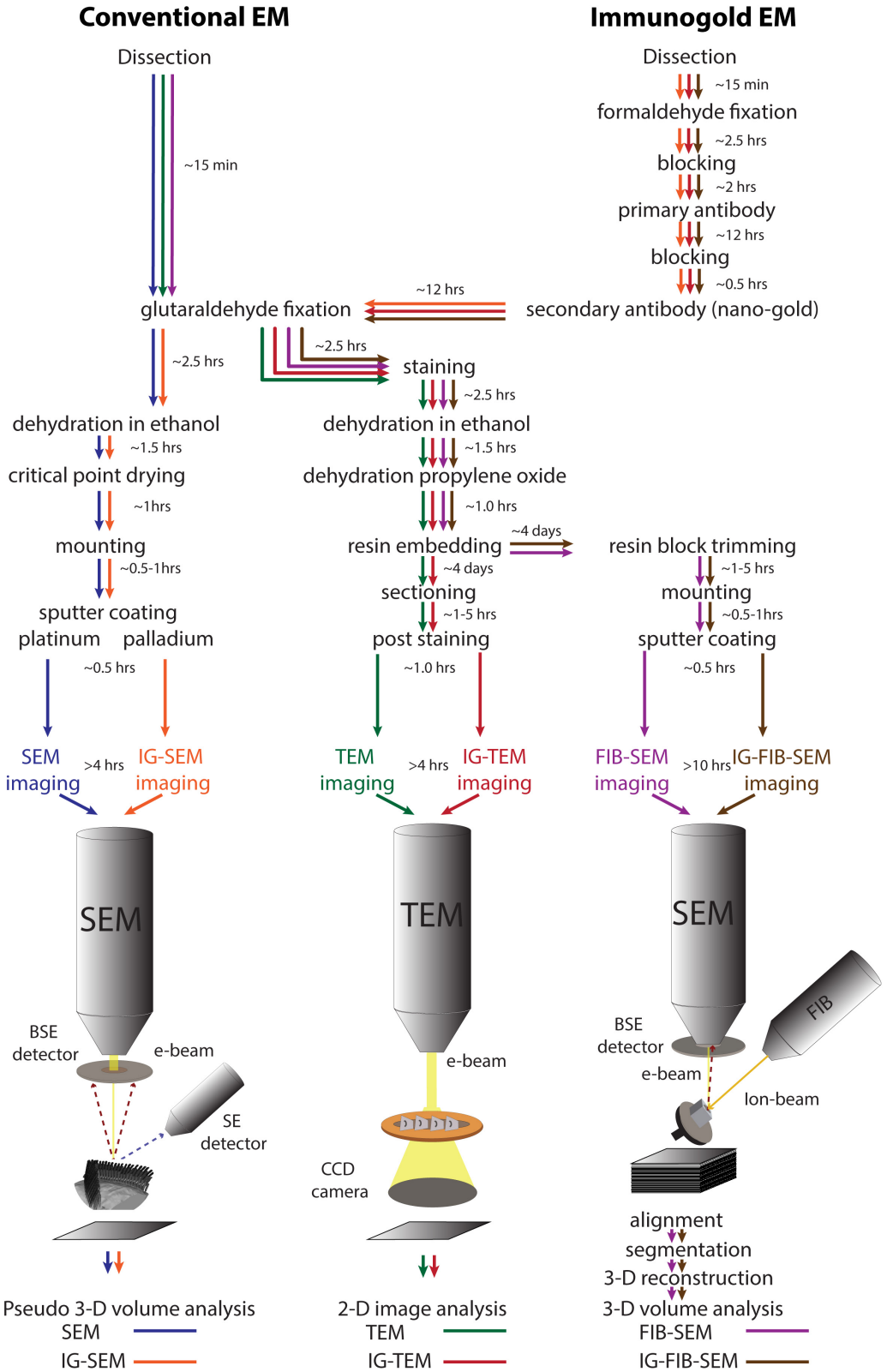


**FIGURE 1 |** A schematic diagram of the work flow for different electron microscopic approaches: conventional SEM (blue), conventional TEM (green), FIB-SEM (magenta), IG-SEM (orange), IG-TEM (red), IG-FIB-SEM (brown). The time ranges refer to the protocols used in this study. SE, secondary electrons; BSE, backscattered electrons.

samples are dehydrated at 0°C in an ascending series of ethanol concentrations, as described for SEM, according to the following schedule:

- 25% ethanol two times for 2 min each.
- 50% ethanol two times for 2 min each.
- 70% ethanol two times for 5 min each.
- 80% ethanol two times for 5 min each.
- 95% ethanol three times for 5 min each.
- Absolute ethanol two times for 10 min each.
- Propylene oxide/ethanol (1:1) two times for 10 min each.

Next, samples are equilibrated in propylene oxide three times for 15 min each.

Alternatively, the dehydration can be paused at the 70% ethanol step and the tissue sample can be stored for a day or two in the cold to minimize loss of lipids.

### *Embedding*

After the sample is dehydrated, the intermediate solvent such as propylene oxide has to be replaced with a liquid resin that can be polymerized or cured to form a solid block with good sectioning properties.

Samples are infiltrated and embedded in propylene oxide/epoxy resin mixtures as follows:

- 3:1 solution of propylene oxide/epoxy embedding medium for 4–6 h.
- 1:1 solution of propylene oxide/epoxy embedding medium for 4–8 h.
- 1:3 solution of propylene oxide/epoxy embedding medium for 8 h.
- Araldite 502/Embed 812 embedding medium with accelerator for 12 h.

A sufficient amount of embedding resin is added. In each step, the vials are carefully tilted to the sides to ensure that the tissue pieces are fully immersed in embedding resin.

Flat embedding molds (EMS, 70900) are suitable for cochlear samples, as they allow a more accurate orientation of the tissue. Those molds are made from transparent silicon rubber and have elongated recesses 3–5 mm deep. Before transferring the sample into the mold, a small elongated piece of paper is placed with the printed sample identifier (e.g., 06356/p79) opposite the assigned sample location. The molds are filled with Araldite 502/Embed 812 embedding medium with the accelerator. The tissue pieces are transferred into the molds using a plastic inoculating loop. Once the samples are fully immersed in the resin solution, a toothpick is used to align the sample for correct orientation under a dissecting microscope. The samples are polymerized in the oven at 60°C for 48 h.

### *Sectioning*

*Preparation of semi-thin sections (0.7–1.5 μm).* Semi-thin sections can initially be cut, stained with 1% methylene blue/1% sodium borate solution and examined under a light microscope to identify the region of the block containing the organ of Corti and its spatial orientation in the block (**Figure 2**).

The block is placed into the holder and mounted to the ultramicrotome adapter so the sample is viewed under a dissecting microscope while trimming. A new, single-edged razor blade is used to trim the faces of the block and its edges to form a trapezoid. Unwanted plastic is removed as much as possible. The block is further trimmed with a TrimTool 90 (EMS, Diatome TT-90).

To find the best orientation for sectioning, semi-thin sections are first cut and stained with methylene blue to examine the tissue. The block is sectioned with a diamond knife or glass knife until the tissue is revealed and then a ribbon of 0.7–1.5 μm sections is cut. Several drops of $dH_2O$ are placed on the glass slide. The sections are transferred onto the water drops and then the slide is placed on a plate preheated to 70–90°C to allow the drops to evaporate and the sections to adhere to the slide. A large drop of methylene blue stain is added onto the sections and the slide is kept on a hot plate for 45–60 s, ensuring that the stain solution does not evaporate. Afterward, the slide is washed with distilled water thoroughly, dried, and examined under a light microscope. The tissue is stained in varying intensities of blue. The sample is mounted with glycerol, covered with a coverslip and observed with a transmitted-light microscope (**Figure 2**). Depending on semi-thin section results, the block is additionally trimmed or the angle of the trimming is adjusted if the orientation of the tissue is not satisfactory.

*Preparation of ultrathin sections (60–100 nm).* Before sectioning, the diamond knife edge is checked to be wet, and the level of water is adjusted in the knife boat. An eyelash on a short stick is used to move the water onto the knife edge.

As the 60–100 nm sections are cut and floated on the water, they are seen as silvery in color. Formvar/carbon-coated copper grids with a slot (EMS, FCF2010-CU) are used to pick up sections floating on the surface of the water. The sections are manipulated with the eyelash so that they can be captured with an empty slot grid. The grids are dried by touching a filter paper, then placed in a slotted storage box.

Until recent improvement in diamond knife production, glass knives (ultramicrotomy grade) fitted with appropriately sized plastic knife boats for water reservoirs were the preferred tools for sectioning. It often makes sense for those learning sectioning to start with glass knives before using a diamond knife. The glass knives are sharper than diamond knives, at least for a few minutes, and are far less expensive. Knife makers are commonly found in most EM laboratories.

### *Post staining*

Staining should be performed in a closed Petri dish with a dental wax-coated bottom. Ten or twenty grids can be accommodated at once. Before use, uranyl acetate and lead citrate solutions should be centrifuged in Eppendorf tubes at 12,000–14,000 rpm for 3 min.

For uranyl acetate, a Petri dish is prepared with drops of 5% methanolic uranyl acetate. Grids are placed onto drops with the tissue oriented downward, toward the liquid, and incubated for 5 min. Grids are picked individually and rinsed quickly (one dip) in 50% methanol, then twice in $dH_2O$ (twenty dips each grid). Limit the exposure of uranyl acetate to light during staining.

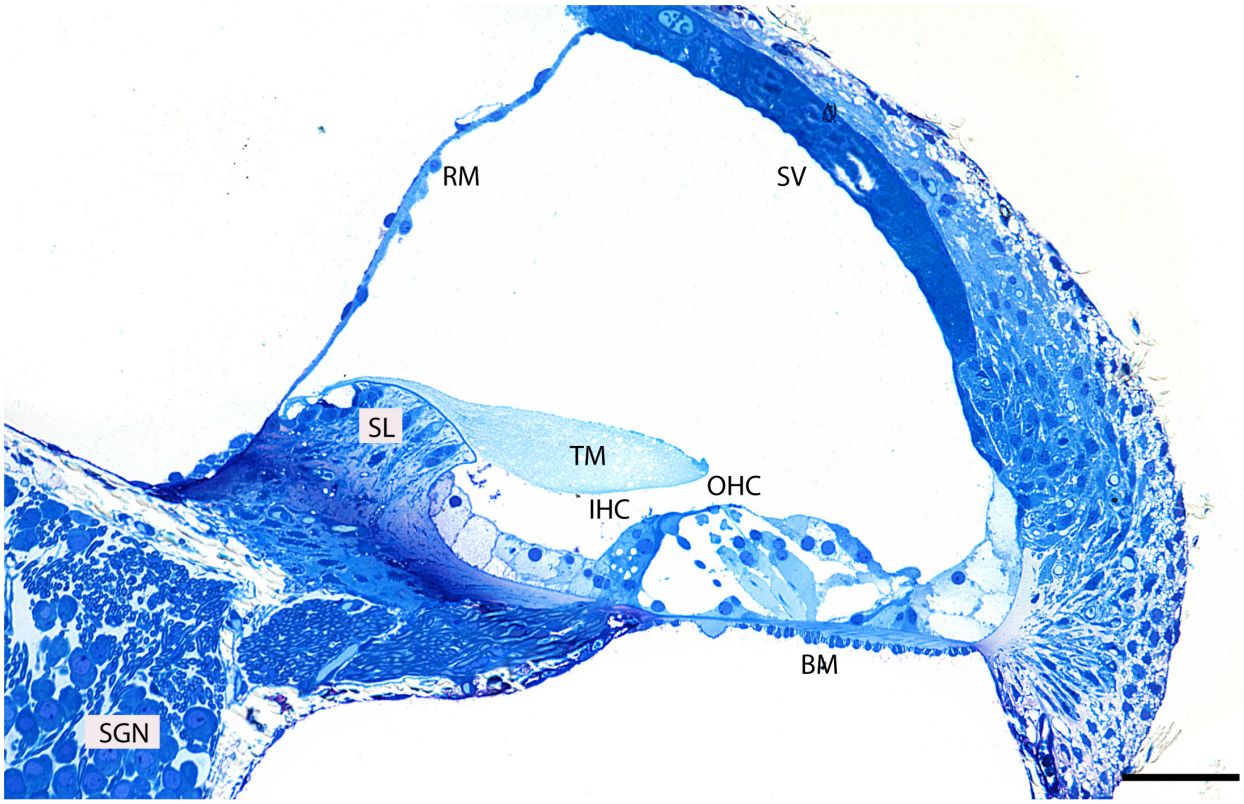


**FIGURE 2 |** Representative image of a semi-thin (0.5 μm) methylene blue-stained resin section taken from the middle region of an adult mouse cochlea. Basilar membrane (BM), inner hair cell (IHC), outer hair cells (OHC), tectorial membrane (TM), spiral limbus (SL), Reissner's membrane (RM), spiral ganglion neurons (SGN), stria vascularis (SV). Scale bar 500 μm.

The grids are dried by touching the filter paper. To prevent the formation of precipitates, the grids are thoroughly rinsed and completely dried before beginning the lead citrate staining step.

For lead citrate, a Petri dish is similarly prepared with drops of lead citrate. A few sodium hydroxide pellets are put around these drops. These prevent precipitates when lead solution reacts with $CO_2$ from the air. Grids are placed onto drops with the tissue facing downward and incubated for 5 min. Grids are picked individually and rinsed twice in $dH_2O$ (twenty dips each). The grids are dried by touching a filter paper and placed in a slotted storage box. Once samples are processed according to the protocol described above, the ultrathin sections are examined with a TEM.

### *Imaging*

Grids were imaged with a JEOL 1200EX microscope operating at 80 kV. Images were captured with an Advanced Microscopy Techniques camera at 3488 × 2580 pixel resolution.

## Protocol for Focused-Ion-Beam Scanning Electron Microscopy

The resin blocks for FIB-SEM are made by following steps 1–4 (*fixation, staining, dehydration, embedding*) as described in the section "Protocol for Conventional Transmission Electron Microscopy."

### *Resin block trimming*

As for TEM, the block is placed into the ultramicrotome holder and trimmed using a TrimTool 90 (EMS, Diatome TT-90) to remove unwanted plastic as much as possible. The block is further trimmed with the TrimTool 90 until the embedded tissue is exposed. Semi-thin sections are cut and stained with a methylene blue solution (see section "Preparation of Semi-Thin Sections"), and examined under a light microscope to identify the region of the block containing the organ of Corti with properly oriented rows of inner or outer hair cells.

### *Mounting and sputter coating*

Next, the trimmed area of the block is cut off using a new razor blade to a height of about 3 mm. An SEM specimen stub mount compatible with the FIB-SEM microscope is used. The ultra-smooth carbon adhesive tab (EMS, 77827-12) is placed on the aluminum specimen stub, and the top protective layer is peeled off. Next, the trimmed resin sample is carefully picked up with fine forceps and is mounted in the center of the specimen stub, with the working surface facing upward. Silver Conductive Adhesive 503 (EMS, 12686-15) is placed on the carbon adhesive tab around the sample to increase sample conductivity, minimizing charging; then the sample is sputter-coated with 5–10 nm of platinum.

### *Image acquisition, image alignment, segmentation, 3-D reconstruction, 3-D volume analysis*

A 3-D serial dataset is obtained on a FEI Helios 660 FIB-SEM microscope using the "Auto Slice and View G3" operating software (FEI). The image acquisition, image processing, and 3-D volume segmentation are performed as previously described (Ivanchenko et al., 2020a).

## Protocol for Immunogold SEM, Immunogold TEM, Immunogold FIB-SEM

We find it convenient to keep each cochlea throughout the immunolabeling steps in the 1.5 Eppendorf tubes in which they were fixed. It helps to avoid evaporation of the solutions during incubation steps, maintains the concentration of reagents, and significantly reduces the amount of antibody used. During solution exchange, the cochlea remains at the bottom of the tube and the pipet does not touch it. In each step, the tubes are carefully tilted to the side to ensure that the tissue pieces are fully immersed in the solution.

### *Fixation*

P1–P3 explants are fixed immediately after dissection with 4% formaldehyde in HBSS with calcium and magnesium, no phenol red (pH 7.2) for 2 h at room temperature. The samples are rinsed three times in HBSS with calcium and magnesium, no phenol red (pH 7.2) for 10 min.

P4–P7 explants are prefixed immediately after dissection with 4% formaldehyde in HBSS with calcium and magnesium, no phenol red (pH 7.2) for 10–15 min, and then transferred to HBSS with calcium and magnesium, no phenol red (pH 7.2). Using fine forceps under a dissecting microscope, the tectorial membrane overlying the hair cells is pulled away to expose the sensory epithelium. The organ of Corti is postfixed with 4% formaldehyde in HBSS with calcium and magnesium, no phenol red (pH 7.2) for 2 h at room temperature. Samples are rinsed three times in HBSS with calcium and magnesium, no phenol red (pH 7.2) for 10 min.

### *Blocking*

Samples are blocked in 10% normal goat serum (100 μl per tube) for 2 h at room temperature to reduce background from non-specific binding and Fc receptor binding sites.

### *Incubation with primary antibody*

The blocking solution is carefully removed from the tubes and 50 μl of primary antibody is added per tube. The samples are incubated with primary antibodies overnight at 4°C. Extra care is taken in adding each antibody solution to the corresponding labeled tube. Next, they are rinsed three times in HBSS with no calcium or magnesium, no phenol red (pH 7.2) for 10 min.

### *Incubation with secondary antibody*

Samples are blocked again in 10% normal goat serum for 30 min at room temperature. The blocking solution is removed and the samples are incubated overnight at 4°C with secondary antibody solution (diluted 1:30 in blocking solution). Following the secondary antibody application, the samples are rinsed three times in no calcium or magnesium HBSS 3x for 10 min each.

### *Post fixation and other steps*

For IG-SEM, follow steps 1–4 in the section "Protocol for Conventional Scanning Electron Microscopy." After samples are mounted they are sputter coated with 5-nm palladium using the coater manufacturer's guidelines. The stubs are transferred to a suitable holder and stored in the desiccator before imaging. The samples are observed in a field-emission SEM with a backscatter electron detector using the manufacturer's guidelines. In this study, SEM images were taken with a Hitachi S-4700 field-emission SEM, or FEI Helios 660 FIB-SEM microscope. During the imaging process, the best signal is obtained using the following parameters of the electron beam: voltage 10 kV, current 50 μA, and working distance of 6–8 mm.

For IG-TEM, samples are then processed following steps 1–7 as described in the section "Protocol for Conventional Transmission Electron Microscopy."

For IG-FIB-SEM, samples are then processed following steps 5–7 in the section "Protocol for Focused-Ion-Beam Scanning Electron Microscopy."

# RESULTS

Although TEM, SEM, and FIB-SEM use very different imaging systems, the sample preparation for them shares many common steps. These have been developed over many years in our laboratory and others', and they have been optimized to address the special challenges of imaging stereocilia of the mammalian cochlea and other inner ear organs. Detailed protocols for each are in the section "Materials and Methods," and are summarized in **Figure 1**. To illustrate these methods, we describe sequential analysis of hair-cell stereocilia using the different approaches.

First, to evaluate the gross anatomy of the mouse cochlea and its orientation in the resin block, we analyzed semi-thin plastic sections stained with 1% methylene blue (**Figure 2**). Clearly visible is the organ of Corti which together with the basilar membrane separates the scala media from the scala tympani. It is composed of mechanosensory hair cells and non-sensory supporting cells.

To explore surface specializations of cochlear hair bundles, we used scanning electron microscopy. Conventional low magnification SEM using SE detection in wild-type mice revealed one row of inner hair cells (IHCs) and three rows of outer hair cells (OHCs), separated by supporting cells (**Figure 3A**). Both types of hair cells have actin-filled stereocilia at their apical surfaces in rows of increasing height (**Figures 3B,C**, **4**). At this age (P5), stereocilia are cross-linked by a variety of links. Conventional SEM of neonatal cochlea showed that tip links connected the tips of adjacent stereocilia along the hair bundle's axis of sensitivity (**Figures 3D**, **4B–E'**). These tip links include single filaments, forked filaments, and "double" tip links which have been described previously in developing cochleas (Alagramam et al., 2011). Lateral links connecting adjacent stereocilia are frequently seen (**Figures 3B,D**). The surface of the stereocilia is rough indicating a cell coat material or glycocalyx.

Scanning electron microscopy of adult cochlea showed well-organized hair bundles in IHCs and OHCs (**Figure 4**).

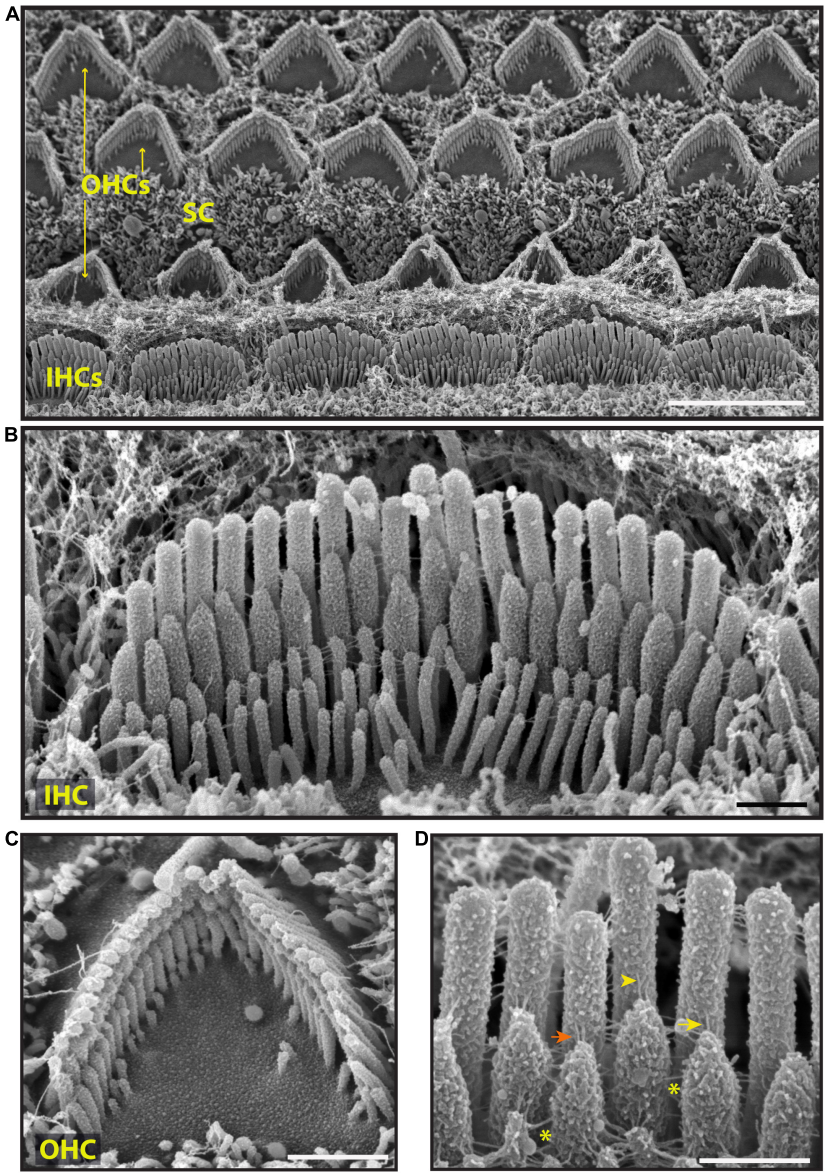


**FIGURE 3 |** Representative scanning electron micrographs of hair bundles of the neonatal (P5) wild-type mouse cochlea. **(A)** Low magnification micrograph shows an overview of the organ of Corti with three rows of OHCs (yellow arrows), one row of IHCs and supporting cells (SC). **(B–D)** High magnification micrographs of an IHC **(B,D)** and an OHC **(C)** bundles. Tip links connect the tips of adjacent stereocilia along the hair bundle's axis of sensitivity. These include single tip link filaments (yellow arrow), forked tip links (yellow arrowhead), and "double" tip links from one stereocilium tip (orange arrow). Lateral links (yellow asterisks) spanning the gap between stereocilia are frequently observed. The surface of the stereocilia is rough suggesting the presence of a cell coat material. Samples were sputter-coated with 5 nm platinum and imaged with a field-emission SEM (Hitachi S-4700) using SE detection mode. Scale bars: **(A)** 5 μm; **(B,C)** 1 μm; **(D)** 500 nm.

In OHC bundles the stereocilia surface appeared to be relatively smooth suggesting the absence of the cell-coat material at that age (**Figure 4**). Horizontal top connectors connected the stereocilia within a single row (**Figures 4B–D**) and between adjacent rows. Tectorial membrane attachment crowns were observed on the tallest row of OHC stereocilia (**Figures 4B,C**). The adjacent stereocilia of both IHCs and OHCs were interconnected by tip links formed by PCDH15 and CDH23 proteins (Kazmierczak et al., 2007; **Figures 4B,C,E**').

To identify proteins associated with these specializations, we used immunogold SEM. We first processed neonatal (P6) wild-type mouse cochlea immunostained with anti-PCDH15 primary antibody and colloidal gold-conjugated secondary antibody. We acquired images with SEM using the backscatter electron detector to distinguish the gold beads from the sputter-coated palladium on the surface. Gold beads associated with anti-PCDH15 were observed at the tips of stereocilia and often were associated with the tip links (**Figures 5A,B**). We also stained cochleas with anti-stereocilin (STRC) antibodies (**Figure 5C**). STRC is thought to

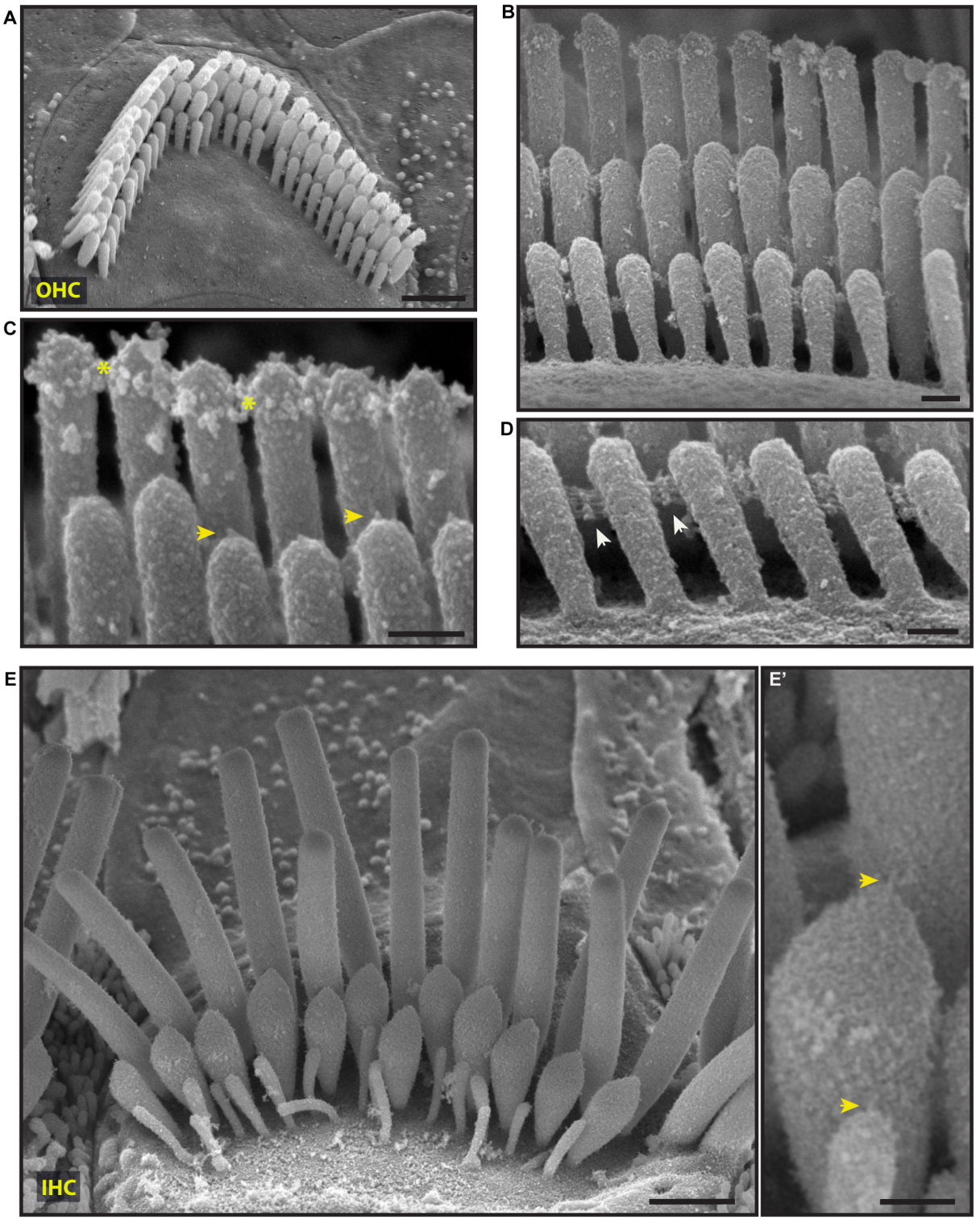


**FIGURE 4 |** Representative scanning electron micrographs of hair bundles of the adult, wild-type mouse cochlea. **(A–D)** Mature OHC bundles from the middle region of the cochlea. OHC bundles contain tip links (yellow arrows in **C**), tectorial membrane attachment crowns (yellow asterisks in **C**), and horizontal top connectors (white arrows in **D**). The stereocilia surface appears to be relatively smooth suggesting the absence of the cell-coat material. **(E,E')** Mature IHC bundle from the middle region of the cochlea. Tip links (yellow arrows in **E'**) connect the tips of adjacent stereocilia. The surface of the stereocilia is relatively smooth in appearance which indicates the absence of stereocilia coat. Samples were processed with the modified OTOTO protocol, sputter-coated with 5 nm platinum, and imaged using SE mode. Scale bars: **(A,E)** 1 μm; **(B–D,E')** 100 nm.

participate in the TM attachment crown and perhaps horizontal top connectors (Verpy et al., 2001, 2011). In a secondary electron image (**Figure 5C**, right), knobby structures observed at the tips of the tallest stereocilia represent the tectorial membrane attachment crowns (see also **Figures 4B,C**). In a backscatter image of the same bundle (**Figure 5C**, left), gold beads bound to anti-STRC antibodies decorated the knobs, indicating that the attachment crowns are composed in part of STRC.

To better visualize actin within hair cells, the surface coat on the apical surface, and extracellular links, we used TEM. We used two TEM sample staining protocols on P4 neonatal wild-type mouse cochleas—either a brief 1% tannic acid treatment to highlight the links and actin filaments (**Figure 6A**), or an overnight 5% tannic acid treatment to highlight the surface coat (**Figure 6B**). Actin filaments were observed in the stereocilia, the rootlets, and the cuticular plate (**Figure 6A**; Tilney et al., 1980; Pacentine et al., 2020). Stereocilia were filled with parallel electron-dense actin filaments. Actin-containing rootlets anchored stereocilia to the cell body. The cuticular plate contained a network or mesh of actin, made up of filaments with no specific orientation or directionality. Cell surface specializations such as tip links, ankle links, and transient lateral links were observed on the hair bundles of OHCs (**Figures 6A,B**). On samples stained with 5% tannic acid, an electron-dense cell coat was seen over the entire stereociliary surface and cell membrane over the cuticular plate (**Figure 6B**).

We then processed for TEM samples that had been immunostained with anti-PKHD1L1 primary antibody and colloidal gold-conjugated secondary antibody. PKHD1L1 participates in forming the stereocilia surface coat, causing hearing loss when absent from the hair cells (Wu et al., 2019). Anti-PKHD1L1 10-nm gold beads were localized toward the tips of OHC stereocilia (**Figures 7A,B**) and were often associated with the surface coat, which was seen as a dense, uniform fuzz on the membrane (**Figure 7B**). No gold beads were associated with the tip links or the transient lateral links connecting neighboring stereocilia, suggesting that PKHD1L1 does not participate in forming links between stereocilia but may attach stereocilia to other structures.

To evaluate the distribution of the tip-link protein PCDH15 at the surface of stereocilia, we used FIB-SEM to collect serial EM data sets of neonatal (P1) IHC stereocilia immunostained with anti-PCDH15 primary antibody and colloidal gold-conjugated secondary antibody (12 nm gold). Serial data sets were collected, objects of interest were identified and outlined based on image contrast contours (segmented), and objects were 3-D reconstructed using Dragonfly and Amira software packages (**Figure 8**). These revealed that in neonatal cochlea, PCDH15 was localized at the tips and along the surfaces of the stereocilia, suggesting that it was a component of tip inks and transient lateral links (**Figure 8** and **Supplementary Movie 1**).

# DISCUSSION

In this study, we aimed to describe and compare different EM imaging techniques commonly used to study hair cells of the inner ear. Although the EM methods have been used for years, various efforts to improve the outcomes have been undertaken. Step-by-step, we described conventional and immunogold TEM, SEM, FIB-SEM providing practical advice for both beginners and experts, and incorporated many years of personal experience in using these approaches in the inner ear research. In our experiments, we used mouse cochlear tissue, however, these protocols with minor modifications also can be applied to the inner ears of other species.

## Specimen Preparation for Electron Microscopy

The introduction of artifacts is one of the most common problems in EM, which makes it difficult to judge whether a cell's ultrastructure is properly represented in the final images. Specific indications of possible artifacts include distortion and disorganization of hair cell bundles, loss of cell-surface specializations, loss of continuity and irregularity of the cell membranes, disparity in the preservation of adjacent cells of the same type, swollen and empty spaces in the cytoplasm and the perinuclear space, and disorganization of the organelles and filamentous structures. Several additional criteria may be used to evaluate the presence of artifacts. First, if the final appearance of the sample conflicts with previously published ultrastructure of the tissue, it is more likely an artifact than an important new discovery. Second, images should be consistent with those biochemical and physiological data that have structural correlates and are well described. Thus characterizing how a genetic mutation affects ultrastructure is especially difficult as mutational effects could be confused with artifacts from sample preparation. In practice, the best test is a comparison of the mutant sample with a control sample of normal morphology prepared in parallel. Following recommendations available in the literature (Bozzolla and Russell, 1998) and protocols described by other groups (Reynolds, 1963; Heywood and Resnick, 1981; Pickles et al., 1984; Furness and Hackney, 1985; Glauert and Lewis, 1998; Verpy et al., 2001, 2011; Goodyear et al., 2005; Michel et al., 2005; Ahmed et al., 2006; Harris et al., 2006; Kazmierczak et al., 2007; Grillet et al., 2009; Fischer et al., 2012; Indzhykulian et al., 2013; Kizilyaprak et al., 2014; Fang et al., 2015; Miranda et al., 2015; Jones, 2016; Parker et al., 2016; Velez-Ortega et al., 2017; Velez-Ortega and Frolenkov, 2019), we used fixation, staining, immunolabeling, dehydration, embedding reagents, and conditions that minimize these factors.

### Cochlear Dissection

A critical first step of sample preparation is cochlear dissection. Hair cells with their rows of fine stereocilia are very delicate structures and the integrity of hair cell bundles can be easily disrupted during dissection. Researchers must perfect their cochlear dissection technique before carrying out meaningful electron microscopy experiments. The dissection and most processing steps should be performed under the visual control of a dissecting microscope. To assess preservation of structure during dissection, light microcopy of samples in which actin is stained with phalloidin can be helpful in preliminary experiments (Landegger et al., 2017). The removal of the tectorial membrane

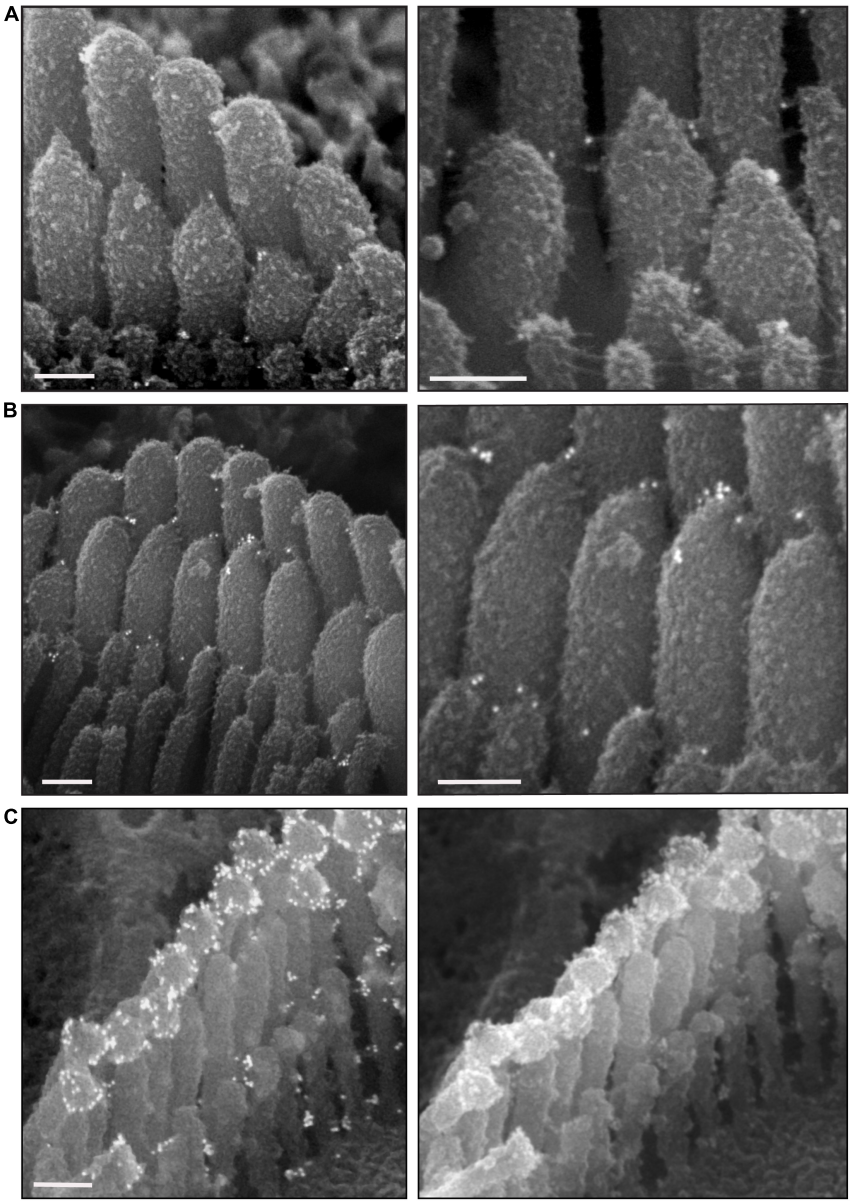


**FIGURE 5 |** Representative immunogold scanning electron micrographs of OHC hair bundles of the neonatal (P6) wild-type mouse cochlea. Samples in **(A,B)** were immunostained with anti-PCDH15 primary antibody and gold-conjugated secondary antibody, sputter-coated with 5 nm palladium, and imaged with backscatter electron detectors on different microscopes. **(A,B)** Were prepared in parallel. Gold beads (12 nm) localize mostly at the tips of shorter-row stereocilia. **(A)** Sample imaged with a field-emission SEM (Hitachi S-4700) using BSE detection mode (semiconductor BSE detector). Right panel is higher magnification. **(B)** Sample imaged with a field-emission FEI Helios 660 FIB-SEM using BSE detection mode (high contrast solid-state BSE detector, CBS). Right panel is higher magnification. **(C)** Sample was immunostained with anti-STRC primary and gold-conjugated secondary antibodies, using a protocol similar to that in methods, and imaged (left) with a Helios 660 FIB-SEM using BSE or (right) with a Hitachi S-4700 using SE detectors. Scale bars: **(A–C)** 200 nm.

is also problematic for the integrity of hair cells; it requires steady hands, proper tools, and experience (Landegger et al., 2017). In TEM a tectorial membrane can usually be kept in place, in SEM in adults, the dehydration nearly always lifts the tectorial membrane from the stereocilia and it curls back to reveal the tops of the hair cell as well as stereocilia imprints on the surface of the tectorial membrane. It goes further up and back after critical point drying. However, in SEM in neonates or any EM that involves antibody labeling, it is important to fully expose the sensory epithelium. This problem is eliminated in post-embedding labeling. We found that slight prefixation of the sample with 4% formaldehyde for 10–15 min makes the tectorial membrane removal easier and minimizes damage to the stereocilia in this step.

Transfer of the samples is also particularly important; ideally, the sample should always be immersed in liquid and the sensory epithelium should never touch the surface of the pipet or

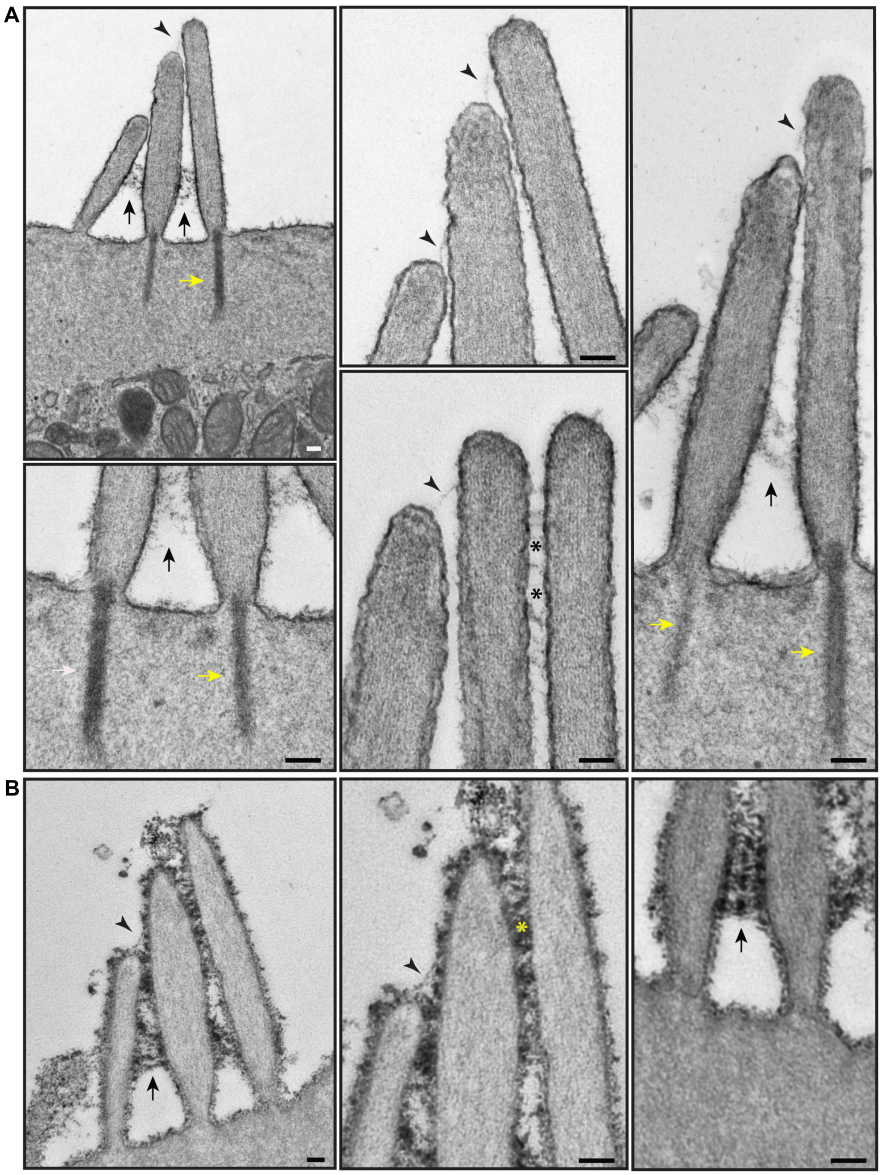


**FIGURE 6 |** Representative transmission electron micrographs of OHC hair bundles of the neonatal (P4) wild-type mouse cochlea. **(A)** Samples stained with 1% tannic acid (1 h). **(B)** Samples stained with 5% tannic acid (overnight). In **(A,B)** adjacent stereocilia (short, middle, tall) are seen to be connected by tip links (black arrowheads), lateral links (asterisks), and ankle links (black arrows). Yellow arrows point to the rootlets. The cell coat material is better visible on the samples stained with 5% tannic acid. It appears at the surface of stereocilia and the apical non-stereociliary surface. **(A,B)** Samples were imaged with a JEOL 1200EX microscope operating at 80 kV. Scale bars: **(A,B)** 100 nm.

other instruments. Finally, the dissection time should be as short as possible. Even though the dissection medium (often Leibovitz's L-15 medium) is enriched with amino acids, vitamins, inorganic salts, and other components to maintain cell health and survival in environments without $CO_2$ equilibration, there is a risk of autolysis. Autolysis causes not only bad preservation of ultrastructure but may also destroy antigenic sites and cause false-negative immunogold results (Jones, 2016). The best results are obtained if the fixative reacts with the sample within seconds after the removal from the cochlea.

## Fixation

Fixation is also one of the most important steps in sample preparation for EM. The goal of fixation is to stabilize cellular organization enough that ultrastructural relationships are preserved despite the subsequent rather drastic treatments of dehydration, embedding, and exposure to the electron beam (Riemersma, 1968). Aldehydes are the most widely used fixatives in EM. For optimal preservation of ultrastructure, a relatively strong glutaraldehyde fixative at a concentration of 2.5% is the primary choice. It contains two functional aldehyde groups

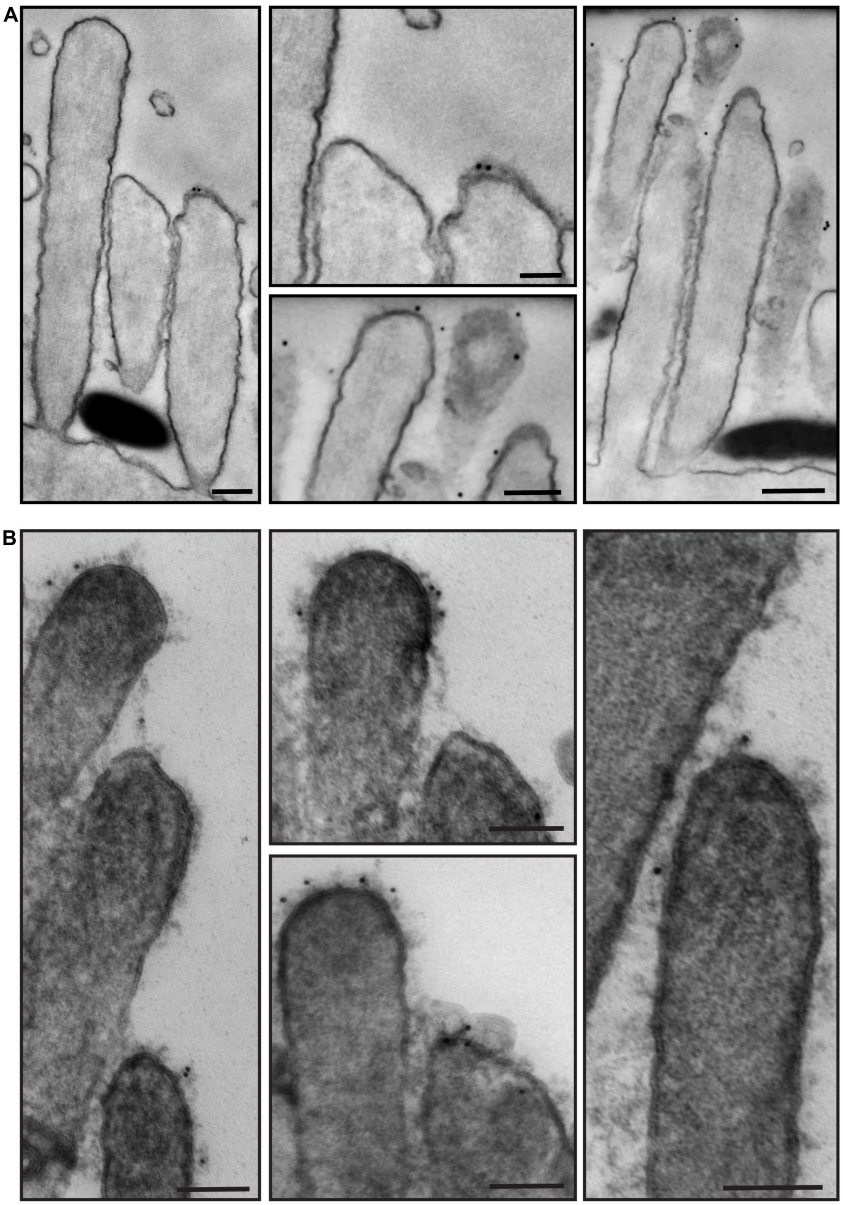


**FIGURE 7 |** Representative immunogold transmission electron micrographs of OHC hair bundles in neonatal (P4) wild-type mouse cochlea. Samples immunostained with anti-PKHD1L1 primary antibody and gold-conjugated secondary antibody. Gold beads (10 nm) localize near the tips of stereocilia. **(A,B)** Were prepared in parallel, however in **(B)** post-staining with uranyl acetate and lead citrate significantly increased contrast of stereocilia cores and surface coat. **(A,B)** Samples were imaged with a JEOL 1200EX microscope operating at 80 kV. Scale bars: **(A)** 200 nm; **(B)** 100 nm.

which react with cellular components, especially with the amino groups in proteins, forming cross-links and resulting in good preservation of ultrastructure. In EM, tannic acid is a useful addition to aldehyde fixation. It does serve as a fixative but has very slow penetration and needs to be used in combination with another fixative such as glutaraldehyde or osmium tetroxide (Glauert and Lewis, 1998). Besides its fixative properties, it enhances the electron density of heavy metals (osmium tetroxide, uranyl acetate, and lead citrate) resulting in increased contrast of extracellular structures, such as the surface coat and stereocilia links. It is less effective for staining intracellular structures but still helps to reveal actin filaments of stereocilia.

Some antigens are extremely sensitive to cross-linking by glutaraldehyde, and this fixative can compromise antibody labeling. For immunogold experiments, formaldehyde is used as a primary fixative as it is a more "gentle" fixative and keeps epitopes accessible for antibodies. The cost is the inevitable loss of some ultrastructural details. For optimal preservation of both immunoreactivity and cell ultrastructure, the formaldehyde fixation step is followed by post-fixation

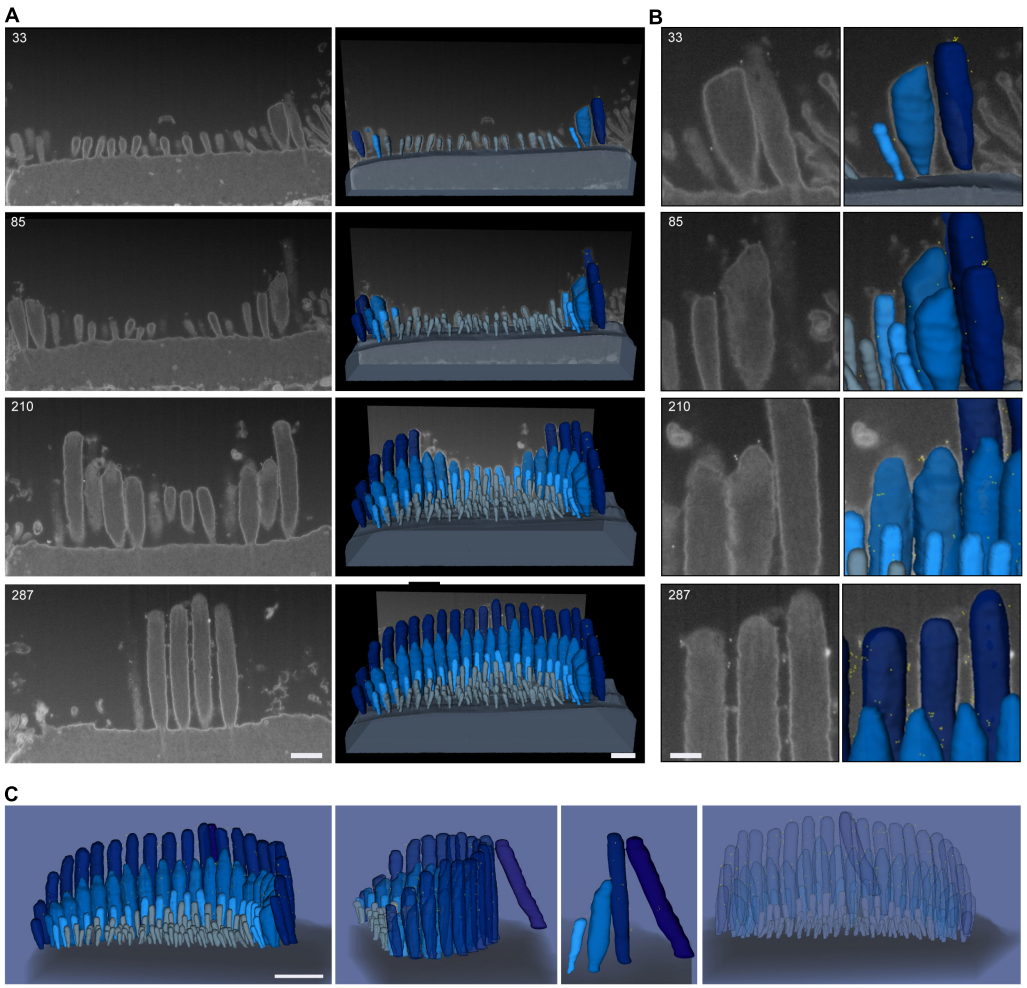


**FIGURE 8 |** Representative FIB-SEM of IHC hair bundles of neonatal (P1) mouse cochlea. Samples were immunostained with anti-PCDH15 primary antibody and gold-conjugated secondary antibody (12 nm gold). **(A)** *Left,* representative FIB-SEM micrographs from four single planes; *right,* a 3-D rendering of the FIB-SEM image stack. **(B)** An inset from **(A)** showing a closer view of the stereocilia and gold beads at their tips. Sample was imaged with a field-emission FEI Helios 660 FIB-SEM using BSE detection mode. **(C)** 3-D representation of an IHC stereocilia bundle labeled with anti-PCDH15 immunogold (12 nm) (426 serial FIB-SEM cross sections, at 10 nm milling step; yellow, gold beads; blue, stereocilia; light gray, microvilli; dark gray, cell body). At this age, PCDH15 is diffusely located near stereocilia tips. Scale bars: **(A)** 500 nm; **(B)** 200 nm; **(C)** 1 μm.

with glutaraldehyde after immunolabeling is completed. Specific attention should be paid to fixation time and temperature. Over-fixation and under-fixation can lead to false-negative or false-positive immunolabeling. The temperature during fixation should be close to the same as when the cochlea was dissected, since changes in temperature can affect the surface morphology of the sensory epithelium. In our experiments, these steps are usually done at room temperature.

For small samples such as neonatal cochlear explants, immersion in the fixative is a preferred method. For adult cochlea, in which the organ of Corti microdissection is more challenging and time-consuming, intracardial perfusion is often a preferred method of primary fixation. However, we did not observe significant differences in ultrastructure when a whole cochlea was quickly dissected out from the temporal bone and moved to the fixative in less than a minute. For this procedure the cochlea is gently and slowly perfused with 4% formaldehyde/1% glutaraldehyde via the round and oval windows until the solution was washed out of the small hole at the apex; it is next postfixed with 2.5% glutaraldehyde. Karnovsky's fixative (2% formaldehyde/2.5% glutaraldehyde) can be used as an alternative solution. Thereafter, the microdissection is performed in the already fixed sample. The advantage of using formaldehyde/glutaraldehyde or Karnovsky's fixative is based on the ability of formaldehyde to penetrate more rapidly to stabilize the cell structure, and glutaraldehyde simultaneously but more slowly permanently cross-link proteins.

## Buffers

Besides the selection of the appropriate fixative, it is important to use the right buffer. Traditionally the buffers used for EM are designed to have a similar osmolality to native tissue (300 mOsmol). Phosphate buffer is widely used because it mimics the composition of extracellular fluid and is not toxic

to cells. However, it has a number of practical disadvantages. The most important is that it is incompatible with calcium, in that calcium phosphate forms a precipitate which can be very visible on the surface of stereocilia. Also, calcium ions are needed to preserve stereocilia links. Finally, stock phosphate buffer solution can be easily contaminated with microorganisms. None of these apply to cacodylate buffer, which is the favored buffering solution used with fixatives in specimen preparation for electron microscopy. Cacodylate buffer prevents microprecipitation, and ultrastructural preservation is excellent. For the samples processed for immunogold labeling, HBSS is the preferable buffer in the fixation and immunolabeling steps. As discussed above, formaldehyde causes gentle fixation and HBSS helps to maintain physiological pH and osmotic balance in under-fixed cells. It also provides essential inorganic ions, such as calcium, to preserve ultrastructural details during immunostaining steps.

## Staining

In order to postfix and enhance the contrast of the cell ultrastructures, samples are usually stained with osmium tetroxide, often in combination with potassium ferrocyanide. The osmium tetroxide slowly reacts with proteins, including histone proteins, helping to preserve the associated DNA (Bozzolla and Russell, 1998). It also postfixes and stains phospholipids of the cell membrane and organelles. The process of interaction between osmium and potassium ferrocyanide is poorly understood but observations show that glycogen staining is enhanced by post-fixation with osmium tetroxide in the presence of ferrocyanide: there is usually more staining of cell-surface specializations and cell membranes (Wu et al., 2019). However, osmium stops the activity of enzymes in the cell which leads to cell hardening. Samples become extremely fragile and can be easily damaged by rough pipetting. The use of osmium tetroxide is additionally problematic for immunolabeling because it results in complete loss of antigenicity. Thus, it has to be applied when samples are already immunogold labeled. In some post-embedding immunogold techniques, osmium was used and good labeling still had been achieved (Flechsler et al., 2020).

## Dehydration

Since most embedding media are not soluble in water, it is necessary to dehydrate fixed samples by passing them through a sequence of dehydrating solutions that are fully soluble with the embedding medium. The most broadly used dehydrating agents are ethanol, acetone, and propylene oxide (Bozzolla and Russell, 1998). The major problem of dehydration is the shrinkage of the cells as a result of the extraction of lipids and water from the sample (Bozzolla and Russell, 1998). A gradual increase in ethanol concentration prevents tissue shrinkage during the dehydration step. The following factors, which minimize the loss of lipids during the dehydration step, should be considered: (1) maintaining calcium ions in the fixative and washing solutions; (2) postfixation with osmium tetroxide and potassium ferrocyanide; (3) shorter duration for dehydration steps; (4) processing at 0°C; and (5) use of gentle lipid solvents such as ethanol, acetone.

## Embedding, Trimming, Sectioning, and Post-staining

In TEM or FIB-SEM the dehydrated sample should be infiltrated with an epoxy resin which is then polymerized to a solid block with good sectioning properties. Epoxy resins (e.g., Araldite 502/Embed 812, Epon 812, Spurr's resin, Durcupan) have considerable advantages as embedding media for EM, in comparison with the acrylic resins. Their volume changes very little during polymerization, they harden uniformly, they have good sectioning properties, and they are very stable under an electron beam. Acrylic resins (Lowicryls, LR-White) are transparent and have a low viscosity as the temperature is lowered, so specimens can be infiltrated and the resin can be polymerized at low temperature. Additionally, LR-White is a hydrophilic acrylic resin and can be used for post-embedding immunolabeling techniques.

For TEM, individual ultrathin sections, 60–100 nm in thickness, are sectioned using an ultramicrotome with a diamond knife and are picked manually onto a metal support grid. We use copper formvar/carbon-coated grids with a slot, and a transparent support film suspended across the slot. These grids allow us to mount the sections as flat as possible on support materials. Grids for TEM can be post-stained with heavy metals that significantly enhance electron-scattering, resulting in increased contrast in the electron microscope (**Figures 6**, **7**). But post-staining of ultrathin sections is not absolutely necessary and samples can be imaged without it (**Figure 7**). We recommend keeping some grids unstained as a backup.

In FIB-SEM the resin block with the sample is trimmed using an ultramicrotome until the embedded tissue is exposed, then it is mounted on the specimen stub oriented with the working surface upward. Silver conductive adhesive is placed on the carbon adhesive tab around the sample to increase conductivity and minimize charging, and the sample is sputter-coated with 5–10 nm of platinum.

## Critical Point Drying

During SEM sample preparation the absolute alcohol of the dehydrated sample needs to be removed, but the surface tension of the alcohol can distort the tissue if air-dried. To allow drying, the alcohol is replaced with liquid $CO_2$ in a critical point dryer. At the right temperature and pressure (the "critical point," 31.1°C and 73.8 bar), the gas and the liquid phases become identical and the visible boundary between them vanishes, reducing surface tension to zero, resulting in instant evaporation of $CO_2$. The structure of the hair bundles is expected to remain largely intact after the gas has been slowly released from the chamber. The dried sample is then mounted on the specimen stub covered with a carbon adhesive tab, and sputter coated. To improve the sample conductivity, silver colloidal paint can be used but is more difficult to apply, especially with small samples.

## Sputter Coating

The coating of SEM samples with a conductive metal is a required step to optimize the microscope performance during imaging. It allows non-conductive SEM samples to become conductive so that the charge of incident electrons is carried away. Otherwise the electric field created by a charged sample would distort

the incident electron beam. Coating thus enables higher sample stability under the electron beam and better resolution. During our protocol development for conventional SEM, we have tested chromium, cobalt, aluminum, copper, carbon, platinum, and palladium coating materials, and found that a 5 nm coating with platinum gives an acceptable resolution of fine stereocilia structures such as tip links and other cell surface specializations. For immunolabeling with colloidal gold samples, we instead use a 5 nm coating with palladium, as previously reported (Indzhykulian et al., 2013). Platinum has nearly the same atomic number (78) as gold (79), and so antibody-coupled gold beads cannot easily be distinguished from a platinum coating using the energy of the BSE. Palladium has a much lower atomic number (46); it allows sufficient contrast with gold while also offering good resolution. Other coating materials have also been used, including carbon (Goodyear et al., 2010). It is also possible to observe immunogold particles on samples prepared with the OTOTO technique (Heywood and Resnick, 1981; Osborne and Comis, 1991; Han et al., 2020), which is sometimes necessary in adult cochlear samples. However, while OTOTO reduces charging, osmium (atomic number 76) partially masks the gold, making the detection more challenging.

The sensory epithelium is not flat, but is a convoluted surface with stereocilia bundles angled to the basilar membrane. The uniform deposition of coating material on the surface of the stereocilia is very important for good conductivity but not possible if the deposition from the target material is perpendicular to the specimen stub surface. The samples should be tilted and rotated to achieve a continuous coating. Most sputter coaters can be equipped with such "planetary" rotating platforms. In our hands, the best result is achieved when the deposition of the palladium or platinum occurs when the stage with the sample is rotating and tilted 35° toward the target for two-thirds of the total deposition time, and 10° away from the target for one-third of the total time.

### Immunogold Labeling

Immunogold EM was historically more often used with TEM. However, with new methods, it has become possible to apply these techniques in SEM. Most developed protocols include specific labeling with a primary antibody, either directly conjugated to gold beads (direct labeling) or subsequently labeled with a secondary antibody conjugated to gold beads (indirect labeling). Primary antibodies can be monoclonal or polyclonal. Polyclonal antibodies bind to multiple epitopes and are more sensitive, while the monoclonal antibodies recognize a single epitope, thereby being more specific (Magaki et al., 2019). A primary antibody should be raised in a different species from the species in which it is used, to avoid cross-reactivity (Boykins et al., 2016). It is also necessary to have a well-characterized antibody that can efficiently recognize the epitope after formaldehyde fixation.

In this work, we used indirect labeling, where the primary antibody is unconjugated, and labeling of the primary antibody is achieved with a gold-conjugated secondary antibody. The advantage of the indirect procedure is that a variety of commercial secondary antibodies are available, reducing the cost. The main disadvantage is that the gold beads are located anywhere within a radius of ∼10–15 nm around the epitope site, due to the length of antibodies.

The concentration of antibody that will provide the strongest staining of the target antigen and lowest background staining must be determined by serial dilutions of a concentrated antibody. It is advisable to start with the dilution recommended by the manufacturer, and also consider one dilution 2–3-fold above it and one dilution below (Magaki et al., 2019).

Double labeling for two proteins can be achieved with EM if the two primary antibodies are raised in different species, so the respective secondary antibodies can differentially recognize them, and if the secondary antibodies are conjugated to colloidal gold of different sizes (e.g., 6-nm, 10-nm, 12-nm, and 18-nm gold). Extensive controls are absolutely essential for the analysis of the results. Some level of non-specific binding (background) is always possible but it is important to minimize it.

In this study, we developed a pre-embedding procedure for proteins that are expressed extracellularly on the surface of the stereocilia. The protocol uses HBSS during the immunolabeling steps, and an additional post-labeling fixation step with glutaraldehyde to minimize ultrastructural loss. For TEM and FIB-SEM samples, in addition to post-fixation with glutaraldehyde, we applied tannic acid and osmium tetroxide to stabilize the antibody complexes and to prevent ultrastructural degradation that appears during the dehydration and heating steps associated with embedding in epoxy resins.

## Electron Microscopy Techniques

There is no single recommendation on which approach or tool is the best choice to answer a specific biological question. More and more techniques are becoming available, and each has its advantages and limitations regarding the resolution, sample area, volume to be analyzed, time for sample preparation and imaging, difficulties in microscope operation which are usually the main factors to be considered when a decision to use one or other approach has to be made (**Table 1**).

### Conventional and Immunogold Transmission Electron Microscopy

Transmission electron microscopy historically was a preferable method for ultrastructural examination of hair cells based on its sub-nanometer resolution. Deposition of heavy metals such as uranyl acetate and lead citrate onto cellular structures increases the contrast but reduces the resolution. The grids are then inserted into the microscope and a small area of interest (10–20 μm) is selected for imaging. Accelerated electrons pass through the sample and are focused onto a CCD camera detector, with 0.2–0.5 nm pixel size. Scattering of the electrons by heavy metals in the sample generates dark regions in the resulting image. TEM imaging is parallel in nature, with each pixel on the image corresponding to a relevant location within the focal plane of the imaging area and all pixels are collecting electrons simultaneously. TEM is a non-destructive technique and the specimens can be imaged multiple times for larger field sizes or at higher resolution.

**TABLE 1 |** Key parameters of different EM methods.

| | TEM | IG-TEM | SEM | IG-SEM | FIB-SEM | IG-FIB-SEM |
|---|---|---|---|---|---|---|
| **Equipment** | Fume hood, dissecting microscope, ultramicrotome, light microscope, TEM (80–100 kV) | | Fume hood, dissecting microscope, critical point dryer, sputter coater, SEM with BSE detector | | Fume hood, dissecting microscope, ultramicrotome, light microscope, sputter coater, FIB-SEM | |
| **Time for sample preparation** | 5 days | 7 days | 7–24 h | 2–3 days | 5 days | 7 days |
| **Measurements** | 2-Dimensional | | Pseudo 3-Dimensional | | 3-Dimensional | |
| **Achievable resolution** | Transmitted electrons *x*, *y*: ∼0.2–0.5 nm, z: 60–100 nm (limited by section thickness) | | Secondary electrons *x*, *y*: ≥0.5 nm | Backscattered electrons *x*, *y*: ≥2 nm | Backscattered electrons *x*, *y*: ∼ 2 nm, z: ∼5–20 nm | |
| **Dimensions** | *x*, *y*: <50 μm (more is possible but not reasonable) | | *x*, *y*: <50 μm | | *x*, *y*, *z*: ∼ 20 μm (more is possible but not reasonable) | |
| **Non-destructive /Destructive** | Non-destructive approach | | Non-destructive approach | | Destructive approach | |
| **Preinspection of the area of interest** | Possible | | Possible | | Not possible in detail until the milling process is started | |
| **Imaging time** | - Several hours and more<br>- Time depends on user experience and quality of the samples<br>- A number of manual adjustments are needed<br>- Structures of interest in each section have to be selected by the user | | | | - Tens of hours and more, depending on the volume<br>- Time depends highly on experience<br>- A number of manual adjustments are needed<br>- No need to select individual profiles of the same cell<br>- The cell is sequentially sectioned and imaged in an automated fashion | |
| **Application** | Sections of hair cell including stereocilia, kinocilia, general organelles, cell nucleolus, membrane, cell surface specializations (links, coat) | Same as TEM plus individual proteins immunolabeled with gold beads | Hair bundle surface topography, stereocilia links | Same as SEM plus cell-surface proteins immunolabeled with gold beads | -Visualization and 3-D reconstruction of entire hair cell or area of hair cell including stereocilia, kinocilia, organelles, cell nucleolus, membrane<br>-Visualization and reconstruction of links is possible but challenging | Individual proteins immunolabeled with gold beads |

Beam alignment, stigmation, and focusing are basic settings that affect the quality of a TEM image. These have to be adjusted by the operator, at magnifications higher than used for imaging. The optimal parameters depend widely on the application. Generally, higher voltages, smaller apertures, and smaller spot sizes make the resolution higher. However, compromise often is necessary to optimize the settings. Astigmatism and spherical and chromatic aberrations are all factors that can affect imaging quality. Of course, a perfectly aligned microscope is essential for generating high-quality data.

Transmission electron microscopy also has some disadvantages. The embedding preparation of biological tissue means the resolution 0.2–0.5 nm is not easily achievable because of limitations such as the molecular graininess of the polymerized resin, the "fuzziness" of extended biological molecules, and the additional coatings added by staining. However, certain applications allow a high resolution to be achieved (e.g., negative staining). Manual sectioning for TEM often generates artifacts in the sections such as holes, folds, shrinkage, and stretching. There is also limited control of the sectioning plane. Staining steps may result in precipitation of heavy metals, which can cause holes in the formvar film or loss of sections. The success of TEM very much depends on the skill of the operator, and on accuracy in collecting and imaging each ultrathin section. Only a relatively small area can be imaged in detail, and low penetration of the electron beam and aberrations limit samples to a thickness of 60–100 nm. Also, TEM provides only two-dimensional information unless multiple serial sections are collected, imaged and reconstructed into a 3-D volume. On the other hand, TEM imaging does not require specialized equipment beyond that common to a basic EM laboratory and is therefore relatively inexpensive.

## Conventional and Immunogold SEM

Interpreting the two-dimensional images of TEM micrographs is challenging, especially in understanding the plane of the section through the tissue. Thus SEM is better at representing a sample with a complex surface. SEM images are formed by the detection of SE or BSE that are emitted when the electron beam hits the surface of the sample. SE are ejected from atoms of the sample by inelastic collision by beam electrons, and collected by a detector placed to the side. Contrast is produced by a difference in emission when the beam hits the surface at varying angles, creating the sense of shadow in the image. These images provide detailed topographic information with a resolution close to 0.5–1 nm. Secondary electron imaging is an ideal mode with which to investigate a complex structure like a cochlear sensory epithelium, and to assess hair cell number; bundle morphology; planar cell polarity; shape, length, width of stereocilia; and stereocilia links. BSE are generated when incident beam electrons are elastically scattered by atoms in the sample back toward the source, and are collected by a donut-shaped detector concentric with the incident beam. Backscatter electron generation depends on the atomic number of atoms in the sample

and so can distinguish different metals. Backscatter imaging is typically used for immunogold SEM, to create strong contrast of the gold beads labeling the tissue.

Biological samples are composed of low atomic number elements and when the electron beam interacts with the sample, electrons can penetrate deeply, causing loss of signal and decrease in sample resolution. Appropriate coating or metal impregnation, and adequate imaging settings should be considered to optimize the imaging conditions. Generally, an electron beam of lower voltage is more suitable for biological samples because it does not penetrate into the sample as deeply as with higher accelerating voltage; however, it produces a weaker signal and lower instrument resolution. For 5 nm platinum-coated samples, 3–5 kV provides adequate secondary electron signal and good resolution of surface features such as stereocilia links (**Figure 3**). A higher accelerating voltage (10 kV or more) may result in a poor image due to deep penetration of the electron beam and high charging of the samples. Charging is a phenomenon that gives rise to anomalous contrast due to the fact that the amount of the electrons emitted from the specimen is larger than the incident electrons in some locations of the specimen surface and is commonly observed at low conductive specimens. Notably, tip links are not well resolved by high-voltage electron beams because the high-energy electrons pass through them instead of scattering off them; a low-voltage (∼5 kV) beam is needed. When a low accelerating voltage is used, instrument resolution can be retained by use of a field-emission electron source.

Samples processed with the osmium-based OTOTO method (**Figure 4**) can be imaged at 3–10 kV with good resolution, low charging, and good stability of the stereocilia under the beam. This protocol works better in adult cochlea samples which usually have higher charging even after platinum coating.

For immunogold SEM, the use of a backscatter detector allows detection of colloidal gold and thus localization of specific proteins. With IG-SEM, the protein of interest has to be on the surface—either extracellular or exposed—so the antibody-conjugated gold particles can reach the epitope at the time of labeling and are also accessible to the electron beam. Therefore IG-SEM can be an ideal tool for analyzing the composition and spatial distribution of stereocilia surface specializations. Immunogold samples can be concurrently imaged with a backscatter detector to detect gold distribution, and with a secondary electron detector for hair-cell surface topology. For immunogold labeled and 5-nm-palladium-coated samples, 10 kV with 50 μA current provides an adequate image of the stereocilia and good detection of gold beads at the surface of stereocilia (**Figure 5**).

One of the advantages of SEM is the depth-of-field capacity. Relatively large objects like dozens of hair cells can be imaged—all in focus—when the working distance is set accordingly. Shortening the working distance improves the resolution but limits the focal depth. For high-resolution images, a working distance of ∼6 mm is generally quite good. For low magnification images, a working distance of 6–10 mm is better. A final advantage of SEM is that it is usually non-destructive: samples can be imaged multiple times with lower or higher magnification or to re-examine them for new features. Note, though, that stereocilia bundles are often prone to charging, and high magnification imaging of a single hair bundle can cause visible damage.

## Conventional and Immunogold Focused-Ion-Beam Scanning Electron Microscopy

The development of powerful microscopes, hybrid imaging technologies (FIB-SEM, SBF-SEM), digital image acquisition, and increased computer storage and speed have enabled 3-D reconstruction of large data sets from large volumes with high resolution (Bullen et al., 2015; Katsuno et al., 2019; Wu et al., 2019; Hadi et al., 2020; Ivanchenko et al., 2020a; Hua et al., 2021; Lu et al., 2021; Payne et al., 2021). One of these promising approaches is FIB-SEM, which generates 3-D images of large volumes with a resolution close to that of TEM. In FIB-SEM, a sample is embedded in a resin block, as for sectioning for traditional TEM, but thin sections are sequentially milled off by an ion beam. Each freshly generated block surface is imaged with an SEM. By repeating the milling and imaging hundreds or thousands of times, a serial 3-D data set is generated as a stack of consecutive images. Usually, the serial images are obtained with the SEM backscatter imaging mode and appear inverted (compared to TEM images) so that high electron-dense areas (heavy metal stained) show up as light and low electron-dense areas are dark (**Figure 8**). The volumetric data set is then aligned, segmented and 3-D reconstructed using Dragonfly, Amira, or other software packages (Ivanchenko et al., 2020a).

Focused-ion-beam scanning electron microscopy can produce high-resolution data sets of large volumes (Ivanchenko et al., 2020a), but the imaging sessions are time-consuming and expensive. Finding an appropriate area of interest is necessary for obtaining reliable serial images within a reasonable time. A specific site usually is pre-selected with the overview image taken from flat block surfaces of the exposed tissue using a backscatter detector. Pre-selection requires deep knowledge of cochlear morphology. As we previously described (Ivanchenko et al., 2020a), appropriate zoom and milling steps are chosen and the area is imaged at high resolution, for instance with the Auto Slice and View G3 operating software associated with the FEI Helios 660 FIB-SEM.

In FIB-SEM, high resolution is generally achieved at the cost of volume, whereas high volumes are achieved at the cost of resolution. The optimal parameters vary widely with the scientific question and compromise often is necessary. In modern FIB-SEM microscopes, such as the FEI Helios 660, overnight imaging can generate volumes of up to 20 μm × 20 μm × 10 μm, with a milling step (virtual slice thickness) of 5–20 nm. Resolution near ∼2–3 nm can be achieved. Another benefit of FIB-SEM—besides the improvement of X-Y-Z resolution—is the ability to image a small volume of the sample without destroying the rest of the block surface, which allows subsequent milling of other regions of interest from the same sample (Peddie and Collinson, 2014).

What resolution do we need for hair-cell imaging? The resolution obtainable in TEM is 0.2–0.5 nm, and similar resolution is also achievable in SEMs where the size of the

electron probe ultimately limits the resolution to 0.5–2 nm. The FIB-SEM provides X-Y resolution near ∼2–3 nm and Z-resolution is the user-defined milling thickness of 5–20 nm. For stereocilia as small as 100 nm in diameter, the pixel size in any dimension should ideally be less than 20 nm. However, much higher X-Y resolutions of 1–5 nm are required to visualize subcellular structures such as tip links, actin filaments, and organelles, or the gold beads on the immunolabeled samples. There is also no single opinion about the Z-step. From our experience, 10–20 nm is good enough to obtain reliable data sets for 3-D reconstruction of hair cell bundles. It is important to note that the electron beam images the freshly exposed surface, but it also penetrates into the resin block, so some of the high-contrast information collected from the scan belongs to the tissue positioned slightly below the surface. For example, a 12-nm gold bead yielding high-contrast backscatter electrons is visible 1–2 slices before it is exposed at the surface of the resin block, at which point it will display its maximum signal intensity.

Although conventional FIB-SEM does not provide information about protein composition or localization, FIB-SEM on immunogold-labeled samples can be used for high-resolution volumetric protein mapping. With the 3-D data set, one can computationally segment subcellular or suborganellular regions with high precision and evaluate spatial distribution of gold beads within that region, enabling a quantitative composition–location–ultrastructure correlation (Ivanchenko et al., 2020a). Labeling of extracellular proteins of interest is compatible with preservation of ultrastructure, and while it is possible to perform immunogold-FIB-SEM in samples with intracellularly labeled proteins, use of permeabilization agents such as Triton X-100 or saponin is unavoidable, resulting in widespread ultrastructural damage (Bozzolla and Russell, 1998). Some other limitations apply: during the "slice and view" process the cell can't be reexamined because of the destructive nature of the technique; there is no way to increase the contrast with post-staining; the tissue needs to be heavily stained before embedding in resin; and the FIB-SEM method requires expensive specialized equipment and highly specialized user training.

Despite the resolution and versatility of all these EM techniques, they still require a deep understanding of methods used and design of proper controls. Postprocessing and analysis of EM data should be carried out by experts with experience in interpreting specific features in the grayscale EM world. The manual segmentation and analysis of large datasets is time-consuming. Speed and insight may come from new machine-learning based tools that can automate segmentation, reconstruction, and data analysis, which in turn would bring tremendous progress to the field. Some progress has been made in the development of machine learning algorithms (Hagita et al., 2018), but they have been limited to defined structures such as mitochondria (Dietlmeier et al., 2013), synapses (Lin et al., 2020), and muscle (Caffrey et al., 2019). Despite a high level of collaboration in the field, online sharing of methods and data analysis code, and terabyte-sized data sets, many automated methods are not accessible to beginners or non-experts and are limited to the specific applications for which they were developed. They may need to be optimized or trained again for other applications. Furthermore, development of machine learning algorithms is also a time-consuming and extensive process that requires lots of manually generated training data and will be carried out by experts in the field. Still, we can expect more powerful and greater accessibility of sophisticated analysis algorithms as data science is integrated with these advances in imaging physics.

## Conclusion

In summary, a number of EM techniques can be chosen to generate structural data at a range of resolutions matched to the research question and capabilities. Although guidelines like the ones described above are available, the best approach preferably should be selected with the help of an expert in the field. A large variety of strategies and EM tools is now widely accessible and is no longer restricted to a few electron microscopy labs providing versatility of obtained data.

## DATA AVAILABILITY STATEMENT

The original contributions presented in the study are included in the article/**Supplementary Material**, further inquiries can be directed to the corresponding author.

## ETHICS STATEMENT

The animal study was reviewed and approved by the Animal Care Committee of Harvard Medical School.

## AUTHOR CONTRIBUTIONS

MI carried out conventional and immunogold TEM, SEM, and FIB-SEM microscopy, analyzed the data, created figures, and wrote the manuscript. AI carried out anti-STRC SEM and FIB-SEM microscopy, analyzed the data, oversaw the project, and helped to write the manuscript. DC analyzed the data, oversaw the project, and helped to write the manuscript. All authors contributed to the article and approved the submitted version.

## FUNDING

Research reported in this publication was supported by the Bertarelli Foundation, and by the National Institute on Deafness and Other Communication Disorders through grants DC016932 and DC002281 (to DC) and DC017166 (to AI). This work was performed in part at the Harvard University Center for Nanoscale Systems (CNS), a member of the National Nanotechnology Coordinated Infrastructure Network (NNCI), which is supported by the National Science Foundation under NSF award 1541959.

## ACKNOWLEDGMENTS

We appreciate advice on FIB-SEM microscopy from Austin Akey and Stephan Kraemer (Harvard University), and on

TEM and SEM from Maria Ericsson, Anja Nordstrom, and Louise Trakimas (HMS Electron Microscopy Facility, Harvard Medical School). We greatly appreciate assistance with laboratory management from Bruce Derfler and animal care from Yaqiao Li (Harvard Medical School), and sample preparation for STRC labeling from Olga Strelkova. We thank Jinwoong Bok (Yonsei University College of Medicine, Seoul, South Korea) for providing anti-STRC antibodies. We especially appreciate institutional support to Harvard Medical School from the Bertarelli Foundation.

## SUPPLEMENTARY MATERIAL

The Supplementary Material for this article can be found online at: https://www.frontiersin.org/articles/10.3389/fcell.2021.744248/full#supplementary-material

**Supplementary Movie 1 |** 3-D localization of PCDH15 in a P1 IHC using immunogold FIB-SEM. A 3-D reconstruction of an OHC stereocilia bundle from 426 serial FIB-SEM cross sections, at a 10 nm milling step. Tissue was labeled with anti-PCDH15 and a gold-conjugated secondary antibody (12 nm). Yellow, gold beads; blue, stereocilia; gray, cell body.

## REFERENCES

Ahmed, Z. M., Goodyear, R., Riazuddin, S., Lagziel, A., Legan, P. K., Behra, M., et al. (2006). The tip-link antigen, a protein associated with the transduction complex of sensory hair cells, is protocadherin-15. *J. Neurosci.* 26, 7022–7034. doi: 10.1523/JNEUROSCI.1163-06.2006

Alagramam, K. N., Goodyear, R. J., Geng, R., Furness, D. N., van Aken, A. F., Marcotti, W., et al. (2011). Mutations in protocadherin 15 and cadherin 23 affect tip links and mechanotransduction in mammalian sensory hair cells. *PLoS One* 6:e19183. doi: 10.1371/journal.pone.0019183

Assad, J. A., Shepherd, G. M., and Corey, D. P. (1991). Tip-link integrity and mechanical transduction in vertebrate hair cells. *Neuron* 7, 985–994. doi: 10.1016/0896-6273(91)90343-x

Auer, M., Koster, A. J., Ziese, U., Bajaj, C., Volkmann, N., Wang da, N., et al. (2008). Three-dimensional architecture of hair-bundle linkages revealed by electron-microscopic tomography. *J. Assoc. Res. Otolaryngol.* 9, 215–224. doi: 10.1007/s10162-008-0114-2

Baena, V., Schalek, R. L., Lichtman, J. W., and Terasaki, M. (2019). Serial-section electron microscopy using automated tape-collecting ultramicrotome (ATUM). *Methods Cell Biol.* 152, 41–67. doi: 10.1016/bs.mcb.2019.04.004

Beurg, M., Fettiplace, R., Nam, J. H., and Ricci, A. J. (2009). Localization of inner hair cell mechanotransducer channels using high-speed calcium imaging. *Nat. Neurosci.* 12, 553–558. doi: 10.1038/nn.2295

Bock, D. D., Lee, W. C., Kerlin, A. M., Andermann, M. L., Hood, G., Wetzel, A. W., et al. (2011). Network anatomy and in vivo physiology of visual cortical neurons. *Nature* 471, 177–182. doi: 10.1038/nature09802

Bohne, B. A., and Harding, G. W. (1993). Combined organ of Corti/modiolus technique for preparing mammalian cochleas for quantitative microscopy. *Hear. Res.* 71, 114–124. doi: 10.1016/0378-5955(93)90027-X

Boykins, L. G., Jones, J. C., Estrano, C. E., Schwartzbach, S. D., and Skalli, O. (2016). Pre-embedding double-label immunoelectron microscopy of chemically fixed tissue culture cells. *Methods Mol. Biol.* 1474, 217–232. doi: 10.1007/978-1-4939-6352-2_13

Bozzolla, J. J., and Russell, L. D. (1998). *Electron Microscopy; Principles and Techniques for Biologists*, 2nd Edn. Boston, MA: Jones & Bartlett Publishers.

Bullen, A., West, T., Moores, C., Ashmore, J., Fleck, R. A., MacLellan-Gibson, K., et al. (2015). Association of intracellular and synaptic organization in cochlear inner hair cells revealed by 3D electron microscopy. *J Cell Sci.* 128, 2529–2540. doi: 10.1242/jcs.170761

Caffrey, B. J., Maltsev, A. V., Gonzalez-Freire, M., Hartnell, L. M., Ferrucci, L., and Subramaniam, S. (2019). Semi-automated 3D segmentation of human skeletal muscle using focused ion beam-scanning electron microscopic images. *J. Struct. Biol.* 207, 1–11. doi: 10.1016/j.jsb.2019.03.008

Chen, Q., Mahendrasingam, S., Tickle, J. A., Hackney, C. M., Furness, D. N., and Fettiplace, R. (2012). The development, distribution and density of the plasma membrane calcium ATPase 2 calcium pump in rat cochlear hair cells. *Eur. J. Neurosci.* 36, 2302–2310. doi: 10.1111/j.1460-9568.2012.08159.x

Denk, W., and Horstmann, H. (2004). Serial block-face scanning electron microscopy to reconstruct three-dimensional tissue nanostructure. *PLoS Biol* 2:e329. doi: 10.1371/journal.pbio.0020329

Dietlmeier, J., Ghita, O., Duessmann, H., Prehn, J. H., and Whelan, P. F. (2013). Unsupervised mitochondria segmentation using recursive spectral clustering and adaptive similarity models. *J. Struct. Biol.* 184, 401–408. doi: 10.1016/j.jsb.2013.10.013

Dow, E., Jacobo, A., Hossain, S., Siletti, K., and Hudspeth, A. J. (2018). Connectomics of the zebrafish's lateral-line neuromast reveals wiring and miswiring in a simple microcircuit. *Elife* 7:e33988. doi: 10.7554/elife.33988

Dror, A. A., and Avraham, K. B. (2010). Hearing impairment: a panoply of genes and functions. *Neuron* 68, 293–308. doi: 10.1016/j.neuron.2010.10.011

Fang, Q., Indzhykulian, A. A., Mustapha, M., Riordan, G. P., Dolan, D. F., Friedman, T. B., et al. (2015). The 133-kDa N-terminal domain enables myosin 15 to maintain mechanotransducing stereocilia and is essential for hearing. *Elife* 4:e08627. doi: 10.7554/elife.08627

Fettiplace, R. (2017). Hair cell transduction, tuning, and synaptic transmission in the mammalian cochlea. *Compr. Physiol.* 7, 1197–1227. doi: 10.1002/cphy.c160049

Fischer, E. R., Hansen, B. T., Nair, V., Hoyt, F. H., and Dorward, D. W. (2012). Scanning electron microscopy. *Curr. Protoc. Microbiol.* 2:2. doi: 10.1002/9780471729259.mc02b02s25

Flechsler, J., Heimerl, T., Pickl, C., Rachel, R., Stierhof, Y. D., and Klingl, A. (2020). 2D and 3D immunogold localization on (epoxy) ultrathin sections with and without osmium tetroxide. *Microsc. Res. Tech.* 83, 691–705. doi: 10.1002/jemt.23459

Furness, D. N., and Hackney, C. M. (1985). Cross-links between stereocilia in the guinea pig cochlea. *Hear. Res.* 18, 177–188. doi: 10.1016/0378-5955(84)90041-8

Furness, D. N., Katori, Y., Mahendrasingam, S., and Hackney, C. M. (2005). Differential distribution of beta- and gamma-actin in guinea-pig cochlear sensory and supporting cells. *Hear. Res.* 207, 22–34. doi: 10.1016/j.heares.2005.05.006

Furness, D. N., Lawton, D. M., Mahendrasingam, S., Hodierne, L., and Jagger, D. J. (2009). Quantitative analysis of the expression of the glutamate-aspartate transporter and identification of functional glutamate uptake reveal a role for cochlear fibrocytes in glutamate homeostasis. *Neuroscience* 162, 1307–1321. doi: 10.1016/j.neuroscience.2009.05.036

Furness, D. N., Mahendrasingam, S., Ohashi, M., Fettiplace, R., and Hackney, C. M. (2008). The dimensions and composition of stereociliary rootlets in mammalian cochlear hair cells: comparison between high- and low-frequency cells and evidence for a connection to the lateral membrane. *J. Neurosci.* 28, 6342–6353. doi: 10.1523/jneurosci.1154-08.2008

Garcia, J. A., Yee, A. G., Gillespie, P. G., and Corey, D. P. (1998). Localization of myosin-Ibeta near both ends of tip links in frog saccular hair cells. *J. Neurosci.* 18, 8637–8647. doi: 10.1523/JNEUROSCI.18-21-08637.1998

Gay, H., and Anderson, T. F. (1954). Serial sections for electron microscopy. *Science* 120, 1071–1073. doi: 10.1126/science.120.3130.1071

Geleoc, G. S., and Holt, J. R. (2003). Developmental acquisition of sensory transduction in hair cells of the mouse inner ear. *Nat Neurosci* 6, 1019–1020. doi: 10.1038/nn1120

Gillespie, P. G., and Walker, R. G. (2001). Molecular basis of mechanosensory transduction. *Nature* 413, 194–202. doi: 10.1038/35093011

Glauert, A. M., and Lewis, P. R. (1998). *Biological Specimen Preparation for Transmission Electron Microscopy*. Princeton, N.J: Princeton University Press.

Goodyear, R. J., Forge, A., Legan, P. K., and Richardson, G. P. (2010). Asymmetric distribution of cadherin 23 and protocadherin 15 in the kinocilial links of avian sensory hair cells. *J. Comp. Neurol.* 518, 4288–4297. doi: 10.1002/cne.22456

Goodyear, R. J., Marcotti, W., Kros, C. J., and Richardson, G. P. (2005). Development and properties of stereociliary link types in hair cells of the mouse cochlea. *J. Comp. Neurol.* 485, 75–85. doi: 10.1002/cne.20513

Gopal, S., Chiappini, C., Armstrong, J. P. K., Chen, Q., Serio, A., Hsu, C. C., et al. (2019). Immunogold FIB-SEM: combining volumetric ultrastructure visualization with 3D biomolecular analysis to dissect cell-environment interactions. *Adv. Mater.* 31:e1900488. doi: 10.1002/adma.201900488

Grillet, N., Xiong, W., Reynolds, A., Kazmierczak, P., Sato, T., Lillo, C., et al. (2009). Harmonin mutations cause mechanotransduction defects in cochlear hair cells. *Neuron* 62, 375–387. doi: 10.1016/j.neuron.2009.04.006

Hackney, C. M., Mahendrasingam, S., Penn, A., and Fettiplace, R. (2005). The concentrations of calcium buffering proteins in mammalian cochlear hair cells. *J. Neurosci.* 25, 7867–7875. doi: 10.1523/JNEUROSCI.1196-05.2005

Hadi, S., Alexander, A. J., Velez-Ortega, A. C., and Frolenkov, G. I. (2020). Myosin-XVa controls both staircase architecture and diameter gradation of stereocilia rows in the auditory hair cell bundles. *J. Assoc. Res. Otolaryngol.* 21, 121–135. doi: 10.1007/s10162-020-00745-4

Hagita, K., Higuchi, T., and Jinnai, H. (2018). Super-resolution for asymmetric resolution of FIB-SEM 3D imaging using AI with deep learning. *Sci. Rep.* 8:5877. doi: 10.1038/s41598-018-24330-1

Han, W., Shin, J. O., Ma, J. H., Min, H., Jung, J., Lee, J., et al. (2020). Distinct roles of stereociliary links in the nonlinear sound processing and noise resistance of cochlear outer hair cells. *Proc. Natl. Acad. Sci. U.S.A.* 117, 11109–11117. doi: 10.1073/pnas.1920229117

Harris, K. M., Perry, E., Bourne, J., Feinberg, M., Ostroff, L., and Hurlburt, J. (2006). Uniform serial sectioning for transmission electron microscopy. *J. Neurosci.* 26, 12101–12103. doi: 10.1523/JNEUROSCI.3994-06.2006

Hasson, T., Gillespie, P. G., Garcia, J. A., MacDonald, R. B., Zhao, Y., Yee, A. G., et al. (1997). Unconventional myosins in inner-ear sensory epithelia. *J. Cell Biol.* 137, 1287–1307. doi: 10.1083/jcb.137.6.1287

Heywood, P., and Resnick, S. (1981). Application of the thiocarbohydrazide-osmium coating technique to scanning electron microscopy of the inner ear. *Acta Otolaryngol.* 91, 183–187. doi: 10.3109/00016488109138498

Hua, Y., Ding, X., Wang, H., Wang, F., Lu, Y., Neef, J., et al. (2021). Electron microscopic reconstruction of neural circuitry in the cochlea. *Cell Rep.* 34:108551. doi: 10.1016/j.celrep.2020.108551

Indzhykulian, A. A., Stepanyan, R., Nelina, A., Spinelli, K. J., Ahmed, Z. M., Belyantseva, I. A., et al. (2013). Molecular remodeling of tip links underlies mechanosensory regeneration in auditory hair cells. *PLoS Biol.* 11:e1001583. doi: 10.1371/journal.pbio.1001583

Ivanchenko, M. V., Hanlon, K. S., Devine, M. K., Tenneson, K., Emond, F., Lafond, J. F., et al. (2020b). Preclinical testing of AAV9-PHP.B for transgene expression in the non-human primate cochlea. *Hear. Res.* 394, 107930. doi: 10.1016/j.heares.2020.107930

Ivanchenko, M. V., Cicconet, M., Jandal, H. A., Wu, X., Corey, D. P., and Indzhykulian, A. A. (2020a). Serial scanning electron microscopy of anti-PKHD1L1 immuno-gold labeled mouse hair cell stereocilia bundles. *Sci. Data* 7:182. doi: 10.1038/s41597-020-0509-4

Ivanchenko, M. V., Hanlon, K. S., Hathaway, D. M., Klein, A. J., Peters, C. W., Li, Y., et al. (2021). AAV-S: a versatile capsid variant for transduction of mouse and primate inner ear. *Mol. Ther. Methods Clin. Dev.* 21, 382–398. doi: 10.1016/j.omtm.2021.03.019

Jones, J. C. (2016). Pre- and post-embedding immunogold labeling of tissue sections. *Methods Mol. Biol.* 1474, 291–307. doi: 10.1007/978-1-4939-6352-2_19

Kachar, B., Parakkal, M., Kurc, M., Zhao, Y., and Gillespie, P. G. (2000). High-resolution structure of hair-cell tip links. *Proc. Natl. Acad. Sci. U.S.A.* 97, 13336–13341. doi: 10.1073/pnas.97.24.13336

Karavitaki, K. D., and Corey, D. P. (2010). Sliding adhesion confers coherent motion to hair cell stereocilia and parallel gating to transduction channels. *J. Neurosci.* 30, 9051–9063. doi: 10.1523/JNEUROSCI.4864-09.2010

Katsuno, T., Belyantseva, I. A., Cartagena-Rivera, A. X., Ohta, K., Crump, S. M., Petralia, R. S., et al. (2019). TRIOBP-5 sculpts stereocilia rootlets and stiffens supporting cells enabling hearing. *JCI Insight* 4:e128561. doi: 10.1172/jci.insight.128561

Kazmierczak, P., Sakaguchi, H., Tokita, J., Wilson-Kubalek, E. M., Milligan, R. A., Muller, U., et al. (2007). Cadherin 23 and protocadherin 15 interact to form tip-link filaments in sensory hair cells. *Nature* 449, 87–91. doi: 10.1038/nature06091

Kizilyaprak, C., Daraspe, J., and Humbel, B. M. (2014). Focused ion beam scanning electron microscopy in biology. *J. Microsc.* 254, 109–114. doi: 10.1111/jmi.12127

Landegger, L. D., Dilwali, S., and Stankovic, K. M. (2017). Neonatal murine cochlear explant technique as an in vitro screening tool in hearing research. *J. Vis. Exp.* 124:55704. doi: 10.3791/55704

Lin, Z., Wei, D., Jang, W. D., Zhou, S., Chen, X., Wang, X., et al. (2020). Two stream active query suggestion for active learning in connectomics. *Comput. Vis. ECCV* 12363, 103–120. doi: 10.1007/978-3-030-58523-5_7

Lu, Y., Wang, F., Wang, H., Bastians, P., and Hua, Y. (2021). Large-scale 3D imaging of mouse cochlea using serial block-face scanning electron microscopy. *STAR Protoc.* 2:100515. doi: 10.1016/j.xpro.2021.100515

Magaki, S., Hojat, S. A., Wei, B., So, A., and Yong, W. H. (2019). An introduction to the performance of immunohistochemistry. *Methods Mol. Biol.* 1897, 289–298. doi: 10.1007/978-1-4939-8935-5_25

Mahendrasingam, S., Bebb, C., Shepard, E., and Furness, D. N. (2011). Subcellular distribution and relative expression of fibrocyte markers in the CD/1 mouse cochlea assessed by semiquantitative immunogold electron microscopy. *J. Histochem. Cytochem.* 59, 984–1000. doi: 10.1369/0022155411421801

Mahendrasingam, S., Fettiplace, R., Alagramam, K. N., Cross, E., and Furness, D. N. (2017). Spatiotemporal changes in the distribution of LHFPL5 in mice cochlear hair bundles during development and in the absence of PCDH15. *PLoS One* 12:e0185285. doi: 10.1371/journal.pone.0185285

Michel, V., Goodyear, R. J., Weil, D., Marcotti, W., Perfettini, I., Wolfrum, U., et al. (2005). Cadherin 23 is a component of the transient lateral links in the developing hair bundles of cochlear sensory cells. *Dev. Biol.* 280, 281–294. doi: 10.1016/j.ydbio.2005.01.014

Miranda, K., Girard-Dias, W., Attias, M., de Souza, W., and Ramos, I. (2015). Three dimensional reconstruction by electron microscopy in the life sciences: an introduction for cell and tissue biologists. *Mol. Reprod. Dev.* 82, 530–547. doi: 10.1002/mrd.22455

Mogensen, M. M., Rzadzinska, A., and Steel, K. P. (2007). The deaf mouse mutant whirler suggests a role for whirlin in actin filament dynamics and stereocilia development. *Cell Motil. Cytoskeleton* 64, 496–508. doi: 10.1002/cm.20199

Osborne, M. P., and Comis, S. D. (1991). Preparation of inner ear sensory hair bundles for high resolution scanning electron microscopy. *Scanning Microsc.* 5, 555–564.

Osborne, M. P., Comis, S. D., and Pickles, J. O. (1984). Morphology and cross-linkage of stereocilia in the guinea-pig labyrinth examined without the use of osmium as a fixative. *Cell Tissue Res.* 237, 43–48. doi: 10.1007/bf00229198

Pacentine, I., Chatterjee, P., and Barr-Gillespie, P. G. (2020). Stereocilia rootlets: actin-based structures that are essential for structural stability of the hair bundle. *Int. J. Mol. Sci.* 21:324. doi: 10.3390/ijms21010324

Parker, A., Chessum, L., Mburu, P., Sanderson, J., and Bowl, M. R. (2016). Light and electron microscopy methods for examination of cochlear morphology in mouse models of deafness. *Curr. Protoc. Mouse Biol.* 6, 272–306. doi: 10.1002/cpmo.10

Payne, S. A., Joens, M. S., Chung, H., Skigen, N., Frank, A., Gattani, S., et al. (2021). Maturation of heterogeneity in afferent synapse ultrastructure in the mouse cochlea. *Front. Synaptic Neurosci.* 13:678575. doi: 10.3389/fnsyn.2021.678575

Peddie, C. J., and Collinson, L. M. (2014). Exploring the third dimension: volume electron microscopy comes of age. *Micron* 61, 9–19. doi: 10.1016/j.micron.2014.01.009

Phelps, J. S., Hildebrand, D. G. C., Graham, B. J., Kuan, A. T., Thomas, L. A., Nguyen, T. M., et al. (2021). Reconstruction of motor control circuits in adult Drosophila using automated transmission electron microscopy. *Cell* 184, 759–774. doi: 10.1016/j.cell.2020.12.013

Pickles, J. O., Comis, S. D., and Osborne, M. P. (1984). Cross-links between stereocilia in the guinea pig organ of Corti, and their possible relation to sensory transduction. *Hear. Res.* 15, 103–112.

Reynolds, E. S. (1963). The use of lead citrate at high pH as an electron-opaque stain in electron microscopy. *J. Cell Biol.* 17, 208–212.

Richardson, G. P., de Monvel, J. B., and Petit, C. (2011). How the genetics of deafness illuminates auditory physiology. *Annu. Rev. Physiol.* 73, 311–334. doi: 10.1146/annurev-physiol-012110-142228

Riemersma, J. C. (1968). Osmium tetroxide fixation of lipids for electron microscopy. A possible reaction mechanism. *Biochim. Biophys. Acta* 152, 718–727. doi: 10.1016/0005-2760(68)90118-5

Sakaguchi, H., Tokita, J., Muller, U., and Kachar, B. (2009). Tip links in hair cells: molecular composition and role in hearing loss. *Curr. Opin. Otolaryngol. Head Neck Surg.* 17, 388–393. doi: 10.1097/MOO.0b013e3283303472

Siemens, J., Lillo, C., Dumont, R. A., Reynolds, A., Williams, D. S., Gillespie, P. G., et al. (2004). Cadherin 23 is a component of the tip link in hair-cell stereocilia. *Nature* 428, 950–955. doi: 10.1038/nature02483

Spoendlin, H., and Brun, J. P. (1974). The block-surface technique for evaluation of cochlear pathology. *Arch. Otorhinolaryngol.* 208, 137–145. doi: 10.1007/bf00453927

Tilney, L. G., Derosier, D. J., and Mulroy, M. J. (1980). The organization of actin filaments in the stereocilia of cochlear hair cells. *J. Cell Biol.* 86, 244–259. doi: 10.1083/jcb.86.1.244

Van Camp, G. S. R. (2021). *Hereditary Hearing Loss Homepage*. Available online at: https://hereditaryhearingloss.org/ (accessed August 30, 2021).

Velez-Ortega, A. C., Freeman, M. J., Indzhykulian, A. A., Grossheim, J. M., and Frolenkov, G. I. (2017). Mechanotransduction current is essential for stability of the transducing stereocilia in mammalian auditory hair cells. *Elife* 6:e24661. doi: 10.7554/eLife.24661.001

Velez-Ortega, A. C., and Frolenkov, G. I. (2019). Building and repairing the stereocilia cytoskeleton in mammalian auditory hair cells. *Hear. Res.* 376, 47–57. doi: 10.1016/j.heares.2018.12.012

Verpy, E., Leibovici, M., Michalski, N., Goodyear, R. J., Houdon, C., Weil, D., et al. (2011). Stereocilin connects outer hair cell stereocilia to one another and to the tectorial membrane. *J. Comp. Neurol.* 519, 194–210. doi: 10.1002/cne.22509

Verpy, E., Masmoudi, S., Zwaenepoel, I., Leibovici, M., Hutchin, T. P., Del Castillo, I., et al. (2001). Mutations in a new gene encoding a protein of the hair bundle cause non-syndromic deafness at the DFNB16 locus. *Nat. Genet.* 29, 345–349. doi: 10.1038/ng726

Vranceanu, F., Perkins, G. A., Terada, M., Chidavaenzi, R. L., Ellisman, M. H., and Lysakowski, A. (2012). Striated organelle, a cytoskeletal structure positioned to modulate hair-cell transduction. *Proc. Natl. Acad. Sci. U.S.A.* 109, 4473–4478. doi: 10.1073/pnas.1101003109

Wang, H., Wang, S., Lu, Y., Chen, Y., Huang, W., Qiu, M., et al. (2021). Cytoarchitecture and innervation of the mouse cochlear amplifier revealed by large-scale volume electron microscopy. *J. Comp. Neurol.* 529, 2958–2969. doi: 10.1002/cne.25137

Wood, M. B., Nowak, N., Mull, K., Goldring, A., Lehar, M., and Fuchs, P. A. (2021). Acoustic trauma increases ribbon number and size in outer hair cells of the mouse cochlea. *J. Assoc. Res. Otolaryngol.* 22, 19–31. doi: 10.1007/s10162-020-00777-w

Wu, X., Ivanchenko, M. V., Al Jandal, H., Cicconet, M., Indzhykulian, A. A., and Corey, D. P. (2019). PKHD1L1 is a coat protein of hair-cell stereocilia and is required for normal hearing. *Nat. Commun.* 10:3801. doi: 10.1038/s41467-019-11712-w

Yin, W., Brittain, D., Borseth, J., Scott, M. E., Williams, D., Perkins, J., et al. (2020). A petascale automated imaging pipeline for mapping neuronal circuits with high-throughput transmission electron microscopy. *Nat. Commun.* 11:4949. doi: 10.1038/s41467-020-18659-3

Zhao, B., and Muller, U. (2015). The elusive mechanotransduction machinery of hair cells. *Curr. Opin. Neurobiol.* 34, 172–179. doi: 10.1016/j.conb.2015.08.006

**Conflict of Interest:** The authors declare that the research was conducted in the absence of any commercial or financial relationships that could be construed as a potential conflict of interest.

**Publisher's Note:** All claims expressed in this article are solely those of the authors and do not necessarily represent those of their affiliated organizations, or those of the publisher, the editors and the reviewers. Any product that may be evaluated in this article, or claim that may be made by its manufacturer, is not guaranteed or endorsed by the publisher.

*Copyright © 2021 Ivanchenko, Indzhykulian and Corey. This is an open-access article distributed under the terms of the Creative Commons Attribution License (CC BY). The use, distribution or reproduction in other forums is permitted, provided the original author(s) and the copyright owner(s) are credited and that the original publication in this journal is cited, in accordance with accepted academic practice. No use, distribution or reproduction is permitted which does not comply with these terms.*

frontiers in Cell and Developmental Biology

ORIGINAL RESEARCH
published: 25 November 2021
doi: 10.3389/fcell.2021.742529

# Dimensions of a Living Cochlear Hair Bundle

*Katharine K. Miller, Patrick Atkinson, Kyssia Ruth Mendoza, Dáibhid Ó Maoiléidigh* and Nicolas Grillet**

*Department of Otolaryngology-Head and Neck Surgery, School of Medicine, Stanford University, Stanford, CA, United States*

The hair bundle is the mechanosensory organelle of hair cells that detects mechanical stimuli caused by sounds, head motions, and fluid flows. Each hair bundle is an assembly of cellular-protrusions called stereocilia, which differ in height to form a staircase. Stereocilia have different heights, widths, and separations in different species, sensory organs, positions within an organ, hair-cell types, and even within a single hair bundle. The dimensions of the stereociliary assembly dictate how the hair bundle responds to stimuli. These hair-bundle properties have been measured previously only to a limited degree. In particular, mammalian data are either incomplete, lack control for age or position within an organ, or have artifacts owing to fixation or dehydration. Here, we provide a complete set of measurements for postnatal day (P) 11 C57BL/6J mouse apical inner hair cells (IHCs) obtained from living tissue, tissue mildly-fixed for fluorescent imaging, or tissue strongly fixed and dehydrated for scanning electronic microscopy (SEM). We found that hair bundles mildly-fixed for fluorescence had the same dimensions as living hair bundles, whereas SEM-prepared hair bundles shrank uniformly in stereociliary heights, widths, and separations. By determining the shrinkage factors, we imputed live dimensions from SEM that were too small to observe optically. Accordingly, we created the first complete blueprint of a living IHC hair bundle. We show that SEM-prepared measurements strongly affect calculations of a bundle's mechanical properties – overestimating stereociliary deflection stiffness and underestimating the fluid coupling between stereocilia. The methods of measurement, the data, and the consequences we describe illustrate the high levels of accuracy and precision required to understand hair-bundle mechanotransduction.

**Keywords: stereocilia, hair cell, mechanotransduction, hair bundle, mouse, deafness, hearing loss, electron microscopy**

OPEN ACCESS

***Edited by:***
*Anthony Wei Peng,*
*University of Colorado Anschutz Medical Campus, United States*

***Reviewed by:***
*Giusy Caprara,*
*University of Colorado Anschutz Medical Campus, United States*
*David Furness,*
*Keele University, United Kingdom*
*A. Catalina Velez-Ortega,*
*University of Kentucky, United States*

****Correspondence:***
*Dáibhid Ó Maoiléidigh*
*dmelody@stanford.edu*
*Nicolas Grillet*
*ngrillet@stanford.edu*

***Specialty section:***
*This article was submitted to Cell Growth and Division, a section of the journal Frontiers in Cell and Developmental Biology*

***Received:*** *16 July 2021*
***Accepted:*** *13 October 2021*
***Published:*** *25 November 2021*

***Citation:***
*Miller KK, Atkinson P, Mendoza KR, Ó Maoiléidigh D and Grillet N (2021) Dimensions of a Living Cochlear Hair Bundle. Front. Cell Dev. Biol. 9:742529. doi: 10.3389/fcell.2021.742529*

## INTRODUCTION

Hair bundles are the mechanosensory organelles of hair cells that detect forces induced by sound in auditory systems, head motion in vestibular systems, or fluid flow in lateral lines. The hair bundle consists of an assembly of stereocilia – cylindrical cellular protrusions with a beveled top and a tapered bottom filled with F-actin (Duvall et al., 1966; Mulroy, 1974; Flock and Cheung, 1977; DeRosier et al., 1980; Tilney et al., 1980; Tilney and Saunders, 1983; Kaltenbach et al., 1994). Stereocilia are arranged in rows of increasing height, forming a staircase (Tilney and Saunders, 1983; Tilney et al., 1988). A single microtubule-based cilium, called the kinocilium, is connected to the stereocilia at a central location behind the tallest row during development, and is maintained

or eliminated in mature hair cells depending on the species and sensory system (Wersall, 1956; Roth and Bruns, 1992). External nanofilaments connect the stereocilia, including tip links that connect the tip of a stereocilium to its taller neighbor (Osborne et al., 1984; Pickles et al., 1984). Mechanical deflection of the hair bundle toward its tallest row extends gating springs, composed of tip links and other elements, which convey forces that modulate mechanotransducer-channel open probability, which in turn drives the hair-cell receptor potential via the influx of potassium ions into the cell (Davis, 1965; Howard and Hudspeth, 1988; Bartsch et al., 2019; Ó Maoiléidigh and Ricci, 2019).

In the rodent auditory organ, the cochlea, hair-bundle development begins embryonically. Hair bundles form a staircase by birth, acquire mechanosensitivity at P0-P1, and reach maturity after P21 (Lim and Anniko, 1985; Roth and Bruns, 1992; Kaltenbach et al., 1994; Zine and Romand, 1996; Waguespack et al., 2007; Lelli et al., 2009; Kim and Fettiplace, 2013; Pan et al., 2013; Beurg et al., 2018; Krey et al., 2020; Trouillet et al., 2021). From P0-P21, hair-bundle morphology changes drastically, with stereocilia increasing or decreasing in height and width depending on their row (Tilney et al., 1980; Tilney and DeRosier, 1986; Roth and Bruns, 1992; Kaltenbach et al., 1994; Krey et al., 2020). Stereociliary height and hair-bundle morphology stabilize in adulthood.

Each mature hair bundle has a distinct number of stereocilia with defined dimensions depending on the species, sensory organ, position within their organ, hair-cell type (e.g., inner hair cells, outer hair cells (OHCs), or vestibular hair cells), and row within a bundle (Wright, 1984; Kaltenbach et al., 1994; Zine and Romand, 1996; Ricci et al., 1997; Xue and Peterson, 2006; Xiong et al., 2012; Yarin et al., 2014). For example, mature apical rodent cochlear hair bundles are taller than basal hair bundles and have fewer stereocilia per row (Garfinkle and Saunders, 1983; Lim, 1986; Roth and Bruns, 1992; Kaltenbach et al., 1994). Although genetic mutations that cause hearing loss often affect the number of stereocilia and their dimensions, their effects on hair-bundle mechanics are not well-understood (Petit and Richardson, 2009; Richardson and Petit, 2019).

Stereociliary dimensions determine the mechanical response of a hair bundle to a stimulus: for example, a stereocilium's height determines its stiffness, and the geometrical relationship between neighboring stereocilia determines their coupling by fluid and the gating-spring extension in response to stereociliary deflection (Howard and Ashmore, 1986; Howard and Hudspeth, 1988; Crawford et al., 1989; Jacobs and Hudspeth, 1990; Geisler, 1993; Pickles, 1993; Zetes, 1995; Furness et al., 1997; Zetes and Steele, 1997; Karavitaki and Corey, 2010; Baumgart, 2011; Kozlov et al., 2011; Hadi et al., 2020). Determining a hair bundle's mechanical properties is challenging experimentally and often relies on mathematical models of the hair bundle (Crawford and Fettiplace, 1985; Howard and Hudspeth, 1987; Kozlov et al., 2011; Powers et al., 2012, 2014; Ó Maoiléidigh and Hudspeth, 2013; Nam et al., 2015; Gianoli et al., 2017; Milewski et al., 2017; Cartagena-Rivera et al., 2019; Tobin et al., 2019). However, models require prior knowledge of stereociliary dimensions. If these measurements have not been determined for living hair bundles, models either make assumptions or use values obtained from electron microscopy (EM) (Furness et al., 1997; Smith and Chadwick, 2011; Zetes et al., 2012; Ó Maoiléidigh and Hudspeth, 2013; Nam et al., 2015).

While EM can achieve sub-nanometer resolution, the preparation method is deleterious to the tissue: the tissue is strongly fixed with glutaraldehyde (and in some cases further post-fixed with osmium tetroxide) and dehydrated in successive ethanol baths. Samples are then either embedded in a resin to generate thin sections imaged by Transmission EM (TEM), or dried in a critical-point drying chamber, after replacement of ethanol by liquid-CO2, coated with a thin metal layer, and observed by SEM (Bozzola and Russell, 1992). These EM sample preparation steps induce dimensional distortions. TEM samples are less subject to these distortions due to the presence of a supporting liquid surrounding the sample until the resin hardens, whereas all fluids are removed during SEM sample drying (Nordestgaard and Rostgaard, 1985). A major limitation of TEM, however, is that it produces clear results only for small numbers of cells, because capturing structures of interest within a TEM section is difficult. In comparison, conventional SEM allows direct imaging of the entire ultrastructure of a large number of cells, but the sample preparation induces substantial tissue shrinkage. Therefore, stereociliary dimensions obtained by SEM are underestimated to a large extent, but the magnitude of this shrinkage has not been well-quantified (Jensen et al., 1981). Still, SEM has been valuable for performing relative comparisons, such as between samples of different genotypes or between groups undergoing different treatments (Hunter-Duvar, 1978; Holme and Steel, 2002; Gagnon et al., 2006; Webb et al., 2011; Xiong et al., 2012; Lelli et al., 2016; Vélez-Ortega et al., 2017; Trouillet et al., 2021).

In addition to SEM, stereociliary dimensions have been measured in mildly-fixed samples – incubating in paraformaldehyde for 30 min, permeabilizing the tissue, labeling the actin-core of stereocilia using fluorescently labeled phalloidin, and finally imaging with fluorescence microscopy. With conventional light microscopy, stereociliary dimensions can be determined with a lateral resolution of about 200 nm and with recent technological improvements in super-resolution fluorescence microscopy, the resolution can be further improved (Schermelleh et al., 2019; Krey et al., 2020). However, it remains unclear whether mild paraformaldehyde fixation affects these measurements.

Live stereociliary dimensions have rarely been determined, resulting in limited information about the live morphology of different types of hair bundles. Because the available live-cell studies used different techniques and the imaged hair bundles differ greatly in their morphology, this data cannot be combined to create a complete description of a given hair bundle. These studies include: fluorescent imaging of overexpressed actin-EGFP in P2-P5 mouse utricular stereocilia (Drummond et al., 2015), fluorescent labeling of the stereociliary membrane with a lipophilic dye in P8-P9 rat IHCs (George et al., 2020), light-microscopy of isolated vestibular bullfrog hair cells (Jacobs and Hudspeth, 1990) or P7-P10 rat IHC hair bundles lying flat on the apical hair-cell surface (Tobin et al., 2019), and scanning ion conductance microscopy of the surface of P4 rat

IHC hair bundles (Vélez-Ortega and Frolenkov, 2016; Galeano-Naranjo et al., 2021). In summary, a complete set of stereociliary heights, widths, and separations has still not been determined for living hair bundles. Moreover, the size differences between live, mildly-fixed, and SEM-processed preparations remain unknown. Determining scaling factors between preparations will allow us to impute live stereociliary dimensions from fixed preparations, which will be especially useful for rare samples such as human hair cells (Wright, 1981, 1984; Jeffries et al., 1986; Lavigne-Rebillard and Pujol, 1986, 1987, 1990).

To address the question of living hair-bundle dimensions, we focused on the mouse – the mammalian genetic animal model for inherited hearing loss. We accurately measured the stereociliary height, width, and separation of apical IHCs from P11 littermate C57BL/6J mice imaged under live, mildly-fixed, or SEM-prepared conditions. We found that live and mildly-fixed bundles have similar stereociliary dimensions, while SEM preparation reduced all stereociliary dimensions by similar amounts. Using the shrinkage factors for SEM, we were able to impute live dimensions that were too small to be measured optically. We also show how calculations of stereociliary stiffness, fluid coupling between stereocilia, and the geometric relationship between gating-spring extension and stereociliary deflection are affected when SEM-determined measurements are used instead of live dimensions.

# RESULTS

## Live and Mildly-Fixed Apical Inner-Hair-Cell Stereocilia Have Similar Heights

Hair-bundle investigations are typically performed in the mouse from P0 to P11, when the cochlear bone can be removed with less damage to the hair cells than at older ages (Kim and Fettiplace, 2013; Asai et al., 2018; Corns et al., 2018; Trouillet et al., 2021). For comparison with previous studies, we imaged and measured stereociliary dimensions in C57BL/6J wild-type (WT) mice at postnatal day (P) P11. We focused on IHCs in the apical cochlear turn, because their stereocilia are tall and wide (Garfinkle and Saunders, 1983). To avoid the heterogeneity found within the most apical IHCs, we focused on hair bundles from the 90th to 160th IHCs from the apex (**Figure 1A**). This is 7–20% of the cochlear length, measured from the apex, corresponding to the 5–8.5 kHz characteristic-frequency range in adults (Müller et al., 2005). At P11, the tallest IHC stereociliary row (row 1) is 2–3 times taller than the second row (row 2), which facilitated measurements (**Figures 1B,C**). To further reduce measurement variability due to maturation differences, we used animals from a single litter in each experiment. To preserve hair-cell viability, apical cochlear turns were dissected in the extracellular solution used for mechanotransduction electrophysiological recordings (George et al., 2020). We stained individual cochleae from a single animal in one of two ways. One cochlea was live-stained for 5 min with a lipophilic dye that becomes strongly fluorescent upon binding to cell membranes. Imaging was performed immediately and for a maximum duration of 37 min using a confocal microscope in Airyscan mode equipped with an immersion lens (**Figure 1D**). The other cochlea was mildly fixed (30 min in 4% paraformaldehyde at room temperature), permeabilized, stained with phalloidin-Alexa488, which labels the stereociliary actin-core, and imaged immediately after the corresponding live sample using the same optical settings and lens (**Figure 1E**). Hair-bundle image stacks were reconstructed and analyzed as 3-D objects with Imaris (Oxford Instruments) software. Stereocilium heights from row 1 and row 2 were measured by manually placing measurements points at the stereociliary bases and tops in 3-D space. We defined the top as the location where the fluorescence signal suddenly decayed, and the base as the narrow end of stereociliary taper (**Supplementary Movies 1–3**). For comparison with SEM (see below), we focused on fully visible stereocilia, or row 1 stereocilia abutting a fully visible row 2 stereocilium, excluding the stereocilia at row edges. All measurements are presented to the nearest 0.01 μm ± standard deviation (SD).

In our first set of experiments, we stained the IHC stereociliary membrane with Di-4-ANEPPDHQ (Di-4) lipophilic vital dye and compared measurements with mildly-fixed bundles stained with phalloidin-Alexa488. The height of row 1 stereocilia was 5.76 ± 0.65 μm in the Di-4 live condition and 5.56 ± 0.35 μm in the mildly-fixed condition (**Figure 1F** and **Supplementary Figure 1A**). The live and mildly-fixed row 1 heights were statistically different due to the large number of samples (because the data was rarely normal, the Mann-Whitney U test was used here and hereafter for comparisons unless stated otherwise; $P = 0.0027$), but the percentage difference was small (magnitude ≤ 10%) and highly uncertain (magnitude similar to or smaller than its SD) (percentage difference = −4 ± 13% relative to Di-4) (**Figure 1F**). Small percentage differences are unlikely to be biologically important and we cannot ascribe biological importance to highly uncertain percentage differences (Hughes and Hase, 2010). Row 2 stereociliary heights from the Di-4 live condition were also similar to the mildly-fixed condition (Di-4: 2.00 ± 0.43 μm, mildly-fixed 1.95 ± 0.38 μm, $P = 0.22$) (**Figure 1F**). Average stereociliary heights per hair bundle were not statistically different between conditions (row 1: 5.76 ± 0.60 μm for Di-4 vs. 5.57 ± 0.24 μm for mildly-fixed, $P = 0.21$; row 2: 2.03 ± 0.39 μm for Di-4 vs. 1.95 ± 0.22 μm for mildly-fixed, $P = 0.32$) (**Figure 1G** and **Supplementary Figure 1B**).

To confirm the results obtained with Di-4, we performed a second set of experiments using a chemically unrelated vital fluorescent lipophilic dye, FM 4-64FX (Thermo Fisher Scientific, F34653) and phalloidin-Alexa488 (**Figures 1H,I** and **Supplementary Movie 3**). As with Di-4, FM 4-64FX emits fluorescence when integrated into the membrane, but not when in solution. With another WT C57BL/6J mouse litter (P11 but earlier in development than the first), row 1 stereociliary height was 4.99 ± 0.52 μm for FM 4-64FX and 4.80 ± 0.40 μm for the mildly-fixed condition (**Figure 1J** and **Supplementary Figure 1C**). As with Di-4, while the heights between conditions were statistically different ($P < 0.0001$, percentage difference = 4 ± 13% relative to FM 4-64FX),

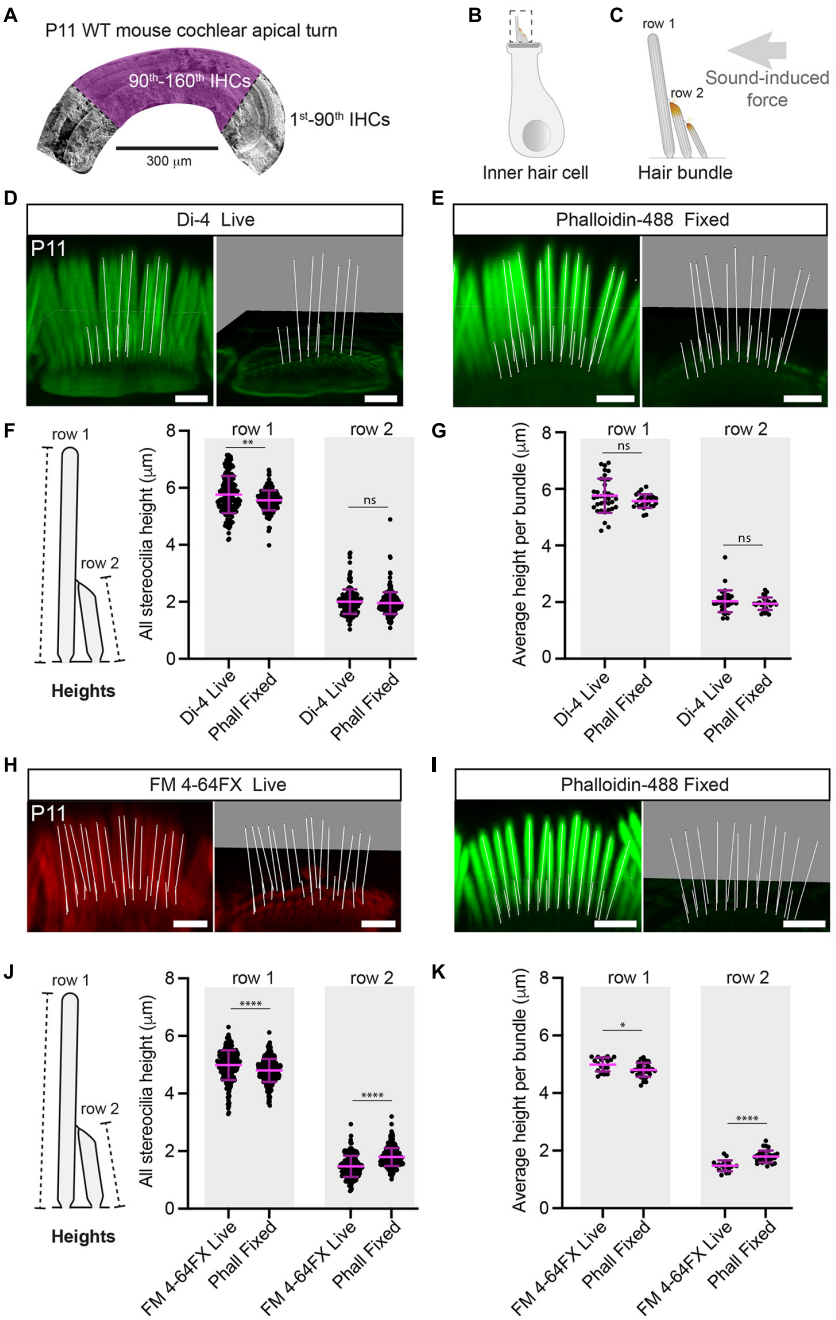


**FIGURE 1 |** Stereociliary heights are the same in live-stained and mildly-fixed conditions. **(A)** Hair-bundle dimensions were measured in a spatially well-defined segment of the P11 WT apical cochlea, highlighted here in purple on an SEM micrograph. The number of inner hair cells (IHCs) are indicated before and within the segment of interest. **(B)** A hair bundle is shown protruding from the apical surface of an inner hair cell. **(C)** A cochlear hair bundle consists of stereocilia arranged in rows of graded height, which are deflected by sound-induced forces, leading to the opening of mechanosensitive ion channels at the tips of rows 2 and 3. Scale bars: 2 μm. Representative 3-D reconstructed images are shown for Di-4 live **(D)** and phalloidin-488 mildly-fixed **(E)** bundles. Lines (white) represent the height measurements for row 1 (tallest) and row 2 stereocilia and are shown with and without the stereociliary volumes. Scale bars: 2 μm. **(F)** Stereociliary heights are shown from P11 WT IHCs live-stained with Di-4 (row 1: 195 stereocilia, row 2: 165 stereocilia, 3 cochleae, 3 animals) or with phalloidin after mild fixation (row 1: 219 stereocilia, row 2: 240 stereocilia, 3 cochleae, 3 animals). Error bars represent the mean ± SD. Di-4 and phalloidin heights differ statistically for row 1 (Mann-Whitney U tests were used here and in figures hereafter, $P = 0.0027$, percentage difference = –4 ± 13% relative to Di-4) and but not for row 2 ($P = 0.22$). These small (magnitude ≤ 10%) and highly uncertain (magnitudes similar to or smaller than their SDs) percentage differences are unlikely to be biologically important, biological importance cannot be ascribed to highly uncertain percentage differences. **(G)** Di-4 and phalloidin average stereociliary heights per bundle do not differ statistically for row 1 and row 2 (36 hair bundles, 3 cochleae, 3 animals for Di-4; 26 hair bundles, 3 cochleae, 3 animals for phalloidin; row 1: $P = 0.21$, row 2: $P = 0.32$). Representative 3-D reconstructed images are shown for FM 4-64FX live **(H)** and phalloidin-488 mildly-fixed **(I)** IHC hair bundles from a slightly less mature P11 WT litter. Lines (white) represent the height measurements and are shown with and without stereociliary volumes. Scale bars: 2 μm. **(J)** Stereociliary heights are shown from slightly less mature P11 WT IHCs live-stained with FM 4-64FX (row 1: 419 stereocilia, row 2: 408 stereocilia, 2 cochleae, 2 animals) or phalloidin after

*(Continued)*

**FIGURE 1 |** mild fixation (row 1: 233 stereocilia, row 2: 224 stereocilia, 2 cochleae, 2 animals). FM 4-64FX and phalloidin heights differ statistically for row 1 and for row 2 ($P < 0.0001$ for both, row 1 percentage difference = –4 ± 13% relative to FM 4-64FX, row 2 percentage difference = 22 ± 33% relative to FM 4-64FX), but the differences are small and/or highly uncertain, implying no biological importance. **(K)** Average stereociliary heights per bundle are shown for row 1 and row 2 using FM 4-64FX (18 hair bundles, 2 cochleae, 2 animals) and phalloidin (33 hair bundles, 2 cochleae, 2 animals). Although row 1 and 2 heights are statistically different between conditions, their percentage differences are small and/or highly uncertain, implying no biological importance (row 1: $P = 0.017$, percentage difference = –4 ± 7% relative to FM 4-64FX; row 2: $P < 0.0001$, percentage difference = 22 ± 19% relative to FM 4-64FX. Horizontal lines indicate comparisons using the Mann-Whitney U test: ns $P > 0.05$, *$P < 0.05$, **$P < 0.01$, ***$P < 0.001$, ****$P < 0.0001$.

the percentage difference was too small and uncertain to be biologically important (**Figure 1J**). Row 2 stereociliary heights in the FM 4-64FX live condition were statistically different to the mildly-fixed condition, but the percentage difference was too uncertain to be ascribed biological importance (FM 4-64FX live: 1.47 ± 0.37 μm, mildly-fixed 1.79 ± 0.31 μm, $P < 0.0001$, percentage difference = 22 ± 33% relative to FM 4-64FX) (**Figure 1J**). Similar results were found when comparing the average stereociliary heights per hair bundle: both row 1 and row 2 stereociliary heights were statistically different between conditions, but the row 1 percentage difference was small, and the row 2 percentage difference was highly uncertain (row 1: 4.99 ± 0.24 μm, row 2: 1.48 ± 0.19 μm for FM 4-64FX live vs. row 1: 4.81 ± 0.24 μm; row 2: 1.80 ± 0.21 μm for mildly-fixed; row 1, percentage difference = −4 ± 7% relative to FM 4-64FX, $P = 0.017$; row 2, percentage difference = 22 ± 19% relative to FM 4-64FX, $P < 0.0001$) (**Figure 1K** and **Supplementary Figure 1D**). In summary, the stereociliary heights measured in live conditions with vital lipophilic dyes were comparable to the heights measured after mild fixation and phalloidin staining, implying that either technique can be used to determine the heights of living stereocilia.

To establish how stereociliary height varies within a given hair bundle, we determined the coefficient of variation for rows 1 and 2 of each hair bundle (**Supplementary Figures 2A,B**). These data indicate low variability within each bundle. However, we noticed outlier heights within each bundle (**Supplementary Figure 1**), which we investigated by determining row 1 stereociliary heights relative to their position within the row using our mildly-fixed phalloidin samples (FM 4-64X litter). Each stereocilium was numbered relative to the central stereocilium (see below for the definition) (**Supplementary Figure 2C**). Stereocilia at position 1 were statistically taller than the central and the last stereocilia, but percentage differences were highly uncertain (position 0–1 percentage difference = −11 ± 14% relative to position 1, position 1-last percentage difference = −19 ± 17% relative to position 1; $P < 0.0001$ for both) (**Supplementary Figures 2D,E**). Although there were outliers within each bundle, these outliers did not occur at systematic positions within a row.

## Live-Stained Apical Inner-Hair-Cell Stereocilia of Slightly Different Ages Have Different Heights but Similar Widths

Less than a 1-day difference in age can cause large differences in stereociliary height, as can be seen in our data above. Although both litters were P11, the litter used for the Di-4 comparison (Litter 1) appeared to be slightly more mature than that the one used for the FM 4-64FX comparison (Litter 2). In the mildly-fixed samples from the two litters, there is a large difference in the height of row 1 stereocilia (Litter 1 (Di4): 5.56 ± 0.35 μm, Litter 2 (FM 4-64FX): 4.80 ± 0.40 μm, $P < 0.0001$, percentage difference = −14 ± 10% relative to Litter 1). A similar large difference in height is seen when comparing the two litters using the live-stained conditions (Litter 1 (Di4): 5.77 ± 0.65 μm, Litter 2 (FM 4-64FX): 4.99 ± 0.52 μm, $P < 0.0001$, percentage difference = −13 ± 15% relative to Litter 1) (**Supplementary Figure 3**). Although the heights differ greatly between litters, the percentage differences are highly uncertain. For the mildly-fixed averages per bundle, the height difference between litters is large and the percentage difference has low uncertainty (Litter 1 (Di4): 4.81 ± 0.24 μm, Litter 2 (FM 4-64FX): 5.56 ± 0.24 μm, $P < 0.0001$, percentage difference = −14 ± 6% relative to Litter 1). However, for the live-stained averages per bundle, the heights are statistically different but the percentage difference is highly uncertain (Litter 1 (Di4): 4.99 ± 0.24 μm, Litter 2 (FM 4-64FX): 5.76 ± 0.60 μm, $P < 0.0001$, percentage difference = −13 ± 11% relative to Litter 1).

We next determined the stereociliary widths of live-stained IHCs in the two litters of slightly different age. In each 3-D reconstructed hair bundle, we created a virtual section through the bundle below the beveled portion of row 2 (**Figure 2A**). We determined a stereocilium's width by measuring the shortest line passing through a stereocilium's axis with endpoints on its perimeter's midsection (see section "Materials and Methods," **Supplementary Figure 4**, **and Supplementary Movies 4, 5**). When comparing the two litters using the live-staining conditions, we found no statistical difference between the widths of row 1 stereocilia (Di4: 0.45 ± 0.04 μm, FM 4-64FX: 0.45 ± 0.04 μm, $P = 0.23$) or between those of row 2 stereocilia (Di4: 0.45 ± 0.04 μm, FM 4-64FX: 0.47 ± 0.05 μm, $P = 0.054$) (**Figure 2B** and **Supplementary Figure 5A**). Similarly, we found no statistical difference between the average stereociliary widths per bundle of row 1 (Di4: 0.45 ± 0.03 μm, FM 4-64FX: 0.45 ± 0.03 μm, $P = 0.52$) or row 2 between conditions (Di4: 0.46 ± 0.02 μm, FM 4-64FX: 0.47 ± 0.03 μm, $P = 0.077$) (**Figure 2C** and **Supplementary Figure 5B**). Although the heights changed greatly within 1 day, the widths did not.

## Row 1 and 2 Stereociliary Dimensions Are Drastically Reduced After Scanning-Electron-Microscopy-Sample Preparation

We next compared the live dimensions to dimensions obtained with electron microscopy. We chose conventional SEM (over TEM or Focused Ion Beam-SEM) because it allowed us to take several different measurements from each hair bundle and to

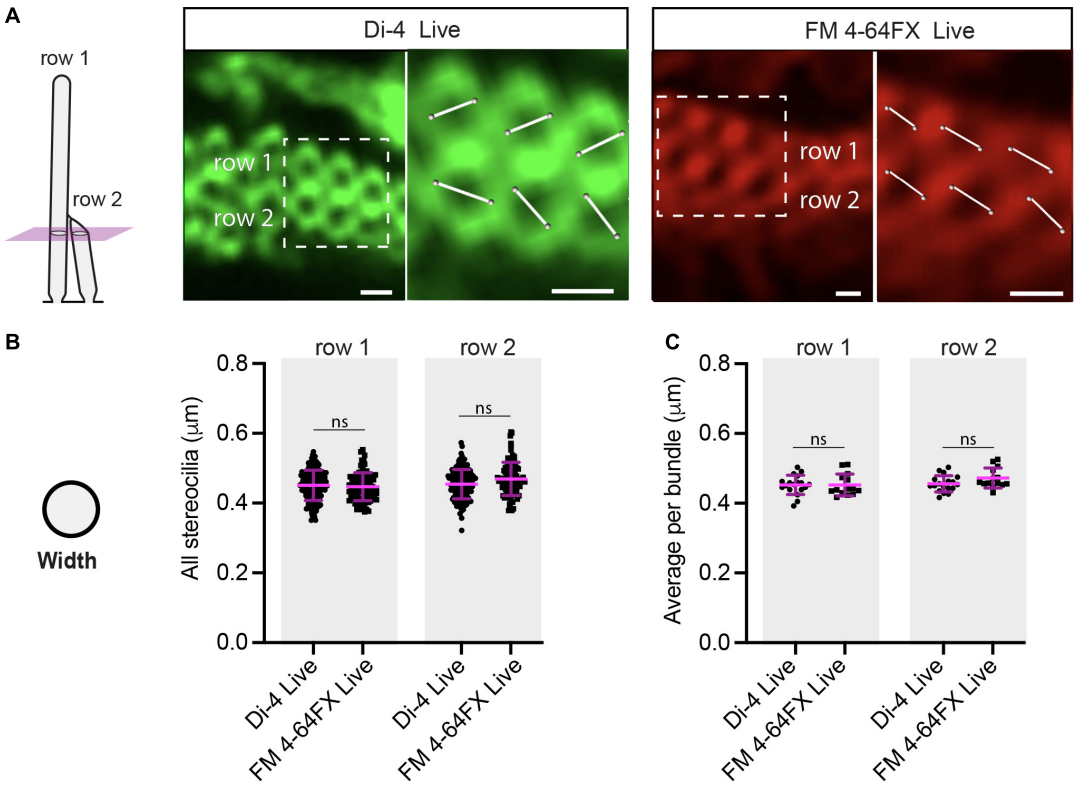


**FIGURE 2 |** Stereociliary widths are the same in Di-4 and FM 4-64FX live-stained bundles of slightly different ages. **(A)** Virtual sections through 3-D reconstructed live-stained hair bundles below the row-2 tips show that stereociliary membranes form rings. Because rings look like distorted ovals, we determined a stereocilium's width in 3-D by measuring the length of the shortest line passing through the ring's center, with endpoints placed on the perimeter's midsection. Scale bars: 0.5 μm. **(B)** No statistical difference was found for row 1 or row 2 stereociliary widths between Di-4 (row 1: 172 stereocilia, row 2: 149 stereocilia, 3 cochleae, 3 animals) and FM 4-64FX conditions (row 1: 101 stereocilia, row 2: 90 stereocilia, 2 cochleae, 2 animals) (row 1: $P = 0.23$, row 2: $P = 0.054$). **(C)** No statistical difference was found for row 1 or row 2 average stereociliary widths per bundle between Di-4 (18 hair bundles, 3 cochleae, 3 animals) and FM 4-64FX conditions (14 hair bundles, 2 cochleae, 2 animals) (row 1: $P = 0.52$, row 2: $P = 0.077$). Horizontal lines indicate comparisons using the Mann-Whitney U test: ns $P > 0.05$.

repeat those measurements across many hair bundles. However, conventional SEM involves a harsh sample-preparation process: the tissue is fixed with paraformaldehyde and glutaraldehyde and subsequently subjected to dehydration. Understanding the extent to which stereociliary dimensions are affected by the SEM preparation process is of paramount importance, as it has been and still is widely used to determine stereociliary dimensions, which inform models of hair-bundle mechanics (Zetes, 1995; Furness et al., 1997; Smith and Chadwick, 2011; Ó Maoiléidigh and Hudspeth, 2013; Nam et al., 2015). Because stereocilia in SEM images are nearly always at an angle relative to the image plane, the absolute heights of stereocilia cannot be measured directly from individual 2-D images (**Figure 3A**). Therefore, to calculate the heights of stereocilia, we used paired images of the same bundle taken at two different angles (images were related by a eucentric rotation centered at the base of row 2, in the middle of the hair bundle), and used geometry to determine the heights from vectors in 3-D space (see section "Materials and Methods"). For stereocilia with visible apical-surface insertion sites, we used the full height measurements of the stereocilia from each image (**Supplementary Figure 6A**). However, for row 1 stereocilia with obscured insertion sites, we selected those that were paired with a row 2 stereocilium with a visible insertion site (**Supplementary Figure 6B**). We then measured the angles and heights of the visible portion of each row 1 stereocilium (from the tip of the row 2 stereocilium to the tip of the row 1 stereocilium) in both images. By using the angles and heights of the row 2 stereocilium and additionally calculating the angle of the apical surface of the hair cell relative to one of the image planes, we could determine the intersection point of the row 1 stereocilium in the apical surface and calculate the full height of the stereocilium. SEM height measurements are accurate only if a stereocilium is straight and close to vertical within an SEM image (Materials and Methods). Because stereocilia at the edge of a row were rarely vertical in SEM images, we measured centrally located stereocilia.

For comparison with the Di-4 live-staining experiment, samples were prepared for SEM from littermates. When comparing the heights obtained from Di-4 live-staining to those calculated from SEM, we found that the stereociliary heights from SEM-samples were greatly reduced both for row 1 and for row 2 (SEM: row 1: 3.46 ± 0.78 μm, percentage difference = −40 ± 18% relative to Di-4; row 2: 1.32 ± 0.23 μm, percentage difference = −34 ± 25% relative to Di-4, $P < 0.0001$ for both) (**Figure 3B**). A similar large reduction was found

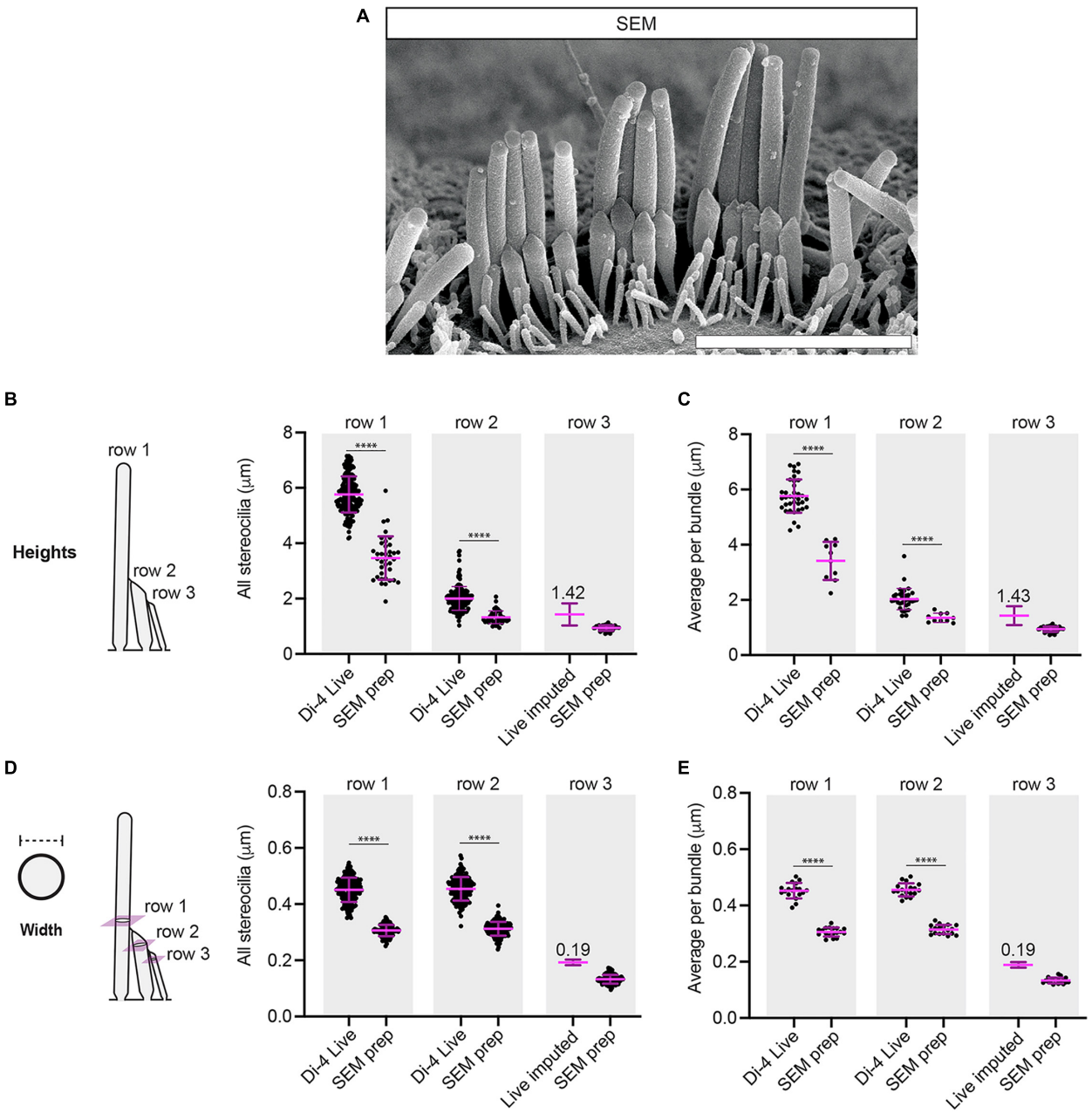


**FIGURE 3 |** SEM preparation greatly reduces the heights and the widths of IHC stereocilia. **(A)** A representative image is shown of a P11 IHC hair bundle used for stereociliary height and width measurements. Scale bar: 3 μm. **(B)** SEM preparation greatly reduces row 1 and row 2 stereociliary heights compared to Di-4 live conditions (SEM: row 1: 37 stereocilia, row 2: 42 stereocilia, row 3: 36 stereocilia, 2 cochleae, 2 animals). **(C)** SEM preparation greatly reduces row 1 and row 2 average stereociliary heights per bundle (SEM: 10 hair bundles, 2 cochleae, 2 animals). **(D)** SEM preparation greatly reduces row 1 and row 2 stereociliary widths compared to Di-4 live conditions (SEM: row 1: 119 stereocilia, row 2: 136 stereocilia, row 3: 116 stereocilia, 2 cochleae, 2 animals). **(E)** SEM preparation greatly reduces row 1 and row 2 average stereociliary widths per bundle (SEM: 18 hair bundles, 2 cochleae, 2 animals). In all panels, row 3 live heights and widths were imputed from the measured SEM row 3 means and SDs, using row 2 means and SDs to determine the scaling factors between SEM and live measurements. Horizontal lines indicate comparisons using the Mann–Whitney *U*-test: $^{****}P < 0.0001$.

when comparing the average height per bundle for both row 1 and row 2 (SEM: row 1: 3.42 ± 0.69 μm, percentage difference = −41 ± 16% relative to Di-4; row 2: 1.35 ± 0.16 μm, percentage difference = −34 ± 22% relative to Di-4, $P < 0.0001$ for both) (**Figure 3C**). While neither the live-lipophilic dye nor the phalloidin were clear enough to obtain row 3 stereociliary measurements, SEM allowed us to determine row 3 heights (0.94 ± 0.10 μm for individual stereocilia; 0.95 ± 0.07 μm for the hair-bundle average). Using these measurements and SEM-shrinkage factors obtained from row 2 Di-4 and SEM

heights, we imputed live row 3 heights (1.42 ± 0.42 μm for all stereocilia; 1.43 ± 0.34 μm for the hair-bundle average) (**Figures 3B,C**).

We also compared width measurements from the Di-4 live staining and the SEM images. Widths for SEM were measured perpendicular to the long axes of fully visible stereocilia and differ negligibly between paired images at different angles. For row 1, widths were taken at a height just above the row 2 tips. For row 2, widths were measured at the widest point across each stereocilium below its tip. We found that row 1 stereociliary widths were greatly reduced after SEM processing compared to Di-4 live-staining, as were row 2 stereociliary widths (SEM: row 1: 0.31 ± 0.02 μm, percentage difference = −32 ± 11% relative to Di-4; row 2: 0.31 ± 0.02 μm, percentage difference = −31 ± 11% relative to Di-4, $P < 0.0001$ for both) (**Figure 3D**). Similar reductions were found for average widths per hair bundle (SEM: row 1: 0.31 ± 0.02 μm, percentage difference = −32 ± 7% relative to Di-4; row 2: 0.31 ± 0.02 μm, percentage difference = −31 ± 7% relative to Di-4, $P < 0.0001$ for both) (**Figure 3E**). As for the height, we were able to determine row 3 widths from SEM (0.13 ± 0.02 μm for all stereocilia; 0.13 ± 0.01 μm for the hair-bundle average) and impute the live widths using SEM-shrinkage factors obtained from row 2 Di-4 and SEM widths (0.19 ± 0.03 μm for all stereocilia; 0.19 ± 0.02 μm for the hair-bundle average) (**Figures 3D,E**).

Taken together, these data show that SEM-preparation greatly reduces the dimensions of stereocilia in comparison to live-stained preparations and, by extension, to mildly-fixed preparations. Furthermore, our multi-condition analysis allows us to impute row 3 stereociliary dimensions that cannot be resolved in live or mildly-fixed phalloidin conditions.

## Separations Between Stereociliary Insertions in the Apical Surface Are Drastically Reduced After Scanning-Electron-Microscopy-Sample Preparation

Beyond the dimensions of individual stereocilia, we wanted to know whether SEM preparation affects the positions of stereocilia relative to each other. To assess this, we focused on the stereociliary insertion points in the apical surface of the hair cells. For live Di-4 stained hair bundles and the corresponding phalloidin-stained samples, we generated virtual sections above the cuticular plate (**Figure 4A** and **Supplementary Movie 6**). To measure the separations between the insertion points by SEM, we developed a procedure to peel away the hair bundles of SEM-samples after sample mounting, using tape, which reveals the insertion points (see section "Materials and Methods") (**Figure 4B**). This method allowed us to image and measure stereocilia in an SEM sample and then image and measure insertions points in the same sample.

First, we measured and compared insertion separations within the same row. Compared to Di-4 staining, the SEM preparation showed reduced separations within row 1 and within row 2 (separation 1-1: 0.60 ± 0.07 μm for Di-4, 0.38 ± 0.05 μm for SEM, percentage difference = −37 ± 14% relative to Di-4; separation 2-2: 0.57 ± 0.07 μm for Di-4, 0.35 ± 0.04 μm for SEM, percentage difference = −39 ± 16% relative to Di-4, $P < 0.0001$ for both) (**Figure 4C**). This reduction was seen also when comparing hair-bundle averages within row 1 and row 2 (separation 1-1: 0.61 ± 0.03 μm for Di-4, 0.38 ± 0.02 μm for SEM, percentage difference = −37 ± 7% relative to Di-4; separation 2-2: 0.57 ± 0.04 μm for Di-4, 0.35 ± 0.02 μm for SEM, percentage difference = −40 ± 8% relative to Di-4, $P < 0.0001$ for both) (**Figure 4D**). We determined the insertion separations within row 3 using SEM (0.25 ± 0.06 μm for all stereocilia; 0.25 ± 0.03 μm for the hair-bundle average) and using the measured Di-4 and SEM row 2-2 separations, we imputed row 3-3 Di-4 insertion separations (0.41 ± 0.12 μm for all stereocilia; 0.42 ± 0.06 μm for the hair-bundle average) (**Figures 4C,D**).

Second, we compared insertion separations between stereocilia of different rows. We found that the row 1 to row 2 insertion separation was greatly reduced by SEM preparation compared to the Di-4 condition (separation 1-2: 0.77 ± 0.12 μm for Di-4, 0.51 ± 0.06 μm for SEM, percentage difference = −34 ± 18% relative to Di-4, $P < 0.0001$) (**Figure 4E**). Again, this observation was seen in the hair-bundle averages (separation 1-2: 0.77 ± 0.10 μm for Di-4, 0.50 ± 0.05 μm for SEM, percentage difference = −34 ± 15% relative to Di-4, $P < 0.0001$) (**Figure 4F**). We could determine the row 2 to row 3 insertion separation by SEM (0.28 ± 0.05 μm for all stereocilia; 0.27 ± 0.04 μm for the hair-bundle average) and impute its Di-4 value (0.42 ± 0.11 μm for all stereocilia; 0.41 ± 0.09 μm for the hair-bundle average) from the measured Di-4 and SEM row 1-2 insertion separations (**Figures 4E,F**).

Third, we compared the insertion separations obtained from live staining to those from mildly-fixed phalloidin samples. All insertion separation measurements were statistically indistinguishable between the two conditions, with the exception of the row 1-2 separation, but this percentage difference was small (all stereocilia: separation 1-1: $P = 0.72$, separation 2-2: $P = 0.77$, separation 1-2: $P < 0.0001$, see **Table 1** for measurements, separation 1-2 for Di-4: 0.77 ± 0.12 μm, separation 1-2 for mildly-fixed: 0.80 ± 0.08 μm, separation 1-2 percentage difference = 4 ± 19% relative to Di-4; per bundle: separation 1-1: $P = 0.50$, separation 2-2: $P = 0.90$, separation 1-2: $P = 0.087$, see **Table 2** for measurements) (**Figures 4C–F**).

In summary, we found that SEM preparation drastically reduces not only stereociliary heights and widths, but also the separation between stereociliary insertion points. Furthermore, we could use our SEM preparation to determine insertion separations that were not clear in live conditions, and impute the corresponding live-cell values.

## Apical Inner-Hair-Cell P11 Stereocilia Are Arranged in Two Wings Separated by a Notch

Our peeled hair-bundle preparation gave us the opportunity to compare the insertion-point positions from many IHCs from the same cochlear location and look for patterns. We noticed that row 1 and 2 stereocilia were always arranged in two wings

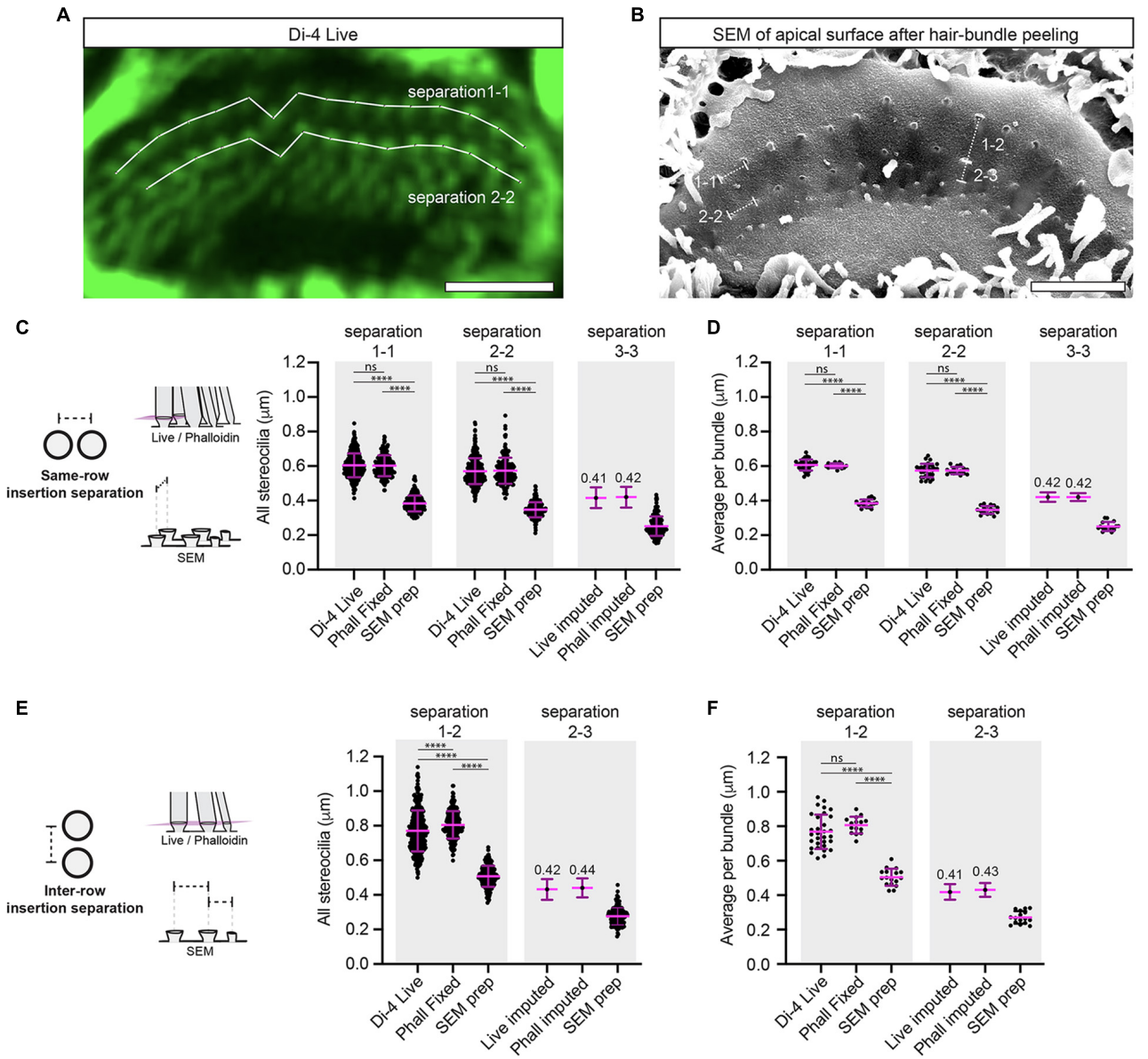


**FIGURE 4 |** SEM preparation greatly reduces the separations between stereociliary insertion points. **(A)** A virtual section is shown through a 3-D reconstructed Di-4 live-stained hair bundle. The optical sectioning plane is parallel to and just above the apical surface and reveals the stereociliary insertion points. Stereociliary insertion separations were measured between the centers of the Di-4 spots. Scale bar: 3 μm. **(B)** A representative SEM image is shown of a hair cell's apical surface with the hair-bundle peeled away using tape. Scale bar: 3 μm. **(C)** The insertion separation between stereocilia within the same row is greatly reduced in SEM compared to Di-4 and phalloidin-stained samples (separation 1-1: SEM: 205 measurements, Di-4: 360 measurements, phalloidin-stained: 191 measurements; separation 2-2: SEM: 180 measurements, Di-4: 348 measurements, phalloidin-stained: 183 measurements; separation 3-3: SEM: 175 measurements; 3 cochleae, 3 animals). Di-4 and phalloidin insertion separations are not statistically different (separation 1-1: $P = 0.72$, separation 2-2: $P = 0.77$). Row 3-3 separations for the Di-4 live and phalloidin-stained condition were imputed from the measured SEM row 3-3 mean and SD using row 2-2 means and SDs to determine scaling factors. **(D)** The average insertion separation per bundle between stereocilia of the same row is greatly reduced in SEM compared to Di-4 and phalloidin-stained samples (separation 1-1: SEM: 17 hair bundles, Di-4: 31 hair bundles, phalloidin-stained: 15 hair bundles; separation 2-2: SEM: 17 hair bundles, Di-4: 31 hair bundles, phalloidin-stained: 15 hair bundles; separation 3-3: 16 hair bundles, 3 cochleae, 3 animals). Di-4 and phalloidin average insertion separations per bundle are not statistically different (separation 1-1: $P = 0.50$, separation 1-1: $P = 0.90$). The row 3-3 insertion separations for the Di-4 live and the phalloidin-stained conditions were imputed from the measured SEM row 3-3 mean and SD using row 2-2 means and SDs to determine scaling factors. **(E)** The insertion separation between stereocilia of different rows is greatly reduced in SEM compared to the live and phalloidin-stained samples (separation 1-2: SEM: 189 measurements, Di-4: 369 measurements, phalloidin-stained: 196 measurements; separation 2-3: 154 measurements, 3 cochleae, 3 animals). Di-4 and phalloidin insertion separations between rows 1 and 2 are statistically different (separation 1-2: $P < 0.0001$). **(F)** The average insertion separation between stereocilia of different rows per bundle is greatly reduced in SEM compared to the live and phalloidin-stained samples (separation 1-2: SEM: 17 hair bundles, Di-4: 31 hair bundles, phalloidin-stained: 15 hair bundles; separation 2-3: SEM: 17 hair bundles; 3 cochleae, 3 animals). Di-4 and phalloidin average insertion separations between rows 1 and 2 per bundle are not statistically different (separation 1-2: $P = 0.087$). Horizontal lines indicate comparisons using the Mann-Whitney U test: ns $P > 0.05$, ****$P < 0.0001$.

**TABLE 1 |** Heights, widths, and insertion separations under Di-4 live, mildly-fixed phalloidin, and SEM-prepared conditions determined from all stereocilia.

| | Row | Live (Di-4) | Light fixation (Phalloidin) | | SEM | |
|---|---|---|---|---|---|---|
| | | Mean ± SD | Mean ± SD | % of Live | Mean ± SD | % of Live |
| Height | 1 | 5.76 ± 0.65 μm (*n* = 195) | 5.56 ± 0.35 μm (*n* = 219) | 96 ± 13 | 3.46 ± 0.78 μm (*n* = 37) | 60 ± 15 |
| | 2 | 2.00 ± 0.43 μm (*n* = 165) | 1.95 ± 0.38 μm (*n* = 240) | 98 ± 28 | 1.32 ± 0.23 μm (*n* = 42) | 66 ± 18 |
| | 3 | 1.42 ± 0.42 μm (imputed from row 2) | 1.39 ± 0.39 μm (imputed from row 2) | ND | 0.94 ± 0.10 μm (*n* = 36) | ND |
| Width | 1 | 0.45 ± 0.04 μm (*n* = 172) | 0.37 ± 0.05 μm (*n* = 210) | 82 ± 13 | 0.31 ± 0.02 μm (*n* = 119) | 68 ± 8 |
| | 2 | 0.45 ± 0.04 μm (*n* = 149) | 0.36 ± 0.04 μm (*n* = 196) | 80 ± 12 | 0.31 ± 0.02 μm (*n* = 136) | 69 ± 8 |
| | 3 | 0.19 ± 0.03 μm (imputed from row 2) | 0.15 ± 0.03 μm (imputed from row 2) | ND | 0.13 ± 0.02 μm (*n* = 116) | ND |
| Same row insertion separation | 1-1 | 0.60 ± 0.07 μm (*n* = 360) | 0.60 ± 0.06 μm (*n* = 191) | 100 ± 15 | 0.38 ± 0.05 μm (*n* = 205) | 63 ± 11 |
| | 2-2 | 0.57 ± 0.07 μm (*n* = 348) | 0.57 ± 0.08 μm (*n* = 183) | 100 ± 19 | 0.35 ± 0.04 μm (*n* = 180) | 61 ± 11 |
| | 3-3 | 0.41 ± 0.12 μm (imputed from separation 2-2) | 0.42 ± 0.12 μm (imputed from separation 2-2) | ND | 0.25 ± 0.06 μm (*n* = 175) | ND |
| Inter row insertion separation | 1-2 | 0.77 ± 0.12 μm (*n* = 369) | 0.80 ± 0.08 μm (*n* = 196) | 104 ± 19 | 0.51 ± 0.06 μm (*n* = 189) | 66 ± 13 |
| | 2-3 | 0.42 ± 0.11 μm (imputed from separation 1-2) | 0.44 ± 0.10 μm (imputed from separation 1-2) | ND | 0.28 ± 0.05 μm (*n* = 154) | ND |

*The number of stereocilia is indicated. ND, not determined.*

**TABLE 2 |** Heights, widths, and insertion separations under Di-4 live, mildly-fixed phalloidin, and SEM-prepared conditions determined from hair-bundle averages.

| | Row | Live (Di-4) | Light fixation (Phalloidin) | | SEM | |
|---|---|---|---|---|---|---|
| | | Mean ± SD | Mean ± SD | % of Live | Mean ± SD | % of Live |
| Height | 1 | 5.76 ± 0.60 μm (*n* = 36) | 5.57 ± 0.24 μm (*n* = 26) | 97 ± 11 | 3.42 ± 0.69 μm (*n* = 10) | 59 ± 13 |
| | 2 | 2.03 ± 0.39 μm (*n* = 36) | 1.95 ± 0.22 μm (*n* = 26) | 96 ± 21 | 1.35 ± 0.16 μm (*n* = 10) | 66 ± 15 |
| | 3 | 1.43 ± 0.34 μm (imputed from row 2) | 1.37 ± 0.25 μm (imputed from row 2) | ND | 0.95 ± 0.07 μm (*n* = 10) | ND |
| Width | 1 | 0.45 ± 0.03 μm (*n* = 18) | 0.37 ± 0.02 μm (*n* = 18) | 82 ± 7 | 0.31 ± 0.02 μm (*n* = 18) | 68 ± 5 |
| | 2 | 0.46 ± 0.02 μm (*n* = 18) | 0.37 ± 0.03 μm (*n* = 18) | 80 ± 8 | 0.31 ± 0.02 μm (*n* = 18) | 69 ± 5 |
| | 3 | 0.19 ± 0.02 μm (imputed from row 2) | 0.16 ± 0.02 μm (imputed from row 2) | ND | 0.13 ± 0.010 μm (*n* = 18) | ND |
| Same row insertion separation | 1-1 | 0.61 ± 0.03 μm (*n* = 31) | 0.60 ± 0.01 μm (*n* = 15) | 99 ± 6 | 0.38 ± 0.02 μm (*n* = 17) | 63 ± 5 |
| | 2-2 | 0.57 ± 0.04 μm (*n* = 31) | 0.57 ± 0.02 μm (*n* = 15) | 100 ± 8 | 0.35 ± 0.02 μm (*n* = 17) | 60 ± 6 |
| | 3-3 | 0.42 ± 0.06 μm (imputed from separation 2-2) | 0.42 ± 0.05 μm (imputed from separation 2-2) | ND | 0.25 ± 0.03 μm (*n* = 16) | ND |
| Inter row insertion separation | 1-2 | 0.77 ± 0.10 μm (*n* = 31) | 0.81 ± 0.05 μm (*n* = 15) | 105 ± 15 | 0.50 ± 0.05 μm (*n* = 17) | 66 ± 11 |
| | 2-3 | 0.41 ± 0.09 μm (imputed from separation 1-2) | 0.43 ± 0.08 μm (imputed from separation 1-2) | ND | 0.27 ± 0.04 μm (*n* = 16) | ND |
| Number of stereocilia | 1 | ND | ND | ND | 16.09 ± 1.51 (*n* = 11) | ND |
| | 2 | ND | ND | ND | 16.00 ± 2.36 (*n* = 10) | ND |
| | 3 | ND | ND | ND | 19.40 ± 0.89 (*n* = 5) | ND |
| Wing angle | 1 | ND | 131°; 95% CI [127°, 135°] (*n* = 13) | ND | ND | ND |
| | 2 | ND | 133°; 95% CI [128°, 139°] (*n* = 13) | ND | ND | ND |

*The number of hair bundles is indicated. ND: not determined.*

separated by a central column of stereocilia that was shifted toward row 3, forming an indentation or notch in the hair-bundle (**Figure 5A**). The notch was most commonly at the center of the bundle, but on rare occasions could be found at an eccentric position (3/24 cases), and in a single case the notch was formed by two columns of shifted stereocilia (data not shown). The notch is likely related to the former insertion position of the kinocilium in the apical surface, the fonticulus (**Figure 5A**;

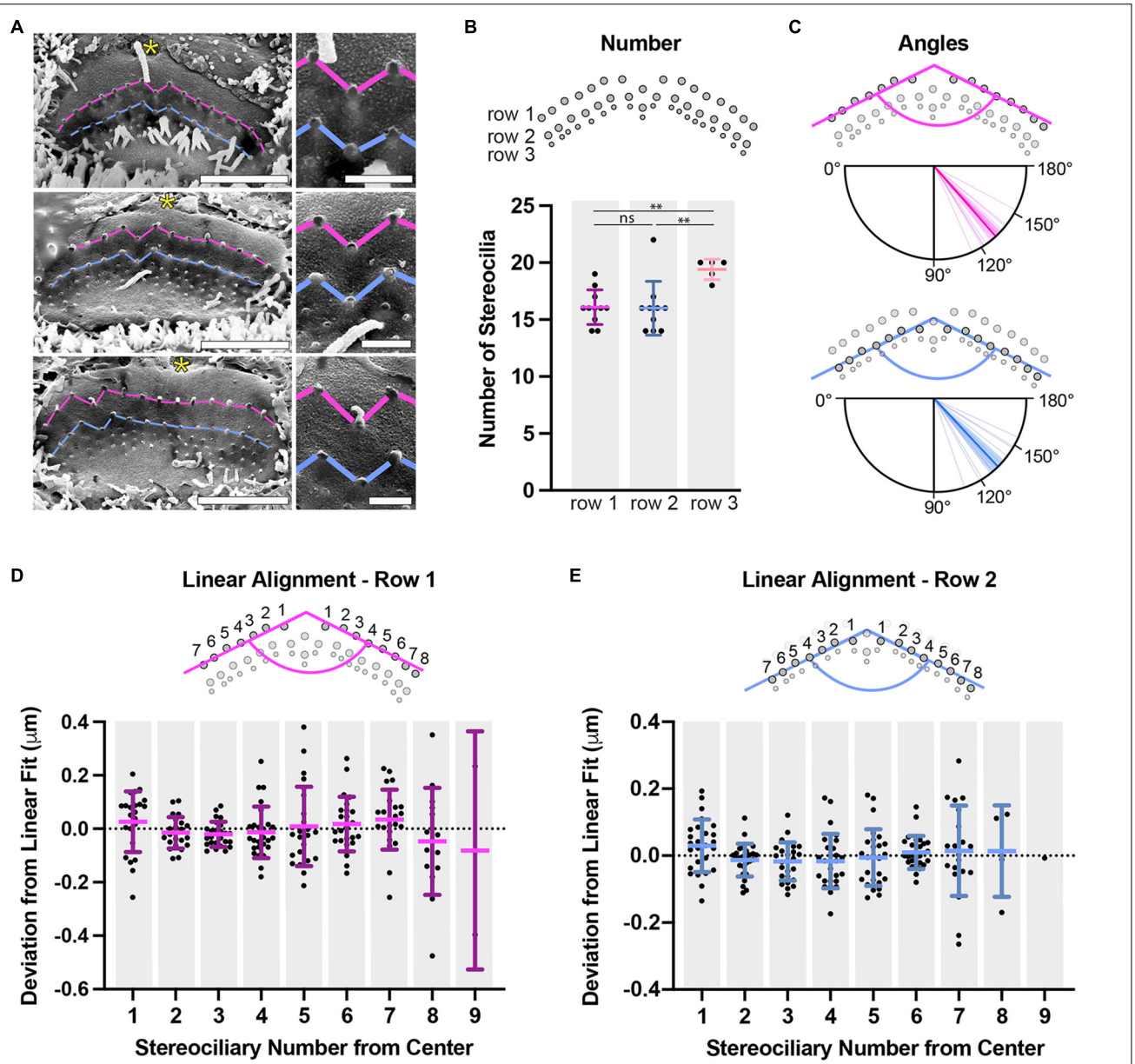


**FIGURE 5 |** Apical IHC P11 stereocilia are arranged in two wings separated by a notch. **(A)** SEM images are shown of peeled IHC apical surfaces. The insertion points are connected by pink lines for row 1 and blue lines for row 2. IHC hair bundles form two wings separated by a central column that is shifted toward row 3, making a notch in the hair bundle. The fonticulus, the former kinocilium insertion point in the apical cell surface, is indicated by a yellow asterisk. Right panels show the notch at higher magnification. Scale bars: full view 2 μm, higher magnification 0.5 μm. **(B)** Stereociliary number per hair cell is shown, determined for each row from peeled hair-bundle SEM pictures (row 1 and 2: 11 hair bundles, row 3: 5 hair bundles). The number of row 1 stereocilia is the same as the number of row 2 stereocilia ($P = 0.59$), but the number of row 3 stereocilia is greater than that of row 1 or 2 (row 3 to 1: $P = 0.0011$, row 3 to 2: $P = 0.010$). **(C)** Hair-bundle angles were measured by identifying all row 1 or row 2 insertion point coordinates within a bundle, fitting each wing to a straight line, and using the line slopes ($n = 13$ hair bundles). Individual measurements are represented by thin lines, means are represented by thick lines, and 95% confidence intervals are represented by transparent colored sectors. **(D)** To determine if row 1 insertion points have additional structure beyond following a straight line, each stereocilium's deviation from a line fit to its wing was determined. Stereocilia were labeled by a number (1–9) increasing from the central column to the edge of each wing. Note that the central column was not included. None of the average deviations for any stereociliary position were statistically different from zero (One sample *T*-test at the 95% confidence level against a mean of 0, Benjamini-Hochberg analysis), implying that there is no additional structure common to all bundles ($n = 13$). **(E)** The approach described in panel D was also applied to row 2 stereocilia (1–8) ($n = 13$). Horizontal lines indicate comparisons using the Mann-Whitney U test: ns $P > 0.05$, $^{**}P < 0.01$.

Kikkawa et al., 2008). The average number of stereocilia per row was similar between row 1 and row 2 (row 1: 16.1 ± 1.5; row 2: 16.0 ± 2.4; $P = 0.59$), but was higher for row 3 (19.4 ± 0.9; $P < 0.01$ for both comparisons) indicating that at this age, there are instances of multiple row 3 stereocilia connecting to a single row 2 stereocilium (**Figures 3A**, **5B**).

To understand the layout of the insertion points further, we quantified and analyzed insertion points from mildly-fixed phalloidin images rather than the shrunken SEM preparations. The insertion-point coordinates of each hair-bundle wing were extracted and plotted. We found that the insertion positions within a wing are well-described by a straight line (row 1, $R^2$ = 0.85 ± 0.12; row 2, $R^2$ = 0.85 ± 0.15). Using the slope of each wing (determined from their linear fits), we calculated the hair-bundle angle for each row. There was a preferred angle for each row ($P < 0.0001$, Rayleigh z test). There was no statistical difference between the mean angle of 131° (95% CI [127°, 135°]) for row 1 and the mean angle of 133° (95% CI [128°, 139°]) for row 2 ($P = 0.69$, circular Mann Whitney U test) (**Figure 5C**). Stereocilia from vestibular end-organs and OHCs have been described as being positioned on a hexagonal or pseudohexagonal grid (Engström and Engström, 1978; Pickles et al., 1984; Comis et al., 1985; Bagger-Sjöbäck and Takumida, 1988; Roth and Bruns, 1992; Tsuprun and Santi, 1998, 2002; Rowe and Peterson, 2004; Beurg et al., 2006; Jacobo and Hudspeth, 2014). We tested whether P11 apical IHC stereocilia were positioned on a hexagonal grid, which implies an angle of 120° between their wings. Both row 1 and row 2 mean angles were statistically larger than 120° refuting the hypothesis (120° was outside the von Mises 95% confidence intervals). Furthermore, the hair-bundle shape could not be described as flat, as the angle was statistically smaller than 180° (180° was outside the von Mises 95% confidence intervals). Finally, we asked whether the stereociliary positions within a wing had additional structure by calculating the deviation of each insertion point from the linear fit line (**Figures 5D,E**). Stereocilia were numbered from 1 to 9 according to their position relative to the central column. None of the means for any of the insertion-position deviations in either row were statistically different from zero (one sample *T*-test against mean 0, Benjamini-Hochberg analysis), implying the absence of additional systematic structure along the hair-bundle wings. The systematic deviation from an angle of 120° and the systematically different separations within rows and between rows imply that IHC stereociliary insertion points lie on a pseudohexagonal grid and that this divergence from a hexagonal grid is not caused by biological variability.

## The Dimensions and Separations of Live Stereocilia

When comparing all of our datasets, we find remarkable consistency in the changes (or lack thereof) that different preparation methods incur (**Figure 6A**). We find that live-stained and mildly-fixed samples have similar heights for both row 1 and row 2, while SEM preparation reduces the height of row 1 (SEM/Live% = 60 ± 15%) and row 2 (SEM/Live% = 66 ± 18%). Similarly, SEM widths are consistently reduced compared with live values (SEM/Live% = 68 ± 8% for row 1, SEM/Live% = 69 ± 8% for row 2). As expected, the stereociliary actin-core width (imaged with phalloidin-488) was smaller than the stereociliary membrane width (row 1 width Phall/Live% = 82 ± 13%, row 2 width Phall/Live% = 80 ± 12%) (**Supplementary Figure 7**), but the percentage difference was highly uncertain. Furthermore, insertion separations are reduced in SEM samples compared to live and mildly-fixed samples for row 1-1 separations (SEM/Live% = 63 ± 11%), row 2-2 separations (SEM/Live% = 61 ± 11%), and row 1-2 separations (SEM/Live% = 66 ± 13%). Calculating the shrinkage factors between different preparations enabled us to determine the live heights, widths, and separations for row 3 stereocilia. The individual measurements (**Table 1**) and averages per bundle (**Table 2**) define the morphology of a living hair bundle with the greatest accuracy and precision to date. Combining the individual measurements, we generated a 3-D representation of an apical IHC hair bundle (**Figure 6B**), which mirrors the 3-D reconstructions from live samples (**Figures 1D,H**), further validating the consistency of the measurements.

## Live-Cell Measurements Determine a Hair Bundle's Mechanical Properties

We took advantage of our multidimensional datasets to determine some of the mechanical properties of the living hair bundle and to test whether these properties are affected by SEM shrinkage. The response of a hair bundle to stimulation is controlled by many factors, including its stiffness, the fluid coupling between stereocilia, and the relationship between channel gating and stereociliary deflection (Corey and Hudspeth, 1983; Ó Maoiléidigh and Hudspeth, 2013; Fettiplace, 2017). We have determined these three factors for an apical P11 IHC.

The stiffness of an IHC bundle is dictated by the stiffnesses of its stereocilia – which are in turn determined by their heights and pivot stiffnesses – and the links between stereocilia. However, we have limited information about these components. Live stereociliary height measurements allow us to determine the extent to which stereociliary stiffness differs between rows owing to differences in stereociliary heights. Stereocilia pivot at their insertion point into the hair-cell's apical surface (Howard and Ashmore, 1986; Crawford et al., 1989; Karavitaki and Corey, 2010; Wang et al., 2021; **Figure 7A**). A stereocilium's deflection stiffness $K_d$ relative to its pivot stiffness $K_p$ is given by

$$\frac{K_d}{K_p} = \frac{1}{H^2}, \tag{1}$$

in which H is the height of the stereocilium. Whether there are differences in pivot stiffness between rows is not known, but the deflection stiffness relative to the pivot stiffness quantifies the extent to which stereociliary height affects the deflection stiffness. The deflection stiffness of a stereocilium increases rapidly when its height decreases (**Figure 7B**). Due to their live-cell height differences, row 1 stiffness is smaller (11 ± 5% of row 2) than that of row 2, which is smaller (60 ± 27% of row 3) than that of row 3. Owing to SEM-sample shrinkage, SEM stiffnesses are larger (219 ± 112 to 308 ± 165%) than the corresponding live-cell stiffnesses.

Pairs of neighboring stereocilia are strongly coupled by the fluid between them (Zetes, 1995; Zetes and Steele, 1997; Baumgart, 2011; Kozlov et al., 2011). Live-cell width measurements allow us to determine the extent to which this

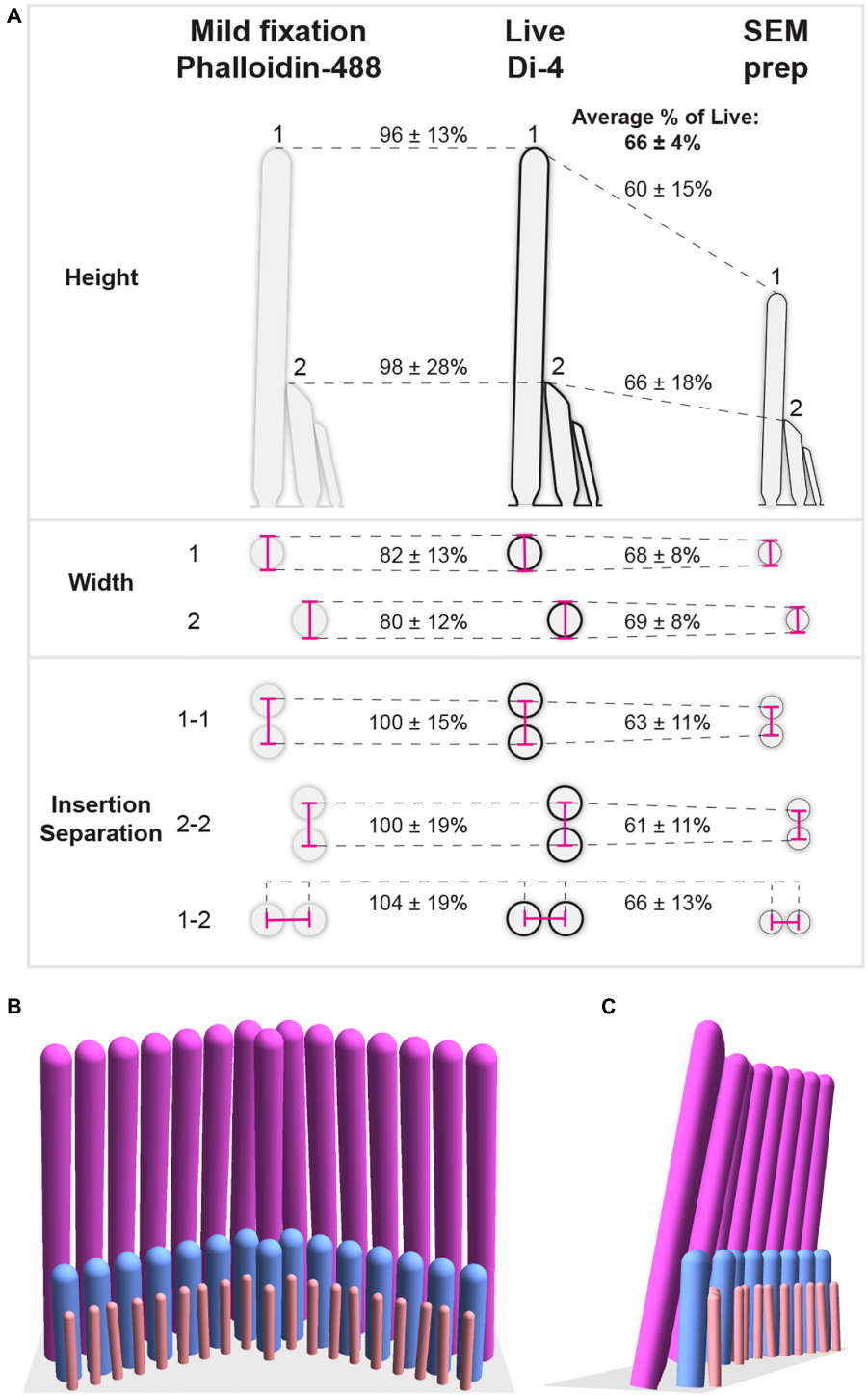


**FIGURE 6 |** Scaling factors between live and mildly-fixed or SEM-prepared conditions and a 3-D model of a P11 apical living IHC hair bundle. **(A)** The illustration summarizes the morphological differences between live (Di-4), mildly-fixed (phalloidin), and SEM-prepared hair bundles. Mean percentages of live hair-bundle dimensions (heights, widths, and insertion separations) are indicated (± SDs). **(B)** A three-dimensional model is shown of a P11 apical living IHC hair bundle based on mean measurements (**Table 1**) and the mean angles and stereociliary numbers (**Table 2**). The angle of row 3's wings has been chosen to be equal to row 2's angle, creating a range of row 2-3 insertion separations (401–489 nm) consistent with measurements (**Figure 4E**). Stereocilia are inclined toward each other as follows: First, row 1 stereocilia are inclined 12° from the vertical toward row 2, in agreement with previous measurements (Furness et al., 1997), and inclined toward each other to create minimum gap of 50 nm between neighboring stereocilia; Second, row 2 stereocilia are inclined toward row 1 stereocilia to create minimum gaps of 20 nm between row 1-2 pairs; Third, each row 3 stereocilium is inclined toward the row 2 stereocilium with the closest insertion point to create minimum gaps of 20 nm between row 2-3 pairs. Since there are more stereocilia in row 3 than in row 2, some row 2 stereocilia are paired with two row 3 stereocilia.

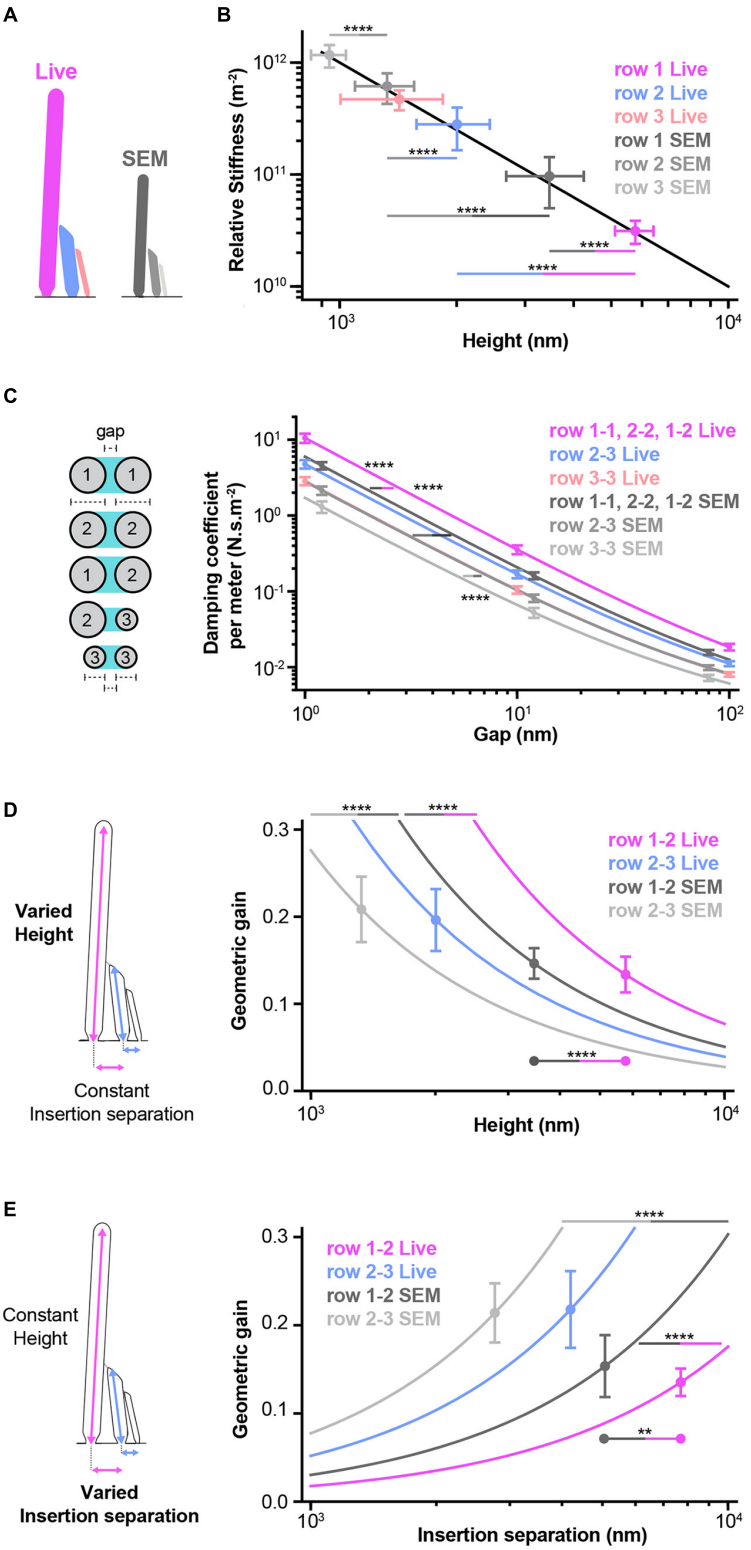


**FIGURE 7 |** Models predict how morphology affects hair-bundle mechanics. **(A)** A schematic summarizes the measurements that were used to generate the results shown in this figure. Live-cell and SEM predictions are, respectively shown in color (pink, blue, and light pink) or shades of gray, according to row identity. All live-cell heights, widths, and separations in this figure correspond to Di-4 measurements. **(B)** A stereocilium's deflection stiffness relative to its pivot stiffness is shown as a function of its height (black line, Eq. 1). The deflection stiffnesses are shown for stereocilia in each row based on live-cell and SEM heights (dots). For row 3, the live-cell height is imputed from the SEM height using a scaling factor based on row 2 live-cell and SEM heights. The live row 1 deflection stiffness is smaller than that of row 2 (asterisks, blue-pink line). Row 1 and 2 live deflection stiffnesses are smaller than those of SEM (asterisks, gray-pink and gray-blue lines). The SEM row 1

*(Continued)*

**FIGURE 7 |** deflection stiffness is smaller than that of row 2, which is smaller than that of row 3 (asterisks, gray lines). **(C)** Fluid-coupling strength (damping coefficient per meter) between two stereocilia is shown as a function of the gap between pairs of stereocilia (Eq. 2). Owing to their similar widths, fluid coupling within and between stereocilia in rows 1 and 2 is similar and is combined into a single group (live-cell widths: 0.45 ± 0.04 μm for row 1, 0.45 ± 0.04 μm for row 2, percentage difference = 1 ± 13% relative to row 1; SEM widths: 0.31 ± 0.02 μm for row 1, 0.31 ± 0.02 μm for row 2, percentage difference = 2 ± 11% relative to row 1). For row 3, the live-cell width is imputed from the SEM width using a scaling factor based on row 1 and 2 live-cell and SEM widths. At any gap size, live row 1-1, 2-2, and 1-2 fluid coupling is larger than that of SEM (asterisks, gray-pink line). At any gap size, SEM row 1-1, 2-2, and 1-2 fluid coupling is larger than that of row 2-3, which is larger than that of row 3-3 (asterisks, gray lines). **(D)** The geometric gain between two stereocilia is shown as a function of the taller stereocilium's height (Eq. 3). At any height, the live row 1-2 geometric gain is larger than that of SEM (asterisks, gray-pink line). At any height, the SEM row 1-2 geometric gain is larger than that of row 2-3 (asterisks, gray line). Geometric gains are shown at the means of measured heights (dots) (row 1-2: live-cell $\gamma_{12}$ = 0.13 ± 0.02, SEM $\gamma_{12}$ = 0.15 ± 0.02, percentage difference = –10 ± 20% relative to live-cell; row 2-3: live-cell $\gamma_{23}$ = 0.20 ± 0.04, SEM $\gamma_{23}$ = 0.21 ± 0.04, percentage difference = –6 ± 26% relative to live-cell). At the means of the measured heights, the row 1-2 live and SEM geometric gains are statistically different, but the percentage difference is highly uncertain (asterisks, gray-pink line between dots). **(E)** The geometric gain is shown as a function of the insertion separation (Eq. 3). At any insertion separation, the live row 1-2 geometric gain is smaller than that of SEM (asterisks, gray-pink line). At any insertion separation, the SEM row 1-2 geometric gain is smaller than that of row 2-3 (gray line). Geometric gains are shown at the means of measured separations (dots) (row 1-2: live-cell 0.14 ± 0.02, SEM 0.15 ± 0.04, percentage difference = –14 ± 28 relative to live-cell; row 2-3: live-cell 0.22 ± 0.04, SEM 0.21 ± 0.03, percentage difference = 2 ± 25% relative to live-cell). At the means of the measured insertion separations, the row 1-2 live and SEM geometric gains are statistically different, but the percentage difference is highly uncertain (asterisks, gray-pink line between dots). **(D,E)** For row 2-3, the live-cell insertion separation is imputed from the SEM separation using a scaling factor based on row 1-2 live-cell and SEM separations. Each dot and error bar represents the mean ± SD. Horizontal lines indicate comparisons using the Mann-Whitney U test: $^{**}P < 0.01$, $^{****}P < 0.0001$. Statistical comparisons with live row 3 values cannot be performed, because these values are imputed from row 1, row 2, and SEM values.

coupling depends on the gap between stereocilia and the extent to which coupling varies across a bundle. At a given height above the apical surface, the fluid-coupling force per unit length equals the relative velocity of the stereociliary pair times a damping coefficient per unit length λ, which depends on the gap between the stereocilia (**Figure 7C**). This damping coefficient quantifies the fluid-coupling strength and depends on the minimum gap $g_m$ between and the widths of the stereociliary pair $w_a$ and $w_b$ at a given height above the apical surface according to (see section "Materials and Methods"):

$$\lambda = \frac{4\mu\pi}{\alpha - \beta - \tanh(\alpha - \beta)}, \tag{2a}$$

in which μ is the viscosity of water and

$$\alpha = \operatorname{arcosh}\left(1 + \frac{g_m w_b}{w_a (w_a + w_b)}\right) \text{ and} \tag{2b}$$

$$\beta = -\operatorname{arcosh}\left(1 + \frac{g_m w_a}{w_b (w_a + w_b)}\right).$$

The minimum gap $g_m$ decreases with distance from the apical surface, causing the fluid-coupling to increase rapidly with distance from the apical surface. Because live-cell row 1 and 2 stereocilia widths were comparable to each other and wider than row 3 stereocilia, fluid coupling within and between rows 1 and 2 is larger (166 ± 21 to 221 ± 42% as $g_m$ decreases) than that between rows 2 and 3, which is in turn larger (139 ± 14 to 167 ± 30% as $g_m$ decreases) than that within row 3. Due to SEM-sample shrinkage, SEM fluid coupling is smaller (57 ± 10 to 76 ± 8% of live) than the corresponding live-cell fluid coupling.

Live-cell measurements of stereociliary heights and insertion separations allow us to determine the relationship between gating-spring extensions and stereociliary deflections. The more a gating-spring extends the greater the probability of mechanotransduction-channel opening (Corey and Hudspeth, 1983; Howard and Hudspeth, 1988; Ó Maoiléidigh and Ricci, 2019). The gating-spring extension between a pair of stereocilia is proportional to the deflection of the taller stereocilium with a constant of proportionality, known as the geometric gain γ, given by

$$\gamma = \frac{s}{H_t}, \tag{3}$$

in which s is the separation between the pair of insertion points and $H_t$ is the height of the taller stereocilium (Howard and Hudspeth, 1988; Jacobs and Hudspeth, 1990; Geisler, 1993; Pickles, 1993; Furness et al., 1997). The geometric gain decreases with the taller stereocilium's increasing height (**Figure 7D**). At a given height, the live-cell row 1-2 geometric gain is larger (184 ± 56% of row 2-3) than the row 2-3 gain, and the SEM gains are smaller (row 1-2: 66 ± 13% of live, row 2-3: 66 ± 21% of live) than their corresponding live-cell gains. At the means of the measured heights, however, the live-cell geometric gains differ little from the corresponding SEM gains (SEM/Live% = 110 ± 21% for row 1-2, SEM/Live% = 106 ± 27% for row 2-3), because SEM-shrinkage is similar for heights and insertion separations (SEM/Live% = 60 ± 15% for row 1 height, SEM/Live% = 66 ± 18% for row 2 height, and SEM/Live% = 66 ± 13% for row 1-2 insertion separation).

The geometric gain increases with insertion separation (Eq. 3, **Figure 7E**). At a given separation, the live-cell row 1-2 gain is smaller (34 ± 8% of row 2-3) than the row 2-3 gain and the SEM gains are larger (row 1-2: 172 ± 44% of live, row 2-3: 149 ± 38% of live) than the corresponding live-cell gains. At the means of the measured separations, however, the live-cell geometric gains differ little from the corresponding SEM gains (SEM/Live% = 113 ± 36% for row 1-2, SEM/Live% = 104 ± 38% for row 2-3), because SEM-shrinkage is similar for heights and insertion separations.

## DISCUSSION

The hair bundle, the mechanosensory organelle of hair cells, is central to our sense of hearing and its pathology. Yet, its live dimensions remained uncertain, which has limited our understanding of the hair bundle's response to mechanical

stimulation. Here, we rigorously measured or imputed the live stereociliary heights, widths, and insertion separations of C57BL/6J mouse P11 cochlear apical IHCs. Parallel sample processing, imaging, and comparisons showed that: 1) SEM preparation results in a hair bundle at a 1:1.5 scale compared to the live preparation while still preserving bundle proportions, which allows SEM dimensions to be converted into live dimensions; and, 2) in contrast to SEM, mildly-fixed/phalloidin-labeled samples have stereociliary heights, widths, and insertion separations similar to those from live conditions, validating mild fixation as a proxy for the living condition. Overall, we have generated the first comprehensive blueprint of a living hair bundle. Finally, we used our blueprint to calculate hair-bundle mechanical properties and showed that SEM measurements lead to the overestimation of stereociliary stiffness and underestimation of the fluid coupling between stereocilia, but accurately estimate the relationship between gating-spring extension and stereociliary deflection due to conservation of proportions. Thus, this study demonstrates the importance of using live hair-bundle dimensions to faithfully investigate hair-bundle function.

## Hair-Bundle Structure

The hair bundle develops at the apical surface of hair cells from the late embryonic stage until adulthood, morphing from a group of brush-border like microvilli to a stereociliary staircase of specific dimensions (Tilney et al., 1980; Tilney and DeRosier, 1986; Roth and Bruns, 1992; Kaltenbach et al., 1994; Waguespack et al., 2007; Krey et al., 2020). The final stereociliary dimensions and arrangement depends on the animal species, sensory organ, position within an organ, and hair-cell type (Garfinkle and Saunders, 1983; Wright, 1984; Kaltenbach et al., 1994; Zine and Romand, 1996; Ricci et al., 1997; Xue and Peterson, 2006; Xiong et al., 2012; Yarin et al., 2014). These hair-bundle variations indicate biological specialization of the structure for particular mechanical stimuli. This structure is still not fully understood at either the mechanical or developmental levels. Obtaining dimensions of unlabeled and live stereocilia is challenging due to their micron-scale heights and nano-scale widths. For these reasons, the vast majority of the reported stereociliary dimensions correspond to either transmission or scanning EM (Lim, 1980; Garfinkle and Saunders, 1983; Pickles et al., 1984; Roth and Bruns, 1992; Holme et al., 2002; Tsuprun et al., 2003; Furness et al., 2008; Zampini et al., 2011; Xiong et al., 2012; Taylor et al., 2015; Tarchini et al., 2016; Hadi et al., 2020) or to fixed, permeabilized, and actin-core labeled experiments (Krey et al., 2020). Although it was previously known that EM sample preparation shrinks cochlear tissue, the extent of this shrinkage at the stereociliary level had not been well quantified, and the consequences of phalloidin-staining preparation remained undetermined (Tilney et al., 1980; Wright, 1981; Forge et al., 1992). Another layer of uncertainty surrounding the previously reported stereociliary dimensions is that most have not been allocated to a well-defined position along the cochlear axis, or well-controlled for age. As we have shown here, controlling for age is critical: even a slight natural delay in development between litters of the same age had a large impact on the stereociliary heights. We minimized biological and experimental variability by limiting our analysis to a defined portion of the apical turn and by comparing cochleae from the same animals treated differentially. We found that the heights of row 1 and row 2 stereocilia were similar when imaged in live or mildly-fixed samples. Much in the same way as larger cochlear dimensions are unaffected by paraformaldehyde fixation (Edge et al., 1998), the micron-scale stereocilia appear to be unaffected, and mild fixation can be used as a proxy for live conditions. SEM sample preparation shrunk all measured dimensions and distances to the same degree (SEM/Live% = 66 ± 3 % on average) relative to the live conditions (**Figure 6** and **Tables 1**, **2**). We used scale factors to convert the SEM measurements of the small row 3 stereocilia to live values. Across all measurements, the average scaling factor between SEM and live measurements was 1:1.51 ± 0.08. In this particular apical cochlear location at P11, in live conditions, IHC row 1 is on average 2.9 times taller than row 2 and 4 times taller than row 3. Row 2 is 1.4 times taller than row 3. The width of rows 1 and 2 are similar and 2.3–2.4 times larger than row 3 widths. Our row 1 and 2 results are consistent with the ones obtained from phalloidin staining of a slightly more basal segment of the mouse cochlea (Krey et al., 2020). In particular, Krey et al. showed that after P7.5 the width of row 1 increases while the width of row 2 decreases, and at P11 that row 1 and row 2 transiently have the same width, as we have observed. The SEM scaling factor we determined can be used for other types of hair bundles as long as their SEM preparation and their SEM dimensions are similar to those reported here. The consequences of other EM sample preparation procedures on stereocilia dimensions would have to be determined; for example, sample preparations for TEM are expected to affect dimensions less than SEM preparation (Nordestgaard and Rostgaard, 1985).

In this study, we have also determined the arrangement of the stereocilia relative to each other in these P11 apical IHCs. To observe the stereociliary insertions, previous studies have used sonication or paper blotting to remove the stereocilia from samples during SEM sample preparation (Tilney and Saunders, 1983; Peterson et al., 1996; Severinsen et al., 2003). In this work, to sequentially image the stereocilia and the insertions of the same sample, we have developed a simple alternative method, using tape to peel-off the stereocilia from mounted SEM-samples. This method gives the added benefit of allowing mounted hair bundles to first be imaged, then peeled off, and finally re-imaged to collect insertion data, thereby allowing measurement of a wide spectrum of dimensions from a single sample. Stereociliary insertion patterns of cochlear hair cells have been reported for bird and turtle (Tilney and Saunders, 1983; Hackney et al., 1993), rodent OHCs (Gulley and Reese, 1977; Comis et al., 1985; Forge et al., 1988, 1991; Roth and Bruns, 1992; Souter et al., 1995; Tsuprun and Santi, 1998; Tsuprun et al., 2003), but rarely for rodent IHCs (Gulley and Reese, 1977; Forge et al., 1988; Furness et al., 2008). Our hair-bundle peeling method allowed us to image by SEM the insertion pattern of a substantial number of cells from the same cochlear location ($n$ = 24). We observed consistently that row 1 and row 2 stereocilia have insertion positions with a central column shifted forward, creating a notch in the hair bundle. When imaging the hair bundle with intact stereocilia using SEM,

the IHC insertion pattern is not evident, which explains why the stereociliary arrangements of rows 1 and 2 in IHCs have been described as forming an almost straight line (Engström and Engström, 1978; Forge et al., 1988; Ciganović et al., 2017). Two reports describe a "W" shape caused by the notch in adult chinchilla and guinea pig, although the insertion positions are not visible (Lim, 1986; Furness and Hackney, 2006). In contrast, a "W" shape caused by the notch in OHCs has been described many times (Lim, 1986; Forge et al., 1988; Roth and Bruns, 1992; Tsuprun et al., 2003; Furness et al., 2008). The notch is likely related to the kinocilium. At P11, the IHC kinocilium is either absent or degenerating, but its former insertion position in the apical surface, the fonticulus, remains and is visible by SEM (Kikkawa et al., 2008). It will be important to further investigate when the notch appears during hair bundle development, if it is maintained at later ages, and finally, if it is seen along the tonotopical axis.

When investigating the shape of the bundle, we found that both the row 1 and row 2 wings of the IHCs form the same angle, that the angle differs from 120 and 180°, and that insertion points along the wings do not diverge systematically from a straight line. Furthermore, insertion separations are not uniform across all rows, with row 1-2 separation being larger than both row 1-1 and row 2-2, all of which are larger than row 2-3 and row 3-3 separations. These observations imply that the IHC insertion positions deviate systematically from a hexagonal array.

Each stereocilium's orientation is defined by two leaning angles, a polar and an azimuthal angle. We did not quantify these angles, as we expect our sample preparations to alter the stereociliary angles from their *in-vivo* states. For example, in Di-4 and phalloidin images, we often see row 1 stereocilia pointing away from each other, splitting the bundle (**Figure 1**). In most cases, SEM preparation causes clear disorganization in the leaning angles (**Figure 3A**). Although the polar angle has previously been measured from TEM images, these measurements also indicate that sample preparation changed the angle (Zetes, 1995; Furness et al., 1997). For some measurements, row 1 leans away from row 2, which is inconsistent with a force balance at rest between insertion-point pivots and links that causes the bundle to move forward when tip links are cut (Tobin et al., 2019). Determining the *in-vivo* leaning angles remains a challenge for future work.

## Hair-Bundle Function

Our understanding of hair-bundle mechanics is based on a combination of experimental data and modeling, which rely on accurate and precise measurements. We found that SEM measurements underestimate IHC bundle dimensions, resulting in greatly overestimated stereociliary stiffness (219 ± 112 to 308 ± 165%) and greatly underestimated fluid coupling (57 ± 10 to 76 ± 8% of live). In contrast, SEM provides good estimates of geometric gains, because heights and insertion separations shrink similar amounts. Similarly, the stiffness of row 1 relative to row 2 (live-cell: 11 ± 5%; SEM: 16 ± 9%) and row 2 relative to row 3 (live-cell: 60 ± 27%: SEM: 53 ± 20%) is well-estimated by SEM, because all heights shrink by similar amounts.

The stiffness of an individual stereocilium determines its deflection in response to stimulation (Corey et al., 2017; Fettiplace, 2017; Ó Maoiléidigh and Ricci, 2019). Here we show that the deflection stiffness of row 1 is 11 ± 5% and 7 ± 2% of rows 2 and 3, respectively, assuming similar pivot stiffnesses. A stiffness gradient within the hair bundle would affect gating of the mechanotransduction channel. However, rootlet differences between the rows might cause pivot-stiffness differences (Furness et al., 2008). How these specializations affect hair-bundle function remains to be determined.

In addition to the effects of stereociliary stiffness on bundle deflection, fluid coupling between stereocilia is very large and is thought to ensure coherent stereociliary motion across a bundle (Zetes, 1995; Zetes and Steele, 1997; Kozlov et al., 2011). This coupling increases rapidly as the gap between pairs of stereocilia decreases, but we lack accurate measurements of the gap size at the point of closest apposition. It is not possible to resolve the smallest gaps optically, but gaps can be resolved using electron microscopy. EM imaged gaps seen in IHCs and OHCs range from 1 to 100 nm, which may imply different amounts of fluid coupling across a bundle or might be a consequence of hair-bundle damage during sample preparation (Osborne et al., 1984; Pickles et al., 1984; Furness and Hackney, 1985; Santi and Anderson, 1987; Furness et al., 1997; Tsuprun et al., 2003; Zampini et al., 2011; Hackney and Furness, 2013). Here we show that fluid coupling at a given gap size within and between rows 1 and 2 is stronger than that between rows 2 and 3, which is again stronger than that within row 3, because stereocilia in rows 1 and 2 are wider than those in row 3.

Finally, gating of the mechanotransduction channel depends on several factors including stereociliary deflections, heights, and insertion separations. The most common formulation of the gating-spring model for mechanoelectrical transduction assumes that all gating springs extend the same amount in response to hair-bundle deflection, characterized by a single geometric gain for each hair cell (Corey and Hudspeth, 1983; Howard and Ashmore, 1986; Howard and Hudspeth, 1988; Crawford et al., 1989; Jacobs and Hudspeth, 1990; Karavitaki and Corey, 2010; Ó Maoiléidigh and Hudspeth, 2013; Corey et al., 2017; Fettiplace, 2017; Tobin et al., 2019; Ó Maoiléidigh and Ricci, 2019). Previous work using TEM indicated that the IHC row 1-2 gating spring extends twice as much as that of row 2-3 (average 167 ± 50%; characteristic frequency 0.27–13 kHz), but was not conclusive owing to measurement uncertainties (Furness et al., 1997). Indeed, only one-to-six stereociliary pairs at each cochlear position were observed, and it is not known whether TEM preparation shrinks hair-bundle dimensions equally or the extent to which it changes the polar leaning angles of the stereocilia – measurements which were used to calculate gating-spring extension relative to hair-bundle deflection (Zetes, 1995). We overcome these limitations by measuring over 150 stereocilia per dimension, by using live-cell, mildly-fixed, and SEM measurements, and by determining that SEM shrinkage is similar across dimensions. To avoid the uncertainty associated with the polar leaning angle, we calculate the geometric gain relative to the taller stereocilium of each pair without accounting for the polar

leaning angle changes the geometric gain very little (<2% for a row 1 angle of 12° toward row 2) (Zetes, 1995; Furness et al., 1997). We find that the row 1-2 geometric gain ($\gamma_{12}$ = 0.14 ± 0.03) is smaller (66 ± 22% of row 2-3) than that of row 2-3 ($\gamma_{23}$ = 0.20 ± 0.06). The geometric gains allow us to determine if row 1-2 and 2-3 gating springs extend similar amounts in response to IHC bundle deflection. For a bundle deflection $X$, the row 1-2 gating spring extends by $\gamma_{12}X = (0.14 \pm 0.03)X$. To a good approximation, row 2 has the same angular displacement as row 1 and the row 2-3 gating spring then extends by $\gamma_{23}\,(H_2/H_1)\,X = (0.07 \pm 0.03)X$, in which $H_1$ and $H_2$ are, respectively the heights of rows 1 and 2. In agreement with previous work, the gating-springs do not extend the same amount: row 1-2 gating-spring extension is double that of row 2-3 (190 ± 79%) (Furness et al., 1997). For small stimuli, this difference will cause row 2 mechanotransduction channels to respond by changing their open probability twice as much as row 3's. Additional experimentation and modeling will be required to understand the full consequences of these differences.

While previous work has provided measurements of IHC bundle morphology using electron and optical microscopy, it has been limited by uncertain cochlear locations, uncertain ages, differences in species, or artifacts in sample-preparation (Garfinkle and Saunders, 1983; Pickles et al., 1984; Holme et al., 2002; Tsuprun et al., 2003; Beurg et al., 2008; Furness et al., 2008; Zampini et al., 2011; Nam et al., 2015; Taylor et al., 2015; Tarchini et al., 2016; Liu et al., 2019; Tobin et al., 2019; Hadi et al., 2020; Krey et al., 2020). Here we control for these uncertainties and show definitively that apical mouse IHC bundles have several morphological specializations. Row 1 is much taller than rows 2 and 3. Stereocilia in rows 1 and 2 are much wider than in row 3. Row 1-2 insertion separations are larger than those within rows 1 and 2, which are larger than those of row 2-3 and those within row 3. Row 1 and 2 angles are larger than 120° and smaller than 180°. Our modeling demonstrates several conspicuous mechanical consequences of IHC bundle specializations, but the functional reasons for these specializations remain elusive.

# CONCLUSION

This work provides the first comprehensive dataset of live hair-bundle dimensions, which are of paramount importance for determining hair-bundle function. Furthermore, the SEM-to-live scaling factor we determined will be instrumental for generating live blueprints from rare samples, such as human hair bundles.

# MATERIALS AND METHODS

## Animals

The Administrative Panel on Laboratory Animal Care (APLAC) at Stanford University (protocol #28278) approved all animal procedures. C56BL/6J adult mice were purchased from Jackson Laboratories (Bar Harbor, ME, United States) and bred to produce pups.

## Cochlear Tissue Preparation

Inner ears of P11 mice of both sexes were dissected from temporal bones at room temperature (RT) in extracellular recording solution containing the following: 145 mM NaCl, 2 mM KCl, 2 mM $CaCl_2$, 1 mM $MgCl_2$, 10 mM 4-(2-hydroxyethyl)-1-piperazineethanesulfonic acid (HEPES), 6 mM Glucose, 2 mM pyruvate, 2 mM ascorbic acid, and 2 mM creatine monohydrate. The pH of the external solution was adjusted to 7.4 by addition of NaOH and osmolality ranged from 304 to 308 mOsmol. The apical turn of the organ of Corti was gently dissected out of the cochlea and the tectorial membrane was removed. To minimize differences due to development, animals from within the same litters were compared. One ear of each animal was used for immediate live imaging, while the other was used for mildly-fixed conditions and imaged after the live one. As shrinkage was expected in SEM samples, cochleae from the littermates of the live and mildly-fixed animals were used for comparisons.

## Live Stereociliary-Membrane Staining

Dissected cochlear apical turns were transferred with a spoon to a dish containing a lipophilic dye and stained for 5 min at RT while protected from light, then transferred to a recording dish with external recording solution and held in place with dental floss ensuring that IHC hair bundles were oriented vertically for imaging. We used the lipophilic dye ANEP (aminonaphthylethenylpyridinium) dye Di-4-ANEPPDHQ (D36802, ThermoFisher Scientific) (MW: 666 g/mlole). The dye was resuspended in 100% ethanol at 1 mg/ml (1.3 mM), and then diluted at 15 μg/ml (19 μM final) in external recording solution before each staining. We also used the lipophilic styryl dye FM 4-64FX (F34653, Invitrogen) (MW: 788 g/mole), which produces low fluorescence in water and intense fluorescence upon binding to the plasma membrane. The dye was resuspended in water at 200 μg/ml (357 μM), and then diluted at 5 μg/ml (9 μM final) in external recording solution before each staining.

## Actin-Core Fluorescent Imaging of Mildly-Fixed Hair Bundles

Dissected cochlear apical turns were transferred with a spoon to a dish containing fixative (4% Paraformaldehyde (PFA) aqueous solution (RT15714, Electronic Microscopy Sciences) in 0.05 mM Hepes buffer pH 7.2, 10 mM $CaCl_2$, 5 mM $MgCl_2$, 0.9% NaCl) and incubated for 30 min at RT. The sample was then transferred to a new dish containing 0.5% Triton and phalloidin-Alexa 488 (A12379) (1/800) in external recording solution for 15 min, causing permeabilization and acting labeling. The sample was then transferred to a recording dish for imaging.

## Live Hair-Bundle Fluorescence Imaging

Live and mildly-fixed IHC hair bundles were imaged in external recording solution using a Zeiss LSM880 microscope in Airyscan mode and a Zeiss Plan Apochromat 40X water immersion 1NA lens and a X7 digital zoom. Di-4-ANEPPDHQ (in lipid, Excitation 472 nm, Emission 615 nm) and phalloidin-488 (Excitation 490 nm, Emission 525 nm) were excited with a

488 nm laser, yielding a theoretical maximum lateral resolution of 246 nm and 210 nm and an axial resolution of 1145 nm and 978 nm. FM 4-64FX (in lipid, Excitation 565 nm, Emission 744 nm) was excited with a 561 nm laser, yielding a theoretical maximum lateral resolution of 298 nm and an axial resolution of 1385 nm. Emission filters used were band-pass at 495–550 nm for phalloidin-488 and long-pass at 570 nm for Di-4-ANEPPDHQ and FM 4-64FX. To limit physical damage to the sample, the laser power used was ∼4.5% for live imaging, and 5–7% for phalloidin staining, in which the maximum laser power was approximately 5.5 μW for the 488 laser and 49.8 μW for the 561 laser. The microscope stage was controlled along the z-axis with a Heidenhain drive, which has a z-axis resolution of 0.05 μm and a z-axis repeatability of ± 0.1 μm. Image stacks of 330-nm thickness encompassing the entire hair bundles (15–20 optical sections per bundle) of 5–8 consecutive IHCs were deconvolved using ZEN software (blue edition, Zeiss).

An imaging system's optical resolution is the smallest distance between two points at which they can be distinguished and depends on the system's point-spread function. The resolution of our system is sufficient to measure row 1 and 2 heights, widths, and insertion separations. The resolution is also sufficient to measure row 2-3 and 3-3 insertion separations, but the fluorescence signal from row 3 was too dim relative to the background to precisely localize row 3 insertion positions. Using 100 nm diameter beads, we determined the point-spread function's full width at half maximum (FWHM) to be 802 ± 25 nm in the axial direction and to be 201 ± 8 nm and 224 ± 12 nm in the lateral directions (488 nm laser, $n = 5$ for each measurement). For distinguishable objects, the optical resolution is larger than the precision in distance measurements (Thompson et al., 2002; von Diezmann et al., 2017). A wider point-spread function causes more variability in a distance measurement because it becomes increasingly difficult to place the measurement points at the desired positions within an image. This variability contributes to the distance standard deviation, which quantifies the precision of a distance measurement. The precision of a measurement is not limited to the width of the point-spread function, however, and can be more than an order of magnitude smaller than this width (Thompson et al., 2002). The standard deviations of our measurements are larger than this achievable limit, because we placed measurement points manually, we are not imaging isolated molecules, and our samples include biological variability. Across all stereociliary measurements based on Di-4 or phalloidin, the smallest lateral standard deviation of 40 nm is consistent with the lateral FWHMs and the smallest axial standard deviation of 350 nm is consistent with the axial FWHM. Averaging measurements per hair bundle reduces the standard deviations further.

## Stereociliary Height, Width, and Insertion-Separation Measurements From Fluorescence Imaging

Airyscan processed stacks were transferred to Imaris (Oxford Instruments, United States) software. The stacks were visualized using the 3-D View interface. The best volume renderings for measurements were obtained when the optical sections were perpendicular to the stereocilia. Stereociliary heights from row 1 and row 2 were measured by manually placing measurement points at the stereociliary base and top in 3-D space. We defined these points as the location at which the fluorescence signal suddenly decays. We determined stereociliary widths at the position just below the beveled portion of row 2. There, we generated a virtual section with the Imaris slicer tool. A stereocilium's cross section looks like a distorted oval because a slice is usually oblique to the stereocilium's axis and a stereocilium's membrane cannot be distinguished from the membranes of neighboring stereocilia when they are closer than the imaging system's optical resolution (**Supplementary Figure 4**). To minimize error caused by this distortion, we determined a stereocilium's width by measuring the length of the shortest line in 3-D, with endpoints placed on the perimeter's midsection, that passes through the center of the stereocilium's ovate cross section. The shortest line in 3-D may not appear to be the shortest in 2-D and may not appear to lie on the midsection in 2-D (**Figure 2A** and **Supplementary Figure 4**).

Insertion separations were determined from phalloidin-stained hair bundles, from the first virtual section parallel to and above the hair cell's apical surface. Separations were defined to be between stereociliary centers.

## Stereociliary Number Count

Using the SEM images of the apical surface of IHCs with the stereocilia peeled off, we identified stereociliary rows using the notch as a reference. Numbers of stereocilia were counted (including the central stereocilia) only for rows that were fully visible. Rows that were obstructed by remaining stereocilia or other objects were not included in the quantification.

## Hair-Bundle Angle Determination and Stereociliary Arrangement

From phalloidin insertion-point images, stereociliary xy-coordinates were extracted (WebPlotDigitizer), plotted, and fit to straight lines. The slope of each hair-bundle wing was determined from their linear fits, and the angle of the bundle was calculated from these slopes. Mean bundle angles were calculated using the vector components, and confidence intervals were determine using a von Mises 95% confidence-interval chart (Batschelet, 1981).

Each stereocilium was assigned a number (1–9) as its distance from the indented central column, with 1 being directly adjacent to the column. The perpendicular deviation of a stereocilium's coordinates from the linear fit line was calculated using

$$r\frac{\left|b + mx_s - y_s\right|}{\sqrt{1 + m^2}}, \tag{4a}$$

in which $(x_s, y_s)$ is the insertion point coordinate, m is the slope of the linear fit, b is the y intercept, and r determines the sign of the deviation, such that r is equal to 1 if

$$\left(y_s - \frac{m\left(x_s + my_s - mb\right)}{m^2 + 1} - b\right) > 0 \tag{4b}$$

and r is equal to −1 if

$$\left(y_s - \frac{m\left(x_s + my_s - mb\right)}{m^2 + 1} - b\right) < 0. \tag{4c}$$

The average deviations were tested against a mean of zero at the 95% confidence level using one-sample *t*-tests and Benjamini-Hochberg analysis (false discovery rate 25%).

## Sample Preparation for Scanning Electronic Microscopy

Samples were prepared as previously described (Trouillet et al., 2021). Briefly, inner ears were isolated in external recording solution, transferred with a spoon to a dish containing fixative (4% Paraformaldehyde aqueous solution (RT15714, Electronic Microscopy Sciences) in 0.05 mM Hepes buffer pH 7.2, 10 mM $CaCl_2$, 5 mM $MgCl_2$, 0.9% NaCl) and incubated for 30 min at RT. The cochleae were then dissected in the fixative to remove the stria vascularis, Reissner's membrane, and the tectorial membrane. The samples were re-fixed in 2.5% glutaraldehyde and 4% PFA in 0.05 mM HEPES Buffer pH 7.2, 10 mM $CaCl_2$, 5 mM $MgCl_2$, and 0.9% NaCl overnight at 4°C, then washed, dehydrated in ethanol (30%, 75%, 95%, 100%, and 100%, 5 min incubation) and brought to the critical drying point using Autosamdri-815A (Tousimis). Cochleae were mounted on 45° beveled-studs using silver paint. The front and back sides of hair bundles were coated with sequential 3 nm palladium depositions (sputter coater EMS150TS; Electron Microscopy Sciences and custom-made stud adaptor). Samples were imaged at 5 kV at a working distance of 4 mm on a FEI Magellan 400 XHR Field Emission Scanning Electron Microscope (Stanford Nano Shared Facilities) and its TLD secondary-electron detector in immersion mode. In this mode, the spatial resolution is 0.8 nm. To limit stereociliary damage and displacement during imaging, the beam current was frequently reduced from 50 to 25 pA or 13 pA. To ensure that beam was not displacing the sample, consecutively scanned images were compared. If a drift was observed, the corresponding hair bundle was not used further. Two stereo-pair images of the same IHC bundle at 20-25,000X were obtained differing by a 5-degree front/back eucentric rotation centered at the insertion point of a row 2 stereocilium located in the middle part of the hair bundle. The microscope was periodically calibrated for measurements using a SIRA-type calibration specimen for ultra-high-resolution modes with 2% or less error between 50 and 350 KX magnifications at our imaging settings.

## Determination of Stereociliary Widths and Heights From Scanning-Electron-Microscopy Pictures

Measured dimensions correspond to hair bundles coated on the back and front with 3 nm of palladium, which approximately equals 1.9% of the diameter of row 1 and 2 stereocilia and 4.6% of the diameter of row 3 stereocilia.

Widths for SEM were measured horizontally across the fully-visible parts of stereocilia. For row 1, widths were measured at a height just above the row-2 tips. For row 2, widths were measured at the widest point across the stereocilia below the tip bevel. For row 3, widths were measured at the widest point across the stereocilia below the tips. To be counted as a row 3 stereocilium, a stereocilium was required to be in front of row 2 in an SEM image and to abut a row 2 stereocilium.

The method we use to determine a stereocilium's height from two tilted SEM images is a corrected version of a published method (Li et al., 2020). Between images, we rotate the sample counterclockwise by an angle α around an axis in the image plane, a eucentric rotation. We chose the rotation axis to be close to the stereocilium's insertion point into the hair cell's apical surface and define a coordinate system with an origin at the insertion point, an x-axis parallel to the rotation axis, and a y-axis in the image plane (**Supplementary Figure 6A**). Let the vectors **A** and **B**, respectively represent the three-dimensional height and positions of the stereocilium before and after the sample rotation and have coordinates $\{x_A, y_A, z_A\}$ and $\{x_B, y_B, z_B\}$ . The vectors $\mathbf{A}'$ and $\mathbf{B}'$ are the projections of the stereocilium onto the image plane and have coordinates $\{x_A, y_A, 0\}$ and $\{x_B, y_B, 0\}$. Using each image, we measure the stereocilium's projected heights $\left|\mathbf{A}'\right|$ and $\left|\mathbf{B}'\right|$ and its angles with the x-axis $\theta_A$ and $\theta_B$. The xy-coordinates of the stereocilium vectors are then given by

$$\begin{aligned} x_A &= \left|\mathbf{A}'\right| \cos\theta_A, \\ y_A &= \left|\mathbf{A}'\right| \sin\theta_A, \\ x_B &= \left|\mathbf{B}'\right| \cos\theta_B, \text{ and} \\ y_B &= \left|\mathbf{B}'\right| \sin\theta_B. \end{aligned} \tag{5}$$

Assuming that the stereocilium is perpendicular to the x-axis, the angle between **A** and **B** is the rotation angle α . We find the height of the stereocilium $H = |\mathbf{A}| = |\mathbf{B}|$ and the z-coordinates $z_A$ and $z_B$ using the law of cosines and the relationships between the height and the coordinates yielding

$$\begin{aligned} H &= \sqrt{\frac{\beta + \sqrt{\beta^2 - 4\left(1-\delta^2\right)\left(x_A y_B - x_B y_A\right)^2}}{2\left(1-\delta^2\right)}}, \\ z_A &= -\sigma(\alpha)\,\sigma\left(y_B - y_A\right)\sqrt{H^2 - \left|\mathbf{A}'\right|}, \text{ and} \\ z_B &= \sigma(\alpha)\,\sigma\left(y_A - y_B\right)\sqrt{H^2 - \left|\mathbf{B}'\right|}, \end{aligned} \tag{6}$$

in which $\delta = \cos\alpha$, $\beta = x_A^2 + x_B^2 + y_A^2 + y_B^2 - 2\delta x_A x_B - 2\delta y_A y_B$, and

$$\sigma(x) = \begin{cases} 1, & x \geq 0 \\ -1, & x < 0 \end{cases}. \tag{7}$$

To find the height of a stereocilium whose insertion point is obscured by a shorter stereocilium **A**, we define the vector **C**

from the tip of the shorter stereocilium to the tip of the obscured stereocilium (**Supplementary Figure 6B**). We define a coordinate system with an origin at the shorter stereocilium's insertion point and measure $\left|\mathbf{A}'\right|$, $\left|\mathbf{C}'\right|$, $\theta_A$, and $\theta_C$. As described above, we find the coordinates of **A** $\{x_A, y_A, z_A\}$ and the coordinates of **C** relative to **A** $\{x_{CA}, y_{CA}, z_{CA}\}$ . The coordinates of the obscured stereocilium's tip relative to the shorter stereocilium's insertion point are then given by

$$\begin{aligned} x_C &= x_{CA} + x_A, \\ y_C &= y_{CA} + y_A, \text{ and} \\ z_C &= z_{CA} + z_A. \end{aligned} \tag{8}$$

We assume that the apical surface plane of the hair cell is related to the first image plane by a counterclockwise rotation around the x-axis through the angle φ. To find φ, we chose two points $M'$ and $N'$ in the image plane that appear to be on the apical surface and that form a line perpendicular to the x-axis. We measure the projected length of the line $\left|M'N'\right|$ and use the method described above to find the true length of the line |MN|. The angle φ is then given by

$$\varphi = \frac{\pi}{2} + \arccos\left(\frac{\left|M'N'\right|}{|MN|}\right). \tag{9}$$

The coordinates of the obscured stereocilium's insertion point Q are then given by

$$\begin{aligned} x_Q &= \frac{x_C z_A - x_A z_C + (x_A y_C - x_C y_A)\tan\varphi}{z_A - z_C + (y_C - y_A)\tan\varphi}, \\ y_Q &= \frac{y_C z_A - y_A z_C}{z_A - z_C + (y_C - y_A)\tan\varphi}, \text{ and} \\ z_Q &= y_Q \tan\varphi. \end{aligned} \tag{10}$$

The height of the obscured stereocilium H is finally given by

$$H^2 = (x_C - x_Q)^2 + (y_C - y_Q)^2 + (z_C - z_Q)^2 . \tag{11}$$

The method we use is based on several assumptions. For unobscured stereocilia, we assume that the rotation axis is in the image plane, the rotation axis is close to the insertion points, the x-axis is parallel to the rotation axis, and the stereocilia are approximately perpendicular to the x-axis. We make the same assumptions for obscured stereocilia along with the assumption that the surface plane is related to the image plane by a rotation around the x-axis. Using artificial images with stereocilia of known height, we estimate the error owing to these assumptions to be less than 10%.

## Hair-Bundle Peeling and Insertion-Separation Measurements

To measure the separation between stereocilia at the hair-cell's apical surface, hair bundles from SEM-prepared samples were peeled-away using a piece of permanent double-sided tape (Scotch, 3M) placed on a fine forceps and gently applied to the hair-cell area. Samples were then reimaged and the number of stereocilia per row and the insertion separations were measured from top-down views. Stereocilia from different rows were paired starting from the most central row 1 stereocilium, which is shifted toward row 3, and then pairing the adjacent stereocilia. If multiple row 3 stereocilia could be paired to a single row 2 stereocilium, measurements were made using the closest stereocilium.

## Fluid Coupling Between Stereocilia

Because inertial fluid forces between stereocilia are negligibly small, we determine the fluid-coupling forces between two stereocilia by solving the corresponding inertialess Stokes equations (Baumgart, 2011). We calculate the fluid-coupling force per unit length between infinitely long parallel cylinders, because at a given height above the apical surface neighboring stereocilia are approximately parallel, have approximately circular cross sections, and their fluid coupling is dominated by forces distant from their ends. We first determine fluid coupling in the lubrication limit, when the gap between stereocilia is much smaller than their widths, by extending previous calculations of the fluid coupling between two cylinders of equal widths to the case in which their widths are not equal (Zetes, 1995; Zetes and Steele, 1997; Baumgart, 2011; Kozlov et al., 2011). In terms of an xy-coordinate system with an origin on the line connecting their centers, the distance g between them is given by

$$g(y) = g_m + r_a + r_b - \sqrt{r_a^2 - y^2} - \sqrt{r_b^2 - y^2}, \tag{12}$$

in which $g_m$ is the minimum gap between the cylinders, and $r_a$ and $r_b$ are their radii (**Supplementary Figure 8**). When $g_m \ll \min\{r_a, r_b\}$ , the distance g is well approximated by

$$g(y) = g_m + \frac{r_a + r_b}{2 r_a r_b} y^2 . \tag{13}$$

When the cylinders come together or move apart along the line connecting their centers with relative velocity **U**, the Poiseuille flow created causes pressure given by

$$\begin{aligned} p(y) &= -12\mu|\mathbf{U}| \int_{-\infty}^{y} \frac{y'}{g(y')^3}\, dy' \\ &= 12\mu|\mathbf{U}| \frac{2 r_a^3 r_b^3}{(r_a + r_b)\left(2 g_m r_a r_b + (r_a + r_b) y^2\right)^2}, \end{aligned} \tag{14}$$

in which μ is the viscosity of water (Zetes, 1995). The magnitude of the force per unit length owing to the pressure is then given by

$$|\mathbf{F_{lub}}| = \int_{-\infty}^{\infty} p\, dy = 3\sqrt{2}\pi\mu \left(\frac{r_a r_b}{g_m (r_a + r_b)}\right)^{\frac{3}{2}} |\mathbf{U}| . \tag{15}$$

Note that $w_a = 2r_a$ and $w_b = 2r_b$ are the cylinder widths (Eq. 2). This calculation for a small gap helps us to determine the fluid coupling satisfying the Stokes equations for a gap of any size. To determine the fluid-coupling force for a gap of any size, we extend a previous calculation of the fluid coupling between two cylinders of equal widths to the case in which their widths are not equal (Wakiya, 1975). Following the notation of Wakiya, consider the two cylinders in bipolar coordinates $\{\alpha, 0\}$ and $\{\beta, 0\}$, and with minimum distances to the y-axis $g_a$ and $g_b$, such that the minimum gap between them is $g_m = g_a + g_b$ (**Supplementary Figure 8**). Using Eqs. 2.5, 2.6, and 2.10 in Wakiya, we find the magnitude of the fluid coupling force between the cylinders is given by

$$|\boldsymbol{F_c}| = \frac{4\mu\pi\,|\boldsymbol{U}|}{\alpha - \beta - \tanh(\alpha - \beta)} = \lambda\,|\boldsymbol{U}| \tag{16}$$

in which $\alpha = \operatorname{arcosh}\left(1 + g_a/r_a\right)$, $\beta = -\operatorname{arcosh}\left(1 + g_b/r_b\right)$, and $\lambda$ is the damping coefficient per unit length. To complete the solution, we determine distances $g_a$ and $g_b$ that are consistent with the equations discussed by Wakiya. We find a constraint for $g_a$ and $g_b$ by matching the leading term of Eq. 16 expanded around $g_a = 0 = g_b$ with the lubrication solution (Eq. 15), yielding

$$\left(\sqrt{\frac{g_a}{r_a}} + \sqrt{\frac{g_b}{r_b}}\right)^2 = \frac{g_m\,(r_a + r_b)}{r_a r_b}. \tag{17}$$

We use this constraint and $g_m = g_a + g_b$ to find

$$g_a = \frac{g_m r_b}{r_a + r_b} \text{ and } g_b = \frac{g_m r_a}{r_a + r_b}. \tag{18}$$

Inserting these expressions into Eq. 16 yields the fluid coupling force for a gap of any size, in which

$$\alpha = \operatorname{arcosh}\left(1 + \frac{g_m r_b}{r_a\,(r_a + r_b)}\right) \text{ and} \tag{19}$$

$$\beta = -\operatorname{arcosh}\left(1 + \frac{g_m r_a}{r_b\,(r_a + r_b)}\right).$$

The fluid-coupling force opposes the relative motion such that $\mathbf{F_c} = -\lambda\mathbf{U}$. We only calculate the fluid-coupling force owing to motion along the line connecting the cylinders' centers, because this force is much larger than fluid-coupling forces caused by other types of relative motion (Zetes, 1995; Zetes and Steele, 1997; Baumgart, 2011; Kozlov et al., 2011).

## 3-D Illustration of the Hair Bundle and Calculus

We used Mathematica 12.1.1.0 (Wolfram Research, Inc., Champaign, IL, United States) to create the 3-D hair-bundle model (**Figures 6B,C**), to calculate the effects of morphology on mechanics (**Figure 7**), and to create **Supplementary Figures 4, 6**.

## Statistical Analyses

Statistical tests performed were described in the text and calculated using Prism 9 (GraphPad Software, San Diego, CA, United States), Excel (Microsoft, Redmond, WA, United States), and Mathematica 12.1.1.0 (Wolfram Research, Inc., Champaign, IL, United States).

# DATA AVAILABILITY STATEMENT

The raw data supporting the conclusions of this article will be made available by the authors upon request.

# ETHICS STATEMENT

The animal study was reviewed and approved by the Administrative Panel on Laboratory Animal Care (APLAC) at Stanford University (protocol #28278), which approved all animal procedures.

# AUTHOR CONTRIBUTIONS

NG and DÓ conceived of the study. PA, KRM, and NG conducted the fluorescence imaging. NG conducted the SEM experiments. KKM, DÓ, and NG performed the analysis. NG and DÓ designed experiments. DÓ performed the mathematical modeling of the hair bundle, derived the fluid-coupling equations, and derived the SEM-height equations. NG, DÓ, and KKM wrote the manuscript. All authors contributed to the article and approved the submitted version.

# FUNDING

The work was funded by the OHNS startup funding and National Institute on Deafness and Other Communication Disorders (NIDCD) grants R01 DC016409-01A1, 1R21DC019457-01, and 2R01 DC003896-21 (PI Anthony Ricci) for NG and 2R01 DC003896-21 (PI Anthony Ricci) for DÓ. The Stanford Nano Shared Facilities were supported by the NSF award ECCS-2026822.

# ACKNOWLEDGMENTS

We thank Teresa Nicolson, Anthony Ricci, and Bertrand Coste for discussions and suggestions about the study, and Sriram Hemachandran for reagents. We would like also to thank Shari and Kenneth Eberts, the Oberndorf Family, and the Stanford Initiative to Cure Hearing Loss for their support.

# SUPPLEMENTARY MATERIAL

The Supplementary Material for this article can be found online at: https://www.frontiersin.org/articles/10.3389/fcell.2021.742529/full#supplementary-material

**Supplementary Figure 1 |** Stereociliary heights differ little between live-stained and mildly-fixed conditions. Points of the same color correspond to stereocilia of the same hair bundle, but color schemes differ between conditions and rows. Data is presented at a higher magnification below each plot. **(A)** Stereociliary heights for all stereocilia are shown from P11 WT IHCs in live Di-4 and mildly-fixed phalloidin conditions. Row 1 Di-4 and phalloidin heights are statistically different, but the percentage difference is small ($P = 0.0027$, percentage difference = $-4 \pm 13\%$ relative to Di-4). Row 2 Di-4 and phalloidin heights are not statistically different ($P = 0.22$). **(B)** Stereociliary heights averaged per hair bundle are shown from P11 WT IHCs in live Di-4 and mildly-fixed phalloidin conditions. Row 1 Di-4 and phalloidin heights are not statistically different ($P = 0.21$). Row 2 Di-4 and phalloidin heights are not statistically different ($P = 0.32$). **(C)** Stereociliary heights for all stereocilia are shown from P11 WT IHCs in live FM 4-64FX and mildly-fixed phalloidin conditions. Row 1 FM 4-64FX and phalloidin heights are statistically different, but the percentage difference is small ($P < 0.0001$, percentage difference = $-4 \pm 13\%$ relative to FM 4-64FX). Row 2 FM 4-64FX and phalloidin heights are statistically different, but the percentage difference is highly uncertain ($P < 0.0001$, percentage difference = $22 \pm 33\%$ relative to FM 4-64FX). **(D)** Stereocilia heights averaged per hair bundle are shown from P11 WT IHCs in live FM 4-64FX and mildly-fixed phalloidin conditions. Row 1 FM 4-64FX and phalloidin heights are statistically different, but the percentage difference is small ($P = 0.017$, percentage difference = $-4 \pm 7\%$ relative to FM 4-64FX). Row 2 FM 4-64FX and phalloidin heights are statistically different, but the percentage difference is highly uncertain ($P < 0.0001$, percentage difference = $22 \pm 19\%$ relative to FM 4-64FX). Horizontal lines indicate comparisons using the Mann-Whitney U test: ns $P > 0.05$, *$P < 0.05$, **$P < 0.01$, ***$P < 0.001$, ****$P < 0.0001$.

**Supplementary Figure 2 |** Stereociliary height coefficient of variation per hair bundle and stereociliary height relative to row 1 stereociliary position. Coefficients of variation (SD/mean) are shown for row 1 **(A)** and row 2 **(B)** stereociliary heights from P11 WT IHCs live-stained with Di-4 or FM 4-64FX or mildly fixed and stained with phalloidin Alexa488 (36 hair bundles, 3 cochleae, 3 animals for Di-4; 25 hair bundles, 3 cochleae, 3 animals for phalloidin; 18 hair bundles, 2 cochleae, 2 animals for FM 4-64FX; 33 hair bundles, 2 cochleae, 2 animals for phalloidin). **(C)** Row 1 stereocilia are labeled with respect to the column forming the notch, which is at position 0 (**Figure 5**). An example of a phalloidin-Alexa488 mildly-fixed P11 IHC hair bundle (FM 4-64X) is labeled with the heights of each row 1 stereocilium. Note that the difference in height between the tallest and shortest row 1 stereocilium is more than 2 μm. Scale bars: 2 μm. **(D)** Row 1 stereociliary heights group by their position within the bundle are shown from phalloidin-Alexa488 mildly-fixed P11 IHCs (33 hair bundles, 2 cochleae, 2 animals) (Litter 2). The phalloidin heights of the position 0 and the position 1 stereocilia are statistically different, but the percentage differences are highly uncertain (stereociliary height: position 0: $4.40 \pm 0.54$ μm; position 1: $4.95 \pm 0.41$ μm; percentage difference = $-11 \pm 14\%$ relative to position 1). **(E)** The heights of the position 1 and the last stereocilia within a hair bundle wing are compared. The comparison is based on measurements of phalloidin-Alexa488 mildly-fixed P11 IHCs (33 hair bundles, 2 cochleae, 2 animals) (Litter 2). The phalloidin heights of the position 1 and the last position stereocilia are statistically different, but the percentage differences are highly uncertain (stereociliary height: position 1: $4.95 \pm 0.41$ μm; last stereocilium: $4.01 \pm 0.75$ μm; percentage difference = $-19 \pm 17\%$ relative to position 1). Horizontal lines indicate comparisons using the Mann-Whitney U test: ****$P < 0.0001$.

**Supplementary Figure 3 |** Comparisons of stereociliary heights from phalloidin and live-stained conditions. **(A)** Row 1 but not row 2 stereociliary heights from P11 WT IHCs with phalloidin-labeling in two independent litters are different owing to developmental variability between litters, but the percentage difference is highly uncertain ($P < 0.0001$ for both row 1 and 2, row 1 percentage difference = $-14 \pm 10\%$ relative to Litter 1, row 2 percentage difference = $-8 \pm 25\%$ relative to Litter 1). **(B)** Average stereociliary height per hair bundle is shown from P11 WT IHCs with phalloidin-labeling in two independent litters. Row 1 and 2 heights are statistically different between the two litters (row 1: $P < 0.0001$, percentage difference = $-14 \pm 6\%$ relative to Litter 1; row 2: $P = 0.0056$, difference = $-8 \pm 16\%$ relative to Litter 1), but the row 2 percentage difference is too small and uncertain to be biologically important. **(C)** Stereociliary heights are shown from P11 WT IHCs with live staining in two independent litters ($P < 0.0001$ both row 1 and 2, row 1 percentage difference = $-13 \pm 15\%$ relative to Litter 1, row 2 percentage difference = $-27 \pm 29\%$ relative to Litter 1). Although the heights are statistically different, the percentage differences are highly uncertain. **(D)** Average stereociliary height per hair bundle is shown from P11 WT IHCs with live staining in two independent litters ($P < 0.0001$ both row 1 and 2, row 1 percentage difference $-13 \pm 11\%$ relative to Litter 1, row 2 percentage difference = $-27 \pm 22\%$ relative to Litter 1). Although the heights are statistically different, the percentage differences are highly uncertain. Magenta lines indicate means ± SDs. Horizontal lines indicate comparisons using the Mann-Whitney U test: **$P < 0.01$, ****$P < 0.0001$.

**Supplementary Figure 4 |** The width of a cylindrical stereociliary section must be measured in 3-D. **(A)** A cylinder's cross section is shown delimited by two planes perpendicular to a cylinder's axis. **(B)** Viewed from the cylinder's axis, a perpendicular cross section appears circular with a uniform perimeter thickness. The ends of a line (black) used to measure the cylinder's width are placed on the perimeter's midsection. The line is chosen to pass though the center of the cylinder's cavity. **(C)** A cross section is shown delimited by two planes oblique to the cylinder's axis. **(D)** Viewed from the cylinder's axis, an oblique cross section appears oval with a nonuniform perimeter thickness. The ends of a line (black) used to measure the cylinder's width are placed on the perimeter's midsection. The line is chosen to be the shortest line that passes through the center of the cylinder's cavity. **(B,D)** Light from planes perpendicular to the cylinder's axis increase the apparent perimeter thickness in 2-D, which creates error in the determination of the cylinder's width in 2-D.

**Supplementary Figure 5 |** Stereociliary widths differ little between Di-4 and FM 4-64FX conditions. Points of the same color correspond to the same hair bundle, but row 1 and 2 color schemes differ between conditions and row. **(A)** Stereociliary widths are shown from P11 WT IHCs live-stained with Di-4 or FM 4-64FX. Data is presented at a higher magnification below each plot. Row 1 Di-4 and FM 4-64FX widths are not statistically different ($P = 0.23$). Row 2 Di-4 and FM 4-64FX widths are not statistically different ($P = 0.054$). **(B)** Stereociliary widths averaged per hair bundle are shown from P11 WT IHCs live-stained with Di-4 or FM 4-64FX. Row 1 Di-4 and FM 4-64FX widths are not statistically different ($P = 0.52$). Row 2 Di-4 and FM 4-64FX widths are not statistically different ($P = 0.077$). Horizontal lines indicate comparisons using the Mann-Whitney U test: ns $P > 0.05$.

**Supplementary Figure 6 |** Schematics for SEM-height determination from paired images. **(A)** A stereocilium is represented by the vector **(A)** in a coordinate frame with an xy-plane coincident with an SEM-image plane. The projection **(A)′** onto the image plane is at an angle $\theta_A$ relative to the x-axis. Rotating the sample counterclockwise around the x-axis changes the coordinates such that the stereocilium is now represented by the vector **(B)**. The projection **(B)′** onto the image plane is at an angle $\theta_B$ relative to the x-axis. **(B)** A stereocilium, represented by **(A)**, has a projection **(A)′** that obscures the base of a taller stereocilium's projection onto the image plane. The vector **(C)′** represents the visible part of the obscured stereocilium in an SEM image and is the projection of the vector **(C)** onto the image plane. The apical surface plane of the hair cell is related to the image plane by a counterclockwise rotation though the angle $\varphi$ . The points N and M on the surface have projections $N'$ and $M'$ onto the image plane, such that the line through $N'$ and $M'$ is perpendicular to the x-axis. A line through **(C)** intersects the surface at the point Q. The distance from Q to the point C is the true height of the obscured stereocilium.

**Supplementary Figure 7 |** Stereociliary width comparison between live, mildly-fixed phalloidin stained, and SEM-prepared samples. **(A)** A cartoon depicts stereociliary cross sections, upon which width measurements are based, corresponding to different sample-preparation methods. Virtual sections were taken through 3-D reconstructed fluorescently labeled hair bundles below row 2's stereociliary tips. In Di-4 and FM 4-64FX live conditions, the staining labels the membrane, forming a ring. In phalloidin-488 mildly-fixed samples, the staining labels the actin core ensheathed by the stereociliary membrane, resulting in an filled-circle narrower than the membranous ring. In SEM preparation, the sample shrinks and the membrane is removed by the dehydration procedure. The dehydrated sample is coated with a thin layer of metal for imaging. **(B)** A representative virtual section trough a phalloidin-488 mildly-fixed hair bundle used for width measurements. Scale bar: 0.5 μm. **(C)** Stereociliary widths are shown from P11 WT IHCs live-stained with Di-4 (row 1: 172 stereocilia, row 2: 149 stereocilia, 3 cochleae, 3 animals), live-stained with FM 4-64FX (row 1: 101 stereocilia, row 2: 90 stereocilia, 2 cochleae, 2 animals), mildly-fixed with phalloidin

(Di-4 litter: row 1: 210 stereocilia, row 2: 189 stereocilia, 3 cochleae, 3 animals) (FM 4-64FX litter: row 1: 318 stereocilia, row 2: 250 stereocilia, 2 cochleae, 2 animals), or prepared for SEM (Di-4 litter: row 1: 119 stereocilia, row 2: 136 stereocilia, 2 cochleae, 2 animals) (FM 4-64FX litter: row 1: 96 stereocilia, row 2: 100 stereocilia, 2 cochleae, 2 animals) (row 1: Di-4 vs. Phall: $P < 0.0001$, percentage difference = $-18 \pm 14\%$ relative to Di-4; Di-4-paired Phall vs. SEM: $P < 0.0001$, percentage difference = $-17 \pm 14\%$ relative to Phall; FM 4-64FX vs. Phall: $P < 0.0001$, percentage difference = $-12 \pm 15\%$ relative to FM; FM-paired-Phall vs. SEM: $P < 0.0001$, percentage difference = $-25 \pm 15\%$ relative to Phall; row 2: Di-4 vs. Phall: $P < 0.0001$, percentage difference = $-20 \pm 14\%$ relative to Di-4; Di-4-paired-Phall vs. SEM: $P < 0.0001$, percentage difference = $-14 \pm 14\%$ relative to Di-4; FM 4-64FX vs. Phall: $P < 0.0001$, percentage difference = $-16 \pm 15\%$ relative to FM; FM-paired-Phall vs. SEM: $P < 0.0001$, percentage difference = $22 \pm 15\%$ relative to Phall). Although the widths are statistically different, most of the percentage differences are highly uncertain. **(D)** Averages of stereociliary widths per bundle are shown from P11 WT IHCs live-stained with Di-4 (rows 1 and 2: 18 hair bundle, 3 cochleae, 3 animals), live-stained with FM 4-64FX (rows 1 and 2: 14 hair bundles, 2 cochleae, 2 animals), mildly-fixed with phalloidin (Di-4 litter: rows 1 and 2: 18 hair bundles, 3 cochleae, 3 animals) (FM 4-64FX litter: rows 1 and 2: 26 hair bundles, 2 cochleae, 2 animals), or prepared for SEM (Di-4 litter. rows 1 and 2: 18 hair bundles, 2 cochleae, 2 animals), (FM 4-64FX litter. rows 1 and 2: 17 hair bundles, 2 cochleae, 2 animals) (row 1: Di-4 vs. Phall: $P < 0.0001$, percentage difference = $-18 \pm 8\%$ relative to Di-4; Di-4-paired-Phall vs. SEM: $P < 0.0001$, percentage difference = $-18 \pm 8\%$ relative to Phall; FM 4-64FX vs. Phall: $P < 0.0001$, percentage difference = $-13 \pm 10\%$ relative to FM 4-64FX; FM 4-64FX -paired-Phall vs. SEM: $P < 0.0001$, percentage difference = $-24 \pm 9\%$ relative to FM 4-64FX; row 2: Di-4 vs. Phall: $P < 0.0001$, percentage difference = $-20 \pm 9\%$ relative to Di-4; Di-4-paired Phall vs. SEM: $P < 0.0001$, percentage difference = $-14 \pm 10\%$ relative to Phall; FM 4-64FX vs. Phall: $P < 0.0001$, percentage difference = $-16 \pm 8\%$ relative to FM 4-64FX; FM 4-64FX -paired-Phall vs. SEM: $P < 0.0001$, percentage difference = $-21 \pm 9\%$ relative to Phall). Although the widths are statistically different, some of the percentage differences are highly uncertain. Horizontal lines indicate comparisons using the Mann-Whitney U test: $^{****}P < 0.0001$.

**Supplementary Figure 8 |** Schematics for fluid-coupling calculations. The cross sections of a pair of neighboring stereocilia with radii $r_a$ and $r_b$ are moving relative to each other with velocity **U** along the line connecting their centers. The gap g (y) between the stereocilia depends on the y-coordinate and has a minimum value $g_m$. The distances $g_a$ and $g_b$ between the y-axis and the stereocilia are used to derive the fluid-coupling force opposing their relative motion.

**Supplementary Movies |** Stereociliary height measurements in representative 3-D reconstructed hair bundles.

**Supplementary Movie 1 |** 3D-reconstructed hair bundles from Di4 live imaging – height measurements.

**Supplementary Movie 2 |** 3D-reconstructed hair bundles from Phalloidin-Alexa488 mildly-fixed imaging – height measurements.

**Supplementary Movie 3 |** 3D-reconstructed hair bundles from FM 4-64FX live imaging – height measurements.

**Supplementary Movie 4 |** 3D-reconstructed hair bundles from Di4 live imaging – width measurements.

**Supplementary Movie 5 |** 3D-reconstructed hair bundles from FM 4-64FX live imaging – width measurements.

**Supplementary Movie 6 |** 3D-reconstructed hair bundles from Phalloidin-Alexa488 mildly-fixed imaging – insertion point separation measurements.

## REFERENCES


Asai, Y., Pan, B., Nist-Lund, C., Galvin, A., Lukashkin, A. N., Lukashkina, V. A., et al. (2018). Transgenic Tmc2 expression preserves inner ear hair cells and vestibular function in mice lacking Tmc1. *Sci. Rep.* 8:12124. doi: 10.1038/s41598-018-28958-x

Bagger-Sjöbäck, D., and Takumida, M. (1988). Geometrical array of the vestibular sensory hair bundle. *Acta Otolaryngol.* 106, 393–403. doi: 10.3109/00016488809122262

Bartsch, T. F., Hengel, F. E., Oswald, A., Dionne, G., Chipendo, I. V., Mangat, S. S., et al. (2019). Elasticity of individual protocadherin 15 molecules implicates tip links as the gating springs for hearing. *Proc. Natl. Acad. Sci. U. S. A.* 166, 11048–11056. doi: 10.1073/pnas.1902163116

Batschelet, E. (1981). *Circular Statistics in Biology*. New York, NY: Academic Press.

Baumgart, J. (2011). *The Hair Bundle: Omniscriptum*. New York, NY: Suedwestdeutscher Verlag fuer Hochschulschriften.

Beurg, M., Cui, R., Goldring, A. C., Ebrahim, S., Fettiplace, R., and Kachar, B. (2018). Mechanotransducer Channels Underlie Tonotopic Conductance Gradients in the Cochlea. *Nat. Commun.* 9:2185. doi: 10.1038/s41467-018-04589-8

Beurg, M., Evans, M. G., Hackney, C. M., and Fettiplace, R. (2006). A Large-Conductance Calcium-Selective Mechanotransducer Channel in Mammalian Cochlear Hair Cells. *J. Neurosci.* 26, 10992–11000. doi: 10.1523/JNEUROSCI.2188-06.2006

Beurg, M., Nam, J.-H., Crawford, A., and Fettiplace, R. (2008). The actions of calcium on hair bundle mechanics in mammalian cochlear hair cells. *Biophys. J.* 94, 2639–2653. doi: 10.1529/biophysj.107.123257

Bozzola, J. J., and Russell, L. (1992). *Electron Microscopy*, 2nd Edn. Boston, MA: John and Bartlett Publishers.

Cartagena-Rivera, A. X., Le Gal, S., Richards, K., Verpy, E., and Chadwick, R. S. (2019). Cochlear outer hair cell horizontal top connectors mediate mature stereocilia bundle mechanics. *Sci. Adv.* 5:eaat9934. doi: 10.1126/sciadv.aat9934

Ciganović, N., Wolde-Kidan, A., and Reichenbach, T. (2017). Hair bundles of cochlear outer hair cells are shaped to minimize their fluid-dynamic resistance. *Sci. Rep.* 7, 1–9. doi: 10.1038/s41598-017-03773-y

Comis, S. D., Pickles, J. O., and Osborne, M. P. (1985). Osmium tetroxide postfixation in relation to the crosslinkage and spatial organization of stereocilia in the guinea-pig cochlea. *J. Neurocytol.* 14, 113–130. doi: 10.1007/BF01150266

Corey, D. P., and Hudspeth, A. J. (1983). Kinetics of the receptor current in bullfrog saccular hair cells. *J. Neurosci.* 3, 962–976. doi: 10.1523/jneurosci.03-05-00962.1983

Corey, D. P., Ó Maoiléidigh, D., and Ashmore, J. F. (2017). "Mechanical Transduction Processes in the Hair Cell," in *Understanding the Cochlea*, Vol. 62, eds G. Manley, A. Gummer, A. Popper, and R. Fay (Cham: Springer).

Corns, L. F., Johnson, S. L., Roberts, T., Ranatunga, K. M., Hendry, A., Ceriani, F., et al. (2018). Mechanotransduction is required for establishing and maintaining mature inner hair cells and regulating efferent innervation. *Nat. Commun.* 9:4015. doi: 10.1038/s41467-018-06307-w

Crawford, A. C., and Fettiplace, R. (1985). The mechanical properties of ciliary bundles of turtle cochlear hair cells. *J. Physiol.* 364, 359–379. doi: 10.1113/jphysiol.1985.sp015750

Crawford, B. Y. A. C., Evans, M. G., and Fettiplace, R. (1989). Activation and adaptation of transducer currents in turtle hair cells. *J Physiol.* 419, 405–434. doi: 10.1113/jphysiol.1989.sp017878

Davis, H. (1965). A model for transducer action in the cochlea. *Cold Spring Harb. Symp. Quant. Biol.* 30, 181–190. doi: 10.1101/sqb.1965.030.01.020

DeRosier, D. J., Tilney, L. G., and Egelman, E. (1980). Actin in the inner ear: The remarkable structure of the stereocilium. *Nature* 287, 291–296. doi: 10.1038/287291a0

Drummond, M. C., Barzik, M., Bird, J. E., Zhang, D., Lechene, C. P., Corey, D. P., et al. (2015). Live-cell imaging of actin dynamics reveals mechanisms of stereocilia length regulation in the inner ear. *Nat. Commun.* 6, 1–10. doi: 10.1038/ncomms7873

Duvall, A. J., Flock, A., and Wersäll, J. (1966). The ultrastructure of the sensory hairs and associated organelles of the cochlear inner hair cell, with reference to directional sensitivity. *J. Cell Biol.* 29, 497–505. doi: 10.1083/jcb.29.3.497

Edge, R. M., Evans, B. N., Pearce, M., Richter, C. P., Hu, X., and Dallos, P. (1998). Morphology of the unfixed cochlea. *Hear. Res.* 124, 1–16. doi: 10.1016/s0378-5955(98)00090-2

Engström, H., and Engström, B. (1978). Structure of the hairs on cochlear sensory cells. *Hear. Res.* 1, 49–66.

Fettiplace, R. (2017). Hair cell transduction, tuning, and synaptic transmission in the mammalian cochlea. *Compr. Physiol.* 7, 1197–1227. doi: 10.1002/cphy.c160049

Flock, A., and Cheung, H. C. (1977). Actin filaments in sensory hairs of inner ear receptor cells. *J. Cell Biol.* 75, 339–343. doi: 10.1083/jcb.75.2.339

Forge, A., Davies, S., and Zajic, G. (1988). Characteristics of the membrane of the stereocilia and cell apex in cochlear hair cells. *J. Neurocytol.* 17, 325–334. doi: 10.1007/bf01187855

Forge, A., Davies, S., and Zajic, G. (1991). Assessment of ultrastructure in isolated cochlear hair cells using a procedure for rapid freezing before freeze-fracture and deep-etching. *J. Neurocytol.* 20, 471–484. doi: 10.1007/BF01252275

Forge, A., Nevill, G., Zajic, G., and Wright, A. (1992). Scanning electron microscopy of the mammalian organ of Corti: assessment of preparative procedures. *Scanning Microsc.* 6, 521–525.

Furness, D. N., and Hackney, C. M. (1985). Cross-links between stereocilia in the guinea pig cochlea. *Hear. Res.* 18, 177–188.

Furness, D. N., and Hackney, C. M. (2006). The Structure and Composition of the Stereociliary Bundle of Vertebrate Hair Cells. *Vertebr. Hair Cells* 2006, 95–153. doi: 10.1007/0-387-31706-6_3

Furness, D. N., Mahendrasingam, S., Ohashi, M., Fettiplace, R., and Hackney, C. M. (2008). The Dimensions and Composition of Stereociliary Rootlets in Mammalian Cochlear Hair Cells: Comparison between High- and Low-Frequency Cells and Evidence for a Connection to the Lateral Membrane. *J. Neurosci.* 28, 6342–6353. doi: 10.1523/JNEUROSCI.1154-08.2008

Furness, D. N., Zetes, D. E., Hackney, C. M., and Steele, C. R. (1997). Kinematic analysis of shear displacement as a means for operating mechanotransduction channels in the contact region between adjacent stereocilia of mammalian cochlear hair cells. *Proc. R. Soc. B Biol. Sci.* 264, 45–51. doi: 10.1098/rspb.1997.0007

Gagnon, L. H., Longo-Guess, C. M., Berryman, M., Shin, J.-B., Saylor, K. W., Yu, H., et al. (2006). The chloride intracellular channel protein CLIC5 is expressed at high levels in hair cell stereocilia and is essential for normal inner ear function. *J. Neurosci.* 26, 10188–10198. doi: 10.1523/JNEUROSCI.2166-06.2006

Galeano-Naranjo, C., Catalina Veléz-Ortega, A., and Frolenkov, G. I. (2021). Stereocilia bundle imaging with nanoscale resolution in live mammalian auditory hair cells. *J. Vis. Exp.* 167:e62104.

Garfinkle, T. J., and Saunders, J. C. (1983). Morphology of inner hair cell stereocilia in C57BL/6J mice as studied by scanning electron microscopy. *Otolaryngol. Neck Surg.* 91, 421–426. doi: 10.1177/019459988309100415

Geisler, C. D. (1993). A model of stereociliary tip-link stretches. *Hear. Res.* 65, 79–82. doi: 10.1016/0378-5955(93)90203-d

George, S. S., Steele, C. R., and Ricci, A. J. (2020). Rat Auditory Inner Hair Cell Mechanotransduction and Stereociliary Membrane Diffusivity Are Similarly Modulated by Calcium. *iScience* 23:101773. doi: 10.1016/j.isci.2020.101773

Gianoli, F., Risler, T., and Kozlov, A. S. (2017). Lipid bilayer mediates ion-channel cooperativity in a model of hair-cell mechanotransduction. *Proc. Natl. Acad. Sci. U.S.A.* 114, E11010–E11019. doi: 10.1073/pnas.1713135114

Gulley, R. L., and Reese, T. S. (1977). Regional specialization of the hair cell plasmalemma in the organ of corti. *Anat. Rec.* 189, 109–123. doi: 10.1002/ar.1091890108

Hackney, C. M., and Furness, D. N. (2013). The composition and role of cross links in mechanoelectrical transduction in vertebrate sensory hair cells. *J. Cell Sci.* 126, 1721–1731.

Hackney, C. M., Fettiplace, R., and Furness, D. N. (1993). The functional morphology of stereociliary bundles on turtle cochlear hair cells. *Hear. Res.* 69, 163–175.

Hadi, S., Alexander, A. J., Vélez-Ortega, A. C., and Frolenkov, G. I. (2020). Myosin-XVa Controls Both Staircase Architecture and Diameter Gradation of Stereocilia Rows in the Auditory Hair Cell Bundles. *JARO J. Assoc. Res. Otolaryngol.* 21, 121–135. doi: 10.1007/s10162-020-00745-4

Holme, R. H., and Steel, K. P. (2002). Stereocilia defects in waltzer (Cdh23), shaker1 (Myo7a) and double waltzer/shaker1 mutant mice. *Hear. Res.* 169, 13–23. doi: 10.1016/s0378-5955(02)00334-9

Holme, R. H., Kiernan, B. W., Brown, S. D. M., and Steel, K. P. (2002). Elongation of hair cell stereocilia is defective in the mouse mutant whirler. *J. Comp. Neurol.* 450, 94–102.

Howard, J., and Ashmore, J. F. (1986). Stiffness of sensory hair bundles in the sacculus of the frog. *Hear. Res.* 23, 93–104.

Howard, J., and Hudspeth, A. J. (1987). Mechanical relaxation of the hair bundle mediates adaptation in mechanoelectrical transduction by the bullfrog's saccular hair cell. *Proc. Natl. Acad. Sci. U.S.A.* 84, 3064–3068. doi: 10.1073/pnas.84.9.3064

Howard, J., and Hudspeth, A. J. (1988). Compliance of the hair bundle associated with gating of mechanoelectrical transduction channels in the Bullfrog's saccular hair cell. *Neuron* 1, 189–199. doi: 10.1016/0896-6273(88)90139-0

Hughes, I., and Hase, T. (2010). *Measurements and Their Uncertainties: A Practical Guide to Modern Error Analysis*. Oxford: Oxford University Press.

Hunter-Duvar, I. M. (1978). A technique for preparation of cochlear specimens for assessment with the scanning electron microscope. *Acta Otolaryngol.* 85, 3–23. doi: 10.3109/00016487809122718

Jacobo, A., and Hudspeth, A. J. (2014). Reaction-diffusion model of hair-bundle morphogenesis. *Proc. Natl. Acad. Sci. U. S. A.* 111, 15444–15449. doi: 10.1073/pnas.1417420111

Jacobs, R. A., and Hudspeth, A. J. (1990). Ultrastructural correlates of mechanoelectrical transduction in hair cells of the bullfrog's internal ear. *Cold Spring Harb. Symp. Quant. Biol.* 55, 547–561. doi: 10.1101/sqb.1990.055.01.053

Jeffries, D. J., Pickles, J. O., Osborne, M. P., Rhys-Evans, P. H., and Comis, S. D. (1986). Crosslinks between stereocilia in hair cells of the human and guinea pig vestibular labyrinth. *J. Laryngol. Otol.* 100, 1367–1374. doi: 10.1017/s002221510010115x

Jensen, O. A., Prause, J. U., and Laursen, H. (1981). Shrinkage in preparatory steps for SEM - A study on rabbit corneal endothelium. *Albrecht Von Graefes Arch. Klin. Exp. Ophthalmol.* 215, 233–242. doi: 10.1007/BF00407662

Kaltenbach, J. A., Falzarano, P. R., and Simpson, T. H. (1994). Postnatal development of the hamster cochlea. II. Growth and differentiation of stereocilia bundles. *J. Comp. Neurol.* 350, 187–198. doi: 10.1002/cne.903500204

Karavitaki, K. D., and Corey, D. P. (2010). Sliding adhesion confers coherent motion to hair cell stereocilia and parallel gating to transduction channels. *J. Neurosci.* 30, 9051–9063. doi: 10.1523/JNEUROSCI.4864-09.2010

Kikkawa, Y. S., Pawlowski, K. S., Wright, C. G., and Alagramam, K. N. (2008). Development of outer hair cells in Ames waltzer mice: Mutation in protocadherin 15 affects development of cuticular plate and associated structures. *Anat. Rec.* 291, 224–232.

Kim, K. X., and Fettiplace, R. (2013). Developmental changes in the cochlear hair cell mechanotransducer channel and their regulation by transmembrane channel–like proteins. *J. Gen. Physiol.* 141, 141–148. doi: 10.1085/jgp.201210913

Kozlov, A. S., Baumgart, J., Risler, T., Versteegh, C. P. C., and Hudspeth, A. J. (2011). Forces between clustered stereocilia minimize friction in the ear on a subnanometre scale. *Nature* 474, 376–379. doi: 10.1038/nature10073

Krey, J. F., Chatterjee, P., Dumont, R. A., O'Sullivan, M., Choi, D., Bird, J. E., et al. (2020). Mechanotransduction-Dependent Control of Stereocilia Dimensions and Row Identity in Inner Hair Cells. *Curr. Biol.* 30, 442.e–454.e. doi: 10.1016/j.cub.2019.11.076

Lavigne-Rebillard, M., and Pujol, R. (1986). Development of the auditory hair cell surface in human fetuses. A scanning electron microscopy study. *Anat. Embryol.* 174, 369–377. doi: 10.1007/bf00698787

Lavigne-Rebillard, M., and Pujol, R. (1987). Surface aspects of the developing human organ of Corti. *Acta Otolaryngol. Suppl.* 436, 43–50.

Lavigne-Rebillard, M., and Pujol, R. (1990). Auditory hair cells in human fetuses: synaptogenesis and ciliogenesis. *J. Electron Microsc. Tech.* 15, 115–122. doi: 10.1002/jemt.1060150204

Lelli, A., Asai, Y., Forge, A., Holt, J. R., and Géléoc, G. S. G. (2009). Tonotopic gradient in the developmental acquisition of sensory transduction in outer hair cells of the mouse cochlea. *J. Neurophysiol.* 101, 2961–2973. doi: 10.1152/jn.00136.2009

Lelli, A., Michel, V., De Monvel, J. B., Cortese, M., Bosch-Grau, M., Aghaie, A., et al. (2016). Class III myosins shape the auditory hair bundles by limiting microvilli and stereocilia growth. *J. Cell Biol.* 212, 231–244. doi: 10.1083/jcb.201509017

Li, S., Mecca, A., Kim, J., Caprara, G. A., Wagner, E. L., Du, T. T., et al. (2020). Myosin-VIIa is expressed in multiple isoforms and essential for tensioning the hair cell mechanotransduction complex. *Nat. Commun.* 11, 1–15. doi: 10.1038/s41467-020-15936-z

Lim, D. J. (1980). Cochlear anatomy related to cochlear micromechanics. A review. *J. Acoust. Soc. Am.* 67, 1686–1695. doi: 10.1121/1.384295

Lim, D. J. (1986). Functional structure of the organ of Corti: a review. *Hear. Res.* 22, 117–146. doi: 10.1016/0378-5955(86)90089-4

Lim, D. J., and Anniko, M. (1985). Developmental morphology of the mouse inner ear: A scanning electron microscopic observation. *Acta Otolaryngol.* 99, 5–69.

Liu, Y., Qi, J., Chen, X., Tang, M., Chu, C., Zhu, W., et al. (2019). Critical role of spectrin in hearing development and deafness. *Sci. Adv.* 5:eaav7803. doi: 10.1126/sciadv.aav7803

Milewski, A. R., Ó Maoiléidigh, D., Salvi, J. D., and Hudspeth, A. J. (2017). Homeostatic enhancement of sensory transduction. *Proc. Natl. Acad. Sci. U. S. A.* 114, E6794–E6803. doi: 10.1093/oso/9780198835028.003.0001

Müller, M., Von Hünerbein, K., Hoidis, S., and Smolders, J. W. T. (2005). A physiological place-frequency map of the cochlea in the CBA/J mouse. *Hear. Res.* 202, 63–73. doi: 10.1016/j.heares.2004.08.011

Mulroy, M. J. (1974). Cochlear anatomy of the alligator lizard. *Brain. Behav. Evol.* 10, 69–87. doi: 10.1159/000124303

Nam, J. H., Peng, A. W., and Ricci, A. J. (2015). Underestimated Sensitivity of Mammalian Cochlear Hair Cells Due to Splay between Stereociliary Columns. *Biophys. J.* 108, 2633–2647. doi: 10.1016/j.bpj.2015.04.028

Nordestgaard, B. G., and Rostgaard, J. (1985). Dimensional changes of isolated hepatocytes during processing for scanning and transmission electron microscopy. *Micron Microsc. Acta* 16, 65–75.

Ó Maoiléidigh, D., and Hudspeth, A. J. (2013). Effects of cochlear loading on the motility of active outer hair cells. *Proc. Natl. Acad. Sci. U. S. A.* 110, 5474–5479. doi: 10.1073/pnas.1302911110

Ó Maoiléidigh, D., and Ricci, A. J. (2019). A Bundle of Mechanisms: Inner-Ear Hair-Cell Mechanotransduction. *Trends Neurosci.* 42, 221–236.

Osborne, M. P., Comis, S. D., and Pickles, J. O. (1984). Morphology and cross-linkage of stereocilia in the guinea-pig labyrinth examined without the use of osmium as a fixative. *Cell Tissue Res.* 237, 43–48. doi: 10.1007/BF00229198

Pan, B., Géléoc, G. S., Asai, Y., Horwitz, G. C., Kurima, K., Ishikawa, K., et al. (2013). TMC1 and TMC2 are components of the mechanotransduction channel in hair cells of the mammalian inner ear. *Neuron* 79, 504–515.

Peterson, E. H., Cotton, J. R., and Grant, J. W. (1996). Structural variation in ciliary bundles of the posterior semicircular canal. Quantitative anatomy and computational analysis. *Ann. N. Y. Acad. Sci.* 781, 85–102. doi: 10.1111/j.1749-6632.1996.tb15695.x

Petit, C., and Richardson, G. P. (2009). Linking genes underlying deafness to hair-bundle development and function. *Nat. Neurosci.* 12, 703–710.

Pickles, J. O. (1993). A model for the mechanics of the stereociliar bundle on acousticolateral hair cells. *Hear. Res.* 68, 159–172. doi: 10.1016/0378-5955(93)90120-p

Pickles, J. O., Comis, S. D., and Osborne, M. P. (1984). Cross-links between stereocilia in the guinea pig organ of Corti, and their possible relation to sensory transduction. *Hear. Res.* 15, 103–112. doi: 10.1016/0378-5955(84)90041-8

Powers, R. J., Kulason, S., Atilgan, E., Brownell, W. E., Sun, S. X., Barr-Gillespie, P. G., et al. (2014). The local forces acting on the mechanotransduction channel in hair cell stereocilia. *Biophys. J.* 106, 2519–2528. doi: 10.1016/j.bpj.2014.03.034

Powers, R. J., Roy, S., Atilgan, E., Brownell, W. E., Sun, S. X., Gillespie, P. G., et al. (2012). Stereocilia Membrane Deformation: Implications for the Gating Spring and Mechanotransduction Channel. *Biophys. J.* 102, 201–210. doi: 10.1016/j.bpj.2011.12.022

Ricci, A. J., Cochran, S. L., Rennie, K. J., and Correia, M. J. (1997). Vestibular type I and type II hair cells. 2: Morphometric comparisons of dissociated pigeon hair cells. *J. Vestib. Res.* 7, 407–420. doi: 10.3233/ves-1997-7504

Richardson, G. P., and Petit, C. (2019). Hair-bundle links: Genetics as the gateway to function. *Cold Spring Harb. Perspect. Med.* 9:a033142. doi: 10.1101/cshperspect.a033142

Roth, B., and Bruns, V. (1992). Postnatal development of the rat organ of Corti - II. Hair cell receptors and their supporting elements. *Anat. Embryol.* 185, 571–581. doi: 10.1007/BF00185616

Rowe, M. H., and Peterson, E. H. (2004). Quantitative analysis of stereociliary arrays on vestibular hair cells. *Hear. Res.* 190, 10–24. doi: 10.1016/s0378-5955(03)00395-2

Santi, P. A., and Anderson, C. B. (1987). A newly identified surface coat on cochlear hair cells. *Hear. Res.* 27, 47–65. doi: 10.1016/0378-5955(87)90025-6

Schermelleh, L., Ferrand, A., Huser, T., Eggeling, C., Sauer, M., Biehlmaier, O., et al. (2019). Super-resolution microscopy demystified. *Nat. Cell Biol.* 21, 72–84. doi: 10.1038/s41556-018-0251-8

Severinsen, S. Å, Jørgensen, J. M., and Nyengaard, J. R. (2003). Structure and Growth of the Utricular Macula in the Inner Ear of the Slider Turtle Trachemys scripta. *JARO J. Assoc. Res. Otolaryngol.* 4, 505–520. doi: 10.1007/s10162-002-3050-6

Smith, S. T., and Chadwick, R. S. (2011). Simulation of the response of the inner hair cell stereocilia bundle to an acoustical stimulus. *PLoS One* 6, 2–6. doi: 10.1371/journal.pone.0018161

Souter, M., Nevill, G., and Forge, A. (1995). Postnatal development of membrane specialisations of gerbil outer hair cells. *Hear. Res.* 91, 43–62.

Tarchini, B., Tadenev, A. L. D., Devanney, N., and Cayouette, M. (2016). A link between planar polarity and staircase-like bundle architecture in hair cells. *Dev* 143, 3926–3932. doi: 10.1242/dev.139089

Taylor, R., Bullen, A., Johnson, S. L., Grimm-Günter, E. M., Rivero, F., Marcotti, W., et al. (2015). Absence of plastin 1 causes abnormal maintenance of hair cell stereocilia and a moderate form of hearing loss in mice. *Hum. Mol. Genet.* 24, 37–49. doi: 10.1093/hmg/ddu417

Thompson, R. E., Larson, D. R., and Webb, W. W. (2002). Precise nanometer localization analysis for individual fluorescent probes. *Biophys. J.* 82, 2775–2783. doi: 10.1016/s0006-3495(02)75618-x

Tilney, L. G., and DeRosier, D. J. (1986). Actin filaments, stereocilia, and hair cells of the bird cochlea. IV. How the actin filaments become organized in developing stereocilia and in the cuticular plate. *Dev. Biol.* 116, 119–129. doi: 10.1016/0012-1606(86)90048-5

Tilney, L. G., and Saunders, J. C. (1983). Actin filaments, stereocilia, and hair cells of the bird cochlea I. Length, number, width, and distribution of stereocilia of each hair cell are related to the position of the hair cell on the cochlea. *J. Cell Biol.* 96, 807–821. doi: 10.1083/jcb.96.3.807

Tilney, L. G., Derosier, D. J., and Mulroy, M. J. (1980). The organization of actin filaments in the stereocilia of cochlear hair cells. *J. Cell Biol.* 86, 244–259. doi: 10.1083/jcb.86.1.244

Tilney, L. G., Tilney, M. S., and Cotanche, D. A. (1988). Actin filaments, stereocilia, and hair cells of the bird cochlea. V. How the staircase pattern of stereociliary lengths is generated. *J. Cell Biol.* 106, 355–365. doi: 10.1083/jcb.106.2.355

Tobin, M., Chaiyasitdhi, A., Michel, V., Michalski, N., and Martin, P. (2019). Stiffness and tension gradients of the hair cell's tip-link complex in the mammalian cochlea. *Elife* 8, 1–25. doi: 10.7554/eLife.43473

Trouillet, A., Miller, K. K., George, S. S., Wang, P., Ali, N.-E.-S., Ricci, A., et al. (2021). Loxhd1 Mutations Cause Mechanotransduction Defects in Cochlear Hair Cells. *J. Neurosci.* 41, 3331–3343. doi: 10.1523/JNEUROSCI.0975-20.2021

Tsuprun, V., and Santi, P. (1998). Structure of outer hair cell stereocilia links in the chinchilla. *J. Neurocytol.* 27, 517–528.

Tsuprun, V., and Santi, P. (2002). Structure of outer hair cell stereocilia side and attachment links in the chinchilla cochlea. *J. Histochem. Cytochem.* 50, 493–502. doi: 10.1177/002215540205000406

Tsuprun, V., Schachern, P. A., Cureoglu, S., and Paparella, M. (2003). Structure of the stereocilia side links and morphology of auditory hair bundle in relation to noise exposure in the chinchilla. *J. Neurocytol.* 32, 1117–1128. doi: 10.1023/B:NEUR.0000021906.08847.d2

Vélez-Ortega, A. C., and Frolenkov, G. I. (2016). Visualization of live cochlear stereocilia at a nanoscale resolution using hopping probe ion conductance microscopy. *Methods Mol. Biol.* 1427, 203–221. doi: 10.1007/978-1-4939-3615-1_12

Vélez-Ortega, A. C., Freeman, M. J., Indzhykulian, A. A., Grossheim, J. M., and Frolenkov, G. I. (2017). Mechanotransduction current is essential for stability of the transducing stereocilia in mammalian auditory hair cells. *Elife* 6, 1–22. doi: 10.7554/eLife.24661

von Diezmann, L., Shechtman, Y., and Moerner, W. E. (2017). Three-Dimensional Localization of Single Molecules for Super-Resolution Imaging and Single-Particle Tracking. *Chem. Rev.* 117, 7244–7275. doi: 10.1021/acs.chemrev.6b00629

Waguespack, J., Salles, F. T., Kachar, B., and Ricci, A. J. (2007). Stepwise morphological and functional maturation of mechanotransduction in rat outer hair cells. *J. Neurosci.* 27, 13890–13902. doi: 10.1523/JNEUROSCI.2159-07.2007

Wakiya, S. (1975). Application of Bipolar Coordinates to the Two-Dimensional Creeping Motion of a Liquid. II. Some Problems for Two Circular Cylinders in Viscous Fluid. *J. Phys. Soc. Japan* 39:113.

Wang, Y., Steele, C. R., Puria, S., and Ricci, A. J. (2021). In situ motions of individual inner-hair-cell stereocilia from stapes stimulation in adult mice. *Commun. Biol.* 4:958. doi: 10.1038/s42003-021-02459-6

Webb, S. W., Grillet, N., Andrade, L. R., Xiong, W., Swarthout, L., Della Santina, C. C., et al. (2011). Regulation of PCDH15 function in mechanosensory hair cells by alternative splicing of the cytoplasmic domain. *Development* 138, 1607–1617.

Wersall, J. (1956). Studies on the structure and innervation of the sensory epithelium of the cristae ampulares in the guinea pig; a light and electron microscopic investigation. *Acta Otolaryngol. Suppl.* 126, 1–85.

Wright, A. (1981). Scanning electron microscopy of the human cochlea–the organ of Corti. *Arch. Otorhinolaryngol.* 230, 11–19. doi: 10.1007/BF00665375

Wright, A. (1984). Dimensions of the cochlear stereocilia in man and the guinea pig. *Hear. Res.* 13, 89–98. doi: 10.1016/0378-5955(84)90099-6

Xiong, W., Grillet, N., Elledge, H. M., Wagner, T. F. J., Zhao, B., Johnson, K. R., et al. (2012). TMHS is an integral component of the mechanotransduction machinery of cochlear hair cells. *Cell* 151, 1283–1295.

Xue, J., and Peterson, E. H. (2006). Hair bundle heights in the utricle: Differences between macular locations and hair cell types. *J. Neurophysiol.* 95, 171–186. doi: 10.1152/jn.00800.2005

Yarin, Y. M., Lukashkin, A. N., Poznyakovskiy, A. A., Meißner, H., Fleischer, M., Baumgart, J., et al. (2014). Tonotopic morphometry of the lamina reticularis of the guinea pig cochlea with associated microstructures and related mechanical implications. *JARO J. Assoc. Res. Otolaryngol.* 15, 1–11. doi: 10.1007/s10162-013-0420-1

Zampini, V., Rüttiger, L., Johnson, S. L., Franz, C., Furness, D. N., Waldhaus, J., et al. (2011). Eps8 regulates hair bundle length and functional maturation of mammalian auditory hair cells. *PLoS Biol.* 9:e1001048. doi: 10.1371/journal.pbio.1001048

Zetes, D. E. (1995). *Mechanical and Morphological Study of the Stereocilia Bundle in the Mammalian Auditory System*. Ph. D. thesis. Stanford, CA: Stanford University.

Zetes, D. E., and Steele, C. R. (1997). Fluid–structure interaction of the stereocilia bundle in relation to mechanotransduction. *J. Acoust. Soc. Am.* 101, 3593–3601. doi: 10.1121/1.418320

Zetes, D. E., Tolomeo, J. A., and Holley, M. C. (2012). Structure and Mechanics of Supporting Cells in the Guinea Pig Organ of Corti. *PLoS One* 7:e49338. doi: 10.1371/journal.pone.0049338

Zine, A., and Romand, R. (1996). Development of the auditory receptors of the rat: A SEM study. *Brain Res.* 721, 49–58. doi: 10.1016/0006-8993(96)00147-3

**Conflict of Interest:** The authors declare that the research was conducted in the absence of any commercial or financial relationships that could be construed as a potential conflict of interest.

**Publisher's Note:** All claims expressed in this article are solely those of the authors and do not necessarily represent those of their affiliated organizations, or those of the publisher, the editors and the reviewers. Any product that may be evaluated in this article, or claim that may be made by its manufacturer, is not guaranteed or endorsed by the publisher.

*Copyright © 2021 Miller, Atkinson, Mendoza, Ó Maoiléidigh and Grillet. This is an open-access article distributed under the terms of the Creative Commons Attribution License (CC BY). The use, distribution or reproduction in other forums is permitted, provided the original author(s) and the copyright owner(s) are credited and that the original publication in this journal is cited, in accordance with accepted academic practice. No use, distribution or reproduction is permitted which does not comply with these terms.*

frontiers in Cell and Developmental Biology

ORIGINAL RESEARCH
published: 30 November 2021
doi: 10.3389/fcell.2021.709442

# Actin Crosslinking Family Protein 7 Deficiency Does Not Impair Hearing in Young Mice

*Benjamin L. Gilbert[1,2†], Shaoyuan Zhu[1,2†], Ahlam Salameh[1†], Shenyu Sun[1,2], Kumar N. Alagramam[1] and Brian M. McDermott Jr.[1,2,3,4*]*

[1] Department of Otolaryngology–Head and Neck Surgery, Case Western Reserve University School of Medicine, Cleveland, OH, United States, [2] Department of Biology, Case Western Reserve University, Cleveland, OH, United States, [3] Department of Genetics and Genome Sciences, Case Western Reserve University School of Medicine, Cleveland, OH, United States, [4] Department of Neurosciences, Case Western Reserve University School of Medicine, Cleveland, OH, United States

To enable hearing, the sensory hair cell contains specialized subcellular structures at its apical region, including the actin-rich cuticular plate and circumferential band. ACF7 (actin crosslinking family protein 7), encoded by the gene *Macf1* (microtubule and actin crosslinking factor 1), is a large cytoskeletal crosslinking protein that interacts with microtubules and filamentous actin to shape cells. ACF7 localizes to the cuticular plate and the circumferential band in the hair cells of vertebrates. The compelling expression pattern of ACF7 in hair cells, combined with conserved roles of this protein in the cytoskeleton of various cell types in invertebrates and vertebrates, led to the hypothesis that ACF7 performs a key function in the subcellular architecture of hair cells. To test the hypothesis, we conditionally target *Macf1* in the inner ears of mice. Surprisingly, our data show that in young, but mature, conditional knockout mice cochlear hair cell survival, planar cell polarity, organization of the hair cells within the organ of Corti, and capacity to hear are not significantly impacted. Overall, these results fail to support the hypothesis that ACF7 is an essential hair cell protein in young mice, and the purpose of ACF7 expression in the hair cell remains to be understood.

**Keywords: hair cell, hearing, MACF1, microtubule-actin crosslinking factor 1, ACF7, ABR (auditory brainstem response), cuticular plate**

OPEN ACCESS

***Edited by:***
*Zhigang Xu,*
*Shandong University, China*

***Reviewed by:***
*Guoqiang Wan,*
*Nanjing University, China*
*Jeremy Duncan,*
*Western Michigan University, United States*

****Correspondence:***
*Brian M. McDermott Jr.*
*bmm30@case.edu*

*† These authors have contributed equally to this work*

***Specialty section:***
*This article was submitted to Cell Growth and Division, a section of the journal Frontiers in Cell and Developmental Biology*

***Received:*** *13 May 2021*
***Accepted:*** *01 September 2021*
***Published:*** *30 November 2021*

***Citation:***
*Gilbert BL, Zhu S, Salameh A, Sun S, Alagramam KN and McDermott BM Jr (2021) Actin Crosslinking Family Protein 7 Deficiency Does Not Impair Hearing in Young Mice. Front. Cell Dev. Biol. 9:709442. doi: 10.3389/fcell.2021.709442*

## INTRODUCTION

In mammals, the mechanosensitive hair cells in the cochlea of the inner ear are responsible for hearing (Hudspeth, 2005). These cells convert mechanical stimuli associated with pressure changes in the air into electrical responses that are forwarded to the brain. In the cochlea, hair cells are arranged into three rows of outer hair cells (OHCs) and one row of inner hair cells (IHCs) in a particular polarity axis, establishing a specific planar cell polarity (PCP) (May-Simera and Kelley, 2012; Ezan and Montcouquiol, 2013). Disruption of hair cell PCP, ototoxic or noise-induced damage to hair cells, or a decrease in their numbers cause sensorineural hearing loss (Petit and Richardson, 2009; Walsh et al., 2010; Lu and Sipe, 2016).

Hair cells each have a precise array of actin-based stereocilia that insert into a dense actin-based meshwork known as the cuticular plate (Pollock and McDermott, 2015). Proteins that

shape the stereocilia are required for hearing and balance (Petit and Richardson, 2009; Richardson et al., 2011). Furthermore, proteins that regulate actin and microtubule filaments may be essential for establishing the cuticular plate and PCP (Goodrich and Strutt, 2011; Copley et al., 2013). Yet, little is known about the roles the proteins that shape the cuticular plate play in hearing and balance. Moreover, the function of the cuticular plate itself with regard to hair bundle development, maintenance, and function is unclear. One potential function is that the cuticular plate provides rigidity to the apical surface of the hair cell to anchor the stereocilia in place (Pollock and McDermott, 2015; Pacentine et al., 2020).

Actin crosslinking family protein 7 (ACF7), encoded by mouse microtubule actin cross-linking factor 1 (*Macf1*), is a member of the spectraplakin family of proteins and contains an F-actin-binding domain near the N-terminus and a microtubule-binding domain near the C-terminus (Suozzi et al., 2012; Goryunov and Liem, 2016; Hu et al., 2016; Zhang et al., 2017). ACF7 is widely expressed across the tissues of metazoans, displaying significant evolutionary conservation (Voelzmann et al., 2017). Previously, we demonstrated in both zebrafish and mouse hair cells that ACF7 reliably localizes to the cuticular plate, the circumferential band, and additionally coats the lumen of the fonticulus, a region that holds the basal body, an organelle subjacent to the kinocilium (Antonellis et al., 2014). The subcellular localization of ACF7 and its ability to bind both actin and microtubule filaments suggest that ACF7 could be involved in integrating cytoskeletal elements to apical structures, a union that may be essential for the cell's integrity and function. ACF7 additionally may be necessary in the formation and maintenance of the cuticular plate (Kodama et al., 2003; Brown, 2008). Recent studies on conditionally targeted mice using a *Foxg1-Cre* driver and floxed *Macf1* showed that ACF7 is required for normal kinocilium length in the cochlea (May-Simera et al., 2016). However, since these mice die at E18.5, it is unknown if ACF7 is required in the mature mouse for hair cell structure or hearing.

Herein, we investigate the role of ACF7 in hearing and the hair cell's structure and function by conditionally targeting ACF7 in mouse hair cells. Our results suggest that a deficiency in ACF7 does not significantly impact hair cell structure or function.

# MATERIALS AND METHODS

## Mouse Husbandry

Protocols for housing and handling of mice were approved by Case Western Reserve University's Institutional Animal Care and Use Committee. CD1 *Pax2-Cre* [Tg(Pax2-cre)1Akg] mice (Ohyama and Groves, 2004) were obtained from the Mutant Mouse Resource & Research Center (stock #10569). We used $Macf1^{fl/-}$ (Wu et al., 2008), $Macf1^{fl/+}$, $Macf1^{fl/fl}$, and $Macf1^{+/-}$; *Pax2-Cre* mouse lines. Each strain was outcrossed with FVB/NJ mice for at least seven generations. Specifically, C57BL/6 $Macf1^{fl/fl}$ mice were outcrossed to FVB/NJ mice (Wu et al., 2008). In addition, to improve the likelihood of Cre-mediated recombination in the cochlea, we generated a germline transmissible knockout allele by crossing $Macf1^{fl/+}$ with BALB/c *CMV-Cre* mice (Tg(CMV-Cre)1Cgn/J obtained from the Jackson Laboratory stock #003465), with resulting $Macf1^{+/-}$; *CMV-Cre* offspring outcrossed to FVB/NJ mice (Schwenk et al., 1995) for more than seven generations before use in generating experimental data. Note, early publications of $Macf1^{fl}$ describe *loxP* sites flanking exons 6 and 7 (Wu et al., 2008); however, after modern genomic analyses, the *loxP* sites were shown to flank exons 11 and 13. Ai3-YFP [$Gt(ROSA)26Sor^{tm3(CAG-EYFP)Hze}$] (Madisen et al., 2010) reporter mice were crossed to *Pax2-Cre* mice. One-month old or P5 mice of either sex were used for experiments.

## Mice Genotyping

Mouse genotypes were determined by a standard PCR amplification procedure (Truett et al., 2000). Floxed and wildtype *Macf1* alleles were genotyped using forward primer (F1′: 5′-AAAGAAACGGAAATACTGGCC-3′; exon 10) and reverse primer (R1′: 5′-GCAGCTTAATTCTGCCAAATTC-3′; exon 11). $T_{A(annealing)}$ = 56°C; $T_{E(extension)}$ = 1 min. The *Macf1* knock out (KO) allele was separately genotyped using the forward primer F1′ with reverse primer targeting exon 14 (R2′: 5′-AAAGAAACGGAAATACTGGCC-3′; $T_A$ = 50°C; $T_E$ = 2.5 min) (Fassett et al., 2013). The *Pax2-Cre* allele was genotyped with the primer pair F′ (5′-GCCTGCATTACCGGTCGATGCAACGA-3′) and R′ (5′-GTGGCAGATGGCGCGGCAACACCATT-3′). $T_A$ = 67°C; $T_E$ = 1 min (Truett et al., 2000). PCR was conducted in a thermocycler (Applied Biosystems™ SimpliAmp™ Thermal Cycler and on a Bio-Rad PTC-200 DNA Engine® Cycler).

## Cochlear Labeling and Imaging

One-month old mice cochleae were dissected and fixed in 4% paraformaldehyde in 1× phosphate-buffered saline (PBS) overnight at 4°C. Apical, middle, and basal turns of cochleae were defined according to **Supplementary Figure 1** (Gilels et al., 2017). The tissue was rinsed three times in 1× PBS for 10 min each and decalcified with 1 mM ethylenediaminetetraacetic acid (EDTA) at 4°C for 2–3 days. Cochleae were blocked and permeabilized simultaneously with 0.05% Triton-X100 (Sigma) and 10% goat serum solution in 1× PBS for 2 h at room temperature. To visualize cells, the tissue was washed and labeled with anti-myosin7a (Proteus Biosciences, Inc.) primary antibody at a 1:500 dilution with blocking solution at 4°C overnight. After three, 5-min washes in blocking solution, tissue was labeled with secondary antibodies at a 1:1,000 dilution for Alexa Fluor 488 IgG (Invitrogen) and a 1:70 dilution for Alexa Fluor 633 phalloidin (Invitrogen) at 4°C overnight, washed, mounted (ProLong Diamond Antifade Mountant), and imaged on a TCS SP8 confocal microscope (Leica). Ai3-YFP/*Pax2-Cre* mice were imaged at an excitation wavelength of 512 nm for YFP.

Whole-mount immunolabeling of cochleae was performed with anti-ACF7 (Karakesisoglou et al., 2000) and mouse anti-acetylated tubulin (T6793; Sigma) as described by Pataky et al. (2004), with modifications being a 1 h fixation, 2 h permeabilization, and 2 h blocking (1% bovine serum albumin)

(Pataky et al., 2004). Anti-ACF7 rabbit polyclonal antiserum against amino acids 1,622–1,817 of a partial sequence of the primary ACF7 isoform was used (Bernier et al., 1996; Karakesisoglou et al., 2000). Anti-ACF7 and anti-acetylated tubulin were used at a 1:100 dilution overnight at 4°C. Treatment with goat anti-rabbit and anti-mouse Alexa Fluor 488 IgG (1:200) and Alexa Fluor 633 phalloidin (1:50) occurred for 2 h at room temperature. Mounting and imaging were conducted as above.

## Cell Enumeration and Organelle Length Measurement

For hair cell enumeration, outer and inner hair cells were manually counted using LAS X software (Leica). A hair cell was considered present when the hair bundle and cuticular plate were observed and myosin7a signal detected (Raphael and Altschuler, 1991; Anttonen et al., 2014; Monzack et al., 2015). We used the hair cells from the entire cochlea for calculations. To calculate the percent of present hair cells we used: % hair cells present = present hair cells/(missing + present hair cells) × 100. For organelle length measurements, we measured kinocilia of all useable cells from the apical turn in a confocal series similar to methods described by May-Simera et al. (2016). Kinocilium length measurements of hair cells labeled with anti-acetylated tubulin in P5 mice were obtained with LAS X software (Leica).

## Auditory-Evoked Brainstem Response (ABR)

Mice of one month of age were anesthetized with a ketamine hydrochloride and xylazine hydrochloride solution (100 and 20 mg/kg, respectively) via intraperitoneal injection, and kept on a homeothermic heating pad at 37°C for the duration of sedation. Platinum subdermal needle electrodes were placed below the pinna of the left and right ears to record the ABRs, and on the back of the mice for electrical grounding (Akil et al., 2016; Geng et al., 2017). Electrical responses of the cochlear ganglion neurons and the nuclei were recorded at different levels of pure tone frequencies played for 100 ms at 8, 16, and 32 kHz (Intelligent Hearing System SmartEP 4.20 system). The lowest sound pressure level (SPL) that could generate an electrical response at the ABR thresholds of these different frequencies was considered. To evaluate if the lack of ACF7 has an impact on ABR thresholds, *Macf1*$^{fl/-}$*; Pax2-Cre* mice were tested with control littermates under the same testing conditions. The intensities of SPL ranged from 100 dB SPL to 20 dB SPL, in 10 dB SPL intervals, and the responses were averaged over 1,024 sweeps. Tones were presented to mice via high-frequency transducers placed in the ear, with ABRs recorded in a soundproofed and closed, free-field system. ABR thresholds were determined post-procedure by identifying the lowest stimulus level that yielded a detectable ABR waveform at various time points.

## Statistics and Analysis

All statistics were performed with GraphPad Prism version 8. Data are reported as mean ± SEM or SD. Comparisons between groups were tested with unpaired two-tailed Student's *t*-tests. R-Studio was used to generate circular histograms (RStudio, Inc.).

# RESULTS

## Generation of a *Macf1* Conditional Knockout in the Ear

To understand the requirement of ACF7 in hair cells of mammals, we used a genetic approach. Because mice that lack ACF7 die pre-implantation (Kodama et al., 2003; Chen et al., 2006), we conditionally targeted the associated gene by using the genetically modified mouse *Macf1*$^{fl/-}$, which has two *loxP* sites flanking a region encompassing exons 11 through 13 (Wu et al., 2008). This genetic strain has been successful in revealing the role of the ACF7 protein as a cytoskeletal integrator in other cell types as deletion of these exons are predicted to shift the coding sequence of downstream exons and has been shown to produce cells that are devoid of ACF7 (Fassett et al., 2013). In addition, we applied a strategy that used a *Pax2-Cre* allele as a Cre-driver line. Pax2 is expressed throughout the otic placode at E9.5 and thus should excise exons that are in-between *loxP* sites in all of the cells in the developing inner ear, including the hair cells in the cochlea (Ohyama and Groves, 2004; **Figure 1**).

Initially, to visualize Cre expression in the organ of Corti, *Pax2-Cre* mice were crossed with the Cre recombinase reporter Ai3-YFP (Madisen et al., 2010). In Ai3-YFP, transcription of the YFP reporter only occurs following Cre mediated excision of a premature stop codon. We observed YFP expression in most inner and outer hair cells (**Figure 1B**), indicating that the Pax2 driver has the spatial and temporal expression to knock out ACF7 in hair cells.

To determine if this stratagem was effective at eliminating ACF7 from hair cells, we labeled the organ of Corti of *Macf1*$^{fl/-}$*; Pax2-Cre* and control mice with ACF7 antiserum and phalloidin to mark the actin of the cuticular plate (Karakesisoglou et al., 2000). In control inner hair cells, ACF7 localized to the cuticular plate and the circumferential band; however, the target protein was absent from inner hair cell cuticular plates and circumferential bands in the *Macf1*$^{fl/-}$*; Pax2-Cre* mice, demonstrating that this gene targeting strategy was successful (**Figure 1C**). We did not observe labeling of outer hair cells in control and experimental groups. This could be because of different mounting procedures. Here, we use whole-mount labeling; however, previously we labeled cultured cochleae, indicating that labeling of outer hair cells may be sensitive to the immunological procedure (Antonellis et al., 2014). Since labeling of the cuticular plate and circumferential band is absent in inner hair cells, the conditional targeting strategy was effective.

## ACF7 Deficiency Does Not Affect Hair Cell Survival

To determine if the presence of ACF7 is required for the survival of hair cells in any of the three turns of the cochlea, tissue of *Macf1*$^{fl/-}$*; Pax2-Cre* and control mice were labeled for myosin7a

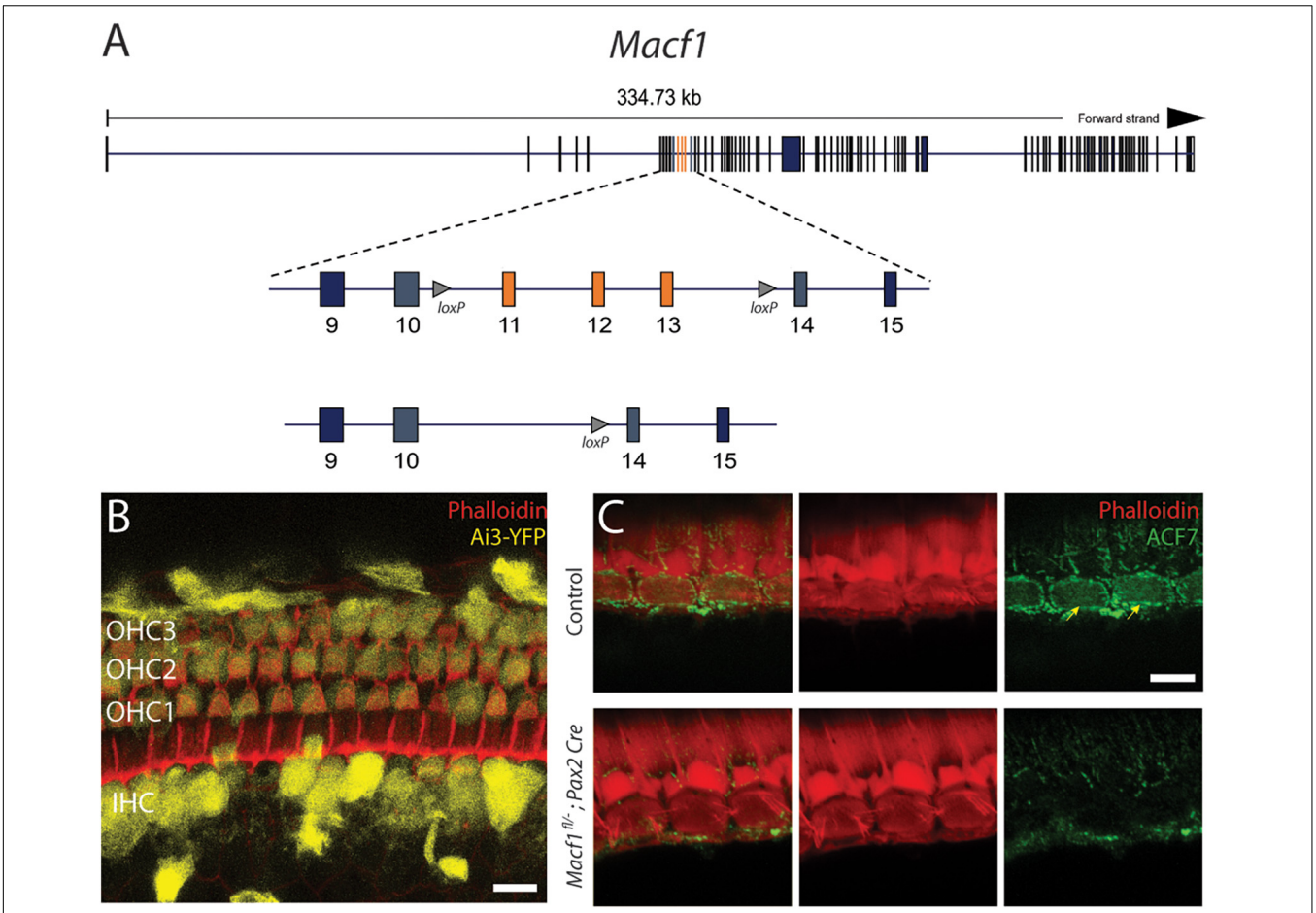


**FIGURE 1 |** Conditional gene ablation of *Macf1* in mouse inner ear hair cells. **(A) (top)** Schematic of the *Macf1* genomic locus. **(middle)** Enlarged view of exons 9–15 are displayed. Exons 11–13 (orange) are flanked by *loxP* sites (triangles). **(B)** Representative confocal micrograph of a segment of the apical turn (∼8 kHz) of a cochlea from a Cre reporter Ai3-YFP mouse at one month of age that expresses Cre driven by the *Pax2* promoter, generated to determine the efficacy of Cre-mediated recombination in hair cells. Cells that express YFP (yellow) indicate successful Cre-mediated recombination. Hair cells of the cochlea express YFP. Phalloidin (red) labels actin of cells. Scale bar = 10 μm. **(C)** Representative confocal micrographs of IHCs from the middle turns (∼16 kHz) of cochleae of one-month old mice labeled with anti-ACF7 antibody [**(top)** sibling control; **(bottom)** *Macf1*$^{fl/-}$; *Pax2-Cre*)]. Anti-ACF7 and phalloidin depicted in green and red, respectively. Arrows show cuticular plates with ACF7 antibody labeling. Hair bundles that appear missing are present but out of focus. Scale bar = 5 μm.

and for actin using phalloidin (**Figure 2**). *Macf1*$^{fl/-}$; *Pax2-Cre* mice are indistinguishable from their littermate controls, showing no apparent defects in the organ of Corti in either hair cells or supporting cells (**Figures 2A–F**). Quantification of hair cells between *Macf1*$^{fl/-}$; *Pax2-Cre* and control littermates in one-month old mice revealed similar numbers of hair cells (**Figures 2G,H**), indicating that ACF7 is not required for hair cell survival in any of the cochlear turns.

## Hair Cell PCP Is Unperturbed in ACF7 Deficient Organ of Corti

Since ACF7 has a compelling localization pattern in and around the cuticular plate, we tested the hypothesis that this protein may be involved in PCP. *Macf1*$^{fl/-}$; *Pax2-Cre* mice and littermate controls were examined for defects in PCP by labeling actin followed by a hair bundle orientational assay on the organ of Corti (**Figures 3A,A′,B,B′**). The orientation of individual stereociliary bundles at the approximate midpoints along the lengths of the cochleae (**Figures 3D,E**) were measured and plotted in circular histograms (**Figure 3C**). Average bundle deviation from the midlateral axis of hair bundles across different animals were measured for *Macf1*$^{fl/-}$; *Pax2-Cre* mice and control mice (**Figure 3F**). In each row, OHC1, OHC2, OHC3, or IHC, there was no significant difference in the average stereociliary bundle deviation between the *Macf1*$^{fl/-}$; *Pax2-Cre* mice and the controls.

## ACF7 Deficiency Reduces Kinocilium Length in Postnatal Mice

In prenatal mice, ACF7 is required for normal kinocilia lengths (May-Simera and Kelley, 2012). Therefore, we tested if kinocilia lengths were altered in P5 *Macf1*$^{fl/-}$; *Pax2-Cre* mice, a timepoint during cochlear development that was chosen because it is before the kinocilia degenerate (Wang and Zhou, 2021) but

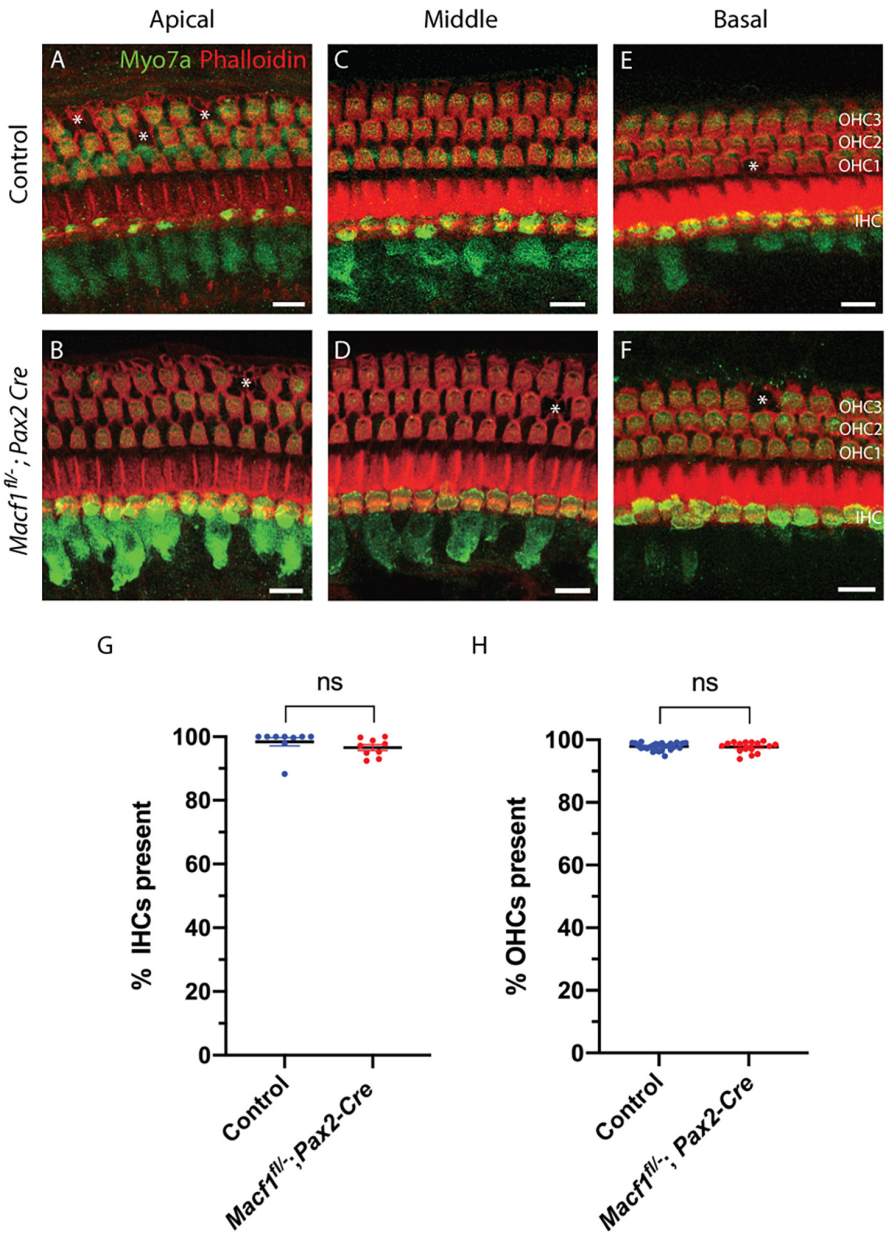


**FIGURE 2 |** Hair cell viability is not impacted by conditional ablation of *Macf1*. **(A,C,E)** Micrographs of cochlear hair cells of control animals along apical **(A)** (*Macf1*$^{fl/+}$*; Pax2-Cre*), middle **(B)** (*Macf1*$^{fl/-}$), and basal **(C)** (*Macf1*$^{fl/-}$) segments of the organ of Corti. **(B,D,F)** Images of cochleae from conditional knockout animals along the apical, middle, and basal segments. Myosin7a and phalloidin localization displayed in green and red, respectively. Each missing outer hair cell is indicated by an asterisk. **(G,H)** Mean percentages ± SEM of inner **(G)** ($p$ = 0.26, $n$ = 9 cochleae from 7 *Macf1*$^{fl/-}$ mice, $n$ = 9 cochleae from 6 *Macf1*$^{fl/-}$; *Pax2-Cre* mice) and outer **(H)** ($p$ = 0.76, $n$ = 26 cochleae from 18 *Macf1*$^{fl/-}$ mice, $n$ = 16 cochleae from 11 *Macf1*$^{fl/-}$; *Pax2-Cre* mice) hair cells present. Each data point represents one cochlea. Scale bar = 10 μm.

should still also reflect defects in kinocilia formation if they do exist in these conditional knockout animals. Using anti-acetylated tubulin to label the kinocilia and confocal microscope software for measurements, we showed that the mean length of kinocilia from control mice is 2.49 ± 0.02 μm (mean ± SEM) (**Figure 4**). In contrast, the mean length of kinocilia from the *Macf1*$^{fl/-}$; *Pax2-Cre* mice is 2.20 ± 0.01 μm. The significant reduction of mean kinocilium length in the conditional knockout mice demonstrates that ACF7 is required for normal kinocilium length after birth.

## ACF7 Deficiency Does Not Affect Hearing

To further investigate whether the lack of ACF7 has an impact on inner hair cell function, we compared ABR thresholds of *Macf1*$^{fl/-}$*; Pax2-Cre* mice to littermate control mice. We

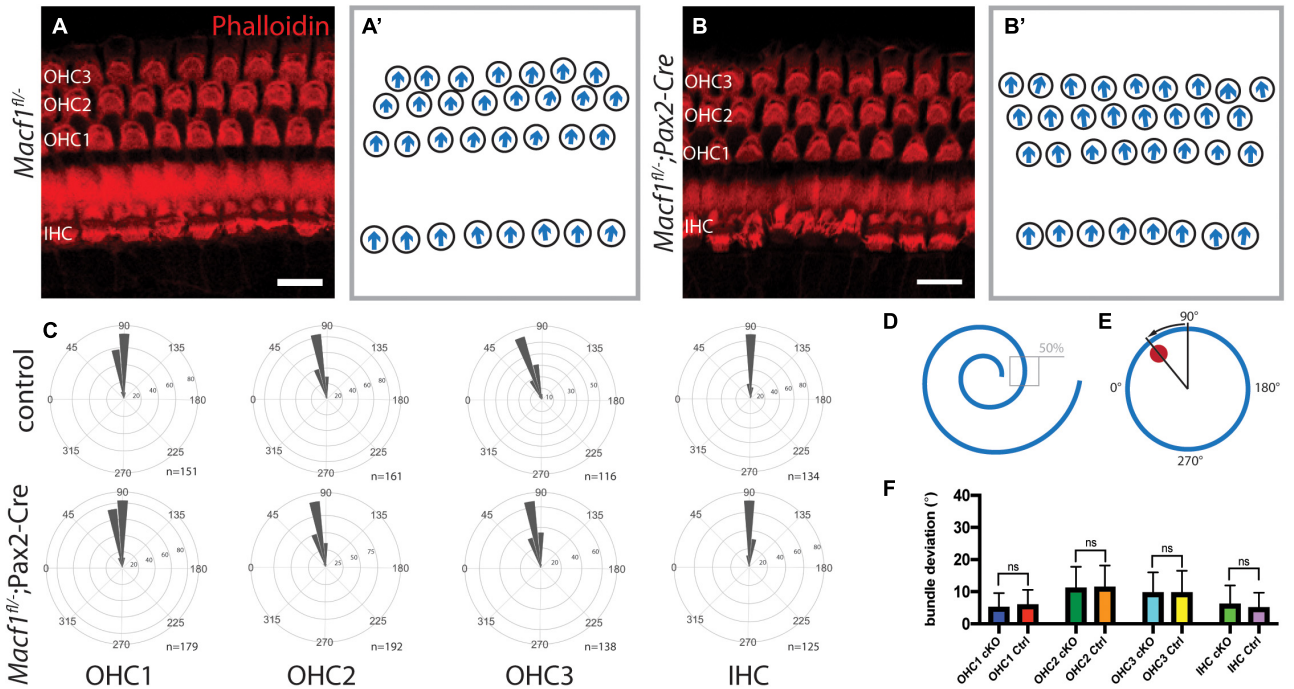


**FIGURE 3 |** Auditory hair cell PCP is not affected in *Macf1*$^{fl/-}$*; Pax2-Cre* mice. **(A,A′,B,B′)** Cochlear hair cells of one-month old mice, labeled with phalloidin (red), demonstrate hair bundle orientations. **(A,B)** Maximum projections of stacks of confocal images and **(A′,B′)** associated schematics of hair bundle orientations. The stacks are centered around the cuticular plate level and do not capture the full bundle lengths of all cells, but are meant to reveal PCP only. **(C)** Orientations of stereociliary bundles plotted on circular histograms for all hair cells from the middle turn of the cochlea (∼50% cochlear length). 0° is directed toward the apical turn of the cochlea, and 180° is toward the base. Bin width is 10°. The total number of represented hair cells is shown by each histogram (*n*). Scale bars = 10 μm. **(D)** Schematic indicating the region located at ∼50% along the length of a cochlea for stereociliary bundle orientation analyses. **(E)** A representative schematic of a single hair bundle demonstrating the angular measurement for quantifying stereociliary bundle deviation. The red dot marks the position of the kinocilium, and the arrow shows the deviation. **(F)** Averaged bundle deviation from the mediolateral axis of a hair bundle for *Macf1*$^{fl/-}$; *Pax2-Cre* (cKO) and control mice. For orientation and bundle deviation assays, the number of mice analyzed is $n = 5$ for *Macf1*$^{fl/-}$; *Pax2-Cre* and $n = 4$ ($n = 2$ for *Macf1*$^{fl/-}$, $n = 2$ for *Macf1*$^{fl/+}$; *Pax2-Cre*) for controls. Error bars show standard deviation. There is no statistical significance between *Macf1*$^{fl/-}$; *Pax2-Cre* and control mice. Calculated using a two-tailed Student's *t*-test ($p = 0.129$ for OHC1, $p = 0.678$ for OHC2, $p = 0.959$ for OHC3, $p = 0.110$ for IHC).

observed no significant difference (**Figure 5**) in ABR thresholds between the two groups at one-month of age. ABR thresholds (Mean ± SEM) for the control group were 23.9 ± 2.2 (8 kHz), 29.4 ± 1.7 (16 kHz), and 30.0 ± 5 (32 kHz); in contrast, ABR thresholds for the *Macf1*$^{fl/-}$; *Pax2-Cre* group were 25.0 ± 6.6 (8 kHz), 33.8 ± 5.2 (16 kHz), and 31.3 ± 3.5 (32 kHz).

## DISCUSSION

In the present study, the role of ACF7 in hair cell structure and function was examined using the inner ear-specific conditional knockout mouse *Macf1*$^{fl/-}$; *Pax2-Cre*. Our previous data showed that in the hair cells of zebrafish and mice, ACF7 displays a compelling localization pattern in and around the cuticular plate (Antonellis et al., 2014). The expression pattern of ACF7 in hair cells combined with its role as a cytoskeleton integrator leads to the hypothesis that ACF7 is an essential hair cell protein. To our surprise, our studies showed that ACF7 deficiency does not appear to negatively impact hair cell integrity or function beyond a modest reduction in the kinocilium length, similar to what was initially reported by May-Simera et al., 2016. In agreement with these findings, young, but mature, *Macf1*$^{fl/-}$; *Pax2-Cre* mice do not exhibit hearing defects.

A recent study investigating the role of ACF7 in platelets using *Macf1*$^{fl}$ to conditionally knockout the gene also revealed that ACF7 was not required for proper function in certain contexts. These findings are relevant because, similar to hair cells, platelets have a robust cytoskeletal structure that is required for the cell to survive and function properly (Schurr et al., 2019). This suggests that both hair cells and platelets have possible redundancy of the cytoskeleton proteins to safeguard their precise structure that is essential for their function. A suitable candidate with potential redundant function in hair cells is the other member of the spectraplakin family, bullous pemphigoid antigen 1 (BPAG1), which shares a similar primary amino acid sequence similarity with ACF7 and is also expressed in cochlear hair cells (Leonova and Lomax, 2002; Voelzmann et al., 2017). *Bpag1* mutations can yield phenotypes similar to those of *Macf1* mutants (Suozzi et al., 2012; Ali et al., 2017). On a cellular level, *Bpag1* mutation is primarily categorized by severe cytoskeletal disruption in a plethora of tissues, producing distinctive neurological, muscular, and skin conditions. Interestingly, a human patient was recently

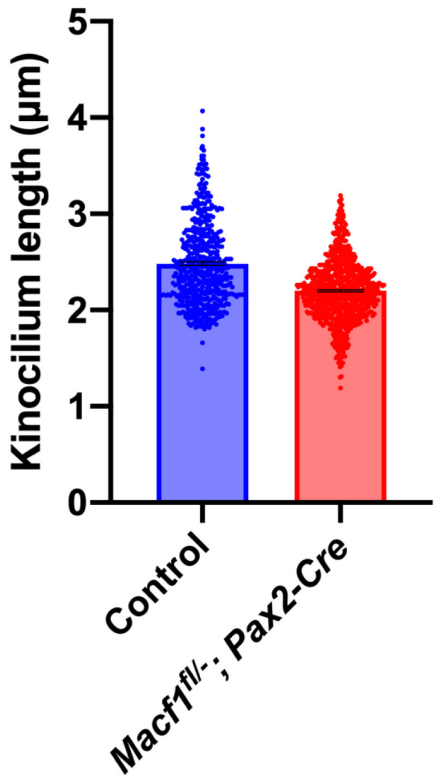


**FIGURE 4 |** Kinocilium length measurements of *Macf1*$^{fl/-}$*; Pax2-Cre* and sibling control mice. Bar graph depicts mean lengths of outer hair cell kinocilia from the apical cochlear turns of P5 mice. The control group's (blue; *Macf1*$^{fl/-}$) mean kinocilium length is 2.49 ± 0.02 µm ($n$ = 527 hair cells from 3 cochleae from 3 mice). The mean length for the conditional knockout group (red) is 2.20 ± 0.01 µm ($n$ = 766 hair cells from 3 cochleae from 3 mice). $P < 0.0001$ calculated using an unpaired Student's $t$-test.

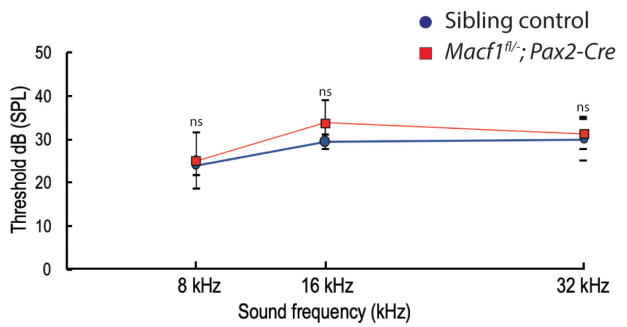


**FIGURE 5 |** Auditory brainstem response (ABR) thresholds of *Macf1*$^{fl/-}$*; Pax2-Cre* and sibling control mice. Thresholds at 8, 16, and 32 kHz show no statistical significance between *Macf1*$^{fl/-}$*; Pax2-Cre* mice and controls. $n$ = 5 control mice and $n$ = 6 *Macf1*$^{fl/-}$*; Pax2-Cre* mice. Error bars are represented as the standard deviation and significance was determined with an unpaired Student's $t$-test. dB, decibels.

identified with compound mutations for *BPAG1* that additionally resulted in the development of early and progressive bilateral hearing loss, suggesting that BPAG1 may in fact be relevant to hearing (Cappuccio et al., 2017). Given our data and the literature, it is plausible that the expression of BPAG1 in cochlear hair cells rescues the cells from what would otherwise perturb hair cells in the conditional *Macf1* knockout.

There are other possible explanations as to why there is no observable hair cell phenotype in *Macf1*$^{fl/-}$; *Pax2-Cre* mice beyond a modest reduction in kinocilium length. First, it is possible that ACF7 is not required for hair cell structure and function at all. It is also plausible that ACF7 plays a role during a small window of time during development, and there are deficits that exist during this period; however, there is recovery sometime afterward, similar to what has been observed in mutant mice that have defects in factors that govern PCP (Copley et al., 2013). Additionally, it may be that ACF7 plays a more protective role in mature hair cells, rather than a function during development. Acoustic over stimulation has the potential to permanently damage the hair cell stereocilia and hair cell function. Perhaps the localization of ACF7 to the cuticular plate provides stability to the rootlets of the stereocilia in order to render some degree of resilience to the stereocilia bundles against noise-induced damage. Additionally, the loss of ACF7 in conditional mutants may not have physiological impacts until later in life and cause the early onset of age-related hearing loss. These hypotheses could be tested in the future by evaluating the resistance of conditional knockout *Macf1* mice to noise-induced hearing loss and by studying mice at more mature time points.

In summary, there are several possible functions for ACF7 in the hair cells of mice; however, evidence to support a role for ACF7 in cochlear hair cell development and function beyond the kinocilium is lacking for the time points examined. Nevertheless, our study showed that a compelling localization pattern of a protein in hair cells may not equate to a critical role for that protein in the cell; examples in the literature are consistent with this. Specifically, annexin A5 is one of the most abundant proteins in stereocilia; however, it was found to be dispensable for stereocilia development and function (Krey et al., 2016). The purpose of ACF7 expression in hair cells beyond a role in kinocilium length remains to be understood.

## DATA AVAILABILITY STATEMENT

The raw data supporting the conclusions of this article will be made available by the authors, without undue reservation.

## ETHICS STATEMENT

The animal study was reviewed and approved by the Case Western Reserve University Institutional Animal Care and Use Committee.

## AUTHOR CONTRIBUTIONS

BG and SZ: fluorescence labeling and imaging. BG, AS, and SS: genetics. AS, BG, SZ, KA, and BM: experimental design. AS and BG: ABRs. BG, SZ, AS, KA, and BM: manuscript writing and

editing. All authors contributed to the article and approved the submitted version.

## FUNDING

This work was supported by grants DC016827 (AS), DC009437 (BM), and the Center for Clinical Research and Technology at University Hospitals Cleveland Medical Center (BM).

## ACKNOWLEDGMENTS

We would like to thank M. Basch for *Pax2-Cre* and Ai3-YFP mice and advice. C57BL/6 *Macf1*$^{fl/fl}$ mice and anti-ACF7 antiserum were generously gifted by Elaine Fuchs. We acknowledge R. Stepanyan for advice on ABR experiments and the Rhee lab for technical advice. We acknowledge the members of our laboratory who provided discussion and comments on this manuscript.

## SUPPLEMENTARY MATERIAL

The Supplementary Material for this article can be found online at: https://www.frontiersin.org/articles/10.3389/fcell.2021.709442/full#supplementary-material

**Supplementary Figure 1 |** Representative whole-mount immunofluorescence on cochleae from experimental and control mice. **(A,B)** *Macf1*$^{fl/-}$; *Pax2-Cre* and control cochleae labeled with phalloidin (red) and a myosin7a antibody (green). For display, each whole cochlea divided in two is shown minus the hook region. **(C)** Schematics of cochlear regional boundaries. Incisions were made to sever the apical and basal regions from the middle turn. The cochleae were divided isometrically. Scale bar 50 μm.

## REFERENCES

Akil, O., Oursler, A. E., Fan, K., and Lustig, L. R. (2016). Mouse auditory brainstem response testing. *Bio Protoc.* 6:e1768.

Ali, A., Hu, L., Zhao, F., Qiu, W., Wang, P., Ma, X., et al. (2017). BPAG1, a distinctive role in skin and neurological diseases. *Semin. Cell Dev. Biol.* 69, 34–39. doi: 10.1016/j.semcdb.2017.06.005

Antonellis, P. J., Pollock, L. M., Chou, S. W., Hassan, A., Geng, R., Chen, X., et al. (2014). ACF7 is a hair-bundle antecedent, positioned to integrate cuticular plate actin and somatic tubulin. *J. Neurosci.* 34, 305–312. doi: 10.1523/jneurosci.1880-13.2014

Anttonen, T., Belevich, I., Kirjavainen, A., Laos, M., Brakebusch, C., Jokitalo, E., et al. (2014). How to bury the dead: elimination of apoptotic hair cells from the hearing organ of the mouse. *J. Assoc. Res. Otolaryngol.* 15, 975–992. doi: 10.1007/s10162-014-0480-x

Bernier, G., Mathieu, M., De Repentigny, Y., Vidal, S. M., and Kothary, R. (1996). Cloning and characterization of mouse ACF7, a novel member of the dystonin subfamily of actin binding proteins. *Genomics* 38, 19–29. doi: 10.1006/geno.1996.0587

Brown, N. H. (2008). Spectraplakins: the cytoskeleton's swiss army knife. *Cell* 135, 16–18. doi: 10.1016/j.cell.2008.09.023

Cappuccio, G., Pinelli, M., Torella, A., Alagia, M., Auricchio, R., Staiano, A., et al. (2017). Expanding the phenotype of DST-related disorder: a case report suggesting a genotype/phenotype correlation. *Am. J. Med. Genet. A* 173, 2743–2746. doi: 10.1002/ajmg.a.38367

Chen, H. J., Lin, C. M., Lin, C. S., Perez-Olle, R., Leung, C. L., Liem, R. K., et al. (2006). The role of microtubule actin cross-linking factor 1 (MACF1) in the Wnt signaling pathway. *Genes Dev.* 20, 1933–1945. doi: 10.1101/gad.1411206

Copley, C. O., Duncan, J. S., Liu, C., Cheng, H., and Deans, M. R. (2013). Postnatal refinement of auditory hair cell planar polarity deficits occurs in the absence of Vangl2. *J. Neurosci.* 33, 14001–14016. doi: 10.1523/jneurosci.1307-13.2013

Ezan, J., and Montcouquiol, M. (2013). Revisiting planar cell polarity in the inner ear. *Semin. Cell Dev. Biol.* 24, 499–506. doi: 10.1016/j.semcdb.2013.03.012

Fassett, J. T., Xu, X., Kwak, D., Wang, H., Liu, X., Hu, X., et al. (2013). Microtubule actin cross-linking factor 1 regulates cardiomyocyte microtubule distribution and adaptation to hemodynamic overload. *PLoS One* 8:e73887. doi: 10.1371/journal.pone.0073887

Geng, R., Omar, A., Gopal, S. R., Chen, D. H., Stepanyan, R., Basch, M. L., et al. (2017). Modeling and preventing progressive hearing loss in usher syndrome III. *Sci. Rep.* 7:13480.

Gilels, F., Paquette, S. T., Beaulac, H. J., Bullen, A., White, P. M., et al. (2017). Severe hearing loss and outer hair cell death in homozygous Foxo3 knockout mice after moderate noise exposure. *Sci. Rep.* 7:1054.

Goodrich, L. V., and Strutt, D. (2011). Principles of planar polarity in animal development. *Development* 138, 1877–1892. doi: 10.1242/dev.054080

Goryunov, D., and Liem, R. K. (2016). Microtubule-Actin cross-linking factor 1: domains, interaction partners, and tissue-specific functions. *Methods Enzymol.* 569, 331–353. doi: 10.1016/bs.mie.2015.05.022

Hu, L., Su, P., Li, R., Yin, C., Zhang, Y., Shang, P., et al. (2016). Isoforms, structures, and functions of versatile spectraplakin MACF1. *BMB Rep.* 49, 37–44. doi: 10.5483/bmbrep.2016.49.1.185

Hudspeth, A. J. (2005). How the ear's works work: mechanoelectrical transduction and amplification by hair cells. *C R Biol.* 328, 155–162. doi: 10.1016/j.crvi.2004.12.003

Karakesisoglou, I., Yang, Y., and Fuchs, E. (2000). An epidermal plakin that integrates actin and microtubule networks at cellular junctions. *J. Cell Biol.* 149, 195–208.

Kodama, A., Karakesisoglou, I., Wong, E., Vaezi, A., and Fuchs, E. (2003). ACF7: an essential integrator of microtubule dynamics. *Cell* 115, 343–354.

Krey, J. F., Drummond, M., Foster, S., Porsov, E., Vijayakumar, S., Choi, D., et al. (2016). Annexin A5 is the most abundant membrane-associated protein in stereocilia but is dispensable for hair-bundle development and function. *Sci. Rep.* 6:27221.

Leonova, E. V., and Lomax, M. I. (2002). Expression of the mouse Macf2 gene during inner ear development. *Brain Res. Mol. Brain Res.* 105, 67–78. doi: 10.1016/s0169-328x(02)00394-7

Lu, X., and Sipe, C. W. (2016). Developmental regulation of planar cell polarity and hair-bundle morphogenesis in auditory hair cells: lessons from human and mouse genetics. *Wiley Interdiscip. Rev. Dev. Biol.* 5, 85–101. doi: 10.1002/wdev.202

Madisen, L., Zwingman, T. A., Sunkin, S. M., Oh, S. W., Zariwala, H. A., Gu, H., et al. (2010). A robust and high-throughput cre reporting and characterization system for the whole mouse brain. *Nat. Neurosci.* 13, 133–140. doi: 10.1038/nn.2467

May-Simera, H., and Kelley, M. W. (2012). Planar cell polarity in the inner ear. *Curr. Top. Dev. Biol.* 101, 111–140. doi: 10.1016/b978-0-12-394592-1.00006-5

May-Simera, H. L., Gumerson, J. D., Gao, C., Campos, M., Cologna, S. M., Beyer, T., et al. (2016). Loss of MACF1 abolishes ciliogenesis and disrupts apicobasal polarity establishment in the retina. *Cell Rep.* 17, 1399–1413. doi: 10.1016/j.celrep.2016.09.089

Monzack, E. L., May, L. A., Roy, S., Gale, J. E., and Cunningham, L. L. (2015). Live imaging the phagocytic activity of inner ear supporting cells in response to hair cell death. *Cell Death Differ.* 22, 1995–2005. doi: 10.1038/cdd.2015.48

Ohyama, T., and Groves, A. K. (2004). Generation of Pax2-Cre mice by modification of a Pax2 bacterial artificial chromosome. *Genesis* 38, 195–199. doi: 10.1002/gene.20017

Pacentine, I., Chatterjee, P., and Barr-Gillespie, P. G. (2020). Stereocilia rootlets: actin-based structures that are essential for structural stability of the hair bundle. *Int. J. Mol. Sci.* 21:324. doi: 10.3390/ijms21010324

Pataky, F., Pironkova, R., and Hudspeth, A. J. (2004). Radixin is a constituent of stereocilia in hair cells. *Proc. Natl. Acad. Sci. U S A.* 101, 2601–2606. doi: 10.1073/pnas.0308620100

Petit, C., and Richardson, G. P. (2009). Linking genes underlying deafness to hair-bundle development and function. *Nat. Neurosci.* 12, 703–710. doi: 10.1038/nn.2330

Pollock, L. M., and McDermott, B. M. Jr. (2015). The cuticular plate: a riddle, wrapped in a mystery, inside a hair cell. *Birth Defects Res. C Embryo Today* 105, 126–139. doi: 10.1002/bdrc.21098

Raphael, Y., and Altschuler, R. A. (1991). Scar formation after drug-induced cochlear insult. *Hear. Res.* 51, 173–183. doi: 10.1016/0378-5955(91)90034-7

Richardson, G. P., de Monvel, J. B., and Petit, C. (2011). How the genetics of deafness illuminates auditory physiology. *Annu. Rev. Physiol.* 73, 311–334. doi: 10.1146/annurev-physiol-012110-142228

Schurr, Y., Spindler, M., Kurz, H., and Bender, M. (2019). The cytoskeletal crosslinking protein MACF1 is dispensable for thrombus formation and hemostasis. *Sci. Rep.* 9:7726.

Schwenk, F., Baron, U., and Rajewsky, K. (1995). A cre-transgenic mouse strain for the ubiquitous deletion of loxP-flanked gene segments including deletion in germ cells. *Nucleic Acids Res.* 23, 5080–5081. doi: 10.1093/nar/23.24.5080

Suozzi, K. C., Wu, X., and Fuchs, E. (2012). Spectraplakins: master orchestrators of cytoskeletal dynamics. *J. Cell Biol.* 197, 465–475. doi: 10.1083/jcb.201112034

Truett, G. E., Heeger, P., Mynatt, R. L., Truett, A. A., Walker, J. A., Warman, M. L., et al. (2000). Preparation of PCR-quality mouse genomic DNA with hot sodium hydroxide and tris (HotSHOT). *Biotechniques* 29:52, 54.

Voelzmann, A., Liew, Y. T., Qu, Y., Hahn, I., Melero, C., Sánchez-Soriano, N., et al. (2017). Drosophila Short stop as a paradigm for the role and regulation of spectraplakins. *Semin. Cell Dev. Biol.* 69, 40–57. doi: 10.1016/j.semcdb.2017.05.019

Walsh, T., Shahin, H., Elkan-Miller, T., Lee, M. K., Thornton, A. M., Roeb, W., et al. (2010). Whole exome sequencing and homozygosity mapping identify mutation in the cell polarity protein GPSM2 as the cause of nonsyndromic hearing loss DFNB82. *Am. J. Hum. Genet.* 87, 90–94. doi: 10.1016/j.ajhg.2010.05.010

Wang, D., and Zhou, J. (2021). The kinocilia of cochlear hair cells: structures, functions, and diseases. *Front. Cell Dev. Biol.* 9:715037. doi: 10.3389/fcell.2021.715037

Wu, X., Kodama, A., and Fuchs, E. (2008). ACF7 regulates cytoskeletal-focal adhesion dynamics and migration and has ATPase activity. *Cell* 135, 137–148. doi: 10.1016/j.cell.2008.07.045

Zhang, J., Yue, J., and Wu, X. (2017). Spectraplakin family proteins - cytoskeletal crosslinkers with versatile roles. *J. Cell Sci.* 130, 2447–2457.

**Conflict of Interest:** The authors declare that the research was conducted in the absence of any commercial or financial relationships that could be construed as a potential conflict of interest.

**Publisher's Note:** All claims expressed in this article are solely those of the authors and do not necessarily represent those of their affiliated organizations, or those of the publisher, the editors and the reviewers. Any product that may be evaluated in this article, or claim that may be made by its manufacturer, is not guaranteed or endorsed by the publisher.

*Copyright © 2021 Gilbert, Zhu, Salameh, Sun, Alagramam and McDermott. This is an open-access article distributed under the terms of the Creative Commons Attribution License (CC BY). The use, distribution or reproduction in other forums is permitted, provided the original author(s) and the copyright owner(s) are credited and that the original publication in this journal is cited, in accordance with accepted academic practice. No use, distribution or reproduction is permitted which does not comply with these terms.*

# Advantages of publishing in Frontiers

**OPEN ACCESS**
Articles are free to read for greatest visibility and readership

**FAST PUBLICATION**
Around 90 days from submission to decision

**HIGH QUALITY PEER-REVIEW**
Rigorous, collaborative, and constructive peer-review

**TRANSPARENT PEER-REVIEW**
Editors and reviewers acknowledged by name on published articles

**Frontiers**
Avenue du Tribunal-Fédéral 34
1005 Lausanne | Switzerland

**Visit us:** www.frontiersin.org
**Contact us:** frontiersin.org/about/contact

**REPRODUCIBILITY OF RESEARCH**
Support open data and methods to enhance research reproducibility

**DIGITAL PUBLISHING**
Articles designed for optimal readership across devices

**FOLLOW US**
@frontiersin

**IMPACT METRICS**
Advanced article metrics track visibility across digital media

**EXTENSIVE PROMOTION**
Marketing and promotion of impactful research

**LOOP RESEARCH NETWORK**
Our network increases your article's readership